BEHAVIOUR AND ANALYSIS OF REINFORCED CONCRETE WALLS SUBJECTED TO REVERSED CYCLIC LOADING

D. Palermo

F. J. Vecchio

May 2002

ABSTRACT

Details of two large-scale wide-flanged structural walls, tested under cyclic displacements, are presented. Results indicate that axial loads, although relatively small, and adjoining flange walls had a significant effect on the strength, ductility, and failure mode of the test specimens. The behaviour of the walls was dominated by shear related mechanisms, and as a consequence, the web elements sustained heavy damage.

Secondary effects are examined and discussed, and include the in-plane horizontal expansion of the web wall and the elongation of the flange walls, which affect the failure load and failure mechanisms of structural walls. Such data is useful in understanding behaviour and corroborating analyses.

The series of wall tests conducted will complement the literature with data on structural walls in which the response is dominated by shear mechanisms, and with data involving complex wall configurations in which three-dimensional effects may be influential. Currently, the literature is lacking in these areas.

Formulations are presented for concrete subjected to cyclic loading in the compression and tension regimes. The proposed models were implemented into a two-dimensional nonlinear finite element program, applicable to reinforced concrete membrane structures. The algorithm is based on a secant stiffness formulation employing the smeared rotating crack concept. This analytical work is one of the first to implement formulations for cyclic load analysis based on the rotating crack model. Enhancements in the modeling include nonlinear unloading, degradation in the reloading

stiffness based on the amount of strain recovered during unloading, improved plastic offset formulations, and partial unloading/reloading rules.

Analyses of structural walls currently available in the literature, and those tested as part of this research, demonstrate that the proposed concrete cyclic models provide reasonably accurate simulations of behaviour, indicating that the Modified Compression Field Theory formulations can be adapted for general load history analysis using a secant stiffness formulation. Further analyses of reinforced concrete shear panels have identified areas of the concrete modeling requiring improvements.

ACKNOWLEDGEMENTS

The author expresses his sincerest thanks and appreciation to Professor Frank J. Vecchio for his continued guidance, patience, and encouragement throughout this research project.

Thanks are also extended to the staff of the Structures Laboratory at the University of Toronto. They include Mehmet Citak, for his help in designing the formwork and testing apparatus for the test specimens; Peter Heliopoulos and John McDonald, for installing the instrumentation and data acquisition system used during testing; John Buzzeo and Alan McClenaghan, for fabricating the testing apparatus; Joel Babbin, for his help in building the test specimens and constant encouragement; and Renzo Basset, for managing the duties of the laboratory staff.

This work would not have been possible without the help from the numerous graduate and undergraduate students. To all of them, thank you. A further thanks is extended to Professor E. Bentz, for the use of TRIXpost, which immensely simplified the modeling process.

Most important has been the support of family; Giuseppe and Dorina Palermo; and Sofia, Mike, and Alessia Ianni-Palarchio. I would also like to extend my warmest gratitude to my dear friends, Helen Asfis and Gianni Gagliardi. Their continual support and constant encouragement has allowed me to fulfill my academic ambitions.

The financial support of the Natural Sciences and Engineering Research Council, University of Toronto, and Professor Frank J. Vecchio is gratefully acknowledged.

TABLE OF CONTENTS

LIST OF FIGURES

CHAPTER 1 - INTRODUCTION

CHAPTER 2 – LITERATURE REVIEW

CHAPTER 3 – FINITE ELEMENT FORMULATIONS

CHAPTER 4 – EXPERIMENTAL PROGRAM

CHAPTER 5 – EXPERIMENTAL RESULTS

CHAPTER 8 – APPLICATION TO SHEAR PANELS & SHEAR WALLS

LIST OF TABLES

NOTATION

a , $a_{\max}$	=	maximum aggregate size in concrete mix design
C_t	=	tension stiffening parameter for concrete
c	=	loading rate parameter for concrete in compression
c_p	=	plastic strain coefficient for concrete in compression
c_r	=	reloading coefficient for concrete in compression
c_u	=	unloading parameter for concrete in compression
E_C , E_O	=	initial modulus of concrete
$\overline{E}_c$	=	secant stiffness modulus of concrete
E_{close}	=	crack-closing stiffness modulus of concrete in tension
E_{cm}	=	unloading stiffness modulus of concrete in compression
E_{c4}	=	reloading stiffness modulus of concrete in tension
E_{c5}	=	initial unloading stiffness modulus of concrete in tension
E_{c6}	=	unloading stiffness modulus at zero stress for concrete in tension
E_m	=	tangent stiffness of reinforcement at previous maximum strain
E_p	=	equivalent plastic strain for concrete in compression
E_r	=	unloading modulus of reinforcement
E_{re}	=	envelope return point tangent modulus of concrete in compression
E_s	=	initial modulus of reinforcement
$\overline{E}_s$	=	secant stiffness modulus of reinforcement
$E_{\sec}$	=	secant modulus at peak compressive stress
E_{sh}	=	strain hardening modulus of reinforcement
E_u , E_{c2}	=	initial unloading stiffness of concrete in compression
E_{u1}	=	secant and initial tangent moduli of concrete in tension
E_{u2}	=	secant and initial tangent moduli of concrete in compression
E_1 , E_{c3}	=	compressive unloading stiffness at zero stress in concrete
E_2 , E_r , E_{c1}	=	compressive reloading stiffness of concrete
F_C	=	normalized compressive stress at the common point of concrete
F_E	=	normalized compressive stress of concrete
f_{bc}	=	concrete stress calculated from base curve in compression
f_{bt}	=	concrete stress calculated from base curve in tension

f_c	=	normal stress of concrete
f'_c, σ_c, f'_{co}	=	peak compressive strength of concrete cylinder
f'_{cc}	=	compressive stress of confined concrete
f_{ci}	=	compressive stress on the crack surface
f_{close}	=	crack-closing stress for concrete in tension
f_{cm}	=	concrete stress corresponding to maximum compressive strain
f_{cx}	=	average stress in the concrete in the x-direction
f_{cy}	=	average stress in the concrete in the y-direction
f_m	=	stress in reinforcement corresponding to previous maximum strain
$f_{\max}$	=	maximum compressive stress of concrete for current unloading cycle
f_{new}	=	compressive reloading stress at envelope unloading strain in concrete
f_r, f_{un}, $\hat{\sigma}_{c2}$, f_{2c}	=	unloading stress on the envelope curve for concrete in compression
f_{re}	=	compressive stress at envelope return point of concrete
f_{ro}	=	compressive stress at the onset of reloading in concrete
f_{scri}	=	local stress in reinforcement at crack location
f_{si}	=	average stress for i-th reinforcement component
f_{stab}	=	stress on the stability limit for concrete in compression
f_{sx}	=	average stress in the reinforcement in the x-direction
f_{sy}	=	average stress in the reinforcement in the y-direction; yield stress of reinforcement
f_{su}	=	ultimate stress of reinforcement
f_{s-1}	=	stress in reinforcement from previous load step
f'_t, σ_t, f_t, f_{cr}	=	cracking stress of concrete in tension
f_{tm}	=	concrete stress corresponding to maximum tensile strain
ft_{stab}	=	stress on the stability limit for concrete in tension
f_{yi}, f_{syi}	=	yield stress for i-th reinforcement component
f_{yx}	=	yield stress of reinforcement in the x-direction
f_{yy}	=	yield stress of reinforcement in the y-direction
F_{calc}	=	predicted lateral load from finite element analysis
$F_{\exp}$	=	measured lateral load
K_o	=	fracture parameter of concrete in compression
n	=	shape factor
n_p, n_u, n_r	=	power term

S	=	compressive strain ratio on the unloading branch in concrete; equivalent compressive stress of concrete
S_E	=	normalized compressive strain of concrete
S_C	=	normalized compressive strain at the common point of concrete
S_{erpu}	=	envelope reloading strain ratio for concrete in compression
S_{eu}	=	compressive unloading strain ratio on the envelope curve in concrete
S_P, ε_{can}	=	normalized plastic strain for concrete in compression
S_{ppu}	=	partial compressive unloading strain ratio of concrete
S_{pu}, S_p	=	plastic strain ratio for concrete in compression
$tf_{\max}$	=	maximum tensile stress of concrete for current unloading cycle
tf_{ro}	=	tensile stress of concrete at the onset of reloading
t_{ro}	=	tensile strain of concrete at the onset of reloading
U_{erpu}	=	envelope reloading stress ratio for concrete in compression
U_{eu}	=	compressive envelope unloading stress of concrete
$U_{\max}$	=	normalized peak compressive cylinder stress of concrete
U_{ppu}	=	partial compressive unloading stress ratio where reloading commences in concrete
U_{pu}	=	partial compressive unloading stress ratio of concrete
U_{relo}	=	compressive stress ratio on the reloading curve in concrete
U_{unlo}	=	compressive stress ratio on the unloading curve in concrete
ν_{ci}	=	shear stress along crack surface
$\nu_{ci\max}$	=	maximum shear stress possible on a crack surface
ν_{cxy}	=	average shear stress of concrete relative to the x, y-axes
ν_{xy}	=	shear stress on element relative to the x, y-axes
w	=	crack width
α	=	orientation of reinforcement
β	=	compression softening parameter for concrete
β_d	=	damage indicator for concrete in compression
β_t	=	damage indicator for concrete in tension
Δ	=	strain increment of concrete
Δ_{calc}	=	predicted displacement from finite element analysis
$\Delta_{\exp}$	=	measured displacement
ε_a	=	common strain for concrete in compression
ε_c, ε	=	compressive strain of concrete
ε_{cc}, ε_p	=	strain corresponding to maximum concrete compressive stress
ε_{cen}	=	difference between unloading and plastic normalized strains

ε_{cf}	=	tensile strain due to stress in concrete
ε_{ci}^{e}	=	elastic component of concrete strain in i-direction
ε_{ci}^{p}	=	plastic component of concrete strain in i-direction
ε_{cmi}	=	maximum compressive strain in i-direction for concrete
ε_{cr}	=	cracking strain for concrete in tension
ε_{cx}	=	average strain of concrete in x-direction
ε_{cy}	=	average strain of concrete in y-direction
ε_{c2}	=	principal compressive strain of concrete
ε_{c1}	=	principal tensile strain of concrete, compressive strain in the transverse direction in concrete
ε_{e}	=	equivalent strain of concrete
ε_{i}	=	current stress of reinforcement
ε_{m}	=	maximum strain of reinforcement from previous cycles
$\varepsilon_{\max}$	=	maximum strain for current cycle
$\varepsilon_{\min}$	=	minimum strain for current cycle
ε_{o} , ε_{co} , $\varepsilon_{c}^{'}$	=	strain at peak compressive stress in concrete cylinder
ε_{r} , ε_{1} , ε_{pl} , ε_{c}^{p}	=	residual (plastic) strain of concrete
ε_{re}	=	compressive strain at envelope return point of concrete
ε_{rec}	=	strain recovered during unloading in concrete
ε_{rn} , ε_{un} , $\hat{\varepsilon}_{c2}$, ε_{2c}	=	compressive unloading strain on the envelope curve of concrete
ε_{ro}	=	compressive strain at the onset of reloading in concrete
ε_{sh}	=	strain of reinforcement at which strain hardening begins
ε_{si}^{p}	=	plastic component of strain in reinforcement
ε_{si}^{e}	=	elastic component of strain in reinforcement
ε_{sx}	=	average strain of reinforcement in x-direction
ε_{sy}	=	average strain of reinforcement in y-direction; yield strain
ε_{s-1}	=	strain of reinforcement from previous load step
ε_{t}	=	tensile strain of concrete
ε_{tm}	=	maximum tensile strain of concrete
$\varepsilon_{t\max}$, $\hat{\varepsilon}_{c1}$, ε_{1c}	=	unloading strain on the envelope curve for concrete in tension
ε_{u}	=	strain at peak cylinder stress of concrete; strain at unloading in concrete; ultimate strain of reinforcement
ε_{x}	=	strain in the element in the x-direction
ε_{y}	=	strain in the element in the y-direction
ε_{y} , ε_{sy}	=	yield strain of reinforcement

ε_1	=	average principal tensile strain of element
ε_2	=	average principal compressive strain of element
ε_{1cm}	=	maximum compressive strain in the transverse direction in concrete
ε_{2tm}	=	maximum tensile strain in the transverse direction in concrete
γ_{cmxy}	=	shear strain associated with maximum compressive strains in concrete
γ_{cxy}^{p}	=	plastic shear strain of concrete relative to x, y-axes
γ_{xy}	=	shear strain relative to the x, y-axes
ρ_h	=	reinforcement ratio in the horizontal direction
ρ_i	=	reinforcement ratio for i-th reinforcement component
ρ_v	=	reinforcement ratio in the vertical direction
ρ_x	=	reinforcement ratio in the x-direction
ρ_y	=	reinforcement ratio in the y-direction
σ, σ_{c2}, f_{c2}	=	principal compressive stress of concrete
σ_{c1}, f_{c1}	=	principal tensile stress of concrete
σ_p, f_p	=	peak principal compressive stress of concrete
σ_t	=	tensile stress of concrete
$\sigma_{t\max}$, $\hat{\sigma}_{c1}$, f_{1c}	=	unloading stress from the envelope curve for concrete in tension
σ_x	=	stress applied to element in the x-direction
σ_y	=	stress applied to element in the y-direction
θ	=	inclination of principal strains in concrete
θ_c	=	inclination of principal stresses in concrete
θ_{ni}	=	angle of orientation between reinforcement and crack surface

CHAPTER 1

Introduction

1.1 BACKGROUND

In the analysis of reinforced concrete structures subjected to general loading conditions, realistic constitutive models and analytical procedures are required to produce reasonably accurate simulations of behaviour. Models that provide accurate simulations under reversed cyclic loading are less common than models applicable to monotonic loading. The smeared crack approach tends to be the most favoured in the context of fixed cracks. In fixed crack formulations, separate models are required to model the normal stress and shear stress hysteretic behaviour. This, however, is at odds with test observations. When equal amounts of reinforcement are provided in the longitudinal and transverse directions, cracks experience minimal rotation, and a fixed crack procedure will provide an accurate simulation. However, under the more general case of varying amounts of reinforcement, which is common in practice, the fixed crack assumption may not realistically represent behaviour. The approach used herein for reversed cyclic loading is based on a smeared rotating crack approach, which more accurately models the response of cracked reinforced concrete under general loading conditions.

In addition to utilizing a realistic procedure, the constitutive models for cyclic loading of concrete should capture the actual behaviour. The shape of the unloading and reloading curves of concrete should accurately predict the energy dissipation of the structure and the damage of the material due to load cycling. Partial unloading/reloading

rules must be considered, as structural components may partially unload and then partially reload during a seismic event. The models should not be limited to the compressive behaviour alone and should include the tensile behaviour. The latter also plays a key role in the overall behaviour of reinforced concrete structures.

In the design of buildings, reinforced concrete shear walls act as major earthquake resisting members. These structural walls provide an efficient bracing system and offer great potential for lateral load resistance. The properties of these seismic shear walls dominate the seismic response of the buildings and, therefore, it is important to evaluate the response of the walls appropriately. The evaluation is important in assessing the seismic performance. The use of realistic concrete models will, therefore, improve the evaluation of the lateral load resisting components.

1.2 ANALYSIS OF STRUCTURES

The design of reinforced concrete structures is routinely based on linear elastic analyses. These structures normally meet or exceed strength and serviceability requirements of present codes. However, such structures may not be representative of the most efficient or economical design. This is true for the design and analysis of seismic shear walls. Cracking of concrete, deformation under service loads, safety and function under seismic loading, ultimate capacity, or collapse mechanisms are some of the associated concerns. In such situations, more accurate nonlinear analysis methods can be employed. To assess the seismic nature of reinforced concrete shear walls commonly found in nuclear reactor buildings, for example, nonlinear response analytical methods and ultimate strength methods have to be developed to a sufficient level of confidence.

Over the past 20 years, research at the University of Toronto has been directed toward improving analysis procedures. The philosophy has been to concentrate on the formulation of simple, but realistic, material behaviour models for reinforced concrete. The same philosophy has been extended to the formulation of unloading/reloading rules for concrete.

Programs VecTor2 and VecTor3, developed at the University of Toronto[1, 2], have the capability of simulating the cyclic response of reinforced concrete structures. The constitutive models for concrete in compression and tension reported by Vecchio[3] were provisional. More realistic unloading and reloading curves for concrete in compression and tension were implemented into VecTor2 as part of this research work. These nonlinear finite element programs are based on a secant stiffness formulation using a total-load iterative procedure, and employ the smeared rotating crack approach. The programs employ the compatibility, equilibrium, and constitutive formulations of the Modified Compression Field Theory[4] (MCFT). VecTor2 is applicable to concrete membrane structures. It employs a 4-noded (8 degree of freedom) constant strain element, which assumes a linear displacement field across the boundary of the element. A 3-noded, constant strain, triangular element is also available. VecTor3 is utilized for concrete solids and is essentially the 3-D equivalent to VecTor2. An 8-noded (24 degree of freedom) brick element that assumes linear displacement fields is typically used. A 6-noded wedge element is also available. Reinforcement is typically modeled as smeared throughout the element, but can also be represented discretely by truss bar elements. More detail of the analytical procedures employed for arbitrary loading conditions will be discussed later.

1.3 MODIFIED COMPRESSION FIELD THEORY

Research efforts at the University of Toronto led to the formulation of the MCFT for concrete in shear[4]. The constitutive laws in the theory are a result of over 200 reinforced concrete panels tested in pure shear or in combination of shear and axial loads. From these tests, stress-strain relationships for cracked concrete under plane stress conditions were derived. The MCFT is a fully rotating, smeared crack model that represents cracked concrete as an orthotropic material with its own stress-strain characteristics. Equilibrium, compatibility, and constitutive relationships are formulated in terms of average stresses and average strains. Directions of average principal stress and directions of average principal strains in the concrete are assumed to coincide, and consideration to local stress conditions at crack locations is also given.

In the MCFT formulations, cracked concrete was treated as distinctly different from plain uncracked concrete. A compression softening relationship accounted for the reduced compressive strength and stiffness of cracked concrete, when subjected to high tensile strains in the direction normal to the compression, relative to uncracked uniaxially compressed concrete. Consideration was also given to tension stiffening to represent the post-cracking average tensile stresses that exist in the concrete between cracks.

Although the accuracy and reliability of the MCFT in its original form have been generally good, some deficiencies have been revealed with respect to panel elements[5]. The two main weaknesses in the computational model responsible, in large part, for the inaccuracies include: the enforced alignment of principal stress and strain directions, and the handling of crack shear stresses. These deficiencies were addressed by the Disturbed Stress Field Model[5] and include slip deformations at crack locations caused by shear

stresses not necessarily zero at the crack surface. Slip deformations result in a deviation between the average principal stresses and the apparent concrete average principal strains. The latter is handled by allowing the principal stress direction to diverge from the apparent principal strain direction. The formulations of the MFCT will be presented in Chapter 3.

Various nonlinear finite element procedures have been developed incorporating the MCFT[6].

1.4 NUPEC STUDY

To assess the seismic safety factor of nuclear reactor buildings, the Nuclear Power Engineering Corporation of Japan (NUPEC) recently conducted a comprehensive experimental investigation. Two large-scale flanged shear walls, U-1 and U-2, were subjected to dynamic loading using a high-performance shaking table. The results of the tests were made available to participants of the Seismic Shear Wall International Standard Problem (SSWISP) Workshop[7] for the following purposes:

1. To clarify the behaviour of seismic shear walls up to ultimate state.
2. To improve the reliability of nonlinear seismic response analysis and ultimate strength evaluation codes.
3. To provide information for quantifying code uncertainties and to highlight areas of the code needing improvement in the future.
4. To suggest necessary experiments to reduce the technical ambiguities of seismic shear walls at the ultimate state.

The test specimens were constructed to represent the box-type wall of a nuclear reactor building. The design process consisted of three prototypes leading to a final H-shaped wall configuration. The initial prototype consisted of a hollow box-shaped wall section. The walls were 3000 mm in length and 75 mm thick. The second prototype was based on a half model of the original box section, resulting in a channel wall section. The flange walls were 1500 mm in length. The third prototype consisted of a transformation of the previous channel section to an equivalent I section, with the reinforcement ratio for both the vertical and horizontal reinforcement at approximately 1.2%. The tested specimens were altered from the final prototype design. The thickness of the flanges were changed from 75 mm to 100 mm, and the flange lengths were increased to 3000 mm to increase the natural frequency in the direction perpendicular to the vibration of the test. To keep the same flexural strength as the prototype, the vertical reinforcement ratio in the flanges was reduced. On the other hand, the horizontal reinforcement was assumed not to directly effect the strength of the specimen, so the same spacing as the web wall was applied. The prototypes considered in the design process are shown in Figure 1.1.

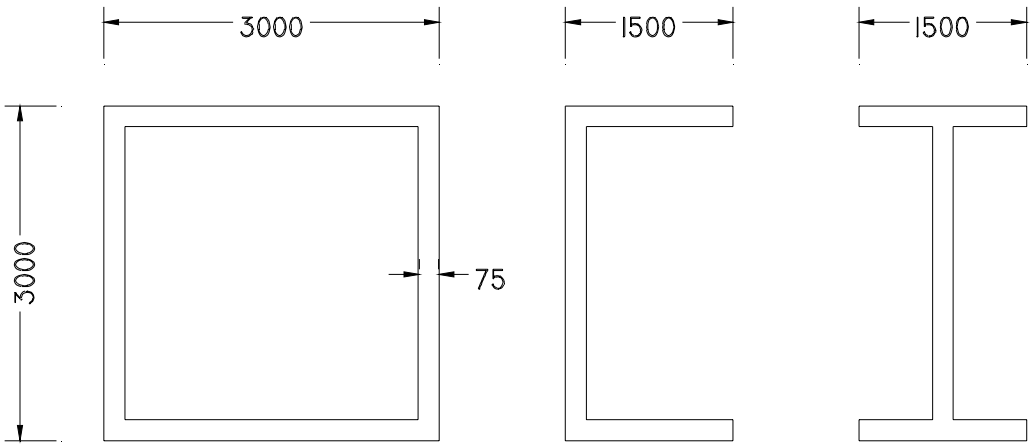

Figure 1.1 NUPEC Prototypes

The base slab of the tested specimens had dimensions of 5000 x 5000 x 1000 mm, and served to simulate a rigid foundation. The top slab, through which the loading was applied, was 4000 x 4000 x 760 mm. The walls consisted of an H cross section, with flange walls 2980 mm in length, 2020 mm in height, and 100 mm in thickness. The web wall, which connected the two flanges, was 2900 mm long, 2020 mm high, and 75 mm thick. Figure 1.2 is a top view of specimen U-1, and Figures 1.3 and 1.4 are sides of the web and flange walls, respectively.

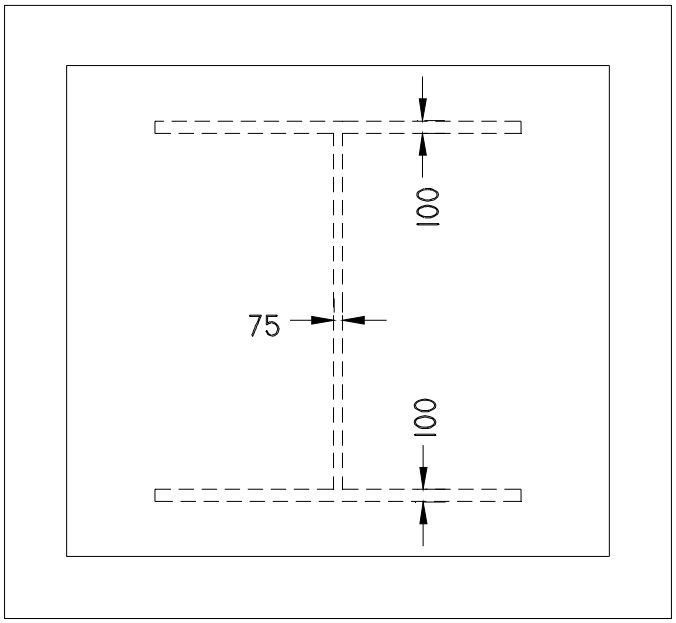

Figure 1.2 Top View of NUPEC Specimen

The base slab was reinforced with D29 deformed reinforcing bars (29 mm diameter) at a typical spacing of 210 mm in an orthogonal gird. The reinforcement consisted of a top and bottom layer. The top slab contained an orthogonal grid with D25 deformed bars at a spacing of 210 mm. Similar to the base slab, there was a top and bottom layer. The walls were reinforced with D6 deformed reinforcing bars. The web section contained an

inside and outside face of reinforcement spaced at 70 mm horizontally and vertically. The flanges also contained an inner and outer layer of reinforcement. The horizontal spacing was constant at 70 mm, and vertically the bars were spaced at 70 mm near the web wall and 175 mm near the flange tips. Figure 1.5 is a top view of the reinforcement layout of the web and flange walls.

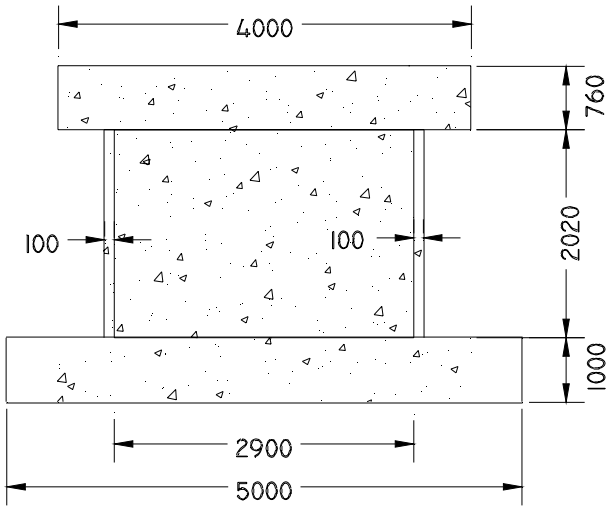

Figure 1.3 Side View of U-1 Web Wall

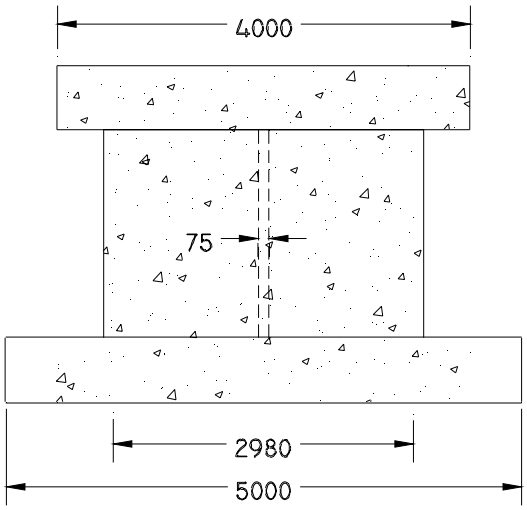

Figure 1.4 Side View of U-1 Flange Wall

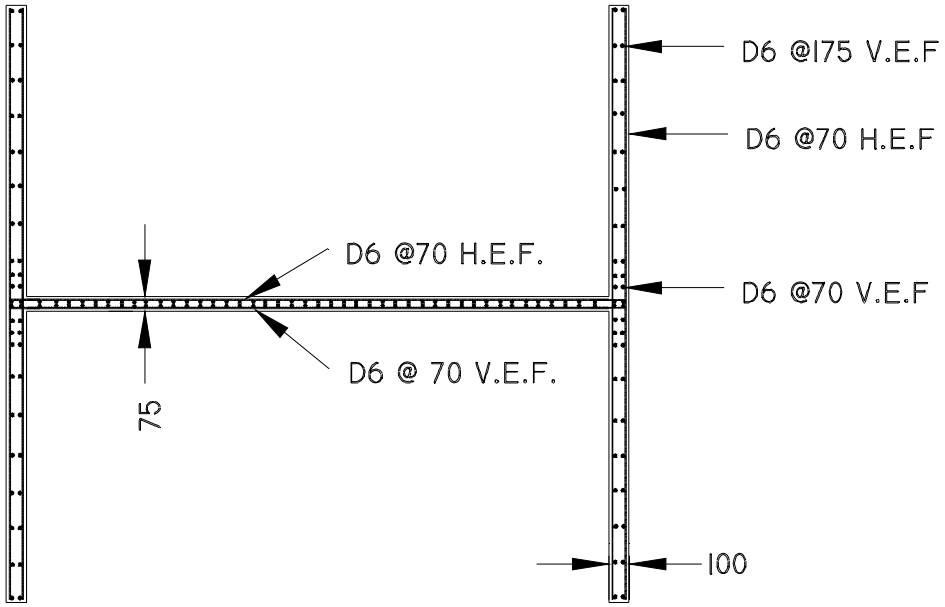

Figure 1.5 Top View of NUPEC Reinforcement

In 1994, NUPEC sponsored an international competition, with the primary objective of determining the reliability of techniques for the nonlinear response analysis and ultimate strength evaluation of seismic shear walls. Analytical results from 24 participating organizations worldwide were submitted to NUPEC. The calculations were based on finite element method (FEM) static monotonic and static cyclic analyses, FEM dynamic analyses, simplified static and dynamic analyses, and lumped-mass dynamic analyses. Figures 1.6 and 1.7 show the analytical results of the calculated maximum load and the calculated displacement at maximum load for the FEM static analyses, respectively. It is evident from the competition results that the ability to calculate the peak strength of shear walls under seismic excitations is not well established. More importantly, however, is the apparent inability to accurately calculate structure ductility.

The results indicate that the methods and models used were able to calculate the maximum load more accurately than the displacement at maximum load. The maximum load reported by NUPEC was 1636 kN and the corresponding displacement was 10.96 mm. The analytical maximum load results varied from 65 to 115% of the experimental value, with the majority of the participants underestimating the peak strength. The variation was, however, smaller than that of the displacement at the maximum load. The range for the calculated displacement varied from 35 to 180% of the experimental value for those participants that submitted results. The majority of calculations underestimated the ductility of the shear walls.

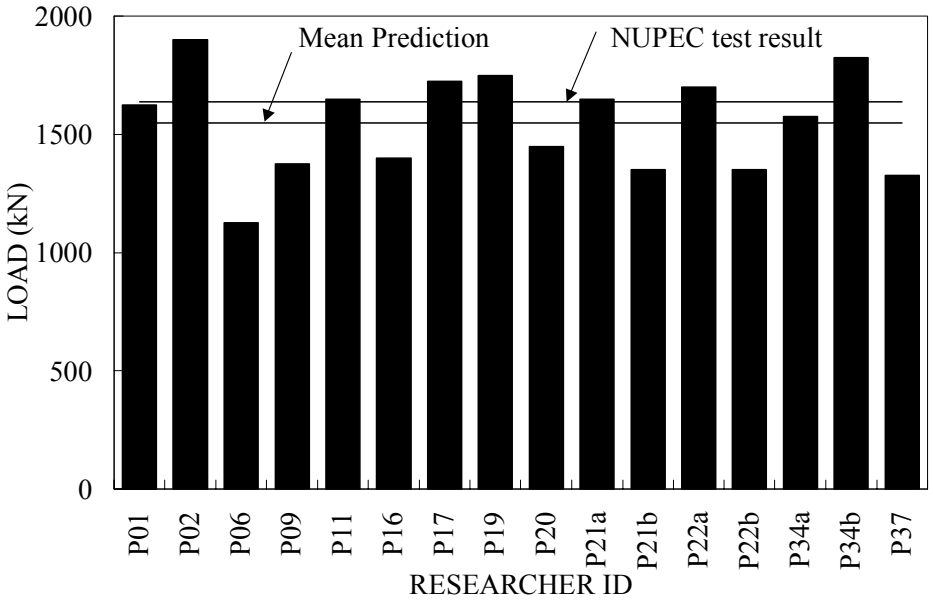

Figure 1.6 Maximum Calculated Load

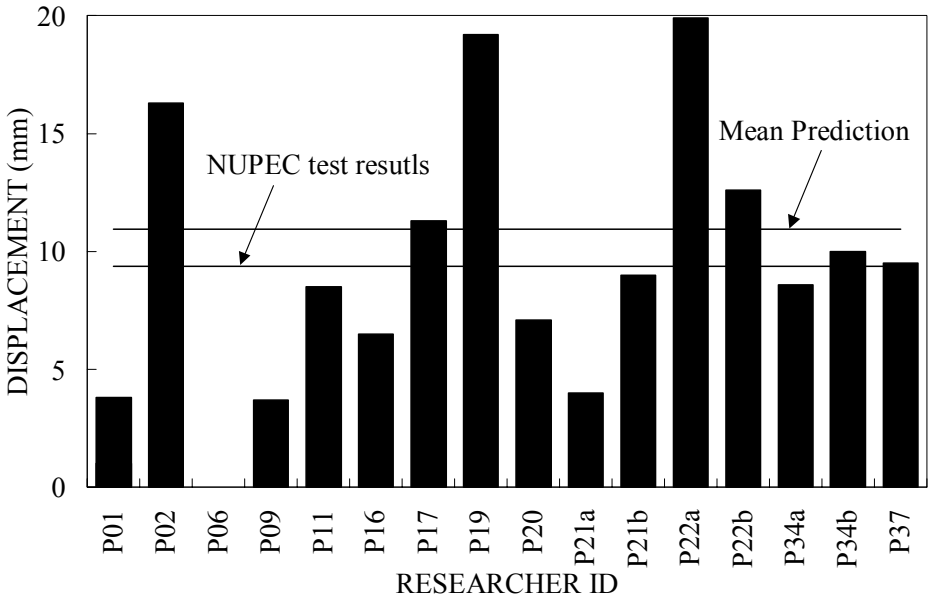

Figure 1.7 Displacement Calculated at Maximum Load

These apparent difficulties with accurately modeling strength and ductility of reinforced concrete shear walls led to the experimental portion of this research project, in which large-scale flanged structural walls were tested under conditions of cyclic loading.

The analytical work consisted of formulating improved models for concrete subjected to cyclic loads.

1.5 OVERVIEW OF EXPERIMENTAL PROGRAM

An experimental program was conducted on two large-scale flanged reinforced concrete structural walls patterned after the NUPEC specimens. Two specimens, DP1 and DP2, were tested. The original test specimens were also repaired (DP1R and OHSW1, respectively) and tested to failure. Testing of specimen DP1[8] and DP1R[9] consisted of imposed lateral cyclic displacements under a constant applied axial load. The second series of tests differed in terms of loading. DP2 was subjected to lateral cyclic displacements without externally applied axial load, and OHSW1[10] consisted of lateral monotonic displacements under an applied axial load.

The specimens were constructed with stiff top and bottom slabs. The top slab (4415 x 4000 x 640 mm) served to distribute the horizontal and axial loads to the walls of the structure. The bottom slab (4415 x 4000 x 620 mm), clamped to the laboratory strong floor, simulated a rigid foundation. The slabs were reinforced with No. 30 deformed reinforcing bars at a spacing of 350 mm in each direction, with a top and bottom layer. The web wall, 2885 mm in length, 2020 mm in height, and 75 mm in thickness, was reinforced with D6 reinforcing bars. The bars were spaced 140 mm horizontally and 130 mm vertically in two parallel layers. The two flange walls were approximately 3050 mm long, 2020 mm high, and 95 mm thick for DP1 and 100 mm thick for DP2. The flanges were also reinforced with D6 reinforcing bars, spaced 140 mm horizontally, and vertically the bars were spaced at 130 mm near the web wall and 355 mm near the tips of

the flanges. The concrete clear covers in the walls and slabs were 15 mm and 50 mm, respectively.

The two walls had nominally identical dimensions and reinforcement, and were similar to the NUPEC specimens. The concrete used in DP1 and DP2 was supplied by a local ready mix plant and was of comparable strength, but the concrete in DP1R was significantly higher in strength, as a result of being batched in-house. Specimen OHSW1 also had a higher concrete strength, even though it was cast with the same mix as DP1 and DP2.

Further details pertaining to the geometry, material properties, and loading application will be discussed later. The focus herein is on DP1 and DP2; details pertaining to DP1R and OHSW1 can be found elsewhere[9, 10].

1.6 OVERVIEW OF ANALYTICAL PROGRAM

The apparent inability to accurately estimate the strength and ductility of shear walls indicates that increased work and attention should be directed towards improving cyclic and ductility models for concrete in compression and tension.

The focus of the analytical work was to develop improved rules for unloading and reloading for concrete. The formulations, presented later, were implemented into a nonlinear finite element program assuming smeared rotating cracks and based on a secant stiffness approach. Plastic offset strains, arising from the unloading process, for concrete and reinforcement are incorporated into the analysis through use of the prestrain approach[3]. The models, discussed in more detail later, include a nonlinear unloading branch from the backbone curve in compression and tension. The backbone curves are

represented by the monotonic response curves and account for compression softening and confinement for the compression regime. In tension, the backbone curve includes tension stiffening. Reloading follows a linear path to the backbone curve, and damage due to cycling is accounted for by degradation to the reloading stiffness. Essentially, the reloading path does not return to the backbone curve at the previous unloading strain, but at a larger strain. Offset strain models in compression and tension, and stiffness values describing the shape of unloading and reloading are defined. The modeling also includes partial unloading and partial reloading formulations. The modeling is based on previous stress and strain history, and strain parameters. The models have been corroborated against the DP test walls, Portland Cement Association (PCA) walls, and walls tested at Imperial College, denoted as SW. These analyses are discussed further in subsequent chapters.

1.7 RESEARCH OBJECTIVES

This research project is aimed at improving the hysteretic modeling of reinforced concrete structures and to formulating the necessary models in a manner compatible with the Modified Compression Field Theory. The models are to be formulated in the context of smeared rotating cracks; for both compression and tension stress regimes. Relative to the more traditional fixed crack formulations; the alternative approach used herein is intended to reproduce behaviour where progressive reorientation of cracks has been observed. This includes situations such as beams, where the transverse direction is typically lightly reinforced and yielding of the reinforcement occurs. The models can also be effectively used to simulate the response of structural elements where the crack

direction remains relatively fixed, including the shear walls tested as part of this research project. Therefore, relative to a fixed crack approach, the assumption of rotating cracks will provide insignificant improvement in simulating the response of some shear walls subjected to reversed loading conditions. However, marked improvements will be evident in the more general case where reinforcement tends to vary in the longitudinal and transverse direction.

Specific objectives of this research are to:

1. Determine realistic shapes for unloading and reloading curves for concrete. These can be modeled as nonlinear or linear. A Ramberg-Osgood formulation will be used to describe the unloading branch, as tests have indicated that unloading is nonlinear. Reloading can be accurately simulated with a simple linear formulation.
2. Propose partial unloading/reloading response curves for concrete. Unloading will be described by a Ramberg-Osgood formulation, and a simple linear formulation will define the reloading portion.
3. Define plastic offset strains. The offset strains define the path of the unloading curve, and will be used as a parameter to determine the degree of damage experienced by the concrete due to load cycling.
4. Define values of moduli of elasticity for unloading and reloading. The reloading branches require two stiffness parameters: one to capture the damage imposed on the concrete due to load cycling, and the other to establish the path of the concrete during partial reloading. Two additional stiffness values are required to fully model the unloading curve: one describes the

initial unloading stiffness and the second indicates the stiffness at the end of the unloading process.

5. Propose models for the damage experienced in the concrete in compression and tension due to cycling. In turn, the damage parameters will determine the stiffness of the reloading curves.
6. Account for reduced stiffness on subsequent cycles.
7. Incorporate the formulations into a nonlinear finite element program based on a secant stiffness algorithm, employing the smeared rotating crack procedure. A criticism of the secant stiffness approach has been that it cannot be effectively used to model response to cyclic loading.
8. Verify the hysteretic models using the secant stiffness algorithm at the material level against cylinder tests currently available in the literature.
9. Demonstrate the applicability of the models to reinforced concrete panels tested at the University of Toronto, and structural walls tested as part of this research project and those tested by other researchers.
10. Complement the literature with tests on structural walls in which the response is dominated by shear mechanisms. Researchers have tended to use flexure-dominant walls to corroborate constitutive models. These walls, however, may not be a proper test for concrete cyclic models.
11. Complement the literature with tests involving more complex configurations, in which three-dimensional effects may be influential.

Beyond the hysteresis models, the experimental data collected will be useful in investigating such effects as: the ratcheting effect of the reinforcement; the influence of

bond slip, which has the effect of diminishing the development of post-cracking tensile stresses in the concrete; and the influence of crack shear-slip, which is used to determine the divergence in rotation between the principal stress and principal strain directions. These, however, are beyond the scope of this research project.

1.8 REPORT LAYOUT

The chapters to follow contain an extensive and critical review of cyclic models currently available in the literature (Chapter 2), a review of the finite element formulations utilized by in-house programs VecTor2 and VecTor3 (Chapter 3), a description of the experimental program executed as part of this research project (Chapter 4), and a summary of the qualitative and quantitative results of the experimental program (Chapter 5). The focus of Chapter 6 is a discussion of phenomenological wall behaviours; the analytical modeling is covered in Chapter 7; and Chapter 8 contains finite element analyses highlighting the advancements of the proposed models. Finally, conclusions and recommendations for future research are found in Chapter 9. Other pertinent information is listed in the Appendices at the end of the report.

CHAPTER 2

Literature Review

2.1 CYCLIC MODELS

2.1.1 Background

In the analysis of reinforced concrete structures, a number of diverse approaches have been used for material modeling. These include plasticity-based procedures, fracture mechanics, and various nonlinear elastic models. In the last case, approaches range from discrete to smeared crack models, and from fixed to rotating crack models. Researchers working in each of these areas generally have been successful in producing models that yield results of acceptable accuracy for conditions of monotonic loading.

Models that provide accurate simulations of behaviour under general loading conditions, and specifically under reversed cyclic loading, are less common. The smeared crack approach tends to be the procedure most commonly employed. Many researchers have documented models assuming fixed crack directions, and have demonstrated reasonable correlation to experimental results. Less common are procedures incorporating the rotating crack assumption, which is more realistic of observed structural behaviour.

2.1.2 Pioneering Work

Sinha, Gerstle, and Tulin[11] were the first researchers to describe qualitatively and quantitatively the stress-strain response of concrete under cyclic loading. At the time of

their work, there was a complete lack of information on the behaviour of concrete subjected to cyclic loading.

Qualitatively their work was instrumental in providing the following contributions:

1. Concrete produces unloading and reloading curves with pronounced hysteresis. Straight-line representation for both unloading and reloading neglects the hysteresis effects.
2. There exists an envelope curve that the stress-strain paths under cyclic loading do not exceed. It may be considered unique and identical with the stress-strain response obtained under monotonic loading.
3. Unloading can be represented by a quadratic equation, and reloading with a straight line.
4. The point at which the reloading curve crosses the unloading curve forms a shakedown limit. Stresses above this limit lead to additional strains, while maximum stresses at or below this limit do not. Essentially, closed loops will be formed below this limit.

A flaw in their initial assumption, which is reflected in their modeling, is that the unloading and reloading curves remain independent of previous load history. Therefore, relations determined from one set of load histories can be utilized to predict the behaviour of the material for any general history of loading. Figure 2.1 is a representation of the modeling assumptions. Karsan and Jirsa[12] later demonstrated that unloading and reloading are not unique and are dependent on the previous load history.

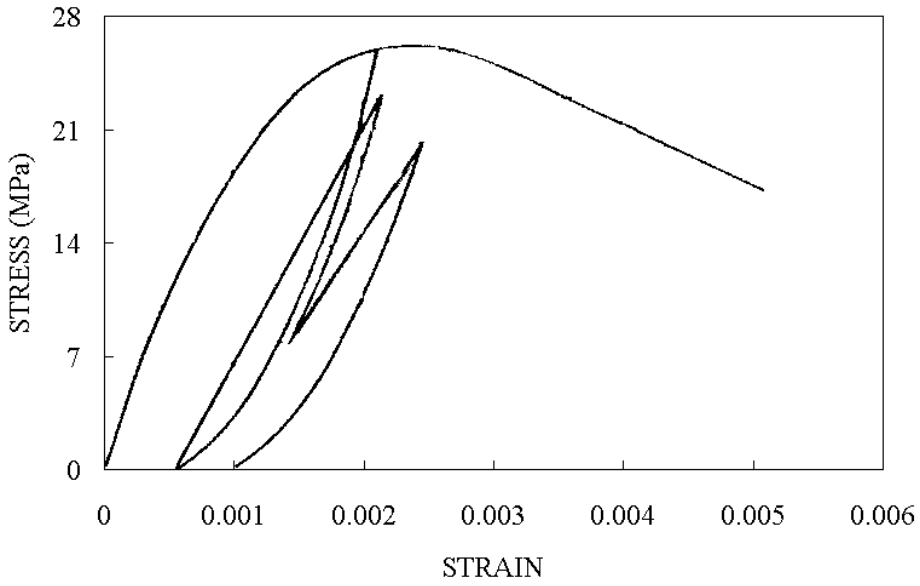

Figure 2.1 Generalized Stress-Strain Curve for Concrete, taken from Sinha, Gerstle, and Tulin.[11]

Karsan and Jirsa set out an experimental program consisting of 46 short rectangular columns of plain concrete to investigate further the findings of Sinha, Gerstle, and Tulin. They concluded that there exists an envelope curve that can be represented by the monotonic response of similar concrete properties, and that the envelope curve is reasonably approximated by the Smith-Young expression given by:

$$F_E = 0.85 S_E^{(1-S_E)} \tag{2.1}$$

where F_E, S_E are normalized stress and strain parameters, normalized with respect to the cylinder compressive strength and the cylinder strain at peak stress, respectively.

The researchers, based on the experimental results, provided a more rigorous definition of the stability limit (shakedown limit). They found that intersecting points of unloading and reloading to the envelope curve constitute an upper limit of the shakedown

limit. This was termed the common point limit. Introducing cycles with lower stress levels caused the point of intersection to be lowered, eventually leading to a stabilized point. This lower bound was referred to as the stability limit. Stresses below the stability limit did not cause additional strains. The common point limit and the stability limit were modeled exponentially in a form similar to the envelope curve, and calculated as:

$$F_C = \beta \frac{S_C}{0.315 + 0.77\beta} e^{\left[1 - S_C / (0.315 + 0.77\beta)\right]} \tag{2.2}$$

where F_S, S_C are the stress and strain ratios at the common point, respectively, and β accounts for change in limits. A value of 0.76 is used for the common point limit, and a value of 0.63 for the stability limit.

Karsan and Jirsa were the first to establish nonrecoverable compressive strains in concrete, commonly referred to as plastic strains that arise during unloading to a zero stress level. Plastic strains influence the shape of the unloading and reloading curve, thus these curves are not unique and are dependent on the previous loading history. A model was formulated describing the relationship of the plastic strains with the strain at the onset of unloading (maximum strain in the history of loading) by the following expression:

$$S_P = 0.145 S_E^{\,2} + 0.13 S_E \tag{2.3}$$

where S_p is the normalized plastic strain, and S_E is the normalized unloading strain.

Second-degree polynomials were used for unloading and reloading as illustrated in Figure 2.2.

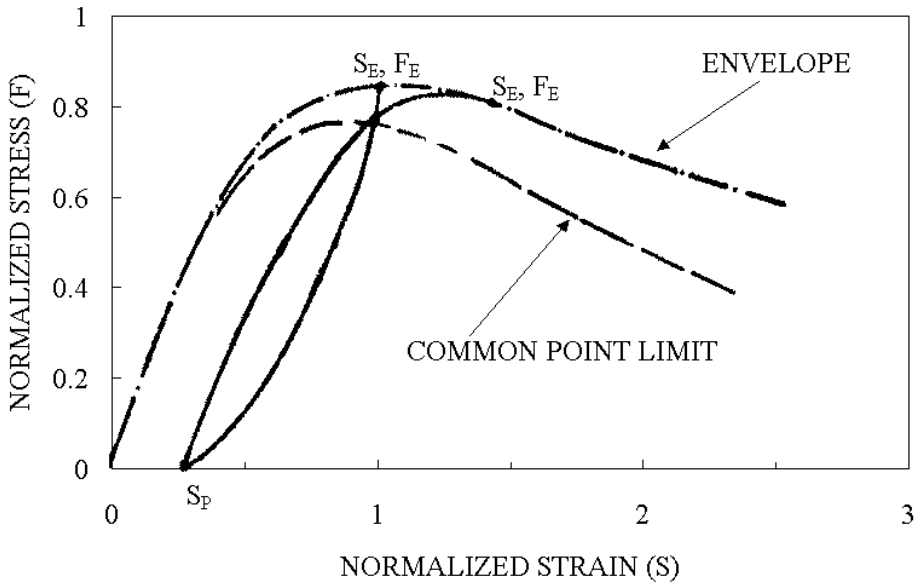

Figure 2.2 Loading and Unloading Curves, taken from Karsan and Jirsa[12]

There is little gain in modeling the reloading curves as nonlinear (e.g. parabolic) considering the increased complexity of the computations; data indicates that a linear approximation provides reasonable results. The assumed reloading curves address the damage in the concrete due to cycling, as the reloading stress at the previous maximum strain is less than the previous unloading stress. The formulations were established and corroborated to uniaxially loaded cylinders and produced results that compared well.

Park, Kent, and Simpson[13] conducted one of the first experimental investigations on reinforced concrete members subjected to cyclic loading. The experimental program consisted of applying cyclic loads to beam-column sub assemblies. Analytical models were proposed for concrete and reinforcement to reproduce moment-curvature responses. Figure 2.3 is a schematic of the proposed concrete model.

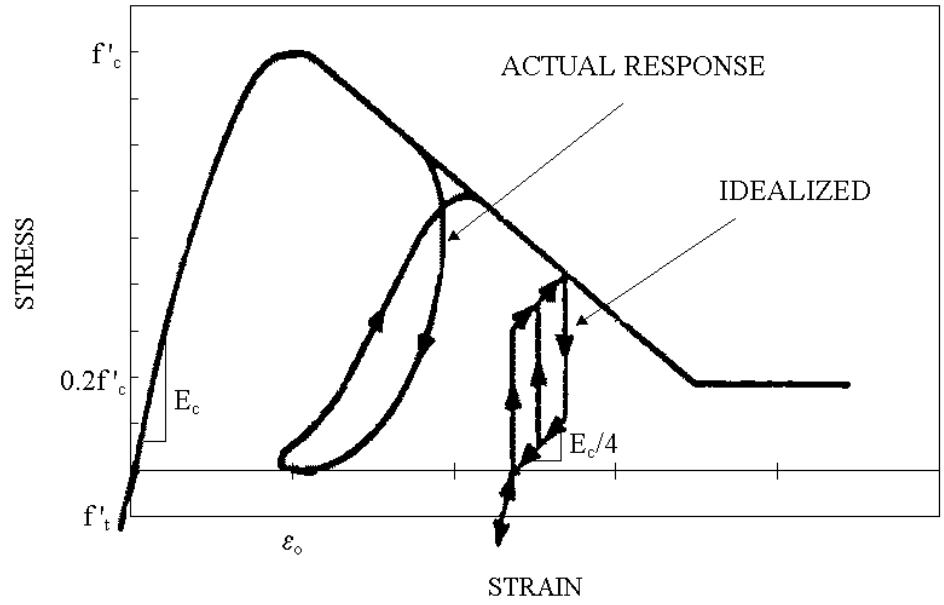

Figure 2.3 Stress-Strain Curve for Concrete, taken from Park, Kent, and Sampson[13]

A Ramberg-Osgood formulation is utilized to describe the response of reinforcement. To model the concrete, a piecewise approach is used. Although simple to understand and compute, the model does not accurately reproduce the unloading and reloading curves of actual behaviour. It incorrectly assumed that, upon unloading, 75 % of the previous stress is lost without a decrease in strain. The unloading response is then incorrectly assumed to follow a linear slope of 25 % of the initial tangent modulus to a zero stress level. In this approach, the plastic strain is independent of the unloading strain as established by other researchers[12]. Reloading begins with an increase in stress, identical to that of the unloading branch, without an increase in strain, followed by a linear slope to the backbone curve. It is also assumed that reloading terminates at the previous maximum unloading stress. Thus, the damage that concrete experiences due to cycling is

neglected. Pre-cracking tensile stresses in the concrete is considered in the modeling; however, no consideration is given to tension stiffening.

The models were implemented into a computer program based on a layered approach. The theoretical responses compared reasonably well with the experimental responses, even though an unrealistic concrete model was used. The experimental responses seemed to be dominated by yielding of the reinforcement, and therefore, the concrete response was not as critical. The concrete modeling becomes more critical in cases where the reinforcement does not yield and the behaviour of the structure is controlled by shear or crushing of the concrete. In this case, the above models would prove unsatisfactory.

The emergence of finite elements for reinforced concrete made it possible to analyze complex structures including structures subjected to seismic type forces. Darwin and Pecknold[14] were the first to report a finite element procedure that incorporated cyclic loading. An incremental, iterative, tangent stiffness approach was adopted. However, at the time, no test data was available to corroborate the approach for the case in which principal axes rotate.

The experimental results of Karsan and Jirsa were utilized in formulating the hysteretic response of the concrete under cyclic loading given by Figure 2.4.

The plastic strain, calculated from the Karsan and Jirsa model, defined the ending and starting points, respectively, for the unloading and reloading curves. A line extending from the plastic strain, through the common point, and terminating at the envelope curve represented the reloading path. Three straight lines approximated unloading: the first with the initial tangent slope; the second parallel to the reloading curve; and the third with zero

slope. The transition between the first and second line produced a turning point. The turning point and common point were based on experimental data to capture the energy dissipation. The tension response of the concrete was assumed to be linear elastic brittle, and no consideration was given to tension stiffening.

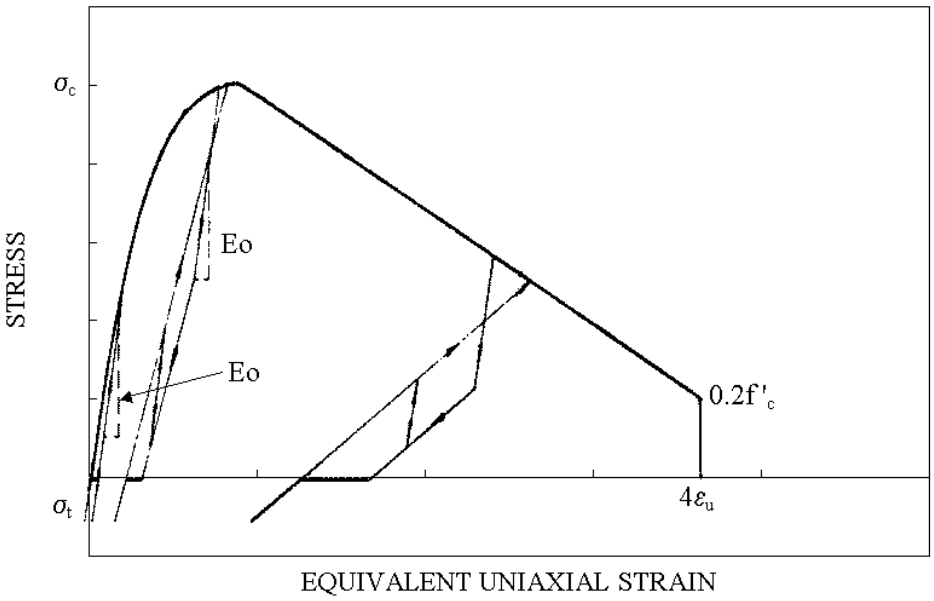

Figure 2.4 Model for Concrete Under Cyclic Loading, taken from Darwin and Pecknold[14]

The models were corroborated against a shear panel for only two and one half cycles. The analytical results provided reasonable results for the first cycle, but began to deviate during the second cycle. The latter seemed to be more a function of the finite element procedure than the cyclic formulations for the concrete. In terms of the modeling, the linear reloading branch, which considers damage due to cycling, is realistic of the actual behaviour. The unloading branch is slightly deficient; it contains a region of zero slope that produces zero stress in the concrete while the concrete is unloading. A simple quadratic formulation would produce a more realistic response.

The effect of biaxial cyclic compression on concrete was ignored in the earlier works. Buyukozturk and Tseng[15] investigated this behaviour by subjecting 127 x 127 mm flat concrete plates of 25 mm thickness to cyclic loading in one direction, with a constant confining strain in the orthogonal direction. Analysis of the experimental data provided insight into the biaxial cyclic behaviour of concrete and was concluded to be consistent with the uniaxial cyclic loading behaviour of concrete. The similarities include:

1. Concrete exhibits typical hysteretic behaviour where the area within the hysteresis loops, representing the energy dissipated during a cycle, becomes larger as the unloading strain increases.
2. Reloading curves are nearly linear up to the intersection with the unloading curve, after which there is a softening in the response.
3. The unloading curves are slightly nonlinear with a marked increase in curvature near the residual strain.
4. A continuous degradation of the concrete is reflected in the decrease of the slopes of the reloading curves.
5. The plastic strains are dependent on the strain at unloading and are not affected by the confining strains.

To further their work, the researchers proposed formulations for concrete under cyclic loading including the effects of confinement. The model was based on an incremental orthotropic formulation and used an equivalent one-dimensional approach to represent the multiaxial behaviour. It was essentially a tangent stiffness approach. The Popovics[16] curve was used to describe the envelope response of concrete in compression and is presented in the equivalent stress-strain form as:

$$\frac{\sigma}{\sigma_p} = \frac{n}{n-1+\left(\frac{\varepsilon_e}{\varepsilon_p}\right)^n}\left(\frac{\varepsilon_e}{\varepsilon_p}\right) \tag{2.4}$$

where σ_p is the principal peak stress, ε_p is the equivalent strain at peak stress, n is a shape factor, σ is the principal stress, and ε_e is the equivalent strain. The unloading branch was assumed parabolic with a finite stiffness at the onset of unloading, and passing through the plastic strain at zero stress. A relation between the plastic strain and the strain at unloading was determined from the test data as follows:

$$\frac{\varepsilon_r}{\varepsilon_p} = 0.162\left(\frac{\varepsilon_u}{\varepsilon_p}\right) + 0.334\left(\frac{\varepsilon_u}{\varepsilon_p}\right)^2 \tag{2.5}$$

where ε_r is the residual (plastic) strain, and ε_u is the strain at unloading. The above formulation produces slightly larger residual strains than that proposed by Karsan and Jirsa. The latter seems to be a lower bound solution. For reloading, the Popovics curve was used with modifications to the initial slope of reloading. The model provided reasonable correlations to the test data and can be implemented into a nonlinear finite element algorithm based on a tangent stiffness approach. The tests and formulations, however, did not consider confinement in the out-of-plane direction.

Much of the pioneering work discussed above provides a benchmark for which current and future analytical modeling can be derived. A discussion of the state-of-the-art in constitutive modeling of reinforced concrete subjected to cyclic loading will be presented in the following section.

2.1.3 Constitutive Modeling

Many constitutive models in the literature describe the behaviour of concrete to cyclic loading for a simple uniaxial case. The implementation of these formulations into a nonlinear finite element algorithm may not be a simple task. These models neglect to consider the possibility of principal axes, causing a rotation of the cracks. The literature has documented models that have been implemented into nonlinear finite element programs that have produced reasonable results, which assume a smeared crack approach of fixed directions. In some fixed crack formulations, separate models have been used to model the normal stress and shear stress hysteresis, which is at odds with test observations. Those researchers that have attempted to account for rotating cracks have done so by using a tangent stiffness-based algorithm. The tangent stiffness approach can result in some numerical difficulties. Vecchio[3] was one of the first researchers to present formulations for concrete under general loading for a secant stiffness-based algorithm, employing the smeared rotating crack assumption. A secant stiffness approach has computational advantages over a tangent stiffness approach. A look at some of these models follows.

Yankelevsky and Reinhardt[17,18] reported one-dimensional models separately for concrete in cyclic compression and cyclic tension based on geometric properties of the concrete.

In compression, the concrete model determines a set of 6 focal points that govern pieced linear branches for unloading and reloading. These focal points are solely dependent on the maximum compressive concrete strength, and are located along the initial tangent modulus. This rather simple model is helpful in graphically visualizing the

one-dimensional behaviour of cyclic compressive loading of concrete. Figure 2.5 demonstrates the graphical procedures utilized to form a set of unloading and reloading responses in a nondimensional uniaxial stress-strain coordinate system.

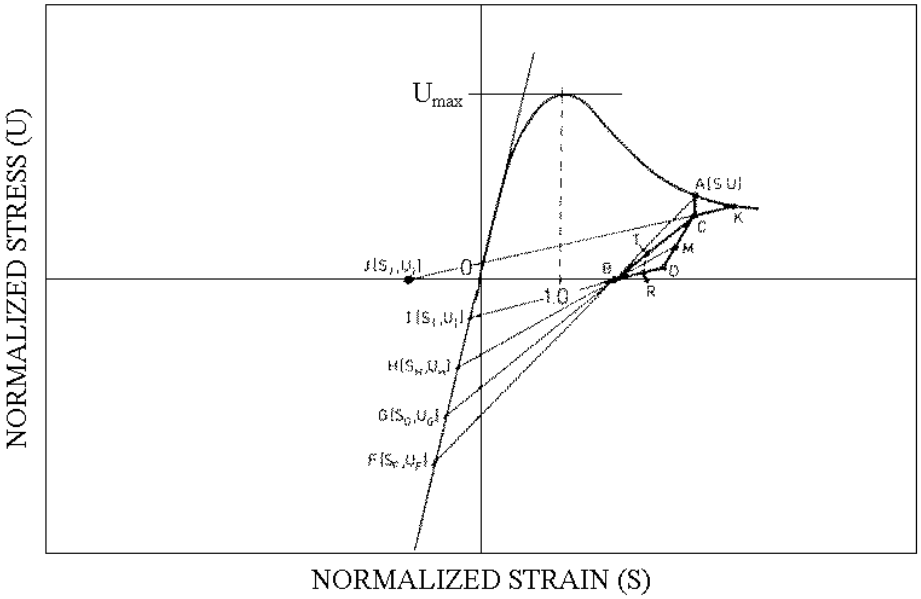

Figure 2.5 Scheme of Focal Points Model, taken from Yankelevsky and Reinhardt[17]

The formulations and focal points are summarized in Ref. 17. The reloading portion CK captures the damage induced in the concrete due to cycling. The model has produced some reasonable results in comparison to cylinder tests; however, in the post-peak region, point D tends to underestimate the stress on the unloading branch. This model serves more as a graphical tool rather than a model conducive to finite element analysis. The unloading branch must consider three separate unloading paths, whereas a simple second-degree parabola would more accurately model the unloading behaviour.

A similar focal point procedure was used to describe the behaviour of concrete subjected to cyclic tension. The model was formulated in the stress-displacement

coordinate system, which is directly applicable to a discrete crack approach. Seven focal points, placed along the tangent to the envelope curve, were defined and deemed dependent on the tensile strength of the concrete. As in the compression response, linear pieced branches described unloading and reloading in tension. Figure 2.6 depicts the focal point model.

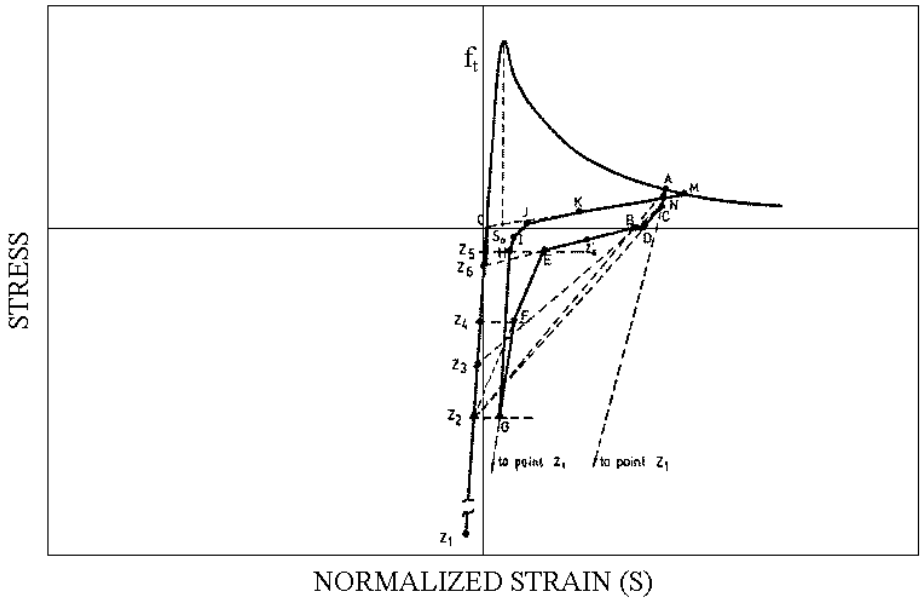

Figure 2.6 Focal Point Model, taken from Yankelevsky and Reinhardt[18]

The above model provides an excellent graphical tool. It captures the damage to the concrete upon reloading, and considers closing of cracks. In the latter, the concrete experiences compressive forces before the cracks are completely closed. However, implementing this model into a finite element algorithm may not be convenient considering the numerous linear responses required to capture the overall cyclic behaviour. The focal point model, describing the cyclic behaviour of concrete, may not be conducive to finite

element programming but does offer a simple graphical representation of the complex behaviour of concrete under cyclic loading.

Yankelevsky and Reinhardt later formulated expressions to model the nonlinear nature of unloading and reloading in tension[19]. It was found that the curvature of the unloading and reloading branches were strongly related to the displacement at unloading and the displacement at reloading, respectively. The expressions used to model the unloading and reloading, formulated in terms of stress-displacement, demonstrated reasonable simulations of behaviour for tests conducted by the researchers. However, the expressions developed depend on the gauge length used in the tests, and transformations are required for test data corresponding to different gauge lengths.

Previous experimental research focused on two types of loading patterns for concrete subjected to uniaxial cyclic loading. The first considered unloading from the envelope curve to zero stress and reloading from the zero stress level to the envelope curve. The second considered repeated unloading and reloading between specified stress levels. The latter is commonly used to determine the fatigue limits of concrete. However, the response of elements in a concrete structure may not fall into either of these two loading patterns. Partial reloading below the envelope curve may follow an unloading phase, and partial unloading to a non-zero stress level may follow reloading. Recently, Bahn and Hsu[20] conducted an experimental program to consider the effect of random cycles in compression. This research consisted of testing 3 x 6 in. (76 x 152 mm) concrete cylinders, and to propose models for the general loading conditions of concrete in compression. Four different loading regimes were employed: monotonic loading; cycles to envelope curve; cycles to common point; and cycles with random loading.

Based on the tests, the following conclusions were made, confirming what previous researchers have stated:

1. The envelope curve for cyclic loading could be represented by the response of concrete to monotonic loading.
2. The residual strains are a function of the strain at unloading, and an increase in the unloading strain causes approximately the same increase in the accumulated residual strain.
3. The unloading and reloading lines do not coincide. The average slope of the unloading and reloading curves is inversely proportional to the plastic strain. This suggests that there is stiffness degradation for the entire stress-strain curve.

The proposed semi-empirical formulations were based on the experimental data and extensive numerical and geometrical simulations to capture the overall behaviour of the concrete. To define the plastic strains, a parabolic expression was adopted, as follows, to fit the experimental data:

$$S_{pu} = c_p (S_{eu})^{n_p} \tag{2.6}$$

where S_{pu} is the plastic strain ratio, S_{eu} is the unloading strain ratio on the envelope curve, c_p is a coefficient of plastic strain, and n_p is an optimum order for the proposed equation type. Based on the test data, c_p is suggested as 0.30 and n_p as 2. The unloading response was modeled by providing a power-type function to the linear unloading response and included partial unloading. The stress on the unloading path is calculated from:

$$U_{unlo} = U_{pu} + c_u\left(U_{eu} - U_{pu}\right)\left(\frac{S - S_p}{S_{eu} - S_p}\right)^{n_u} \tag{2.7}$$

where U_{unlo} is a stress ratio on the unloading curve, U_{eu} is the envelope unloading stress ratio, U_{pu} is the partial unloading stress ratio, S is a strain ratio on the unloading branch, S_p is the plastic strain ratio, S_{eu} is the unloading strain ratio on the envelope curve, and c_u is a parameter of unloading; equal to 0.95. The latter was determined from a trial and error approach of simulating the overall shape of the stress-strain curve. n_u is a power term to reflect the curvature of unloading and is calculated as: $1.0 + \sqrt{S_p}$. It was suggested that the curvature of unloading was related to the plastic strain, thus it was included in the calculation of the power term. To formulate a reloading response, a linear relation was assumed from the last unloading strain ratio to the reloading strain ratio on the envelope curve including the effects of partial unloading, calculated as:

$$U_{relo} = U_{ppu} + c_r\left(U_{erpu} - U_{ppu}\right)\left(\frac{S - S_{ppu}}{S_{erpu} - S_{ppu}}\right)^{n_r} \tag{2.8}$$

where U_{relo} is a stress ratio on the reloading curve, U_{ppu} is the partial unloading stress ratio at which reloading commences, and U_{erpu} is the envelope reloading stress ratio considering the effects of partial unloading. S_{ppu} is the partial unloading strain ratio, and S_{erpu} is the envelope reloading strain ratio. The reloading coefficient c_r is equal to 1.0, and the power term for reloading n_r is equal to 1.0 to reflect the assumed linear response. Figure 2.7 graphically demonstrates the response of the above formulations, considering the more general case of partial unloading and partial reloading.

The reloading strain ratio, for which no formulations were given, was a function of the unloading strain ratio. The proposed model provided excellent agreement with cylinder tests conducted as part of the research, and with cylinders tested elsewhere. The model also considered the general case of partial unloading and partial reloading. However, the formulations were strongly influenced by previous stress history, thus the envelope curve may affect the results. Also, extensive graphical simulations were performed to model the overall cyclic behaviour of concrete, and this may not reflect the true behaviour. The extensive tests conducted provide much needed data to model the general case of partial unloading and partial reloading commonly ignored in most models.

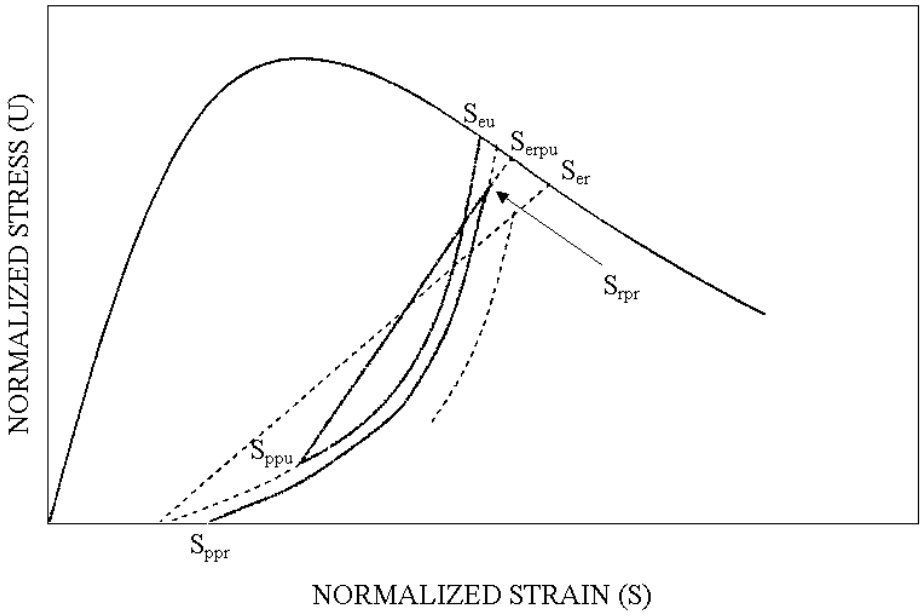

Figure 2.7 Schematic of Unloading and Reloading Response, taken from Bahn and Hsu[20]

Excellent agreement in predicting the behaviour of concrete subjected to cyclic loading against cylinder-type tests have been reported for many of the models proposed thus far. However, models must be applicable to structural members and be able to

provide accurate simulations of the structure's behaviour. Beam-column joints frequently experience load reversals, and realistic models describing the cyclic behaviour are required, which can be easily implemented into computer programs. Seckin[21] conducted a research project investigating the behaviour of exterior beam-column sub-assemblies. Figure 2.8 is a schematic of the proposed concrete cyclic model.

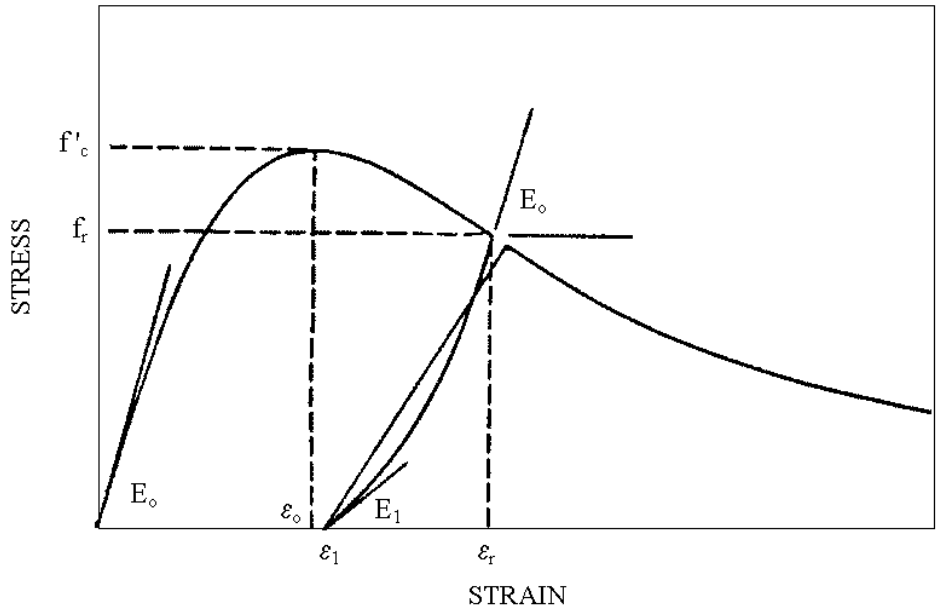

Figure 2.8 Mathematical Model for Concrete, taken from Seckin[21]

Seckin, based on the following assumptions, developed a model for concrete in compression:

1. Tensile strength of concrete is negligible.
2. Reloading curves are represented with straight lines.
3. The monotonic loading response is an upper bound to the reloading curves.
4. The stress-strain point at unloading from the envelope curve defines the unloading curves. The accumulation of plastic strains occurs only from the envelope curve.

The unloading curves, expressed in polynomial form, were derived considering the boundary conditions at the onset of unloading from the envelope curve and at the end of unloading. The unloading stress is computed as:

$$f_c = E_1(\varepsilon - \varepsilon_1) + G(\varepsilon - \varepsilon_1)^N \tag{2.9}$$

where

$$N = \frac{(E_0 - E_1)(\varepsilon - \varepsilon_1)}{f_r - E_1(\varepsilon - \varepsilon_1)} \tag{2.10}$$

$$G = \frac{f_r - E_0(\varepsilon - \varepsilon_1)}{(\varepsilon - \varepsilon_1)^N (1 - N)} \tag{2.11}$$

Through a parametric study, the following was determined:

$$E_1 = E_0\left(1 - 0.7\varepsilon_{rn}^{\ 0.41}\right) \text{ if } \varepsilon_r < 2\varepsilon_0 \tag{2.12}$$

$$E_1 = 0.071E_0 \qquad \text{if } \varepsilon_r \geq 2\varepsilon_0 \tag{2.13}$$

$$\varepsilon_1 = (\varepsilon_{rn} - 0.60)\varepsilon_0 \qquad \geq 0 \tag{2.14}$$

A simpler linear reloading relation was adopted for the reloading portion of the response, and modeled as:

$$f_c = E_2(\varepsilon - \varepsilon_1) \tag{2.15}$$

where

$$E_2 = \frac{7.5E_0}{\varepsilon_1 E_0 + 7.5} \tag{2.16}$$

ε is the current strain, ε_1 is the plastic strain, ε_0 is the strain at peak stress, and ε_{rn} is the unloading strain from the envelope curve, normalized with respect to the strain at peak stress. f_c is the concrete stress, f_r is the stress at unloading from the envelope curve, E_0 is the initial modulus of elasticity of concrete, E_1 represents the stiffness of the unloading response at zero stress, and E_2 is the stiffness of the reloading branch.

Standard cylinders tested under cyclic compressive loadings verified the proposed model, and acceptable results were obtained. The formulations were implemented into a sectional response algorithm, where the section is divided into discrete layers over the height. The computed response demonstrated a good agreement with the experimental results. The proposed model provides formulations that can be easily implemented into a nonlinear finite element program.

In a study by Mander, Priestley, and Park[22], the applicability of cyclic loading models was verified against rectangular and circular columns, and shear walls. The focus of this research was on modeling the response of confined concrete due to confining reinforcement. The proposed models showed good agreement with experimental tests conducted by the researchers. However, the tests involved only one or two cycles of unloading during the entire loading range.

The monotonic loading stress-strain response for concrete was assumed to form the envelope curve for cyclic loading regardless of confinement.

The research produced a unified approach to modeling confinement in columns, including the effects of cyclic loading. The model considered concrete in compression and tension, damage to the compressive response due to cycling, and partial unloading and reloading. Figure 2.9 is a representation of the proposed model.

The model assumed that a Popovics[16] response curve for concrete under monotonic loading formed the envelope for cycling loading in compression, and accounted for the effects of confinement. The compressive stress is given as:

$$f_c = \frac{f'_{cc}\, xr}{r - 1 + x^r} \tag{2.17}$$

where f'_{cc} is the compressive strength of confined concrete.

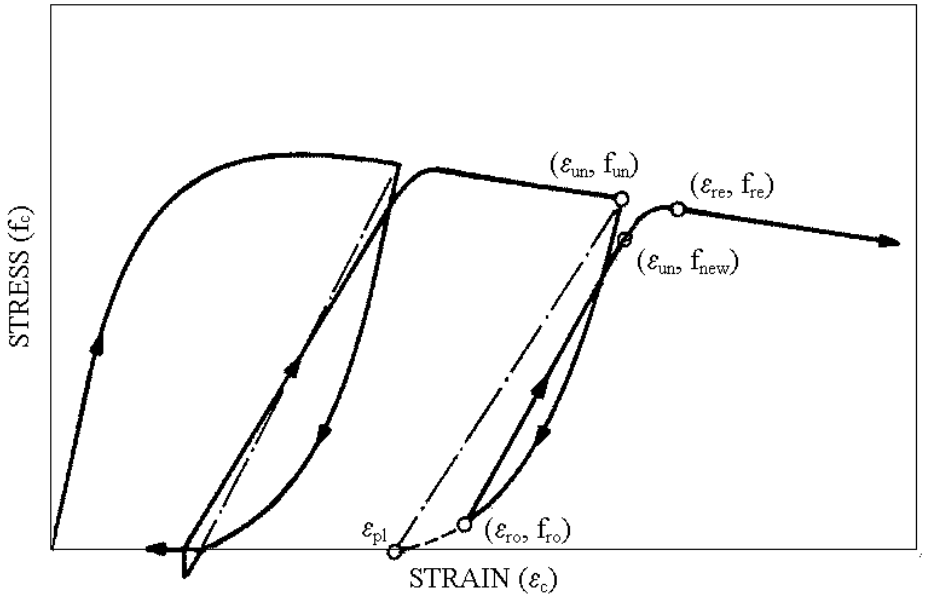

Figure 2.9 Stress-Strain Curves for Reloading Branch, taken from Mander, Priestley, and Park[22]

The parameter x is calculated from.

$$x = \frac{\varepsilon_c}{\varepsilon_{cc}} \tag{2.18}$$

where ε_c is the longitudinal compressive strain, and ε_{cc} is determined from:

$$\varepsilon_{cc} = \varepsilon_{co}\left[1 + 5\left(\frac{f'_{cc}}{f'_{co}} - 1\right)\right] \tag{2.19}$$

where ε_{cc} is the strain corresponding to the maximum stress, and f'_{co} and ε_{co} are the unconfined concrete strength and the corresponding strain. The parameter r is computed according to the following expressions:

$$r = \frac{E_c}{E_c - E_{\text{sec}}} \tag{2.20}$$

where $$E_c = 5000\sqrt{f'_{co}} \tag{2.21}$$

$$E_{\sec} = \frac{f'_{cc}}{\varepsilon_{cc}} \tag{2.22}$$

E_c is the tangent modulus of the concrete, and $E_{\sec}$ is the secant modulus at the peak compressive strength.

The unloading branch in compression was defined by the unloading strain and the plastic strain. The plastic strain was determined from a common strain at the intersection of the initial tangent modulus and the plastic unloading secant slope as follows:

$$\varepsilon_{pl} = \varepsilon_{un} - \frac{(\varepsilon_{un} + \varepsilon_a) f_{un}}{(f_{un} + E_c \varepsilon_a)} \tag{2.23}$$

where $$\varepsilon_a = a\sqrt{\varepsilon_{un}\varepsilon_{cc}} \tag{2.24}$$

and a is the greater of $$a = \frac{\varepsilon_{cc}}{\varepsilon_{cc} + \varepsilon_{un}} \tag{2.25}$$

or $$a = \frac{0.09\varepsilon_{un}}{\varepsilon_{cc}} \tag{2.26}$$

ε_{pl} is the plastic strain due to unloading in compression, f_{un} and ε_{un} are the unloading stress and strain from the envelope curve, and ε_a is a common strain at the intersection of the initial tangent and secant moduli.

The nonlinear nature of the unloading response was modeled by modifying the Popovics envelope curve as follows:

$$f_c = f_{un} - \frac{f_{un} x r}{r - 1 + x^r} \tag{2.27}$$

where $$r = \frac{E_u}{E_u - E_{\sec}} \tag{2.28}$$

$$E_{\sec} = \frac{f_{un}}{\varepsilon_{un} - \varepsilon_{pl}} \tag{2.29}$$

$$x = \frac{\varepsilon_c - \varepsilon_{un}}{\varepsilon_{pl} - \varepsilon_{un}} \tag{2.30}$$

E_u is the initial modulus at the onset of unloading and is calculated as:

$$E_u = bcE_c \tag{2.31}$$

where

$$b = \frac{f_{un}}{f'_{co}} \geq 1 \tag{2.32}$$

$$c = \left(\frac{\varepsilon_{cc}}{\varepsilon_{un}} \right)^{0.5} \leq 1 \tag{2.33}$$

The reloading branches may occur from the unloading curve, or from the cracked state. A linear relation was used to model the response between the reloading strain and the previous envelope unloading strain, and a parabolic curve modeled the response from the unloading strain to the envelope curve. The former is determined from:

$$f_c = f_{ro} + E_r(\varepsilon_c - \varepsilon_{ro}) \tag{2.34}$$

where

$$E_r = \frac{f_{ro} - f_{new}}{\varepsilon_{ro} - \varepsilon_{un}} \tag{2.35}$$

$$f_{new} = 0.92 f_{un} + 0.08 f_{ro} \tag{2.36}$$

E_r is the reloading stiffness, f_{ro} and ε_{ro} are the stress and strain at the onset of reloading, and f_{new} is the new concrete stress on the reloading branch at the previous envelope unloading strain. The parabolic transition portion of the response is computed as:

$$f_c = f_{re} + E_{re}(\varepsilon_c - \varepsilon_{re}) + A(\varepsilon_c - \varepsilon_{re})^2 \tag{2.37}$$

where

$$\varepsilon_{re} = \varepsilon_{un} + \frac{f_{un} - f_{new}}{E_r\left(2 + \frac{f'_{cc}}{f'_{co}}\right)} \tag{2.38}$$

$$A = \frac{E_r - E_{re}}{-4[(f_{new} - f_{re}) - E_r(\varepsilon_{un} - \varepsilon_{re})]} \tag{2.39}$$

E_{re} is the return point tangent modulus, and f_{re} and ε_{re} are the stress and strain at the return point on the envelope curve.

For concrete in tension, a linear loading and unloading response is utilized. Tension stiffening is ignored, and upon cracking, the tensile strength of subsequent loadings is assumed to be zero.

The models were corroborated against columns and shear walls with only one or two unloading cycles during the course of testing.

The models, despite producing good results for limited unloading cycles, have some deficiencies in that:

1. Little or no excursion in the tension regime is considered.
2. Damage due to load cycling is based on stress conditions.
3. The plastic strain model is dependent on the base curve for concrete.
4. To capture the parabolic transition model, although realistic, requires extremely small load increments in a finite element analysis.
5. The formulations do not consider rotation of the principal axes.

2.1.4 Application To Finite Elements

Models that provide accurate simulations of behaviour under reversed cyclic loading conditions tend to model cracks as smeared in the finite element procedure. However, many of these models also consider cracks to be fixed in direction. Thus, under

cyclic loading, cracks that form after an element has cracked in one direction are assumed to be orthogonal to the first set of cracks. This approach requires separate normal and shear stress hysteretic models at the crack surface.

The fixed crack approach, as assumed by Sittipunt and Wood[23], and Okamura and Maekawa[24], has demonstrated reasonable agreement with experimental results. Okamura and Maekawa formulated a compression model for concrete based on fracture mechanics in terms of equivalent stress and equivalent strain. The tension model considered stress transferred to the concrete through bond with the reinforcement and stress transferred through closing of cracks. Shear transfer at a crack was based on a contact density model, and the shear stress was dependant on the ratio of shear displacement to crack width. The compressive response is shown in Figure 2.10.

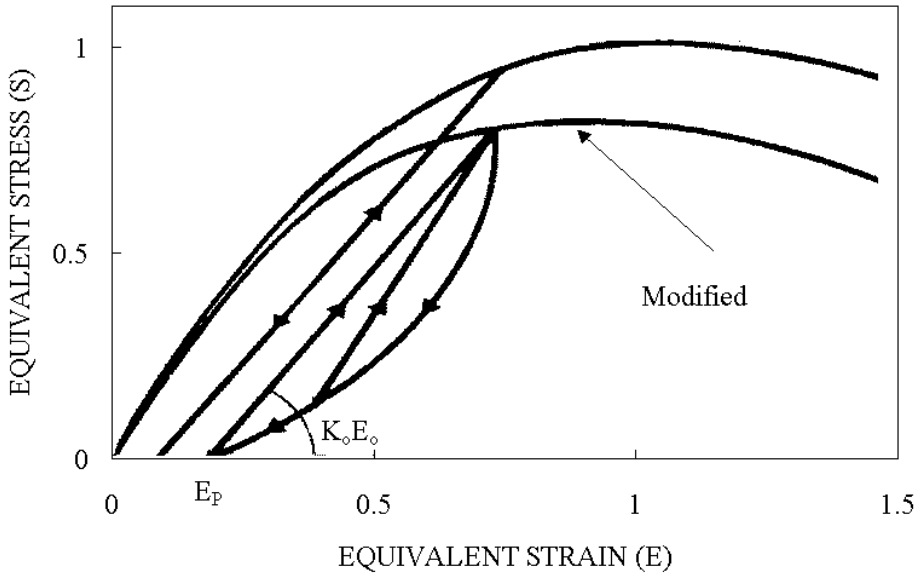

Figure 2.10 Equivalent Stress-Strain Relationship in Compression, taken from Okamura and Maekawa[24]

The tension model comprised of the bond action and closing of cracks is illustrated in Figure 2.11.

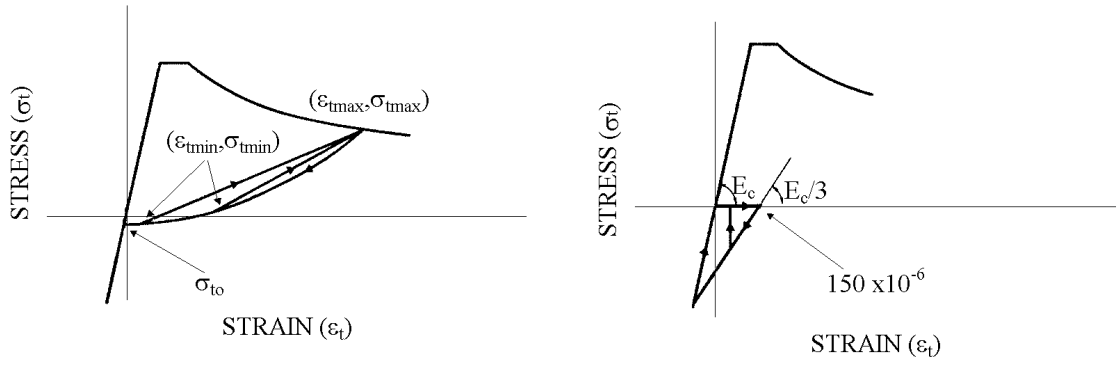

Figure 2.11 Tension Model, taken from Okamura and Maekawa[24]: (a) Bond Action; (b) Closing of Cracks

Initially, unloading and reloading in compression were assumed to follow the same linear path. However, to account for energy dissipation in the concrete under cyclic compressive loading, a nonlinear path was implemented for the unloading branch. The unloading phase begins at the envelope curve with an infinite tangent stiffness and ends at the plastic offset strain. The equivalent plastic strain is determined by the following expression:

$$E_p = c\left(1 - e^{-0.35E}\right) \tag{2.40}$$

where E_p is the equivalent plastic strain, and c is a parameter that accounts for loading rate ($40/7$ for slow loading rate, and $20/7$ for original loading rate). The original loading rate refers to the rate used in the experimental tests. E is the equivalent strain and is a variable in terms of the average strain and the deviation strain, normalized with respect to

the strain at peak stress. The equivalent stress on the reloading path is determined by the following formulation:

$$S = E_o K_o \left(E - E_p\right) \tag{2.41}$$

where

$$K_o = e^{-0.73E\left(1-e^{-1.25E}\right)} \tag{2.42}$$

S is the equivalent stress normalized with respect to the peak stress, and is given in terms of the average stress and the deviation stress. E_o is the elastic modulus, and K_o is a fracture parameter that indicates the reduction of the elastic modulus in the reloading process.

In tension, the model is formulated in terms of stress and strain. The unloading response consists of two contributions: the stress transferred through bond action, and the stresses occurring due to crack closing. The unloading response of the stress transferred through bond action is expressed as follows:

$$\sigma_t - \sigma_{to} = \left(\sigma_{t\max} - \sigma_{to}\right)\left(\varepsilon_t / \varepsilon_{t\max}\right)^2 \tag{2.43}$$

where

$$\sigma_{to} = -0.0016 E_c \varepsilon_{t\max} \tag{2.44}$$

σ_t and ε_t are the tensile stress and strain, respectively, $\sigma_{t\max}$ and $\varepsilon_{t\max}$ are the stress and strain on the envelope curve at the onset of unloading, and E_c is the initial tangent modulus. The stress transferred by closing of cracks in the unloading phase is modeled by a linear response. The contact stress begins when the cracked surfaces come in contact and is considered to occur when the strain on the unloading path is 150×10^{-6}. The response follows a stiffness of $E_c/3$. The stress is considered to be zero as long as the cracked surfaces are not in contact with each other. For reloading, the stress transmitted

through the cracks is assumed to be elastic until the average strain of the concrete becomes zero, after which the contact stress becomes zero.

The concrete cyclic models proposed by the above researchers are advanced over those previously reviewed. Concrete in tension is considered, along with energy dissipation due to load reversals. The tensile cyclic model also attempts to quantify stresses transferred due to closing of cracks. However, the concrete cyclic model fails to capture the damage caused to the concrete both in compression and in tension, and prefers to assume that the reloading paths will meet the envelope curve at the previous envelope unloading strain. Also, the concrete models are applicable to algorithms based on a fixed crack approach.

Less common in the literature are cyclic loading procedures based on a rotating smeared crack approach. Attempts have been made by researchers to account for cyclic loading in a rotating crack procedure, but have either been unsuccessful or have formulated rather simple models for concrete that do not capture the realistic behaviour of cyclic loading. Teigen[25] proposed a simplistic cyclic model for concrete in tension and compression, assuming that simple joint linear paths for unloading and reloading meet at the origin. The model is depicted in Figure 2.12.

In compression, the stress on the unloading or reloading path can be computed from:

$$\sigma_{c2} = E_{u2}\varepsilon_{c2} \tag{2.45}$$

where

$$E_{u2} = \frac{\hat{\sigma}_{c2}}{\hat{\varepsilon}_{c2}} \quad ; \hat{\varepsilon}_{c2} < 0 \tag{2.46}$$

$$E_{u2} = E_c \quad ; \hat{\varepsilon}_{c2} = 0 \tag{2.47}$$

σ_{c2} , ε_{c2} and E_{u2} are the stress, strain and slope of the joint unloading/reloading line in compression. $\hat{\sigma}_{c2}$ and $\hat{\varepsilon}_{c2}$ are stress and strain at the onset of unloading from the envelope curve, and E_c is the initial tangent modulus.

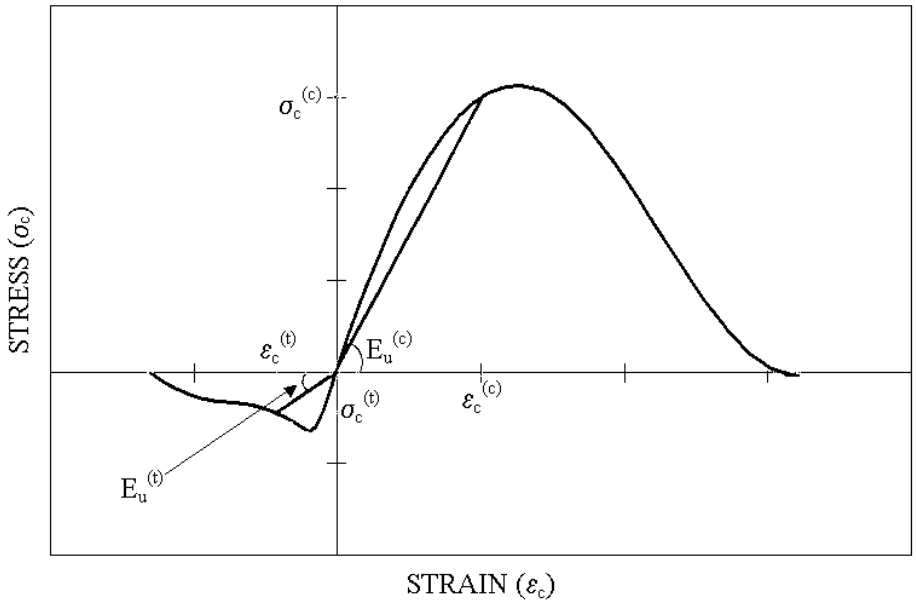

Figure 2.12 Generalized Stress-Strain Relationship for Concrete, taken from Teigen[25]

A similar model was proposed for concrete in tension, and is given by:

$$\sigma_{c1} = E_{u1}\varepsilon_{c1} \tag{2.48}$$

where

$$E_{u1} = \frac{\hat{\sigma}_{c1}}{\hat{\varepsilon}_{c1}} \quad ; \hat{\varepsilon}_{c1} > 0 \tag{2.49}$$

$$E_{u1} = E_c \quad ; \hat{\varepsilon}_{c1} = 0 \tag{2.50}$$

σ_{c1} , ε_{c1} and E_{u1} are the stress, strain and slope of the joint unloading/reloading line in tension, and $\hat{\sigma}_{c1}$ and $\hat{\varepsilon}_{c1}$ are stress and strain at the onset of unloading from the envelope curve.

The proposed formulations neglect hysteresis of the concrete under cyclic loading, ignore plastic offsets due to the unloading phase, and do not account for damage in the concrete due to load cycling. However, the cyclic behaviour of concrete was not a primary objective of the above work, and a simple model was deemed satisfactory. If plastic offsets are ignored, adjustments of the envelope curve are not necessary.

Stevens, Uzumeri, and Collins[26] used a more comprehensive constitutive modeling approach for concrete in a rotating smeared crack context. Figure 2.13 depicts the idealized concrete response.

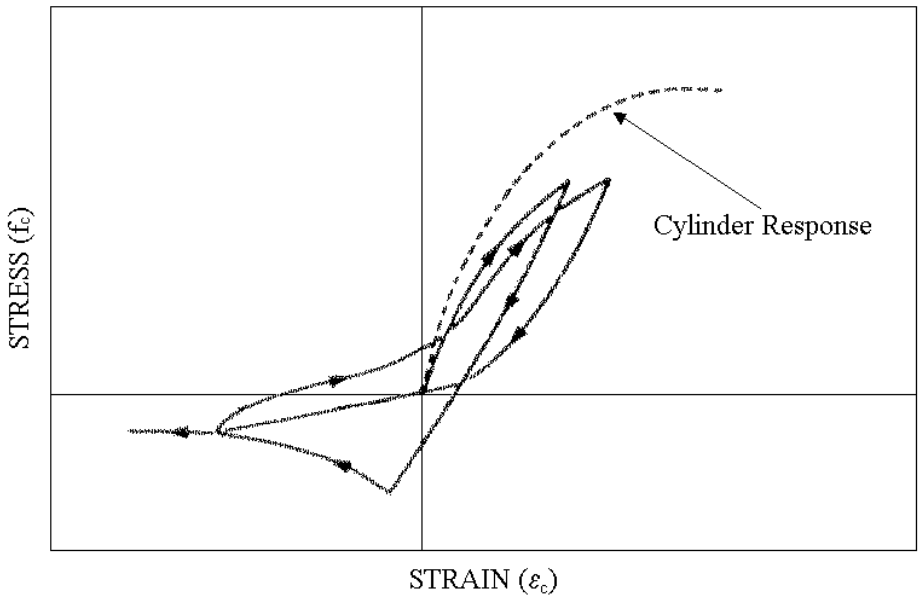

Figure 2.13 Idealized Concrete Response, taken from Stevens, Uzumeri, and Collins[26]

The proposed model will be described qualitatively, and the complex stiffness approach to formulating the expressions can be found elsewhere[26]. Initial loading in compression follows the envelope curve as determined by the monotonic response, and accounts for the effects of compression softening and damage due to biaxial cycling.

Unloading in the uncracked state is relatively stiff until the concrete cracks in tension. The cracking stress is reduced from the monotonic cracking stress, and is a function of the previous maximum compression strain. Beyond cracking, a tension stiffening portion is considered in the response. An initially stiff response characterizes the unloading branch in tension, but rapidly levels off. Before the cracks are completely closed, compressive stresses start to increase, and with increasing compressive strain, the response becomes stiffer. Eventually, when the cracks are closed, a reloading branch in compression in the form of a parabola controls the behaviour. The reloading branch does not return to the previous peak stress and includes damage to the reloading stiffness caused by load cycling. Subsequent unloading in compression, in the cracked state, differs from the response in the uncracked state. The unloading branch is initially similar to that of the uncracked state, but softens considerably and becomes almost linear until it reaches the previous peak tensile stress. The softening portion of the unloading curve causes tensile strains to develop in the concrete under compressive stresses.

The proposed model provided accurate results in comparison to panel tests carried out by the investigators; however, analyses of structures subjected to cyclic loading were lacking, and the solution technique used in the finite element algorithm required improvements. This stiffness approach is able to describe the cyclic behaviour of concrete both in compression and tension; however, it is susceptible to convergence problems in finite element analysis.

The models reviewed herein provide an insight into the behaviour of concrete under cyclic loading; however, no one model captures all the effects experienced by the concrete. More importantly, with regards to this research, is the fact that no models have

been successfully implemented into a nonlinear finite element program based on a rotating smeared crack assumption employing a secant stiffness approach. This is not to say that certain rules proposed by the above researchers cannot be implemented, but consideration needs to be given to rotating of principal axes.

Vecchio[3] recently reported formulations for arbitrary loading conditions for a secant stiffness-based finite element algorithm. A secant stiffness approach is characterized as having excellent convergence and numerical stability. However, a criticism of this approach has been that it cannot be effectively used to model response to general loading. Vecchio used a plastic offset approach to include the effects of cyclic loading. The resulting formulations for cyclic loading demonstrated that the procedure used was stable, compliant and provided accurate simulations of behaviour. The proposed models for concrete in compression and tension under cyclic loading were provisional. A complete description of the procedure and models will be presented in the following chapter.

A key objective of this research project was to improve upon the models proposed by Vecchio for cyclic loading, taking into account the characteristics of the concrete as described by the models reviewed herein.

2.2 SHEAR WALLS

2.2.1 Review

The use of shear walls as the main seismic resisting element in structures seems to be a structurally sound method. Mark Fintel highlighted the excellent performance of shear walls in buildings subjected to severe earthquakes worldwide[27].

The ductile moment resisting frame evolved in the 1950's as the structural system for multi-storey buildings, and remained the main seismic resisting system until the 1970's. The shear wall was later introduced, but was considered undesirable as the main seismic resisting element. Shear walls were expected to suffer severe damage stemming from their brittle response due to the fact that rigid structures attract higher seismic forces. Most post-war structures were, therefore, built with ductile moment resisting frames. However, recorded observations of severe earthquakes in Yugoslavia (1963), Venezuela (1967), California (1971), Nicaragua (1972), Romania (1977), Mexico (1985), and Armenia (1988) revealed otherwise. Hundred of structures, incorporating the ductile moment resisting frame, collapsed due to excessive interstorey drift which caused failures of columns. Buildings designed with shear walls were able to withstand these seismic forces and also exhibited good earthquake performance.

The moment resisting frames used in the early days, which suffered severe damage under seismic forces, are classified as ordinary moment-resisting frames according to current seismic design standards. Stringent detailing provisions for reinforced concrete frames subjected to severe seismic events were not adopted in the US until several years after the 1971 California earthquake, which lead to the special moment-resisting frame. These types of provisions have not been adopted in many countries today.

Engineers confused flexibility with ductility in the early days of seismic design, and as a result, a large number of buildings were built in a flexible manner. These structures were prone to large interstorey drift leading to structural failure. The shear walls, on the other hand, were capable of resisting the interstorey drift associated with the seismic

events noted above. Today, shear walls and special moment resisting frames are commonly incorporated in seismic design of multi-storey buildings.

Incorporating shear walls to resist seismic actions requires the engineer to become aware of the potential failure mechanisms, and to be able to control some of the undesired characteristics. An earthquake-resisting shear wall structure should ensure survival during the largest ground shaking that can be expected. It should also protect components of a building against all but superficial damage during more frequent disturbances of smaller intensity. Proper detailing will ensure structural survival through energy dissipation by hysteretic damping. Paulay[28] was one of the first researchers to provide a design philosophy for shear walls including desirable energy dissipation and potential failure mechanism. A review of his findings follows; however, it is important to note that ideas about designing structural walls have changed in the past 25 years.

Flexural Yielding

Yielding of the flexural reinforcement is a good source of hysteretic damping. In cantilever walls, yielding can be restricted to the base of the wall; therefore, this area requires added attention in detailing. Concrete, however, being a brittle material, should not normally be considered as a significant contributor to the energy dissipation. To ensure the desired ductility, the internal forces in the potential plastic hinge region should be allocated to the reinforcement.

Shear Distortions

Shear resistance after inelastic shear displacements can be attained only when the subsequent imposed displacement is larger than the largest previously encountered displacement. The detrimental effect of shear increases with the magnitude of the shear

stresses, the reduction of the axial compression on the wall section, and the reduction of the height-to-length ratio of the wall.

Limited Ductility

Shear walls with a low height-to-width ratio have more difficulty developing the required energy dissipation owing to the fact that large shear stresses will develop even with a small amount of flexural reinforcement. The reduction in energy dissipation must be recognized and less reliance must be placed on hysteretic damping. The inelastic shear displacements associated with shear sliding across the critical base section can significantly reduce the energy dissipation with progressive cycling of squat walls.

Foundations

Shear walls are cantilever structures; therefore, the critical region is normally the base of the wall. The foundations must be capable of resisting the associated overturning moment if the energy dissipation has been assigned to plastic hinges.

Stability

The danger of premature failure by instability of the section occurs when part of a thin wall section is subjected to large compressive strains. The problem is compounded when cyclic inelastic deformations occur. The use of compact wall sections has been suggested to alleviate the problem.

Confinement

For large compressive zones, the use of confining reinforcement is highly effective to enhance both the compression strain capacity and compression strength of the concrete core.

Failure Modes

The common mode of shear failure is diagonal tension. This is controlled with the use of web reinforcement. Diagonal compression failure of the web wall may occur when large amounts of web reinforcement are required to resist high shear stresses. During reversed cyclic loading, the compression strength of the web is considerably reduced by intersecting diagonal cracks. Near horizontal failure planes may develop in plastic hinge zones along interconnecting cracks. This may lead to a sliding shear failure. Horizontal construction joints may also present a potential weakness.

Diagonal Tension

Shear forces may be transferred across a potential diagonal failure plane by aggregate interlock, by the uncracked flexural compression zone, and by dowel action of the longitudinal reinforcement. These mechanisms, which form part of the concrete contribution, degrade under reversed cyclic loading involving yielding of the flexural reinforcement. In the absence of significant axial compression, it is advisable that the entire design shear force should be resisted by the web reinforcement in potential plastic hinge regions.

Sliding Shear

Sliding shear is the largest single cause for both stiffness and strength degradation in plastic zones. The effects increase with nominal shear stresses, and with reduction of axial compression and with height-to-width ratio of the wall. Effective control of sliding can be conveniently achieved by the use of diagonal reinforcement.

Detailing

Proper and careful detailing of earthquake resisting shear walls is crucial. The boundary zones, when subjected to large compressive strains, require attention. Detailing should consider the full structural interaction of the boundary elements with the web wall, the principal vertical reinforcement should not buckle, and a sufficient area of compressed concrete should be satisfactorily confined against expansion due to large compressive strains.

Squat shear walls are characterized with a height-to-length ratio of less than 2 and have been extensively used in low-rise buildings as seismic load resisting elements. They have also been incorporated into high-rise structures to contribute to the lateral load resistance over the first few stories of a foundation. Squat shear walls typically demonstrate little energy dissipation through their hysteretic behaviour under seismic events. The response of low height-to-length ratio walls is dominated by the strength and ductility of the concrete. The reinforcement typically experiences little yielding prior to concrete crushing. Under seismic loading, more energy dissipation is usually required to ensure the structures perform satisfactorily. Paulay, Priestley, and Synge[29] have investigated the possibilities of achieving acceptable levels of energy dissipation in squat shear walls, mainly by flexural yielding of the reinforcement. Shear failures originating from diagonal tension or compression failure show limited ductility and dramatic degradation in strength and stiffness. For this reason, a more ductile flexural response is desired.

The researchers conducted an experimental program of four squat shear walls with a height-to-length ratio of 0.5. Two of the specimens had rectangular cross sections and

the remaining included small flanges at the end of a central web wall. A rigid foundation was used to clamp the specimens to the laboratory floor, and a stiff top slab ensured an even distribution of the imposed displacements to the wall. Figure 2.14 is a typical test specimen (dimensions in mm).

Two complete cycles at 1, 2, 4, 6, and 8 multiples of the yield displacement were imposed on the shear walls. One rectangular wall and one flanged wall section were reinforced with diagonal reinforcement extending the full height of the wall section. The diagonal reinforcement was anchored into the top and bottom slab.

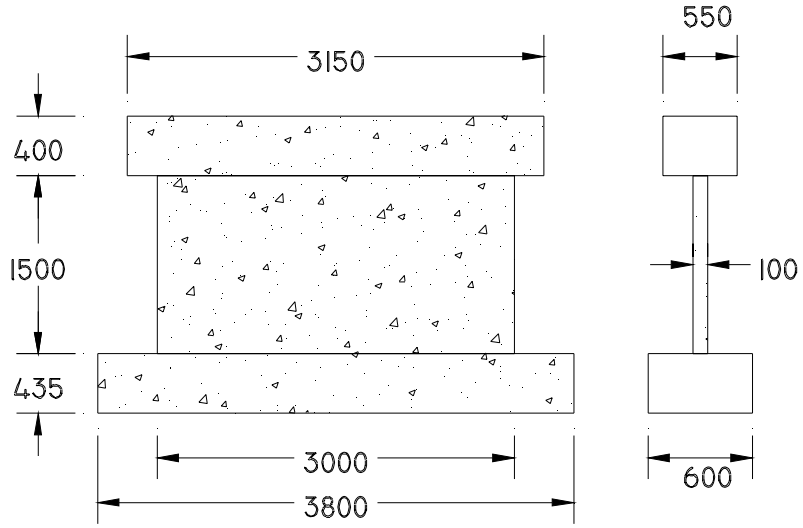

Figure 2.14 Typical Test Unit of Paulay, Priestley, and Synge

The following observations, based on the experimental findings, were reported:

1. It is possible to ensure a predominately flexural response, involving considerable yielding of the flexural reinforcement, for squat shear walls subjected to seismic loading.

2. Suppression of shear failure by diagonal tension or compression is a prerequisite for a flexural response and hence, significant energy dissipation.
3. Squat shear walls are likely to fail due to sliding shear along the base unless specially detailed or subjected to high axial loading. Sliding shear results in the most significant loss of stiffness and strength.
4. Flanged walls are more seriously affected by sliding shear along interconnecting flexural cracks.
5. Diagonal reinforcement considerably improves the seismic response of squat shear walls.
6. The severity of sliding shear increases with increased ductility demand, with decreasing vertical reinforcement, and with a decrease of the flexural compression zone.

2.2.2 Benchmark Structures

The Portland Cement Association (PCA) series of wall tests are widely regarded as benchmarks against which theoretical formulations are calibrated [23, 30]. The specimens represented a one-third-scale model of a five-storey building. The design moment was calculated following the procedures in the ACI building code, and the horizontal shear reinforcement was selected to develop the design moment. The wall series consisted of three wall sections: rectangular, barbell, and flanged. Figure 2.15 shows the dimensions of a typical barbell wall specimen.

Two load histories were used for the specimens: incrementally increasing reversed, and modified reversed. The incrementally increasing reversed loading history consisted of a series of load increments with three complete cycles per displacement level. The

modified reversed loading history was selected from analytical results of dynamic responses of many walls subjected to a wide range of different earthquakes.

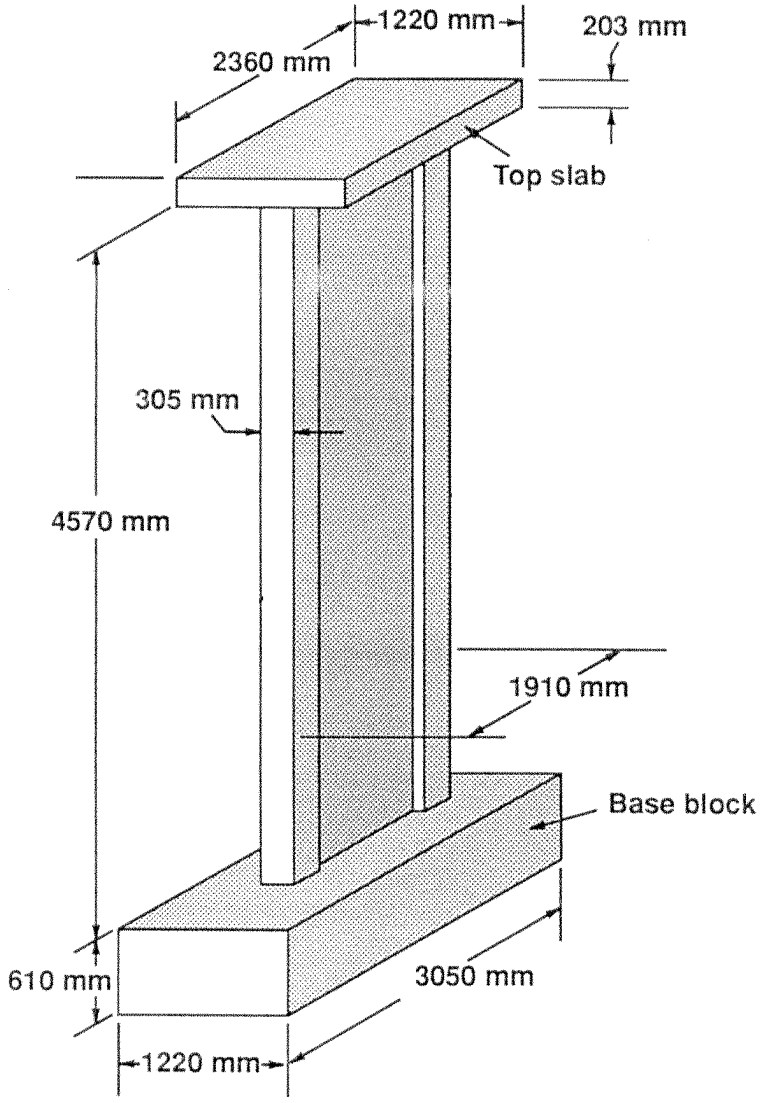

Figure 2.15 Nominal Dimensions of PCA Test Specimen, taken from Oesterle, Fiorato, Johal, Carpenter, Russel, and Corley[30]

Variables of testing included: axial stress, concrete strength, shape, confinement of the boundary elements, and amount of horizontal shear reinforcement. Of the three shapes

tested, only flanged and barbell shaped specimens exhibited web crushing. As large inelastic displacements were applied, one or more of the compressive struts crushed. Crushing usually occurred in the compressive struts that intersected the compression boundary element at the wall base. Load carried by crushed struts was transferred to higher or lower struts depending on the stiffness of the boundary element. As load was transferred, additional struts crushed thus progressively forming either a horizontal or vertical failure plane. In all specimens, web crushing occurred only after significant flexural and shear yielding had taken place. The test results indicated that web crushing is a potential limit on the capacity of structural walls subjected to inelastic load reversals. It is dependent on the magnitude of shear stress and the level of deformation.

Another series of wall tests commonly used to corroborate analytical models are the SW series tested by Pilakoutas and Elnashai[31]. A total of nine walls were tested under severe cyclic loading regimes. Three of the walls (SW1-SW3) were 1:5 scale models, while walls SW4-SW9 were 1:2.5 scale models. A typical test specimen for the SW4-SW9 series is shown in Figure 2.16. Displacements were imposed along the top slab in increments of 2 mm, consisting of two full cycles per displacement level. The shear reinforcement in the web walls was varied to investigate the effect of various degrees of safety margins in shear. Concentrated reinforcement in the boundary elements was used to maximize the flexural capacity, and the web vertical reinforcement was kept nominal. The confinement of the boundary elements varied as a consequence of the variation in shear reinforcement.

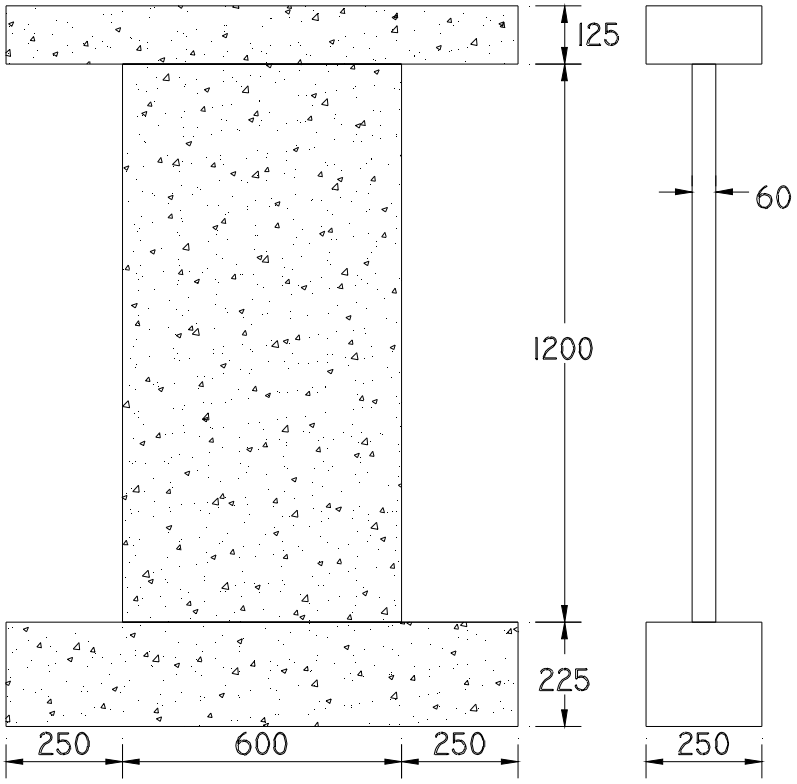

Figure 2.16 Dimensions for SW Series

The researchers reported some of the following observations:

1. Failure mode depended mainly on the amount and distribution of the shear reinforcement.
2. The strength and deformational characteristics of the specimens were not affected significantly by shear reinforcement in excess of the amount required to resist the maximum applied load.
3. Shear force was partly transmitted by the concrete in compression and partly by the horizontal (link) reinforcement that enables shear stresses to be resisted through the concrete in the tensile zone. Failure occurred after yielding of the links, and when the shear resistance of concrete in compression was exceeded.

4. Concrete dilation following cracking caused the extension of the wall in both the longitudinal and lateral directions.
5. Significant extension of the wall in the vertical direction took place following yield due to the accumulation of irrecoverable strains mainly within the plastic hinge zone.

An objective of this research project is to complement the literature with tests on squat shear walls whose deformational characteristics are highly influenced by the performance of the concrete. The PCA and SW walls series were more influenced by flexural effects, and failure ultimately occurred after yielding of the flexural reinforcement. Thus, the hysteretic behaviour of these walls was controlled by the response of the reinforcement. Other key components of this research include the effects of flange walls and axial load.

CHAPTER 3

Finite Element Formulation

3.1 BACKGROUND

In recent years the finite element method has become a very useful and powerful tool in the design and analysis of reinforced concrete structures. Research developments have produced differing approaches in stiffness formulation (tangent stiffness versus secant stiffness), constitutive modeling, and element preference. It has generally been perceived that formulations using higher order elements are preferable, and there has been a tendency to favour the tangent stiffness method. Research at the University of Toronto has demonstrated that the use of a secant stiffness approach utilizing many elements of the lowest order finite element is a viable alternative, yielding excellent accuracy against experimental results. It has long been thought that the secant stiffness approach cannot be effectively used to analyze structures subjected to cyclic loading conditions. The following sections will describe how a secant stiffness-based algorithm can be modified to incorporate general loading using the compatibility, equilibrium, and constitutive formulations of the Modified Compression Field Theory (MCFT).

3.2 MODIFIED COMPRESSION FIELD THEORY

The Modified Compression Field Theory was developed over twenty years ago to replicate the true behaviour of cracked reinforced concrete elements subjected to in-plane

forces. It is a fully rotating smeared crack model that represents concrete as an orthotorpic material. Equilibrium, compatibility, and stress-strain relationships are formulated in terms of average stresses and average strains. Local stress conditions at cracks are also examined. In the formulation, cracked concrete is treated as a new orthotropic material with its own stress-strain characteristics. Central to the theory is the assumption that directions of principal stress and principal strains remain coincident. Compression softening accounting for the reduced compressive strength of concrete in the presence of large transverse tensile strains is quantified. Also, a tension stiffening formulation is proposed to represent the presence of post-cracking tensile stresses in the concrete between cracks.

In formulating the theory, the MCFT assumed the following conditions:

1 Element loads are uniformly distributed.

2 Reinforcement is smeared across the element uniformly.

3 Cracks are smeared and allowed to rotate.

4 Formulations are based on average stresses and average strains.

5 Direction of principal stress coincides with direction of principal strain.

6 The total stress state is a function of the total strain state and is independent of load history.

7 Bond slip between the reinforcement and concrete is ignored.

8 The amount of concrete tensile stress transmitted across cracks is a function of the reserve strength of the reinforcement at the cracks.

An element, as shown in Figure 3.1, is taken to be of uniform thickness, and contains an orthogonal grid of reinforcement. Loads acting on the element's edge planes

are assumed to consist of uniform axial stresses σ_x, σ_y and uniform shear stress τ_{xy}. The deformed shape is defined by two normal strains ε_x, ε_y and a shear strain γ_{xy}.

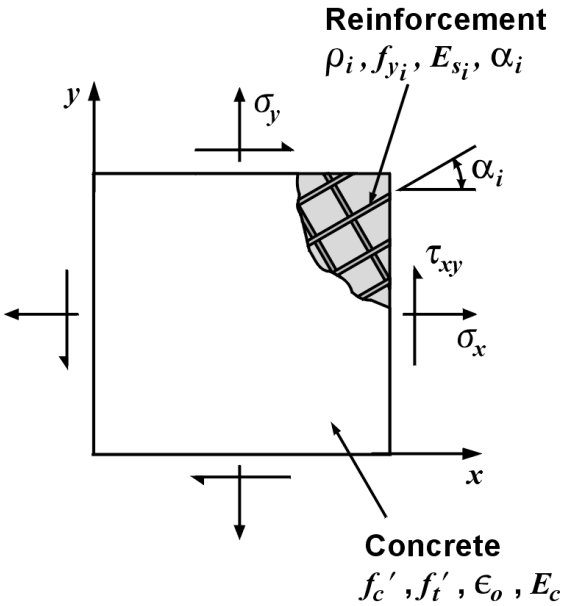

Figure 3.1 Membrane Element, taken from Vecchio[5]

3.2.1 Compatibility Conditions

Compatibility requires that any deformation experienced by the concrete must be matched by an identical deformation of the reinforcement. The MCFT, therefore, assumes that the reinforcement is perfectly anchored to the concrete, and any change in concrete strain is accompanied by an equal change in the reinforcement as follows:

$$\varepsilon_{sx} = \varepsilon_{cx} = \varepsilon_x \tag{3.1}$$

and

$$\varepsilon_{sy} = \varepsilon_{cy} = \varepsilon_y \tag{3.2}$$

where ε_{sx}, ε_{cx}, and ε_x are the average strains in the reinforcement, concrete, and element in the x-direction, respectively. ε_{sy}, ε_{cy}, and ε_y are the average strains in the

reinforcement, concrete, and element in the y-direction. The relations establish a link between the external deformations and the element strains.

If the three element strains ε_x, ε_y, and γ_{xy} are known, then a Mohr's circle of strain (Figure 3.2) can be used to summarize the strains experienced by the element in its principal directions.

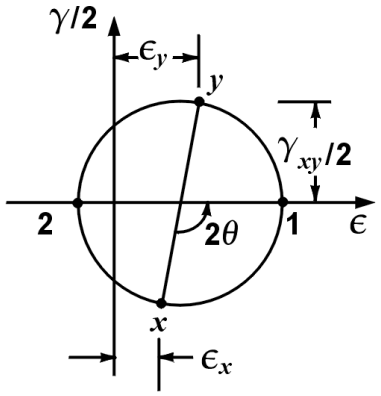

Figure 3.2 Compatibility Relations, taken from Vecchio[5]

The formulations are as follows:

$$\varepsilon_1 = \frac{\varepsilon_x + \varepsilon_y}{2} + \frac{1}{2}\left[\left(\varepsilon_x - \varepsilon_y\right)^2 + \gamma_{xy}{}^2\right]^{\frac{1}{2}} \tag{3.3}$$

$$\varepsilon_2 = \frac{\varepsilon_x + \varepsilon_y}{2} - \frac{1}{2}\left[\left(\varepsilon_x - \varepsilon_y\right)^2 + \gamma_{xy}{}^2\right]^{\frac{1}{2}} \tag{3.4}$$

$$\theta = \tfrac{1}{2}\arctan\left[\frac{\gamma_{xy}}{\varepsilon_y - \varepsilon_x}\right] \tag{3.5}$$

where ε_1 is the average principal tensile strain, ε_2 is the average principal compressive strain, and θ is the inclination of the principal strains.

3.2.2 Equilibrium Relations

Forces applied to the element are resisted by internal stresses in the concrete and in the reinforcement. Equilibrium is satisfied by the following expressions for the case where the reinforcement is orthogonal and aligned with the reference axes:

$$\sigma_x = f_{cx} + \rho_x \cdot f_{sx} \tag{3.6}$$

$$\sigma_y = f_{cy} + \rho_y \cdot f_{sy} \tag{3.7}$$

$$\tau_{xy} = \upsilon_{cxy} \tag{3.8}$$

where f_{cx} and f_{cy} are the average stresses in the concrete in the x- and y-directions, respectively, and v_{cxy} is the average shear stress in the concrete. f_{sx} and f_{sy} are the average stresses in the reinforcement, and ρ_x and ρ_y are the reinforcement ratios in the x- and y-directions. A Mohr's circle of stress, as shown in Figure 3.3, is used to determine the stress conditions in the element.

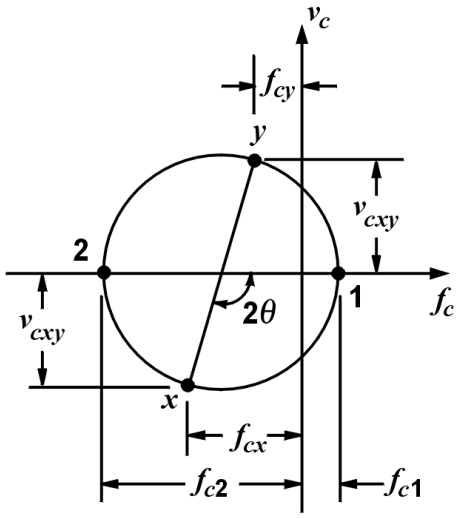

Figure 3.3 Equilibrium Relations, taken from Vecchio[5]

From Mohr's circle, the stresses in the concrete are calculated as:

$$f_{cx} = f_{c1} - v_{cxy} / \tan\theta_c \tag{3.9}$$

$$f_{cy} = f_{c1} - v_{cxy} \tan\theta_c \tag{3.10}$$

where f_{c1} is the average principal tensile stress, and θ_c is the inclination of principal stresses.

The inclusion of tensile stresses in the concrete makes it necessary to check that these stresses can be transmitted across the cracks. In order to transmit the average principal tensile stress due to tension stiffening between cracks, local increases in the reinforcement stresses are necessary at the cracks. The magnitude that can be transmitted is limited by the reserve capacity of the reinforcement, and is determined from:

$$f_{c1} \le \sum_{i=1}^{n} \rho_i \left(f_{yi} - f_{si}\right) \cos^2 \theta_{ni} \tag{3.11}$$

where ρ_i is the reinforcement ratio, f_{si} is the average stress, and f_{yi} is the yield stress for the *i*-th reinforcement component. θ_{ni} is the difference between the angle of orientation of the reinforcement and the normal to the crack surface.

It is also important to note that local increases in reinforcement stresses, at crack locations, leads to the development of shear stresses along the crack surfaces. Equilibrium requirements suggest the following relation for the shear stress:

$$v_{ci} = \sum_{i=1}^{n} \rho_i \left(f_{scri} - f_{si}\right) \cos\theta_{ni} \cdot \sin\theta_{ni} \tag{3.12}$$

where v_{ci} is the shear stress along the crack surface, and f_{scri} is the local stress in the reinforcement.

Theoretically, a maximum shear stress exists that can be resisted on the crack, and was given by Vecchio and Collins[4] as:

$$v_{ci\max} = \frac{\sqrt{f_c'}}{0.31 + \frac{24w}{a+16}} \tag{3.13}$$

where $v_{ci\max}$ is the maximum shear stress possible on a crack surface, a is the maximum aggregate size (mm), and w is the crack width. Slip along the crack surface results if the maximum shear stress is exceeded. However, slip along the crack was not incorporated into the Modified Compression Field Theory. Initially, the theory calculated the shear stress across the crack surface using the following relationship, which was derived from work conducted by Walraven[32]:

$$v_{ci} = 0.18v_{ci\max} + 1.64f_{ci} - 0.82\frac{f^2_{ci}}{v_{ci\max}} \tag{3.14}$$

where f_{ci} is the compressive stress on the crack surface. If the maximum shear stress is exceeded, the MCFT responds by reducing the average tensile stress that can be transmitted across cracks.

The local reinforcement stresses are determined to satisfy the equilibrium condition that the average concrete tensile stresses must be transmitted across the crack, and is computed from:

$$\sum_{i=1}^{n} \rho_i (f_{scri} - f_{si}) \cos^2 \theta_{ni} = f_{c1} \tag{3.15}$$

3.2.3 Constitutive Relations

Constitutive relationships are required to link the average stresses to the average strains for both the reinforcement and the concrete.

The compression response curve of cracked concrete considers a pre-peak and a post-peak branch and is modeled by Hognestad's[33] parabola, which is sufficiently accurate for most applications. The response is described as:

$$f_{c2} = f_p\left[2\left(\varepsilon_2 \big/ \varepsilon_p\right) - \left(\varepsilon_2 \big/ \varepsilon_p\right)^2\right] \text{if} \varepsilon_p < \varepsilon_{c2} < 0 \tag{3.16}$$

$$f_{c2} = f_p\left[1 - \left(\frac{\varepsilon_{c2} - \varepsilon_p}{-2\varepsilon_o - \varepsilon_p}\right)^2\right] \quad \text{if } -2\varepsilon_o < \varepsilon_{c2} < \varepsilon_p \tag{3.17}$$

where f_{c2} and ε_{c2} are the principal compressive stress and strain, f_p and ε_p are the peak compressive stress and the corresponding strain, and ε_o is the strain corresponding to the peak cylinder stress. The peak compressive stress and strain include softening effects caused by the co-existing principal tensile strains and computed as:

$$f_p = -\beta \cdot f_c' \tag{3.18}$$

$$\varepsilon_p = -\beta \cdot \varepsilon_o \tag{3.19}$$

where

$$\beta = 0.35\left(-\varepsilon_1 \big/ \varepsilon_2 - 0.28\right)^{0.8} \tag{3.20}$$

Concrete in tension includes a linear response prior to cracking and a post-cracking response known as tension stiffening. The pre-cracking response is modeled as:

$$f_{c1} = E_c \varepsilon_{c1} \qquad \text{if } 0 < \varepsilon_{c1} < \varepsilon_{cr} \tag{3.21}$$

where

$$\mathrm{E_c} = 2\frac{f_c'}{\varepsilon_o} \tag{3.22}$$

$$\varepsilon_{cr} = \frac{f_t'}{E_c} \tag{3.23}$$

E_c is the initial tangent compressive modulus, ε_{cr} is the cracking strain, ε_{c1} is the principal tensile strain due to stress, and f_t' is the cracking stress. The cracking stress of concrete is based on recent experience with aggregates from the Toronto area, which is described by the following expression:

$$f_t' = 0.65\left(f_c'\right)^{0.33} \tag{3.24}$$

The post-cracking tensile stresses that arise from the interactions between the reinforcement and concrete is computed from:

$$f_{c1} = \frac{f_t'}{1+\sqrt{C_t \varepsilon_{c1}}} \tag{3.25}$$

where C_t is taken as 200 for relatively small elements, or elements containing a closely spaced mesh of reinforcement. For larger-scale elements, $C_t = 500$ is used.

A tri-linear stress-strain relation is used to model the response of reinforcement in tension or compression, given by:

$$f_s = E_s \varepsilon_s \qquad \text{if } 0 < \varepsilon_s < \varepsilon_y \tag{3.26}$$

$$f_s = f_y \qquad \text{if } \varepsilon_y < \varepsilon_s < \varepsilon_{sh} \tag{3.27}$$

$$f_s = f_y + E_{sh}\left(\varepsilon_s - \varepsilon_{sh}\right) \qquad \text{if } \varepsilon_{sh} < \varepsilon_s < \varepsilon_u \tag{3.28}$$

$$f_s = 0 \qquad \text{if } \varepsilon_s > \varepsilon_u \tag{3.29}$$

where f_s is the stress, f_y is the yield strength, E_s is the modulus of elasticity, E_{sh} is the strain hardening modulus, ε_y is the yield strain, ε_{sh} is the strain at the onset of strain hardening, and ε_u is the ultimate strain.

The compatibility, equilibrium, and constitutive relations of the MCFT have been implemented into nonlinear finite elements programs for reinforced concrete, and have demonstrated excellent agreement with experimental results[1, 2, 6].

3.3 CYCLIC LOAD MODELING

A secant stiffness-based finite element algorithm based on the compatibility, equilibrium, and constitutive formulations of the MCFT was recently provisionally modified to allow analysis capability for cyclic loading conditions. The constitutive relations for the concrete and reinforcement were expanded to account for cyclic loading. Plastic offset strains were defined for concrete and reinforcement and were incorporated into the analysis through the use of prestrain forces. The elastic components of strain were used to define the effective secant stiffness, and Mohr's circle techniques were used to track strains experienced during previous loading. Analysis of shear walls has shown that the procedure used is stable and compliant and has potential to provide accurate simulations of behaviour[3].

3.3.1 Plastic Offset Formulation

The basis for modifying a secant stiffness-based algorithm to provide the capability of analyzing cyclic loading conditions is in the handling of plastic offset strains. The plastic strains must be treated as a strain offset, similar to elastic offsets resulting from thermal expansion, shrinkage, or other prestrain effects[3]. Working in the principal stress and principal strain directions, the total strain can be considered to consist of an elastic component and a plastic component, such that:

$$\varepsilon_c = \varepsilon_c^e + \varepsilon_c^p \tag{3.30}$$

where ε_c is the total strain in the concrete, ε_c^e is the elastic strain component, and ε_c^p is the plastic strain component. The effective secant stiffness is then determined from the elastic strain component according to the following:

$$\overline{E}_c = \frac{f_c}{\varepsilon_c^e} \tag{3.31}$$

where $\overline{E}_c$ is the effective secant stiffness and f_c is the current stress in the concrete. Figure 3.4 is a representation of the elastic and plastic components of the concrete strain.

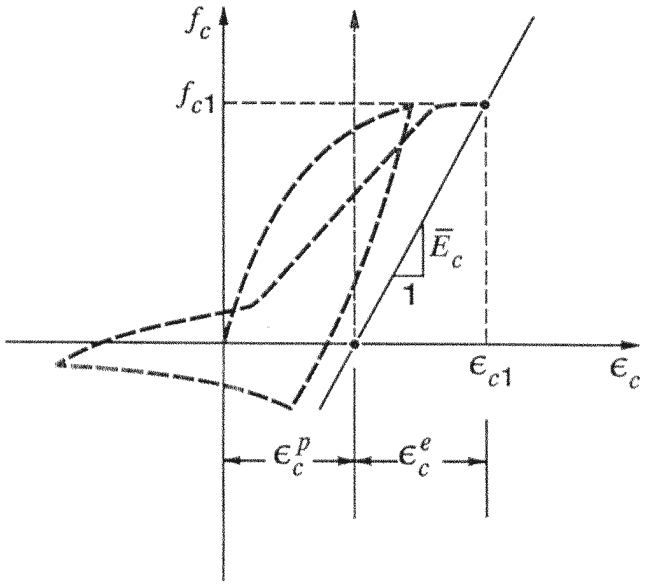

Figure 3.4 Concrete Strain Components, taken from Vecchio[3]

The plastic offsets in the principal directions are resolved into components relative to the reference axes, giving the following vector:

$$\left[\varepsilon_c^p\right] = \begin{bmatrix} \varepsilon_{cx}^p \\ \varepsilon_{cy}^p \\ \gamma_{cxy}^p \end{bmatrix} \tag{3.32}$$

where ε_{cx}^p and ε_{cy}^p are the plastic strains in the x- and y-directions, and γ_{cxy}^p is the shear strain component of the plastic offset. Free joint displacements as functions of the element geometry are determined from the plastic prestrains. The prestrain nodal forces are then computed using the effective stiffness due to the concrete component.

The plastic offsets in the reinforcement are handled in a similar manner. The vector of plastic strains in the reinforcement is:

$$\left[\varepsilon_s^p\right]_i = \begin{bmatrix} \varepsilon_{si}^p \cdot \left(1+\cos 2\alpha_i\right)/2 \\ \varepsilon_{si}^p \cdot \left(1-\cos 2\alpha_i\right)/2 \\ \varepsilon_{si}^p \cdot \sin 2\alpha_i \end{bmatrix} \tag{3.33}$$

where ε_{si}^p is the reinforcement plastic offset, and α_i is the orientation of the reinforcement. The secant stiffness for the reinforcement is computed from:

$$\overline{E}_{si} = \frac{f_{si}}{\varepsilon_{si}^e} \tag{3.34}$$

where $\overline{E}_{si}$ is the effective secant stiffness, and ε_{si}^e is the elastic strain component of the total strain.

The total nodal forces, arising from plastic offsets, consists of the sum of the concrete and the reinforcement contributions. These are added to prestrain forces caused from elastic prestrain effects.

3.3.2 Concrete Plastic Offset Envelope

The procedure requires that the plastic strains occurring in the concrete be retained and defined under rotation of the principal axes. A Mohr's circle is employed to track the plastic offsets in the principal directions as follows:

$$\varepsilon_{c1}^p = \frac{\varepsilon_{cx}^p + \varepsilon_{cy}^p}{2} + \frac{\varepsilon_{cx}^p - \varepsilon_{cy}^p}{2}\cos 2\theta + \frac{\gamma_{cxy}^p}{2}\sin 2\theta \tag{3.35}$$

$$\varepsilon_{c2}^p = \frac{\varepsilon_{cx}^p + \varepsilon_{cy}^p}{2} - \frac{\varepsilon_{cx}^p - \varepsilon_{cy}^p}{2}\cos 2\theta + \frac{\gamma_{cxy}^p}{2}\sin 2\theta \tag{3.36}$$

where ε_{c1}^{p} and ε_{c2}^{p} are the principal plastic strain components. Further plastic straining is accounted for by increments in plastic straining in the principal directions. The envelope of plastic strains relative to the reference axes is updated as follows:

$$\varepsilon_{cx}^{p'} = \varepsilon_{cx}^{p} + \frac{\Delta\varepsilon_{c1}^{p}}{2}(1+\cos 2\theta) + \frac{\Delta\varepsilon_{c2}^{p}}{2}(1-\cos 2\theta) \tag{3.37}$$

$$\varepsilon_{cy}^{p'} = \varepsilon_{y}^{p} + \frac{\Delta\varepsilon_{c2}^{p}}{2}(1-\cos 2\theta) + \frac{\Delta\varepsilon_{c2}^{p}}{2}(1+\cos 2\theta) \tag{3.38}$$

$$\gamma_{cxy}^{p'} = \gamma_{cxy}^{p} + \Delta\varepsilon_{c1}^{p} \cdot \sin 2\theta - \Delta\varepsilon_{c2}^{p} \cdot \sin 2\theta \tag{3.39}$$

where $\Delta\varepsilon_{c1}^{p}$ and $\Delta\varepsilon_{c2}^{p}$ are the increments in the plastic strains in the principal directions.

3.3.3 Maximum Concrete Strains

The common approach to modeling cycling loading is to link the unloading and reloading branches to the backbone curve, which requires knowledge of the maximum strains previously attained. In calculating the maximum strains, rotation of the principal strains must be considered and is handled elegantly by Mohr's circle. The maximum compressive strains in the principal directions are given by:

$$\varepsilon_{cm1} = \frac{\varepsilon_{cmx} + \varepsilon_{cmy}}{2} + \frac{\varepsilon_{cmx} - \varepsilon_{cmy}}{2} \cdot \cos 2\theta + \frac{\gamma_{cmxy}}{2} \cdot \sin 2\theta \tag{3.40}$$

$$\varepsilon_{cm2} = \frac{\varepsilon_{cmx} - \varepsilon_{cmy}}{2} + \frac{\varepsilon_{cmx} - \varepsilon_{cmy}}{2} \cdot \cos 2\theta - \frac{\gamma_{cmxy}}{2} \cdot \sin 2\theta \tag{3.41}$$

where ε_{cm1} and ε_{cm2} are the maximum principal compressive strains, and ε_{cmx}, ε_{cmy}, and γ_{cmxy} are the maximum compressive strains relative to the x- and y-axes. The maximum strains are updated when the current total compressive strains in the principal directions exceed those previously recorded. Therefore, the strain increments are the difference

between the current strains less the previous maximum strain, and the increments are taken as zero when the current strain does not exceed the previous maximum strain. The maximum strains relative to the x- and y-axes are updated as follows:

$$\varepsilon'_{cmx} = \varepsilon_{cmx} + \frac{\Delta\varepsilon_{cm1}}{2}(1+\cos 2\theta) + \frac{\Delta\varepsilon_{cm2}}{2}(1-\cos 2\theta) \tag{3.42}$$

$$\varepsilon'_{cmy} = \varepsilon_{cmy} + \frac{\Delta\varepsilon_{cm2}}{2}(1-\cos 2\theta) + \frac{\Delta\varepsilon_{cm2}}{2}(1+\cos 2\theta) \tag{3.43}$$

$$\gamma'_{cmxy} = \gamma_{cmxy} + \Delta\varepsilon_{cm1} \cdot \sin 2\theta - \Delta\varepsilon_{cm2} \cdot \sin 2\theta \tag{3.44}$$

where $\Delta\varepsilon_{cm1}$ and $\Delta\varepsilon_{cm2}$ are the maximum principal strain increments. A similar approach is used to determine the maximum tensile strains in the concrete.

3.3.4 Constitutive Models For Concrete

The unloading and reloading rules proposed by Vecchio[3] were temporary and employed to demonstrate the analysis capability of a secant stiffness-based algorithm under conditions of cyclic loading. Simple linear responses were adopted for unloading/reloading in both compression and tension.

For compression either the Hognestad[33] or Popovics[16] monotonic response curve can be used to represent the backbone curve and is modified to account for the effects of compression softening and confinement. Figure 3.5 illustrates the compressive response of concrete.

The plastic strain, which defines the slope for both unloading and reloading, is calculated from:

$$\varepsilon_c^p = \varepsilon_c - \varepsilon_p \left[0.87\left(\frac{\varepsilon_c}{\varepsilon_p}\right) - 0.29\left(\frac{\varepsilon_c}{\varepsilon_p}\right)^2 \right] \text{ if } \varepsilon_c > 1.5\varepsilon_p \tag{3.45}$$

$$\varepsilon_c^p = \varepsilon_c - 0.001305\left(\frac{\varepsilon_p}{0.002}\right) \qquad \text{if } \varepsilon_c < 1.5\varepsilon_p \tag{3.46}$$

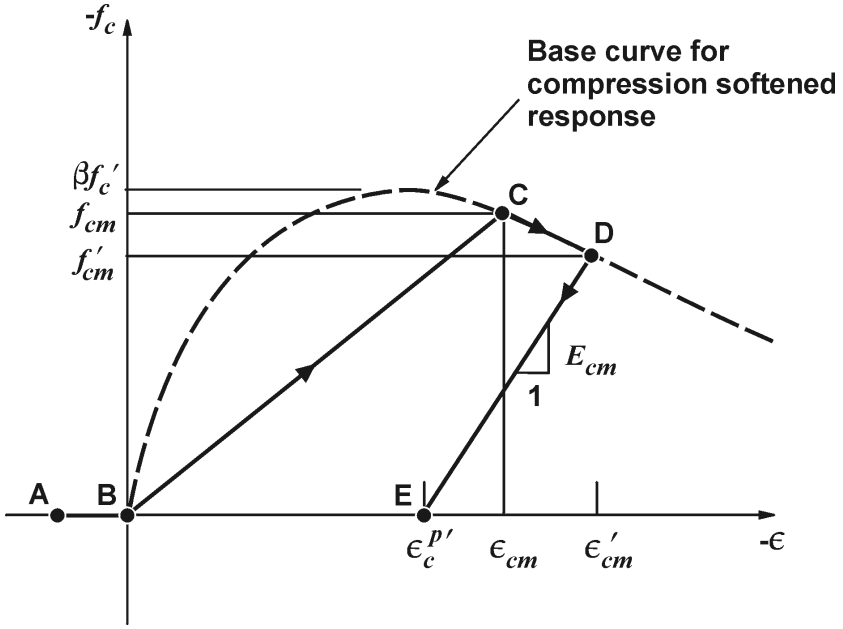

Figure 3.5 Hysteresis Model for Concrete in Compression, taken from Vecchio[3]

The unloading branch produces stresses according to the following relation:

$$f_c(\varepsilon_c) = E_{cm}\left(\varepsilon_c - \varepsilon_c^p\right) \tag{3.47}$$

where

$$E_{cm} = \frac{f_{cm}}{\left(\varepsilon_{cm} - \varepsilon_c^p\right)} \tag{3.48}$$

$f_c(\varepsilon_c)$ is the current stress determined by the unloading model, E_{cm} is the unloading modulus, ε_{cm} is the maximum compression strain attained during previous loading, and f_{cm} is the stress corresponding to ε_{cm}.

The concrete compressive stress on a reloading cycle is calculated as:

$$f_c(\varepsilon_c) = \left(\varepsilon_c - \varepsilon_c^p\right)\frac{f_{cm}}{\left(\varepsilon_{cm} - \varepsilon_c^p\right)} \quad \text{if } \varepsilon_c^p > \varepsilon_c > \varepsilon_{cm} \tag{3.49}$$

$$f_c(\varepsilon_c) = f_{bc}(\varepsilon_c) \qquad \text{if } \varepsilon_c < \varepsilon_{cm} \qquad (3.50)$$

where $f_{bc}(\varepsilon_c)$ is the stress calculated from the base curve.

Implicit in the compression model is the assumption that the compressive stresses remain zero until the cracks completely close. This is at odds with experimental evidence. Upon unloading in tension, cracked surfaces will re-contact at strains greater than zero, thus causing compressive stresses to form while the total strains are tensile.

As shown in Figure 3.6, the tension response considers the pre-cracked response and the tension- stiffened response.

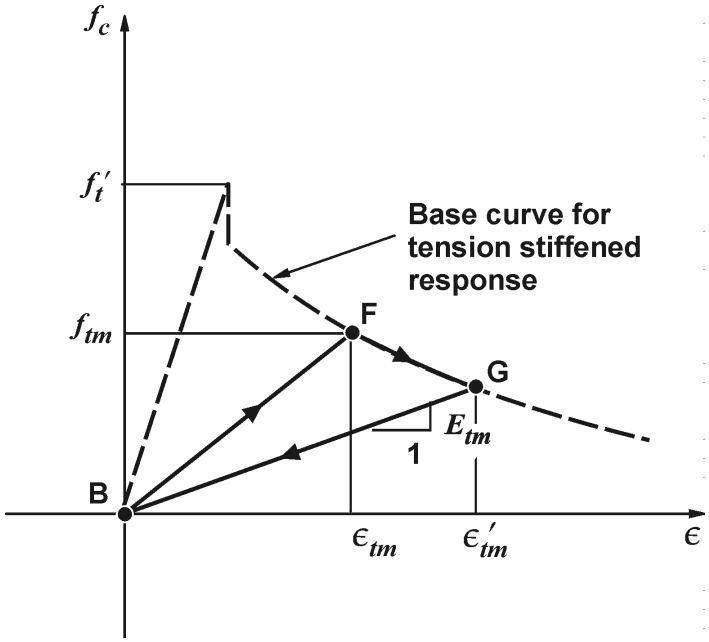

Figure 3.6 Hysteresis Model for Concrete in Tension, taken from Vecchio[3]

The reloading response is calculated by the following two expressions:

$$f_c(\varepsilon_c) = \frac{(\varepsilon_c - \varepsilon_c^p)}{(\varepsilon_{tm} - \varepsilon_c^p)} \cdot f_{tm} \qquad \text{if } \varepsilon_c^p < \varepsilon_c < \varepsilon_{tm} \qquad (3.51)$$

$$f_c(\varepsilon_c) = f_{bt}(\varepsilon_c) \qquad \text{if } \varepsilon_c > \varepsilon_{tm} \qquad (3.52)$$

where ε_{tm} is the maximum tensile strain attained during previous loading, f_{tm} is the stress corresponding to ε_{tm}, and $f_{bt}(\varepsilon_c)$ is the stress calculated from the base curve.

Stresses during unloading are computed from:

$$f_c(\varepsilon_c) = E_{tm}(\varepsilon_c - \varepsilon_c^p) \tag{3.53}$$

where

$$E_{tm} = \frac{f_{tm}}{(\varepsilon_{tm} - \varepsilon_c^p)} \tag{3.54}$$

E_{tm} is the unloading modulus.

Implicit in the tension response is that the base curve is shifted such that it coincides with the plastic offset calculated from the compression regime. Also, no plastic offsets are considered in the tension response; therefore, the unloading and reloading branches pass through the origin.

3.3.5 Constitutive Models for Reinforcement

The monotonic response of the reinforcement is assumed to be tri-linear. The initial response is linear elastic, followed by a yield plateau, and ending with a strain-hardening portion. The hysteretic response of the reinforcement has been modeled after Seckin[21], and the Bauschinger effect is represented by a Ramberg-Osgood formulation illustrated in Figure 3.7.

As with the concrete response, the monotonic response curve is assumed to represent the base curve. The unloading portion of the response follows a linear path and is given by:

$$f_s(\varepsilon_i) = f_{s-1} + E_r(\varepsilon_i - \varepsilon_{s-1}) \tag{3.55}$$

where $f_s(\varepsilon_i)$ is the stress at the current strain of ε_i, f_{s-1} and ε_{s-1} are the stress and strain from the previous load step, and E_r is the unloading modulus.

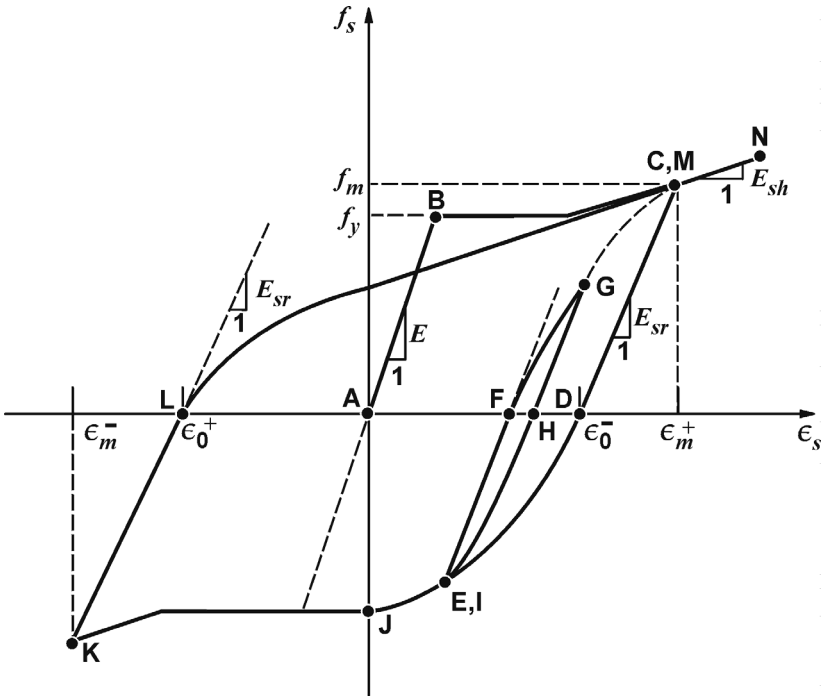

Figure 3.7 Hysteresis Model for Reinforcement, taken from Vecchio[3]

The unloading modulus E_r is calculated from:

$$E_r = E_s \qquad \text{if } (\varepsilon_m - \varepsilon_o) < \varepsilon_y \tag{3.56}$$

$$E_r = E_s\left(1.05 - 0.05\frac{\varepsilon_m - \varepsilon_o}{\varepsilon_y}\right) \quad \text{if } \varepsilon_y < (\varepsilon_m - \varepsilon_o) < 4\varepsilon_y \tag{3.57}$$

$$E_r = 0.85E_s \qquad \text{if } (\varepsilon_m - \varepsilon_o) > 4\varepsilon_y \tag{3.58}$$

where ε_m is the maximum strain attained during previous cycles, and ε_o is the plastic offset strain.

The stresses experienced during the reloading phase are determined from:

$$f_s(\varepsilon_i) = E_r(\varepsilon_i - \varepsilon_o) + \frac{E_m - E_r}{N \cdot (\varepsilon_m - \varepsilon_o)^{N-1}} \cdot (\varepsilon_i - \varepsilon_o)^N \tag{3.59}$$

where

$$N = \frac{(E_m - E_r)(\varepsilon_m - \varepsilon_o)}{f_m - E_r(\varepsilon_m - \varepsilon_o)} \tag{3.60}$$

f_m is the stress corresponding to the maximum strain recorded during previous loading, and E_m is the tangent stiffness at ε_m.

3.4 CURRENT DEFICIENCIES

The models proposed in the previous section have shown to provide reasonably accurate simulations of behaviour of reinforced concrete subjected to reversed cyclic loading. However, for simplicity, linear unloading/reloading responses were assumed, which implicitly contain deficiencies. This argument excludes the model used to represent the reinforcement; researchers have confirmed that the proposed model is a realistic representation of behaviour.

The provisional model for both the tension and compression regime consider unloading to follow a linear path. This has the effect of neglecting energy dissipation that occurs if the load is simply cycled within each domain. The reloading branches for tension and compression do not account for the damage caused due to load cycling. The model incorrectly assumes that the reloading response returns to the base curve at the previous maximum unloading strain. Plastic offsets in tension are ignored, leading to the assumption that the re-contact strain of cracks is zero. Also, no explicit rules were given for the case of partial unloading and partial reloading, which become essential when modeling either the unloading or reloading responses by curves of higher orders.

3.5 OBJECTIVES

Taking into account the deficiencies of the provisional models described in this chapter, and the models proposed by other researchers in Chapter 2 of this report, the focus of this research project was to formulate improved models for cyclic loading. The new models, presented later, were formulated to provide a realistic representation of the hysteretic behaviour of concrete in tension and compression. At the same time, the models were formulated to be compatible with a secant stiffness-based nonlinear finite element program.

The objectives of the new formulations include: unloading curves in tension and compression to account for energy dissipation; reloading curves in tension and compression with consideration to the stiffness degradation due to load cycling; plastic offset models for both tension and compression; a re-contact model for crack-closing; and partial unloading and partial reloading rules for both the tension and compression regime.

CHAPTER 4

Experimental Program

4.1 INTRODUCTION

An experimental program was conducted on two large-scale reinforced concrete walls. Structural walls with low height-to-width ratios are referred to as squat shear walls. They find wide application as seismic load resisting elements in low-rise buildings, and are also major contributors to the lateral load resistance over the first few stories above the foundation level for high-rise structures.

Two specimens, DP1[8] and DP2, were tested. The original test specimens were also repaired and tested to failure: DP1R[9] and OHSW1[10], respectively. The focus of this chapter is on the original test specimens, and includes the geometric properties of the shear walls, the layout of the reinforcement, the construction process, the material properties, the testing rig, the loading application, and the instrumentation used for testing. Information on DP1R and OHSW1 can be obtained from Ref. 9 and 10, respectively.

4.2 GEOMETRIC PROPERTIES

Specimens DP1 and DP2 were nominally identical in geometry to the NUPEC specimens; therefore, a comparison between dynamic testing and static testing can be investigated.

The walls were constructed with stiff top and bottom slabs. The top slab (4415 x 4000 x 640 mm) served to distribute the horizontal and axial loads to the walls of the structures. The bottom slab (4415 x 4000 x 620 mm) was clamped to the laboratory strong floor, and simulated a rigid foundation. The walls consisted of a central web wall connecting to end flange walls. The web wall was 2885 mm in length, 2020 mm in height, and 75 mm in thickness. The two flange walls were approximately 3045 mm long, 2020 mm high, and 95 mm thick for DP1 and 100 mm thick for DP2. Figure 4.1 is a top view of DP1 and DP2.

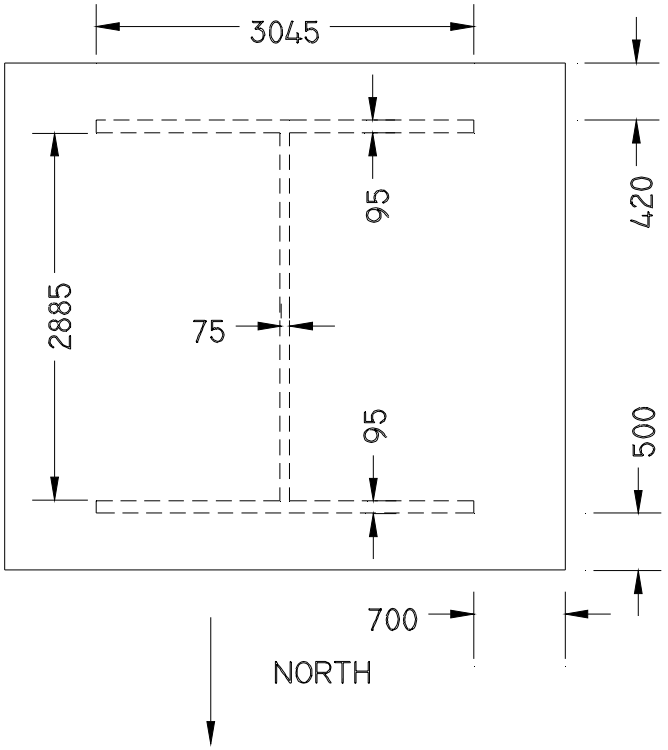

Figure 4.1 Top View of DP1Test Specimen

As indicated in Figure 4.1, the laboratory strong wall was located on the north side of the test specimens. The sectional details of the walls follow in Figures 4.2 and

4.3. Figure 4.2 is a side view of the web wall, and Figure 4.3 is a side view of the flange walls. Note that the flange walls have been indicated as being 95 mm thick, as was the case for DP1. For DP2, the flanges were 100 mm thick.

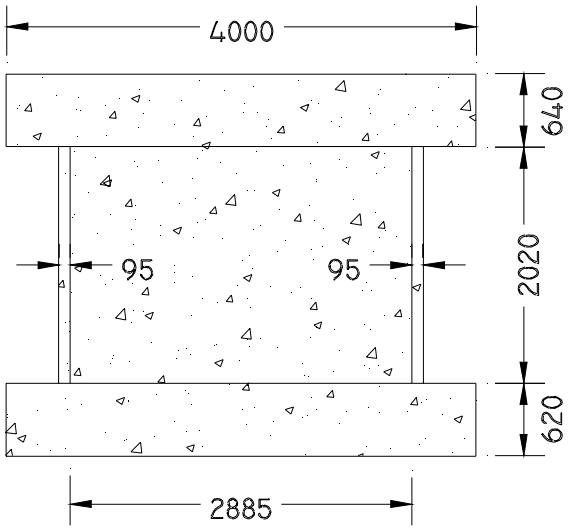

Figure 4.2 Side View of Web Wall

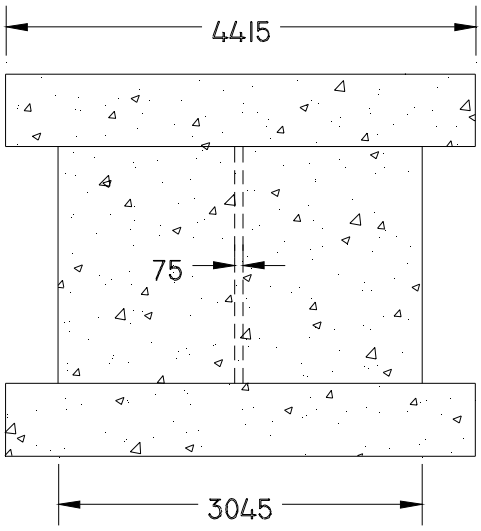

Figure 4.3 Side View of Flange Wall

The only notable dimensional difference between DP1 and DP2 was the thickness of the flange wall. DP1 had a flange thickness 5 mm less than DP2 and was the result of over-tightening the wall ties, which held the wall forms together. (See section 4.4 for construction details.) At the onset of construction of DP1, the objective was to build a wall with a flange thickness of 100 mm, to be consistent with DP2 and the NUPEC test specimens. The photograph in Figure 4.4 shows the southeast portion of the test specimens at the end of construction.

Figure 4.4 Test Specimens After Construction

4.3 REINFORCEMENT DETAILS

The top and bottom slabs were reinforced with No. 30 deformed reinforcing bars at a spacing of 350 mm in each direction, with a top and bottom layer. The equivalent reinforcement ratio for this bar spacing was 0.63% in the top slab and 0.65% for the bottom slab. Development for the slab reinforcement was provided by 90-degree bends and a 500 mm extension beyond the bend at the ends of the bars. A clear cover of 50 mm to the reinforcement was provided. Figure 4.5 is a top view drawing of the slab reinforcement.

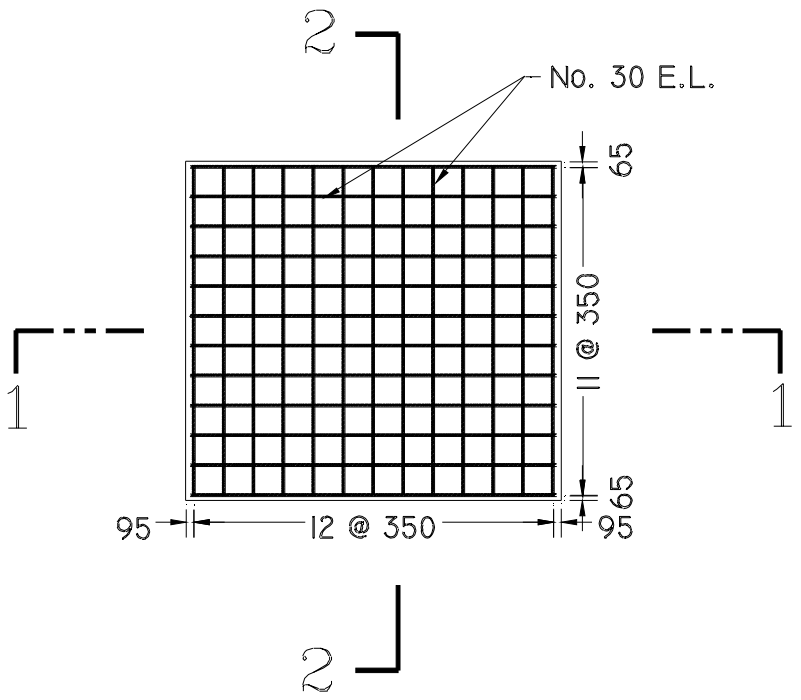

Figure 4.5 Top View of Reinforcement

The following figure, Figure 4.6, is a sectional drawing of Figure 4.5.

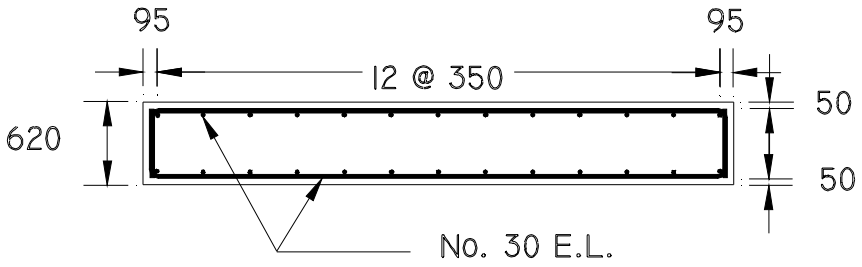

Figure 4.6 Section 1-1

Figure 4.7 is a photograph of the base slab of DP1 prior to casting of the concrete. It depicts the layout of the reinforcement. Note that DP2 was constructed using the base slab of DP1. Further details will be given in subsequent sections.

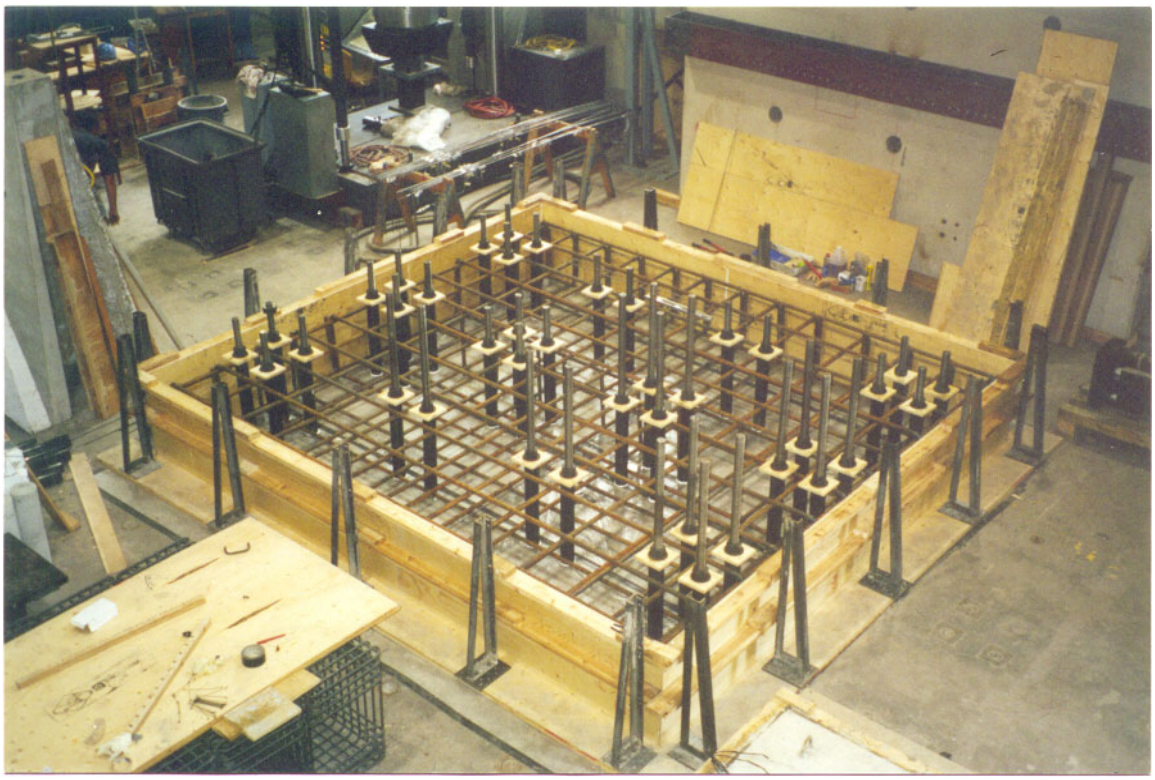

Figure 4.7 Photograph of Slab Reinforcement

The web walls were reinforced with D6 reinforcing bars. The bars were spaced 140 mm horizontally and 130 mm vertically in two parallel layers. The flange walls were also reinforced with D6 reinforcement, spaced 140 mm horizontally, and vertically the bars were spaced at 130 mm near the web wall and 355 mm near the tips of the flanges. The flange walls also contained two layers of reinforcement. For development purposes, the vertical wall reinforcement was extended into the top and bottom slabs to the outer layer of the slab reinforcement. The bars were also fabricated with a 90-degree bend and a 500 mm extension beyond the bend. The horizontal reinforcement in the web walls was anchored into the flange walls by the use of 90-degree bends and a 500 mm extension. The horizontal reinforcement in the flanges did not contain any development details. A

concrete clear cover of 15 mm for all wall reinforcement was provided. Table 4.1 is a list of the reinforcement ratios for the web and flange walls.

Table 4.1 Reinforcement Ratios

Zone	ρ_h (%)		ρ_v (%)	
	DP1	DP2	DP1	DP2
Web Wall	0.737	0.737	0.794	0.794
Inner Flange	0.582	0.553	0.627	0.596
Outer Flange	0.582	0.553	0.230	0.218

Figure 4.8 is a top view layout of the wall reinforcement for specimens DP1 and DP2. Figures 4.9 and 4.10 are drawings of the reinforcement in the flange and web walls, respectively.

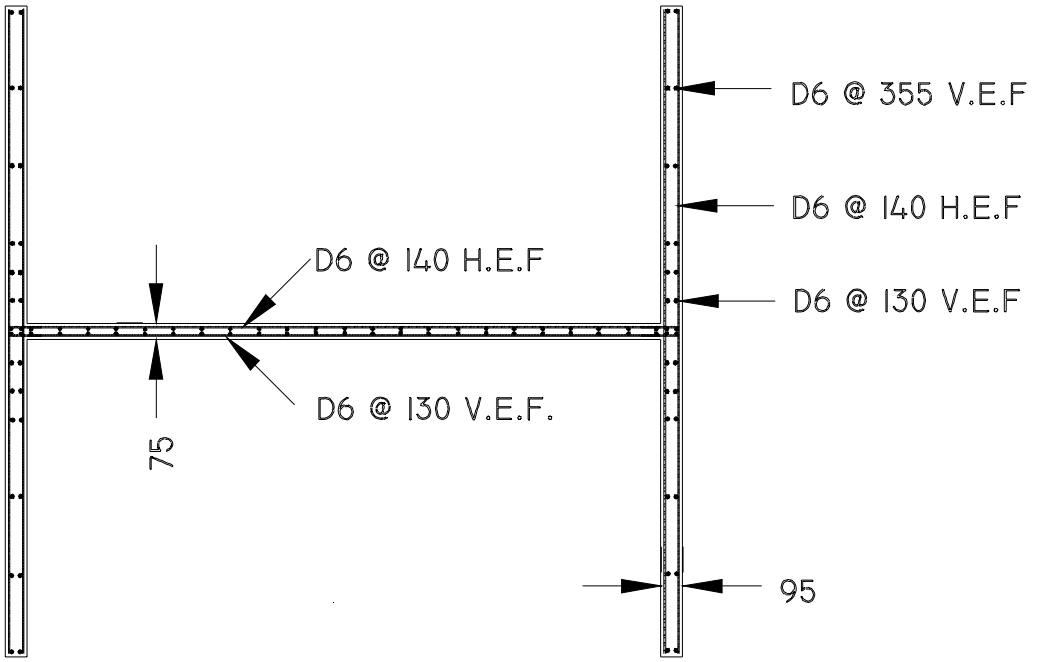

Figure 4.8 Top View of Wall Reinforcement

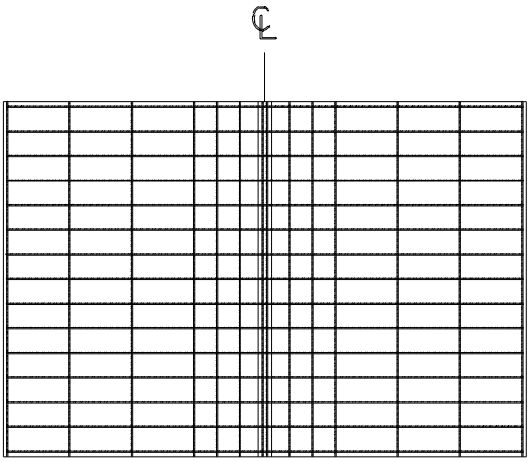

Figure 4.9 Flange Wall Reinforcement

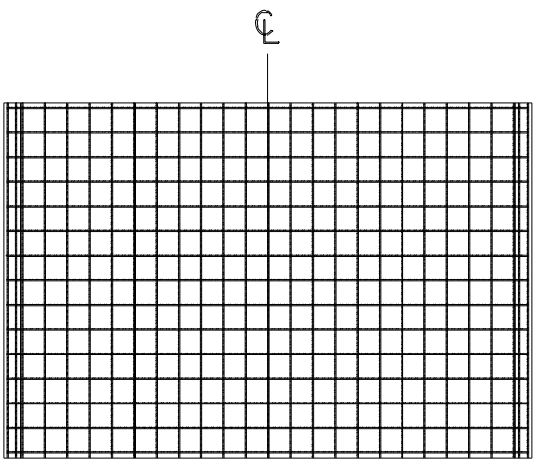

Figure 4.10 Web Wall Reinforcement

The final reinforcement drawing, Figure 4.11, is a detail of the web-flange joint. It shows the length of development for the horizontal web reinforcement into the flange wall. Figure 4.12 is a photograph of the wall reinforcement after casting of the base slab.

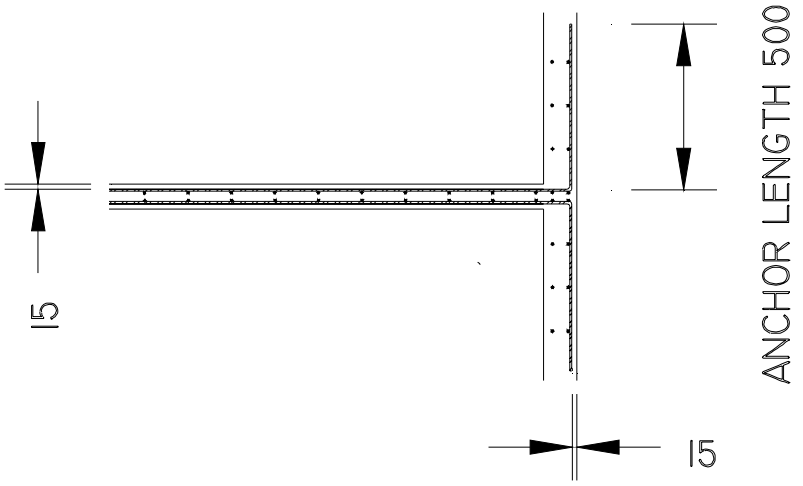

Figure 4.11 Web-Flange Connection

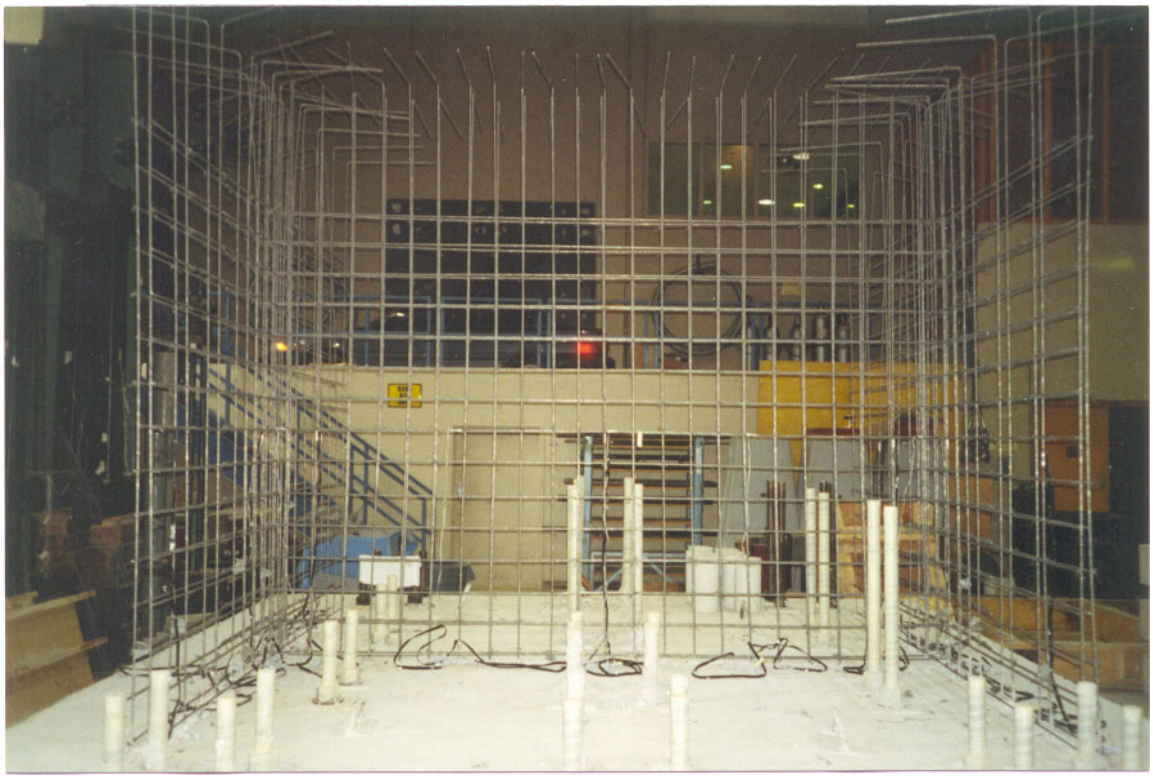

Figure 4.12 Photograph of Wall Reinforcement

4.4 CONSTRUCTION DETAILS

4.4.1 Specimen DP1

Full details pertaining to the construction of DP1 can be obtained in Ref. 8. This section contains a more general description of the construction process.

DP1 was built in three phases: the base slab, the flange and web walls, and the top slab, each requiring 11 m^3, 1.7 m^3, and 11.5 m^3 of concrete, respectively. This three-staged process caused construction joints between the walls and the slabs.

The base slab was constructed on the laboratory strong floor in its place of testing. Prior to casting, the forty floor bolts used to clamp the walls to the laboratory strong floor were anchored in place, and the vertical wall reinforcement was tied to the slab

reinforcement to avoid lap splices. The approximate weight of the base slab after casting was 26 metric tonnes. Figure 4.13 is a picture of the base slab just prior to casting, and Figure 4.14 is a photo of the slab just after casting.

The second phase of construction consisted of casting the flange and web walls. The horizontal reinforcement was tied to the vertical reinforcement, which was anchored into the base slab. The walls were formed, and approximately 1.7 m^3 of concrete was used in the casting operation. Details of the formwork can be found in Ref. 8. Figure 4.15 depicts the walls of DP1 after casting and during the curing process.

Figure 4.13 Base Slab Prior to Casting

Figure 4.14 Base Slab After Casting

Figure 4.15 Walls After Casting

The final phase of building included the construction of the top slab. First the floor of the slab was formed, and then the reinforcement was tied in place. Prior to casting, two sets of four ducts were inserted through the slab. The ducts provided voids through which threaded rods could be inserted as part of the cyclic displacement apparatus. The ducts in each set were spaced 300 mm vertically and 150 mm horizontally. The centre of each set of ducts coincided with the mid-height of the top slab. The two sets of ducts were spaced 1215 mm horizontally from each other. Four additional vertical voids, one at each corner of the slab, were also formed for purposes of applying a constant axial load during testing. Figures 4.16 and 4.17 illustrate the top slab prior to casting and after casting, respectively.

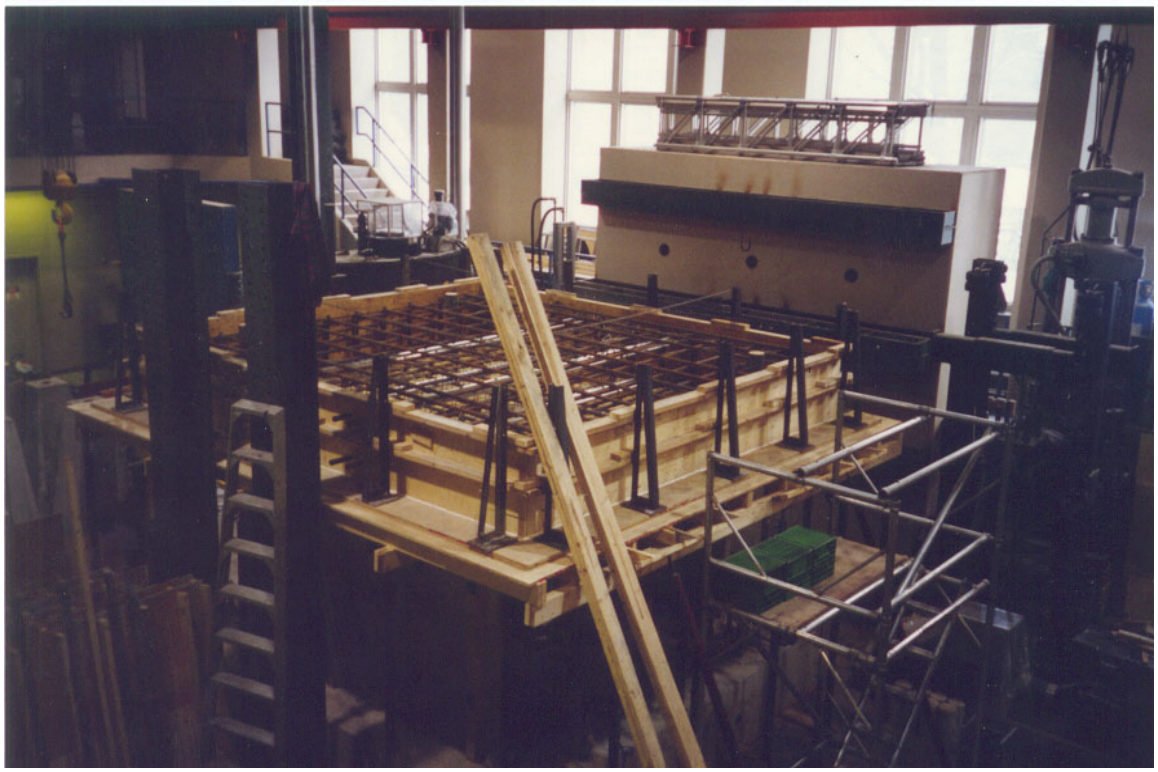

Figure 4.16 Top Slab Prior to Casting

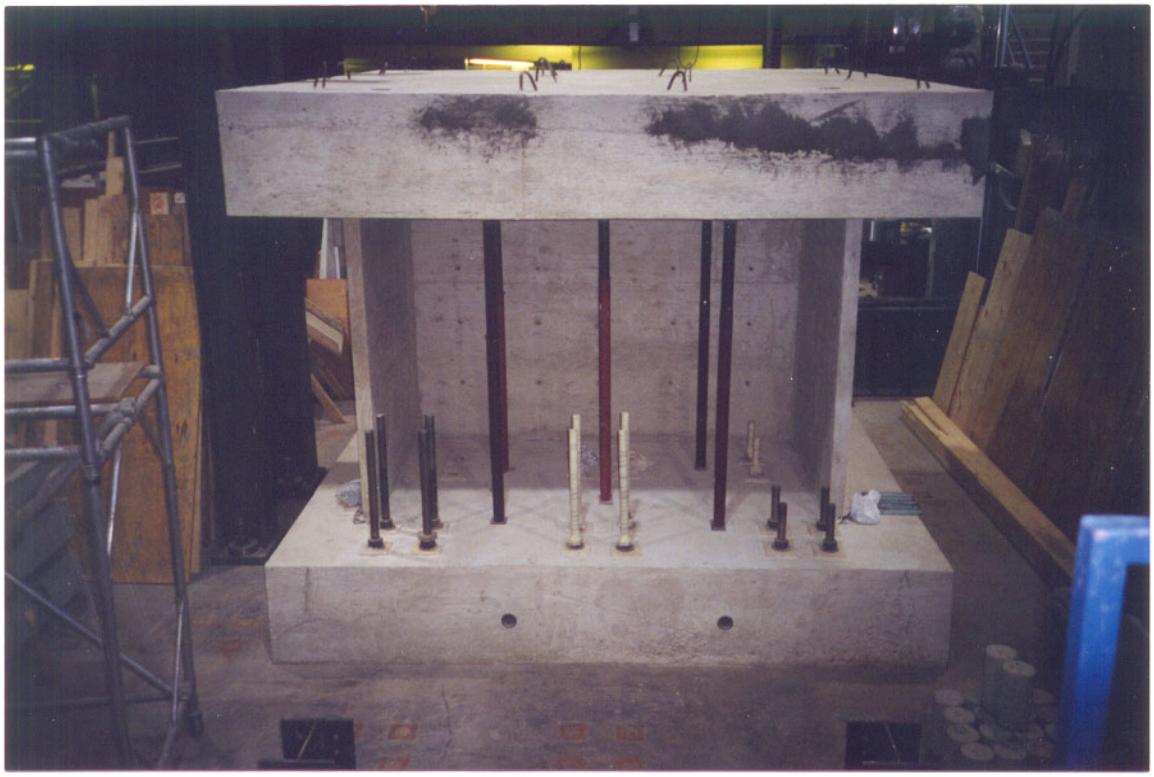

Figure 4.17 Top Slab After Casting

4.4.2 Specimen DP2

The procedures and process to construct DP2 were similar to that of DP1, with the exception that the base slab of DP1 was used to form part of DP2. The base slab of DP2 is illustrated in Figure 4.18.

To develop the wall reinforcement, the vertical bars of the flange and web walls were anchored into the base slab. A rotary hammer drill was used to produce holes 9.5 mm (3/8 in.) in diameter and 305 mm (12 in.) deep into the slab. The holes were cleaned with pressurized air and a brush. Adhesive mortar for setting bars in concrete was injected into the holes using a trigger cartridge. The reinforcement was then inserted into the hole and held for approximately 5 minutes. Prior to anchoring the vertical wall

reinforcement into the slab, samples of reinforcement were tested to ensure that the reinforcement would not slip from the base slab. A series of 1.5 m long D6 reinforcing bars were anchored to the base slab using the anchoring procedure. Pull-out tests, using a hydraulic jack, were performed under three loading conditions: monotonic, one cycle, and two cycles. The cyclic tests consisted of loading and unloading in increments of 0.8 mm of displacements of the reinforcement. The displacements were monitored by a LVDT (Linear Variable Differential Transducer). In all the tests, bond slip of the reinforcement was not evident, and the reinforcement ruptured away from the joint. The tests indicated that this method of anchoring the reinforcement to the base slab was adequate. Figure 4.19 is an illustration of the pull-out tests conducted on the D6 wall reinforcement, and Figure 4.20 is a photograph of DP2 after the vertical reinforcement was anchored to the base slab and just prior to setting the formwork for the walls.

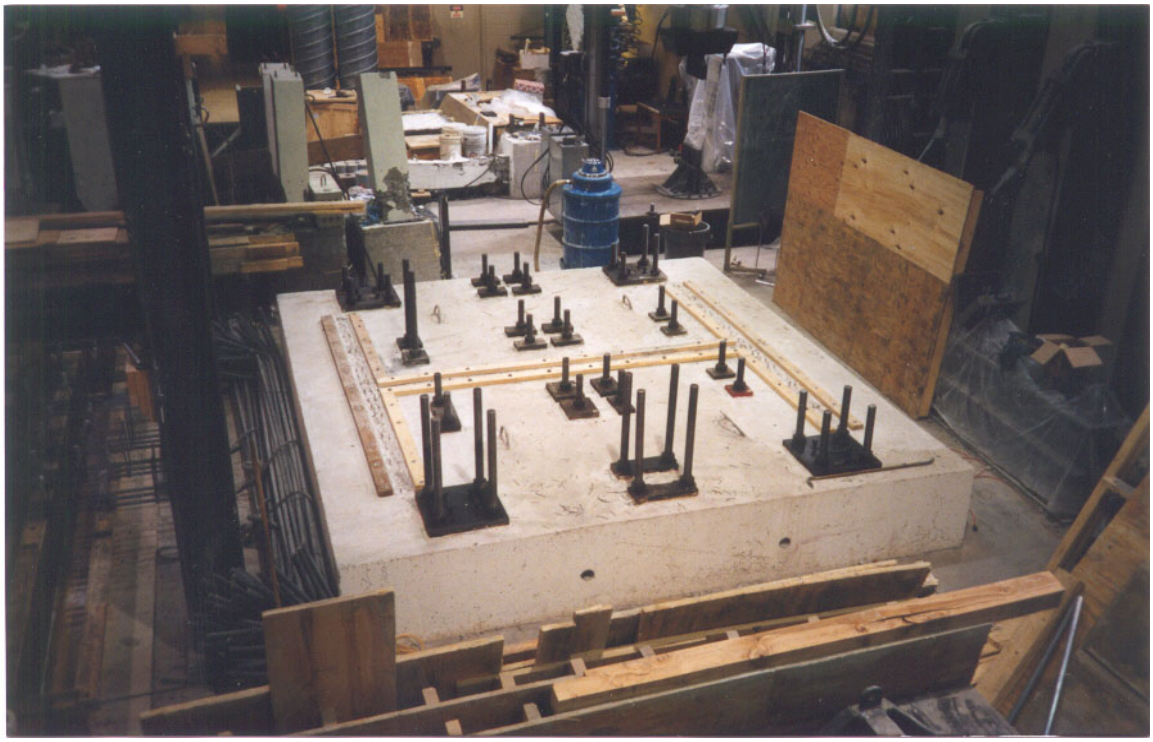

Figure 4.18 Base Slab of DP2

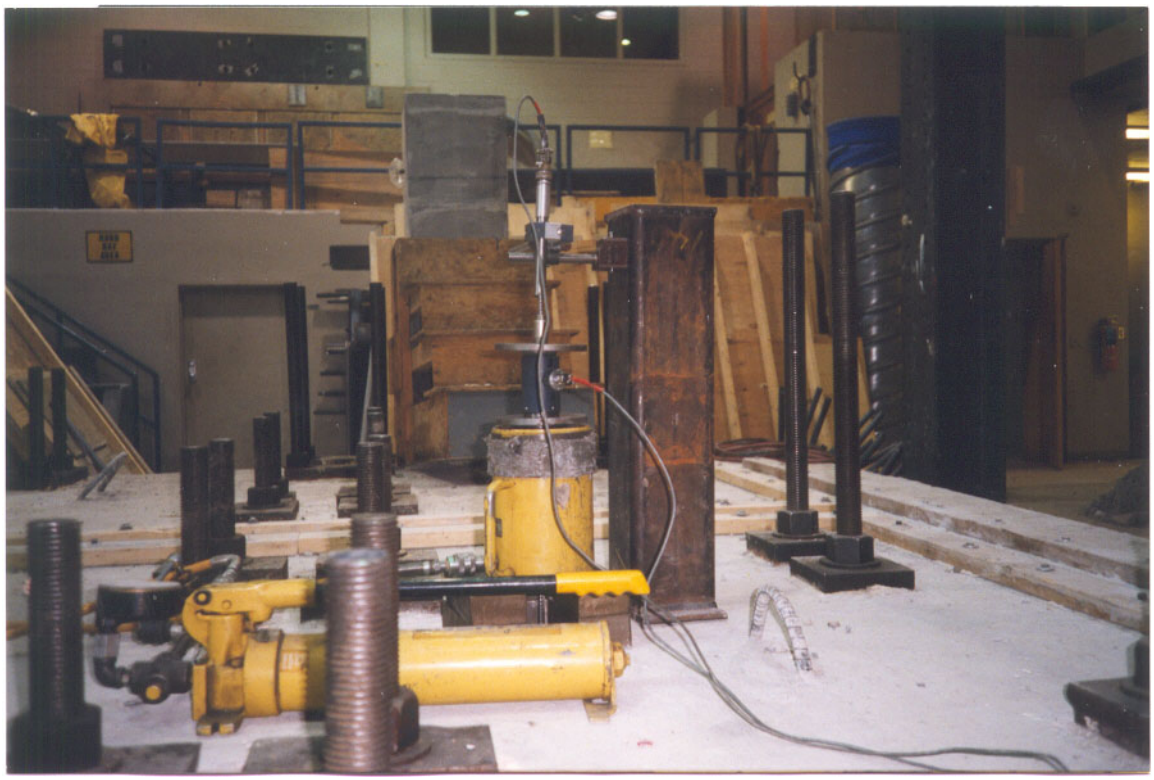

Figure 4.19 Pull-Out Test of Wall Reinforcement

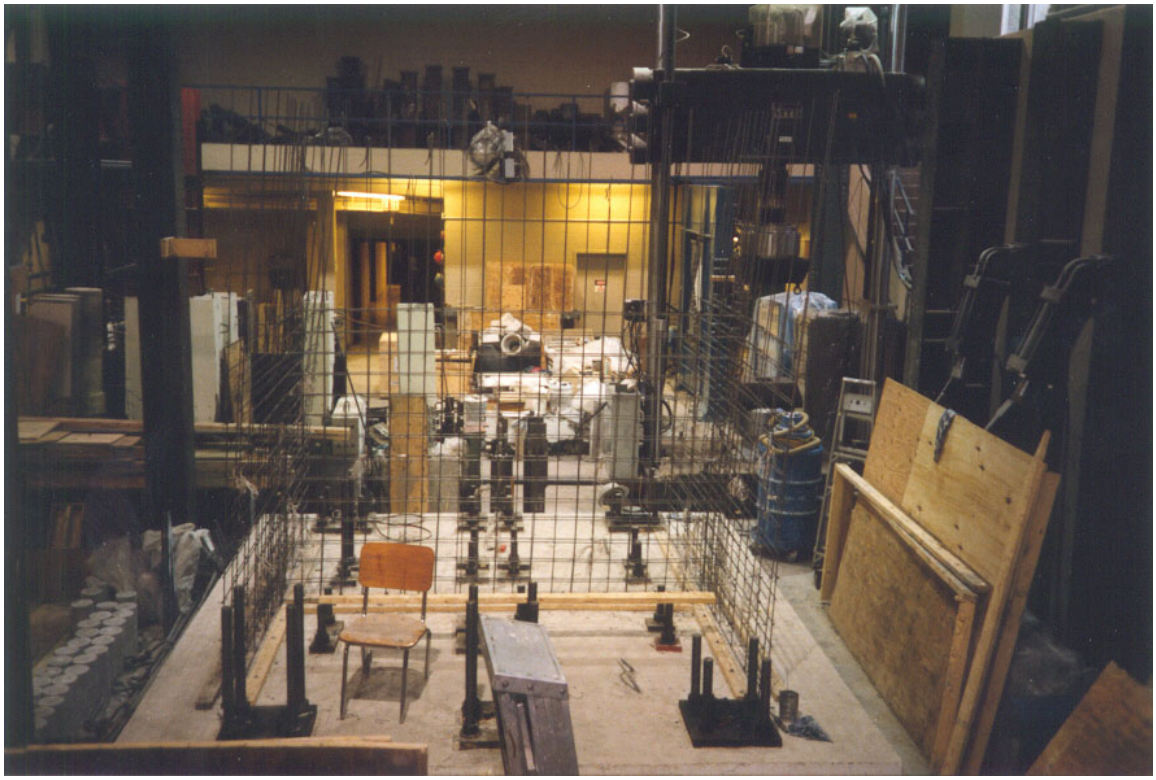

Figure 4.20 Specimen DP2 Wall Reinforcement

4.5 MATERIAL PROPERTIES

4.5.1 Concrete

A local ready mix plant supplied concrete for DP1 and DP2. A typical mix giving a compressive strength of 30 MPa at 28 days was requested for the base and top slabs. The mix included a maximum aggregate size of 10 mm and a slump of 100 mm. On the day of casting, 11.5 m^3 was delivered in two trucks: one containing 7 m^3, and the other 4.5 m^3. At the conclusion of testing, compression cylinder tests were conducted on standard 6 x 12 in. (152 x 305 mm) concrete cylinders batched from each truck. The cylinders were tested on a 5000 kN MTS machine at a loading rate of 0.005 mm/s.

A special order was required for the walls of the specimens. The mix contained 10 mm pea gravel, instead of angular gravel normally used in concrete mixes, and an air content of 3 %. The pea gravel was used to increase the flow of the concrete through the relatively thin wall members. The cement content contained 50 % cement and 50 % slag. Slag is characterized as providing a slower and lower ultimate strength gain. The objective was to attain a compressive strength in the range of 25 MPa, similar to that of the NUPEC specimens. Superplasticizer, which increases the flow of concrete while not affecting the ultimate strength, was also added to the concrete prior to casting to increase the slump from 100 mm to 200 mm. On the day of casting, 2.5 m^3 of concrete was delivered and used to cast the walls and standard cylinders. The cylinders from the wall concrete were tested on the day of testing using the apparatus discussed previously. The mean results of the cylinder tests are given in Table 4.2.

Table 4.2 Concrete Properties

Zone	f'_c (MPa)		ε'_c ($\times 10^{-3}$)		a_{max} (mm)	E_c (MPa)	
	DP1	DP2	DP1	DP2		DP1	DP2
Web Walls	21.7	18.8	2.04	2.12	10	25900	18580
Flange Walls	21.7	18.8	2.04	2.12	10	25900	18580
Top Slab	43.9	38.0	1.93	1.96	10	43700	37570
Base Slab	34.7	34.7	1.90	1.90	10	36900	36900

Figures 4.21 to 4.23 give typical concrete stress-strain responses for each wall element.

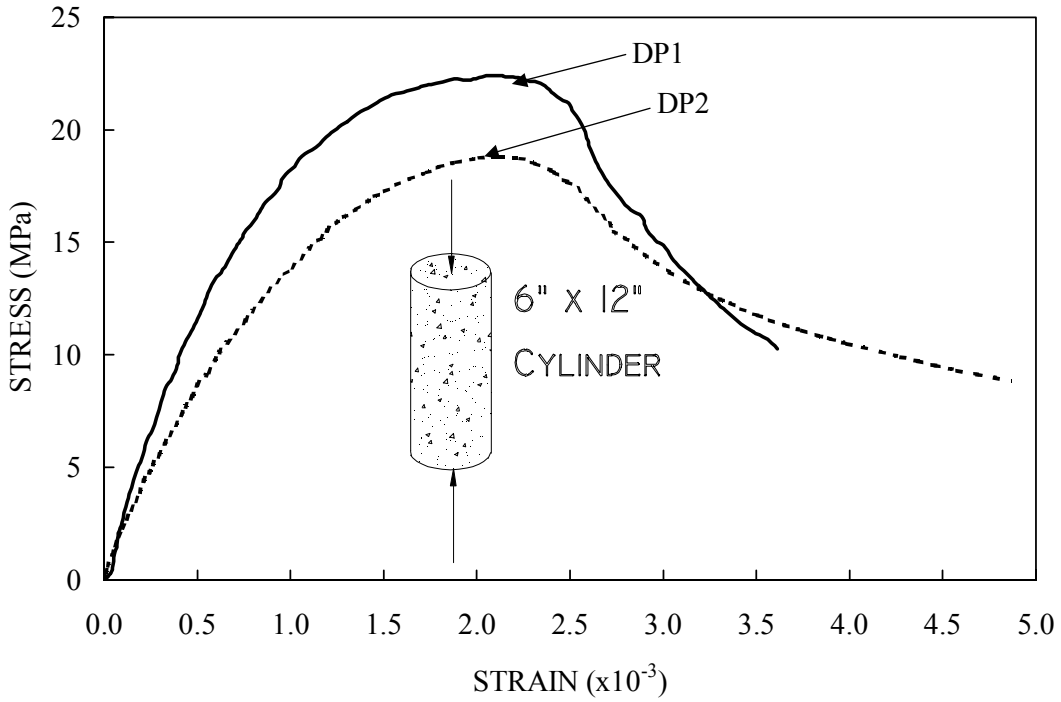

Figure 4.21 Typical Wall Concrete Stress-Strain

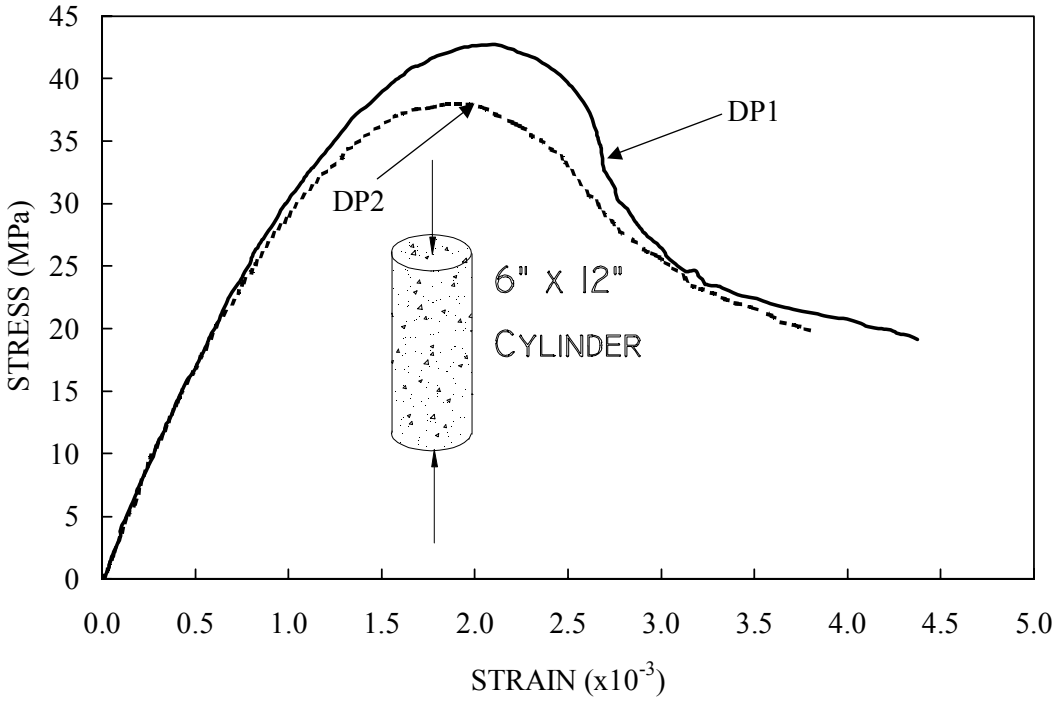

Figure 4.22 Typical Top Slab Concrete Stress-Strain

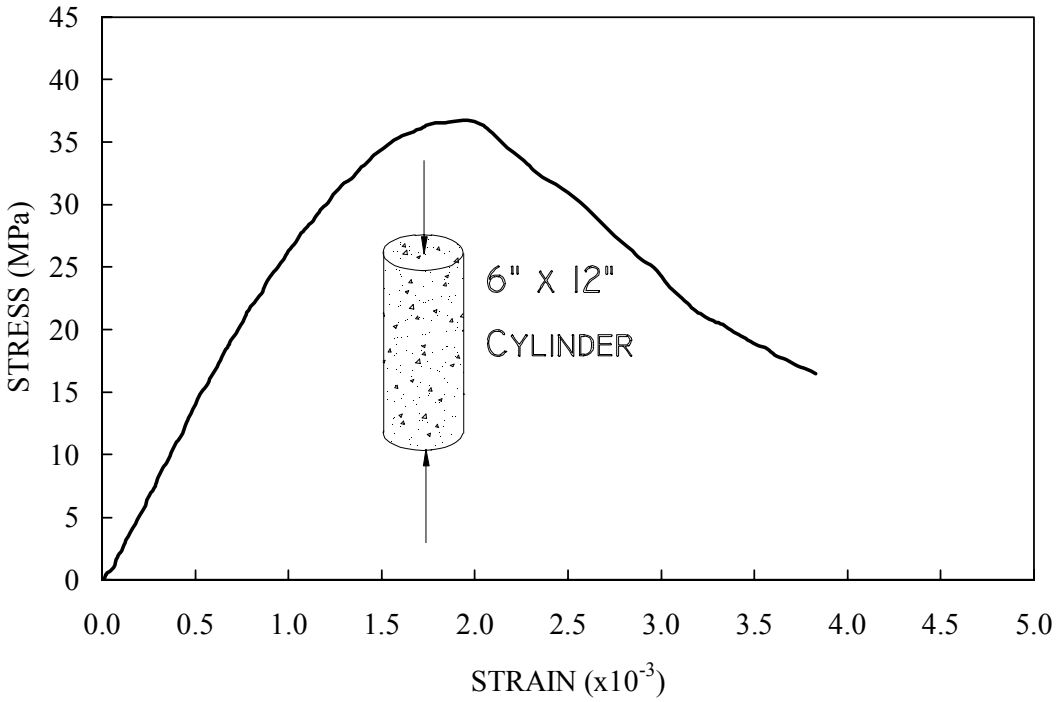

Figure 4.23 Typical Bottom Slab Concrete Stress-Strain

4.5.2 Reinforcement

Two reinforcing bar types were used in the construction of DP1 and DP2: No.30 and D6. The former, used in the top and base slabs, has a nominal diameter of 29.9 mm and a cross sectional area of 700 mm^2. The D6 reinforcing bar, used in the walls as vertical and horizontal reinforcement, has a nominal diameter and cross sectional area of 7.0 mm and 38.71 mm^2, respectively. Coupon tests were performed on samples of each reinforcement on a 1000 kN MTS machine. The mean results of these tests are listed in Table 4.3. Figures 4.24 and 4.25 illustrate typical responses for the D6 and No. 30 bars, respectively.

Table 4.3 Reinforcement Properties

Zone	Type	Nominal Diameter (mm)	ε_{sy} (x 10^{-3})	f_{sy} (MPa)	E_s (MPa)	f_{su} (MPa)
Web Wall	D6	7	3.18	605	190250	652
Flange Wall	D6	7	3.18	605	190250	652
Top Slab	No. 30	29.9	2.51	550	220000	696
Base Slab	No. 30	29.9	2.51	550	220000	696

The D6 reinforcing bars were not heat-treated and, therefore, did not respond with a flat yield plateau. The yield stress was calculated using a 0.2 % offset.

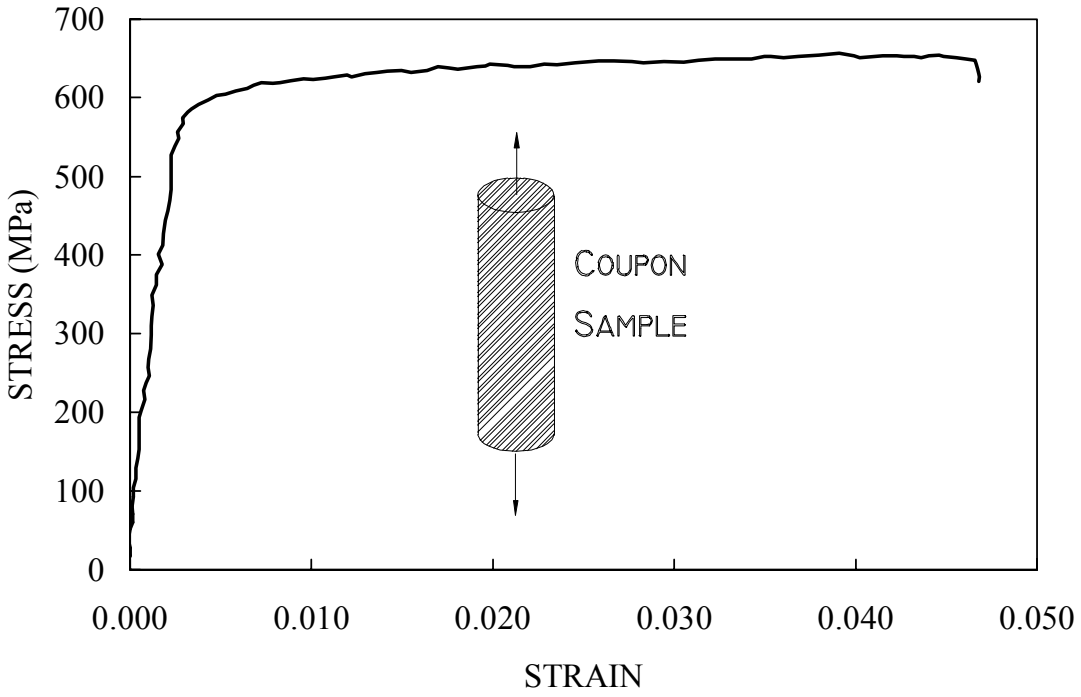

Figure 4.24 Typical Stress-Strain Response for D6 Bar

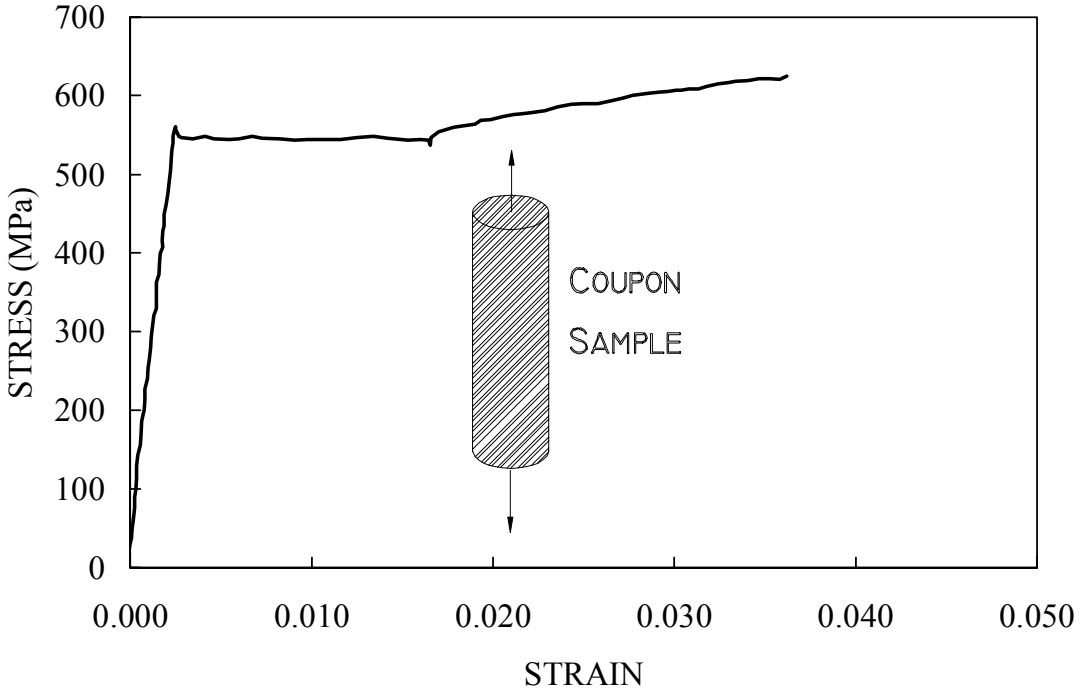

Figure 4.25 Typical Stress-Strain Response for No.30 Bar

4.6 TESTING RIG AND SETUP

The loading scheme for DP1 and DP2 differed slightly. DP1 was subjected to cyclic displacements with a constant axial load applied, whereas the externally applied axial load was removed for DP2.

The cyclic displacements were applied to the top slab on the north side of the specimens through two 1000 kN actuators. The actuators were mounted to the laboratory strong wall, which acted as a reaction frame, and connected to load cells on the top slab of the specimens. In turn, each load cell was bolted to the top slab by four threaded rods, which were inserted into the voids formed during the casting operation as previously discussed. For loading of the specimens away from the strong wall, the experimental lateral load was the sum of the loads measured by load cells mounted to the north end of the top slab; for loading of the specimens toward the strong wall, the horizontal load was the sum of the loads registered by load cells located on the south end of the top slab. The difference in loads measured by the two loads cells, typically, was negligible.

Four 600 kN actuators were installed at each corner of the specimen for the case where an axial load was required. The actuators were mounted to the base slab by floor bolts and connected with a threaded rod to load spreader beams located on the top slab. The threaded rods were inserted through the top slab via voids formed during casting. In turn, the rods were bolted to the spreader beams. The purpose of the spreader beams was to provide a means to distribute the axial load evenly along the top slab. The voids constructed for the threaded rods were approximately 830 mm from the north end and 700 mm from the south end of the top slab, and 400 mm from each side face. The location of the voids was dictated by the location of the floor bolts. Load cells were also

installed between the actuators and the threaded rods to monitor the axial load. To ensure that the axial load for DP1 was distributed uniformly along the length of the spreader beams, Plaster of Paris was placed between the top of the upper slab and the bottom of the spreader beams. Figure 4.26 is an illustration of the set-up used to provide the cyclic displacements to the walls. Figure 4.27 and Figure 4.28 are web wall side views of DP1 and DP2, depicting the loading rig.

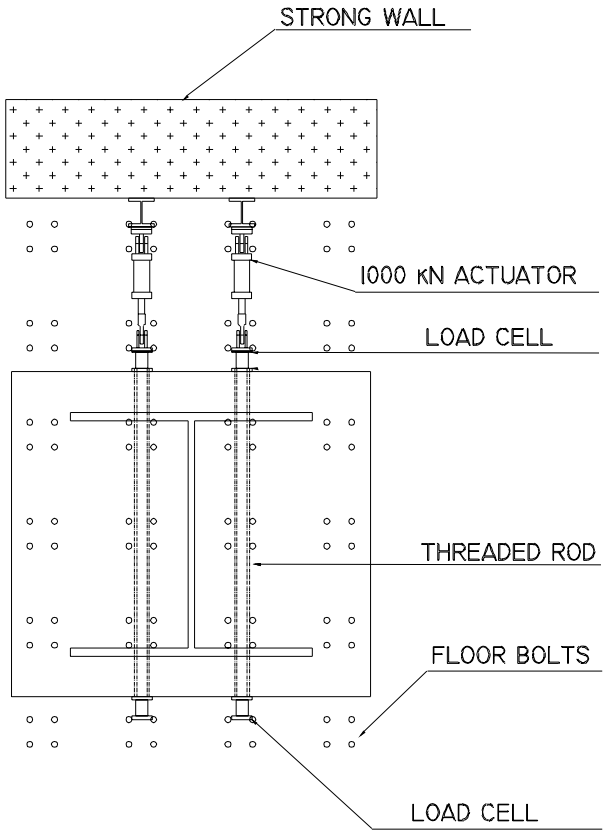

Figure 4.26 Cyclic Loading Set-up

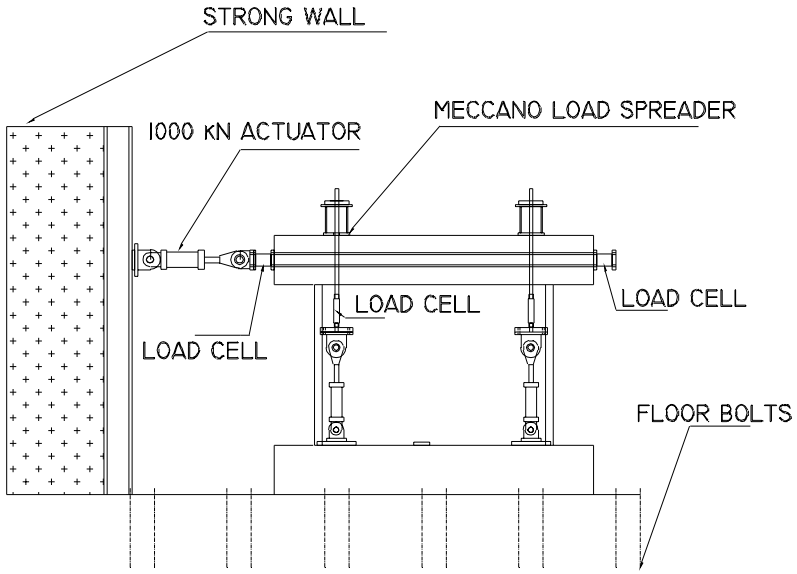

Figure 4.27 DP1 Test Set-up

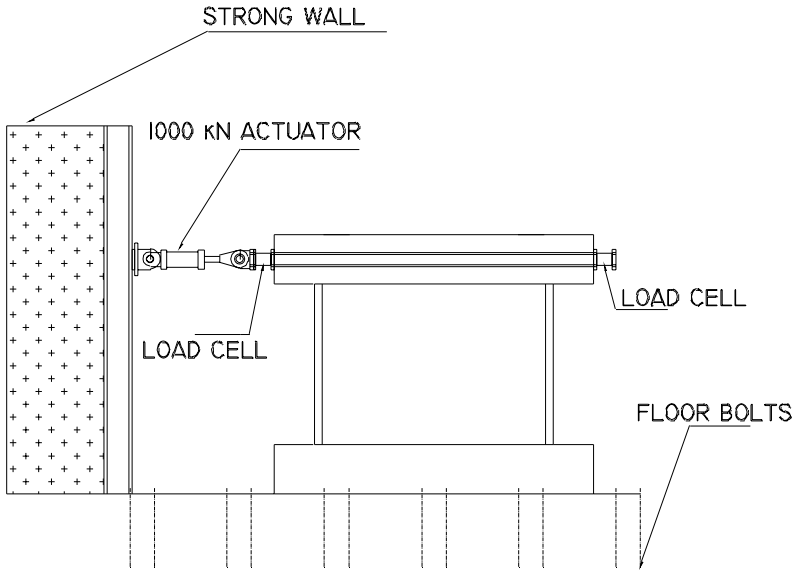

Figure 4.28 DP2 Test Set-up

4.7 DATA ACQUISITION SYSTEM

The test readings originating from the load cells, LVDTs, strain gauges, and Zurich gauges, were recorded by a Heliotronic data acquisition system. The readings were transferred from the acquisition system to a 9816 Hewlett Packard computer. Figure 4.29 is a photograph of the data acquisition system.

Figure 4.29 Data Acquisition System

4.8 LOADING HISTORY

DP1 and DP2 were subjected to cyclic lateral displacements along the axis of the web wall. In addition, DP1 was also loaded with a constant applied axial load of 940 kN. The self-weight of the top slab contributed an additional 260 kN of axial load. After the axial force was applied, the specimens were displaced laterally, along the axis of the web wall,

in increments of 1 mm. Two repetitions at each displacement level were imposed. The lateral loading regime was representative of extreme conditions experienced during a severe earthquake, where a large number of load reversals is expected at low displacements. Displacements at the mid-height of the top slab were monitored on the data acquisition system and served as the reference point for the imposed displacements. Figure 4.30 is a schematic showing the locations of the horizontal and vertical actuators, and Figure 4.31 depicts the cyclic loading history.

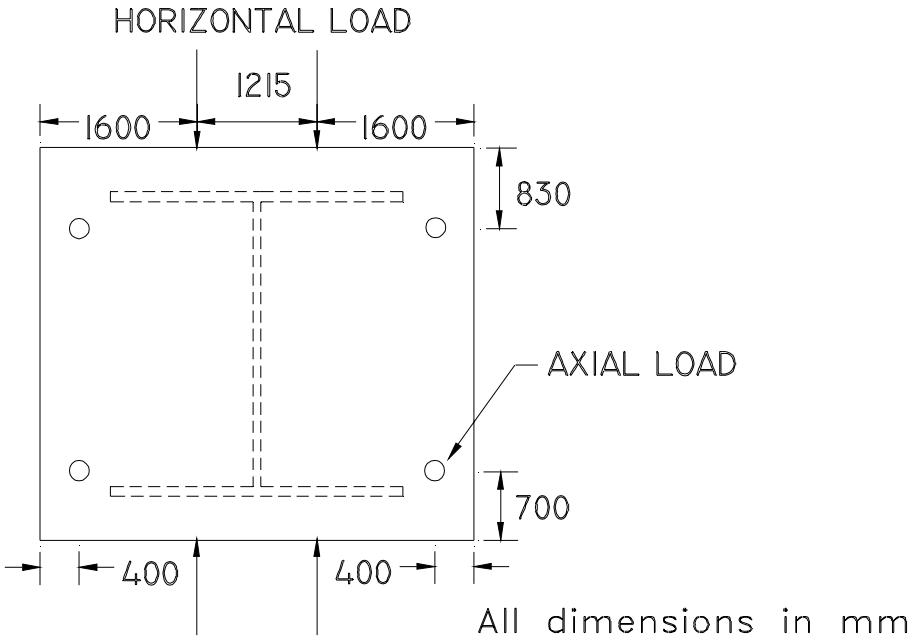

Figure 4.30 Actuator Locations

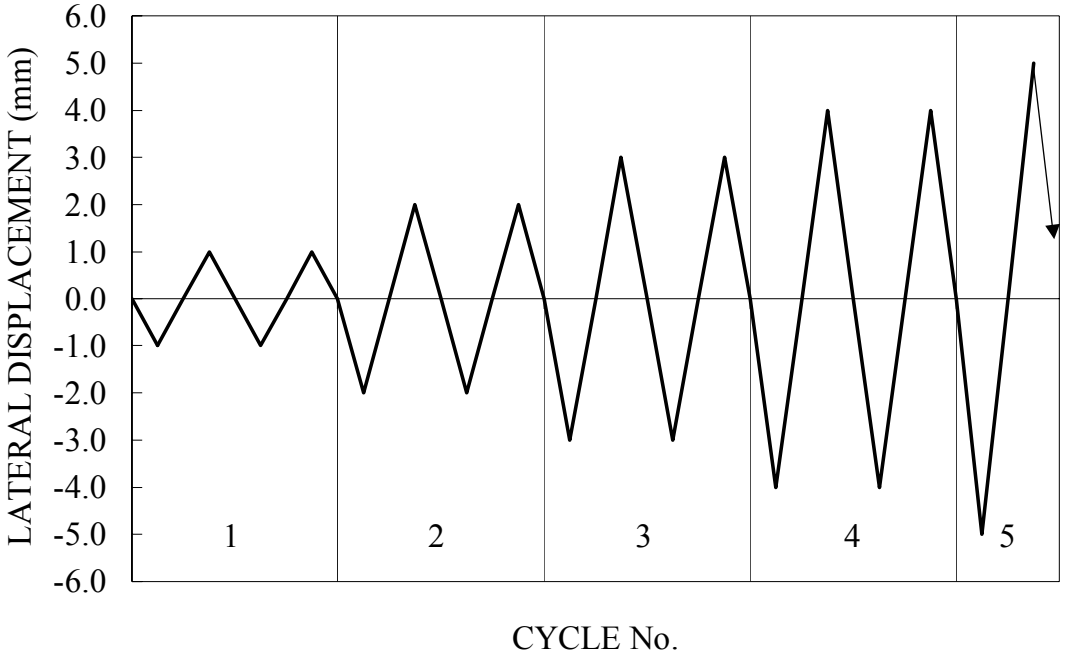

Figure 4.31 Loading History

4.9 INSTRUMENTATION

4.9.1 Electrical Resistance Strain Gauges

Electrical resistance strain gauges were mounted on the D6 reinforcing bars throughout the web and flanges walls to record the strains experienced by the reinforcement during the course of testing. Of the 40 strain gauges used, 18 were located in the web wall. Of these, ten were placed on the reinforcement along the base of the web wall, and the other eight were placed on the reinforcement near the mid-height of the web wall. In the flanges, 14 strain gauges were used to measure the strains near the base of the walls, and eight gauges were installed near the mid-height of the flanges. Some of the strain gauge wires were inadvertently broken and some of the gauges were damaged during the construction process due to the casting operation or vibrating procedures. Figures 4.32 to 4.39 show the location of the strain gauges on DP1 and DP2. The

difference between the two test specimens was in the relative location of each strain gauge. In the figures, a circle is used for those gauges recording vertical strains, and the gauges used to monitor the horizontal strains are identified by a rectangle. The individual strain gauges were also tagged for identification. Strain gauges in the web wall were denoted WV for the vertical strain gauges and WH for the horizontal strain gauges. The WV gauges were further described numerically to indicate the bar number starting from the north end of the specimen. Finally, the gauges were numbered beginning with one. An A denoted the west face of the web, and a B the east face. An example is WV12A5, which refers to a vertical strain gauge located on the west face of the web wall on bar number 12 and having gauge number 5. The same process was used for the gauges in the flange walls. In this case, FV and FH were used to differentiate vertical and horizontal gauges. Further, N and S were used to distinguish between the north and south flange walls, respectively. There was a slight difference in the location of strain gauges in the flanges of the two specimens. In DP2, there was no gauge 9 on the north face, and instead it was placed on the south face as gauge number 12.

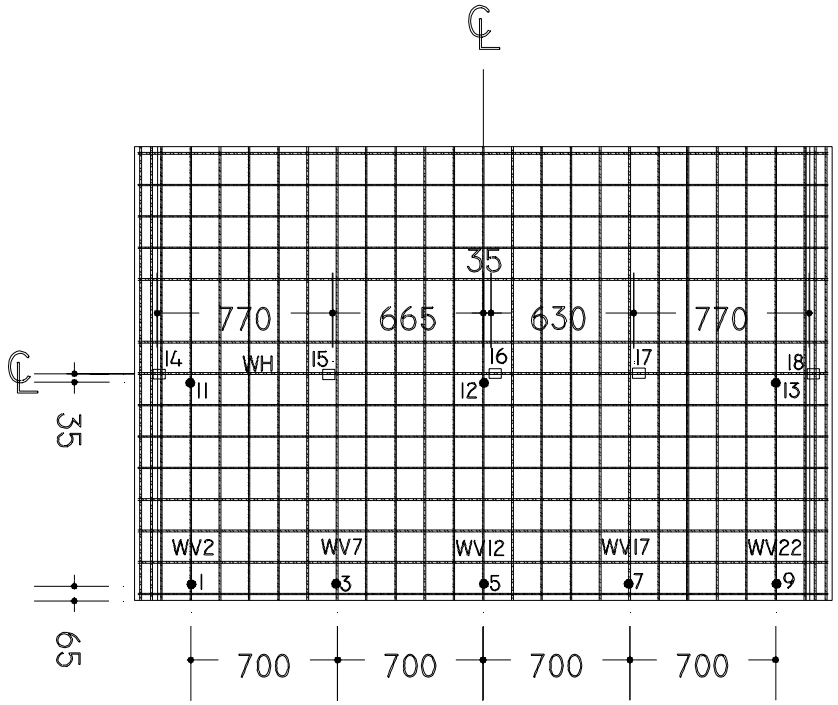

Figure 4.32 DP1 Web Strain Gauges, West Face

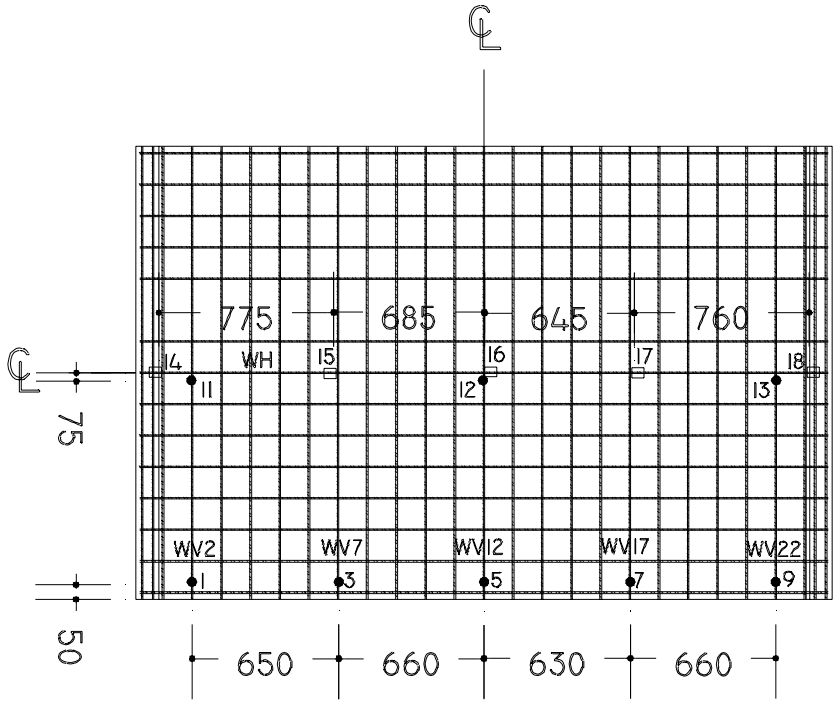

Figure 4.33 DP2 Web Strain Gauges, West Face

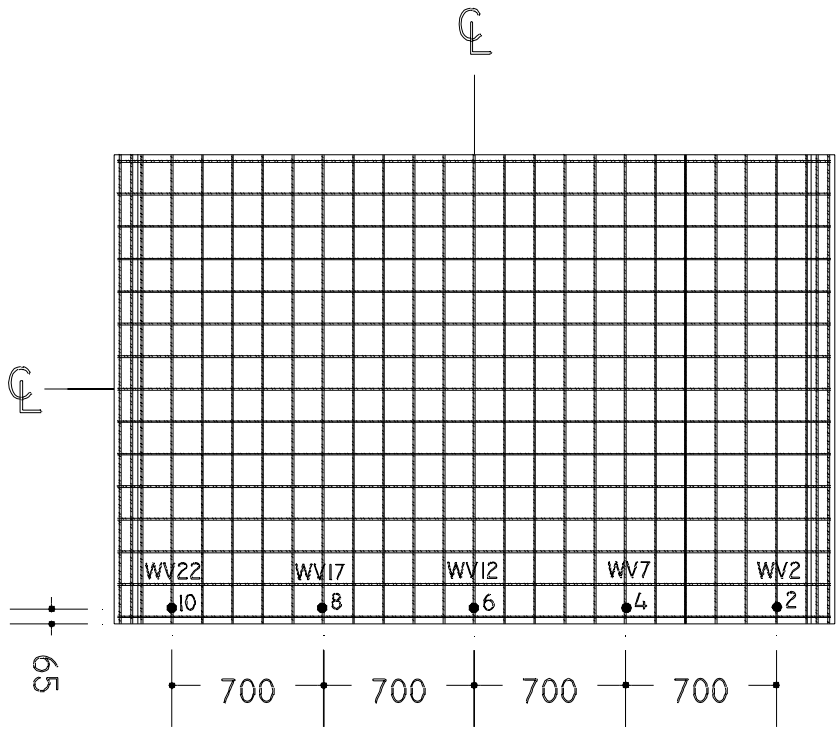

Figure 4.34 DP1 Web Gauges, East Face

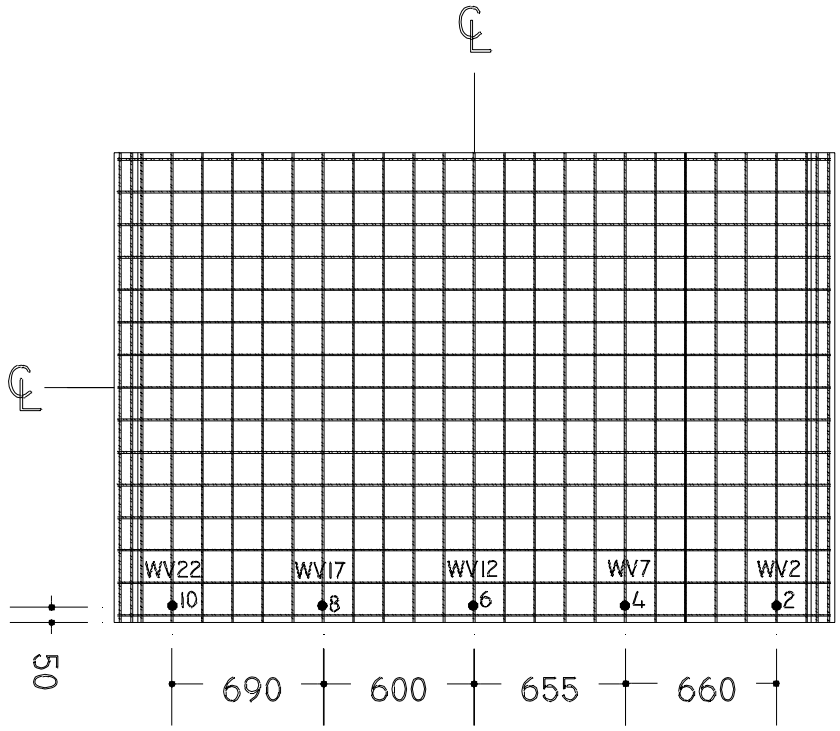

Figure 4.35 DP2 Web Gauges, East Face

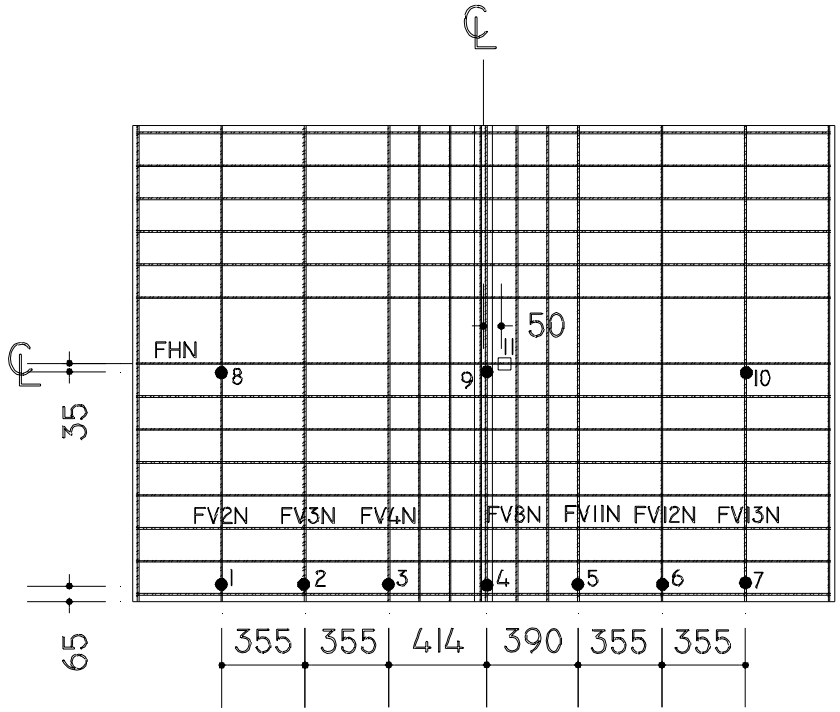

Figure 4.36 DP1 Flange Strain Gauges, North Face

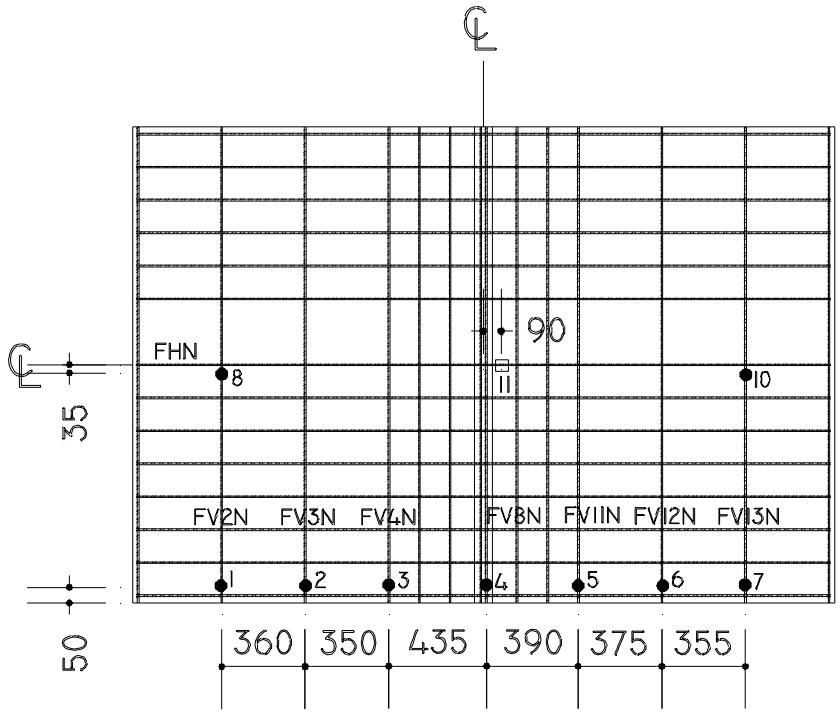

Figure 4.37 DP2 Flange Strain Gauges, North Face

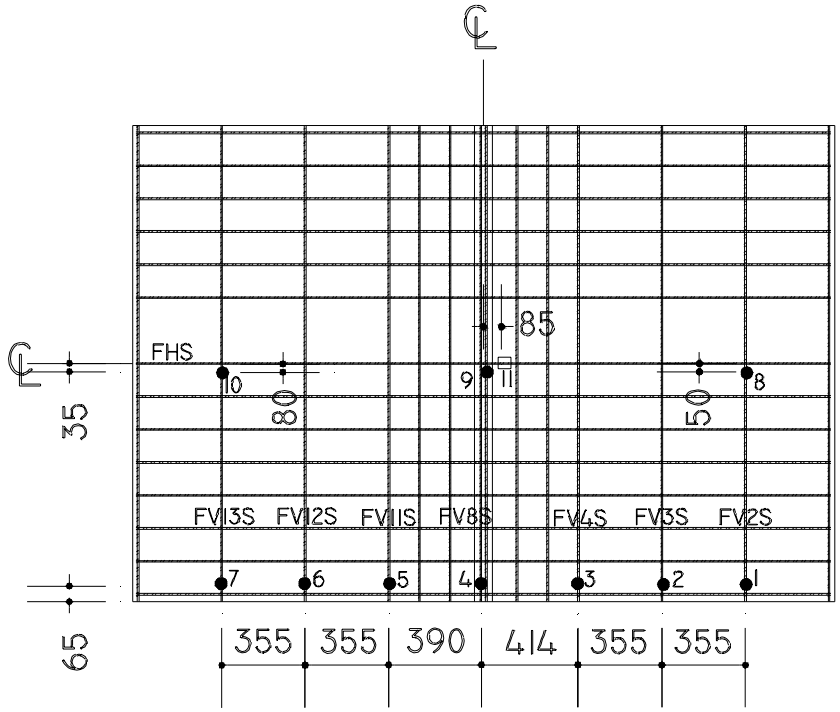

Figure 4.38 DP1 Flange Gauges, South Face

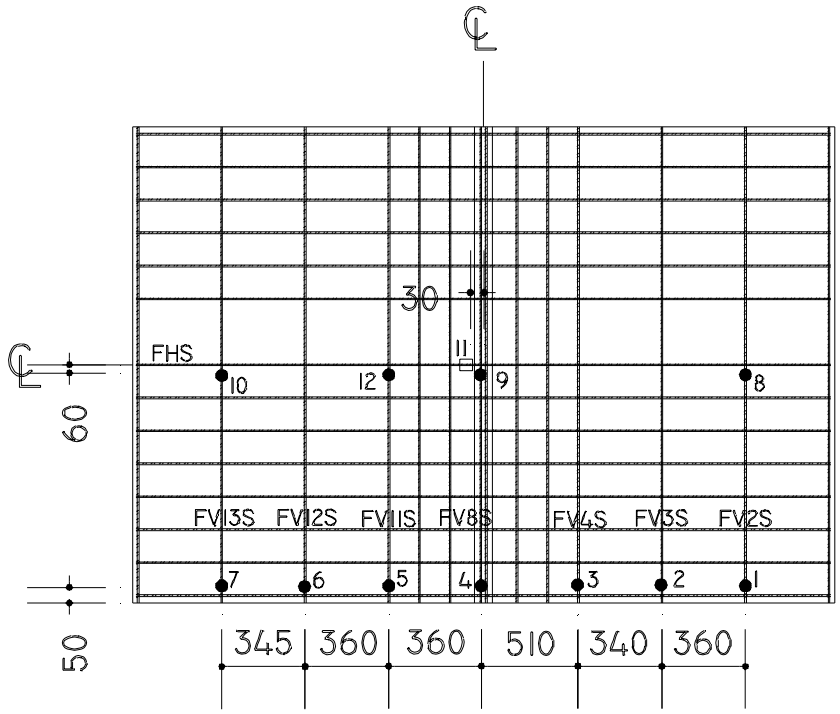

Figure 4.39 DP2 Flange Gauges, South Face

4.9.2 Zurich Gauges

Zurich targets, used with an extensometer to measure the relative displacements between adjacent targets, monitored the surface strains of the concrete and the crack propagation for each displacement level. The targets were mounted to the concrete surface with glue, and epoxy was later placed around each target to provide a stronger bond to the concrete surface.

A total of 54 targets were placed on the flange walls. Of these, 18 gauges were mounted on each of the outer and inner face of the northeast flange wall. The remaining 18 were placed on the outer face of the southwest flange wall. Prior to testing, it was assumed that the main cracking in the flange walls would be flexure-dominant; therefore, only vertical readings between adjacent targets were recorded based on a gauge length of 200 mm.

On the web wall, eight targets were mounted on the east face to measure the surface strains at the north and south toes. A grid 200 x 200 mm was used in this region, where high strains and possible failure by concrete crushing was expected to occur. A 200 mm gauge was used to record horizontal and vertical strains within the grid, and a 283 mm gauge measured the diagonal strains. Figure 4.40 shows the location of the Zurich targets on the outer face of the northeast flange wall. A similar pattern was used for the Zurich targets mounted to the inner northeast and outer southwest flanges. Figure 4.41 indicates the location of the targets placed on the east face of the web wall.

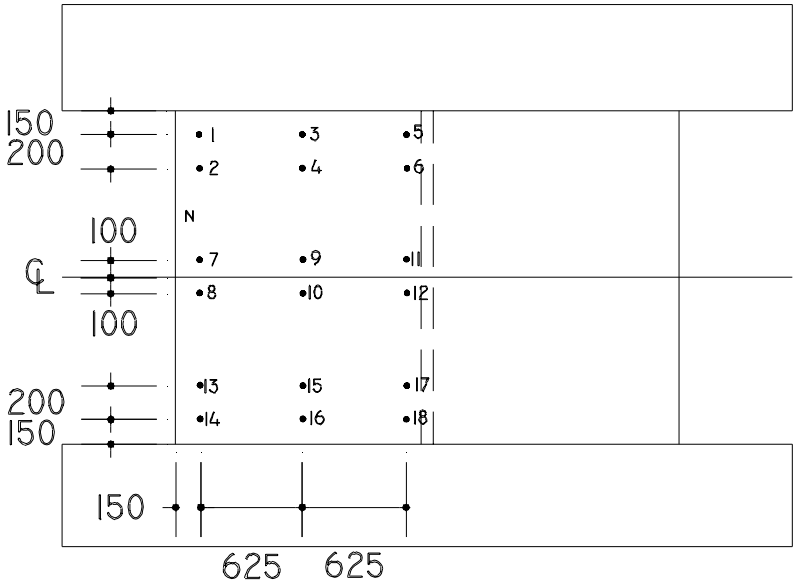

Figure 4.40 Flange Zurich Targets

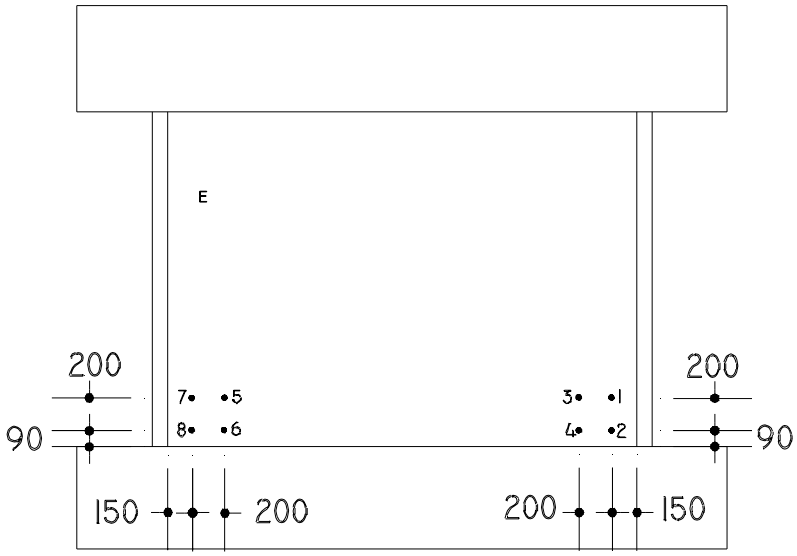

Figure 4.41 Web Zurich Targets

4.9.3 Linear Variable Differential Transducers (LVDTs)

Linear Variable Differential Transducers were installed throughout DP1 and DP2 to monitor displacements. A total of 21 LVDTs were employed. Figures 4.42 and 4.43

show the locations of the instruments from an elevation view of the web wall and a top view of top slab.

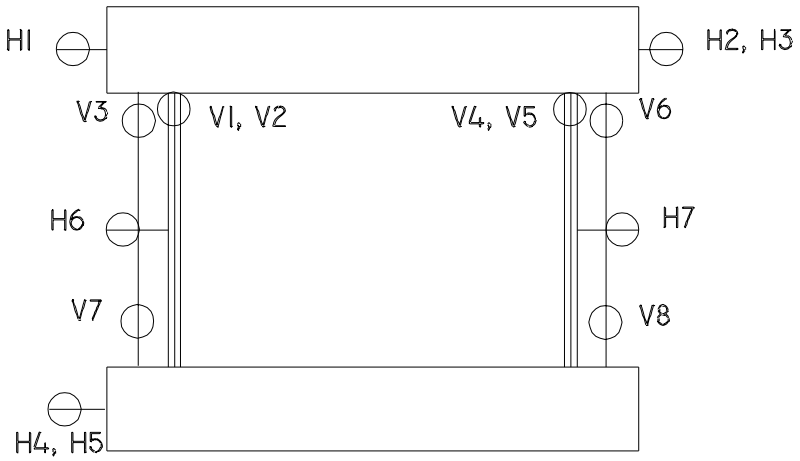

Figure 4.42 Elevation View of LVDTs

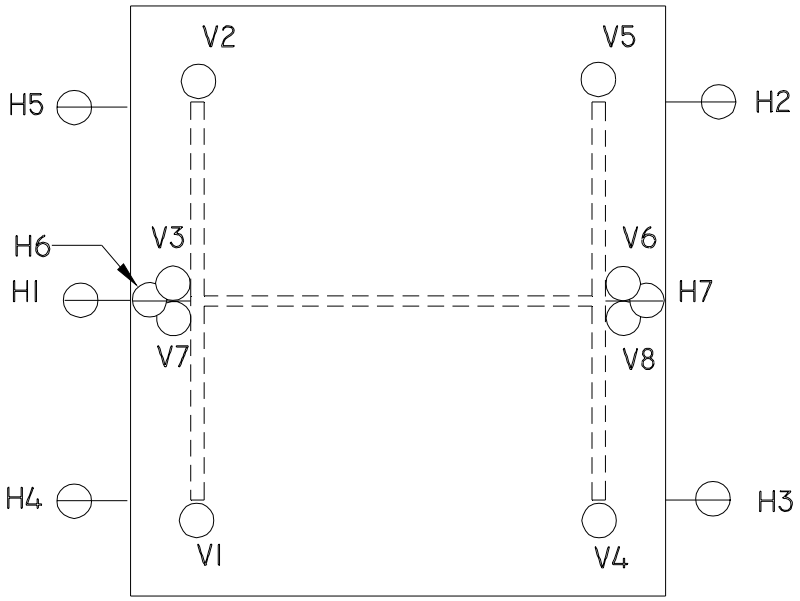

Figure 4.43 Top View of LVDTs

The LVDTs installed to measure horizontal displacements were denoted by an H, and a V labelled those LVDTs used to measure vertical displacements. H1, H2, and H3 LVDTs recorded the horizontal displacement of the top slab, and H4 and H5 recorded the displacements of the base slab relative to the strong floor. H6 and H7 monitored the lateral displacement of the web wall at mid-height and were also used to determine the horizontal expansion of the web. The vertical LVDTs V1 through V6 measured the relative displacement of the top slab to the base slab, and V7 and V8 were mounted near the base slab to record the slip between the flange walls and the base slab.

An additional 6 LVDTs were mounted on the west face of the web wall near the north and south toe, as depicted by Figure 4.44.

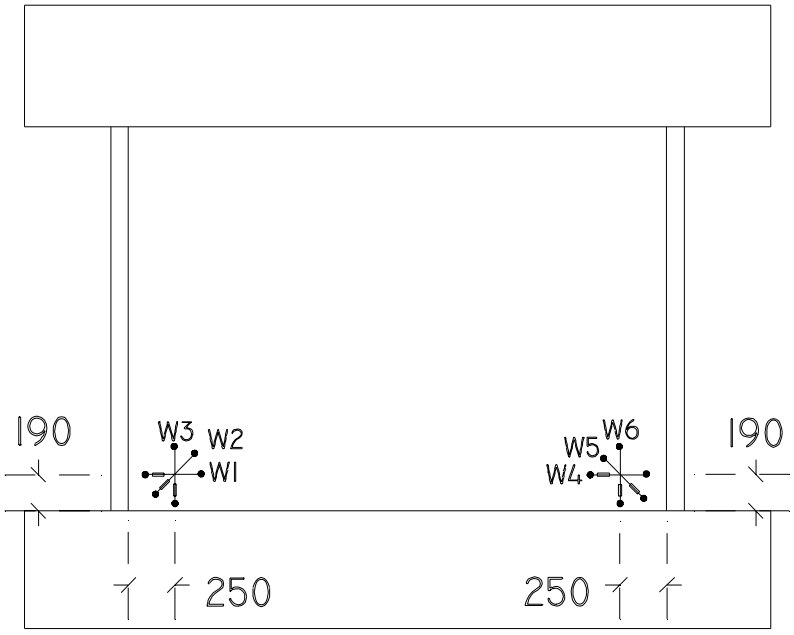

Figure 4.44 Web Wall LVDTs

The web wall LVDTs were labelled as W; W1 and W4 measured the horizontal displacements, W2 and W5 recorded the diagonal displacements, and W3 and W6

monitored the vertical displacements. The point of intersection of each set of LVDTs on the web wall coincided with the centre of the Zurich targets located on the opposite face of the web wall. The initial gauge lengths for the web wall LVDTs were 200 mm for W1, W3, W4, and W6, and 283 mm for W2 and W5.

4.9.4 Sensitivity of Instrumentation

The experimental data presented in Chapters 5 and 6 includes the differences in measured behaviour between the two specimens, and in some cases the differences were rather small. The instruments, as listed in Tables 4.4 and 4.5, were sensitive enough to detect differences according to the precision limits listed.

Table 4.4 Sensitivity of Instrumentation for DP1

Instrument	Identifier	Sensitivity
Load Cells	Horizontal	0.1 kN
	Vertical	0.032 kN
LVDTs	H1, H2, H3	0.001 mm
	H4, H6, H7, V2, V3, V4, V5, V6, V7, V8, W1, W2, W3, W4, W5, W6,	0.000625 mm
	V1, H5	0.0008 mm
Strain Gauges	FV12S6, FV13S10, FV13S7, WV22A13, WV22B10, WH17, WV17B8, WV12B6, WV12A5, WH16, WH14, WH15, WH18, WV7B4, WV7A3, WV2B2, WV2A1, WV17A7, WV22A9, WV12A12, WV2A11, FV13N7, FV13N10, FV8N9, FHN11, FV8N4, FV11N5, FV12N6, FV11S5	2.5 με
	FV2N1, FV4N3, FV2N8, FV3S2, FV8S4, FV4S3, FHS11, FV2S8, FV2S1, FV3N2, FV8S9	2.0 με
Zurich Extensometers	200 mm	2.0 με
	282.8 mm	1.4 με

Table 4.5 Sensitivity of Instrumentation for DP2

Instrument	Identifier	Sensitivity
Load Cells	Horizontal	0.1 kN
	Vertical	0.032 kN
LVDTs	H1	0.0025 mm
	H2, H3	0.0032 mm
	H4, H5, V7, V8	0.000625 mm
	H6, H7, W1, W2, W3, W4, W5, W6	0.00125 mm
	V1, V2, V3	0.0011 mm
	V4, V5, V6	0.001 mm
Strain Gauges	FV11N5, FV13N7, FHN11, FV13N10, FV8N4, FV12N6, FV13S10, FV11S12, FV13S7, FHS11, FV12S6, FV8S4, FV11S5, FV8S9, WH14	2.5 με
	FV2S8, FV4S3, FV2S1, FV3S2, WV22A13, WV22B10, WV22A9, WV12A5, WV12A12, WH16, WV12B6, WH18, WV2A11, WV2B2, WV2A1, WV17B8, WV17A7, WH15, WV7B4, WH17, WV7A3, FV2N1, FV2N8, FV3N2, FV4N3	2.0 με
Zurich Extensometers	200 mm	2.0 με
	282.8 mm	1.4 με

CHAPTER 5

Experimental Results

5.1 INTRODUCTION

The focus herein is to summarize the qualitative and quantitative experimental results from test specimens DP1 and DP2. The qualitative results include photographs of each specimen through the course of testing, displaying the crack patterns, crushing locations, and state of the walls at failure. Readings of crack widths, concrete surface strains, reinforcement strains, and displacements constitute the quantitative results.

5.2 TESTING PROCEDURE

Prior to commencing each test, the instrumentation was connected to the data acquisition system, and the loading actuators were anchored into position. The vertical actuators, in the case of DP1, were loaded to a negligible load to set their position, and the horizontal actuators were linked to the top slab. Before applying the axial load, two sets of Zurich readings were taken as reference points to determine the change in concrete strains throughout the loading regime.

The vertical actuators were first loaded to a combined force of 940 kN. This force, in addition to the self-weight of the top slab, resulted in a total vertical load of 1200 kN and was held constant for the entire duration of testing. DP2 was tested under its self-weight of 260 kN. Zurich readings were also recorded after imposing the vertical load to determine the amount of compressive shortening. The DP1 test spanned 11 days;

therefore, to ensure that the vertical actuators maintained their position, a residual load of 100 kN was maintained at the end of each testing day.

The horizontal actuators were responsible for imposing the cyclic displacements, in increments of 1 mm, to the walls. Two repetitions at each displacement level were imposed. The first cycle consisted of pulling the specimens toward the laboratory strong wall, hereafter referred to as the pull or the negative direction. The displacements were monitored by LVDT H1 located at the centre on the north side of the top slab. Zurich readings were taken at the peak displacement, at zero loads, and at zero displacement for every repetition. At the peak displacement, the load was reduced 5 to 10 % to prevent creep. The LVDTs and the reinforcement strain gauges recorded continuous readings throughout the test. Testing was halted at 15 mm and 10 mm of displacement for DP1 and DP2, respectively, so that a simple and effective rehabilitation could be implemented.

A problem was encountered in the first excursion to –1 mm of displacement in DP1. The threaded rods connecting the horizontal actuators to the top slab had been post-tensioned prior to testing. Therefore, the load recorded corresponds to the difference between the load at 1 mm of displacement and the decompression force. The rods were released of the post-tensioning and the testing resumed without further flaws.

Testing of DP1 and DP2 did not commence soon after casting. Table 5.1 indicates the age of the specimens at the time of testing and the time to complete the test.

Table 5.1 Age of Test Specimens

Specimen	Age of Specimen at Testing (Days)	Time to Complete Testing (Days)
DP1	183	11
DP2	168	8

5.3 CRACKING CHARACTERISTICS

The two specimens exhibited similar cracking patterns throughout the course of testing. Figure 5.1 is a photograph of DP2 just prior to testing. A grid consisting of 15 elements spaced 192 mm horizontally and 16 elements spaced 126 mm vertically, representing the analytical finite element mesh of the web wall, is visible.

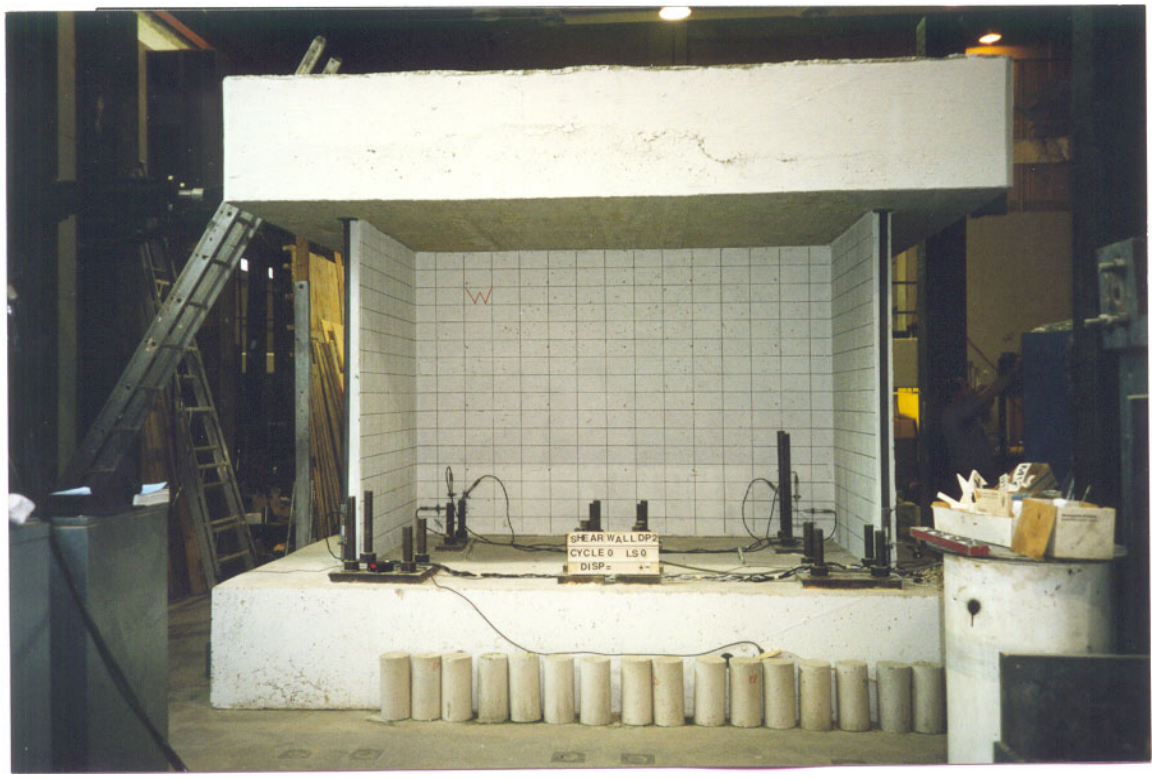

Figure 5.1 Initial State of Test Specimen DP2

Shear cracking initiated at a lateral load of –408 kN with a corresponding displacement of –0.63 mm for DP1, and at –256 kN with a displacement of –0.47 mm for DP2. These cracks surfaced during the first excursion to –1 mm. [The negative quantities refer to pulling of the specimen toward the laboratory strong wall.] Similar loads and displacements were recorded at the onset of shear cracking in the positive direction. The cracking propagated through the thickness of the web wall and was inclined approximately 45 degrees to the horizontal plane. The initial shear cracking, however, seemed to be more widespread in DP1. The initial cracking in DP2 was confined along a diagonal strut that formed through the centre of the web wall. Figures 5.2 and 5.3 depict the initial shear cracking at the end of 1 mm of displacement for DP1 and DP2, respectively. The cracks marked in red, propagating from the top right corner to the bottom left corner of the west face of the web wall, are those that surfaced during the negative excursions. The blue marked cracks, representing the cracking that appeared during the positive displacements, extended from the top left corner to the bottom right corner. Shear cracks continued to appear with increasing displacement. The shear cracks generally extended the full height of the web wall and were inclined approximately 45 degrees to the horizontal. New cracks typically appeared during the first excursion of displacement. During the second excursion, smaller secondary cracks formed between the major shear cracks. By the end of cycle 4 (4 mm of displacement), the web walls were essentially fully cracked. During cycle 5 there was visual evidence of slipping along the crack surfaces. During the unloading phase, the crack surfaces were not capable of re-aligning, causing a grinding of the two surfaces, resulting in localized crushing along the crack surfaces throughout the web wall.

Shear cracks continued to appear up to 8 mm of displacement. Beyond 8 mm of displacement, additional cracking was limited to extensions of previously formed cracks. The maximum shear crack widths recorded were 1.0 mm for DP1 and 0.6 mm for DP2, observed during cycle 13 and cycle 9, respectively. For both specimens, cracks that formed during the later cycles generally remained parallel to the first shear cracks, thus there was no visible evidence of cracks rotating. A subtle difference in web cracking between DP1 and DP2 was the presence of flexure-shear cracks in the toe regions of DP2. Figures 5.4 through 5.9 show the cracking pattern of the west face of the web wall at 4 mm, 8 mm, and the final displacement level for DP1 and DP2.

Similar flexural cracking patterns were observed on the flanges of DP1 and DP2. For DP1, the first flange crack appeared during the first excursion to 3 mm, on the outside surface of the south flange near the flange-web wall intersection. The crack surfaced approximately one-third of the wall height from the top slab. The approximate load and displacement at the onset of cracking were –819 kN and –2.9 mm, respectively. For DP2, the first flange crack surfaced on the south flange wall during the first excursion to 2 mm. The crack surfaced one-quarter of the height of the wall from the base slab, extended the full width of the flange, and propagated through the thickness of the flange. The load and displacement recorded at cracking were –385 kN and –1.19 mm, respectively. Full-width flexural cracks first surfaced at 4 mm of displacement for DP1 and continued to surface to the end of 11 mm of displacement. Full-width flexural cracks, for DP2, continued to appear to the end of 9 mm of displacement.

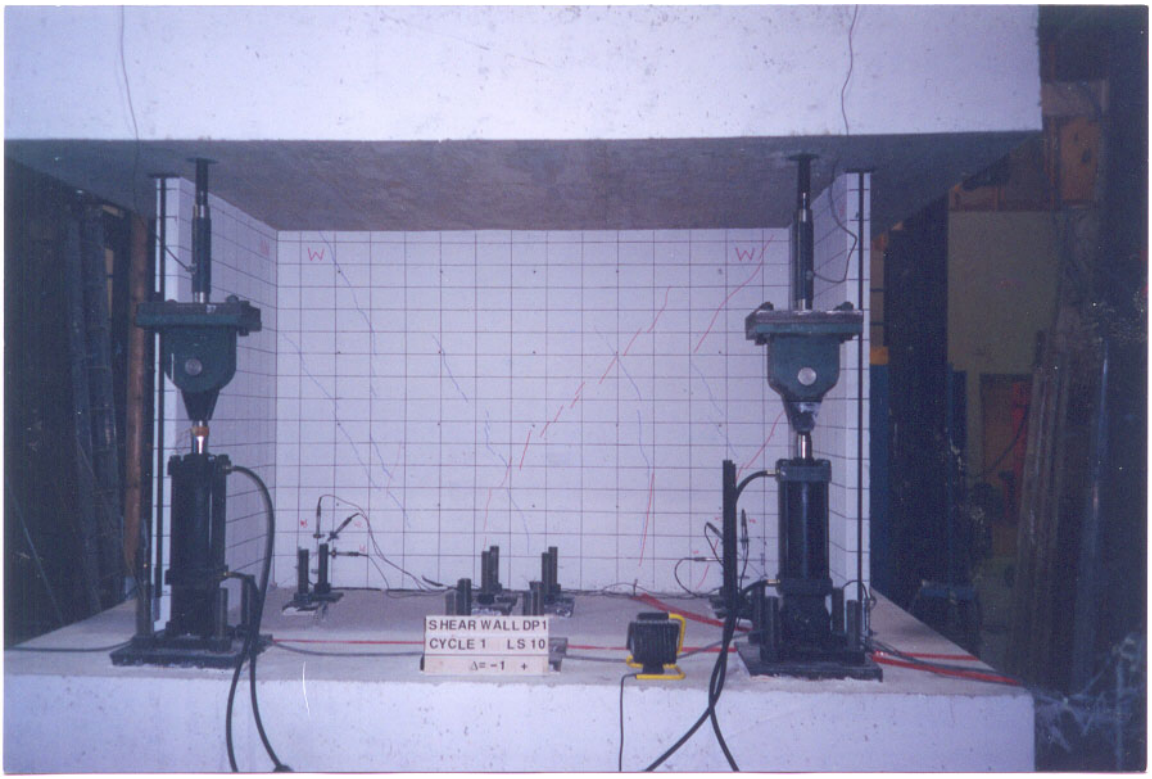

Figure 5.2 DP1 Web Wall After 1 mm Lateral Displacement

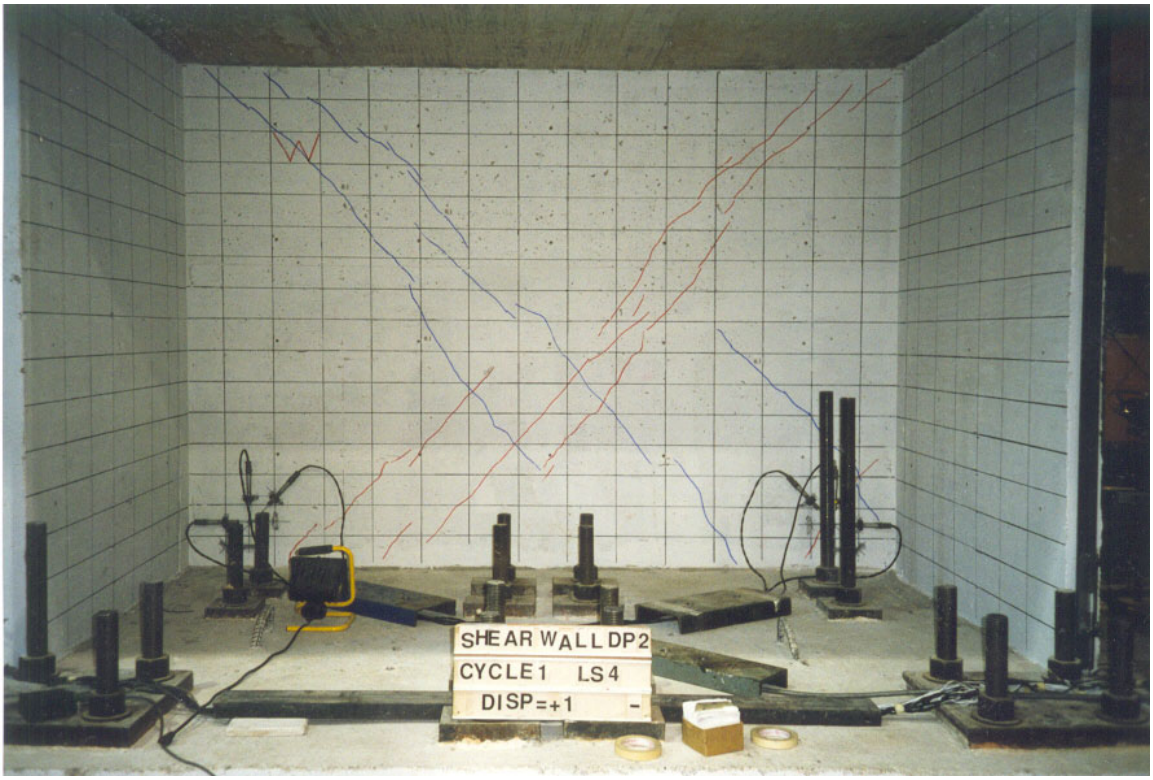

Figure 5.3 DP2 Web Wall After 1 mm Lateral Displacement

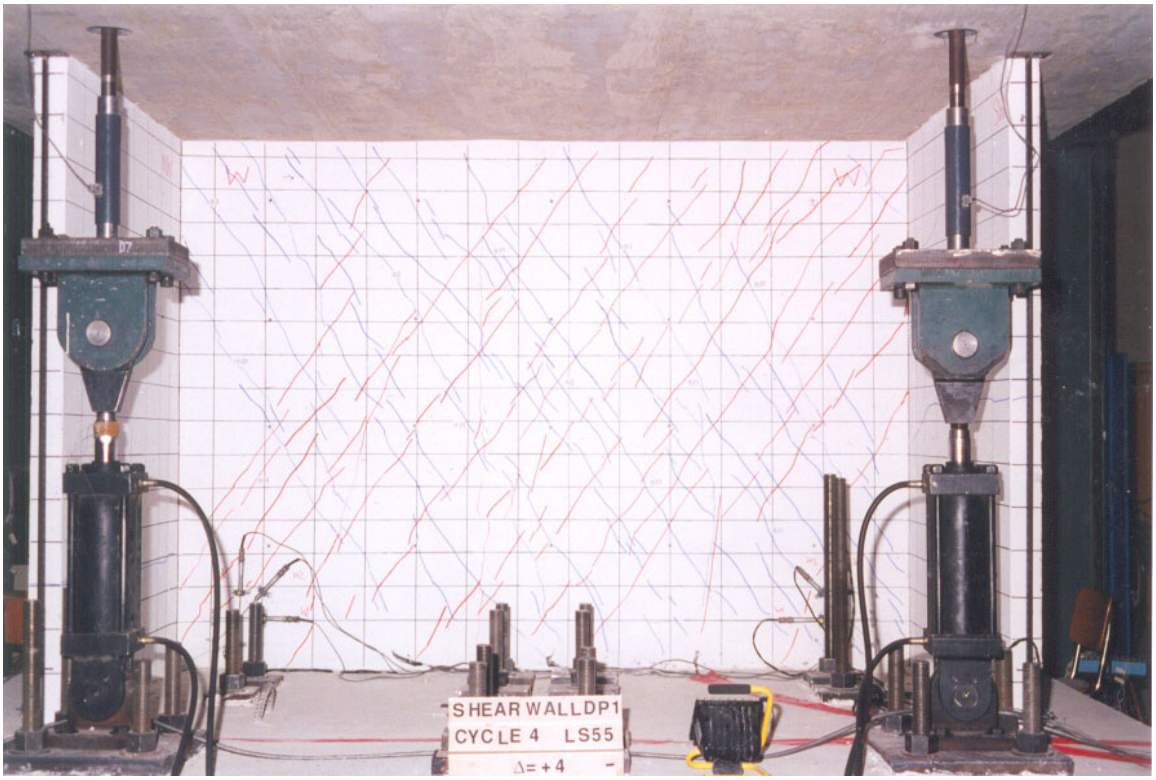

Figure 5.4 DP1 Web Wall After 4 mm Lateral Displacement

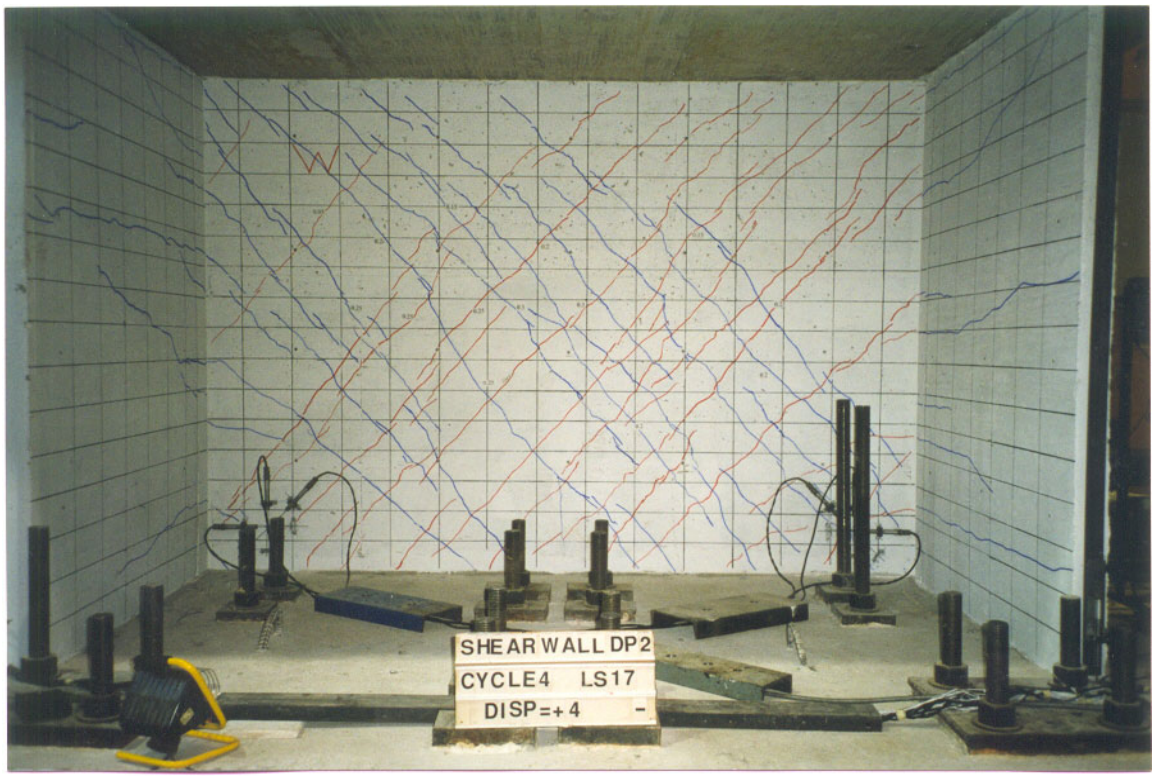

Figure 5.5 DP2 Web Wall After 4 mm Lateral Displacement

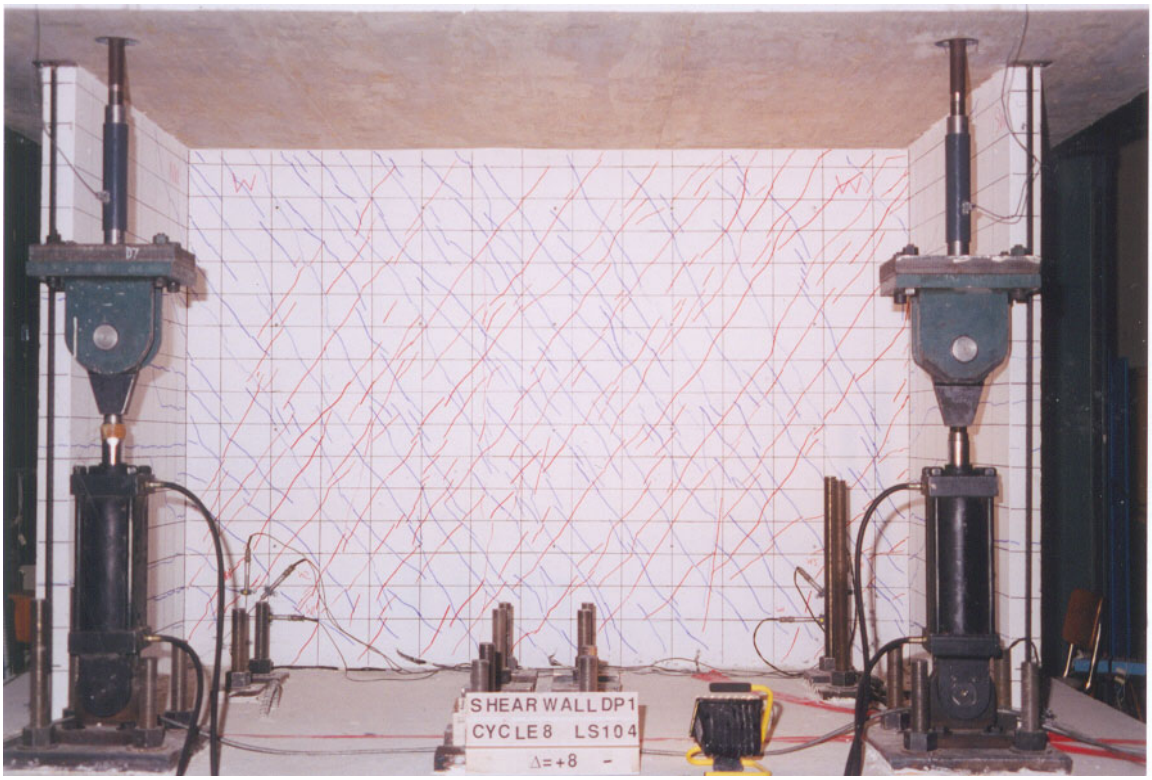

Figure 5.6 DP1 Web Wall After 8 mm Lateral Displacement

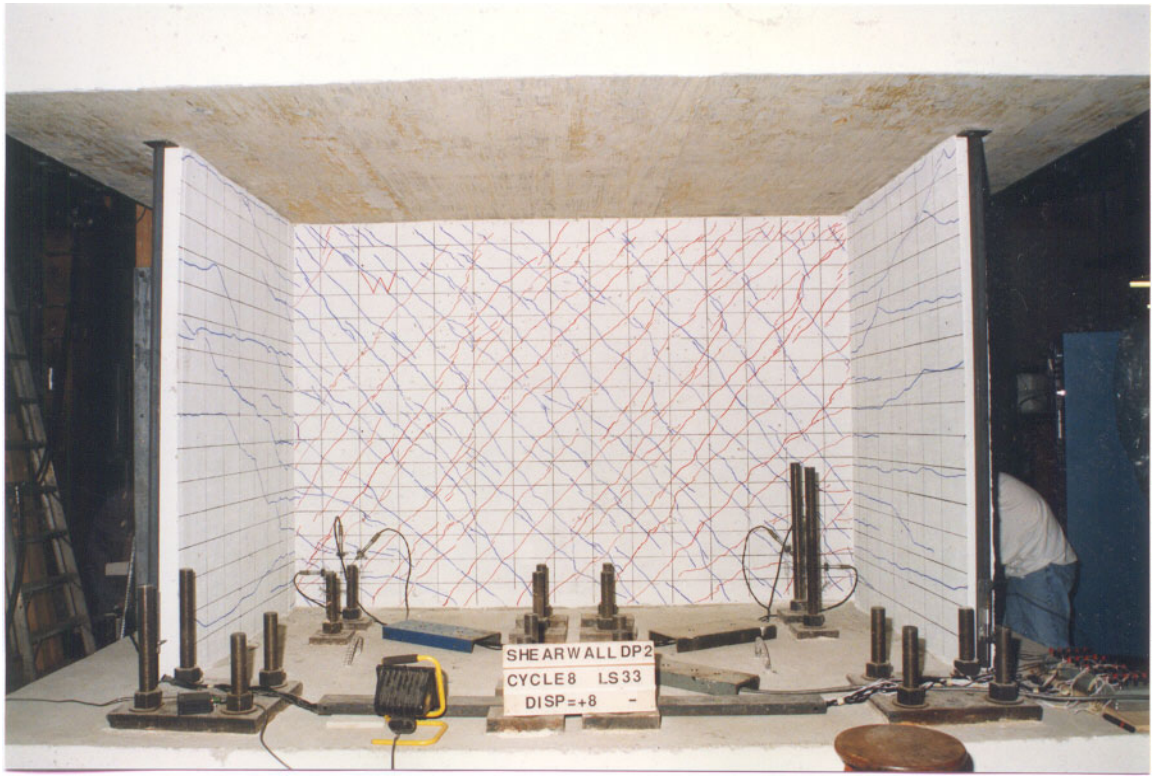

Figure 5.7 DP2 Web Wall After 8 mm Lateral Displacement

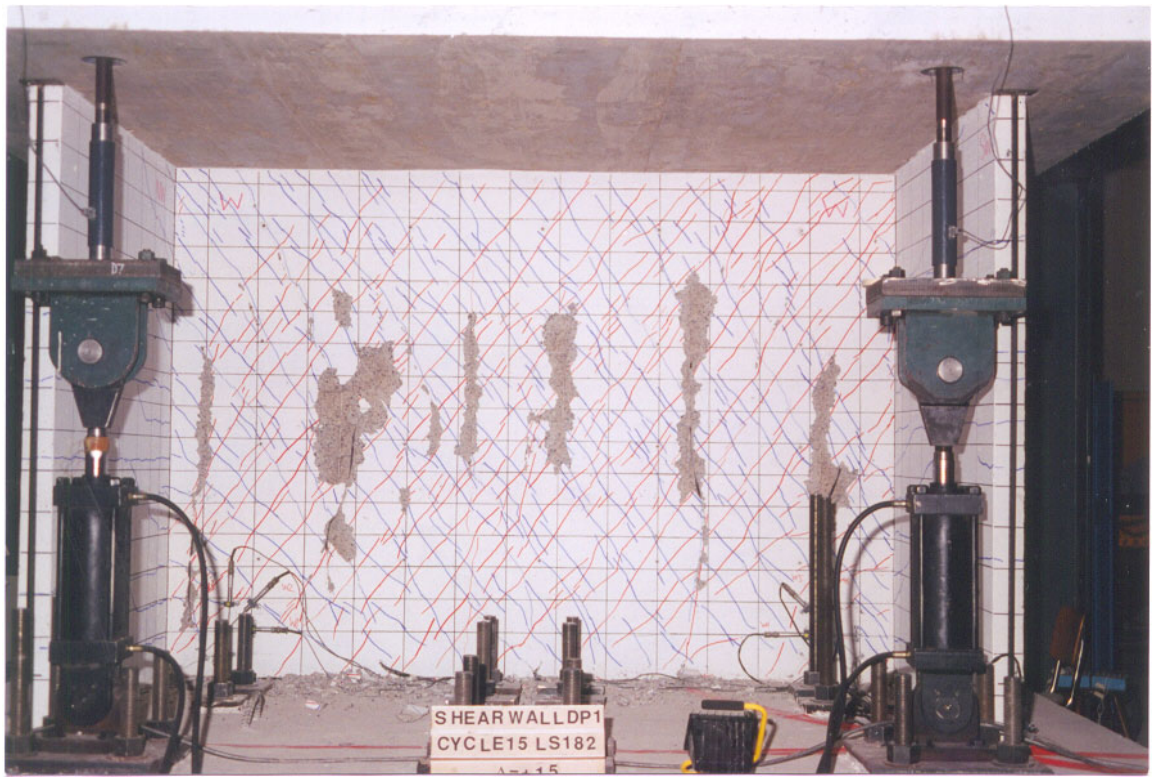

Figure 5.8 DP1 Web Wall at Failure

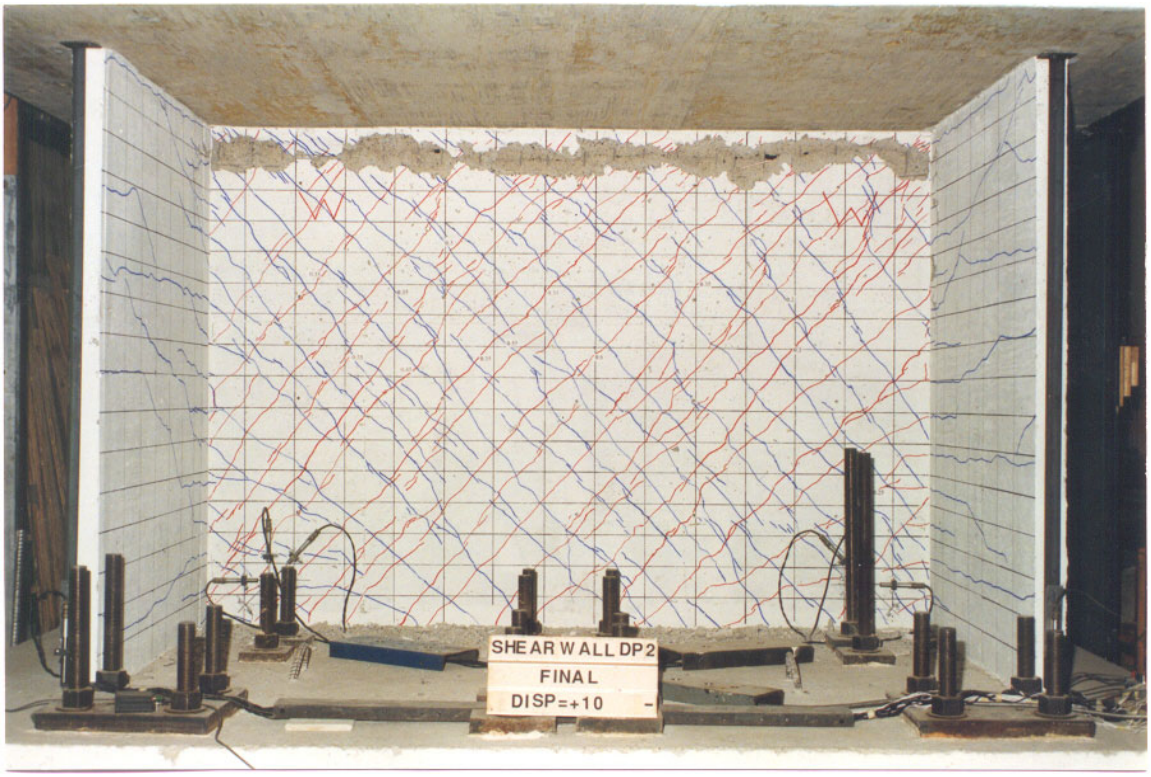

Figure 5.9 DP2 Web Wall at Failure

By the end of testing, four to five major flexural cracks were evident on the flange walls of the two specimens, evenly spaced along the height, and extending the full width and thickness of the wall. Further flange cracking, in the form of U-shape patterns, were concentrated near the flange-web wall intersection. Vertical cracks extending the full height of the flange walls were also visible at the flange-web wall connection.

The location of the maximum flexural crack differed for DP1 and DP2. For DP1, the maximum crack width was measured near the mid-height of the flange, and approximately 50 mm below the top slab for DP2. These crack locations contributed to the failure mechanism of each specimen, as will be discussed later. A maximum flexural crack width of 1.1 mm was recorded during the first excursion to 12 mm of displacement for DP1, and a 1.0 mm crack width occurring during 9 mm of displacement was measured for DP2. Appendix A contains tables reporting the full cracking pattern for each displacement level for the two test specimens. Figures 5.10 and 5.11 are photographs of the north flange wall for DP1 after 4 mm of displacement and the south flange for DP2 after 2 mm, respectively, illustrating the first flexural cracks. Figures 5.12 and 5.13 illustrate the state of DP1 and DP2 after the flange walls were essentially fully cracked, which corresponds to displacements of 11 mm for DP1 and 9 mm for DP2. Finally, Figures 5.14 and 5.15 show the damage in the flange walls at the end of testing.

Figure 5.10 DP1 Flange Wall After 4 mm Lateral Displacement

Figure 5.11 DP2 Flange Wall After 2 mm Lateral Displacement

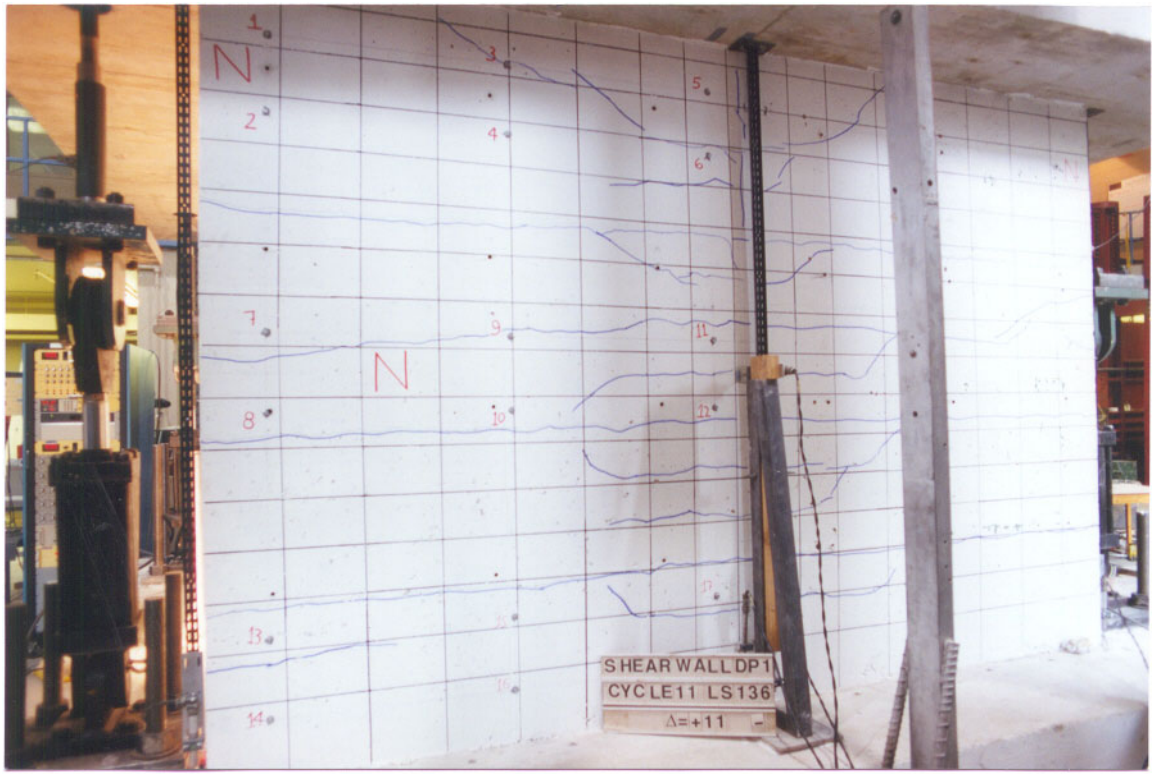

Figure 5.12 DP1 Flange Wall After 11 mm Lateral Displacement

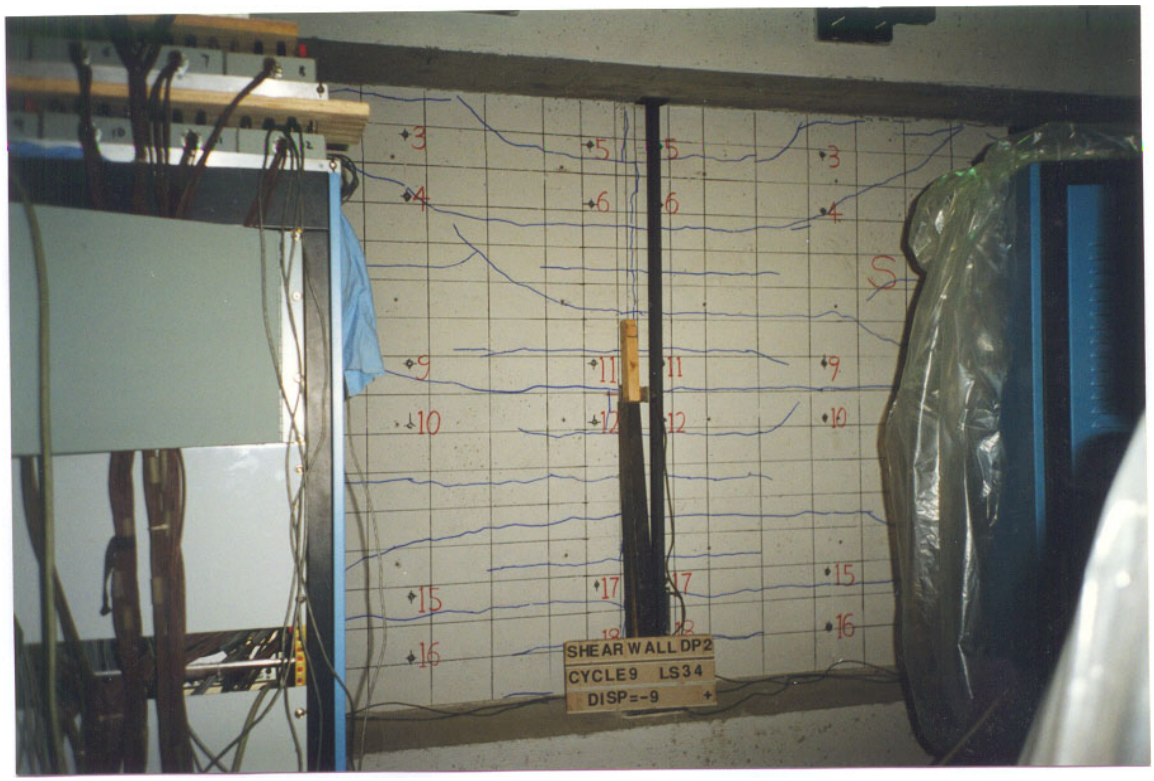

Figure 5.13 DP2 Flange Wall After 9 mm Lateral Displacement

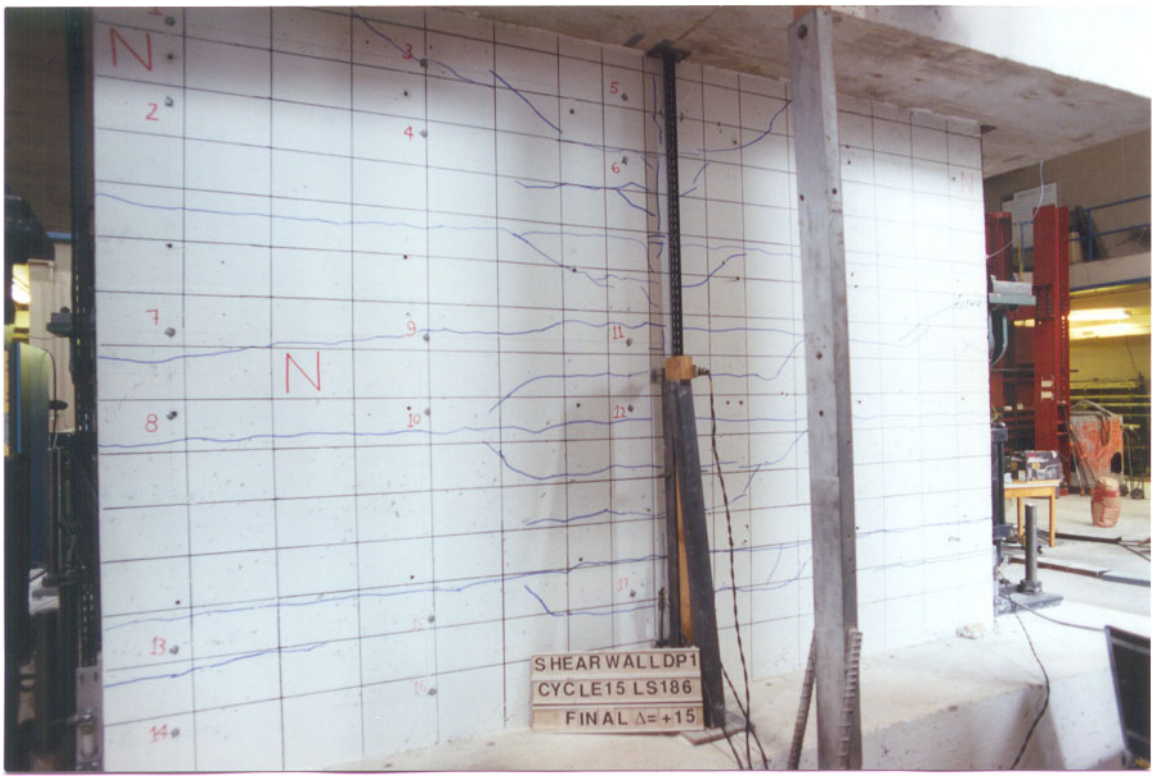

Figure 5.14 DP1 Flange Wall at End of Testing

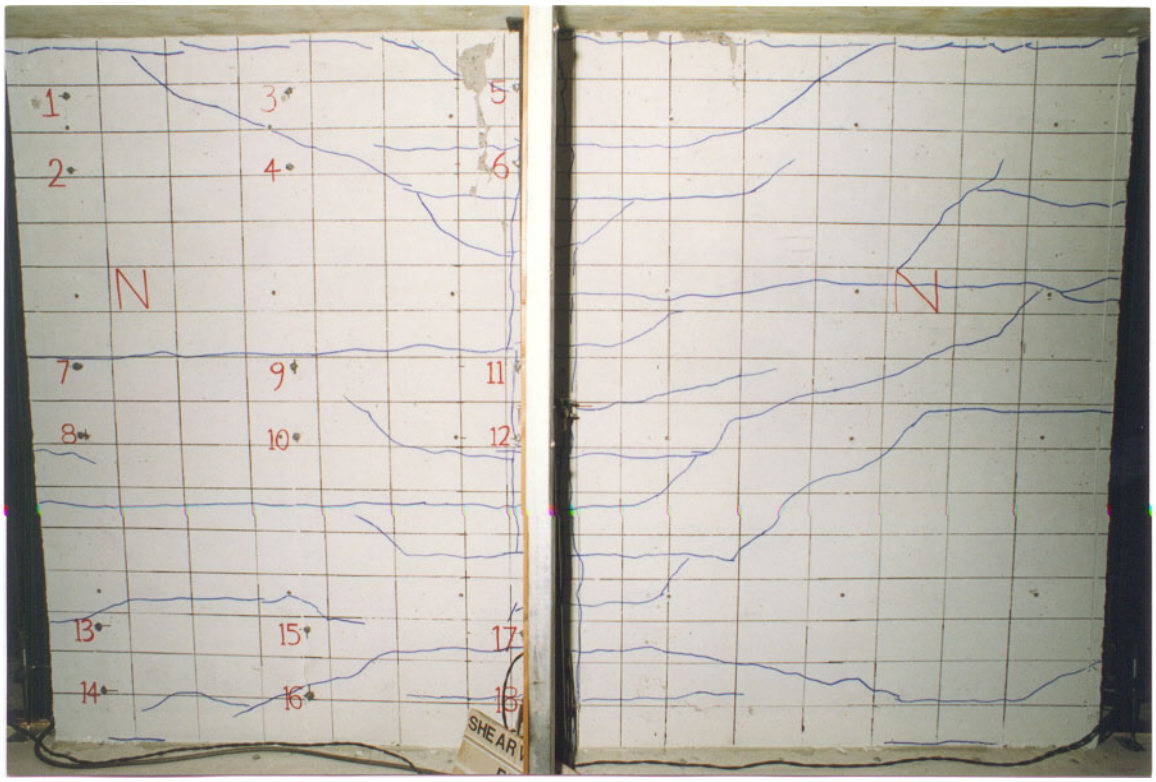

Figure 5.15 DP2 Flange Wall at End of Testing

5.4 LOAD-DEFORMATION RESPONSE

Load-deformation responses of DP1 and DP2 were monitored by 21 LVDTs mounted throughout each test specimen. Three of the LVDTs, H1, H2, and H3 were placed at the mid-height of the top slab to record the lateral displacement. H1 was used to determine the peak displacement for each cycle. The hysteresis response, as recorded by H1, for each wall is shown in Figures 5.16 and 5.17 for DP1 and DP2, respectively.

Testing was terminated after the completion of 15 mm of displacement for DP1. At this point, a significant portion of the descending branch of the load-deformation response had been attained. Maximum loads were recorded in the first excursion to 11 mm. The maximum load and corresponding displacement in the positive direction were 1298 kN and 11.14 mm, respectively; -1255 kN and –11.09 mm for the negative direction loading. Specimen DP2, without externally applied axial load, was not capable of sustaining a ductile post-peak response. The wall failed during the first excursion to 10 mm. Maximum loads were recorded during the first excursion to 9 mm. In the positive direction, a load of 904 kN at a corresponding displacement of 9.15 mm was recorded, and a load of –879 kN at a displacement of –9.08 mm was attained in the negative direction. Figures 5.18 through 5.42 provide the load-deformation responses for each displacement level, as recorded by LVDT H1. The following chapter contains a further discussion of the hysteresis behaviours of each test specimen. [The responses from other LVDTs are available in the Appendices.] The associated phenomenological wall behaviours discussed in Chapter 6 include: twisting of the top slab, horizontal expansion of the web wall, base slip, elongation of the flange walls, and bond slip.

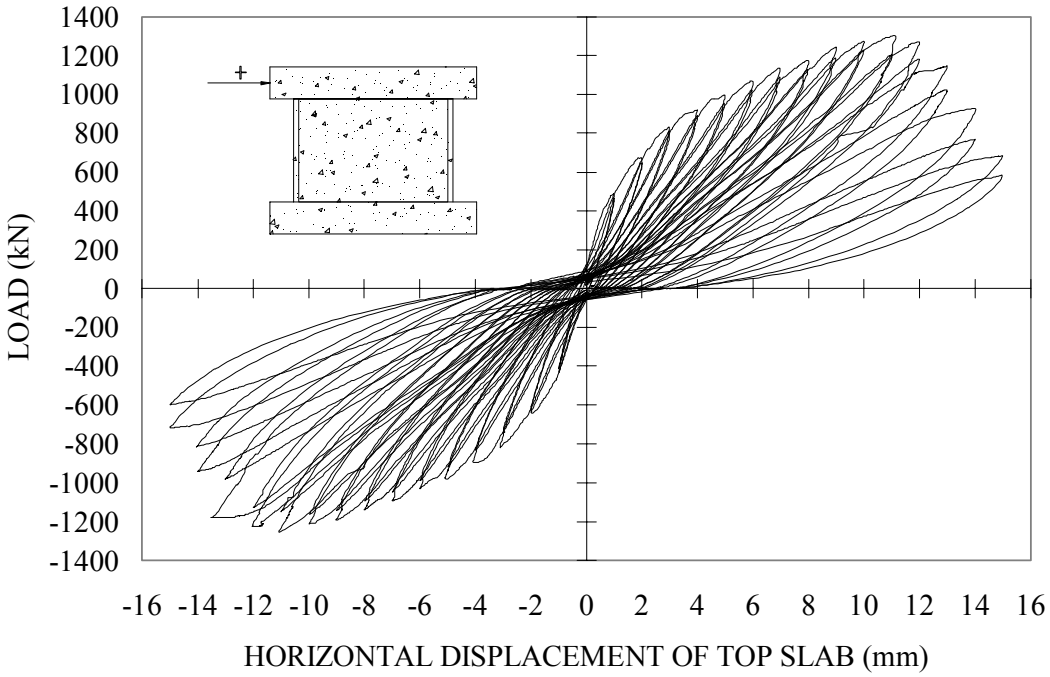

Figure 5.16 DP1 Observed Load-Deformation Response

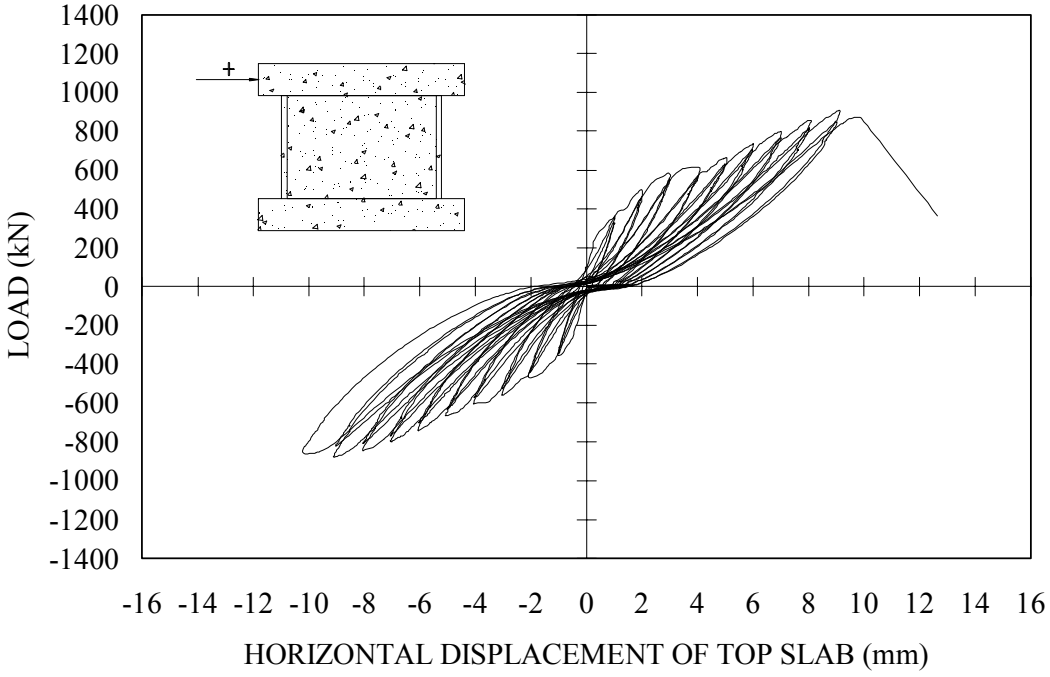

Figure 5.17 DP2 Observed Load-Deformation Response

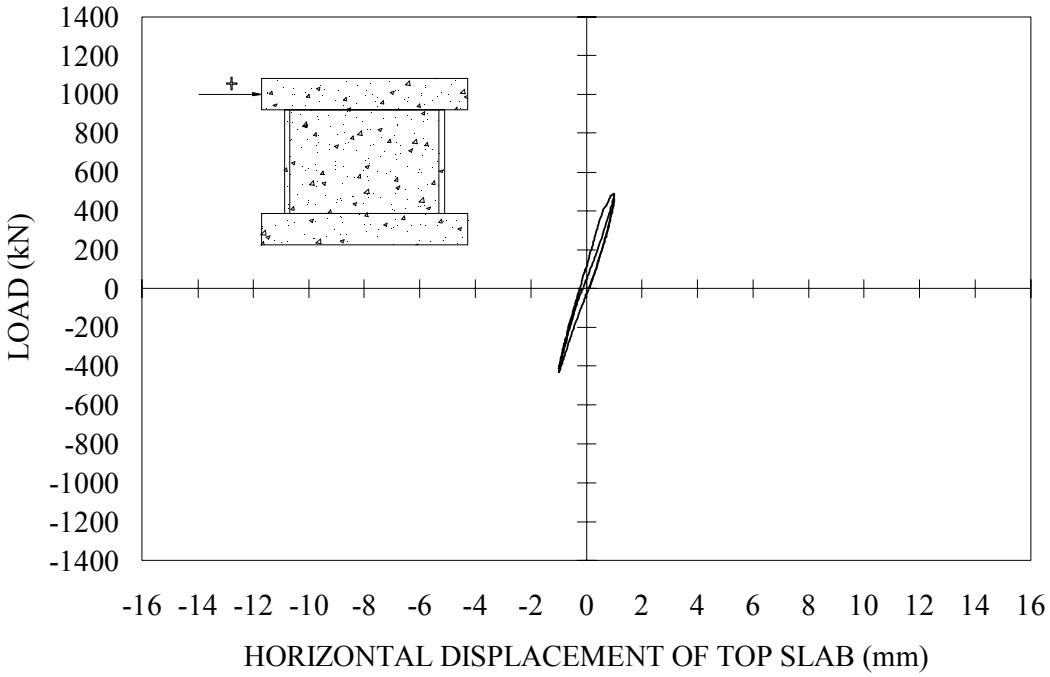

Figure 5.18 DP1 Cycle 1

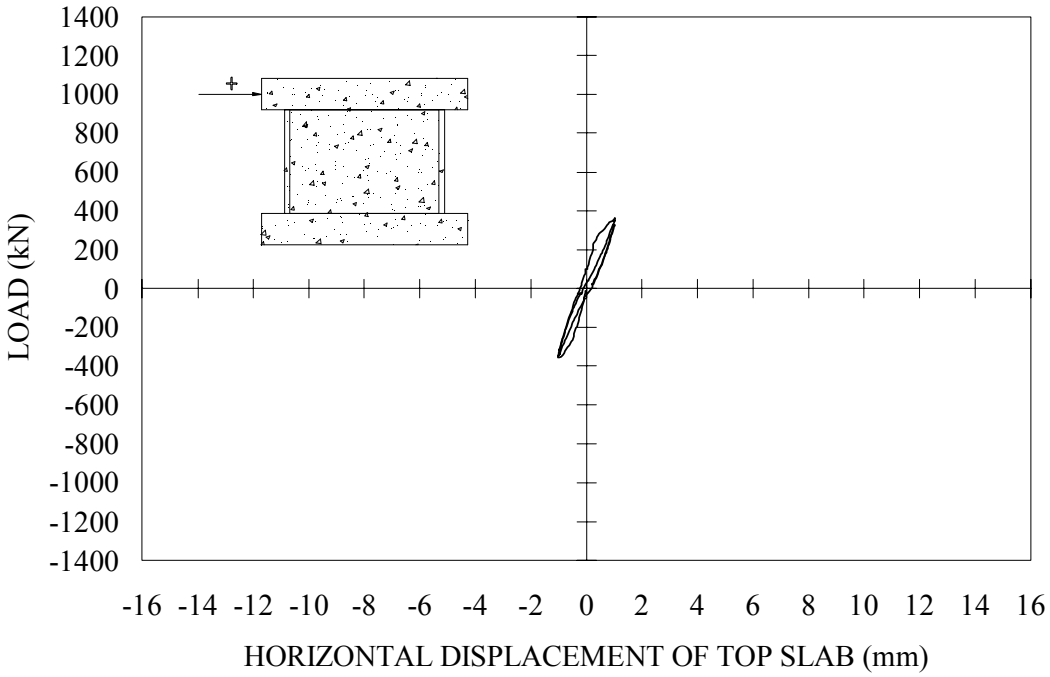

Figure 5.19 DP2 Cycle 1

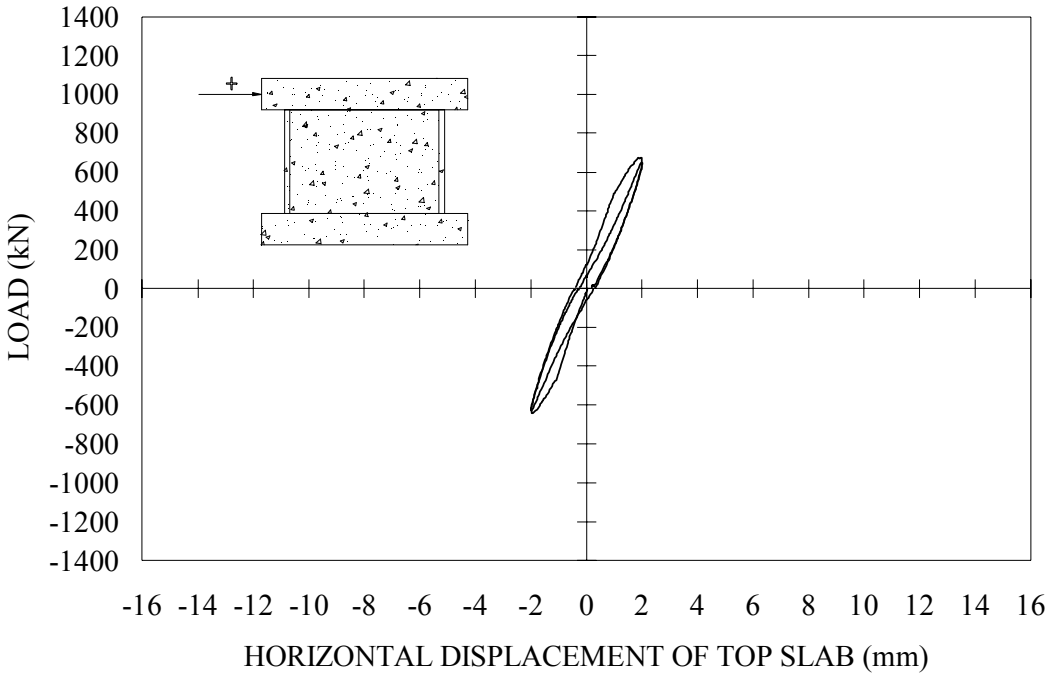

Figure 5.20 DP1 Cycle 2

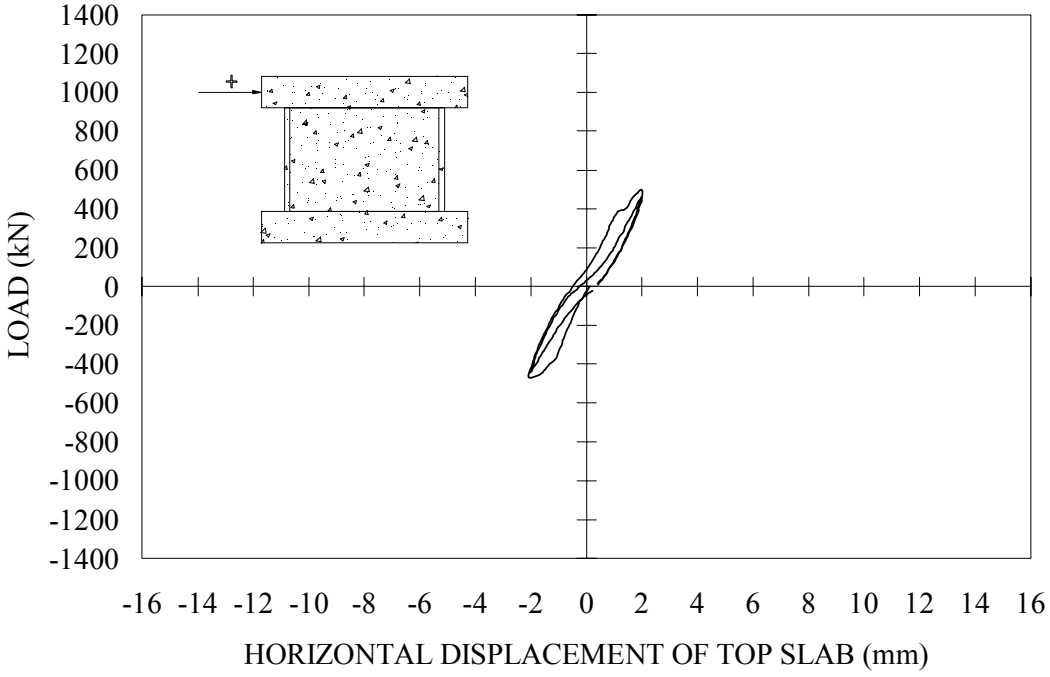

Figure 5.21 DP2 Cycle 2

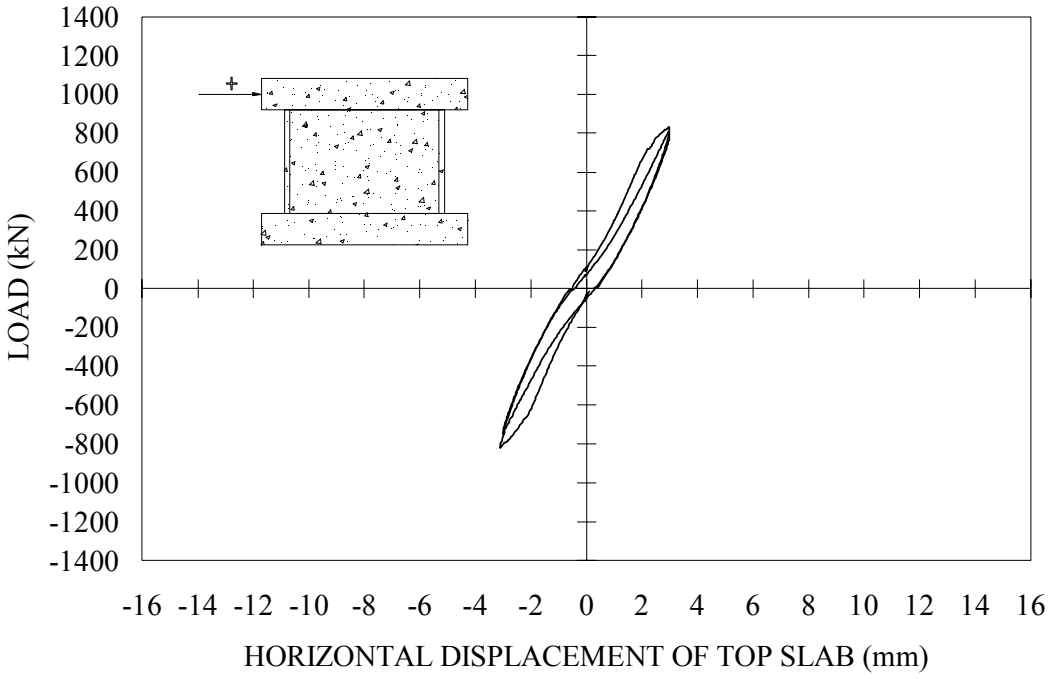

Figure 5.22 DP1 Cycle 3

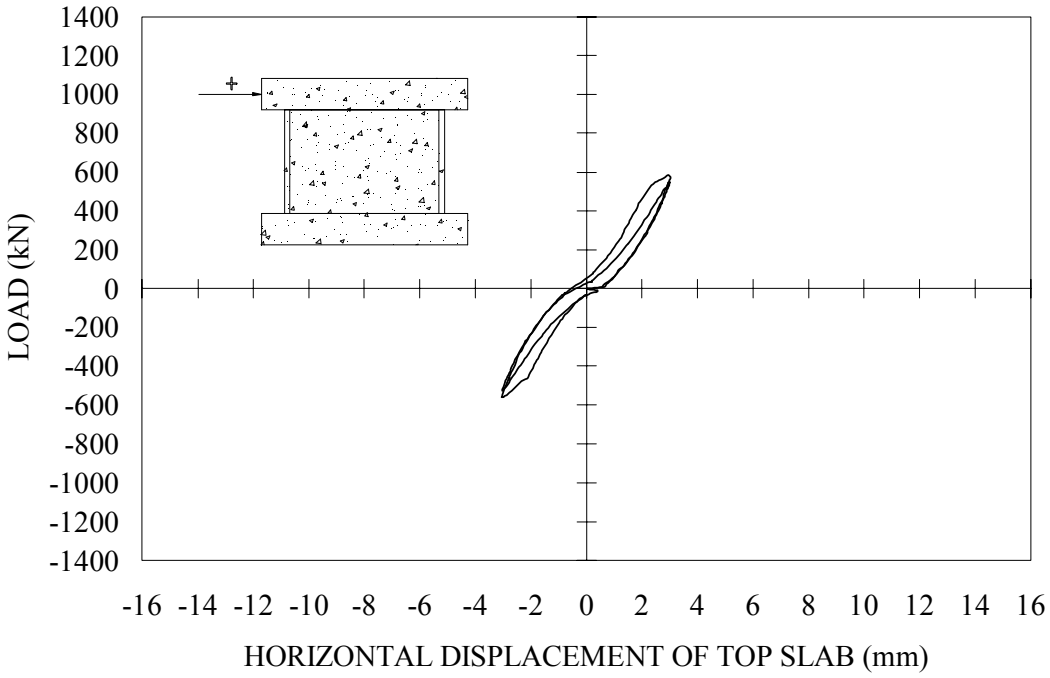

Figure 5.23 DP2 Cycle 3

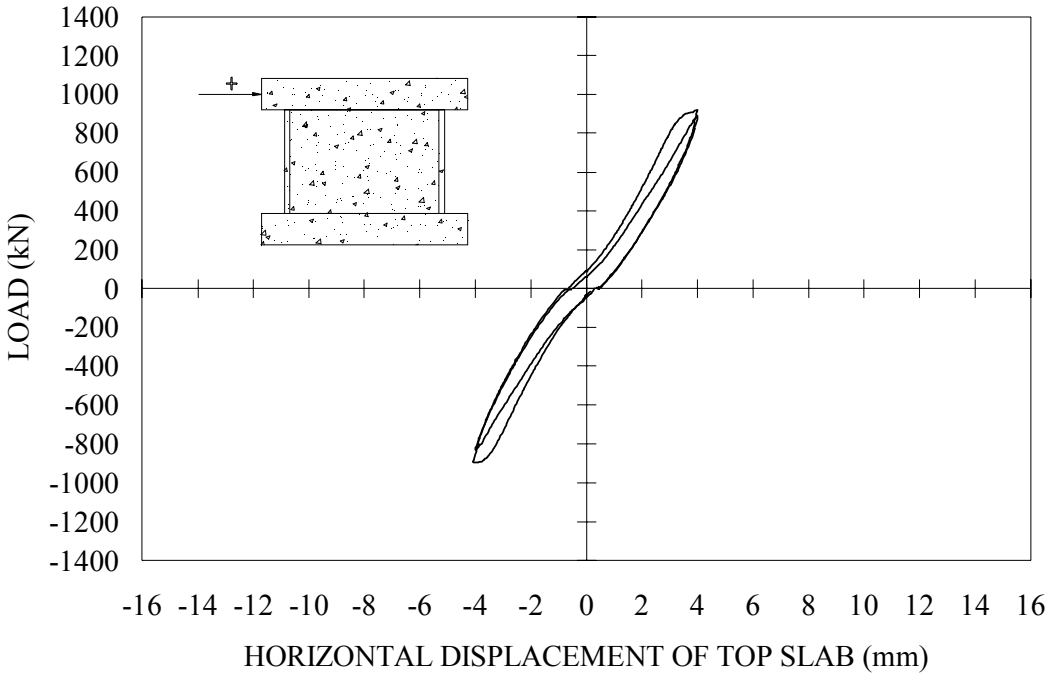

Figure 5.24 DP1 Cycle 4

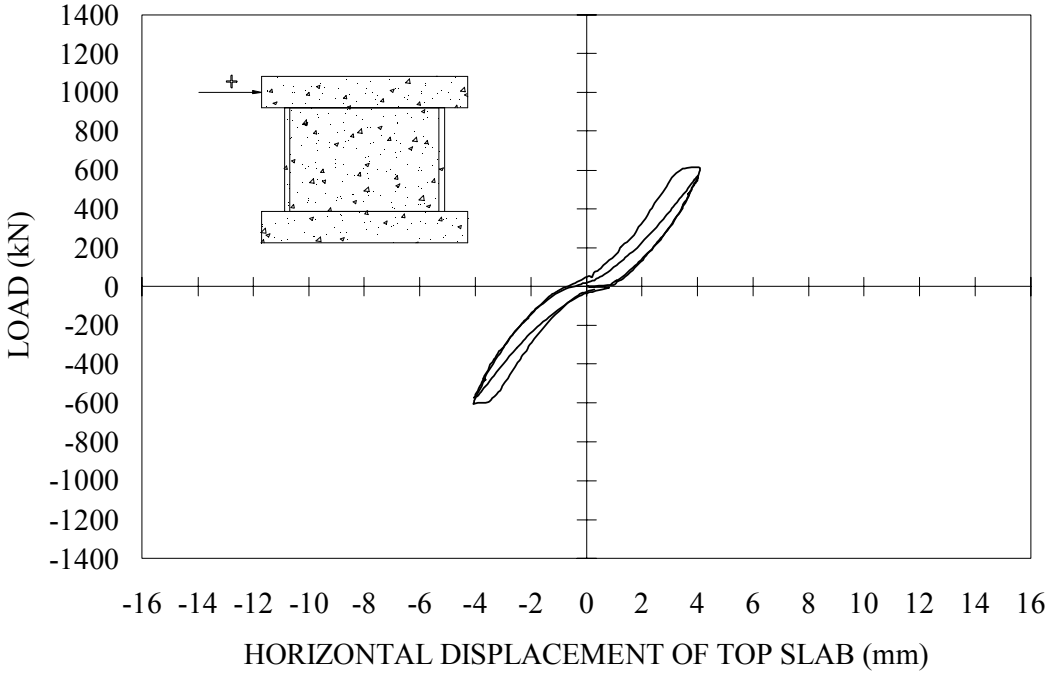

Figure 5.25 DP2 Cycle 4

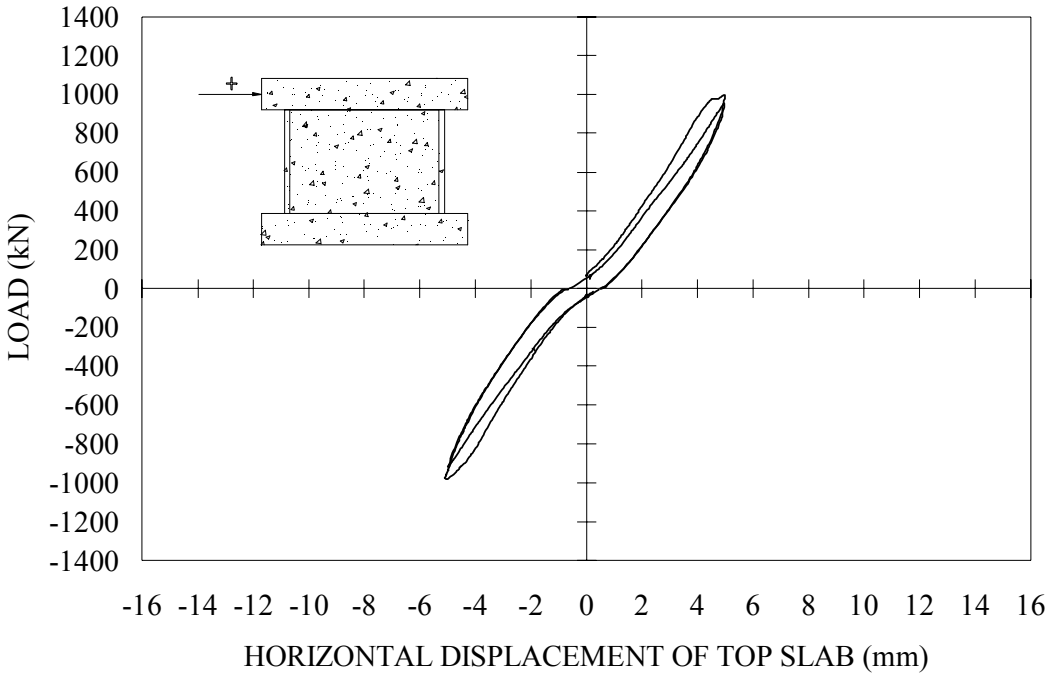

Figure 5.26 DP1 Cycle 5

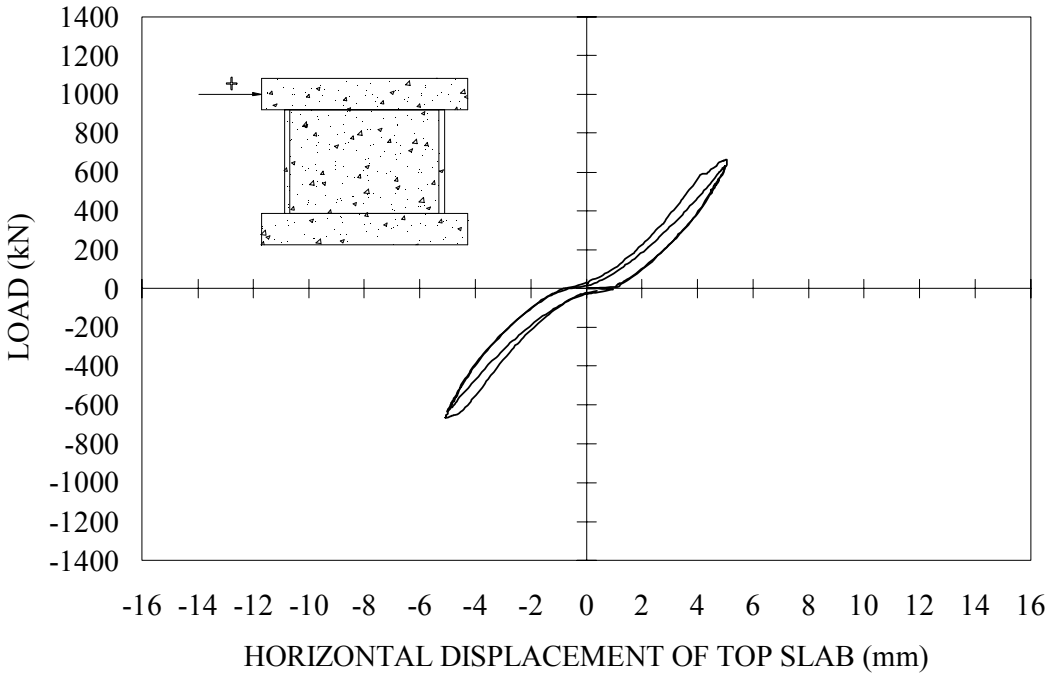

Figure 5.27 DP2 Cycle 5

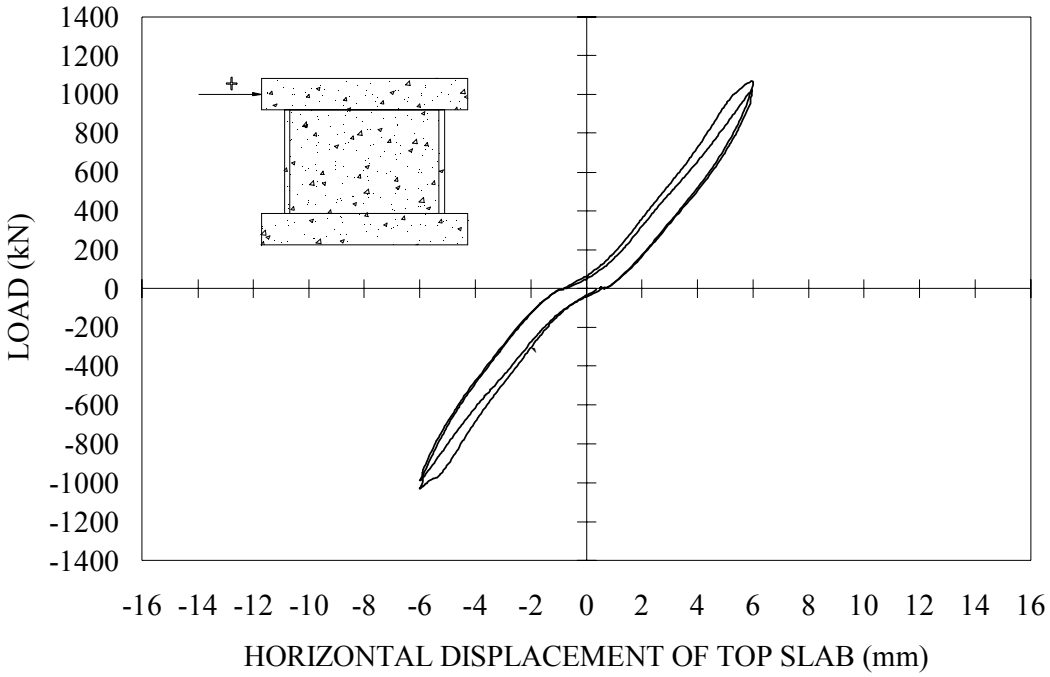

Figure 5.28 DP1 Cycle 6

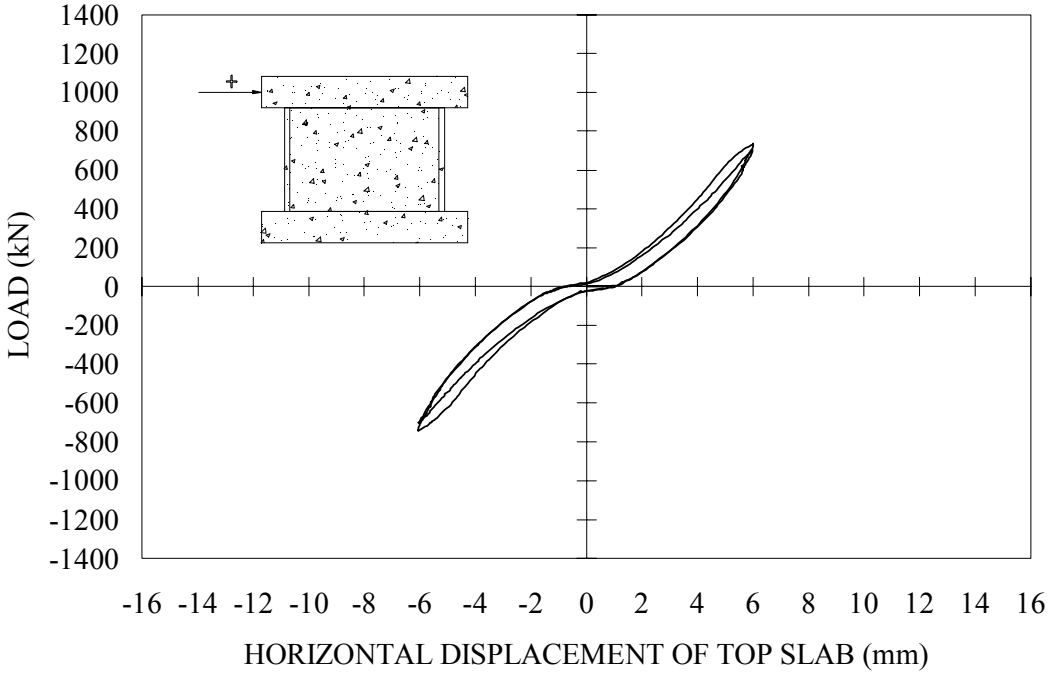

Figure 5.29 DP2 Cycle 6

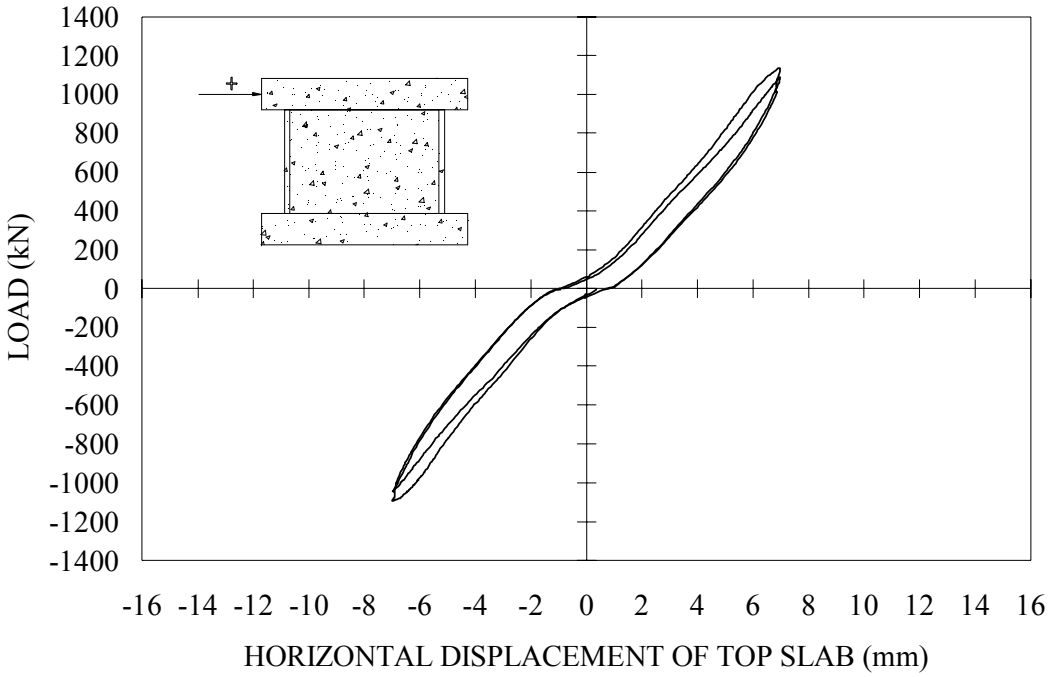

Figure 5.30 DP1 Cycle 7

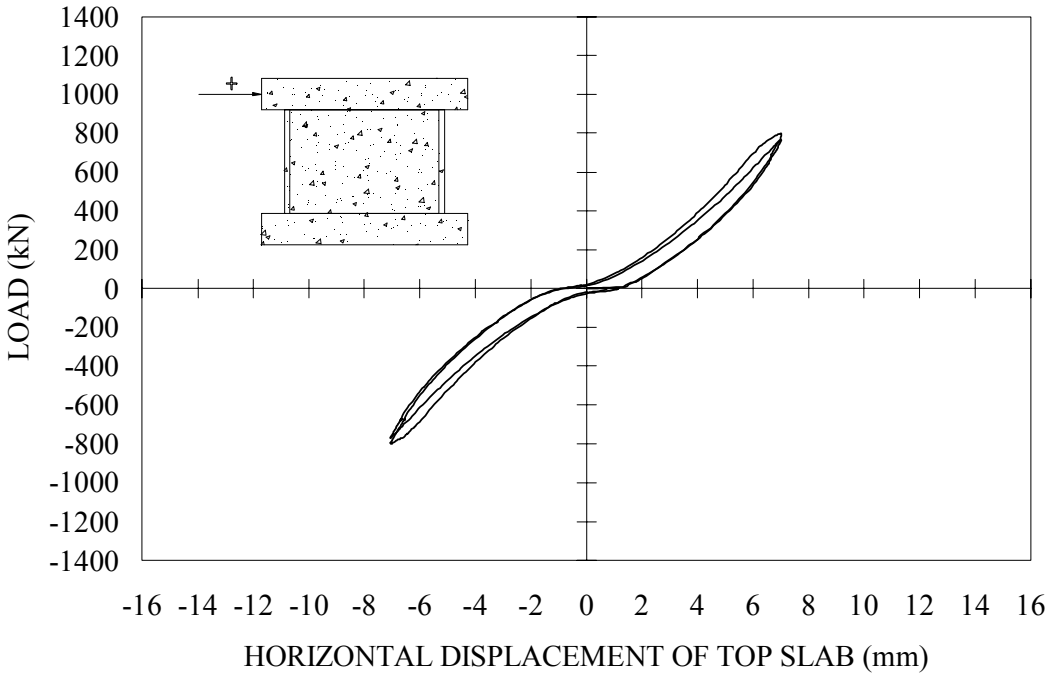

Figure 5.31 DP2 Cycle 7

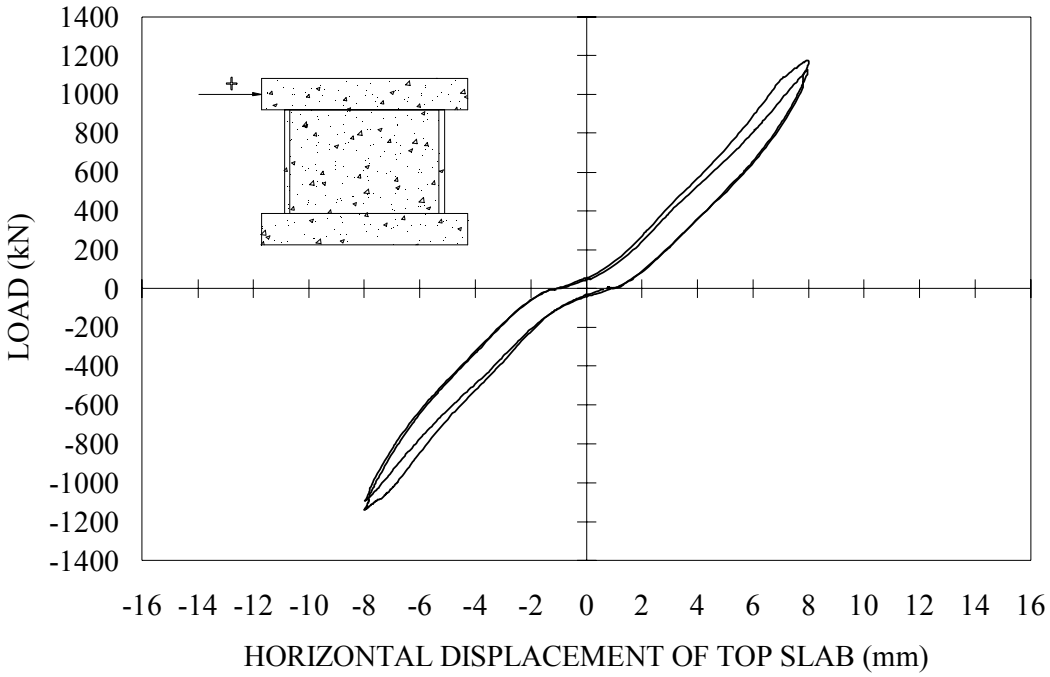

Figure 5.32 DP1 Cycle 8

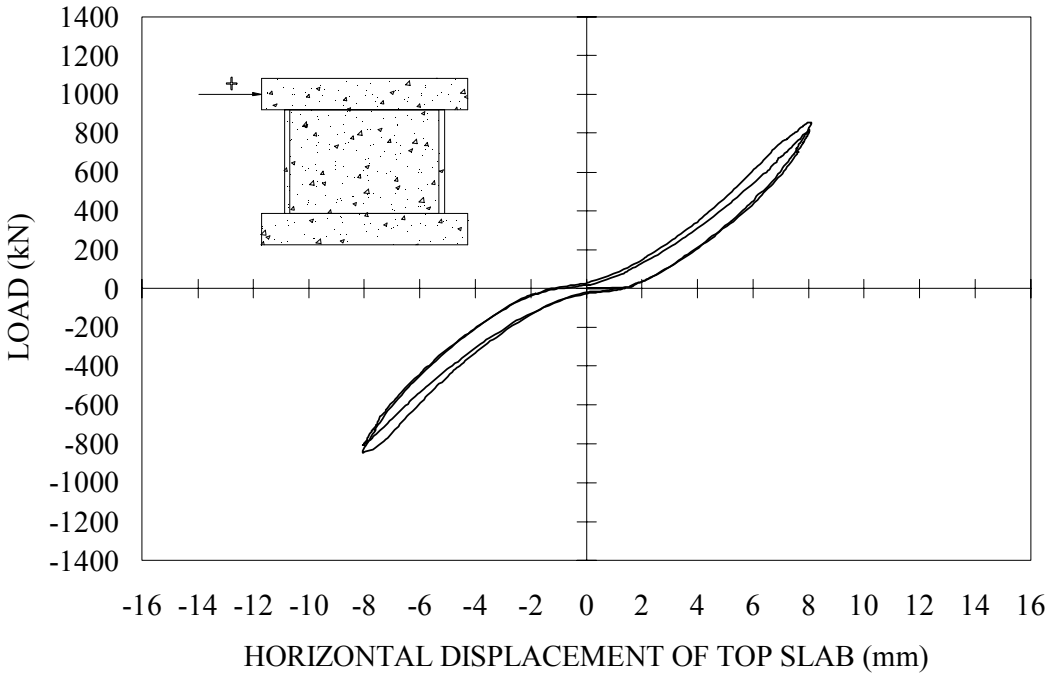

Figure 5.33 DP2 Cycle 8

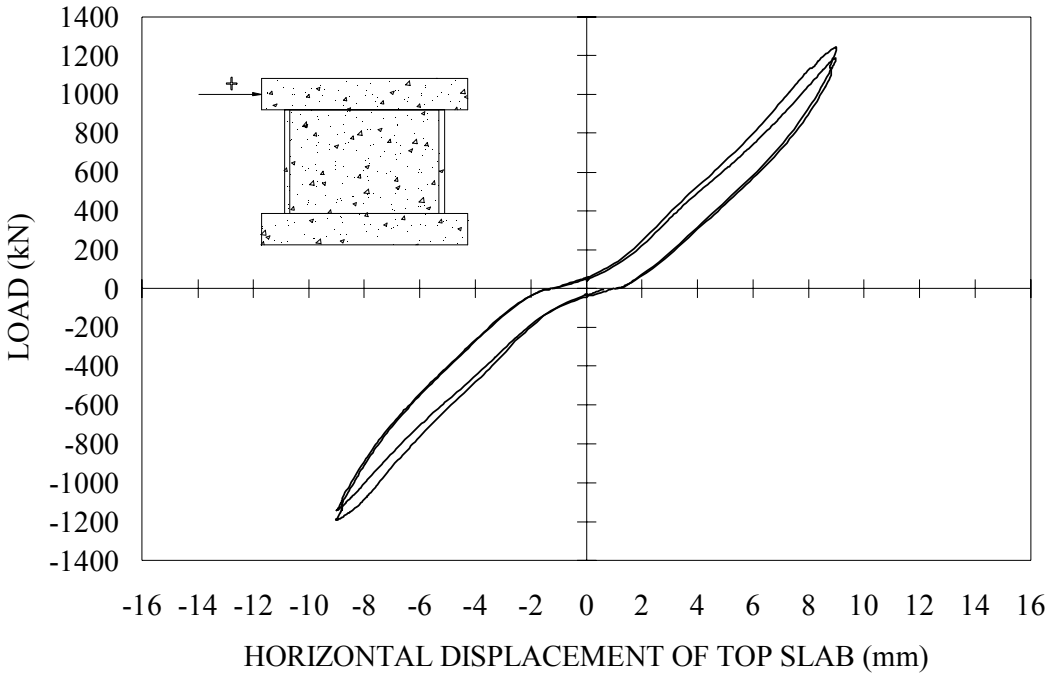

Figure 5.34 DP1 Cycle 9

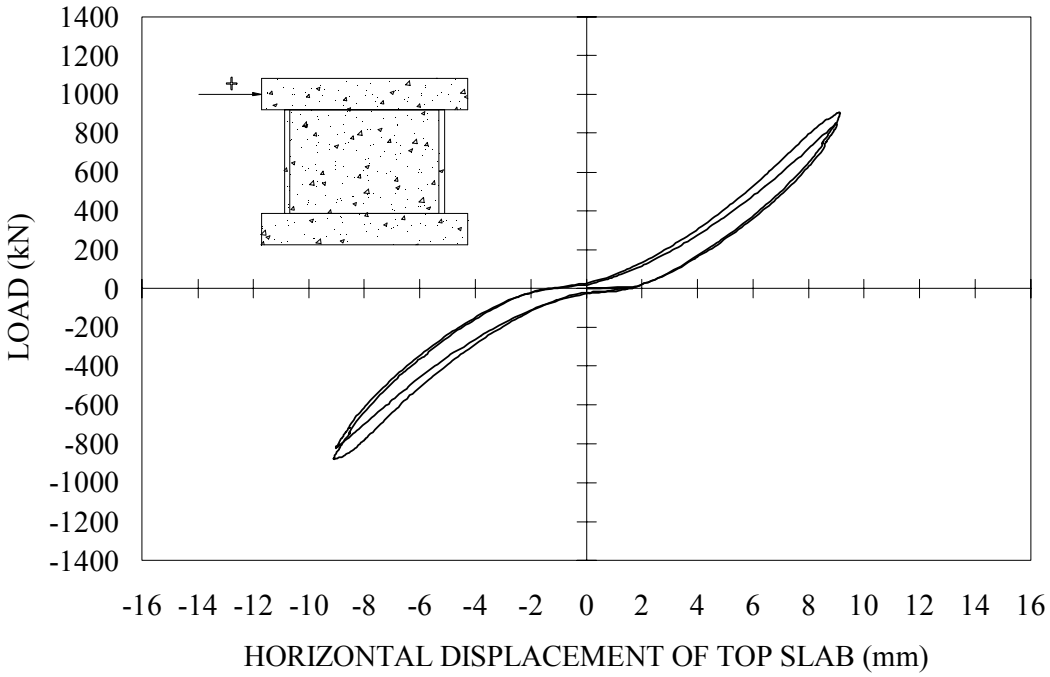

Figure 5.35 DP2 Cycle 9

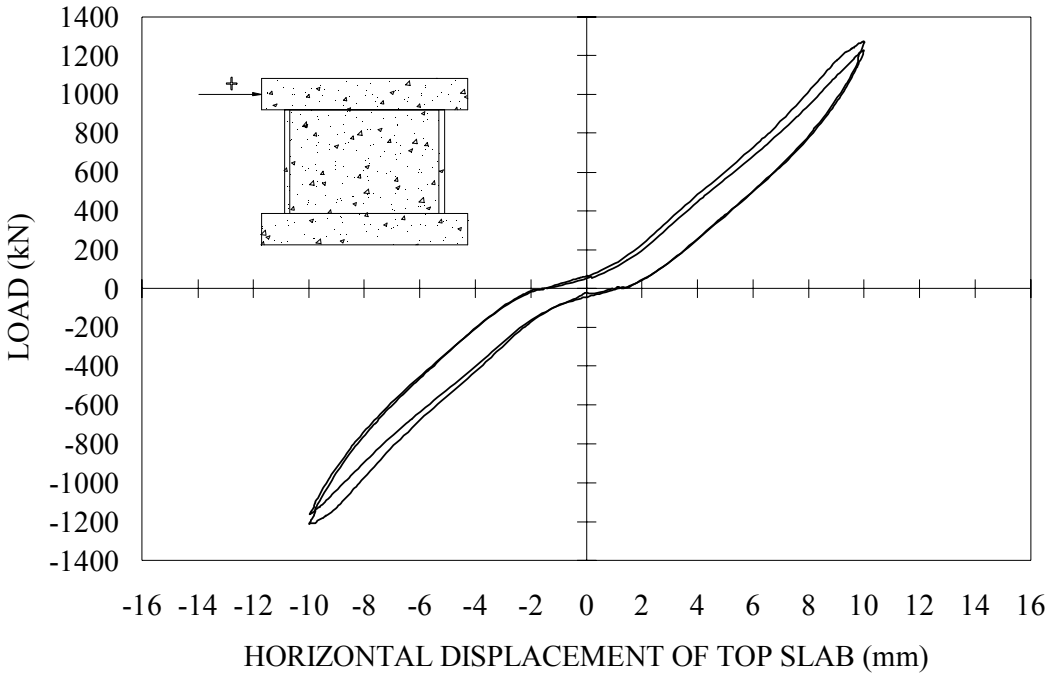

Figure 5.36 DP1 Cycle 10

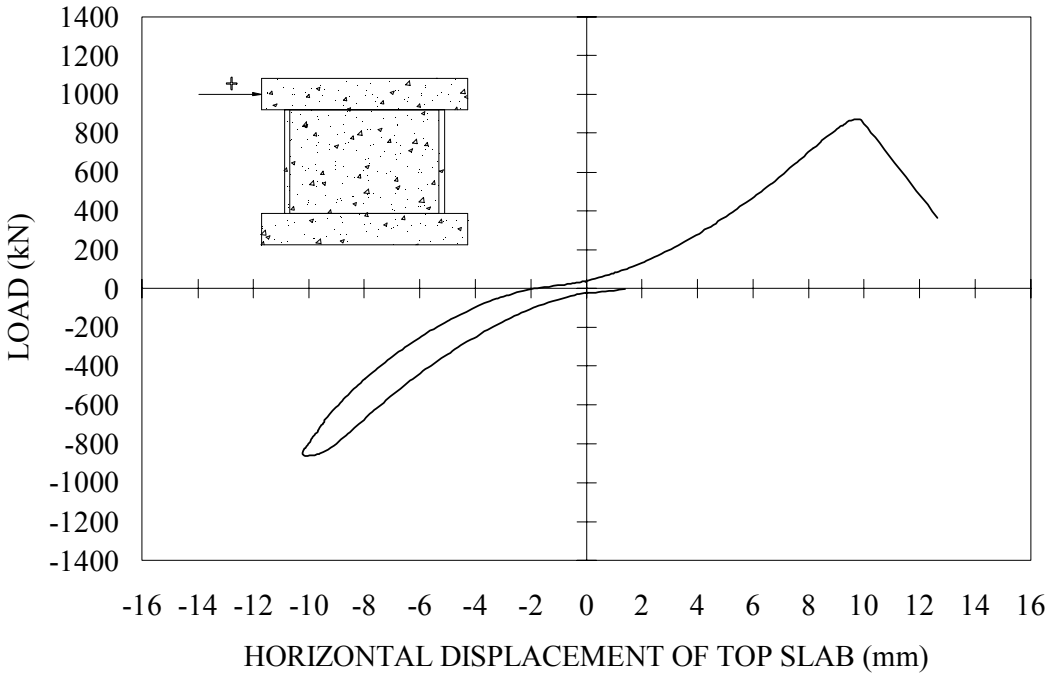

Figure 5.37 DP2 Cycle 10

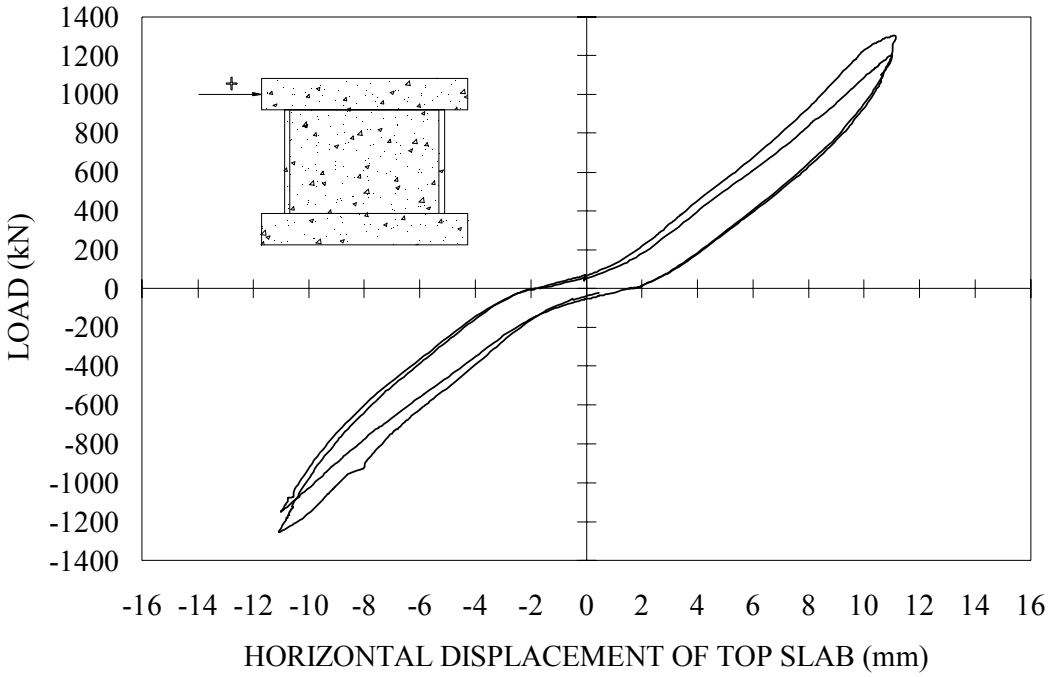

Figure 5.38 DP1 Cycle 11

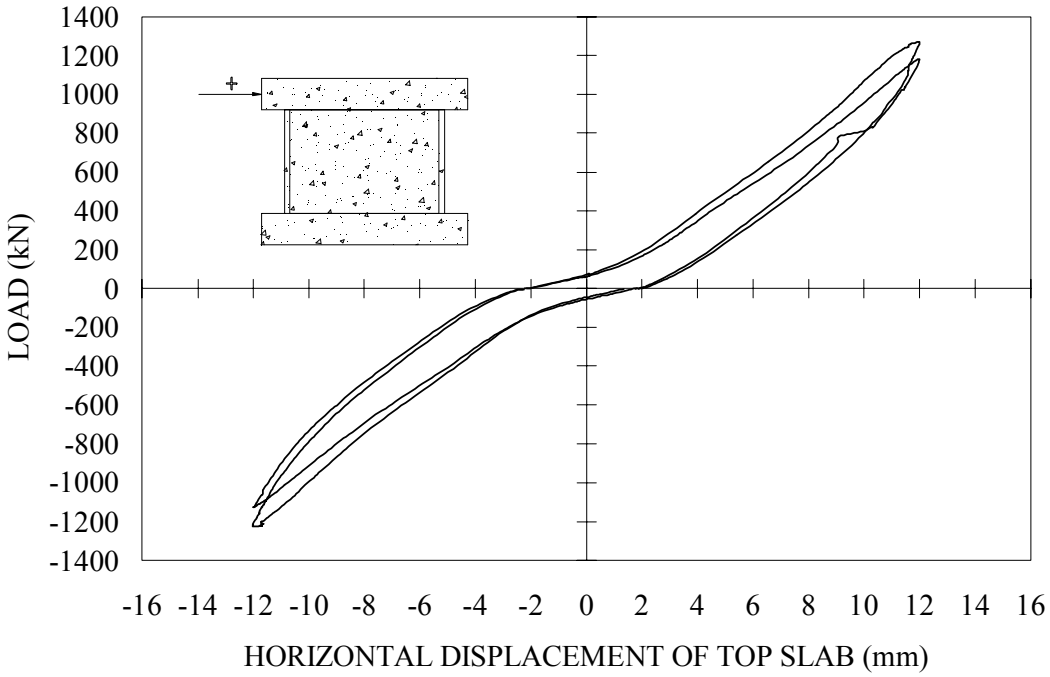

Figure 5.39 DP1 Cycle 12

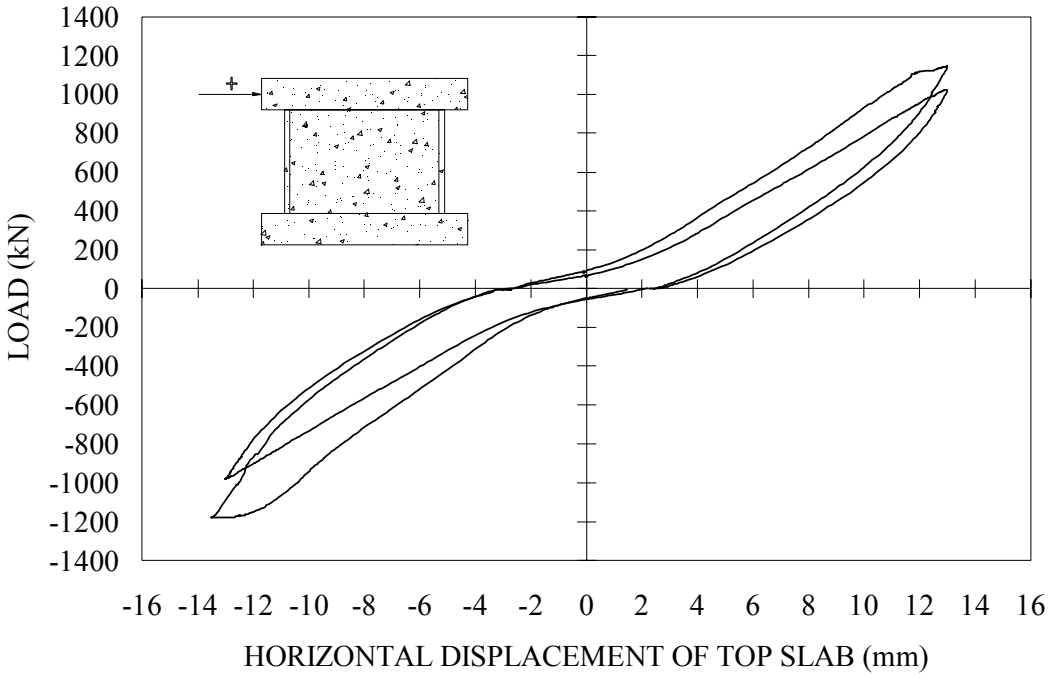

Figure 5.40 DP1 Cycle 13

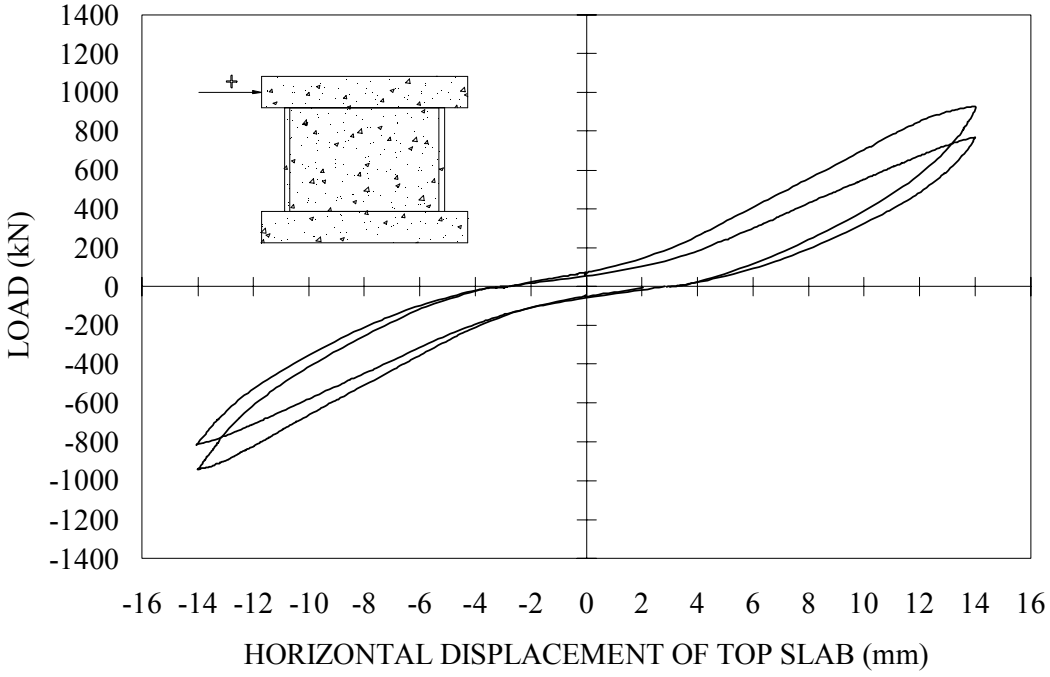

Figure 5.41 DP1 Cycle 14

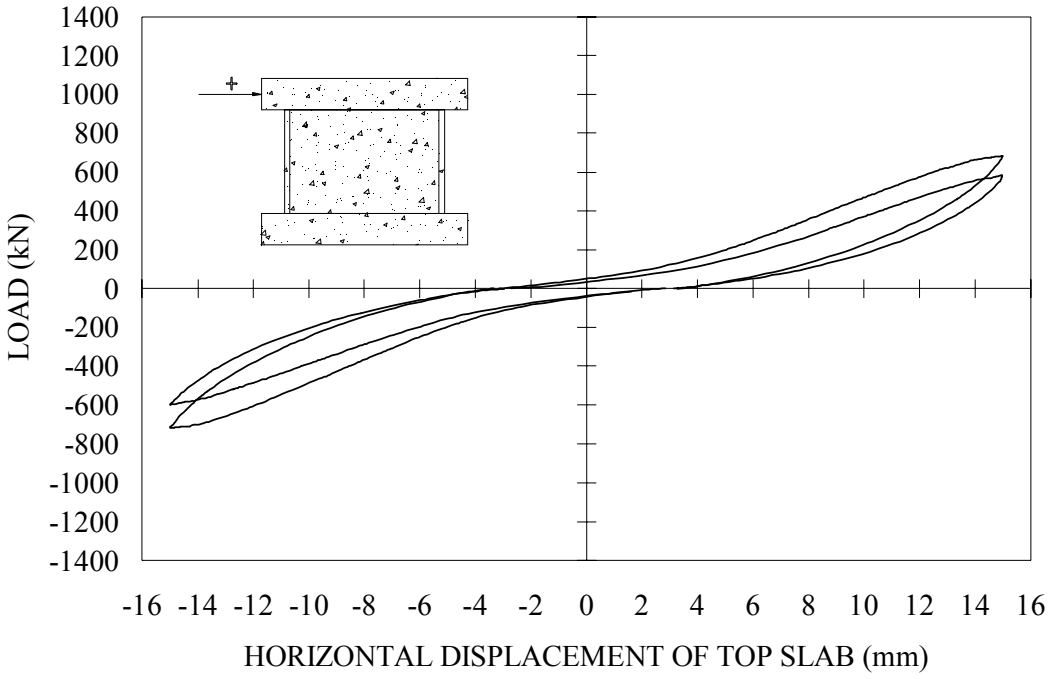

Figure 5.42 DP1 Cycle 15

5.5 FAILURE MODE

Testing was terminated at the completion of cycle 15 (15 mm of displacement) for DP1, at which point a significant portion of the descending branch of the load-deformation response had been attained. Six vertical slip planes, equally spaced along the width of the web wall, were visible. These planes began to form during 11 mm of displacement near the toes of the web, and by the end of cycle 12 four crushing planes were visible. Crushing of the concrete was first observed during cycle 8 in the toe regions of the web wall; spalling of the concrete in this region was evident by the end of cycle 6. Beyond 8 mm of displacement, crushing of the concrete seemed mostly confined along the vertical planes. The flanges experienced flexural cracking; otherwise, no other significant damage was evident. Failure, therefore, seemed to involve severe crushing of

the concrete over a widespread region of the web wall. Figure 5.43 is a photo of the web wall of DP1 at the end of testing.

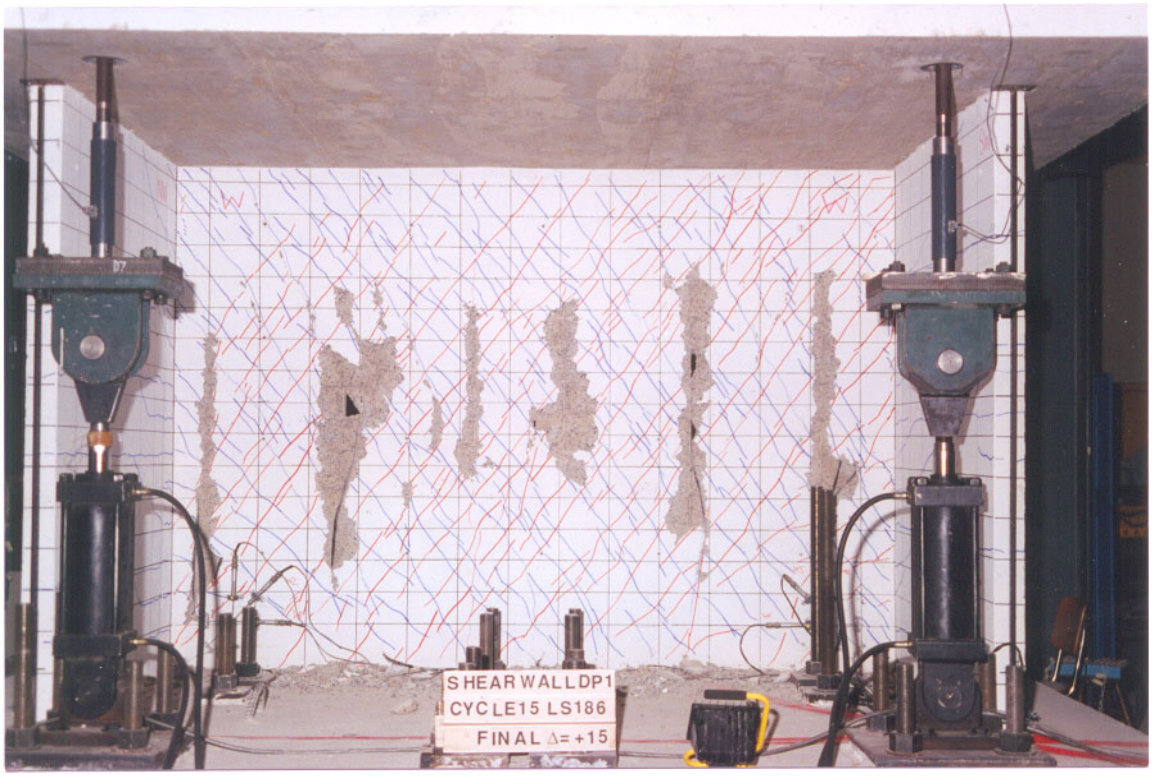

Figure 5.43 DP1 at Failure

Testing of DP2 was halted during the first excursion to +10 mm of displacement, at which point a sudden sliding shear plane formed along the web wall slightly beneath the top slab. The sliding action of the web wall further caused a punching of the flanges near the top slab. The first signs of concrete crushing, however, were observed during cycle 8 at the toes of the web wall, and crushing of the upper corners became visible during cycle 9. By the end of cycle 9, the concrete at the north and south upper corners showed signs of progressive crushing. During cycle 10, crushing of the concrete near the top slab extended toward the centre of the web wall. The bulk of concrete crushing was confined

to a distance of 125 mm from the top slab. Failure, ultimately, involved shear crushing of the concrete followed by sliding. This type of failure is common in squat shear walls; however, the concrete at the toes usually crushes followed by a sliding shear plane near the base of the web wall. There were no signs of flange punching near the base slab. Further discussion involving the mechanisms contributing to the sequence of failure of the specimens is covered in Chapter 6. Figure 5.44 illustrates the state of the web wall of DP2 at failure, and Figure 5.45 is a photo of the upper flange wall illustrating the punching action of the web wall on the flanges.

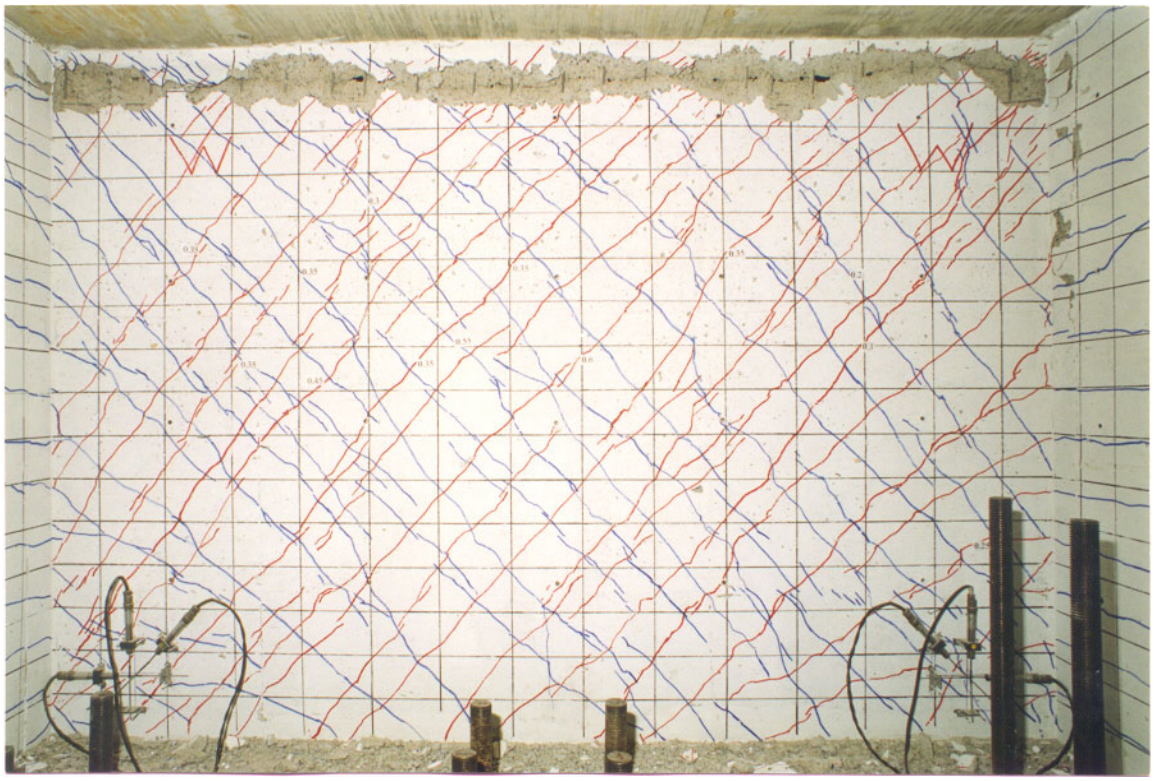

Figure 5.44 DP2 Web Wall at Failure

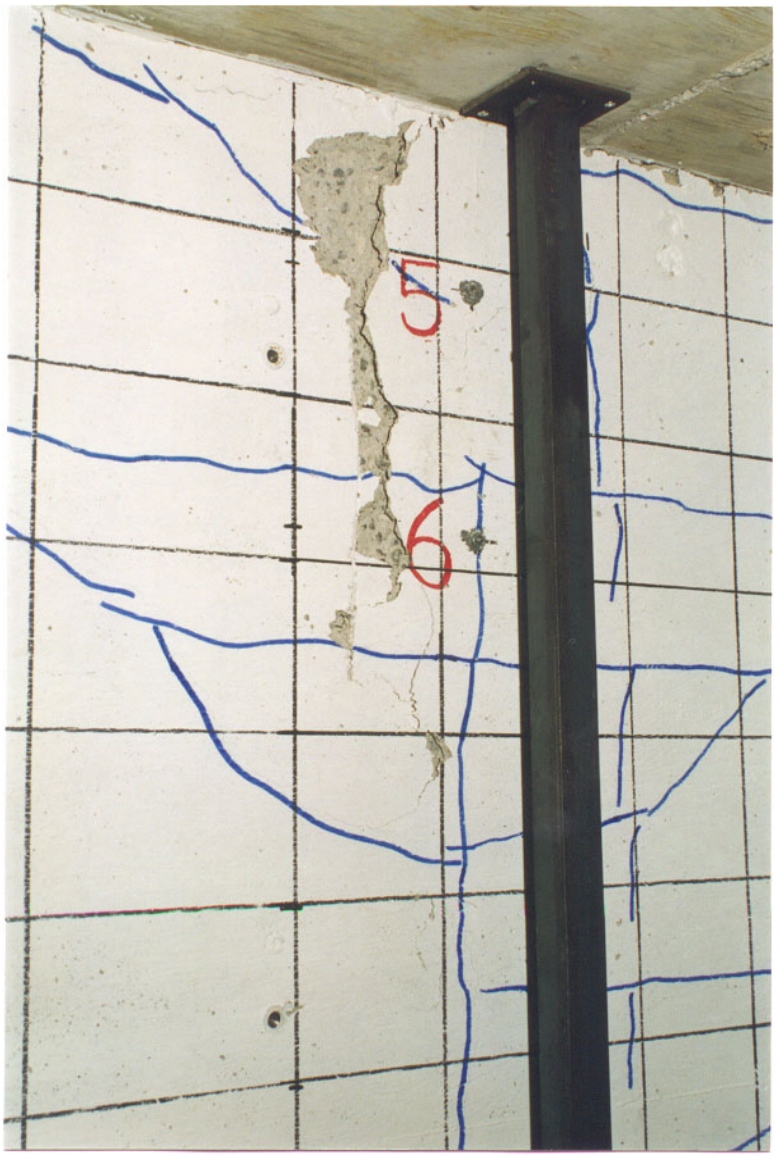

Figure 5.45 DP2 Flange Wall at Failure

5.6 WEB CONCRETE SURFACE STRAINS

This section describes the strains experienced by the concrete at the toes in the web walls. Structural walls subjected to lateral loads typically experience high stresses in the toe regions, and crushing of the concrete within this area is a common contributor to failure. To monitor the strains in the toes, six LVDTs were placed on the east face of the

web wall of each specimen, three for each toe. The instruments were labelled W1 through W6. W1 and W4 recorded the strains in the horizontal direction, W3 and W6 measured the strains in the vertical direction, and the strains experienced along a 45-degree diagonal were measured by W2 and W5. The horizontal and vertical instruments had a gauge length of 200 mm, and that of the diagonal was 282.8 mm. Plotted in Figures 5.46 and 5.47 are the results of W2 for DP1 and DP2, respectively. The remaining plots can be found in Appendix D. A drawing of the specimen is included in the plots, showing the location of the centre point of the grid used to monitor the displacements. Positive strains are tensile and negative strains are compressive.

The responses of W2 demonstrate a general similarity; however, some differences are evident. These include a stiffer response in compression and in tension for DP1, and excursions into the post-peak regime in compression and post-cracking response in tension for DP2. The recorded maximum strains for DP1 in compression and tension were -1.80×10^{-3} and 1.04×10^{-3}, respectively. The corresponding loads were –1097 kN occurring during cycle 11, and 1155 kN occurring during cycle 12, respectively.

The maximum strains for DP2 were recorded just prior to failure (cycle 10) for the compression response and cycle 9 for the tensile regime. The corresponding strains and loads were -2.51×10^{-3} at –862 kN and 1.46×10^{-3} at 904 kN, respectively. It is apparent that the toes in specimen DP2 experienced higher straining. This would be expected in the tensile regime due to the fact that the imposed axial load was removed from DP2; conversely, higher compressive strains would be expected in DP1 under an imposed axial load. The reason to the contrary lies in the mode of failure, and the amount of crushing actually concentrated near the toes regions. Further elaboration will be provided later.

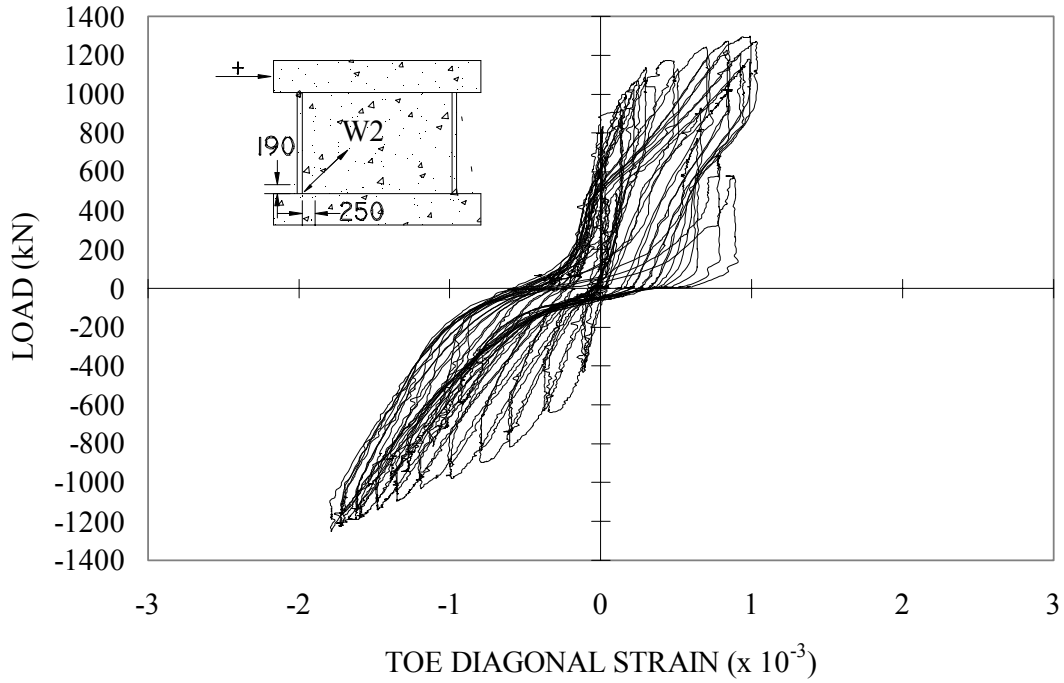

Figure 5.46 DP1 Toe Diagonal Strain

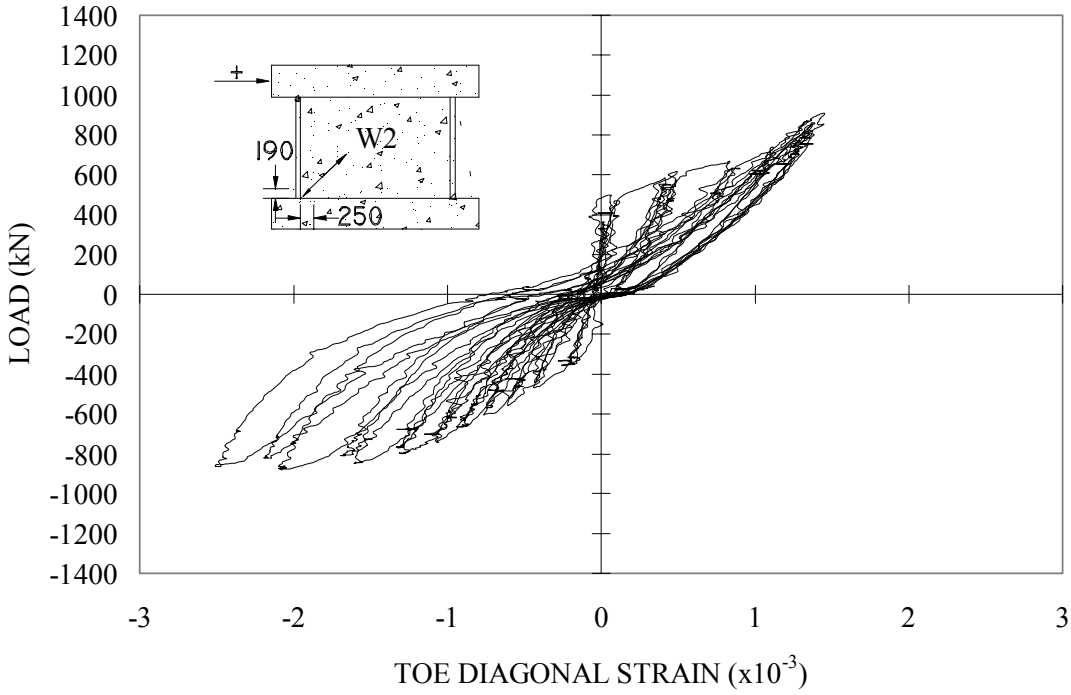

Figure 5.47 DP2 Toe Diagonal Strain

An investigation at cycle 9 revealed that the straining in the toe region was significantly higher in DP2. In compression and tension, strains of -2.09×10^{-3} and 1.46×10^{-3} were recorded for DP2 compared to -1.65×10^{-3} and 0.72×10^{-3} for DP1.

5.7 REINFORCEMENT STRAINS

Of the 40 strain gauges placed in each of DP1 and DP2, only two strain gauges in DP1, WH16 and WH17, recorded strains in excess of yield. The gauges were located on a horizontal reinforcing bar near the mid-height of the web wall. This does not necessarily indicate that reinforcement located elsewhere in the specimens was not yielding. The Zurich readings of the concrete surface strains, presented in the following section, recorded fairly large local strains. This suggests that the reinforcing bars in the flanges were most likely yielding locally throughout the specimen. Figures 5.48 and 5.49 are the responses of gauge WH17 for the two specimens. A yield strain of 3.18×10^{-3} for the wall reinforcement was determined from coupon tests.

The reinforcement in DP1 yielded during the first excursion to 13 mm of displacement. At this point, the structure was in its post-peak range. A maximum strain of 3.55×10^{-3} at a load of 1021 kN was recorded during cycle 13 for DP1, and a strain of 2.0×10^{-3} at –860 kN was recorded during cycle 10 for DP2. During cycle 9 (the peak load displacement for DP2), strain gauge WH17 of specimen DP1 experienced strains of 1.71×10^{-3} and 1.60×10^{-3} during the negative and positive cycles, respectively; whereas, DP2 measured strains of 1.17×10^{-3} and 1.53×10^{-3}. Even though the general response of DP1 and DP2 were similar at the location of the horizontal reinforcement marked by WH17, DP1 experienced larger strains.

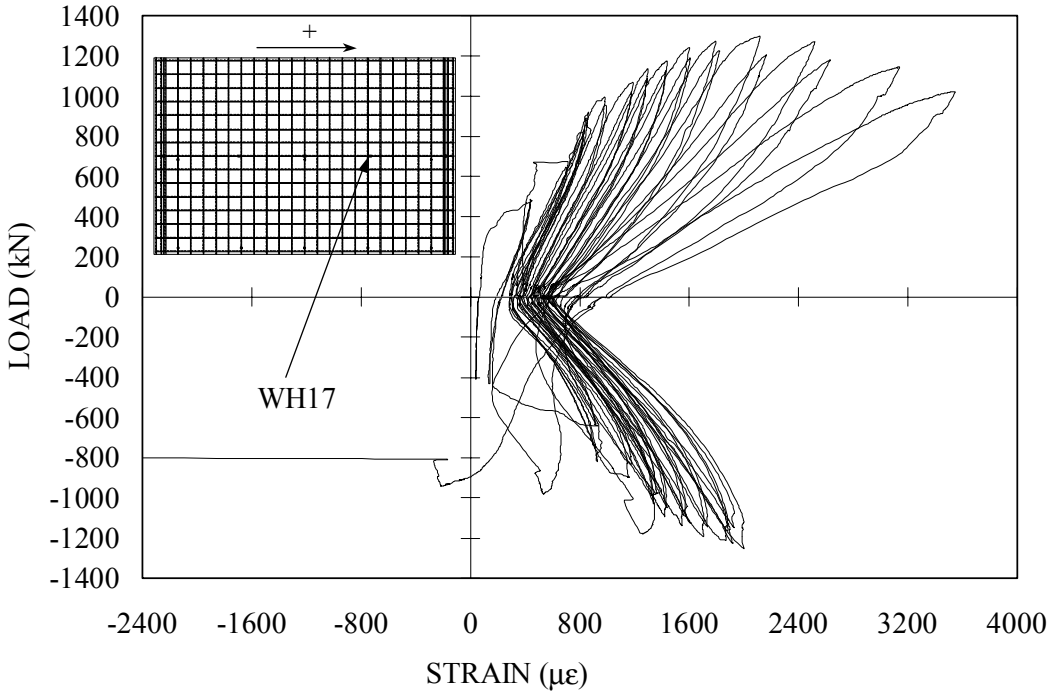

Figure 5.48 DP1 Strain Gauge WH17

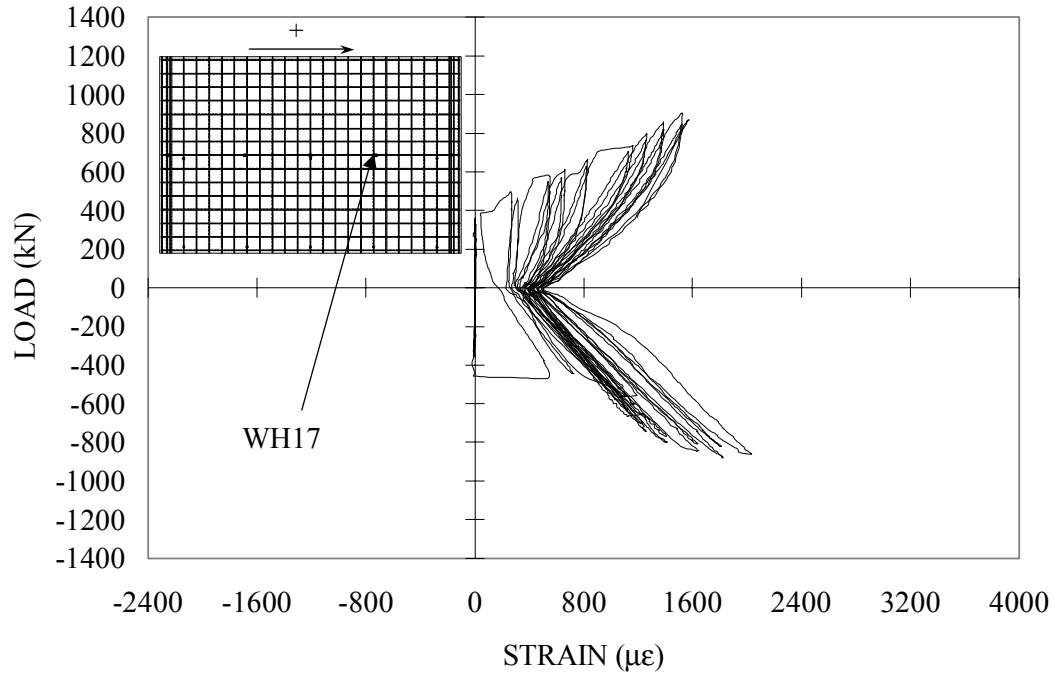

Figure 5.49 DP2 Strain Gauge WH17

The remaining strain gauges recorded high values of strain; however, they were not close to yielding. Gauge WV22B10 provides a typical response of the vertical reinforcement within the web wall and is shown in Figures 5.50 and 5.51 for DP1 and DP2, respectively. The axial load on DP1 appears to have increased the straining in the horizontal web reinforcement, but reduced the strains in the vertical web reinforcement.

The vertical reinforcement of DP1, at the location of WV22B10, indicated significantly more energy dissipation than DP2. More energy was dissipated in DP1 in the post-peak range where the reinforcement significantly influenced the response. The concrete, at that point, was severely damaged and unable to contribute significantly to the lateral load resistance. A direct comparison with DP2 is not possible as failure occurred without realizing a post-peak behaviour. The maximum strain measured in DP1 occurred during the first excursion to cycle 14, with a magnitude of 1.90×10^{-3} occurring at a load of 914 kN. For DP2, WV22B10 recorded a maximum strain of 2.31×10^{-3} at a corresponding load of –879 kN, which occurred during the first excursion to 9 mm of displacement. The maximum strain for DP1 occurred while the reinforcement was in compression, whereas, tension dominated the response for DP2. A comparison at cycle 9 indicates that the amount of compressive straining was similar for both specimens: 0.67×10^{-3} for DP1 and 0.65×10^{-3} for DP2. However, the tensile strains were larger in DP2: 2.31×10^{-3} versus 1.36×10^{-3} for DP1.

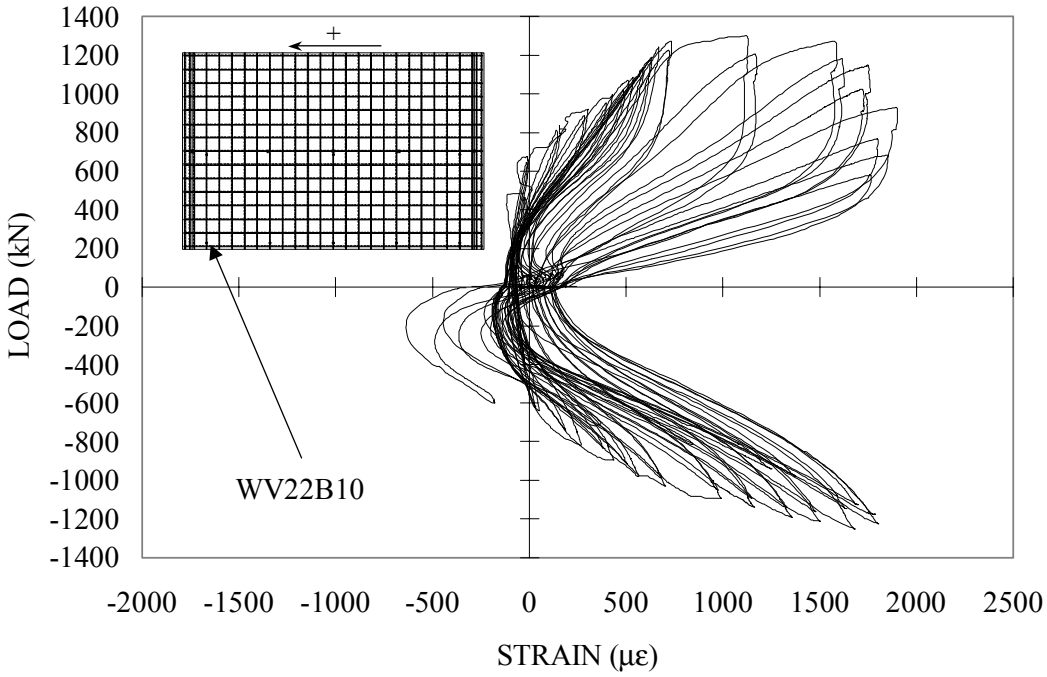

Figure 5.50 DP1 Strain Gauge WV22B10

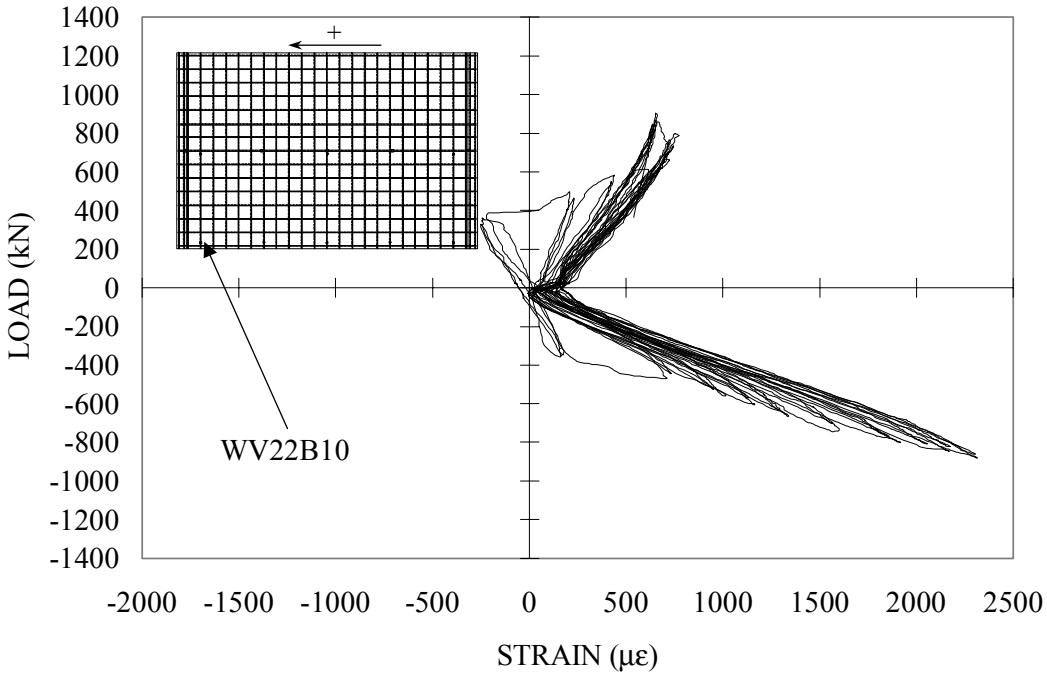

Figure 5.51 DP2 Strain Gauge WV22B10

In general (see Appendix E), the vertical reinforcement in the web wall of DP2 experienced larger strains; however, DP1 experienced more straining in the horizontal reinforcement in the web wall. Also, analysis of the vertical reinforcement near the centre of the webs indicates significant straining, suggesting that the reinforcement contributed to resisting the shear stress on the web wall. The stress due to the flexure was a minimum at the centre of the web wall. Finally, it is evident that the reinforcement experienced large jumps in strain in the first few cycles of displacement. These plateaus corresponded to the point at which the first full-width flexural cracks surfaced on the flange walls. Upon flexural cracking, there was a transfer of force from the concrete to the reinforcement, and this was accompanied by a sudden release of energy.

Strain gauges mounted to the vertical reinforcement in the flanges near the mid-height also demonstrated jumps in the strain within the first few cycles, as shown by gauge FV8N9 in DP1 and FV8S9 in DP2 below. These gauges were located in similar positions in the flange walls; however, for DP1, FV8N9 was in the north wall, and for DP2, FV8S9 was in the south wall. The responses of the reinforcement were similar; however, it appears that more energy was dissipated in the reinforcement of DP1. This was the result of cycling beyond the post-peak in DP1, where the response of the structure was significantly influenced by the reinforcement. Although DP2 was subjected to fewer cycles than DP1, the vertical reinforcement at the mid-height of the structure did experience more straining. Jumps in the strain while the flanges were in tension are also evident. The main flexural cracking extending the full width of the flange wall had surfaced near these gauges. Again, these plateaus corresponded to the occurrence of the first full-width flexural cracks.

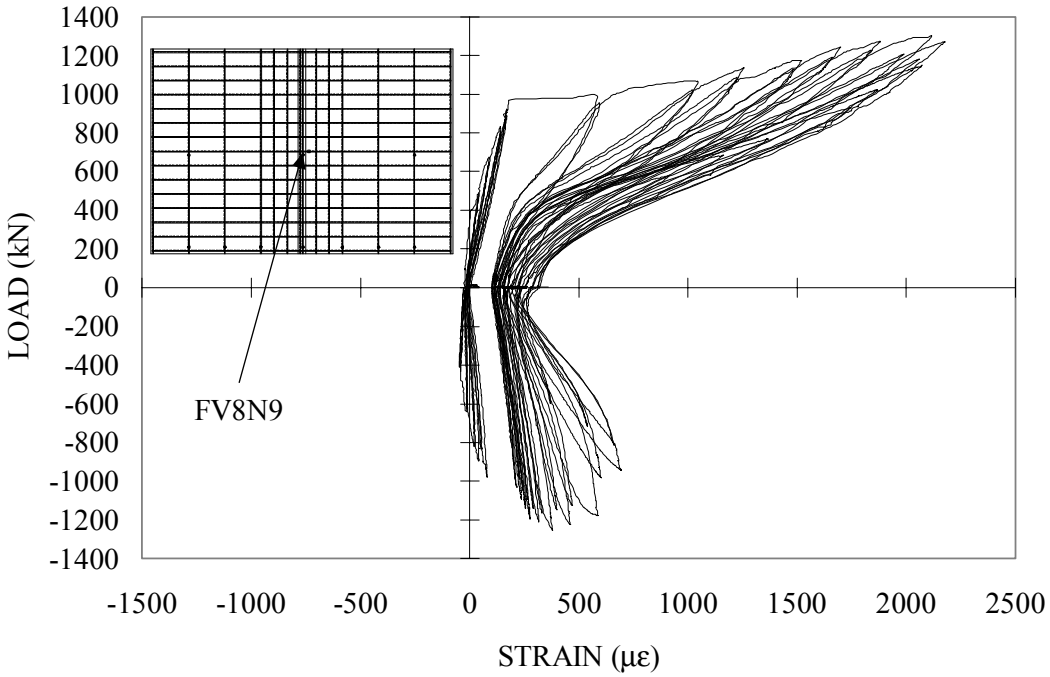

Figure 5.52 DP1 Strain Gauge FV8N9

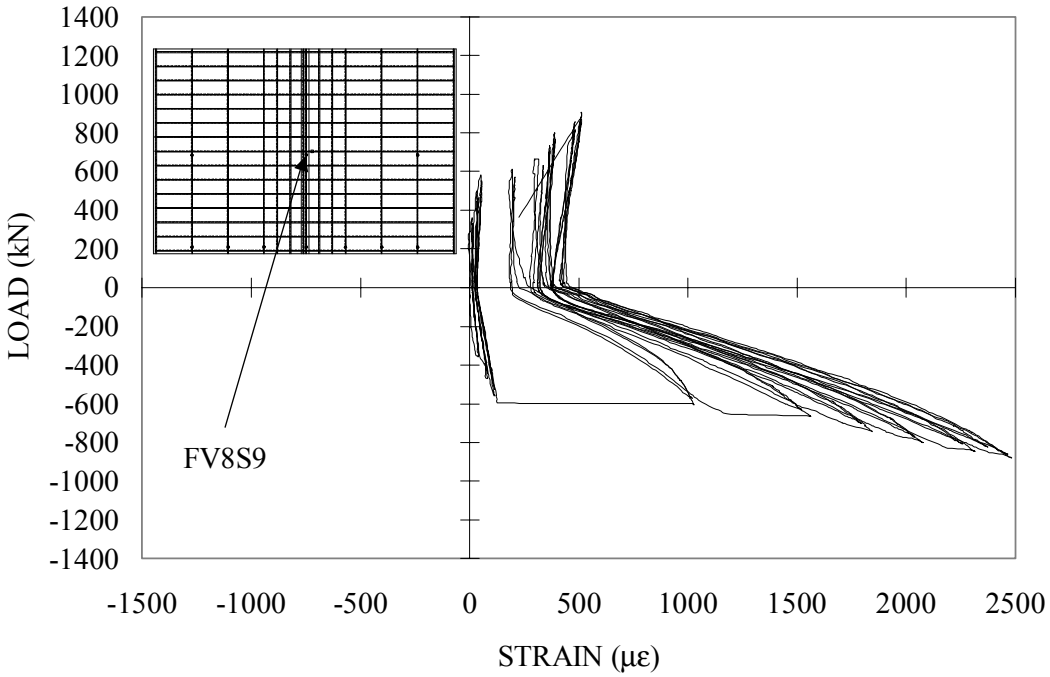

Figure 5.53 DP2 Strain Gauge FV8S9

Gauge FV8N9 in DP1 registered a maximum strain in tension of 2.18 x 10^{-3}, occurring at a load of 1275 kN during the first excursion to 12 mm of displacement, and FV8S9 recorded a strain of 2.48 x 10^{-3} corresponding to –878 kN, which occurred during the peak load cycle (cycle 9). FV8N9 experienced a strain of 1.70 x 10^{-3} during cycle 9, indicating that straining in the vertical reinforcement in the flanges of DP2 was significantly larger than DP1. Two additional plots of gauge FV4S3 located near the base of the south flange wall of each specimen are shown in Figures 5.54 and 5.55, respectively.

The responses of the gauges were similar; however, the gauge in DP2 experienced higher strains in tension. A maximum strain of 1.82 x 10^{-3} and 2.43 x 10^{-3} were recorded for DP1 and DP2, respectively. The corresponding loads were –1207 kN and –878 kN. For DP1, the maximum strain occurred during the first excursion to cycle 12, and during the first excursion to cycle 9 for DP2. During cycle 9, gauge FV4S3 in DP1 experienced a strain of 1.43 x 10^{-3}; thus, DP2 recorded strains nearly double those of DP1 at the peak load cycle for DP2. In general (see Appendix F and G), the vertical reinforcement in the flange walls of DP2 registered higher strains in tension, and the vertical reinforcement of DP1 experienced higher strains in compression. It seems that the axial load imposed on DP1 restrained the accumulation of tensile straining in the flexural reinforcement of the flanges. The externally applied axial load on DP1 also caused an initial compressive strain offset in FV4S9. This was typical of the vertical reinforcement located near the base slab for DP1. (See Appendices E, F and G.)

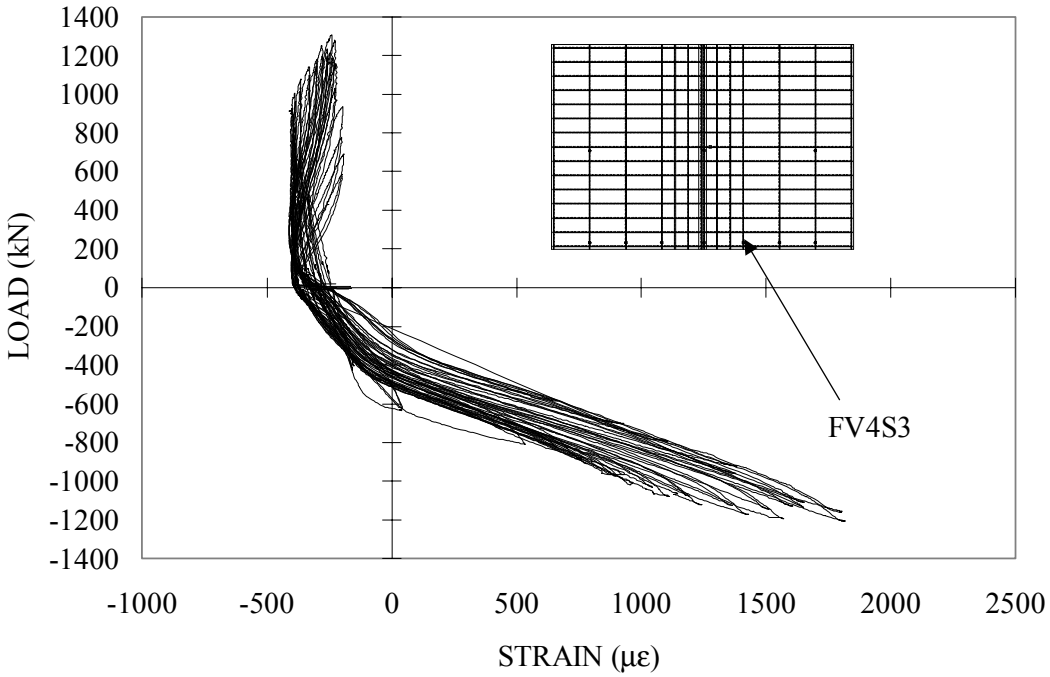

Figure 5.54 DP1 Strain Gauge FV4S3

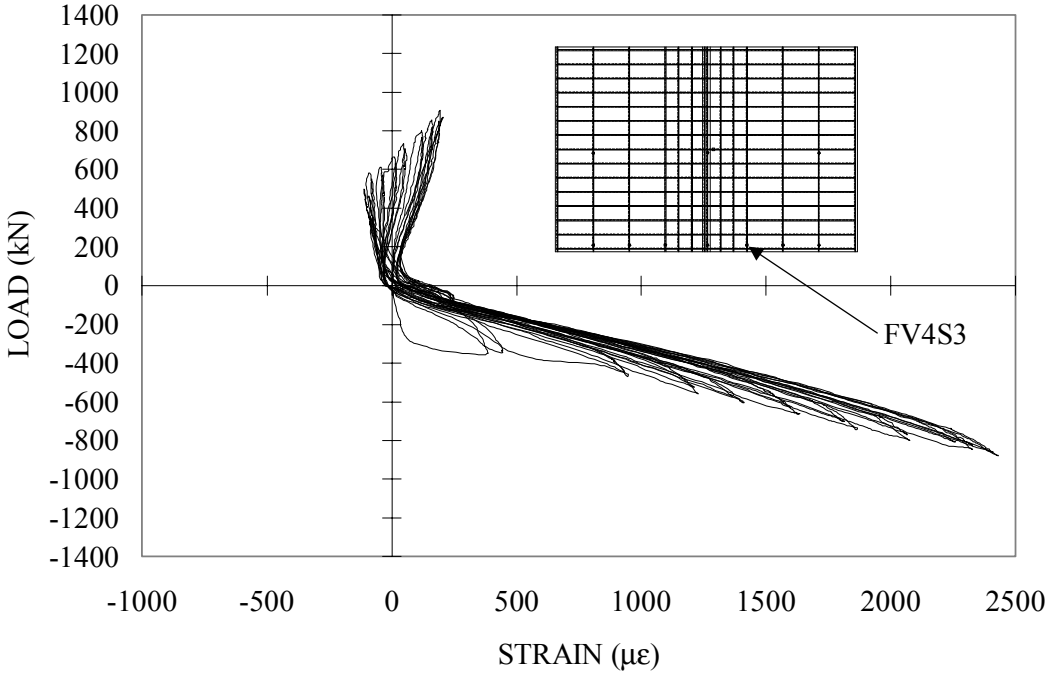

Figure 5.55 DP2 Strain Gauge FV4S3

5.8 CONCRETE SURFACE STRAINS

Zurich targets mounted throughout the specimens served two purposes: to determine the concrete surface strains of adjacent targets, and to determine the average strains in the reinforcement. Figures 5.56 and 5.57 are responses of Zurich targets 9-10S, located at the mid-height of the west half of the outer south flange wall. This set of targets recorded strains in excess of the reinforcement yield strain (3.18×10^{-3}), suggesting that the reinforcement was most likely yielding locally. Targets 9-10S of DP1 enclosed two major full-width flexural cracks, and the same targets of DP2 enclosed one major crack.

The two plots demonstrate generally similar behaviour of the concrete strains on the flange walls. More straining was measured in tension due to the opening of the flexural cracks between the targets. It is also evident that the targets registered tensile strains while the flange was in compression. This was most likely the result of the cracks not realigning perfectly upon unloading. The maximum strain recorded for DP1 occurred during the first excursion to cycles 11 and 12. The peak load was attained during cycle 11, and cycle 12 was the first cycle in the post-peak range. A strain of 5.61×10^{-3} was measured at corresponding loads of –1134 kN and –1090 kN, respectively, for cycle 11 and cycle 12. A maximum strain of 4.04×10^{-3} was recorded for specimen DP2 at a load of –742 kN occurring in the first excursion to 9 mm of displacement. The latter displacement level corresponded to the peak load cycle for DP2. It was difficult to establish any general comparison of the Zurich results of the two tests due to the location of flexural cracking relative to the Zurich targets. Cracks bounded by targets resulted in higher strains in tension.

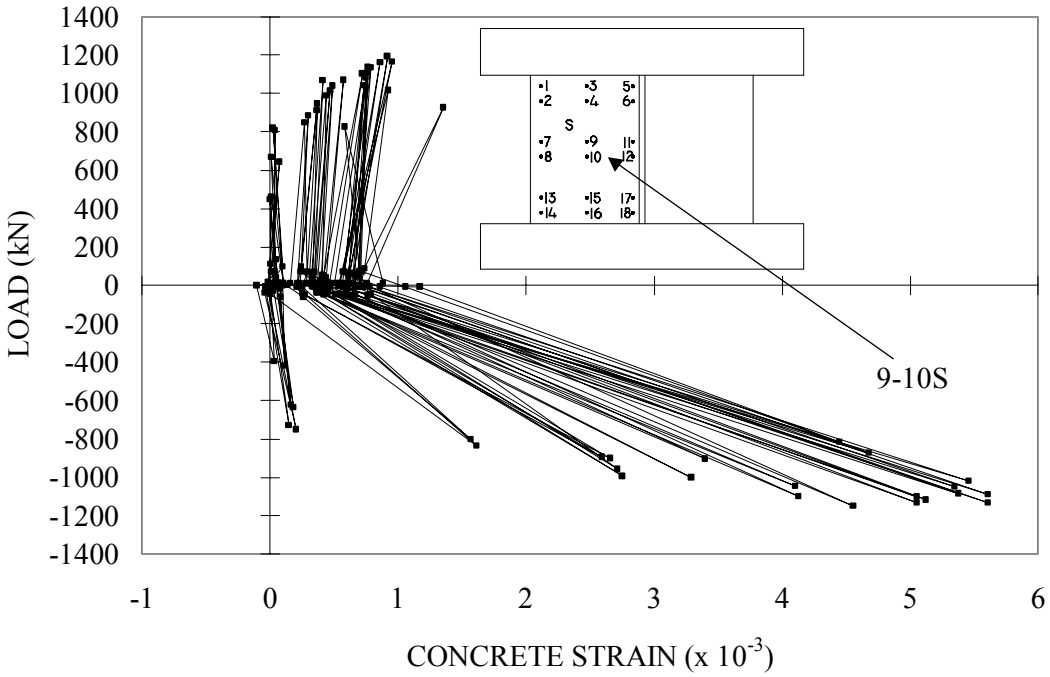

Figure 5.56 DP1 Zurich Targets 9-10S

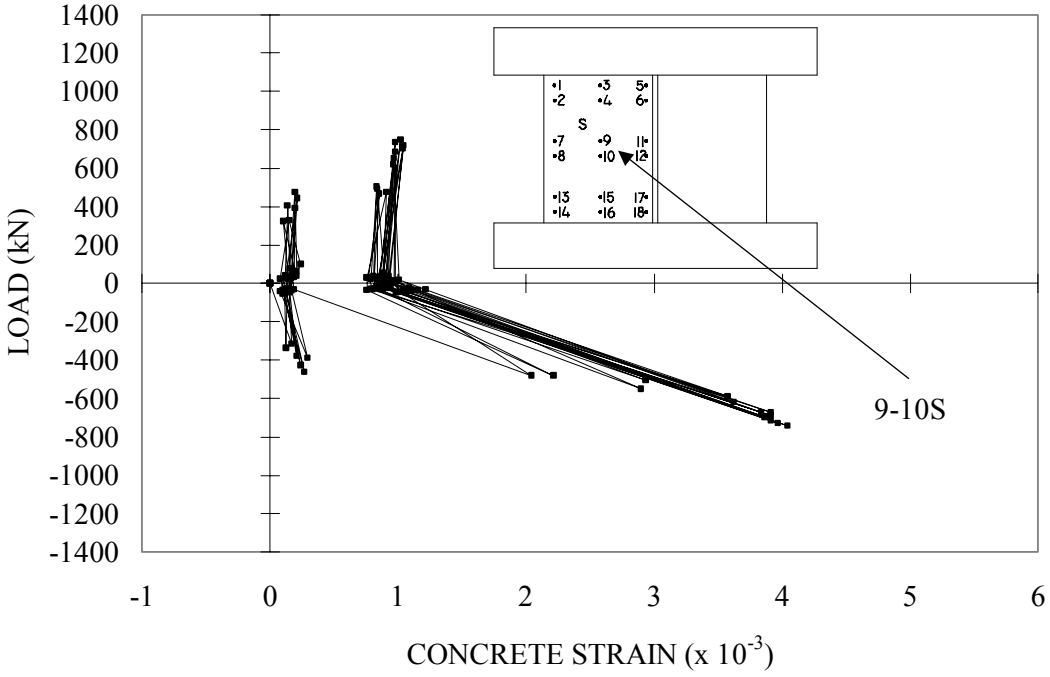

Figure 5.57 DP2 Zurich Targets 9-10S

The responses of targets 2-3E are given in Figures 5.58 and 5.59 to show the diagonal straining in the east web wall at the north toe. The behaviours were similar in tension and compression, and there were no notable differences between the responses.

For DP1, maximum strains of 1.93 x 10^{-3} and -1.99 x 10^{-3} were measured during the first excursion to cycles 12 and 13, respectively. The corresponding loads were 1136 kN and –1019 kN. For DP2, the maximum strains were recorded just prior to failure, during the second excursion to 9 mm of displacement for the positive cycles, and the first excursion to 10 mm of displacement for the negative cycles. The corresponding strains and loads, respectively, were 2.08 x 10^{-3} at 734 kN and –2.37 x 10^{-3} at –688 kN. The remaining Zurich results are available in Appendix H. Of note are targets 3-4N, 17-18N, 3-4S, 7-8S, 13-14S, 17-18S for DP2 and 1-2E for DP1, which registered relatively large strains.

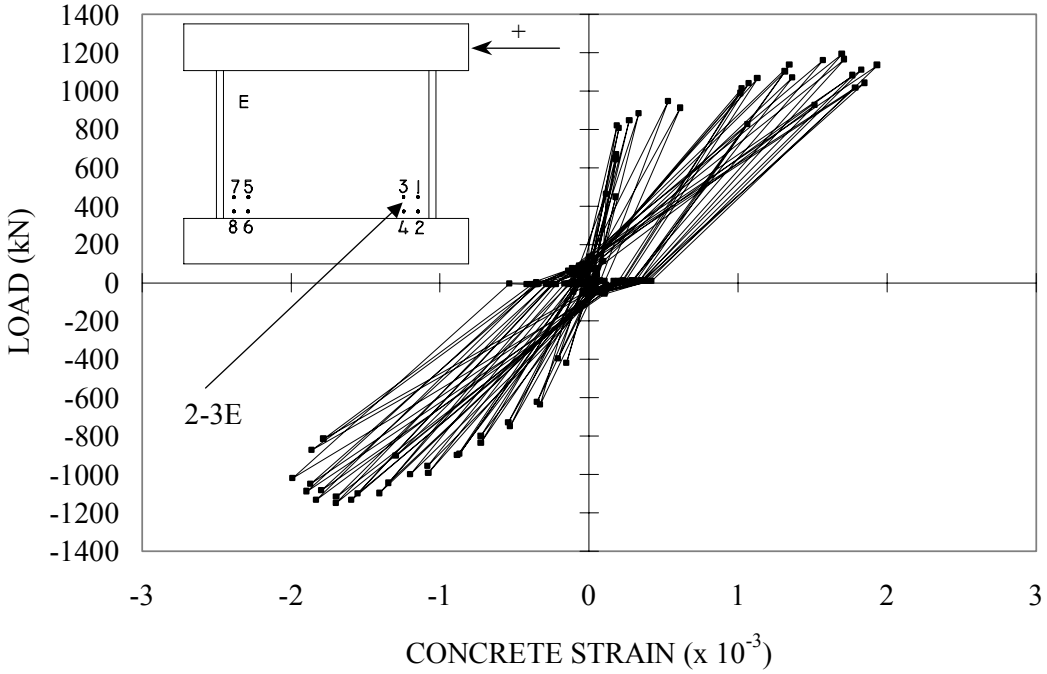

Figure 5.58 DP1 Zurich Targets 2-3E

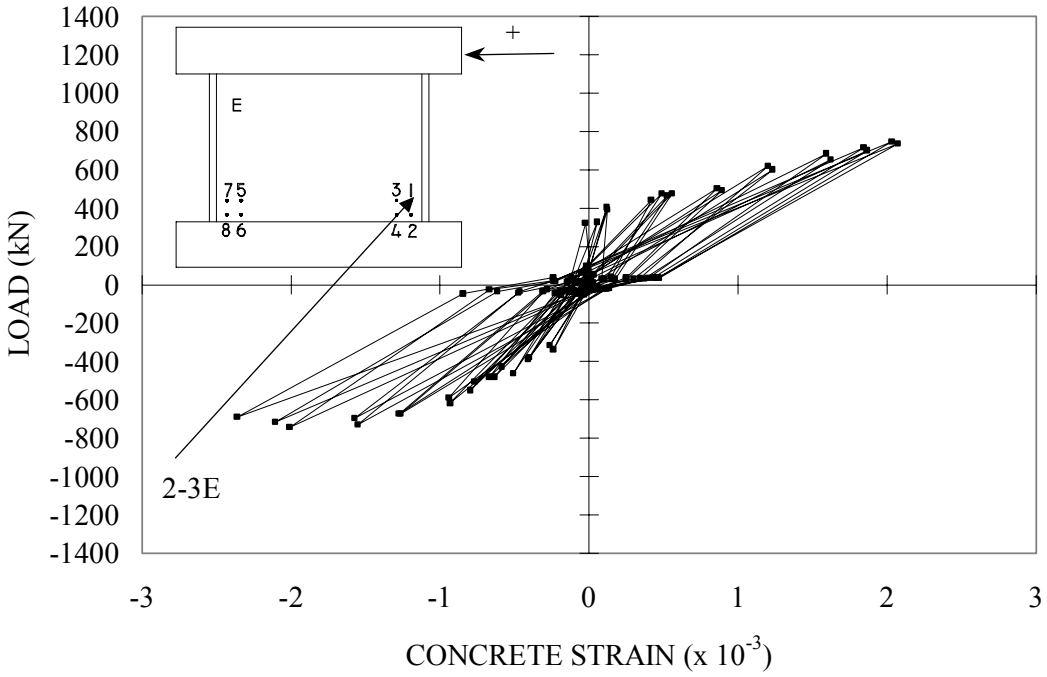

Figure 5.59 DP2 Zurich Targets 2-3E

CHAPTER 6

Discussion of Experimental Results

6.1 INTRODUCTION

The database collected from DP1 and DP2 is potentially useful in understanding the behaviour of structural walls, the effects of lateral loads with and without axial loads, and the effects of flange walls. To investigate static cyclic loading as a viable alternative to dynamic testing, the DP series of shear walls will be compared to the NUPEC U-1 wall.

6.2 STRENGTH AND DEFORMATION CHARACTERISTICS

The experimental results indicate that the presence of a small axial load had a significant effect on the behaviour of the walls subjected to reversed cyclic displacements. The applied axial load of 940 kN, on specimen DP1, was equivalent to an axial stress of 1.18 MPa, or approximately equivalent to 5.4 % of $f'c$. DP2, without externally applied axial load, was only able to attain 70 % of the maximum load resisted by DP1. The maximum load resisted by DP2 occurred at a displacement of 80 % of that experienced by DP1. DP2 did have a cylinder compressive strength 13 % lower than DP1, but the reduction in strength and ductility of DP2 cannot solely be attributed to the lower compressive strength of the concrete. It is apparent that a small amount of axial load enhanced the strength of DP1. Figures 6.1 and 6.2, below, are the envelope responses (maximum load for each displacement level).

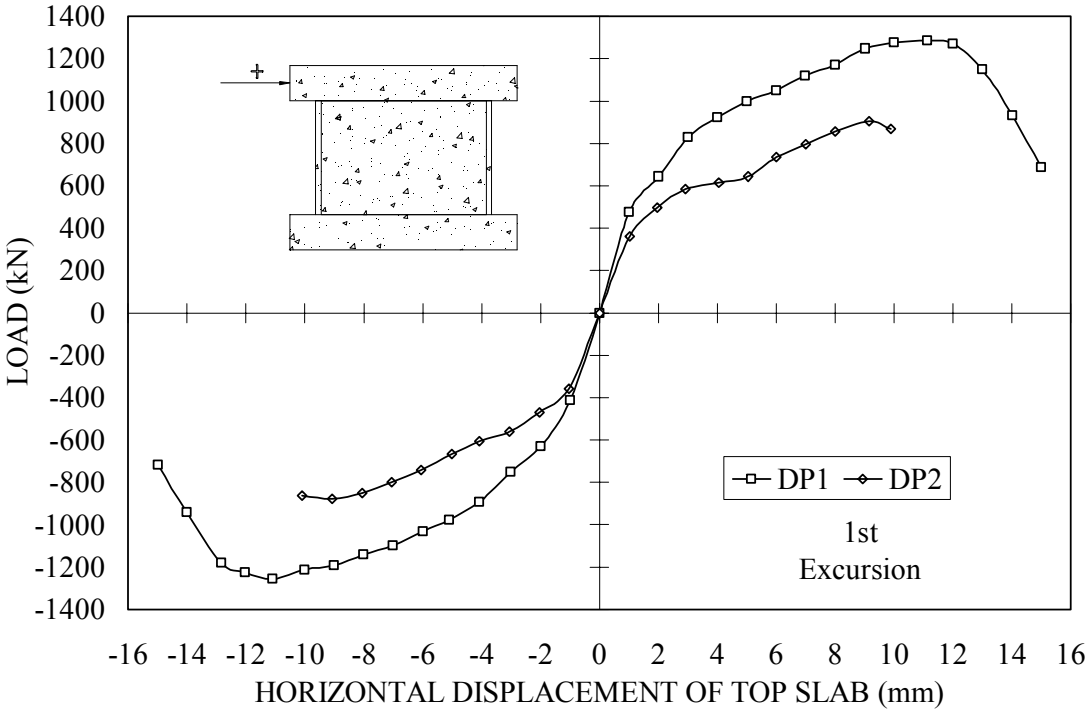

Figure 6.1 First Excursion Response Envelopes

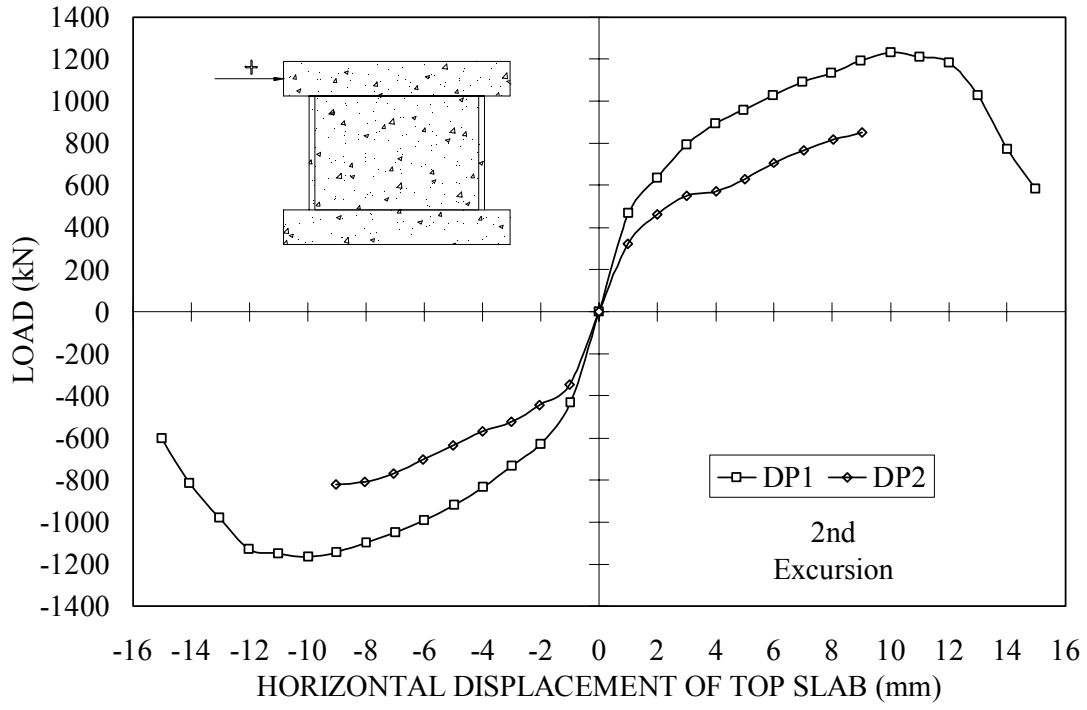

Figure 6.2 Second Excursion Response Envelopes

The envelope responses confirm the significant difference in strength and stiffness between the two walls in the post-cracking regime. DP2 recorded a significantly less stiff response and no post-peak behaviour; however, this appears to be partly a function of the apparently weaker concrete in the upper portion of the web wall, as discussed in further detail in subsequent sections. A comparison of the first excursion for cycle 9 (peak load stage for DP2) for both specimens is shown in Figure 6.3. The responses reveal that DP2 had a significantly lower loading and unloading stiffness. The residual strains, however, were essentially identical for both walls, and as confirmed by other researchers is a function of the maximum strain experienced in the history of loading. DP1 seemed to dissipate more energy than DP2; the hysteresis loops of DP2 seemed to experience more pinching under zero load.

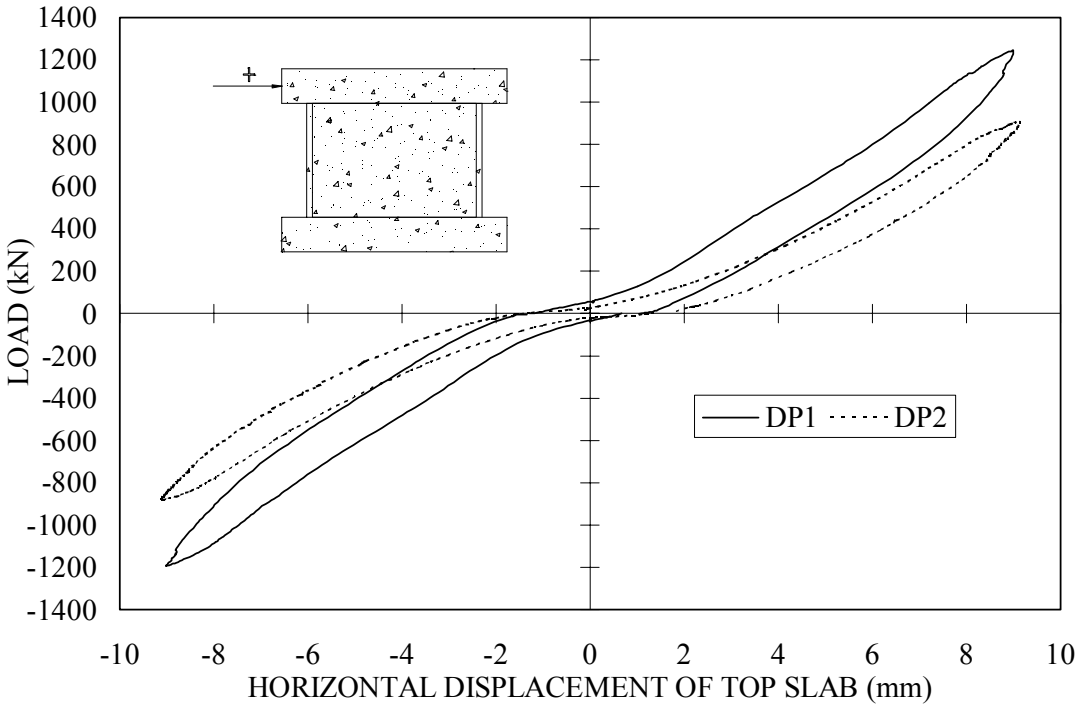

Figure 6.3 Comparisons of Responses at Cycle 9

6.3 HYSTERESIS TRENDS

The load-displacement results for DP1 and DP2 demonstrated similarities in behaviour. Low height-to-width shear walls generally produce hysteresis curves that are highly pinched and exhibit significantly less energy dissipation than would similar walls with a larger height-to-width ratio. More energy is dissipated through the structure in the post-peak range as the concrete begins to soften and the reinforcement approaches yielding. In the pre-peak range, the concrete within the web wall controls the response. The observed responses of DP1 and DP2 were consistent with these trends.

The load-deformation responses of the individual cycles for both specimens, presented in Chapter 5, demonstrated similar loading and unloading characteristics. The unloading curves of the second excursion at each displacement level generally followed the same unloading path as the first. The shape of the unloading path seemed to be dependent on the strain at the onset of unloading and on the residual strain. The residual strains were similar in the two specimens and seemed to be a function of the maximum unloading strain in the history of loading. The reloading branches of the second excursion of displacement followed a similar loading path as the first, but at a lower loading stiffness, resulting in lower peak strengths. The load-deformation curves indicated that the first excursion of a new displacement level followed the loading path of the second excursion of the previous displacement amplitude. This suggests that additional cycles at a specific displacement level would produce negligible damage in comparison to that experienced by the first unloading-reloading cycle. The responses demonstrated this trend until the peak load. During the post-peak response of DP1, the amount of damage experienced during subsequent cycles was significant and similar to

that sustained during the second excursion of the previous displacement. The increased accumulation of damage was a function of the concrete's inability to contribute significantly to the lateral resistance. Specimen DP2 was not able to support this trend; it failed in the first excursion of the first cycle of the post-peak range.

The unloading/reloading curves of the individual displacement levels of the test walls did exhibit some subtle differences. The reloading and unloading branches of DP2 seemed to demonstrate more nonlinearity than DP1. Therefore, it appears that the presence of an axial load affects the general shape of the unloading/reloading curves.

6.4 HORIZONTAL EXPANSION OF WEB WALL

LVDTs H6 and H7 were utilized to determine the horizontal expansion of the web walls (see Figure 4.42). H6 was mounted to the north flange wall at mid-height near the flange-web intersection. H7 was placed at the same location on the south flange wall. The responses of H6 and H7 (see Appendix C) demonstrated similar trends. Higher displacements were recorded by the LVDTs when the respective flanges were in compression. For DP1, H6 measured a maximum of –10.70 mm of displacement at a load of –717 kN during the first excursion to 15 mm of displacement, whereas a maximum displacement of 9.96 mm corresponding to a load of 690 kN was recorded by H7. At the ultimate lateral capacity, H6 measured displacements of –8.03 mm and 2.46 mm for the negative and positive cycles, respectively, and H7 recorded displacements of –2.46 mm and 7.85 mm. For DP2, maximum displacements of the web wall of –6.67 mm for H6 and 6.34 mm for H7 were measured during the first excursion to cycle 10. The corresponding loads were 868 kN and –860 kN, respectively. The displacements

attained at the peaks loads, which occurred during cycle 9, were –6.16 mm and 2.17 mm for H6 and –2.02 mm and 6.09 mm for H7.

The horizontal expansion measures the elongation of the web wall due to crack opening and was calculated from the difference in readings of LVDTs H6 and H7. The crack widths become larger as the reinforcement at the cracks yield, causing a further expansion of the web wall. Essentially, the expansion is a measure of the dilation of the web wall, and indicates the extent of compression softening due to existence of transverse tensile straining. High expansion results in an increased compression softening effect in the web concrete, higher stresses in the web reinforcement, and higher stresses in the restraining flanges. These effects result in a decreased stiffness, and potentially, an earlier failure of the concrete. Figures 6.4 and 6.5 show the horizontal expansion responses of DP1 and DP2. A continuous response for the expansion of DP1 was unavailable; the plot indicates the amount of expansion experienced at peak loads and zero displacements.

It is evident that the web walls experienced a significant amount of horizontal expansion throughout the course of testing, and the responses were similar in both directions of loading. For a particular positive load, H6 recorded the amount of direct displacement due to the imposed displacement; however, H7 recorded larger displacements that consisted of the direct imposed displacement and the displacements associated with web cracking and further opening of previous web cracks. In the negative direction, H6 registered the extension of the web wall due to the effects of cracking.

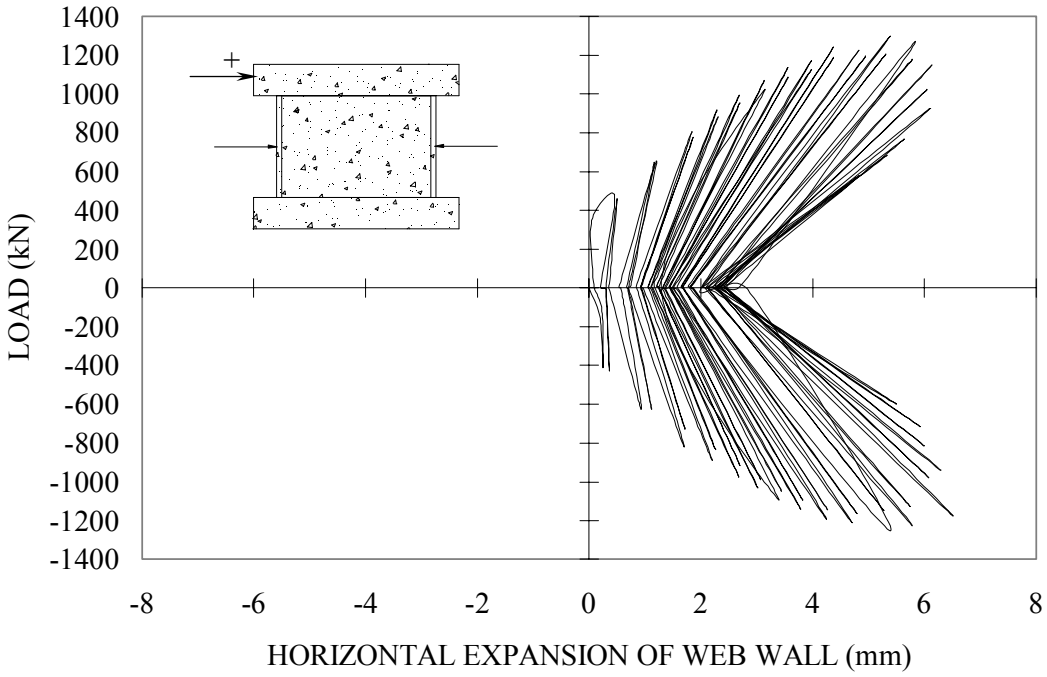

Figure 6.4 DP1 Horizontal Expansion of Web Wall

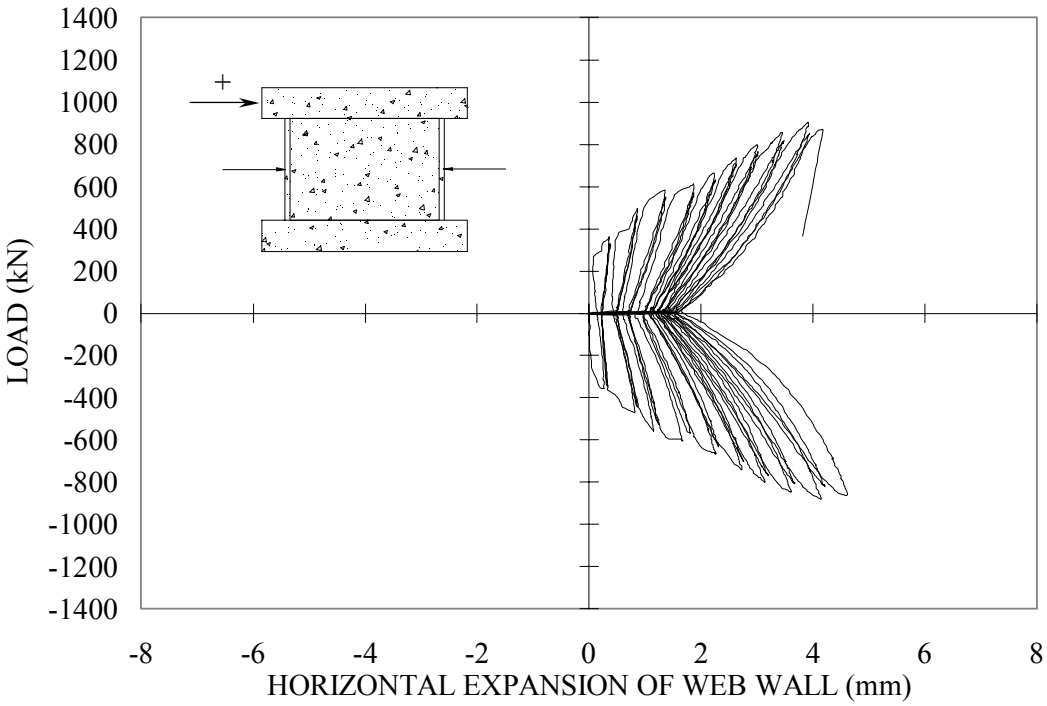

Figure 6.5 DP2 Horizontal Expansion of Web Wall

The maximum horizontal expansion was 6.52 mm for DP1, occurring during the first excursion to 13 mm of displacement at a corresponding load of –1177 kN. For DP2, an expansion of 4.62 mm at a load of –860 kN was calculated during the first excursion to 10 mm of displacement. It appears that DP1 experienced more expansion in the web wall. However, a better indication is to compare the expansion of the webs at 9 mm of displacement, which corresponds to the cycle of maximum loads for DP2. Horizontal expansions of 4.14 mm and 3.92 mm were calculated for the negative and positive directions for DP1, and 4.24 mm and 4.38 mm were observed for DP2. Therefore, the web wall of DP2 did experience slightly more expansion than DP1 at comparable load levels. The axial load on DP1 seemed to have restrained the expansion in web wall. The externally applied axial load has a similar effect as prestressing; it reduced the straining of the transverse reinforcement resulting in less horizontal expansion. Note that the hysteretic response is not significantly pinched and retains relatively large residual strains, suggesting that local strains in the web horizontal reinforcement were large and possibly in excess of yielding.

6.5 ELONGATION OF FLANGE WALLS

LVDTs V1 through V6 monitored the elongations of the flange walls, and were placed at the ends of the flanges and at the flange-web joint (see Figure 4.43). The flange elongation can be used to determine the extent of cracking and yielding of the flexural reinforcement in the flanges. Cycling beyond yielding leads to a ratcheting effect, which describes the vertical stretching of the wall due to the irrecoverable strains that accumulate in the post-yield cycles. For DP2, only V3 recorded values that were not

defective. Figures 6.6 and 6.7 depict the elongation of the north flange wall recorded by LVDT V3. Results of the other LVDTs for DP1 can be obtained from Appendix C and are similar in behaviour. The hysteretic responses of the flange walls are similar for both specimens. Significant elongations of the flanges, while in tension, are evident, due to flexural cracking and the straining of the reinforcement at the cracks. The elongation of the flange walls increased up to the peak load. Beyond the peak load and into the post-peak region, DP1 demonstrated a recovery in the amount of elongation in relation to the peak quantity. This is an indication that yielding of the flexural reinforcement was not widespread, as the displacement in the post-peak regime was not accumulating, but rather, diminishing with increasing lateral displacement. In compression, DP1, under axial stress, demonstrated more contraction to its original height, most likely attributed to the re-alignment of cracks as they closed in compression. The relatively insignificant residual deformations on the flange walls at zero load further indicates that yielding of the flexural reinforcement was not widespread, and most likely confined locally in the vicinity of cracks.

Specimen DP1 experienced 4.18 mm of extension at a load of 1270 kN occurring during cycle 12, and DP2 had an extension of 4.11 mm at a load of 868 kN just prior to failure. A comparison of the flange elongations at 9 mm of displacement reveals that the flanges of DP2 recorded larger displacements than DP1. The corresponding displacements were 4.11 mm and 3.33 mm, respectively. The axial load on DP1 appears to have caused a restraint of the expansion of the flange walls, and the larger residual displacements of DP2 suggest yielding of the flexural reinforcement was more prevalent.

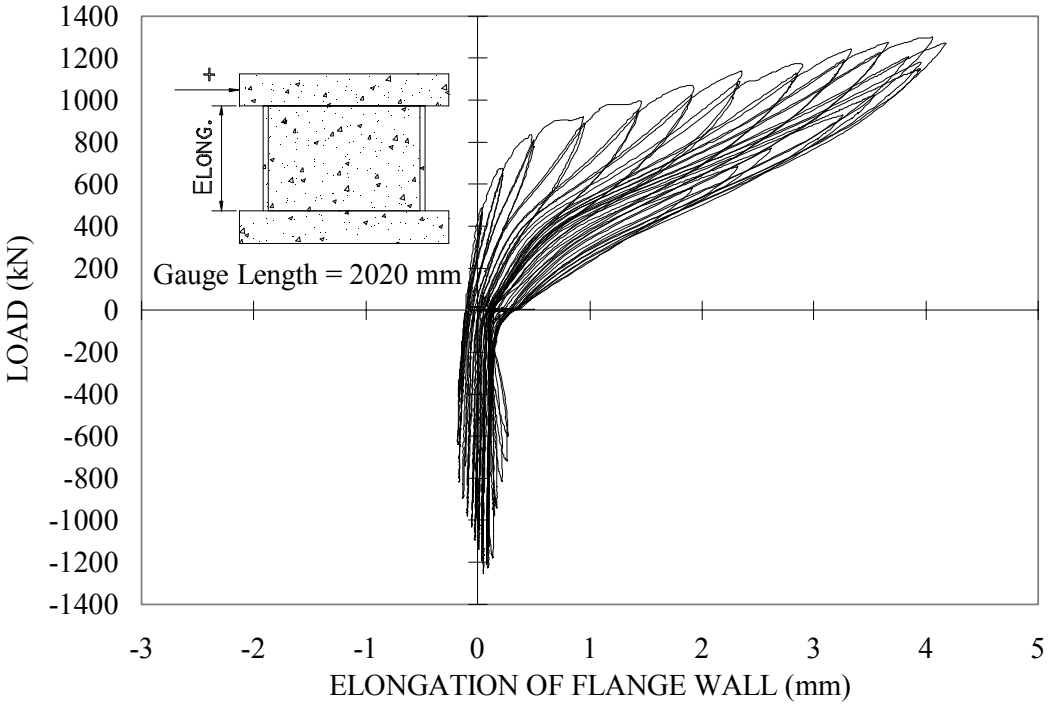

Figure 6.6 DP1 Vertical Displacement of Flange Wall

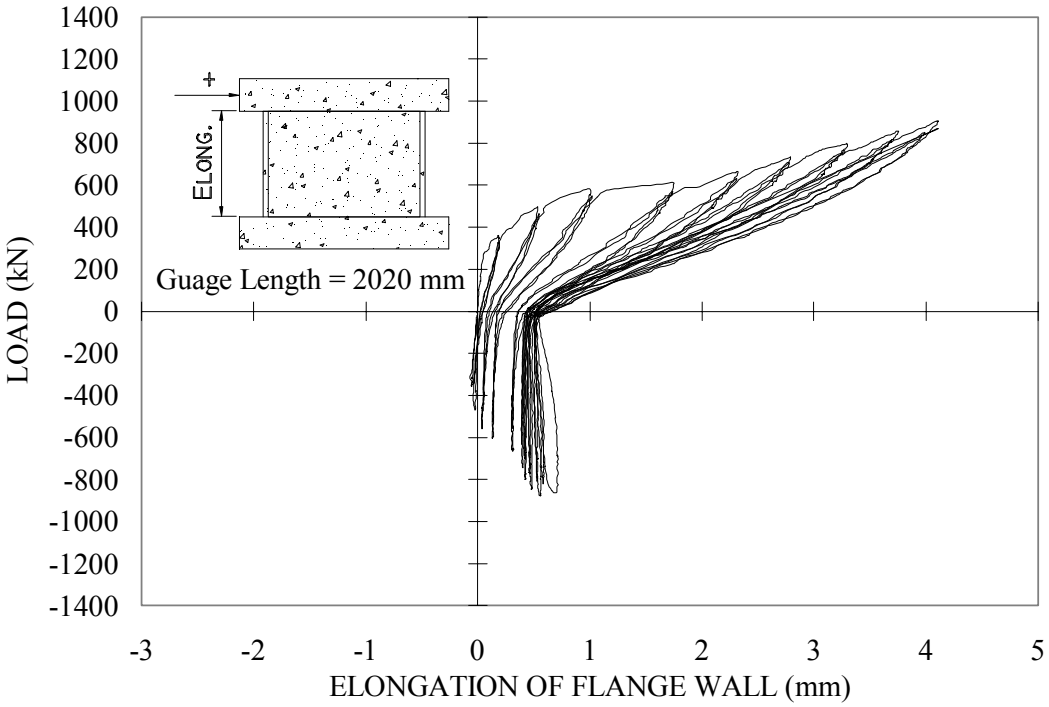

Figure 6.7 DP2 Vertical Displacement of Flange Wall

6.6 BOND SLIP

The remaining vertical LVDTs, V7 and V8, were utilized to monitor the local displacements of the flange walls near the base slab. Figures 6.8 and 6.9 display the vertical displacements recorded by LVDT V7 at the base of the flanges for DP1 and DP2, respectively. The results of V8 can be obtained from Appendix C. The LVDT's were mounted to the flange walls at a distance of 180 mm and 145 mm from the top of the base slab for DP1 and DP2, respectively. The readings measured the elongation of the flange walls locally near the base slab. A comparison of the local elongation of the flange walls with the total elongation is useful in determining the extent of bond slip. The displacements of interest occurred while the flange walls were in tension. The values in compression simply indicate the amount of shortening of the flange walls.

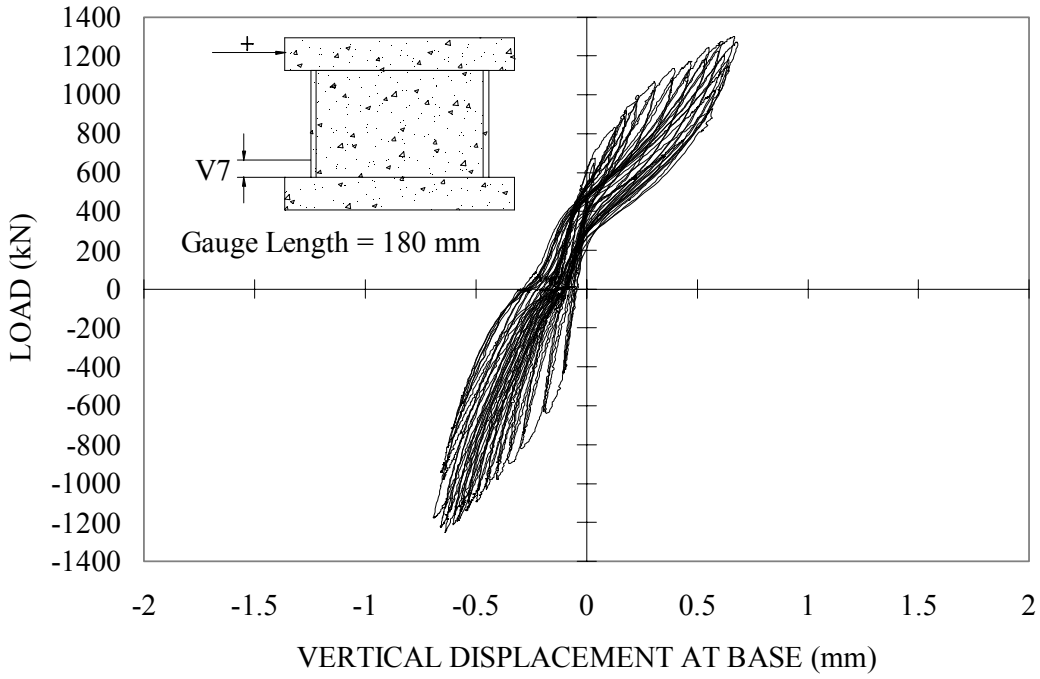

Figure 6.8 DP1 Vertical Displacements at Base

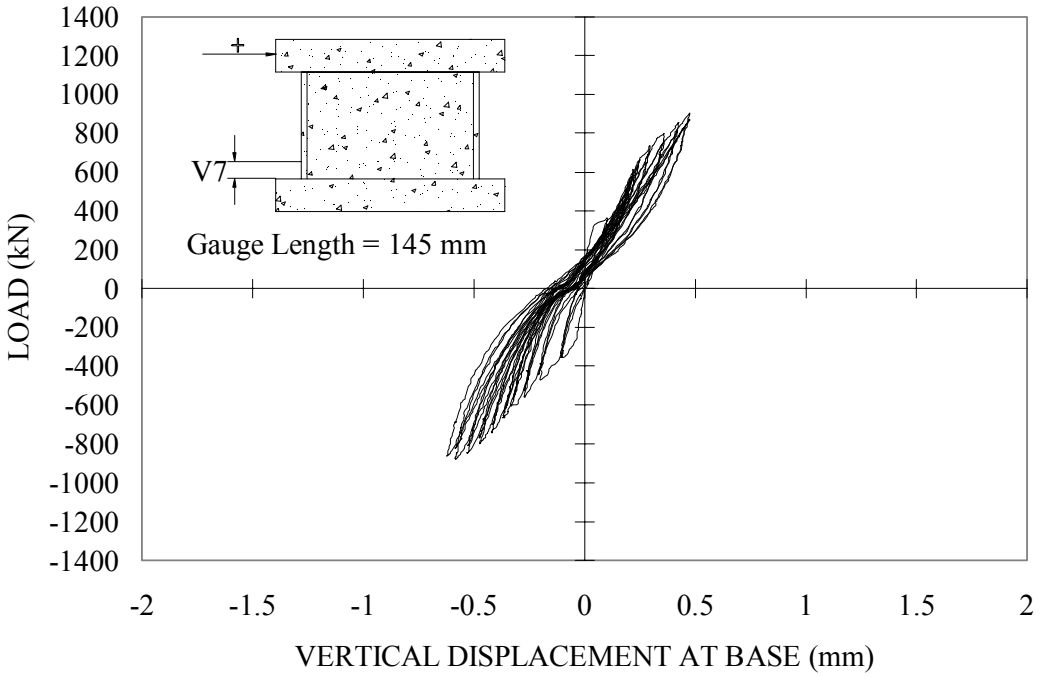

Figure 6.9 DP2 Vertical Displacements at Base

The responses of the two specimens were generally similar; however, the tensile response of DP1 demonstrated a gradual softening with increasing displacement, whereas DP2 remained relatively stiff. The maximum displacement measured in the flange wall of DP1 was 0.68 mm occurring at a load of 1258 kN during cycle 12. For DP2, a maximum displacement of 0.48 mm occurred just prior to failure (cycle 10). Again, it is more appropriate to compare the vertical displacement at the maximum load for DP2, which occurred at 9 mm of displacement. A value of 0.47 mm was attained for DP2, and for DP1, a displacement of 0.55 mm was recorded. A review of the photos of the flange walls, and the notes taken during the course of testing, indicate that some minor flexural cracks were visible at the flange wall-base slab joint. The first sign of cracks near the base for DP1 was recorded at the end of cycle 3 (3 mm of displacement), and by the end

of 2 mm of displacement, cracks near the flange tips were evident for DP2. In the post-peak regime, DP1 demonstrated that the vertical displacements diminished significantly and were not accumulating beyond the maximum lateral resistance. This further indicates that the yielding of flexural reinforcement was not widespread.

Relative to the total vertical displacements, discussed as part of the elongation of the flange walls, the local vertical displacements measured by LVDT V7 were 80 percent larger in DP1 and 64 percent larger in DP2 at the peak load. The majority of this displacement appeared as a crack at the base of the wall. Further, the measured reinforcement strains were large, but not in excess of yield, near the base slab. It may be concluded that some amount of bond slip in the anchorage zone of the vertical reinforcement in the flange walls had taken place, but it appears to be rather small.

6.7 FAILURE MECHANISMS

The presence of axial load, and the stiffness of the flange walls, contributed to the sequence of failure of DP1 and DP2. The failure mechanisms of the two walls were unexpected and not consistent with failures of other shear walls in the literature[29, 34]. The conventional thought on squat shear walls holds that failure can occur by either diagonal tension or diagonal compression[28]. Diagonal tension failure occurs when insufficient horizontal shear reinforcement is placed in the web section of the wall. Diagonal compression failure occurs when the shear stress on the web is large. In the latter case, the concrete in the toe region crushes followed by a sliding shear plane extending along the base of the wall.

Testing of DP1 was terminated at 15 mm of displacement. Beyond the peak load cycle (11 mm), the web wall's ability to resist the horizontal displacements was impaired, and with each successive cycle, the integrity of the concrete continued to diminish. Six vertical slip planes, equally spaced along the web, were evident. These planes began to form during 11 mm of displacement near the toes of the web.

The relatively undamaged flange walls, and the axial load, provided restraint against the opening of shear cracks in the web wall, preventing the conventional form of failure: diagonal tension or diagonal compression followed by sliding shear. The axial stiffness of the flanges restrained the rotation of the top slab. Therefore, shear distortion of the web wall contributed significantly to the lateral displacements relative to displacements due to flexure. Essentially, the restraint provided by externally applied axial load and stiff flange walls restrained the opening of shear cracks, and the significant shear distortion induced large shear stresses vertically in the web wall, leading to the formation of vertical slip planes.

The flange walls experienced flexural cracking; otherwise, no other significant damage was visible. Failure also involved severe crushing of the concrete over a widespread region of the web wall. Oesterle, Fiorato, Johal, Carpenter, Russell, and Corley[30] reported a similar type of failure mechanism for a shear wall with stiff boundary elements.

Testing of DP2 was halted at 10 mm of displacement, at which point the structure had failed by sliding shear of the web wall near the top slab. Possibly weaker concrete in the upper part of the walls initiated failure. On displacing the structure to +10 mm, a sudden sliding shear plane formed along the top of the web wall. The plane extended the

entire length of the web and caused a punching of the north flange wall near the top slab. Initially, flexural cracking first surfaced near the top slab, and a maximum crack width of approximately 1 mm was recorded in this area. Local yielding of the reinforcement in the upper portion of the flange walls, leading to the ratcheting effect, also contributed to the zone of weakness near the top slab. Note, that the concrete at the end of testing in the failure zone was of a brittle nature and reduced to a rubble-like material, further suggesting weaker concrete near the top slab. A further explanation of failure of DP2 near the top slab could be the possible variation of the wall thickness. A thinner wall section would also initiate failure. Although no core samples were taken from the web wall after testing to measure the thickness, the wall ties used during construction ensured that the forms remained in place and that the wall thickness was constant throughout. Twenty wall inserts were placed throughout the web wall and were used to tie the forms together. The wall inserts, which remained in the walls after casting of the concrete, acted as spacers to ensure a web wall thickness of 75 mm. After the forms were removed, the wall inserts were visible and were, for the most part, flush with the web wall faces indicating that the thickness remained constant.

A post-peak response for DP2 was not realized due to the sudden failure after the peak load.

It is important to note that prior to failure of DP1 and DP2, concrete in the area of the toes near the base of the web walls was spalling, and there were also signs of crushing prior to the peak load cycle. The stiffness of the flange walls in DP1 restrained shear cracks from opening and from concentrating the crushing of the concrete in the toe regions. The apparently weaker concrete of DP2 near the top slab caused yielding of the

flexural reinforcement in the flanges, which initiated failure away from the base of the web wall.

6.8 TWISTING OF TOP SLAB

LVDTs H2 and H3 (see Figure 4.43), placed on the south end of the top slab above the ends of the flange wall, served two purposes: to record the lateral displacement of the top slab, and to monitor twisting of the specimen. Twisting of the specimen was a concern at the onset of testing due to the torsionally weak web-flange wall section. For DP1, H2 and H3 measured displacements, which corresponded to the maximum lateral loads. For LVDT H2, a displacement of 12.09 mm was recorded at a corresponding lateral resistance of 1298 kN, and –11.38 mm corresponding to –1255 kN, in the positive and negative directions, respectively. For H3, slightly different displacements were measured. The displacement in the positive direction was 11.16 mm, and –11.36 mm in the negative direction. For specimen DP2, the maximum loads recorded were –879 kN and 904 kN in the negative and positive directions, respectively. For H2, the corresponding displacements were -9.14 mm and 9.15 mm; for H3, -9.24 mm and 8.54 mm. Plots of the responses are available in Appendix C and are similar to the responses of LVDT H1. The discrepancies in displacements at the peak loads indicate that some twisting was present during the test. Twisting was calculated from the algebraic difference in displacements between instruments H2 and H3 and is measured in radians. Figures 6.10 and 6.11 show the hysteretic twisting behaviours of DP1 and DP2, respectively.

From the plots, it is evident that the magnitude of twisting was relatively insignificant. Twisting was also more prevalent in the positive cycles. There seems to be slightly more instability as the specimens were pushed away from the strong wall. The maximum twisting measured for DP1 was 0.32 x 10^{-3} radians at a load of 1271 kN occurring during the first excursion to 12 mm of displacement. With DP2, the maximum twisting occurred during the second excursion to 9 mm of displacement for the positive cycles, and measured 0.2 x 10^{-3} radians at a load of 825 kN. LVDT H2 located on the east side of the top slab recorded larger displacements indicating that the specimens were twisting clockwise during the positive cycles.

Figures 6.10 and 6.11 seem to suggest that DP1 experienced slightly more twisting. However, DP2 failed perhaps prematurely, which will be discussed later, and a comparison of the magnitude of twisting at the peak load (cycle 9) of DP2 would be more representative. DP1 and DP2 experienced maximum rotations of 0.21 x 10^{-3} radians and 0.20 x 10^{-3} radians, respectively, during cycle 9. Thus, both specimens seemed to undergo similar degrees of twisting, and the axial load appears to have had a negligible effect on twisting.

6.9 BASE SLIP

LVDTs H4 and H5 (see Figure 4.42) monitored horizontal displacements of the base slab with respect to the laboratory strong floor. The base slab was post-tensioned to the laboratory strong floor prior to testing; therefore, a negligible amount of slip was measured. Plots of the responses are available in the Appendix C.

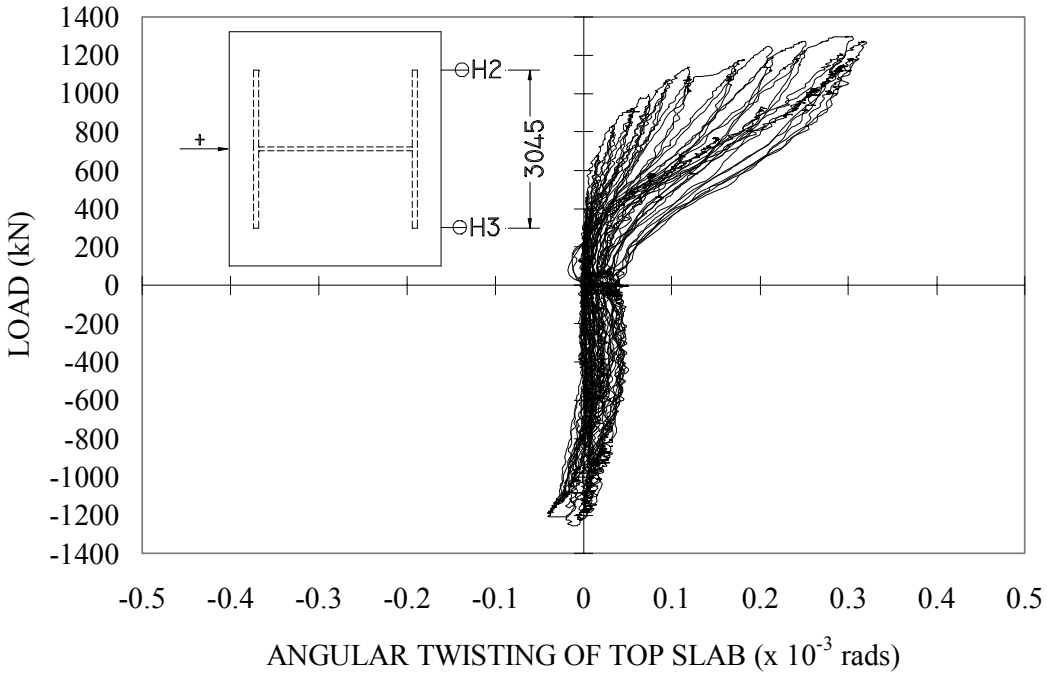

Figure 6.10 DP1 Twisting of Top Slab

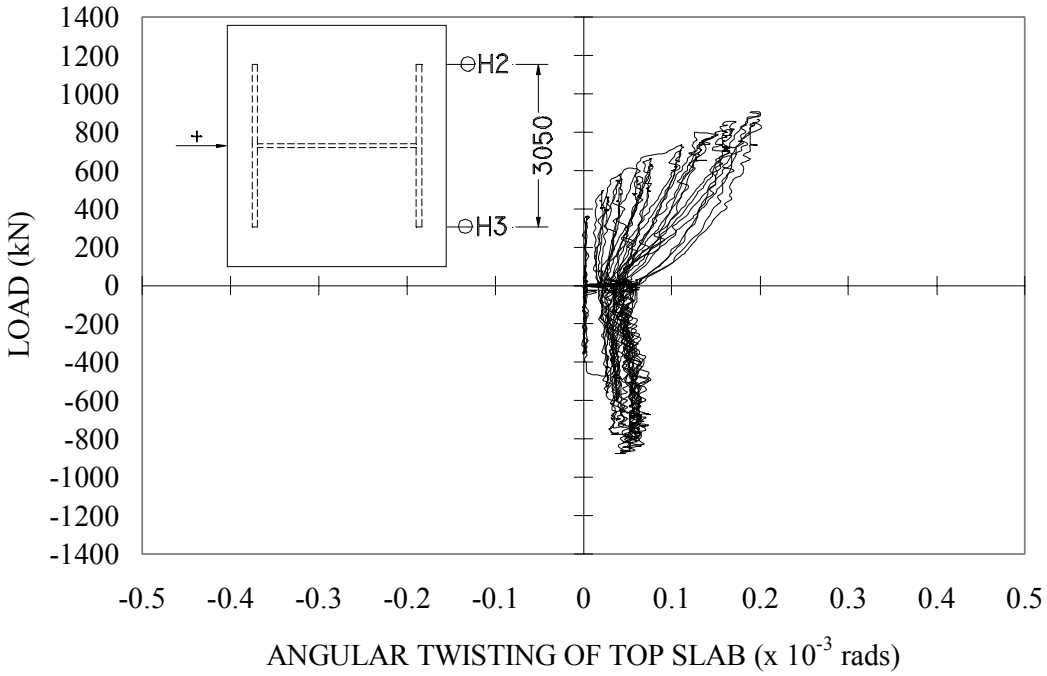

Figure 6.11 DP2 Twisting of Top Slab

6.10 BASE ROTATION

Although no instrumentation was attached to the test specimens to detect rocking of the foundations, the floor bolts were sufficiently post-tensioned to prevent rocking. The forty floor bolts were post-tensioned to 8000 psi (5.62 MPa). Each floor bolt had a cross sectional diameter of 2 in. (50 mm), and therefore, each bolt was post-tensioned to a force of approximately 112 kN. The bottom of the base slab was subjected to an approximate distributed compressive stress of 0.254 MPa. The self-weight of the test specimen provided an additional 0.03 MPa of compressive axial stress at the base. For DP1, the externally applied axial load of 940 kN increased the compressive stress at the base of the specimen by 0.053 MPa. Considering the combined compressive stress of 0.337 MPa at the base of DP1, and using the elastic flexural formula, a lateral load exceeding 1340 kN would be required to cause tensile stresses at the base. The registered maximum horizontal load for DP1 was 1298 kN, suggesting that lift-off did not occur. For DP2, considering the axial compressive stresses of the post-tensioning and the self-weight, a lateral load exceeding 1130 kN would have caused tensile stresses at the base; the maximum load applied during the test was well below at 904 kN

6.11 COMPARISONS TO NUPEC SPECIMEN

Specimen DP1 and the NUPEC specimen U-1 had similar wall geometries, similar reinforcement levels, and were tested under a similar axial load. The top slab of U-1 was 4000 x 4000 x 760 mm and the bottom slab was 5000 x 5000 x 1000 mm. The web wall was 2900 mm in length, 2020 mm in height, and 75 mm in thickness, and was reinforced with D6 reinforcing bars. The reinforcement was spaced 70 mm horizontally and

vertically in two layers. The flange walls were 2980 mm long, 2020 mm high, and 100 mm thick. The flanges were also reinforced with D6 reinforcing bars, spaced 70 mm horizontally, and vertically the bars were spaced at 70 mm near the web wall and 175 mm near the tips of the flanges. The reinforcement in DP1 had approximately double the reinforcement spacing to that of U-1 to maintain a comparable ρf_{sy} ratio. Even though DP1 was tested under static cyclic displacements and the NUPEC specimen was tested dynamically, comparisons are possible by investigating the envelope responses of each specimen.

The maximum load reported by NUPEC was 1636 kN at a displacement of 10.96 mm, and for DP1, the maximum load was 1298 kN at a displacement of 11.14 mm. Specimen U-1 did, however, have a compressive cylinder strength 32 % higher than DP1. The ratio of the peak loads between U-1 and DP1 was 1.26. The discrepancy in strength between the two walls was partly related to the difference in the concrete strengths, but was also a function of the ground motion imposed on U-1. The walls did, however, experience a similar amount of ductility at the ultimate lateral resistance. Figure 6.12 is a plot of the envelope responses of DP1 and U-1.

The stiffer envelope response of U-1 was strongly influenced by the ground motion to which it was subjected. Under seismic conditions, structures do not experience the same straining that they would under static loading, where the structure has time to respond, and creep effects become significant. Essentially, a structure would appear stiffer under dynamic loading relative to a similar structure exposed to an equivalent static loading. Eleven days were required to complete the static cyclic loading of DP1, whereas the dynamic input motion applied to U-1 had a duration of 16 seconds. The

envelope curves of the two responses merely indicate that behaviours were somewhat similar for a specific set of loading conditions, and for this case, static testing can potentially be a viable alternative to dynamic testing.

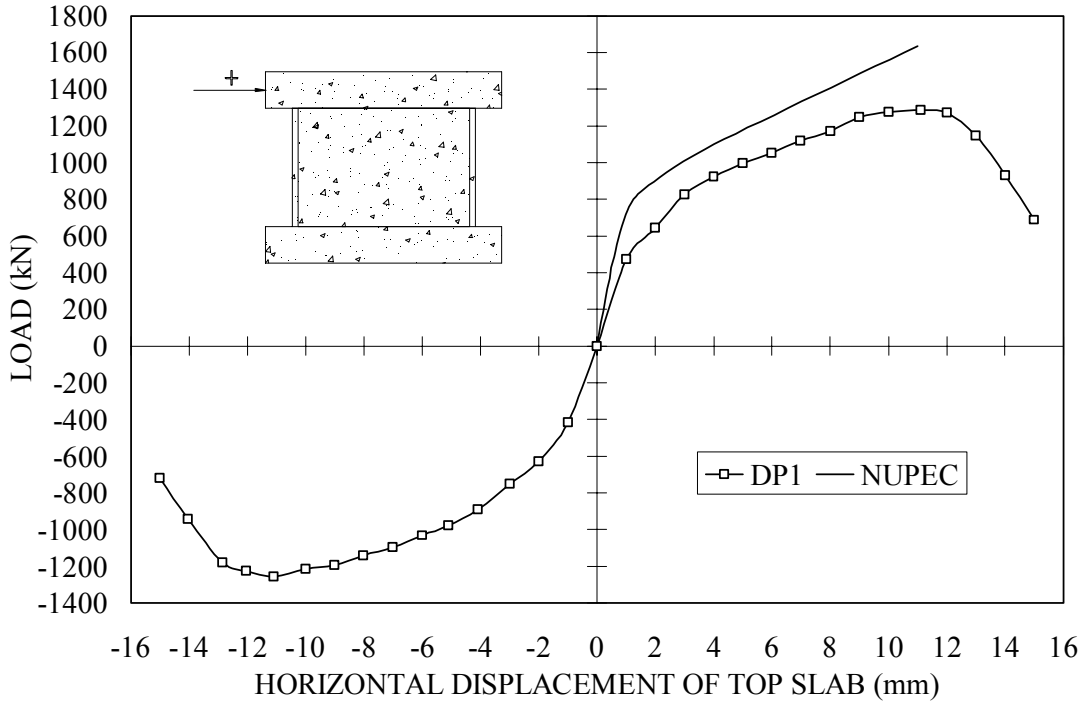

Figure 6.12 Envelope Responses

The modes of failure of the two walls differed somewhat; however, both failure mechanisms were the result of the damage experienced in the web walls, and the stiffness of the flanges at the onset of failure. U-1 failed by crushing of the concrete at the toes of the web wall followed by a sliding shear plane near the base of the wall. The web wall also punched through the flange wall near the base slab. Prior to failure, the flexural reinforcement in the flanges had yielded, and extensive vertical cracking in the flanges near the web wall was visible. The flanges were significantly damaged and provided little restraint to the formation of a sliding shear plane. Whereas, the stiff and relatively

undamaged flange walls of DP1 restrained the expansion of shear cracking in the web wall, thus causing vertical planes of failure.

6.12 SUMMARY OF RESULTS

To conclude this chapter, a summary of the experimental results of DP1 and DP2 are listed in the Table 6.1, highlighting important phenomenon during the course of testing. Figures 6.13 and 6.14 illustrate the locations of damage for each specimen.

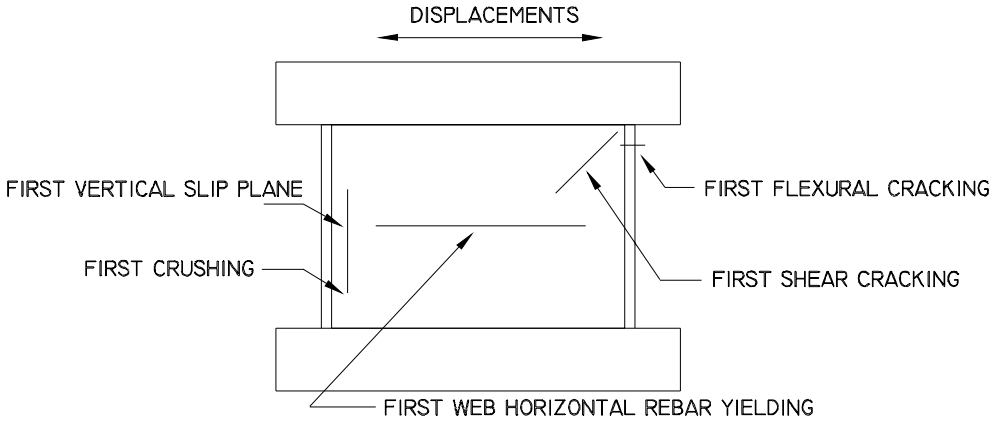

Figure 6.13 DP1 Damage Locations

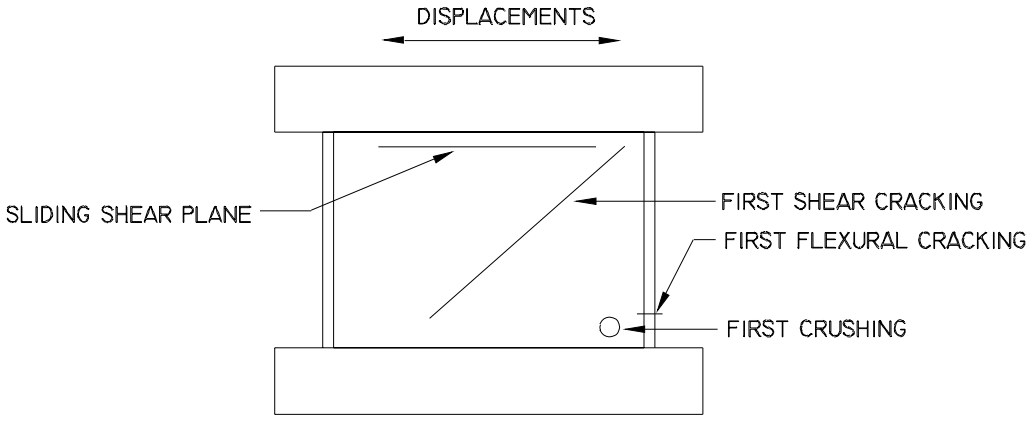

Figure 6.14 DP2 Damage Locations

Table 6.1 Summaries of Results

Phenomena	**Horizontal Displacement (mm)**		**Horizontal Force (kN)**	
	DP1	**DP2**	**DP1**	**DP2**
Flange Wall Initiation point of flexural crack	-2.89 cycle –3	-1.19 cycle -2	-819	-385
Web Wall Initiation point of shear crack	-0.63 cycle –1	-0.47 cycle -1	-408	-256
Flange wall vertical rebar Initiation point of yielding	n/a	n/a	n/a	n/a
Web wall vertical rebar Initiation point of yielding	n/a	n/a	n/a	n/a
Web wall horizontal rebar Initiation point of yielding	11.59 cycle +13	n/a	1079	n/a
Crush point	-8 cycle -8	8 cycle +8	-1141	856
Maximum displacement	-15 cycle -15	-10.22 cycle -10	-717	-852
Maximum load	11.14 cycle +11	9.15 cycle +9	1298	904

CHAPTER 7

Material Modeling & Finite Element Implementation

7.1 INTRODUCTION

The analytical portion of this research project focused on formulating constitutive rules describing the behaviour of cyclically loaded concrete. In particular, the proposed models have been formulated in the context of smeared rotating cracks, both in the compression and tension regimes.

While several models have been presented in the literature, most are not appropriate for the above conditions. Some models assume fixed principal stress directions, and others are based on a fixed crack formulation. No one model captures all the characteristics of the cyclic response behaviour of concrete. The proposed models do, however, have roots in models currently available in the literature, adapted to a rotating crack approach. Comparisons will be made between the proposed models and those reported by other researchers.

It is important to note that the models presented herein are not intended for fatigue analysis and are best suited for a finite number of excursions to a displacement level. Additionally, the linear cyclic models for concrete reported by Vecchio[3] were preliminary at the time they were reported and served to demonstrate the applicability of cyclic loading in a secant stiffness-based algorithm.

7.2 COMPRESSION MODELS

Herein is a discussion of the proposed models for the cyclic compressive behaviour of concrete including unloading/reloading curves, plastic offsets, stiffness degradation, and partial unloading/reloading curves.

7.2.1 Plastic Offset Model

A plastic offset strain is the residual strain that occurs in concrete during unloading to a zero-load level. Essentially, it is the amount of non-recoverable damage. The damage includes the effects of crushing, internal cracking, and the compressing of internal voids.

The plastic strains are largely responsible for the changes in the unloading and reloading slope. The plastic offset is used as a parameter in defining the unloading path and in determining the degree of damage in the concrete due to cycling. The plastic offset also determines the shift in the tension model from the origin and the degree of pinching of the hysteresis loops.

Various plastic offset models for concrete in compression have been proposed in the literature. To allow comparisons to the proposed model (Palermo model), the following models have been included in this study (see Chapter 2 for full details):

1. Karsan and Jirsa $$S_P = 0.145 S_E^{\,2} + 0.13 S_E \tag{7.1}$$

2. Buyukozturk and Tseng $$\frac{\varepsilon_r}{\varepsilon_p} = 0.162\left(\frac{\varepsilon_u}{\varepsilon_p}\right) + 0.334\left(\frac{\varepsilon_u}{\varepsilon_p}\right)^2 \tag{7.2}$$

3. Bahn and Hsu $$S_{pu} = c_p \left(S_{eu}\right)^{n_p} \tag{7.3}$$

4. Mander, Priestley, and Park $$\varepsilon_{pl} = \varepsilon_{un} - \frac{\left(\varepsilon_{un} + \varepsilon_a\right) f_{un}}{\left(f_{un} + E_c \varepsilon_a\right)} \tag{7.4}$$

$$\varepsilon_a = a\sqrt{\varepsilon_{un}\varepsilon_{cc}} \tag{7.5}$$

a is the greater of $$a = \frac{\varepsilon_{cc}}{\varepsilon_{cc} + \varepsilon_{un}} \tag{7.6}$$

$$a = \frac{0.09\varepsilon_{un}}{\varepsilon_{cc}} \tag{7.7}$$

5. Vecchio $$\varepsilon_c^p = \varepsilon_c - \varepsilon_p\left[0.87\left(\frac{\varepsilon_c}{\varepsilon_p}\right) - 0.29\left(\frac{\varepsilon_c}{\varepsilon_p}\right)^2\right] \text{ if } \varepsilon_c > 1.5\varepsilon_p \tag{7.8}$$

$$\varepsilon_c^p = \varepsilon_c - 0.001305\left(\frac{\varepsilon_p}{0.002}\right) \quad \text{if } \varepsilon_c < 1.5\varepsilon_p \tag{7.9}$$

The final model, previously not reported in this manuscript, is that proposed by Stevens, Uzumeri, and Collins[26], and is described by the following expressions:

$$\varepsilon_{can} = \varepsilon_{cen} - \Delta\varepsilon_{cn1} \tag{7.10}$$

where $$\Delta\varepsilon_{cn1} = 0.87\varepsilon_{cen} - 0.145\varepsilon_{cen}^{\ 2} \qquad \varepsilon_{cen} \le 3 \tag{7.11}$$

$$\Delta\varepsilon_{cn1} = 1.305 \qquad \varepsilon_{cen} \ge 3 \tag{7.12}$$

All strain parameters are normalized with respect to the strain at peak cylinder stress for concrete. ε_{can} is the plastic strain and ε_{cen} is the difference between the unloading strain and the plastic strain.

Figure 7.1 is a plot of the aforementioned models plotted against test data reported by Bahn and Hsu[20]. The data is presented in terms of normalized plastic strain and normalized unloading strain, normalized with respect to the strain corresponding to the maximum concrete cylinder stress. A total of 26 test points are included in the plot. The data was part of an experimental project in which 3 x 6 in. (76 x 152 mm) cylinders of normal strength concrete were subjected to random cycles of compressive loading.

Note that the model proposed by Karsan and Jirsa is identical to that suggested by Stevens, Uzumeri, and Collins. The latter was derived using the model of Karsan and Jirsa. The Palermo model is included, and the formulation will be discussed later.

The Bahn and Hsu model best fits the data in Figure 7.1 from which it was derived. The Karsan and Jirsa, and Stevens, Uzumeri, and Collins models appear to represent a lower bound solution. The Buyukozturk and Tseng expression is an upper bound for the entire range of test points, and Vecchio's model seems to also represent an upper limit for the most part. The Mander, Priestley, and Park model produces a residual curve similar to the Karsan and Jirsa response. Mander, Priestley, and Park formulated a plastic offset model assuming the base curve to be represented by Popovics'[16] formulation for concrete under monotonic loading. The formulation is a function of the unloading strain, initial tangent stiffness and unloading stress; whereas, most residual models are solely functions of the unloading strain. Assumptions were required for the model to calculate the unloading stress and the initial tangent modulus. A compressive strength of 30 MPa for concrete, which is reasonable for the normal strength, was assumed. The Mander, Priestley, and Park model, which is dependant on the base curve, produces varying results when used with different base curves. The Palermo model lies between the Karsan and Jirsa, and Bahn and Hsu models for the most part.

To further investigate the plastic offset models, additional data from Karsan and Jirsa[12], and Buyukozturk and Tseng[15] have been plotted in Figures 7.2 and 7.3, respectively.

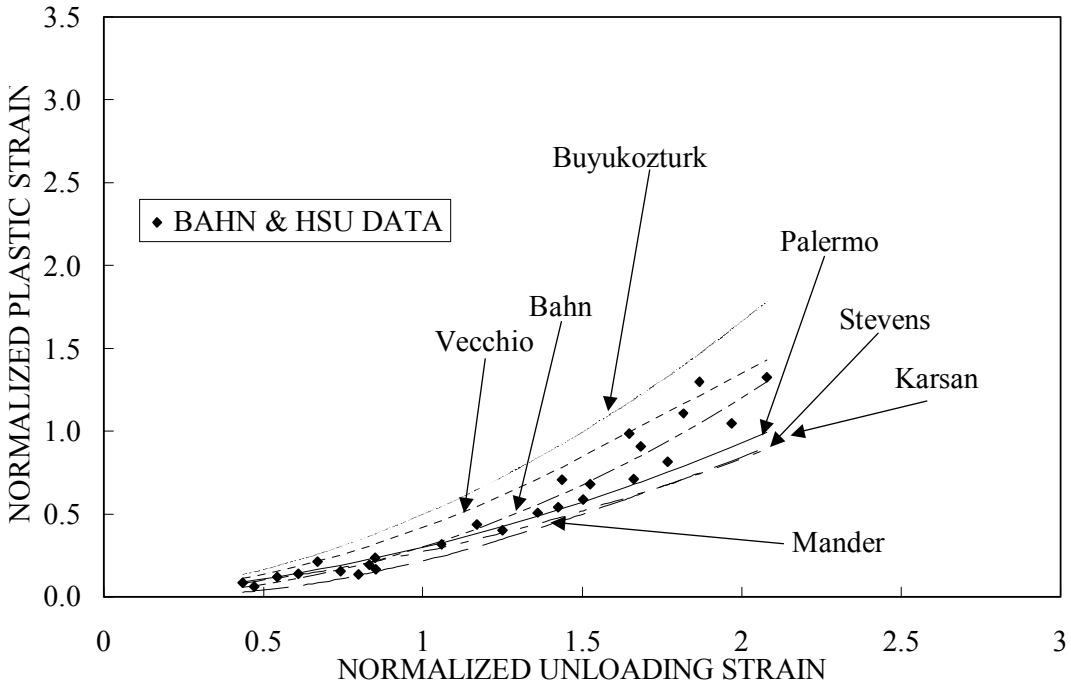

Figure 7.1 Bahn and Hsu Plastic Offset Data

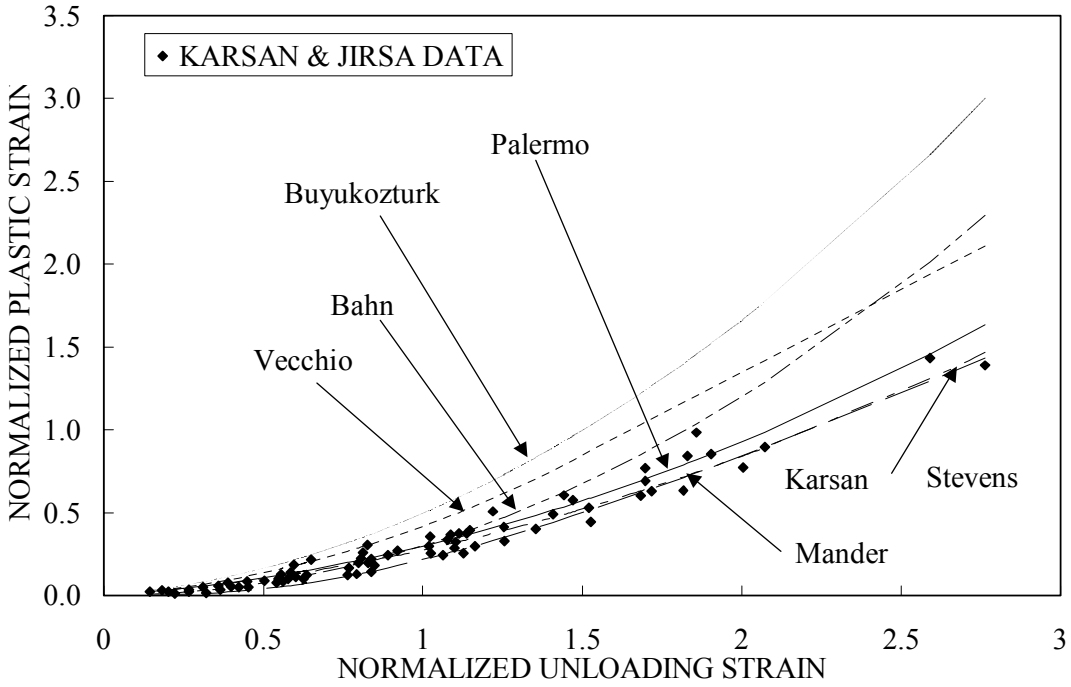

Figure 7.2 Karsan and Jirsa Plastic Offset Data

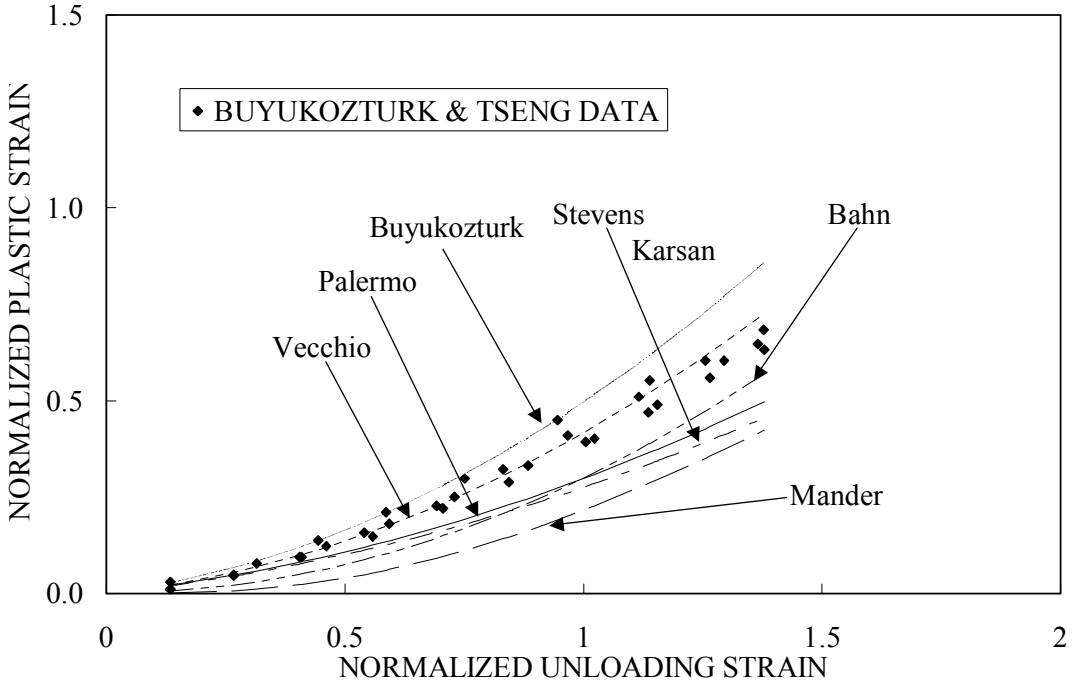

Figure 7.3 Buyukozturk and Tseng Plastic Offset Data

The Karsan and Jirsa results consisted of 74 data points from cyclic load tests on rectangular columns 5 in. (127 mm) high and 3 in. (76 mm) wide. To confine failure to the mid-height, the ends of the columns were flared and reinforced with No. 5 bars.

The model proposed by Karsan and Jirsa best represents the data of Figure 7.2 from which it was formulated. The Buyukozturk and Tseng model forms an upper bound for the most part, and the Palermo model predicts residual strains slightly larger than the Karsan and Jirsa model. The Mander, Priestley, and Park model, assuming Popovics formulation as the base curve, provides a lower bound solution. The Vecchio, and Bahn and Hsu models lie between the upper and lower bound, with the former predicting larger offsets.

The 35 data points obtained from Buyukozturk and Tseng were the results of confined cyclic test on flat concrete plates 5 x 5 x 1 in. (127 x 127 x 25 mm). It was

concluded that the plastic strains were dependent mainly on the strain at unloading and did not seem to be significantly affected by confining stresses and strains. The Buyukozturk and Tseng model represents an upper bound to the data it was derived from, and the Vecchio model seems to best fit the data. The Bahn and Hsu expression appears to form a lower bound solution for the entire rage of test data, closely followed by the Palermo model. The remaining models seem to underestimate the residual strains.

The models presented, for the most part, best suit the data from which they were derived, and no one model seems to be more appropriate. This can be attributed to the test data, where discrepancies between each set of data are evident. To formulate a unified model, the test data from Bahn and Hsu, Karsan and Jirsa, and Buyukozturk and Tseng were combined and plotted, and are given in Figure 7.4 along with the analytical models discussed thus far.

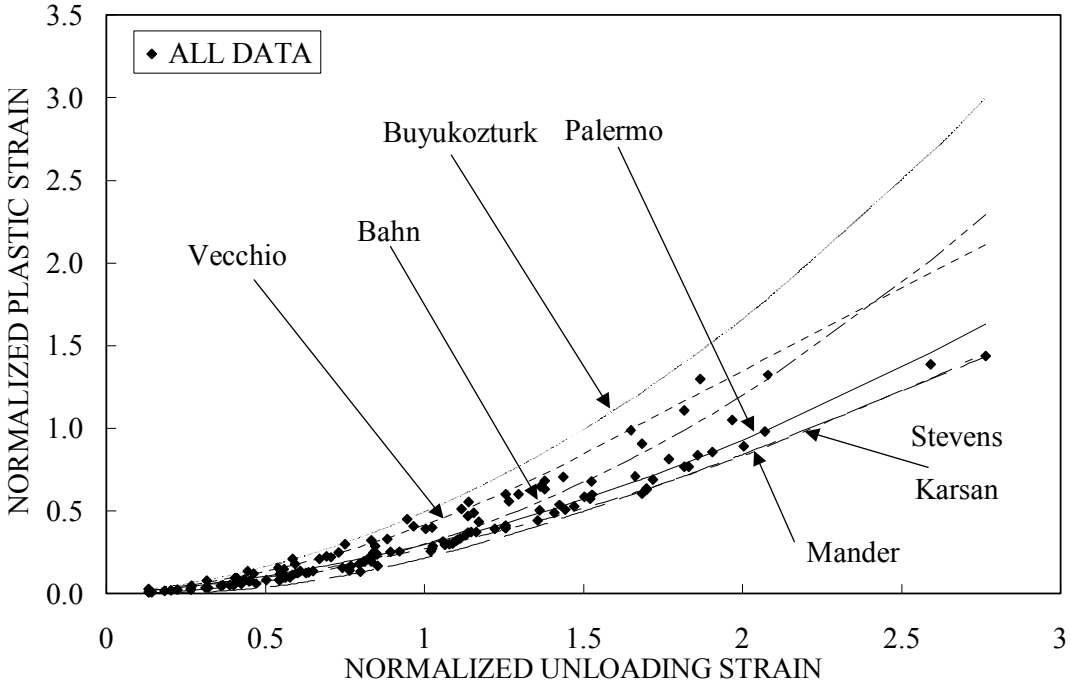

Figure 7.4 Combined Offset Data for Concrete in Compression

The plot indicates that scatter in data is not significant, and a unified model can be formulated to represent the plastic offset strain. The Palermo model was derived from the combined data to best represent the entire range of test results. The Karsan and Jirsa data points, representing 55% of the data, largely influenced the Palermo model. Through regression analysis, a quadratic expression was formulated as:

$$\varepsilon_c^{\ p} = \varepsilon_p \left[0.166 \left(\frac{\varepsilon_{un}}{\varepsilon_p} \right)^2 + 0.132 \left(\frac{\varepsilon_{un}}{\varepsilon_p} \right) \right] \tag{7.13}$$

where $\varepsilon_c^{\ p}$ is the plastic strain, ε_p is the strain at peak stress, and ε_{un} is the strain at the onset of unloading from the base curve. A strain-based approach was used over a stress-based model. A stress-based approach is dependent on the curves used to calculate stresses and can produce varying results; the Mander, Priestley, and Park model being an example. The Palermo model can be re-written to represent the instantaneous plastic strain at any load:

$$\varepsilon_c^{\ p} = \varepsilon_c - \varepsilon_p \left[0.868 \left(\frac{\varepsilon_c}{\varepsilon_p} \right) - 0.166 \left(\frac{\varepsilon_c}{\varepsilon_p} \right)^2 \right] \tag{7.14}$$

where ε_c is the strain in the concrete. The Palermo model predicts smaller plastic offset strains relative to the Vecchio model, thus providing more pinching in the hysteresis loops of concrete in compression. The Karsan and Jirsa expression can be used to represent a lower limit to calculating plastic strains, and the upper limit can be obtained from the Buyukozturk and Tseng model. The plastic offset strain remains unchanged unless the previous maximum strain in the history of loading is exceeded.

7.2.2 Unloading Curves

The unloading response of concrete, in its simplest form, can be represented by a linear expression from the unloading strain to the plastic strain. However, this type of representation is deficient and does not reflect the amount of energy dissipated during an unloading/reloading cycle in compression. Test data of concrete under cyclic loading confirms that the unloading branch is nonlinear. To derive an expression to describe the unloading branch of concrete, a Ramberg-Osgood formulation similar to that utilized by Seckin[21] was adopted. This form of modeling is independent of the base curve and is strongly influenced by the unloading and plastic strains. Formulations based on previous strain history and strain parameters yield better results, as the need to determine previous stress conditions is removed. The general form of the unloading branch of the proposed model is expressed as:

$$f_c(\Delta\varepsilon) = A + B\Delta\varepsilon + C\Delta\varepsilon^N \tag{7.15}$$

where f_c is the stress in the concrete on the unloading curve, and $\Delta\varepsilon$ is the strain increment measured from a strain on the unloading path to the unloading strain. $A, B,$ and C are parameters used to define the general shape of the curve, and N is the Ramberg-Osgood power term. Sets of boundary conditions were used to define the parameters and are illustrated in Figure 7.5.

The initial unloading stiffness is denoted by E_{c2}, and E_{c3} is the unloading stiffness at the intersection with the strain axis. f_p is the peak stress, ε_p is the strain at peak stress, and f_{2c} is the base curve stress at an unloading strain of ε_{2c}. The four sets of boundary conditions used to develop the unloading model include:

1. $\Delta\varepsilon = 0$, $f(\Delta\varepsilon) = f_{2c}$

2. $\Delta\varepsilon = \varepsilon_c^{\,p} - \varepsilon_{2c}$, $f(\Delta\varepsilon) = 0$

3. $\Delta\varepsilon = 0$, $df_c / d\Delta\varepsilon = E_{c2}$

4. $\Delta\varepsilon = \varepsilon_c^{\,p} - \varepsilon_{2c}$, $df_c / d\Delta\varepsilon = E_{c3}$

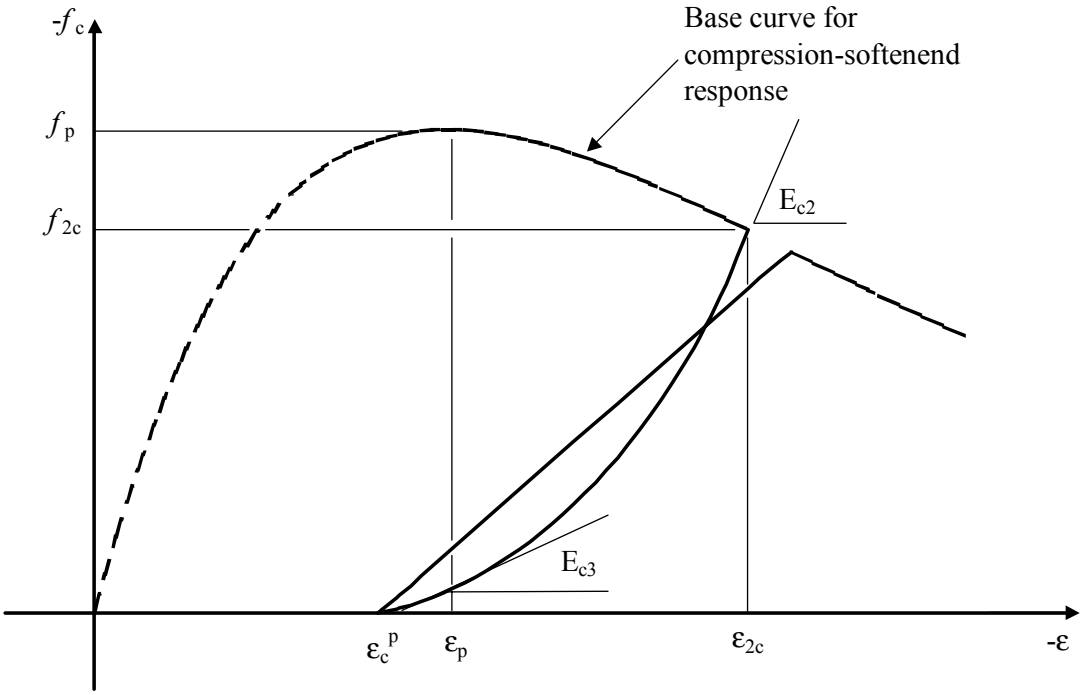

Figure 7.5 Compressive Unloading Parameters

Applying the boundary conditions and simplifying yields:

$$f(\Delta\varepsilon) = f_{2c} + E_{c2}(\Delta\varepsilon) + \left[\frac{(E_{c3} - E_{c2})\Delta\varepsilon^N}{N(\varepsilon_c^{\,p} - \varepsilon_{2c})^{N-1}}\right] \tag{7.16}$$

where $$\Delta\varepsilon = \varepsilon - \varepsilon_{2c} \tag{7.17}$$

and $$N = \frac{(E_{c2} - E_{c3})(\varepsilon_c^{\,p} - \varepsilon_{2c})}{f_{c2} + E_{c2}(\varepsilon_c^{\,p} - \varepsilon_{2c})} \tag{7.18}$$

ε is the instantaneous strain in the concrete. The initial unloading stiffness E_{c2} is assigned a value equal to the initial tangent stiffness E_c, and is routinely calculated as $2f_c'/\varepsilon_0$. The unloading stiffness E_{c3} is defined as $0.071E_c$, and was adopted from the Seckin results. To test the validity of the proposed formulations, the above model (the Palermo model) was plotted against test data from the experimental works of Bahn and Hsu[20], Karsan and Jirsa[12], Seckin[21], and Sinha, Gerstle, and Tulin[11]. The test data of Bahn and Hsu, Seckin, and Sinha, Gerstle, and Tulin are those from tests on standard cylinders, and the Karsan and Jirsa data represents results from short rectangular columns. Also plotted are the unloading responses predicted by the Mander, Priestley, and Park[22], Bahn and Hsu[20], and Vecchio[3] models. Figure 7.6 depicts the results of the various models against data reported by Bahn and Hsu.

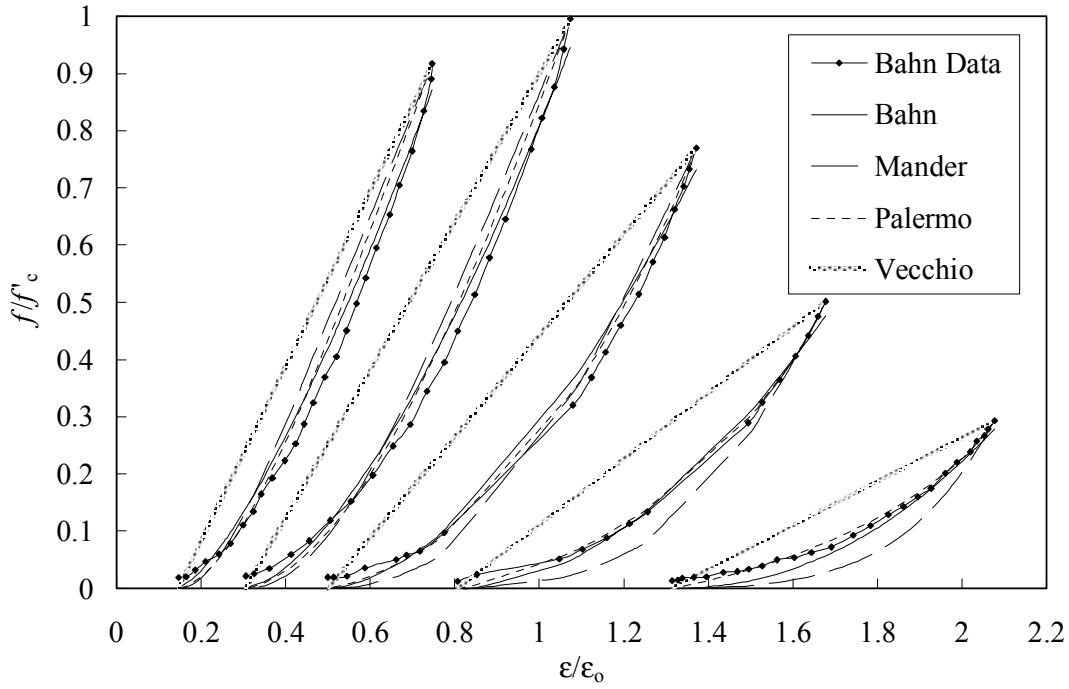

Figure 7.6 Bahn and Hsu Unloading Data

The preliminary linear unloading response of Vecchio dramatically underestimates the nonlinear nature of concrete during the unloading phase, and does not consider the energy dissipation. The Mander, Priestley, and Park model, which seems to overestimate the amount of energy dissipation for the most part, is a modified form of the Popovics[16] stress-strain curve for monotonic loading of concrete. The Palermo, and Bahn and Hsu models appear to represent the test data more accurately. Figure 7.7 shows the results of the models against data reported by Karsan and Jirsa. For this set of data, the Mander, Priestley, and Park model appears to best fit the data for unloading strains larger that $2\varepsilon_o$. For unloading strains less than $2\varepsilon_o$, the Palermo expression provides excellent agreement with the test results. The data provided by Seckin in Figure 7.8 demonstrates that the model proposed herein provides reasonably accurate simulations of test data.

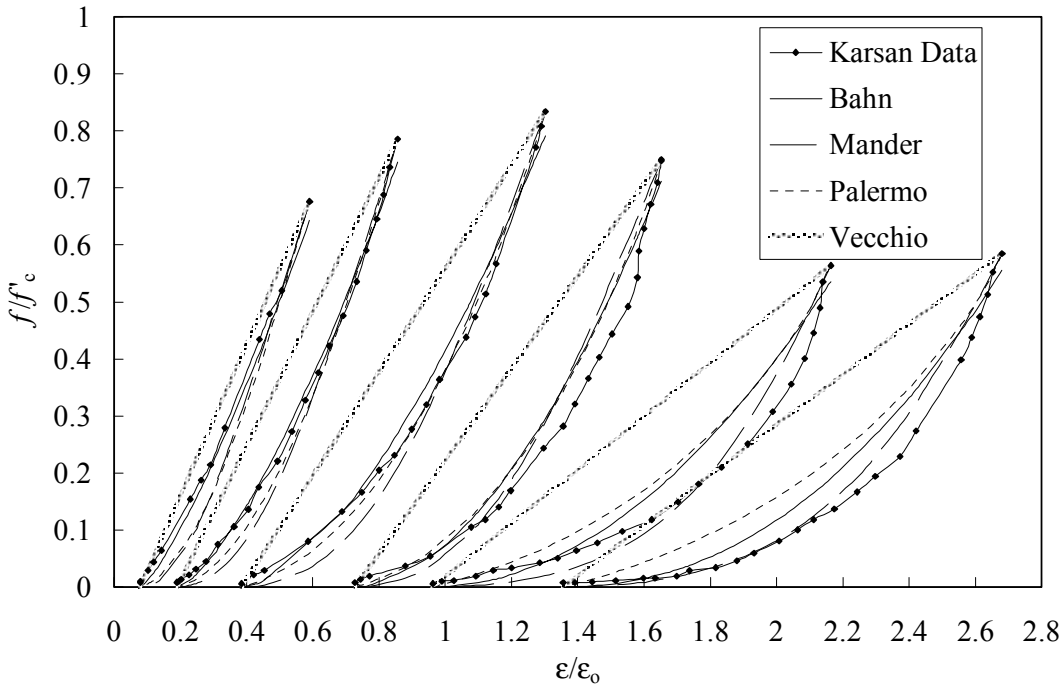

Figure 7.7 Karsan and Jirsa Unloading Data

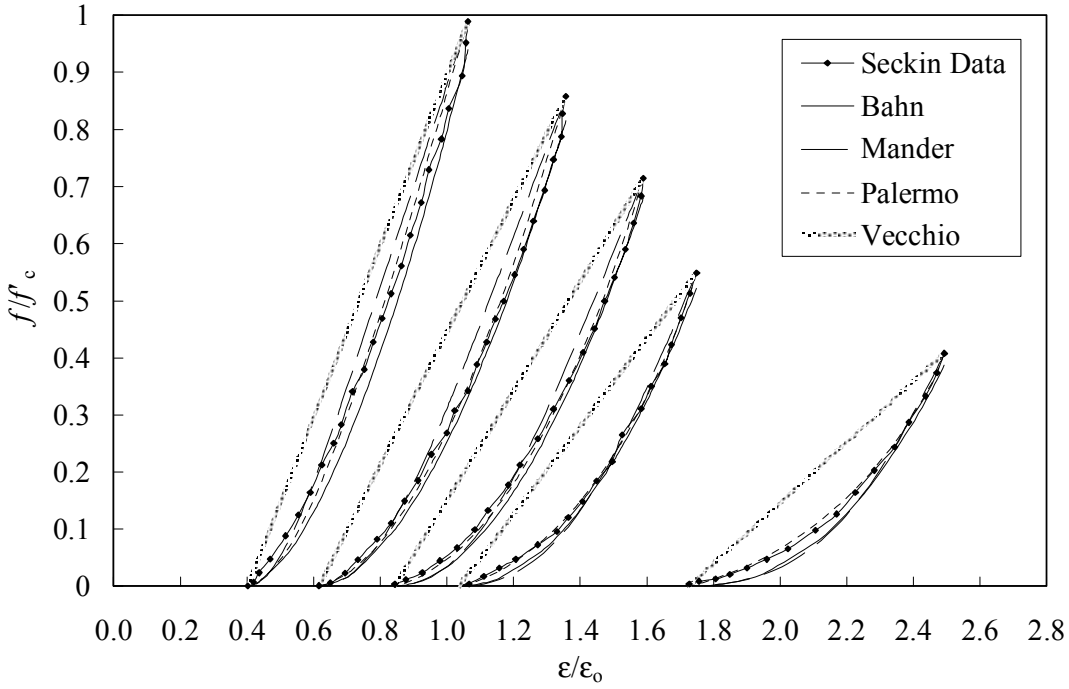

Figure 7.8 Seckin Unloading Data

Figures 7.7 and 7.8 confirm that a linear representation of the unloading curve does not simulate the actual behaviour of concrete. The model proposed by Bahn and Hsu provides excellent agreement with the test data; however, the model is a power function of the straight-line linear response and does not consider the boundary conditions of the concrete in the modeling. Figure 7.9 is a plot of the Palermo and Vecchio models plotted against data from Sinha, Gerstle, and Tulin, to further validate the applicability of the proposed expression.

The strength of the proposed unloading model lies in its independence from any stress-based backbone curve, and considers the boundary conditions at the onset of unloading and at the end of unloading. It also captures the actual nonlinear behaviour of the unloading response, which is strongly influenced by the unloading and plastic strains.

The formulations incorporate unloading and plastic strains as parameters to describe the degree of nonlinearity of unloading.

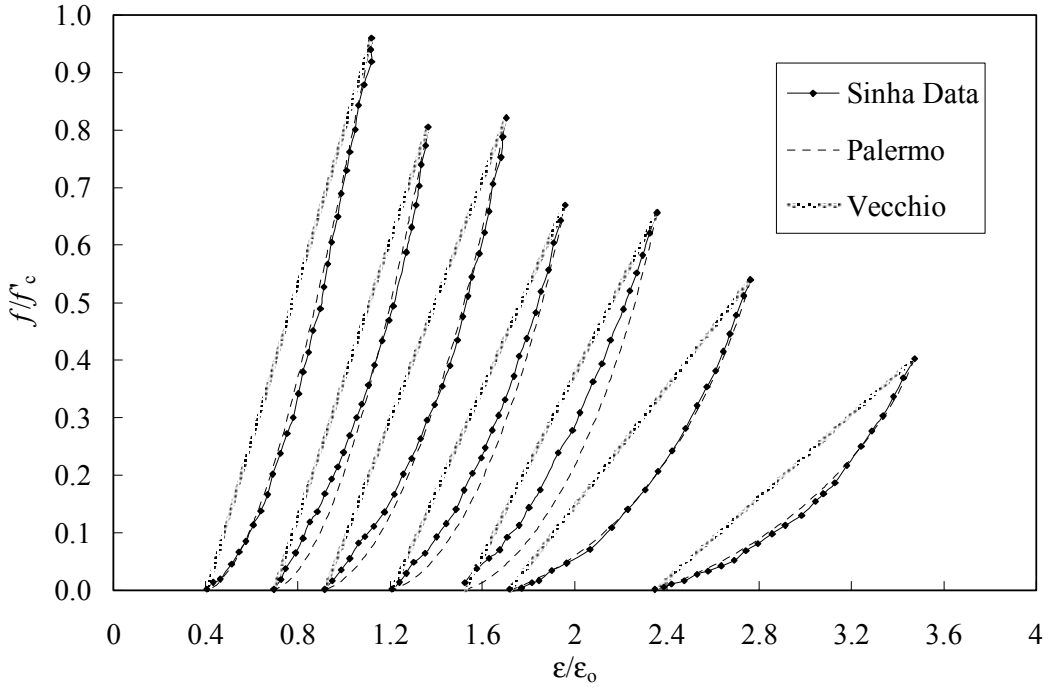

Figure 7.9 Sinha, Gerstle, and Tulin Unloading Data

7.2.3 Reloading Curves

Test data indicates that the reloading curve can be accurately modeled by a linear representation. Most researchers have used this type of a reloading curve, and the same approach is used herein.

An important characteristic of concrete in the reloading phase is that the reloading curve does not intersect the base curve at the previous maximum unloading strain. Further straining, beyond the previous maximum strain, is required for the reloading response to intersect the base curve. This represents damage in the concrete due to the cycling process. Researchers that have modeled this damage do so by defining

a return strain point on the base curve, and by adjusting the reloading branch to intersect the base curve at this point. Seckin modeled the reloading branch by defining the reloading stiffness as a degrading function of the unloading strain. In another approach, Mander, Priestley, and Park defined a new stress point on the reloading path, which corresponded to the previous maximum unloading strain. The new stress point was assumed to be a function of the previous unloading stress and of the stress at reloading reversal. Beyond this point, Mander, Priestley, and Park used a nonlinear function to connect the reloading path to the base curve at a definable return strain. The above models, for the most part, ignore the case of partial unloading and assume the return strain to be a function of the unloading strain, or are stress-based formulations. The approach used here was to define the reloading stiffness as a degrading function, and was determined to be a function of the strain recovery during unloading. The model implicitly considers the case of partial unloading. The reloading stiffness is defined by the following expression:

$$E_{c1} = \frac{(\beta_d \cdot f_{\max}) - f_{ro}}{\varepsilon_{2c} - \varepsilon_{ro}} \tag{7.19}$$

where

$$\beta_d = \frac{1}{1 + 0.10\left(\varepsilon_{rec} / \varepsilon_p\right)^{0.5}} \qquad \text{for } |\varepsilon_c| < |\varepsilon_p| \tag{7.20}$$

$$\beta_d = \frac{1}{1 + 0.175\left(\varepsilon_{rec} / \varepsilon_p\right)^{0.6}} \qquad \text{for } |\varepsilon_c| > |\varepsilon_p| \tag{7.21}$$

and

$$\varepsilon_{rec} = \varepsilon_{\max} - \varepsilon_{\min} \tag{7.22}$$

E_{c1} is the reloading stiffness, β_d is a damage indicator, $f_{\max}$ is the maximum stress in the concrete for the current unloading loop, and f_{ro} is the stress in the concrete at

reloading reversal that corresponds to a strain of ε_{ro}. ε_{rec} is the amount of strain recovered in the unloading process and is the difference between the maximum strain $(\varepsilon_{\max})$ and the minimum strain $(\varepsilon_{\min})$ for the current cycle. The minimum strain is limited by the compressive plastic strain. The damage indicator was established from regression analysis of test data on plain concrete from 4 series of tests: Buyukozturk and Tseng[15], Bahn and Hus[20], Karsan and Jirsa[12], and Yankelevsky and Reinhardt[17]. A total of 31 data points were collected for the pre-peak range (see Figure 7.10) and 33 data points for the post-peak regime (see Figure 7.11). Since there was a negligible amount of scatter between each series of test, the data points were combined in order to formulate the model. Also shown is Figure 7.12, an arbitrary loading cycle depicting the reloading parameters.

Reloading curves as assumed by Vecchio; Mander, Priestley, and Park; Seckin; and that derived herein (Palermo) are plotted against test data reported by Seckin[21] in Figure 7.13. The reloading response for the Palermo model is determined from:

$$f_c = f_{ro} + E_{c1}(\varepsilon_c - \varepsilon_{ro}) \tag{7.23}$$

where f_c and ε_c are the stress and strain on the reloading path.

The Seckin model grossly overestimates the stresses on the reloading path. The expressions are a function of the initial tangent modulus and the plastic offset strain. The model would follow more closely the experimental results if the plastic strains used in the reloading curves were determined from the Seckin plastic offset model.

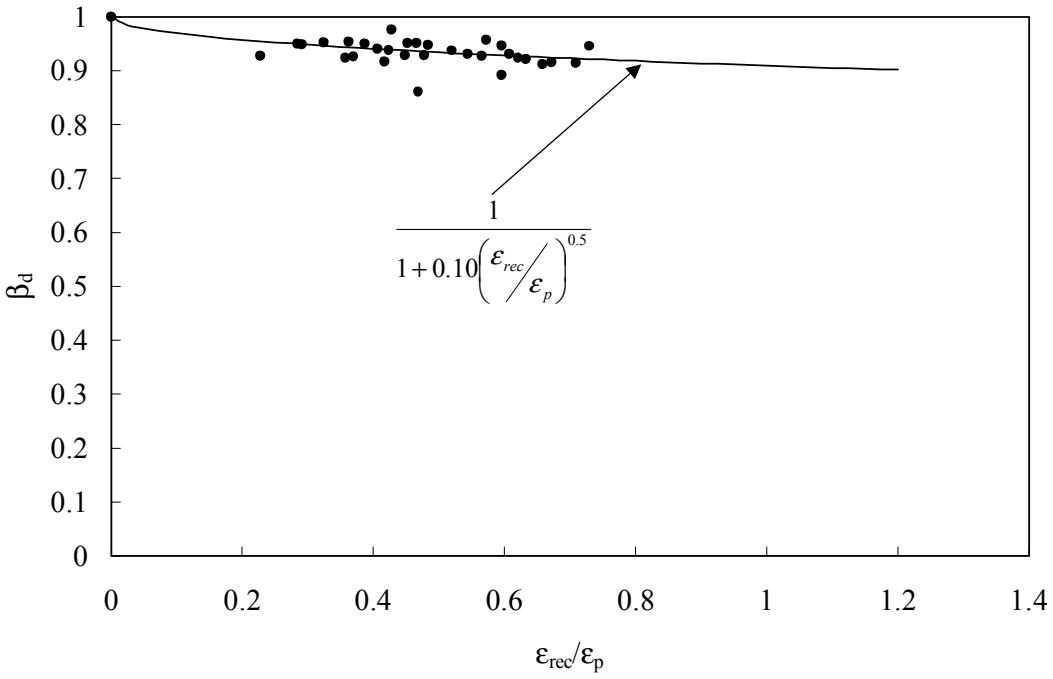

Figure 7.10 Pre-Peak Damage Indicator for Concrete in Compression

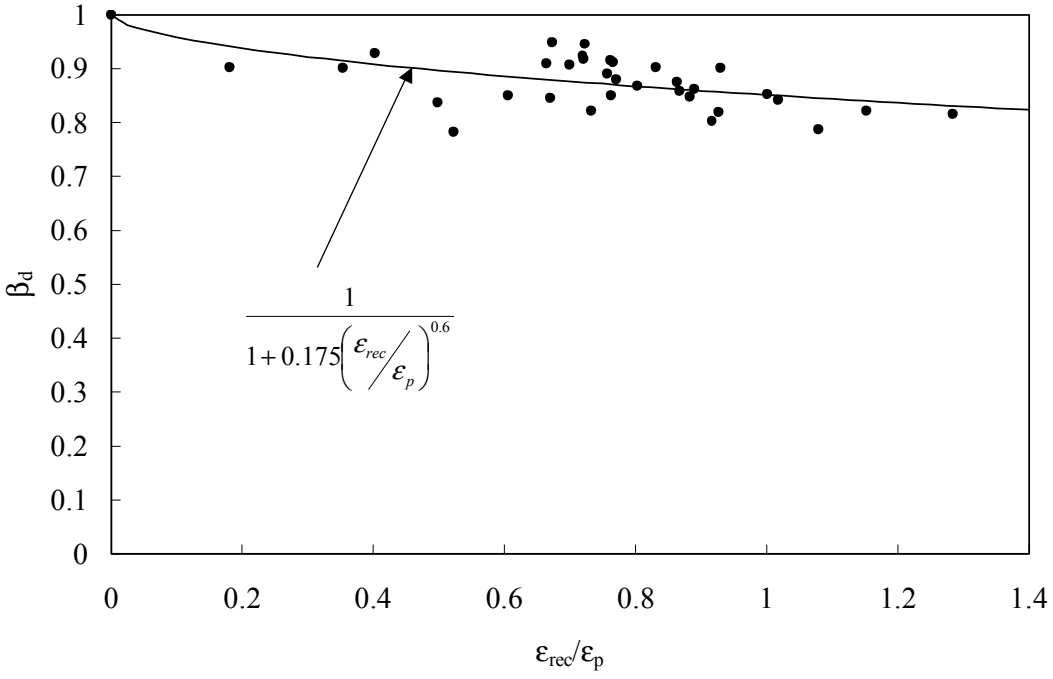

Figure 7.11 Post-Peak Damage Indicator for Concrete in Compression

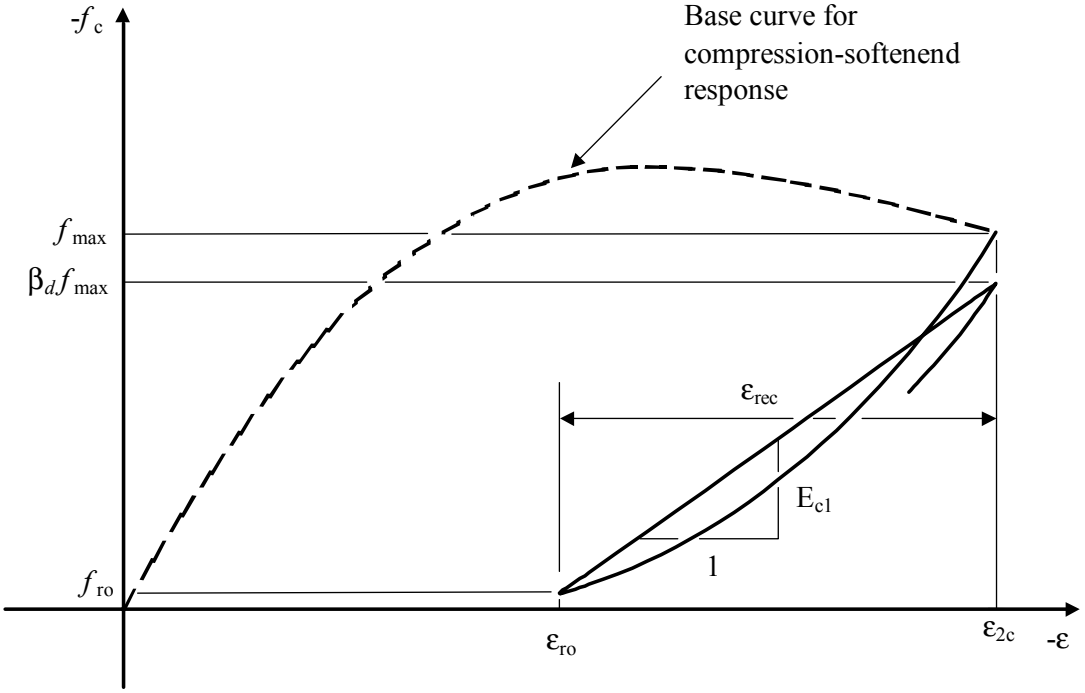

Figure 7.12 Compression Reloading Parameters

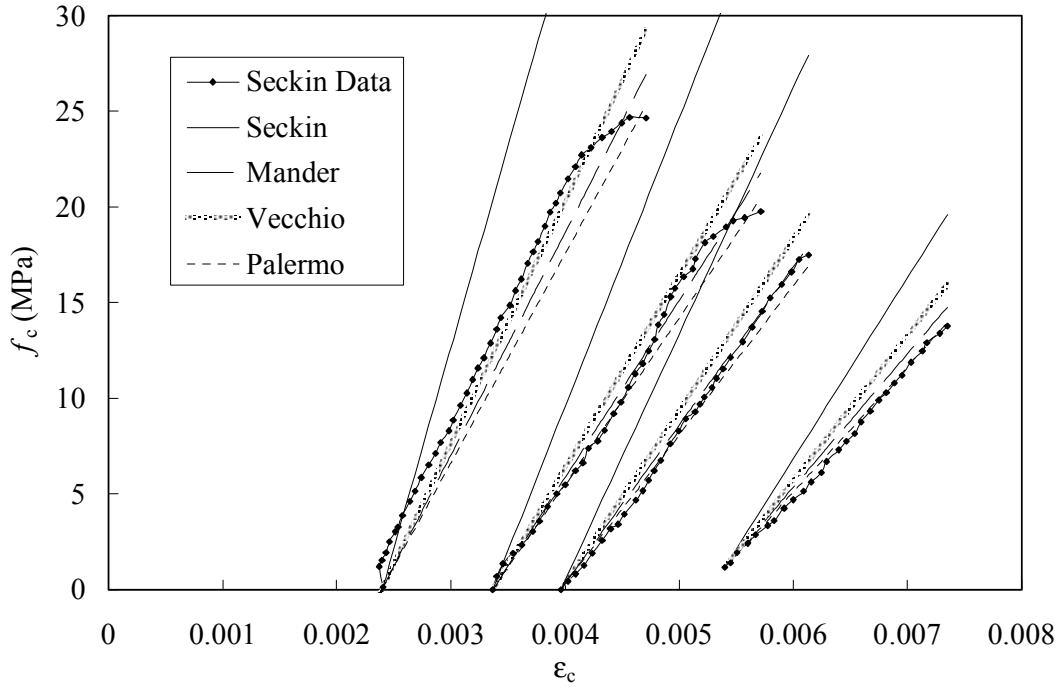

Figure 7.13 Seckin Reloading Data

The reloading curves of Seckin tend to return to the base curve at strains less than the previous maximum unloading strain. This is contradictory with experimental evidence, where the reloading path will intersect the base curve at strains in excess of the pervious maximum unloading strain. The Vecchio model, with increasing unloading strain, generally overestimates the reloading stresses due to the fact that the reloading path meets the base curve at the previous unloading maximum strain, and therefore, neglects the damage induced in the concrete due to cycling. The Mander, Priestley, and Park model and the Palermo model seem to more accurately predict the reloading response. With increasing strain the Palermo model generally provides better results. Both models consider a degrading reloading stiffness; however, Mander, Priestley, and Park's approach is stress-based, and is influenced by the base curve. This deficiency is not evident in the plots, since the reloading curves were established using the unloading point and load reversal point from the test data. Other models available in the literature, based on a return strain point on the base curve, did not contain the necessary information to calculate the return strain point and were not included in Figure 7.13. To reiterate the importance of accounting for damage to concrete under cyclic loading, Figure 7.14 containing reloading curves from Bahn and Hsu[20] in normalized coordinates is reproduced. The reloading model initially assumed by Vecchio, in which reloading returns to the previous unloading strain on the base curve, overestimates the stresses on the reloading path. The models accounting for a degrading reloading stiffness, as assumed by the Mander, Priestley, and Park model, and the Palermo model, provide more accurate simulations of the reloading behaviour. The Seckin response was omitted because it requires knowledge of the peak concrete stress and the corresponding strain.

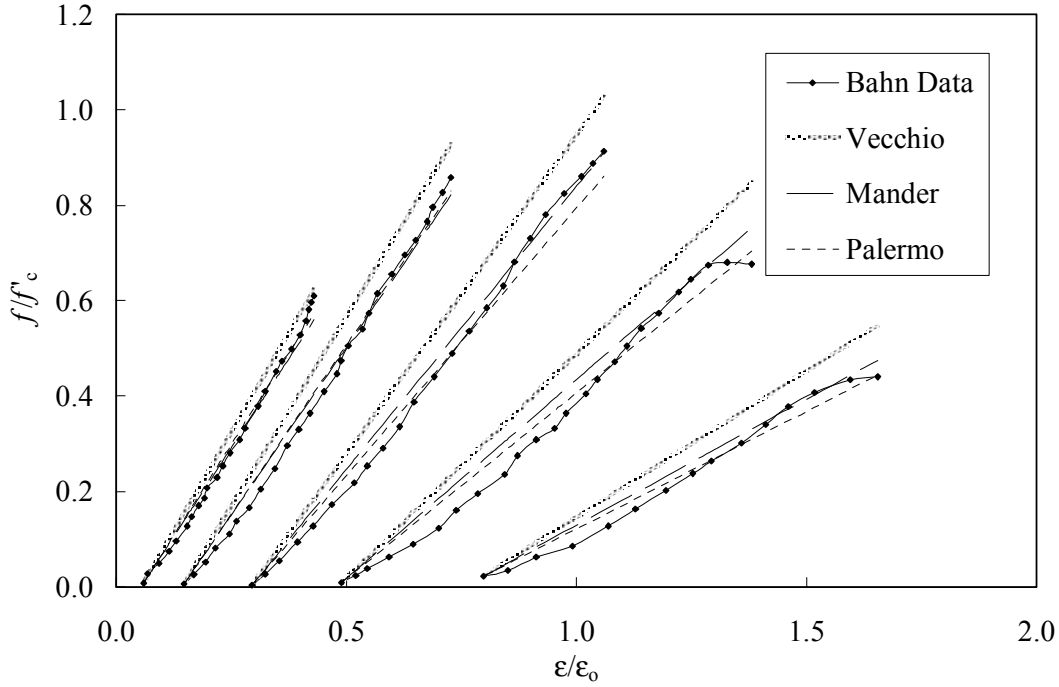

Figure 7.14 Bahn and Hsu Reloading Data

7.2.4 Reloading Stiffness

The proposed reloading stiffness of the previous section considers damage in the concrete due to cyclic loads. A lower limit is placed on the reloading stiffness and is modeled by considering the results from Karsan and Jirsa[12]. The researchers established a stability limit, below which no further damage would be induced in the concrete under cyclic loading. The evolution of the stability limit is based on cycling the concrete to the point of intersection with the unloading path, referred to as the common point. Eventually the hysteresis curves form a closed loop, and no further degradation will occur. The analogy is extended to the previous unloading maximum strain in the present model. Thus, no further damage would be accounted for in the reloading stiffness unless subsequent unloading strains are at least equal to the previous maximum unloading strain.

This will be more evident in later sections when models for partial unloading/reloading are discussed. The curve representing the stability limit is a modified form of the Smith-Young[35] response for concrete subjected to monotonic loading and, in normalized form, is defined as:

$$f/f'_c = 0.7875\left(\varepsilon/\varepsilon_p\right)e^{\left[1-\left(\frac{\varepsilon}{\varepsilon_p}/0.8\right)\right]} \tag{7.24}$$

A plot of the stability limit along with the Smith-Young curve is presented in Figure 7.15.

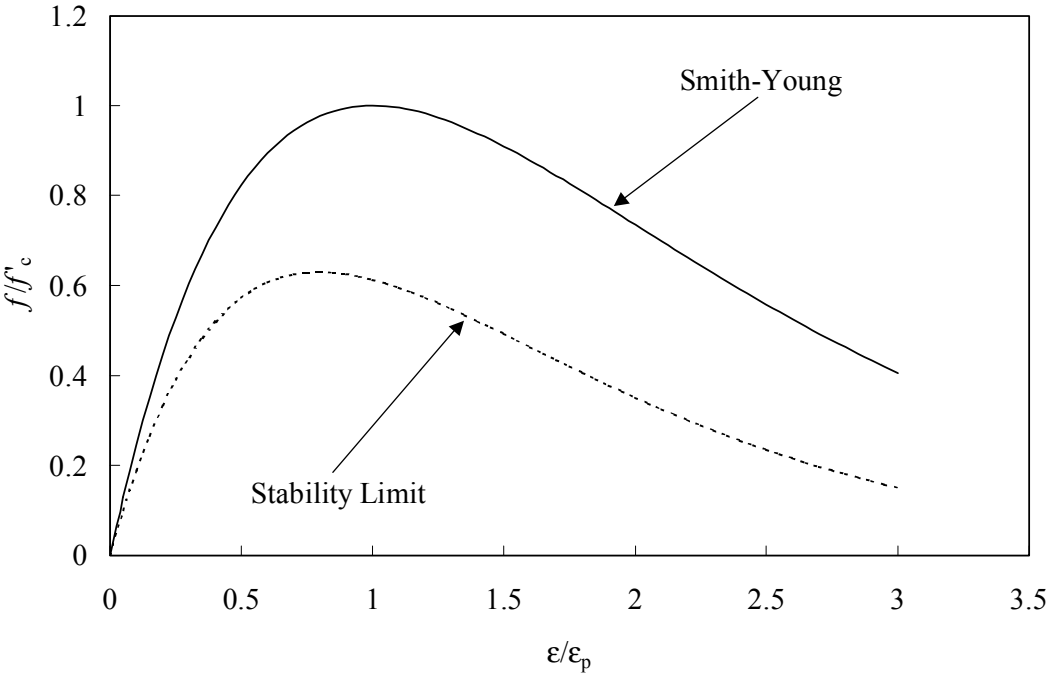

Figure 7.15 Stability Limit for Concrete in Compression

For an arbitrary unloading strain on the base curve, a stress based on the stability expression is determined. The stability stress is used to determine the lower limit on the reloading stiffness and is calculated as:

$$E_{c1} \geq \frac{f_{stab} - f_{ro}}{\varepsilon_{2c} - \varepsilon_{ro}} \tag{7.25}$$

where f_{stab} is the stress on the stability limit curve. Figure 7.16 is a plot of plain concrete subjected to cyclic compressive displacements to the stability limit.

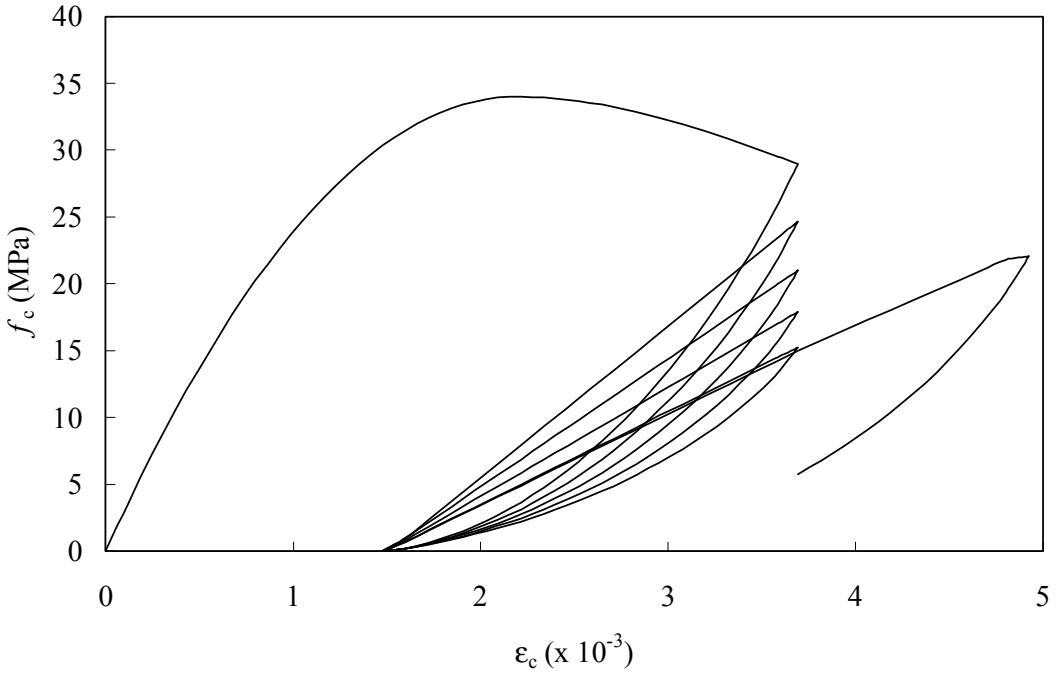

Figure 7.16 Compressive Cycles to Stability Limit

The plain concrete of Figure 7.16 was cycled between 6 mm of displacement and the plastic offset strain. The reloading stiffness was exposed to 4 cycles of degradation, and on the fifth cycle, the stiffness was limited by the stability limit. Implicitly, this approach assumes that the concrete will not fail by fatigue while cycled at strains no greater than the previous maximum unloading strain. Results from Bahn and Hsu[20] seem to suggest that insignificant damage is accumulated when cycles are repeated to the previous maximum unloading strain, and no damage is evident when cycling at strains less than the previous maximum strain.

7.2.5 Partial Unloading/Reloading

Many cyclic models in the literature ignore the behaviour of concrete for the case of partial unloading/reloading. Some models base rules for partial loadings from the full unloading/reloading curves. Some models explicitly consider the case of partial unloading followed by reloading to either the base curve or strains in excess of the previous maximum unloading strain. There seems to be a lack of models considering the case where partial unloading is followed by partial reloading to strains less than the previous maximum unloading strain. This more general case was modeled using the experimental results of Bahn and Hsu[20]. The partial unloading curves are identical to those assumed for full unloading; however, the previous maximum unloading strain and stress are replaced by a variable unloading strain and stress, respectively. The unloading path is defined by the unloading stress and the plastic strain, which remains unchanged unless the previous maximum strain is exceeded. For the case of partial unloading followed by reloading to a strain in excess of the previous maximum unloading strain, the reloading path is defined by the expressions governing full reloading (see Figure 7.17). Figure 7.18 represents the case where concrete is partially unloaded and partially reloaded to strains less than the previous maximum unloading strain.

Five loading branches are required to model the response of Figure 7.18. Unloading curve 1 represents full unloading from the maximum unloading strain to the plastic offset and is calculated from equations 7.16–7.18 for full unloading. Curve 2 defines reloading from the plastic offset strain and is defined by equations 7.19-7.23.

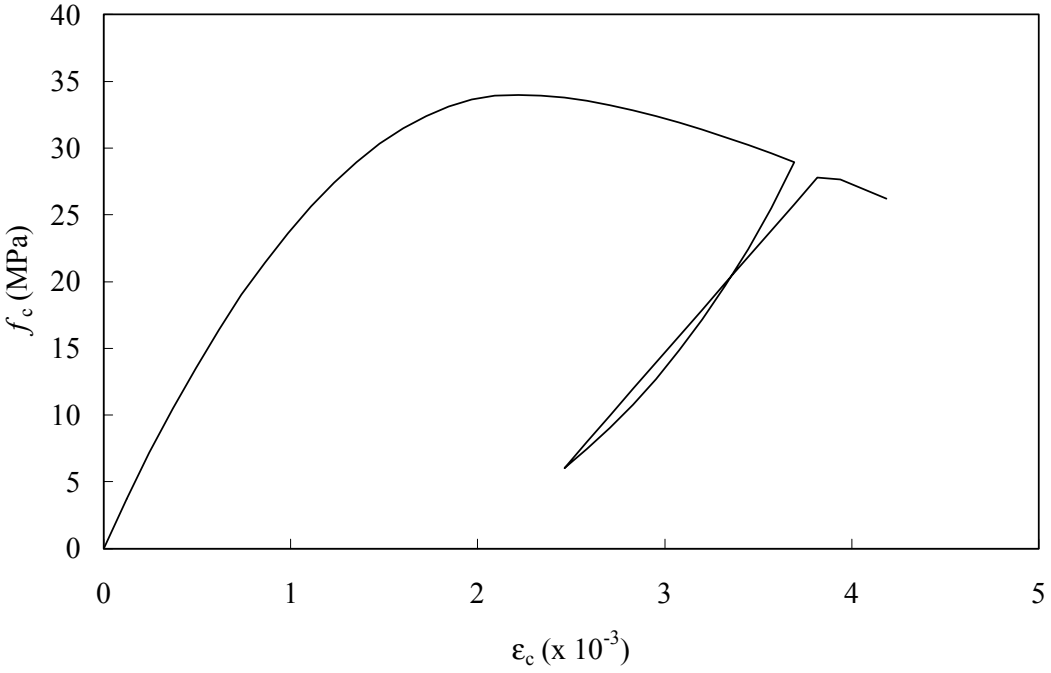

Figure 7.17 Partial Unloading Response for Concrete in Compression

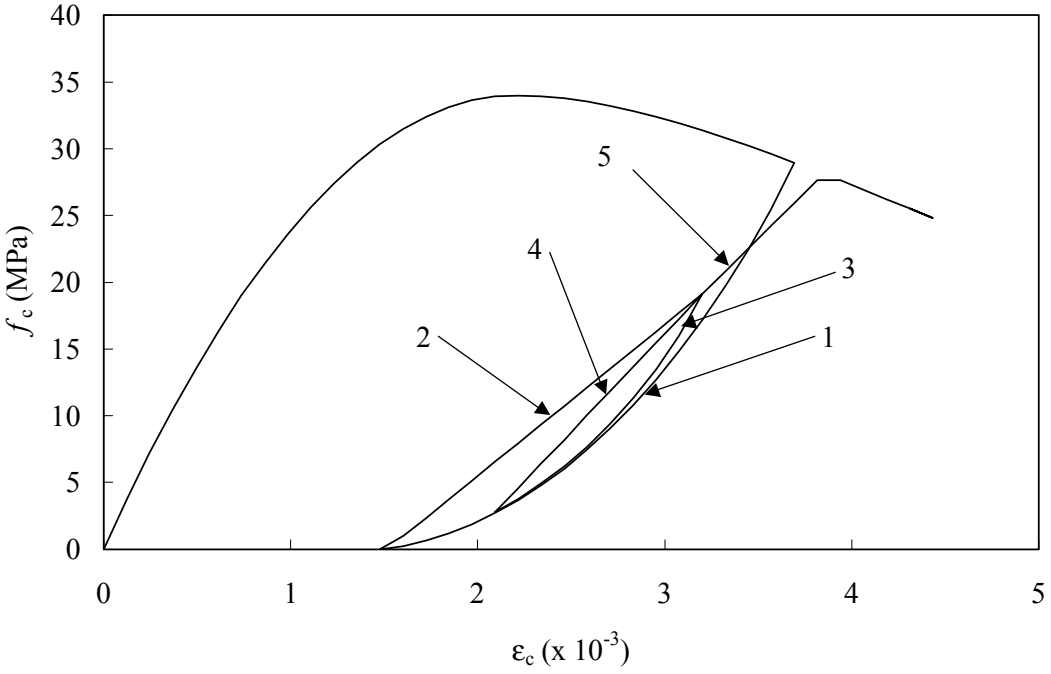

Figure 7.18 Partial Unloading/Reloading for Concrete in Compression

Curve 3 represents the case of partial unloading from a reloading path at a strain less than the previous maximum unloading strain. The expressions used for full unloading are applied, with the exception of substituting the unloading stress and strain for the current cycle for the unloading stress and strain at the previous maximum unloading point. Curve 4 describes partial reloading from a partial unloading branch. The response follows a linear path from the load reversal point to the previous unloading point. No damage is accumulated for loops forming at strains less than the previous maximum unloading strain. This implies that the reloading stiffness is greater than the reloading stiffness of curve 2, and is consistent with test data reported by Bahn and Hsu[20]. The reloading stiffness for curve 4 is represented by the following expression:

$$E_{c1} = \frac{f_{\max} - f_{ro}}{\varepsilon_{\max} - \varepsilon_{ro}} \tag{7.26}$$

and the reloading stress is calculated as:

$$f_c = f_{ro} + E_{c1}(\varepsilon_c - \varepsilon_{ro}) \tag{7.27}$$

Further straining beyond the intersection with curve 2, the response of curve 4 follows the reloading path of curve 5. The latter retains the damage induced in the concrete from the first unloading phase, and the stiffness is calculated as:

$$E_{c1} = \frac{\beta_d \cdot f_{2c} - f_{\max}}{\varepsilon_{2c} - \varepsilon_{\max}} \tag{7.28}$$

The reloading stresses are then determined from the following:

$$f_c = f_{\max} + E_{c1}(\varepsilon_c - \varepsilon_{\max}) \tag{7.29}$$

A partial unloading/reloading cycle from the experimental work of Bahn and Hsu is illustrated in Figure 7.19, and Figure 7.20 is a plot of the response predicted by the Palermo model.

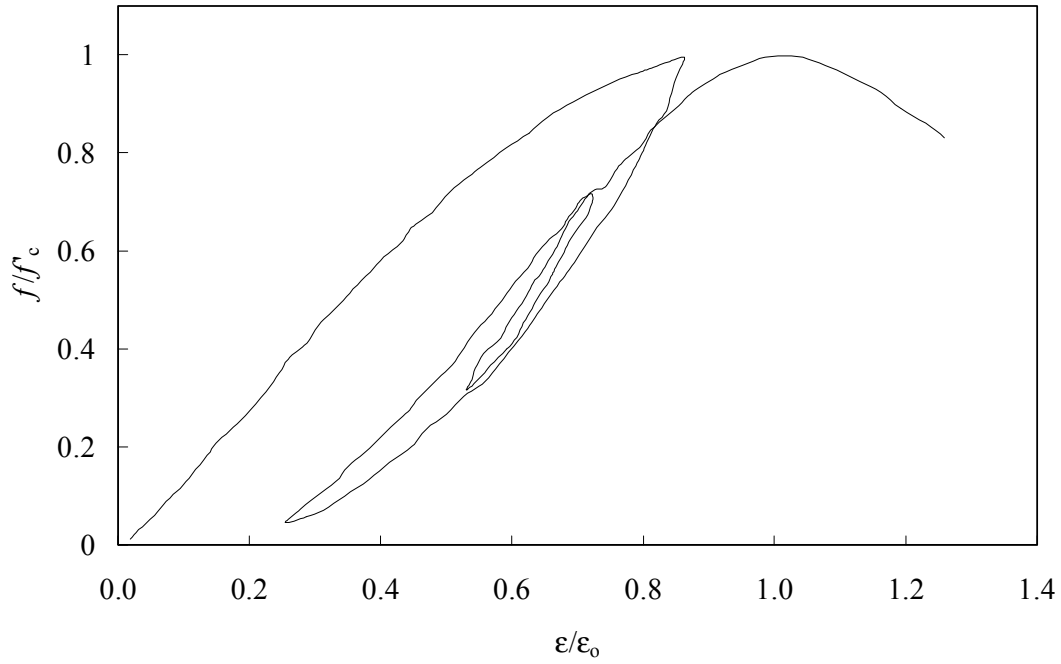

Figure 7.19 Partial Unloading/Reloading Results of Bahn and Hsu

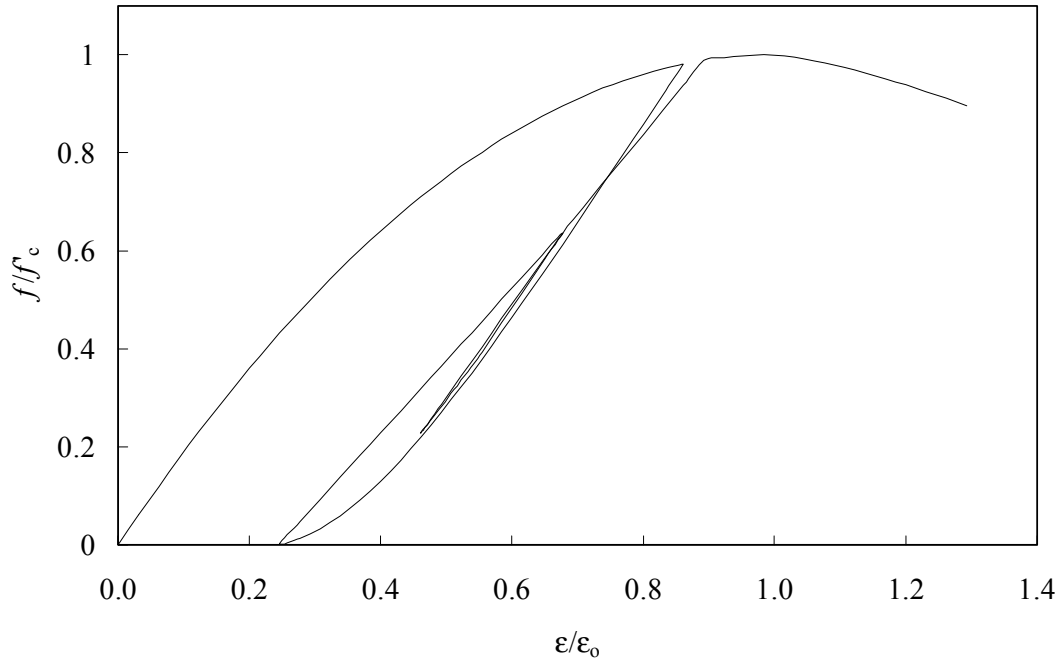

Figure 7.20 Predicted Unloading/Reloading Response

The predicted response using the Palermo model seems to follow the general behavioural patterns of the experimental results; however, it fails to capture the same degree of hysteresis for this set of unloading curves.

7.2.6 Model Response

The formulations presented herein form the constitutive relations for concrete subjected to compressive cyclic loading. Figures 7.21 and 7.22 are plots of the proposed cyclic model, plotted against the experimental results of Bahn and Hsu[20], and Karsan and Jirsa[12], respectively. The Palermo model generally captures the behaviour of concrete under cyclic compressive loading. The nonlinear unloading and linear loading formulations agree well with the data. However, for the Bahn and Hsu experimental curves, the model underestimates the plastic offset strain with increasing unloading strain, and the predicted stresses in the post-peak regime exceed those reported. The latter is the effect of the post-peak ductility curve for the concrete and not the hysteresis model. In this case, a Popovics[16] base curve was selected. Figure 7.22, containing the experimental results of Karsan and Jirsa, shows an improved agreement with the data. The plastic offset strains are similar, and the base curve generally predicts stresses more representative of the data. The Smith-Young[35] curve, which models the envelope response reasonably well, was selected as the base curve. For both sets of experimental curves, it is apparent that the reloading curves become nonlinear beyond the point of intersection with the unloading curves, commonly referred to as the common point. The Palermo model can be easily modified to account for this phenomenon; however, unusually small load steps would be required in a finite element analysis in order to capture this behaviour, and thus, it was determined to be insignificant.

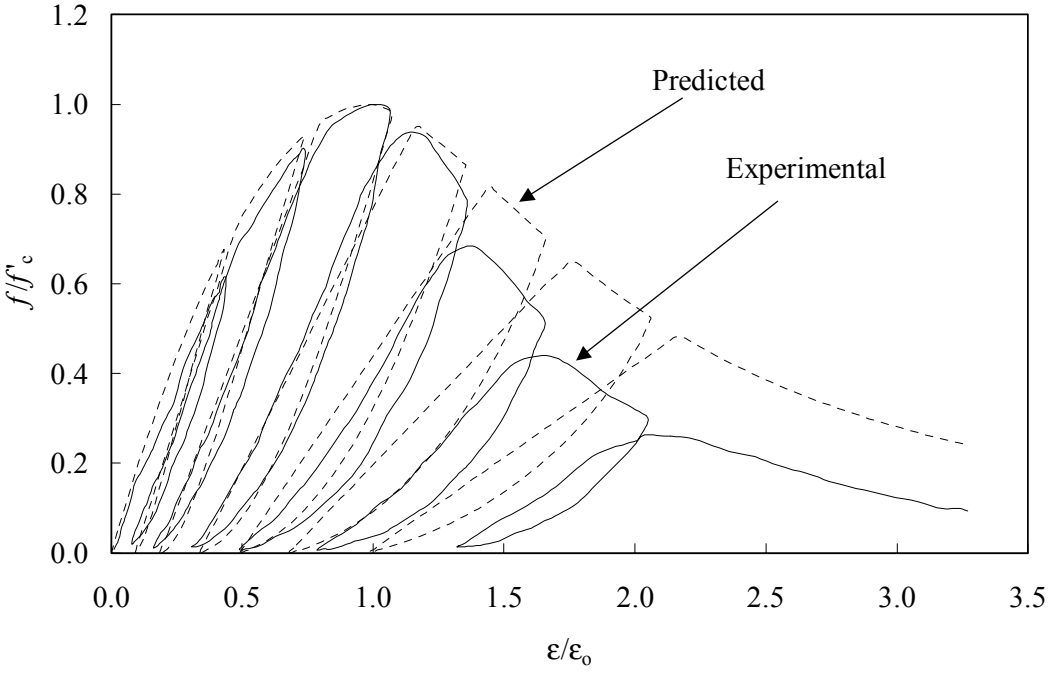

Figure 7.21 Predicted Response Versus Bahn and Hsu Data

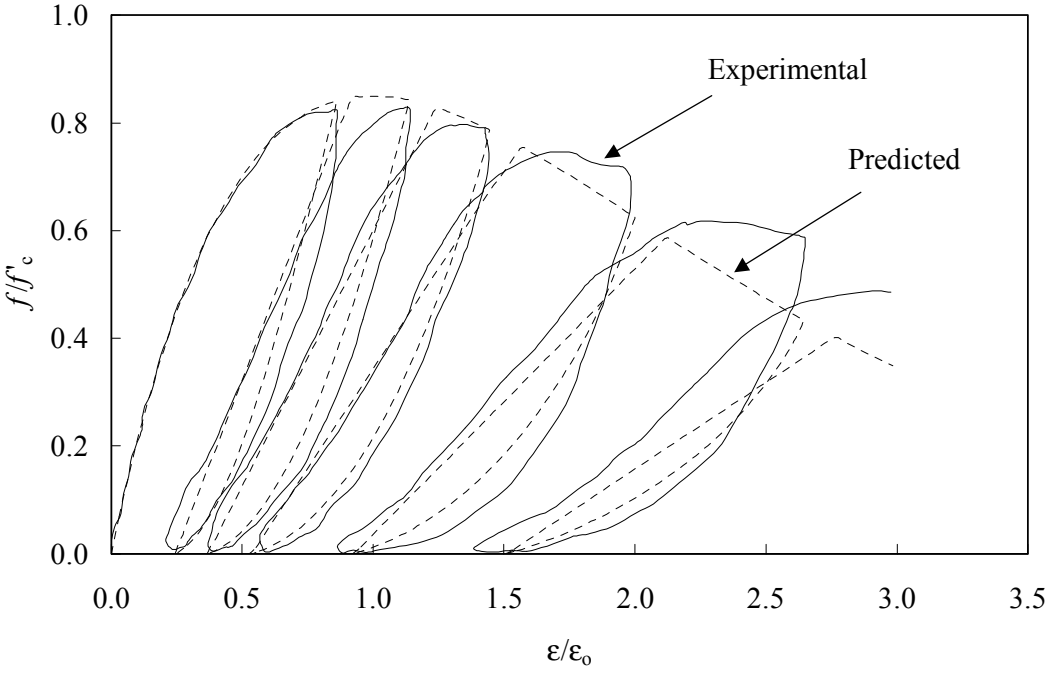

Figure 7.22 Predicted Response Versus Karsan and Jirsa Data

The proper modeling of the post-peak curve significantly affects the hysteresis loops as shown in Figures 7.21 and 7.22 and should be studied further.

7.3 TENSION MODELS

Much less attention has been directed towards the modeling of concrete under cyclic tensile loads. Some researchers consider little or no excursions into the tension stress regime and those who have proposed models assume, for the most part, linear unloading/reloading responses with no plastic offsets. The latter was the approach used by Vecchio in formulating a preliminary tensile model. Stevens, Uzumeri, and Collins[26] reported nonlinear curves based on defining stiffness along the loading paths; however, the models were verified with limited success. Okumura and Maekawa[24] proposed a hysteretic model for cyclic tension, in which a nonlinear unloading curve considered stresses through bond action and through closing of cracks. A linear reloading path was also assumed.

The models proposed in the subsequent sections follows the philosophy used to model concrete under cyclic compressive loadings.

7.3.1 Plastic Offset Model

There seems to exist a lack of research in the literature that is helpful in defining a plastic offset for the case of unloading in tension. The offsets occur when cracked surfaces come into contact during unloading and do not realign. Shear slip along the crack surfaces can also be a contributing factor. Test results from Yankelevsky and Reinhardt[18], and Gopalaratnam and Shah[36] provide data that can be used to formulate a plastic offset model. The researchers were able to capture the softening behaviour of

concrete beyond cracking in displacement-controlled testing machines. The plastic strain, in the proposed tension model, is used to define the shape of the unloading curve, the slope and damage of the reloading path, and the point at which cracked surfaces come into contact. Similar to concrete in compression, the offsets in tension seem to be dependent on the unloading strain from the envelope curve (base curve). The envelope curve in tension is also represented by the monotonic response curve. The proposed offset model, derived using regression analysis, is expressed by the following equation:

$$\varepsilon_c^{\ p} = 146\varepsilon_{1c}^{\ 2} + 0.523\varepsilon_{1c} \tag{7.30}$$

where $\varepsilon_c^{\ p}$ is the tensile plastic offset, and ε_{1c} is the unloading strain from the base curve. Figure 7.23 shows the above model in comparison to the combined data of Yankelevsky and Reinhardt[19], and Gopalaratnam and Shah[36].

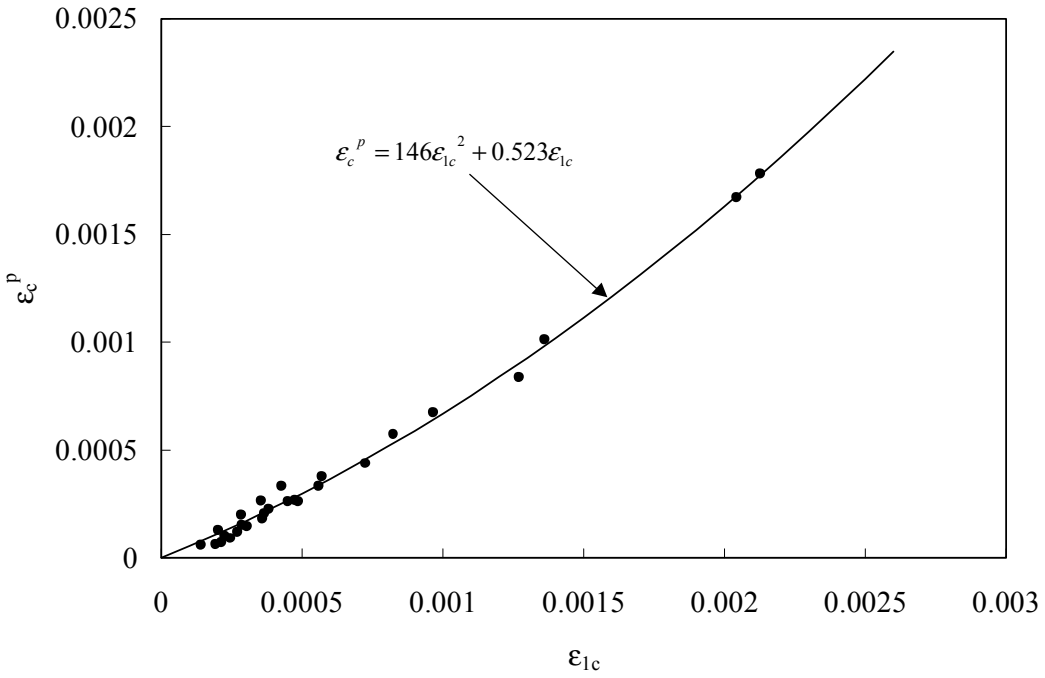

Figure 7.23 Plastic Offset Model for Concrete in Tension

The plastic offset model, plotted against 25 data points, demonstrates excellent agreement with the test data, and confirms that the offset strain is dependent upon the strain at unloading. There exists minimal scatter in the test data of the two series of experimental results used; thereby justifying a combination of the data.

7.3.2 Unloading Curves

Test data indicates that the unloading response of concrete subjected to tensile loading is nonlinear. The common approach has been to model the unloading branch as linear and to ignore the hysteretic behaviour in the concrete due to cycles in tension. The approach used herein was to formulate a nonlinear expression for the concrete that would generate realistic hysteresis loops. To derive the model, a Ramberg-Osgood formulation, similar to that used for concrete in compression, was adopted and is expressed as:

$$f_c = D + F\Delta\varepsilon + G\Delta\varepsilon^N \tag{7.31}$$

where f_c is the tensile stress in the concrete, $\Delta\varepsilon$ is the strain increment measured from a strain on the unloading path to the unloading strain, D, F, and G are parameters that define the shape of the unloading curve, and N is a power term that describes the degree of nonlinearity. Figure 7.24 illustrates the response of concrete subjected to cyclic tensile loading. E_{c5} denotes the initial unloading stiffness, and the unloading stiffness at zero stress is described by E_{c6}. f_t' is the cracking stress and corresponds to a strain of ε_t', and f_{1c} and ε_{1c} are the unloading stress and strain, respectively.

Boundary conditions are required to determine the parameters governing equation 7.31. Referring to Figure 7.24, the following conditions are used:

1. $\Delta\varepsilon = 0$ $\qquad f(\Delta\varepsilon) = f_{1c}$

2. $\Delta\varepsilon = \varepsilon_c^{\,p} - \varepsilon_{1c}$ $\qquad f(\Delta\varepsilon) = 0$

3. $\Delta\varepsilon = 0$ $\qquad df_c / d\Delta\varepsilon = E_{c5}$

4. $\Delta\varepsilon = \varepsilon_c^{\,p} - \varepsilon_{1c}$ $\qquad df_c / d\Delta\varepsilon = E_{c6}$

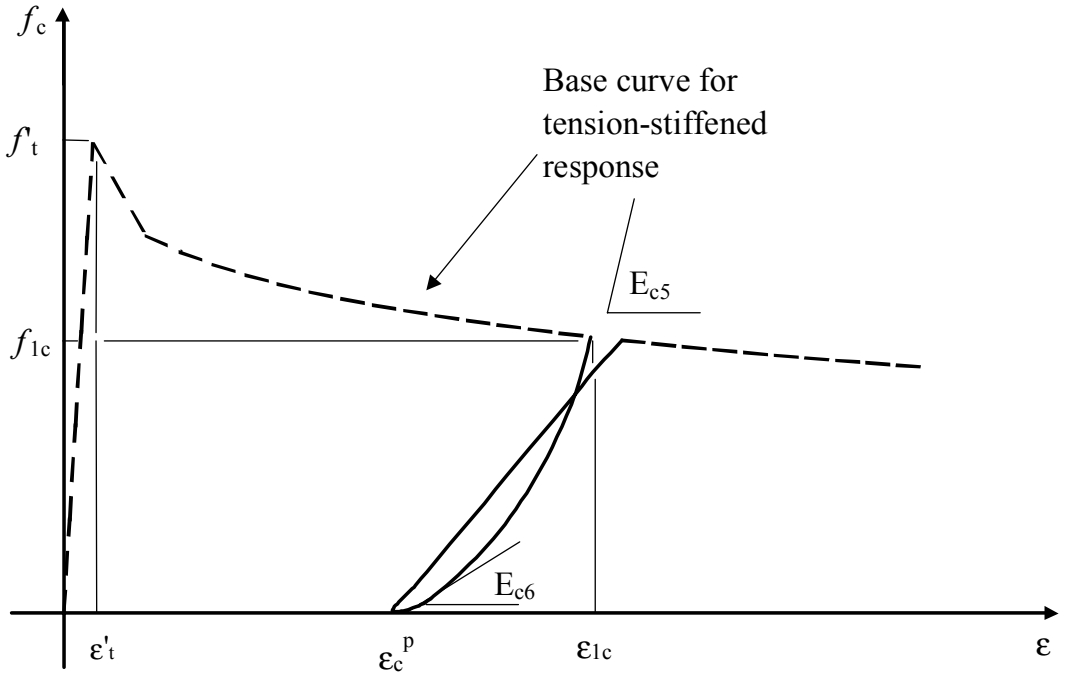

Figure 7.24 Tensile Unloading Parameters

Applying the boundary conditions and simplifying yields:

$$f(\Delta\varepsilon) = f_{1c} - E_{c5}(\Delta\varepsilon) + \left[\frac{(E_{c5} - E_{c6})\Delta\varepsilon^N}{N(\varepsilon_{1c} - \varepsilon_c^{\,p})^{N-1}}\right] \tag{7.32}$$

where $\Delta\varepsilon = \varepsilon_{1c} - \varepsilon$ (7.33)

and $N = \dfrac{(E_{c5} - E_{c6})(\varepsilon_{1c} - \varepsilon_c^{\,p})}{E_{c5}(\varepsilon_{1c} - \varepsilon_c^{\,p}) - f_{1c}}$ (7.34)

ε is the instantaneous strain in the concrete. The initial unloading stiffness E_{c5} is assigned a value equal to the initial tangent stiffness E_c, and is routinely calculated as $2f_c'/\varepsilon_0$. The unloading stiffness E_{c6} was determined from unloading data reported by Yankelevsky and Reinhardt[18]. By varying the unloading stiffness E_{c6}, the following models were found to agree well with the data:

$$E_{c6} = 0.071 \cdot E_c \left(0.001 / \varepsilon_{1c} \right) \qquad \varepsilon_{1c} \le 0.001 \qquad (7.35)$$

$$E_{c6} = 0.071 \cdot E_c \left(0.001 / \varepsilon_{1c} \right) \cdot 0.75 \qquad \varepsilon_{1c} > 0.001 \qquad (7.36)$$

The proposed unloading tensile response is plotted in Figures 7.25 and 7.26 against the Yankelevsky and Reinhardt data along with the Okamura and Maekawa model[24], and the preliminary linear unloading model proposed by Vecchio[3].

The Okamura and Maekawa model, based on the stress transferred through bond action, overestimates the unloading stresses for the entire range of data, owing to the fact that the formulation does not consider a plastic offset strain. The quadratic formulation is a function of the unloading point and a residual stress at the end of the unloading phase. The residual stress is dependent on the initial tangent stiffness and the strain at the onset of unloading. The linear unloading response suggested by Vecchio is a simple representation of the behaviour, but does not capture the nonlinear nature of the concrete, and underestimates the energy dissipation. The model proposed herein provides reasonable simulations of the test results, and captures the nonlinear behaviour and energy dissipation.

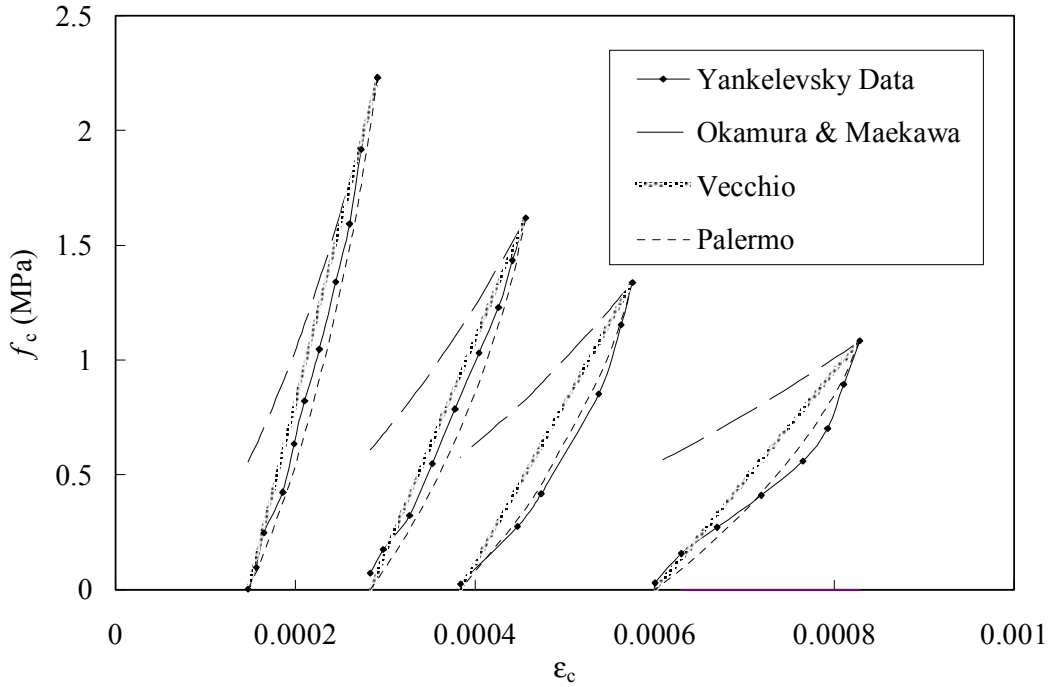

Figure 7.25 Yankelevsky and Reinhardt Unloading Test Results, Part I

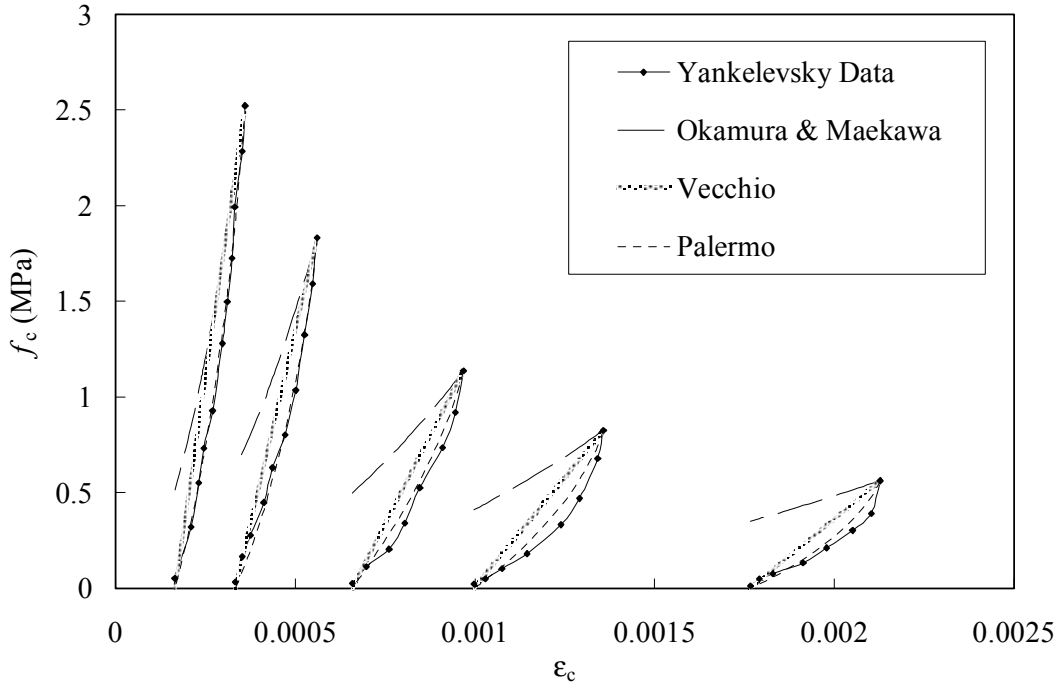

Figure 7.26 Yankelevsky and Reinhardt Unloading Test Results, Part II

7.3.3 Reloading Curves

The state-of-the-art in modeling reloading of concrete in tension is based on a linear representation, as described by Vecchio[3], and Okamura and Maekawa[24]. The response is assumed to return to the base curve at the previous unloading stress and ignores damage inflicted to the concrete due to load cycling. Limited test data confirms that linear reloading sufficiently captures the general response of the concrete; however, it is evident that the reloading stiffness accumulates damage as the unloading strain increases. The approach suggested herein is to model the reloading behaviour as linear, and to account for a degrading reloading stiffness. The latter is assumed to be a function of the strain recovery and is confirmed by test data. The model implicitly considers the case of partial unloading. Figure 7.27 illustrates the parameters of the proposed model.

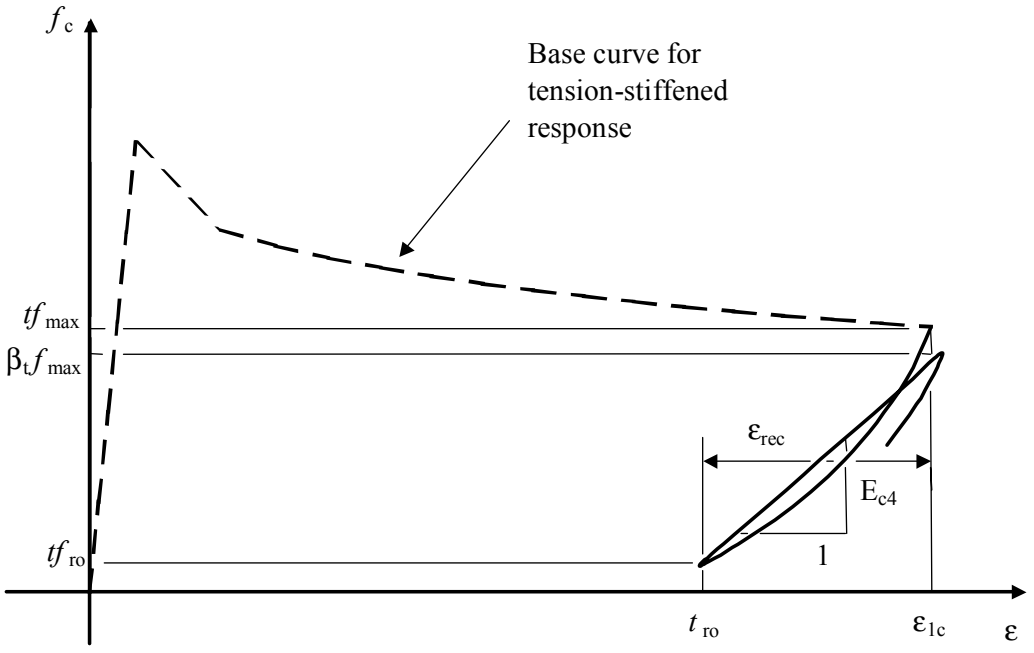

Figure 7.27 Tension Unloading Parameters

The following formulation describes the degrading reloading stiffness:

$$E_{c4} = \frac{(\beta_t \cdot tf_{\max}) - tf_{ro}}{\varepsilon_{1c} - t_{ro}} \tag{7.37}$$

where E_{c4} is the reloading stiffness, β_t is a tensile damage indicator, $tf_{\max}$ is the maximum unloading stress, tf_{ro} is the stress in the concrete at reloading reversal, and corresponds to a strain of t_{ro}. The damage parameter β_t was determined from the following relation:

$$\beta_t = \frac{1}{1 + 1.15(\varepsilon_{rec})^{0.25}} \tag{7.38}$$

where

$$\varepsilon_{rec} = \varepsilon_{\max} - \varepsilon_{\min} \tag{7.39}$$

ε_{rec} is the strain recovered during an unloading phase, and the larger the recovery the greater the degradation of the reloading stiffness. It is the difference between the unloading strain $\varepsilon_{\max}$ and the minimum strain at the onset of reloading $\varepsilon_{\min}$. The formulation was derived with a best-fit line to data reported by Yankelevsky and Reinhardt[18]. A total of 27 points were plotted in Figure 7.28. The minimum strain is limited by the tensile plastic offset strain and assumes there is a negligible effect due to closing of cracks.

The reloading stresses are then calculated as:

$$f_c = \beta_t \cdot tf_{\max} - E_{c4}(\varepsilon_{1c} - \varepsilon_c) \tag{7.40}$$

where f_c is the tensile stress on the reloading curve, which corresponds to a strain of ε_c. A comparison between the proposed model and a typical linear behaviour are plotted in Figure 7.29 against data reported by Gopalaratnam and Shah[36].

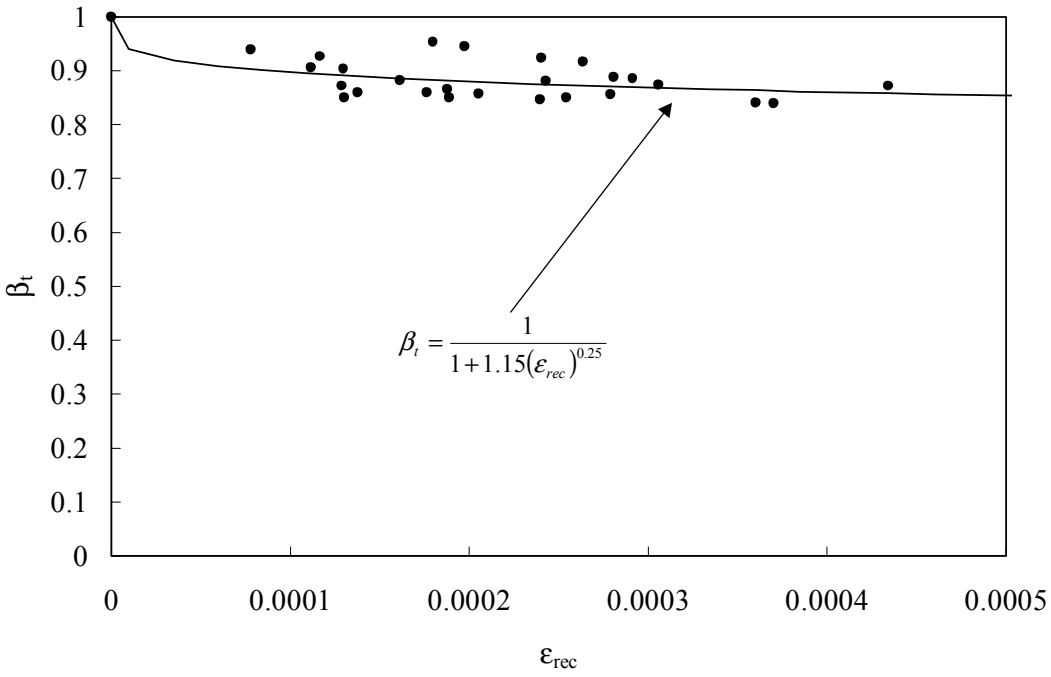

Figure 7.28 Reloading Damage Parameter for Concrete in Tension

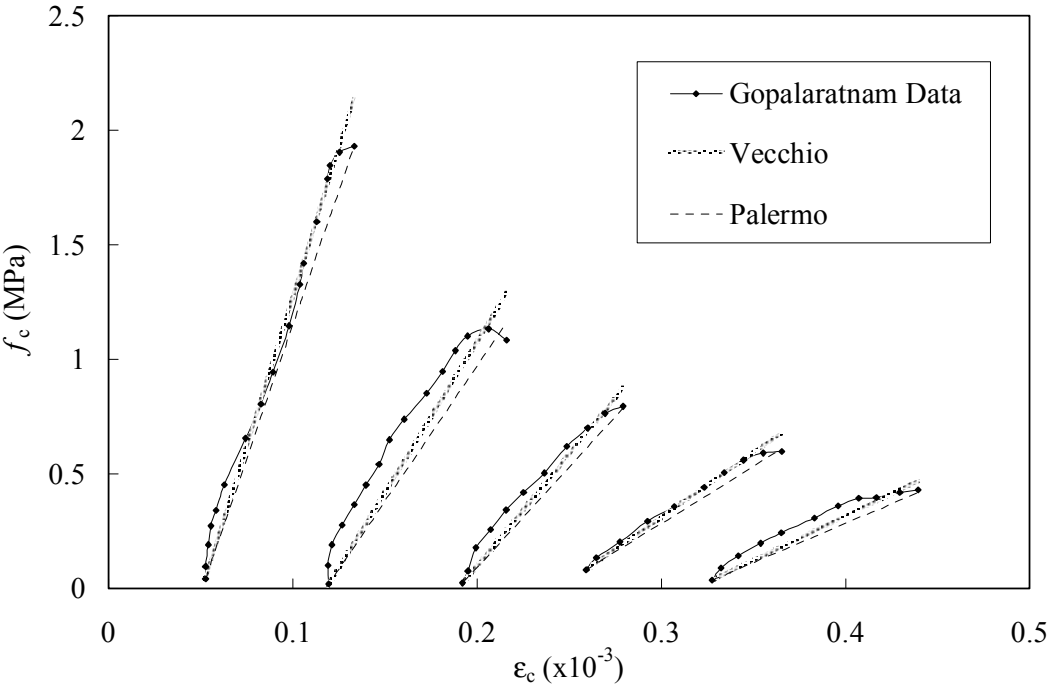

Figure 7.29 Gopalaratnam and Shah Reloading Data

In general, the linear reloading model, as formulated by Vecchio, predicts slightly larger stresses than the model proposed herein (the Palermo model). The Vecchio model assumes that the reloading response will return to the previous unloading stress on the base curve. The Palermo model places more emphasis on modeling the damage incurred in the concrete due to load cycling. The results indicate that the proposed model accurately predicts the degree of damage for any unloading cycle.

7.3.4 Reloading Stiffness

A lower limit has been assumed to exist for the reloading stiffness to prevent a fatigue failure under the condition of repeated cycling to a constant displacement level. While there is a lack of data to confirm such a lower limit, the philosophy adopted follows that established for concrete in compression. Therefore, under cyclic tension, no damage is accumulated in the concrete beyond the first cycle unless the previous maximum strain is reached. The amount of degradation accumulating at a specific displacement is limited by a lower limit. To formulate the model, it was first assumed that the Collins-Mitchell[37] response for tension stiffening formed the base curve response, calculated according to the following expression:

$$f_c = \frac{f_{cr}}{1+\sqrt{500 \cdot \varepsilon_{cf}}} \tag{7.41}$$

where f_c is the post-cracking tensile stress in the concrete, f_{cr} is the cracking stress, and ε_{cf} is the tensile strain due to stress. The minimum reloading stress was determined using the stability limit curve for concrete in compression. For a particular strain, a limiting stress value was determined from the compressive stability limit, and using the Smith-Young[35] base curve, a limit was established for β_d. The latter was multiplied by

the tensile stress at the particular strain in question using the Collins-Mitchell base curve. This stress represents a lower limit on the tensile stress, and hence a limit on β_t, the tensile reloading stiffness degradation factor. A regression analysis was used to fit a curve to represent the data. The model was formulated with a modification to the Collins-Mitchell base curve response. The suggested expression is as follows:

$$f_c = \frac{f_{cr}}{1+\sqrt{4170 \cdot \varepsilon_{cf}}} \tag{7.42}$$

Figure 7.30 shows the proposed stability curve for concrete in tension.

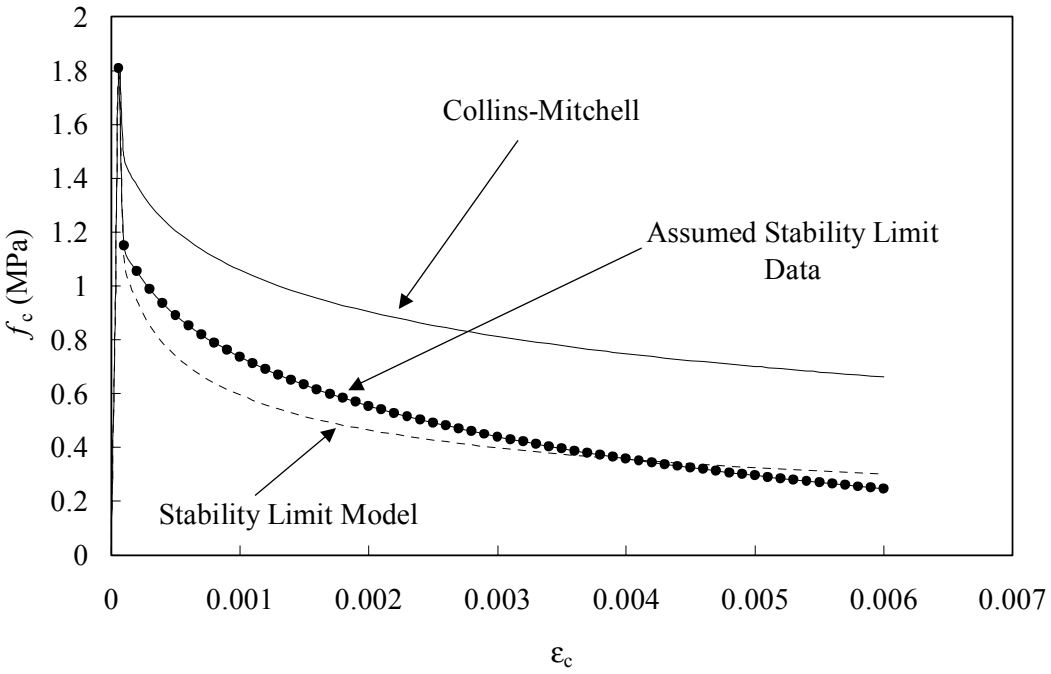

Figure 7.30 Stability Limit for Concrete in Tension

Using the stability limit, the reloading stiffness is limited according to the following expression:

$$E_{c4} \geq \frac{ft_{stab} - tf_{ro}}{\varepsilon_{1c} - t_{ro}} \tag{7.43}$$

where ft_{stab} is the tensile stress on the proposed stability limit. Shown in Figure 7.31 is the response of concrete subjected to repeated cycles at a set displacement level. The concrete element of Figure 7.31 was cycled from a peak displacement of 1.5 mm and a minimum displacement of 0.9 mm. The tensile reloading stiffness experienced four excursions of degradation. During the fifth excursion, the reloading stiffness was limited by the stability limit curve. The use of a limiting reloading stiffness assures that the element will not fail in fatigue while it is subjected to a constant unloading strain. Further damage in the reloading stiffness will only be incurred when the reloading path exceeds the previous maximum unloading strain.

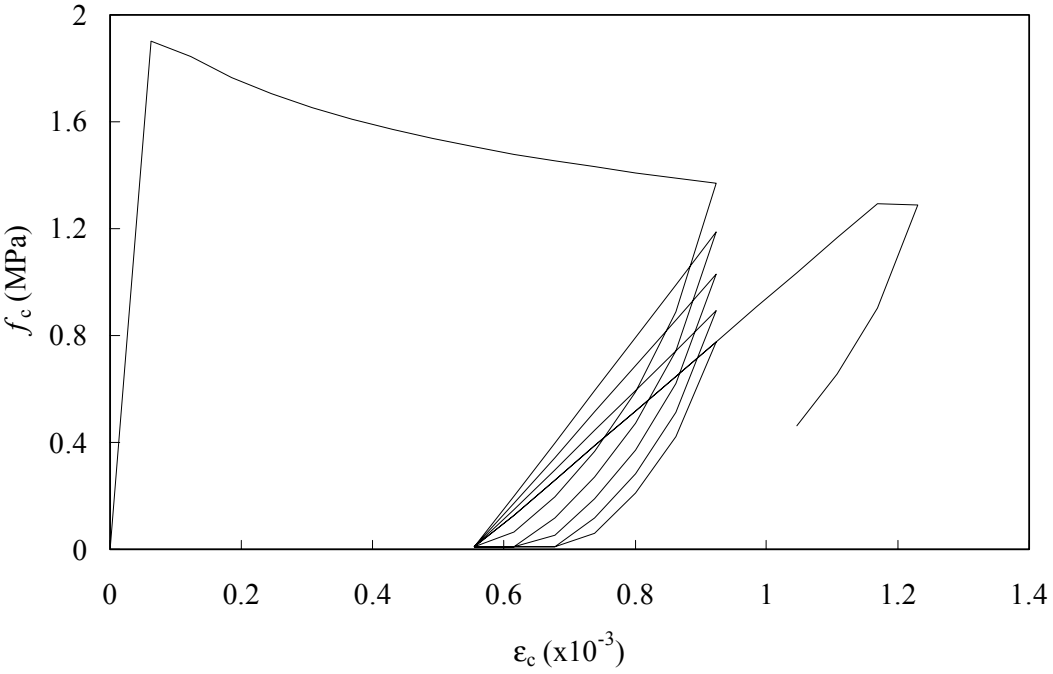

Figure 7.31 Tensile Cycles to Stability Limit

7.3.5 Partial Unloading/Reloading

There is a lack of experimental data or models in the literature that consider the general case of partial unloading followed by partial reloading in the tension stress regime. Proposed herein is a partial unloading/reloading model that directly follows the rules established for concrete in compression. However, no data exists to either confirm or contradict the model. Figure 7.32 depicts the proposed rules for a concrete element, lightly reinforced to allow a post-cracking response.

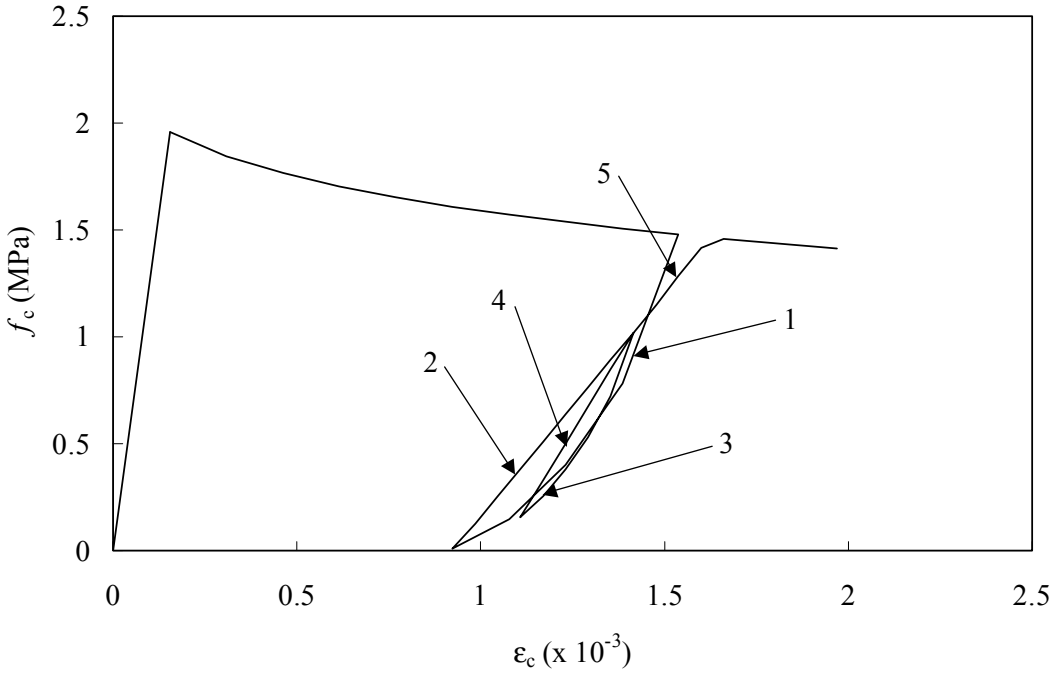

Figure 7.32 Partial Unloading/Reloading for Tension Regime

Curve 1 corresponds to a full unloading response and is identical to that assumed by equations 7.32-7.34. Reloading from a full unloading curve is represented by curve 2 and is computed from equations 7.37-7.40. Curve 3 represents the case of partial unloading from a reloading path at a strain less than the previous maximum unloading

strain. The expressions for full unloading are utilized; however, the strain and stress at unloading, now variables, replace the strain and stress at the previous peak unloading point on the base curve. Reloading from a partial unloading segment is described by curve 4. The response follows a linear path from the reloading stress to the previous unloading strain defining the transition from curve 2 to 3. No damage accumulates for loops that form at strains less than the previous peak unloading strain on the base curve. Therefore, the reloading stiffness of curve 4 is larger than the reloading stiffness for the first unloading/reloading response of curve 2. The partial reloading stiffness defining curve 4 is calculated by the following expression:

$$E_{c4} = \frac{tf_{\max} - tf_{ro}}{\varepsilon_{\max} - t_{ro}} \tag{7.44}$$

and the reloading stress is determined from:

$$f_c = tf_{ro} + E_{c4}\left(\varepsilon_c - t_{ro}\right) \tag{7.45}$$

Further straining along the reloading path of curve 4 results in a change of the reloading path at the intersection with curve 2. Beyond the intersection of curve 2 and 4, the response follows the response of curve 5 and retains the damage induced to the concrete from the first unloading/reloading phase. The stiffness is then calculated as:

$$E_{c4} = \frac{\beta_t \cdot f_{1c} - tf_{\max}}{\varepsilon_{1c} - \varepsilon_{\max}} \tag{7.46}$$

The reloading stresses can then be calculated according to the following expression:

$$f_c = tf_{\max} + E_{c4}\left(\varepsilon_c - \varepsilon_{\max}\right) \tag{7.47}$$

The above formulations for concrete in tension are preliminary and require experimental data to verify their validity. The models are, however, based on realistic assumptions derived from the models suggested for concrete in compression.

7.4 CRACK-CLOSING MODEL

In an excursion returning from the tensile domain, the compressive stresses do not remain at zero until the cracks completely close. Compressive stresses occur in the tensile strain region and begin at the re-contact strain. The re-contact strain is a function of factors such as crack shear slip. There exists a lack of data to form an accurate model for crack-closing, and the model suggested here is based on the models and assumptions suggested by Okamura and Maekawa[24]. Figure 7.33 is a schematic of the proposed model.

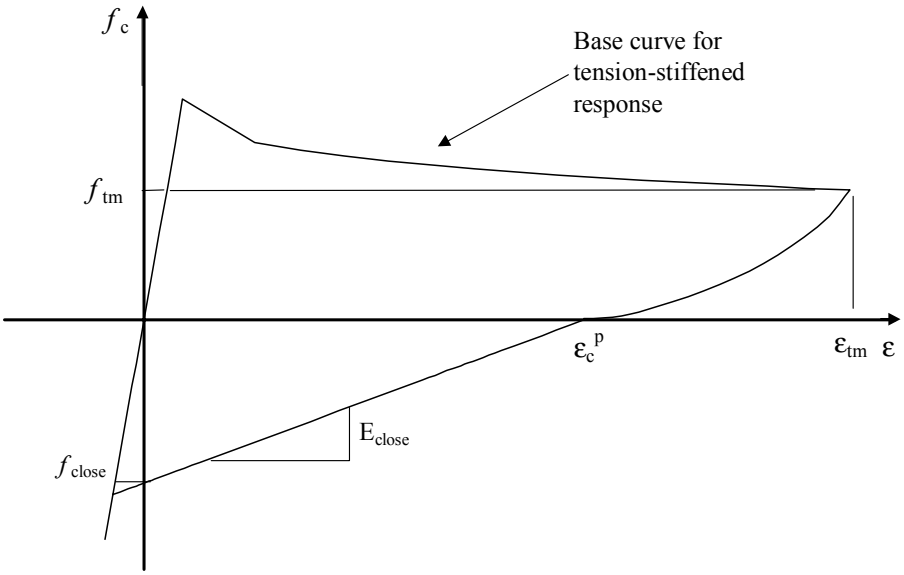

Figure 7.33 Crack-Closing Model

The re-contact strain assumes the plastic offset strain value defined in section 7.3.1. The stiffness of the concrete during closing of cracks, after the two cracked surfaces have come into contact and before the cracks completely close, is smaller than that of crack-free concrete. Once the cracks completely close, the stiffness assumes the initial tangent stiffness value. The crack closing stiffness E_{close} is calculated from:

$$E_{close} = \frac{f_{close}}{\varepsilon_c^{\ p}} \tag{7.48}$$

where $$f_{close} = -E_c\left(0.0016 \cdot \varepsilon_{tm} + 50x10^{-6}\right) \tag{7.49}$$

f_{close} consists of two terms taken from the Okamura and Maekawa model for concrete in tension. The first term represents a residual stress at the completion of unloading due to stress transferred due to bond action. The second terms represents the stress directly related to closing of cracks. The stress on the closing-of-cracks path is then determined from the following expression:

$$f_c = E_{close}\left(\varepsilon_c - \varepsilon_c^{\ p}\right) \tag{7.50}$$

For reloading from the closing-of-cracks regime, the stress in the concrete is assumed to be linear while the cracked surfaces are still in contact, after which the concrete stress assumes the reloading path previously established for tensile reloading of concrete.

7.5 REINFORCEMENT MODEL

The reinforcement model is that assumed by Vecchio[3]. The monotonic response of the reinforcement is assumed to be tri-linear. The initial response is linear elastic, followed by a yield plateau, and ending with a strain-hardening portion. The hysteretic response of the reinforcement has been modeled after Seckin[21], and the Bauschinger effect is represented by a Ramberg-Osgood formulation, as illustrated in Figure 7.34

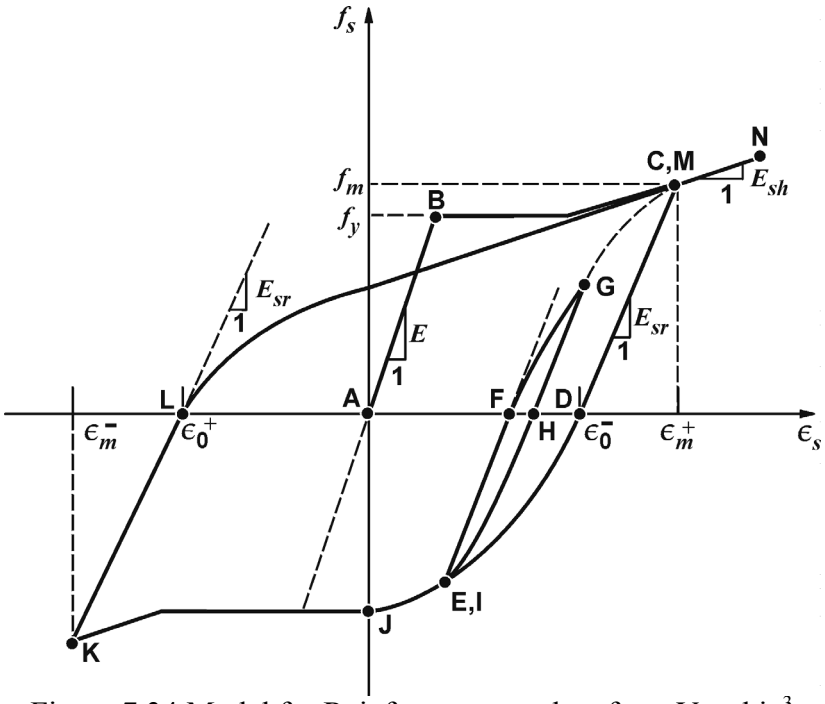

Figure 7.34 Model for Reinforcement, taken from Vecchio[3]

The monotonic response curve is assumed to represent the base curve. The unloading portion of the response follows a linear path and is given by:

$$f_s(\varepsilon_i) = f_{s-1} + E_r(\varepsilon_i - \varepsilon_{s-1}) \tag{7.51}$$

where $f_s(\varepsilon_i)$ is the stress at the current strain of ε_i, f_{s-1} and ε_{s-1} are the stress and strain from the previous load step, and E_r is the unloading modulus and is calculated as:

$$E_r = E_s \qquad \text{if } (\varepsilon_m - \varepsilon_o) < \varepsilon_y \tag{7.52}$$

$$E_r = E_s\left(1.05 - 0.05\frac{\varepsilon_m - \varepsilon_o}{\varepsilon_y}\right) \quad \text{if } \varepsilon_y < (\varepsilon_m - \varepsilon_o) < 4\varepsilon_y \tag{7.53}$$

$$E_r = 0.85E_s \qquad \text{if } (\varepsilon_m - \varepsilon_o) > 4\varepsilon_y \tag{7.54}$$

where E_s is the initial tangent stiffness, ε_m is the maximum strain attained during previous cycles, ε_o is the plastic offset strain, and ε_y is the yield strain.

The stresses experienced during the reloading phase are determined from:

$$f_s(\varepsilon_i) = E_r(\varepsilon_i - \varepsilon_o) + \frac{E_m - E_r}{N \cdot (\varepsilon_m - \varepsilon_o)^{N-1}} \cdot (\varepsilon_i - \varepsilon_o)^N \tag{7.55}$$

where

$$N = \frac{(E_m - E_r)(\varepsilon_m - \varepsilon_o)}{f_m - E_r(\varepsilon_m - \varepsilon_o)} \tag{7.56}$$

f_m is the stress corresponding to the maximum strain recorded during previous loading, and E_m is the tangent stiffness at ε_m.

The same formulations apply for reinforcement in tension or compression. For the first reverse cycle, ε_m is taken as zero and $f_m = f_y$.

7.6 FINITE ELEMENT IMPLEMENTATION

7.6.1 Parameters Retained

Modeling of reinforced concrete, using the plastic offset procedure to provide the analysis capability of arbitrary loading conditions described in Chapter 3, requires parameters to be retained in memory. Thus, the loading history is essential. For concrete in compression, $\varepsilon_c^{\ p}$, the plastic offset strain, must be defined and stored as it forms the backbone of the analysis procedure. The stresses on the unloading and reloading path are linked to the base curve and requires knowledge of f_{2c} and ε_{2c}, the stress and strain corresponding to the previous peak unloading point on the base curve. The reloading curve requires β_d, a reloading stiffness damage indicator; and $\varepsilon_{\max}$ and $\varepsilon_{\min}$, the maximum and minimum strain for any arbitrary cycle, to compute the strain recovery used in calculating β_d. For the case where partial unloading/reloading occurs, the models require f_{ro} and ε_{ro}, the stress and strain at the reloading reversal; $f_{\max}$, the

maximum stress for the current cycle; and E_{c1}, the reloading stiffness, adjusted for cyclic damage. For concrete in tension, the same parameters, but corresponding to tensile stresses and strains, must also be retained in memory. They include: $\varepsilon_c^{\ p}$, f_{1c}, ε_{1c}, β_t, $\varepsilon_{\max}$, $\varepsilon_{\min}$, tf_{ro}, t_{ro}, $tf_{\max}$, and E_{c4}. To accommodate the rotating crack concept, these parameters are first resolved into components relative to the reference axes, resulting in two normal values and a shear value. The components are then stored in memory and later used to define strains and stresses in the principal directions.

For the reinforcement, five parameters are retained for each reinforcement component and they include: $\varepsilon_m^{\ +}$ and $\varepsilon_m^{\ -}$, the maximum positive and negative strain attained; the reinforcement stress and strain from the previous load step f_{si-1} and ε_{i-1}; and the residual strain ε_o.

7.6.2 Model Adjustments

The implementation of models into a rotating crack approach is not a straightforward task. Consideration must be given to the changing of the principal angles. Problems were encountered in implementing the tension models suggested herein. The current approach is deficient in that a tensile plastic offset formulation could not be implemented due to numerical instabilities in the programming. To correct this problem, plastic offsets were omitted, and the unloading stiffness at the completion of unloading (E_{c6}) was modified to fit the unloading data for the case where the plastic offset is zero. This insures that the energy dissipation during unloading in tension is properly captured in the modeling. Using the data reported by Yankelevsky and

Reinhardt[18], a formulation was derived for the unloading stiffness at zero load and is proposed as a function of the unloading strain on the base curve as follows:

$$E_{c6} = -1.1364\left(\varepsilon_{1c}{}^{-0.9905}\right) \tag{7.57}$$

Figure 7.35 shows the above formulation with data from Yankelevsky and Reinhardt.

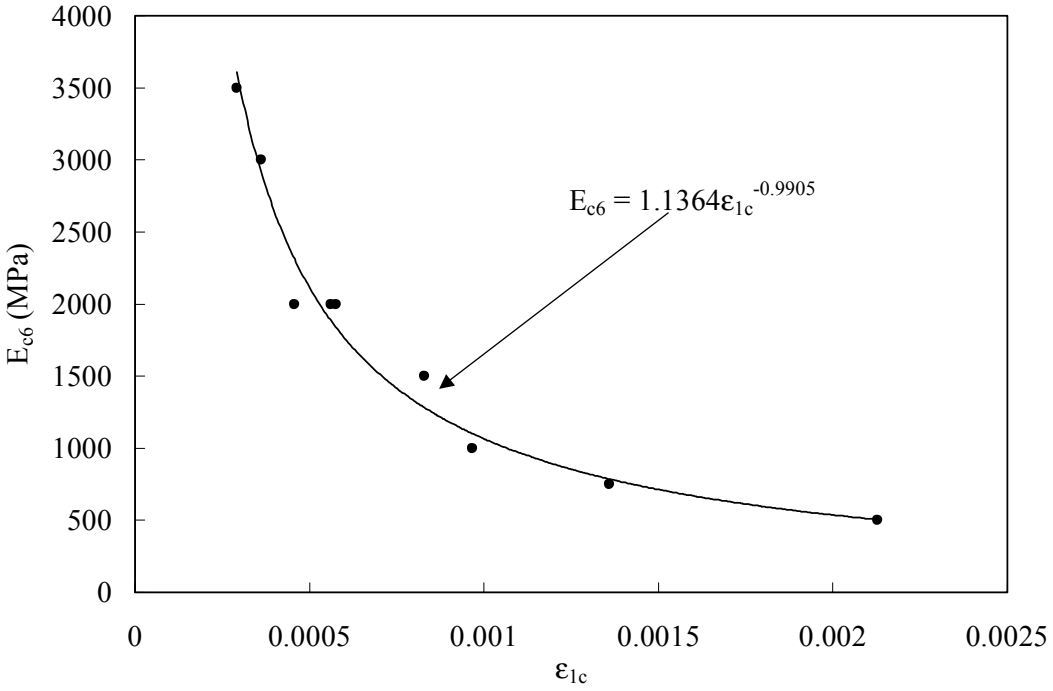

Figure 7.35 Modified Unloading Stiffness

The unloading stiffness data points were determined by fitting the analytical response to the experimental unloading curves, as shown in Figures 7.36 and 7.37. The adjusted unloading stiffness assumes that the plastic offset is zero in the tensile regime, and therefore, a crack-closing model, which initiates at the tensile offset strain, could not be realized. This implies that the compressive stresses remain zero until the cracks completely close. No further adjustments to the models were necessary in the implementation process.

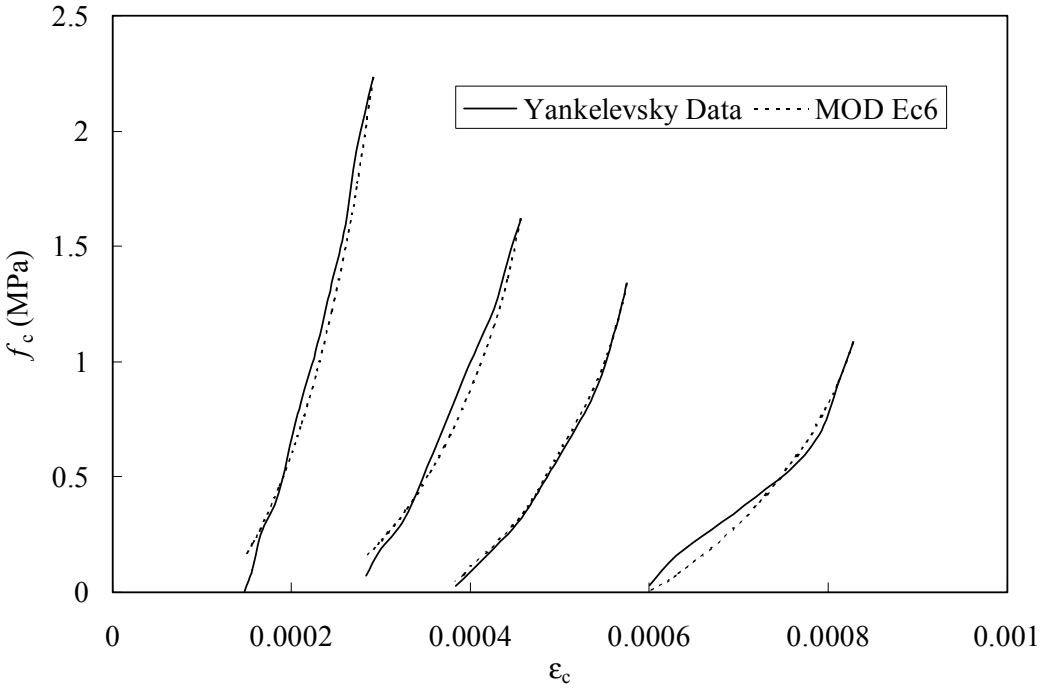

Figure 7.36 Tensile Unloading Curves, Part 1

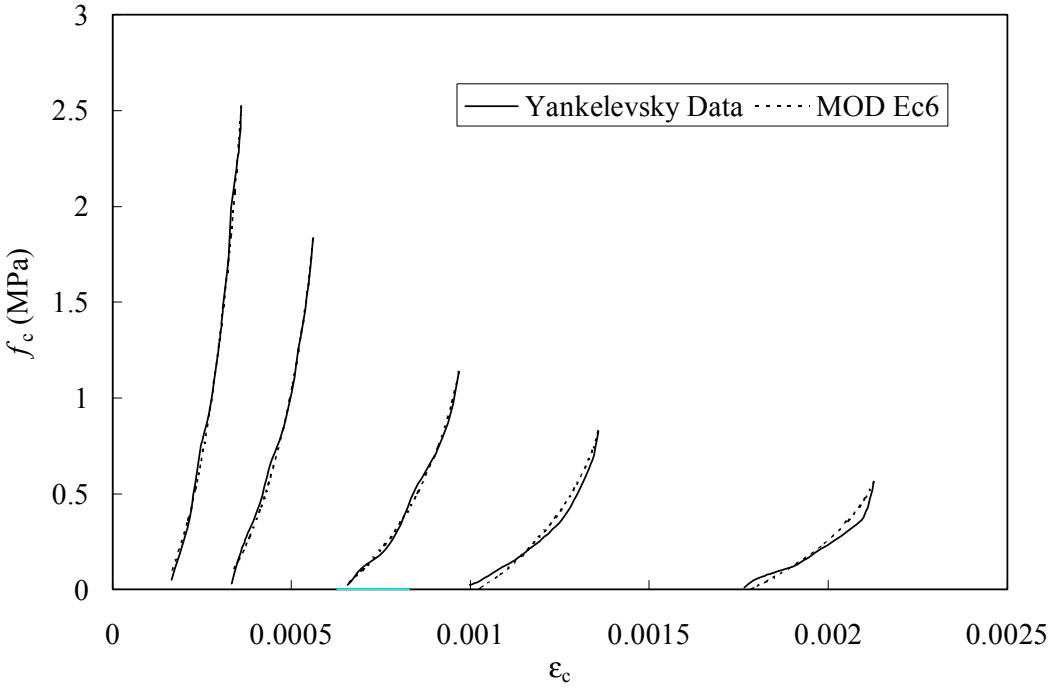

Figure 7.37 Tensile Unloading Curves, Part 2

Chapter 8 contains applications of the models proposed in this chapter to the analysis of actual structures. The finite element analyses to be conducted will consider shear panels and structural walls currently available in the literature.

CHAPTER 8

Application To Shear Walls And Shear Panels

8.1 INTRODUCTION

Corroboration of the cyclic models for concrete proposed in Chapter 7 will include an examination of reinforced concrete shear panels and shear walls tested at the University of Toronto, and reinforced concrete shear wall tests documented in the literature. Namely, walls tested at the Portland Cement Association (PCA) and at Imperial College (SW) will be examined. Program VecTor2, an in-house nonlinear finite element program developed at the University of Toronto, is used to perform the analyses.

8.2 PROGRAM VecTor2

VecTor2, formerly known as TRIX[1], was initially restricted to conditions of monotonic loading. The program was further developed to account for material prestrains, thermal loads, and expansion and confinement effects. The ability to account for material prestrains has recently resulted in analysis capability for reversed cyclic loading. The procedure defines and treats plastic offsets as a strain offset similar to offsets resulting from elastic offsets[3]. The most recent modification to the program has incorporated the capability for analysis of repaired or rehabilitated concrete structures, taking into account the chronology of the loading, damage, and repair[38].

VecTor2 is a two-dimensional nonlinear finite element program, applicable to concrete membrane structures. The program is based on a secant stiffness formulation

using a total-load, iterative procedure, and employing the smeared rotating crack concept. VecTor2 employs the compatibility, equilibrium, and constitutive relations of the Modified Compression Field Theory. Rectangular 4-noded (8 degree of freedom) constant strain elements, as well as triangular 3-noded (6 degree of freedom) constant strain elements are available in the element library. The reinforcement is typically modeled as smeared within the element, but can also be discretely represented by truss bar elements.

The program requires the creation of the following three input files:

- "file".job: The job file contains information regarding the structure name, date, structure file, load file and seed file, loading parameters, averaging factors, convergence limits, and material models.
- "file".s2r: The structure file provides the necessary input to generate the finite element mesh including the number of joints, elements and material types, material properties, and joint coordinates. It also defines the support conditions.
- "file". l2r: The load file defines the loading conditions including joint loads, gravity loads, support displacements, temperature loads, concrete prestrains, and ingress pressures.

An analysis begins by reading the job, structure and load files, and a check is made to see whether a seed file from a previous run is utilized. Initially, linear elastic isotropic material properties are assumed in determining the material component stiffness matrices. The global stiffness matrix is then constructed from the element stiffness matrices. The load vector, which includes prestrain and expansion effects, is formed. Nodal displacements are computed followed by the principal strains and corresponding

directions. Evaluation of the concrete and steel stresses using the constitutive models permits determination of secant moduli and, in turn, new material stiffness matrices. Convergence is then checked and, if satisfied, the load stage is complete. Otherwise, newly calculated stiffness values, based on averaging criteria of the old and new stiffness values, are used to perform another iteration. This process continues until convergence is satisfied or until the maximum number of iterations is reached. Further details are provided elsewhere[1, 39].

8.3 ELEMENT RESPONSE

To describe the new constitutive relations used to model the behaviour of concrete under reversed cyclic loading, a single concrete element subjected to cyclic loading is shown in Figure 8.1.

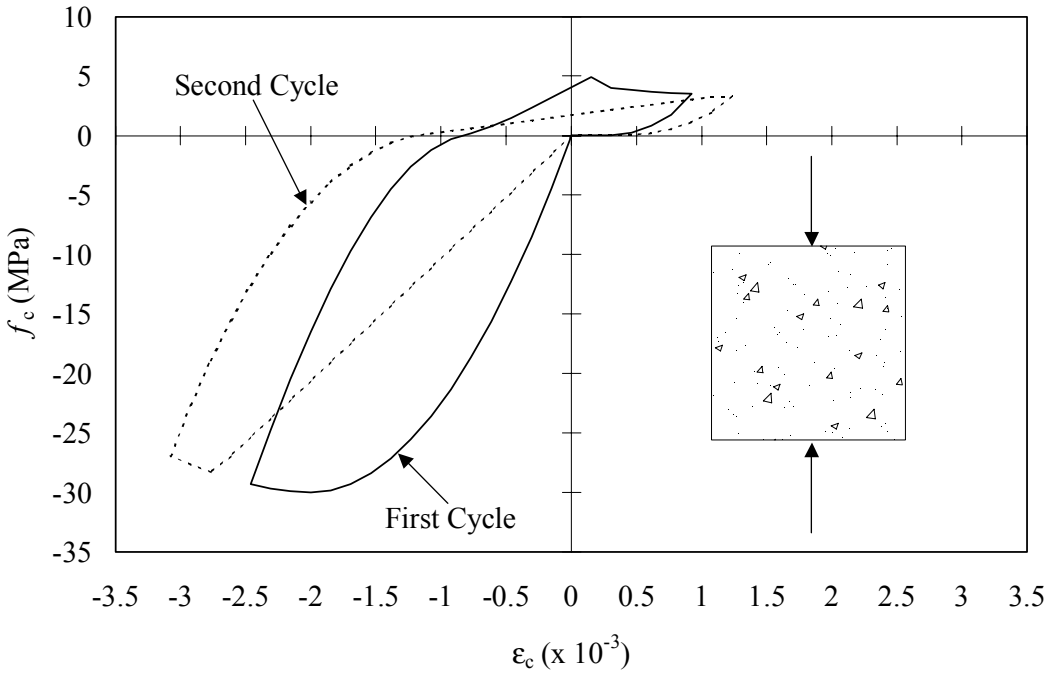

Figure 8.1 Analytical Response of Element Under Uniaxial Cyclic Loading

The concrete element in Figure 8.1 was reinforced in the direction of loading to allow a post-cracking response. The element was loaded in compression to a strain of -2.5×10^{-3} during the first cycle. At that point, the concrete was in its post-peak regime. Unloading terminated at the plastic offset, after which tensile stresses began to develop while the concrete still experienced compressive strains. This is the effect of trying to deform the element to its original position and relieve the residual strains present at the end of unloading. This explicitly caused a shift in the tensile base curve to the compressive plastic offset strain. Loading in tension to a strain of 1×10^{-3} captured the post-cracking response prior to unloading. The unloading phase followed a nonlinear path to the origin, and therefore assumed that the compressive stresses remain zero until the cracks completely closed. This is at odds with observed behaviour, and is currently a numerical stability problem in the program. In the second cycle, the strain was increased by 0.5×10^{-3} for both the compressive and tensile domain. Reloading for both responses included a degrading stiffness, which is evident at the previous maximum unloading strains. Essentially, the reloading curves did not return to the base curve at the previous maximum unloading strains, and required further straining before the base curve was reached. A new plastic strain was defined during the unloading phase, and increased with increasing unloading strain. This again caused a shift in the tensile regime to the new compressive offset value. The above characteristics of concrete subjected to reversed cyclic loading will be applied to more complex structures in subsequent sections.

8.4 APPLICATION TO SHEAR PANELS

8.4.1 PDV Panel Tests

Panel tests, which involve simple elements subjected to well-defined and well-controlled loads, are valuable in assessing the fundamental constitutive behaviour of reinforced concrete. The first series of panels to be analyzed are those tested by Villani[40]. The test program consisted of 890 x 890 x 70 mm orthogonally reinforced panels, named PDV1, PDV2, and PDV3. This study focuses on panels PDV2 and PDV3, both subjected to cyclic loading conditions. The panels were constructed of normal strength concrete and contained 1.82 percent reinforcement in the x-direction and 0.91 percent reinforcement in the perpendicular y-direction. The reinforcement consisted of deformed D5 rebar, with a nominal diameter of 6.0 mm.

The test panels were loaded under conditions of biaxial compression and shear in fixed proportions of f_{nx}:f_{ny}:v = -0.4:-0.4:1.0. Panel PDV2 was subjected to reversed cyclic shear, and PDV3 was tested under unidirectional cyclic loading conditions. Loads were applied in increments of v = 0.5 MPa per load stage until approximately 70 % of the ultimate capacity, and at v = 0.25 MPa thereafter. Table 8.1 contains details of the material properties, and Figure 8.2 is a layout of a typical test specimen.

Table 8.1 PDV Material Properties

Panel	**PDV2**	**PDV3**
f'_c (MPa)	23.7	34.1
ε_o (x 10^{-3})	1.63	1.69
ρ_x (%)	1.82	1.82
f_{yx} (MPa)	282	282
ρ_y (%)	0.91	0.91
f_{yy} (MPa)	282	282

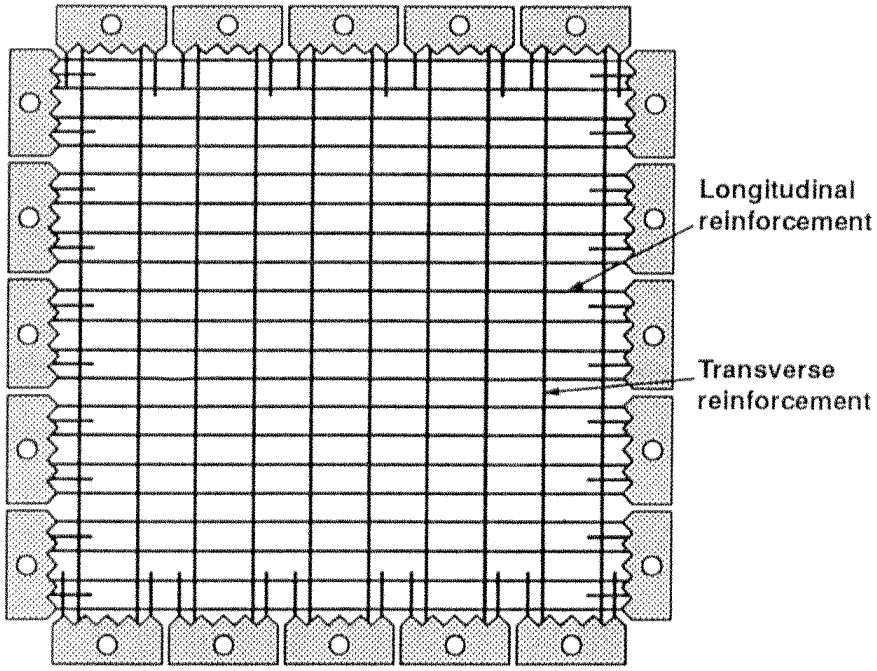

Figure 8.2 PDV Panel Layout, taken from Vecchio[3]

The measured shear stress-shear strain response of Panel PDV3 is shown in Figure 8.3.

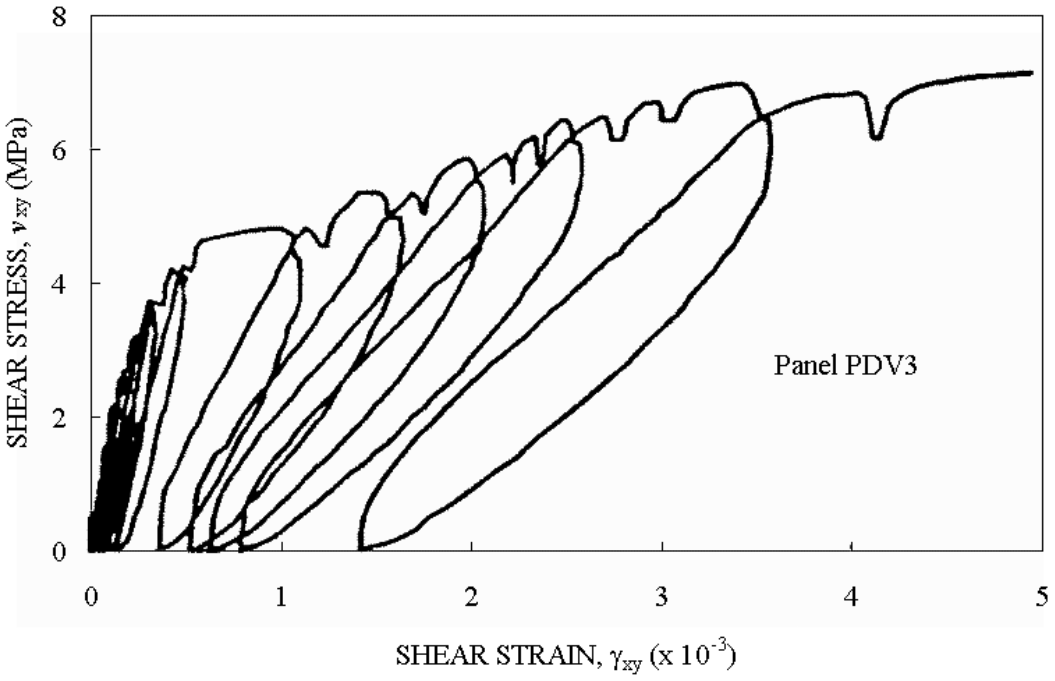

Figure 8.3 Shear Stress-Strain Response of PDV3, taken from Villani[40]

Panel PDV3 failed by shear failure of the concrete occurring coincidently with yielding of the reinforcement in the x-direction. The reinforcement in the y-direction yielded well before failure. A peak shear stress of 7.21 MPa was measured at a corresponding shear strain of approximately 3.4×10^{-3}, and failure propagated during the subsequent reloading cycle. The analytical responses are plotted in Figures 8.4 and 8.5. Figure 8.4 is the calculated response using the preliminary linear cyclic models for concrete initially reported by Vecchio[3], and Figure 8.5 depicts the analysis results incorporating the nonlinear cyclic models suggested in this research report. A single element was used in the finite element mesh, and loads, using force control, were incremented by 0.5 MPa. Under conditions of well-defined and uniform stress conditions, a single element can accurately model behaviour.

Both responses calculated failure to occur immediately following yielding of the reinforcement in both directions. Yielding of the reinforcement in the y-direction preceded yielding in the x-direction. Subsequently, the concrete failed in shear. The analytical calculations seem to overestimate the stiffness of the element, underestimate the peak strength and corresponding shearing strain, and produce significantly less residual strains. A peak shear stress of 6 MPa was calculated, corresponding to shear strains of 2.79×10^{-3} and 2.92×10^{-3} for the linear and nonlinear cyclic models, respectively. Failure occurred during the subsequent load increment. The analysis incorporating the proposed nonlinear cyclic models seems to accurately calculate the damage occurring in the panel during the reloading phases, and produces more energy dissipation. Generally, the nonlinear cyclic models capture a more realistic behaviour of the panel's nonlinear response to cyclic loads.

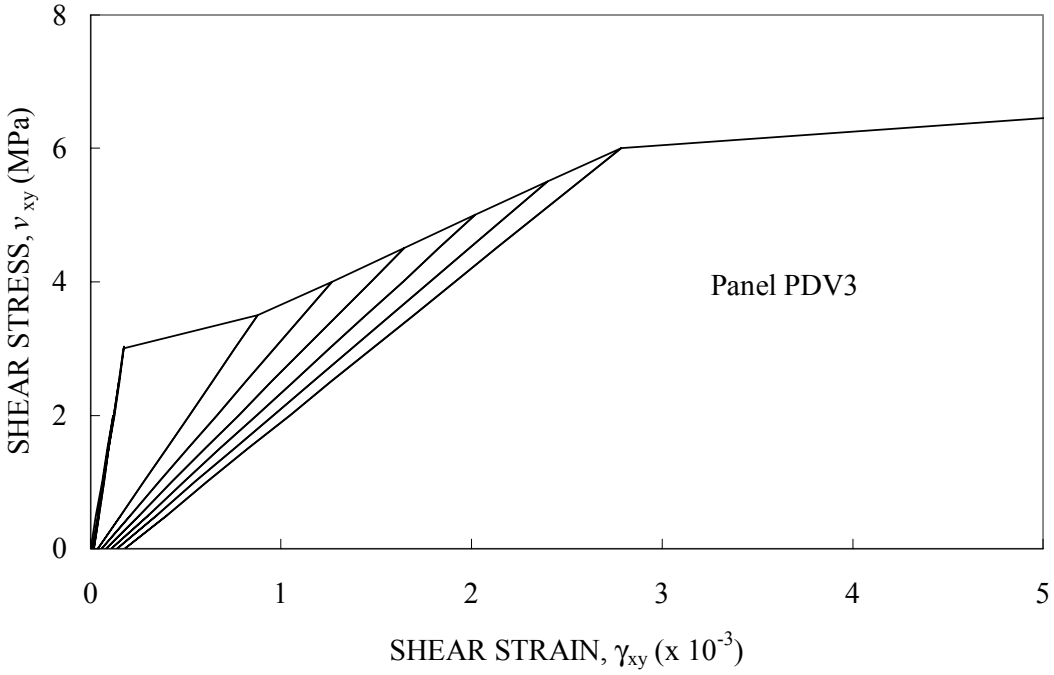

Figure 8.4 Calculated Response of PDV3 Using Linear Cyclic Models

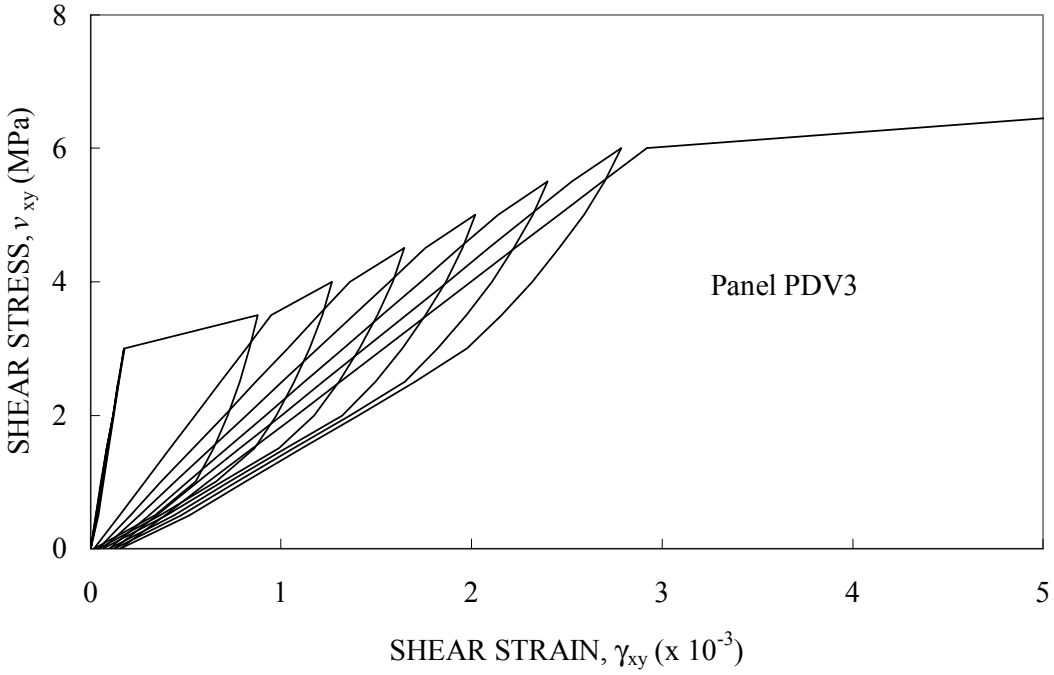

Figure 8.5 Calculated Response of PDV3 Using Nonlinear Cyclic Models

Incorporating a crack-closing model would improve the overall behaviour and better calculate the energy dissipated of the hysteresis loops.

The experimental shear stress-strain response of Panel PDV2 is shown in Figure 8.6. A shear failure of the concrete following yielding of the reinforcement in the x-direction was observed. A peak shear stress of 6.34 MPa was measured at a shear strain of approximately 4.25×10^{-3}, and failure occurred during the subsequent load increment. Shown in Figures 8.7 and 8.8 are the analytical responses of panel PDV2 using the linear and nonlinear cyclic models, respectively. Failure was calculated to occur in the load increment following 5.75 MPa and 6.25 MPa for the analyses using the linear and nonlinear cyclic models, respectively. Shear strains of 3.78×10^{-3} and 4.14×10^{-3} were calculated at the peak shear stresses, respectively. The nonlinear cyclic model calculated more accurately the peak shear stress and shear strain. The mode of failure involved yielding of the reinforcement in the x-direction followed by a shear failure of the concrete. Yielding of the reinforcement in the y-direction was observed well before failure. Similar deficiencies are present in the analyses of panel PDV2: an underestimation of the residual strains, an underestimation of the energy dissipation, and a generally stiffer response.

The calculated behaviour of the nonlinear cyclic model provides a better representation of the actual behaviour of Panel PDV2. It captures the damage in the concrete, which is incorporated in the reloading stiffness, and the hysteresis loops account for more energy dissipation.

Improvements are evident with the proposed nonlinear cyclic models in comparison to the original linear cyclic models. However, deficiencies are still present at

the elemental level. Modeling of reinforced concrete, when controlled by shear failure of the concrete, is a complex phenomenon. Accurately calculating the damage inflicted to the concrete as a result of cyclic shear loading is a controlling factor in properly simulating behaviour. Incorporating a crack-closing model should also provide improvements to the overall elemental behaviour.

Analyses of more complex shear walls, described in subsequent sections, reveals that these deficiencies do not affect the general behaviour of the analysis results. However, improvements at the elemental level can be significant in correctly calculating localized damage, failure modes, and failure loads in shear critical structures.

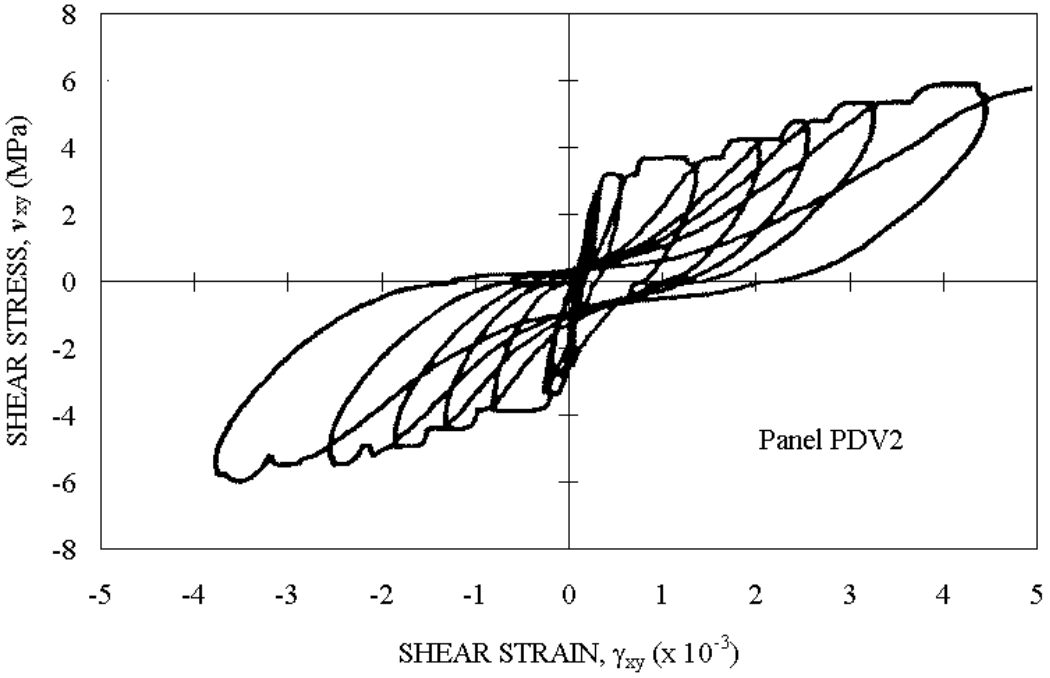

Figure 8.6 Shear Stress-Strain Response of PDV2, taken from Villani[40]

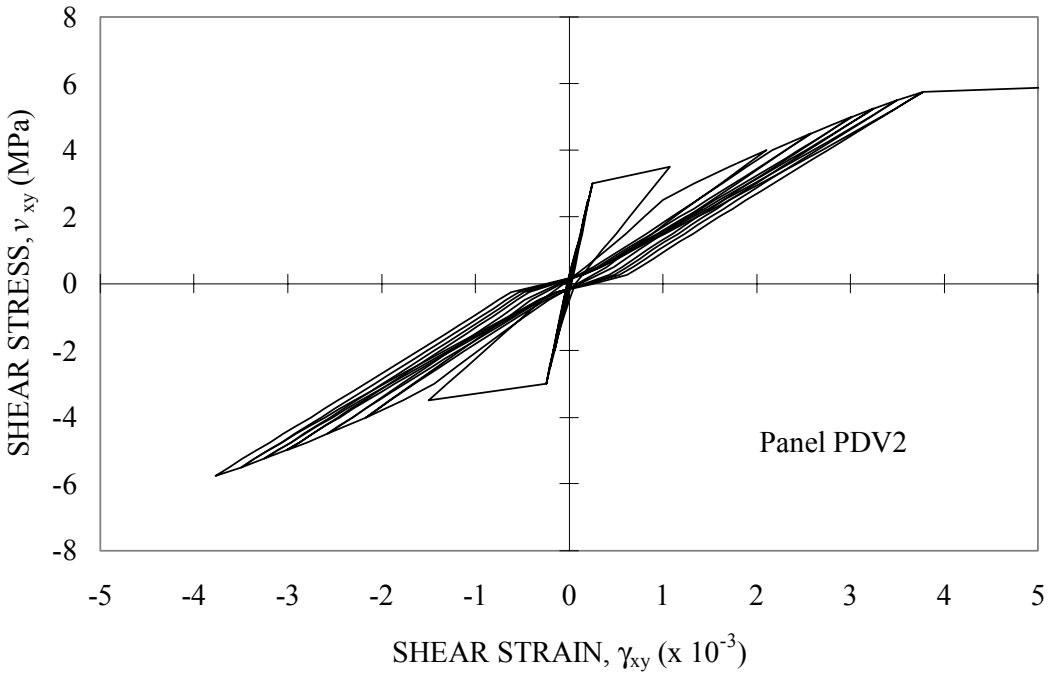

Figure 8.7 Calculated Response of PDV2 Using Linear Cyclic Models

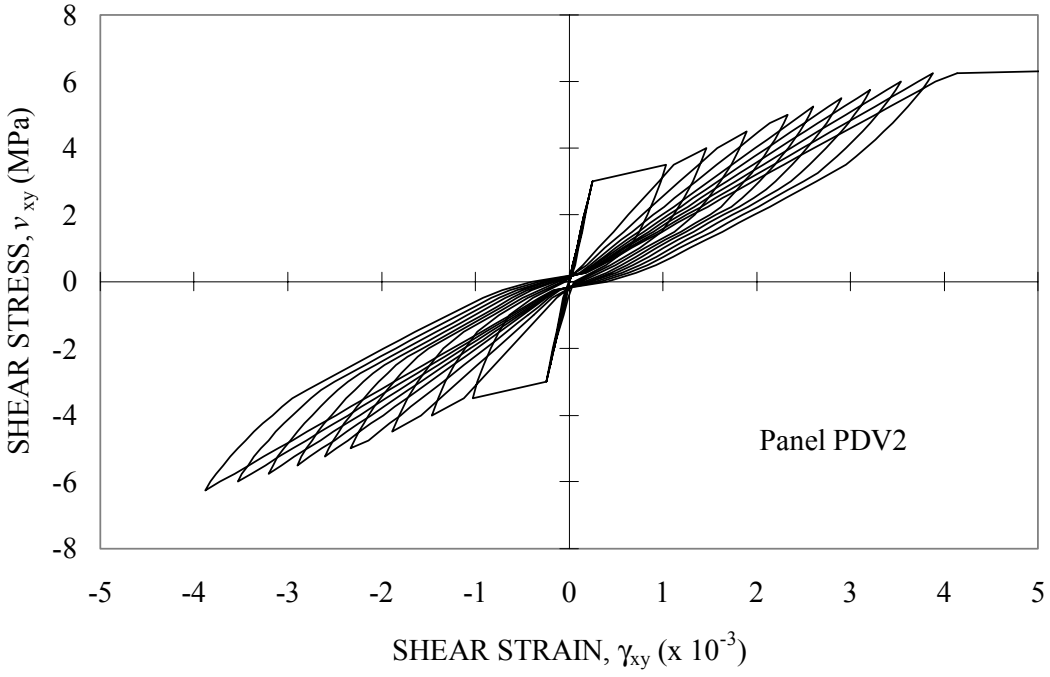

Figure 8.8 Calculated Response of PDV2 Using Nonlinear Cyclic Models

8.4.2 SE Panel Tests

The University of Toronto Shell Element Tester was used to conduct three tests on reinforced concrete elements subjected to reversed cyclic shear. The specimens, 1524 x 1524 x 285 mm in dimension, were orthongonally reinforced, and were designated as SE8, SE9, and SE10[26]. A typical test specimen is shown in Figure 8.9, and the respective material properties are listed in Table 8.2. The test panels were subjected to well-defined and uniform stress conditions, thus the finite element mesh consisted of a single rectangular element. Loading was incremented in steps of 10 percent of the peak shear stress using force control.

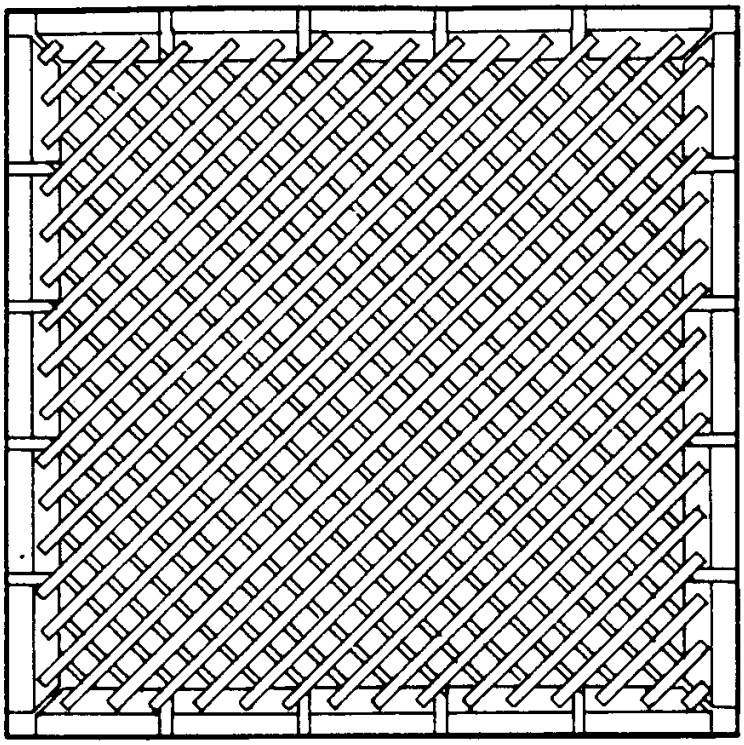

Figure 8.9 SE Specimen Layout, taken from Stevens, Uzumeri, and Collins[26]

Table 8.2 SE Material Properties

Panel	SE8	SE9	SE10
f'_c (MPa)	37.0	44.2	34.0
ε_o (x 10^{-3})	2.60	2.65	2.20
ρ_x (%)	3.0	3.0	3.0
f_{yx} (MPa)	492	422	422
ρ_y (%)	1.0	3.0	1.0
f_{yy} (MPa)	479	422	479

Panel SE8 had reinforcing ratios of 3.0 percent in the x-direction and 1.0 percent in the perpendicular y-direction. The reinforcement consisted of deformed No.20 in the x-direction and deformed No. 10 in the y-direction, with nominal diameters of 19.5 mm and 11.3 mm, respectively. Loading consisted of reversed cyclic shear. Initial shear stresses of 3.98 MPa in the positive direction followed by –4.10 MPa in the negative direction were applied to the panel. In the second cycle, three excursions at a shear stress of 4.51 MPa were imposed on SE8 in both directions of loading. The final load stage consisted of a shear stress of 5.76 MPa. Six complete excursions were resisted at 5.76 MPa, and failure occurred during the seventh excursion at a shear strain of 11.5 x 10^{-3}. Failure ultimately involved a shear failure of the concrete. The y-direction reinforcement yielded during the first excursion to 5.76 MPa. Figure 8.10 is a plot of the shear stress-strain response. The measured response demonstrates pinched hysteresis loops with relatively little energy dissipation that is characteristic of shear mechanisms. The near flat-top response, although, is indicative of yielding of the reinforcement, and the general

behaviour seems controlled by reinforcement yielding. Figures 8.11 and 8.12 are the calculated responses using the linear and nonlinear cyclic concrete models, respectively.

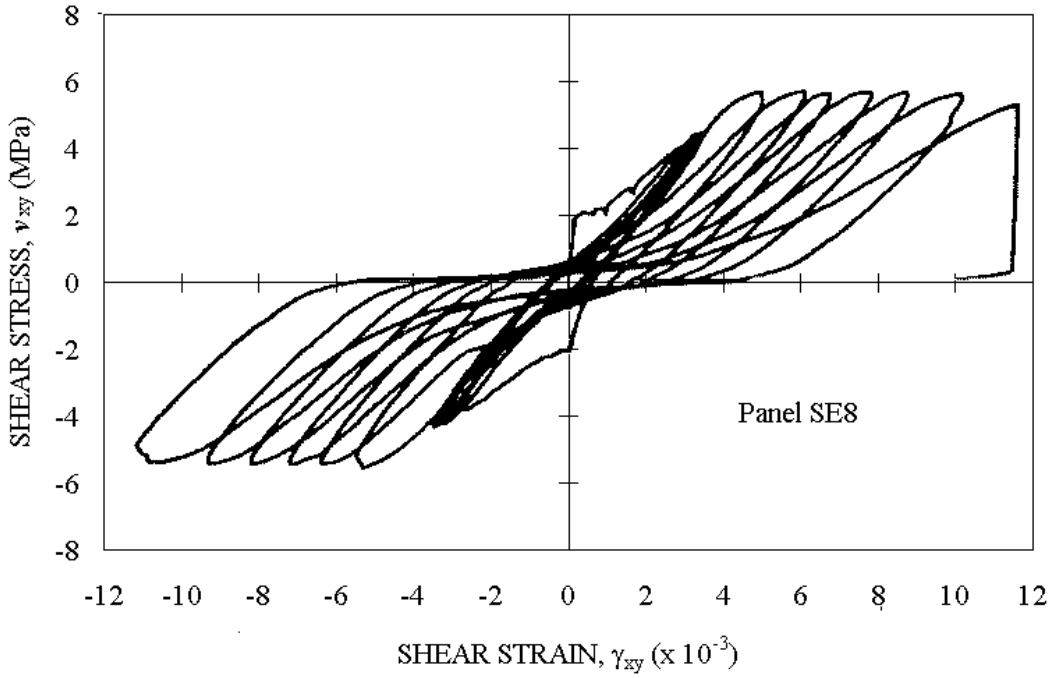

Figure 8.10 Shear Stress-Strain Response of SE8, taken from Stevens, Uzumeri, and Collins[26]

The calculated responses of SE8 demonstrated similar shortcomings to the computed results of the PDV panel series. The assumed responses were significantly stiffer and calculated significantly less damage in concrete in terms of shear strains and residual strains. The calculated behaviours also demonstrated less energy dissipation than recorded. Neither analysis calculated failure in the panel during the seventh excursion to a shear stress of 5.76 MPa. In both analyses, the reinforcement in the x- and y-directions had not yielded; and therefore, failure due to concrete crushing after yielding was not realized. Local reinforcement stresses of 54 % and 95 % of the yield stress were

calculated for the x- and y-directions, respectively. Shear strains of 4.11 x 10^{-3} and 4.13 x 10^{-3} were calculated by the analyses using the linear and nonlinear cyclic models, respectively, which significantly underestimated the actual damage of the panel. The test results indicated that cycling beyond yield caused large strain increments that eventually lead to a shear failure of the concrete.

The response of Figure 8.12, using the nonlinear cyclic model, tends to demonstrate a more realistic behaviour of the panel. More energy dissipation is produced due to the damage parameters incorporated during reloading and the use of nonlinear unloading rules.

Panel SE9 was also loaded in reversed cyclic shear, but had reinforcing ratios of 3.0 percent in both directions. The panel failed at a higher shear stress than panel SE8, but experienced less straining. The response was significantly stiffer, and residual strains were smaller. Failure followed local yielding of the reinforcement in the y-direction and involved crushing of the concrete over a widespread region of the panel. The shear stress-strain response exhibited by SE9 is shown in Figure 8.13, and the computed responses are plotted in Figures 8.14 and 8.15.

Loading consisted of 3 reversed cyclic excursions to 4.51 MPa, 6.39 MPa, 7.81 MPa, and 9.55 MPa. Failure was observed during the third excursion to –9.55 MPa, and a dramatic overall compressive failure of the concrete was visually evident. A shear strain of approximately 8.0 x 10^{-3} was observed at failure. The rounded response, which resembles the concrete base curve, appears to be more influenced by the concrete behaviour.

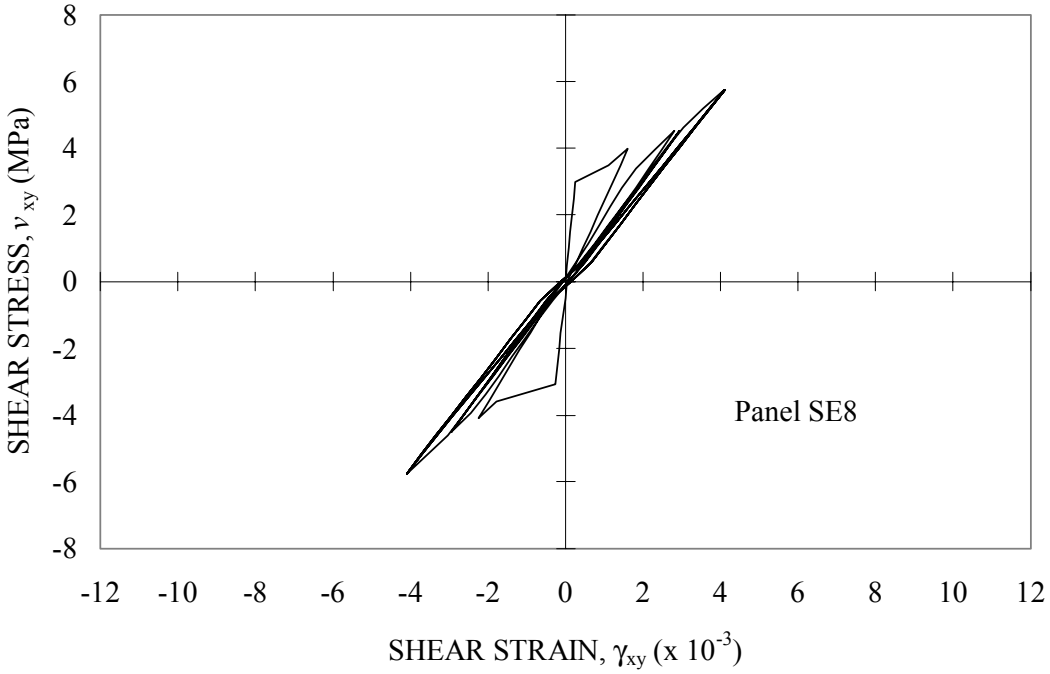

Figure 8.11 Calculated Response of SE8 Using Linear Cyclic Models

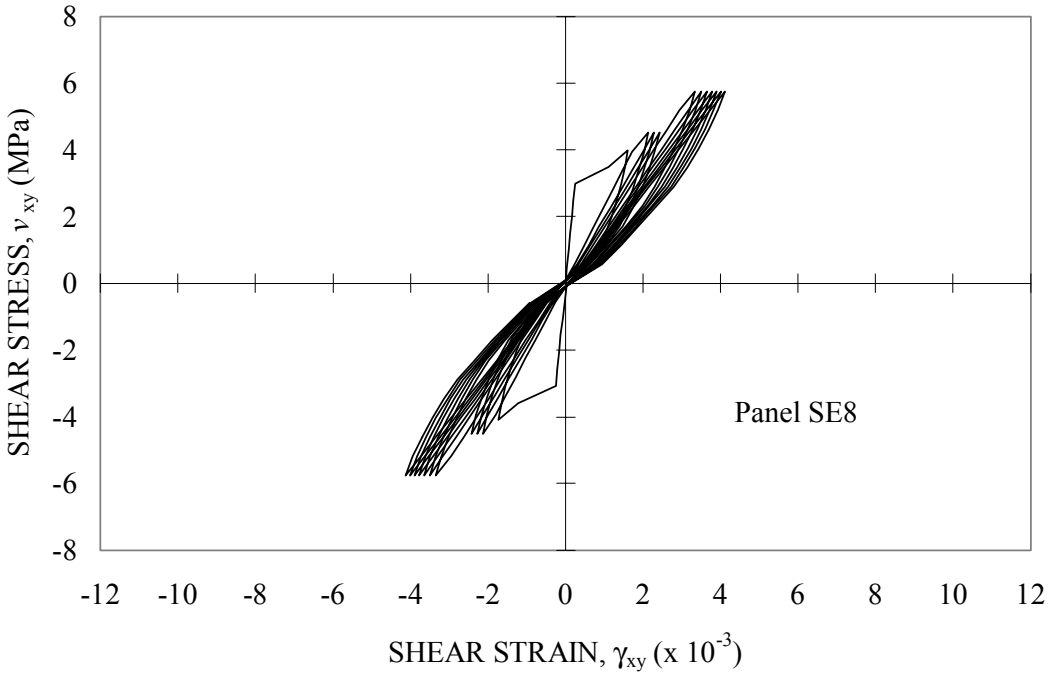

Figure 8.12 Calculated Response of SE8 Using Nonlinear Cyclic Models

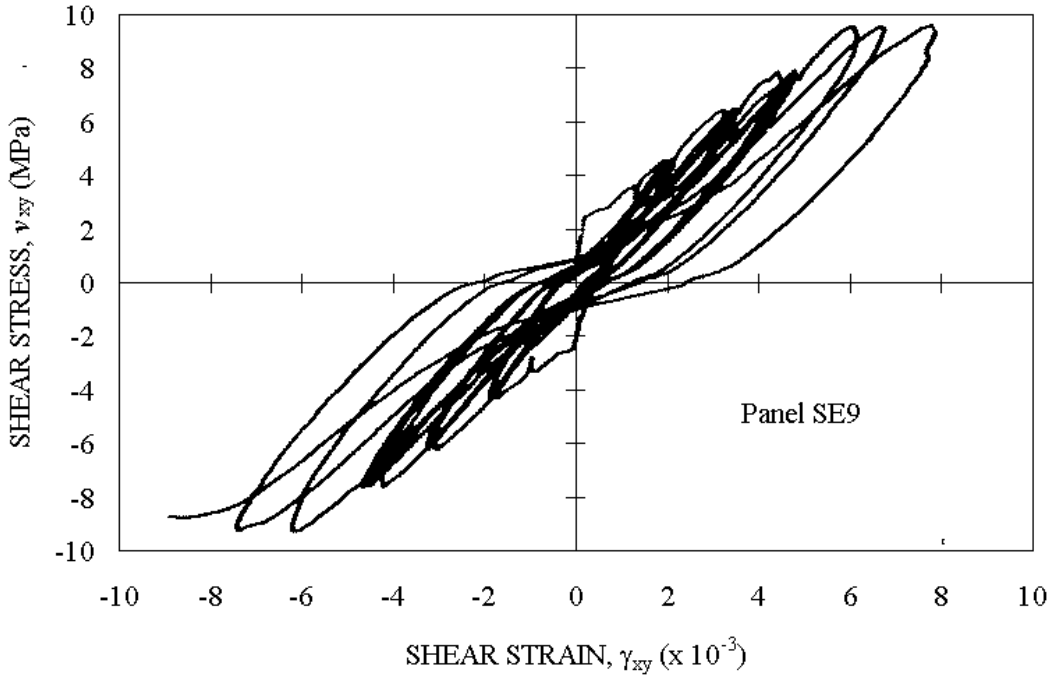

Figure 8.13 Shear Stress-Strain Response of SE9, taken from Stevens, Uzumeri, and Collins[26]

The computed responses of SE9 were unable to calculate failure. The reinforcement had not yielded, preventing strains from accumulating. Locally, the reinforcement attained 78 % of the yield stress in both directions. Both the linear and nonlinear cyclic models calculated a stiffer response and less residual strains. Maximum shear strains of 4.68 x 10^{-3} and 4.78 x 10^{-3} were recorded for the linear and nonlinear cyclic models, respectively, again underestimating the degree of damage experienced. In general, the calculations of the nonlinear cyclic model seemed to demonstrate a more realistic representation of the panel's behaviour and seemed to provide reasonably accurate simulations of the reloading damage.

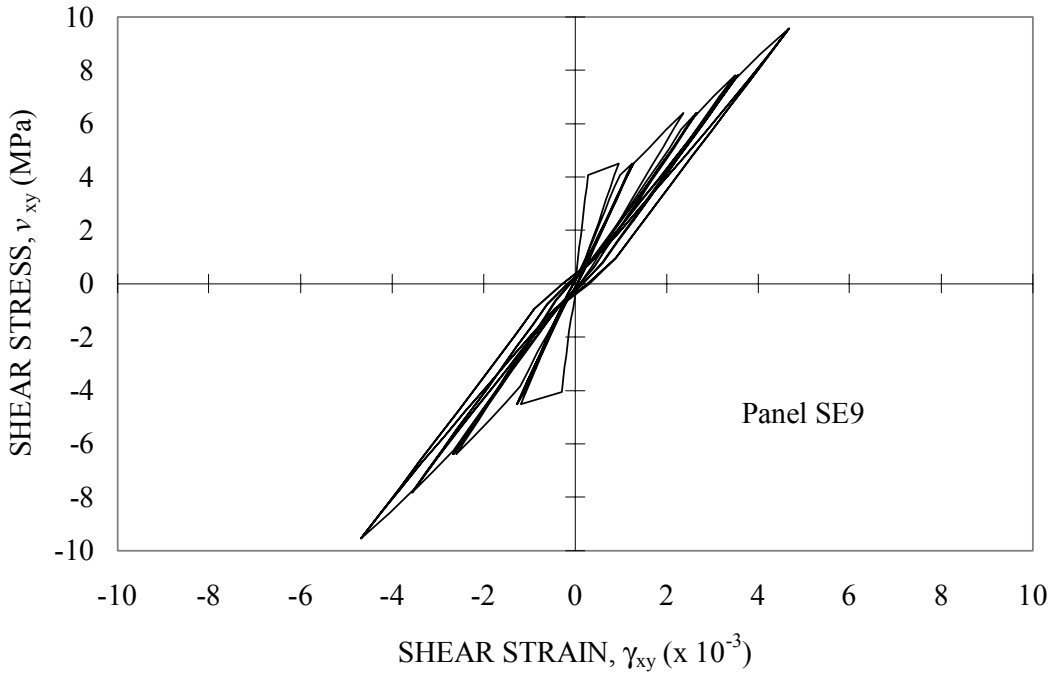

Figure 8.14 Calculated Response of SE9 Using Linear Cyclic Models

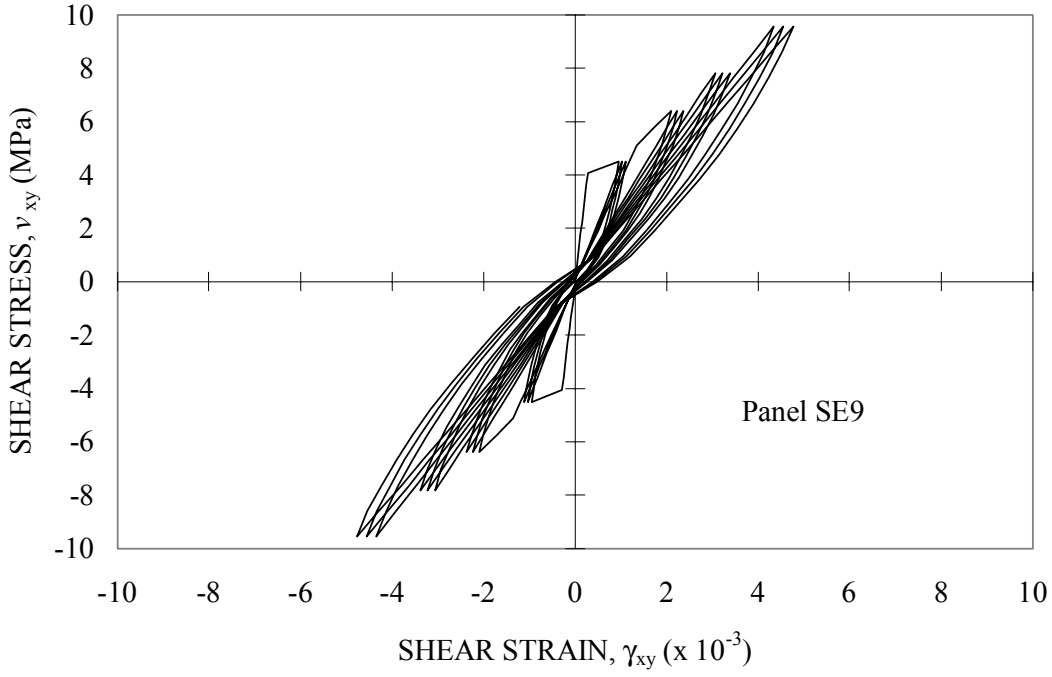

Figure 8.15 Calculated Response of SE9 Using Nonlinear Cyclic Models

As a result of panel SE9 failing at 9.55 MPa after yielding of the reinforcement in the y-direction raises some important issues. The panel was reinforced with identical reinforcement in both the x- and y-directions. Under ideal laboratory conditions, the panel should fail after yielding of the reinforcement in both directions, provided that the panel is not over reinforced, which would cause crushing of the concrete prior to yielding. Therefore, to yield panel SE9, a shear stress of 12.66 MPa is expected. The analysis would provide better results had the panel behaved as was expected.

The last of the SE series of test panels, SE10, was loaded under a combination of shear and biaxial compression. The biaxial compression was one-third of the applied shear stress. Panel SE10 had reinforcing ratios of 3.0 percent in the x-direction and 1.0 percent in the y-direction. The load consisted of three excursions, each to shear stresses of 4.6 MPa, 5.73 MPa, 7.06 MPa, and 8.25 MPa. Failure by widespread crushing occurred during the third excursion to –8.25 MPa, at a shearing strain of approximately -8.0×10^{-3}. Yielding of the reinforcement in the y-direction was measured prior to failure. The observed shear stress-shear strain response is shown in Figure 8.16. The response is similar to SE8 and SE9; demonstrating pinched hysteresis loops with little energy dissipation. The rounded behaviour, similar to SE9, appears to be significantly influenced by the concrete. Beyond yielding, the rate of shear strain accumulation escalated and was evident at a shear stress of 8.25 MPa. The calculated responses are plotted in Figures 8.17 and 8.18.

The calculated responses of the linear and nonlinear cyclic models did not capture the degree of damage measured by panel SE10, and were not capable of calculating failure in the third excursion to 8.25 MPa. The analyses had calculated that the

reinforcement had not yielded; the result was significantly smaller peak shear strains and residual strains. Reinforcement stresses of 60 % and 86 % of yield in the x- and y-directions, respectively, were computed. Coincident with yielding of the reinforcement are large accumulations of shearing strains and residual strains, which were not realized by the calculated responses. The linear and nonlinear cyclic models calculated maximum shear strains of 4.68 x 10^{-3} and 4.36 x 10^{-3}, respectively. The analysis results of the nonlinear cyclic model depicted a more realistic representation of the actual behaviour of the specimen; however, the linear cyclic model recorded a slightly larger shearing strain.

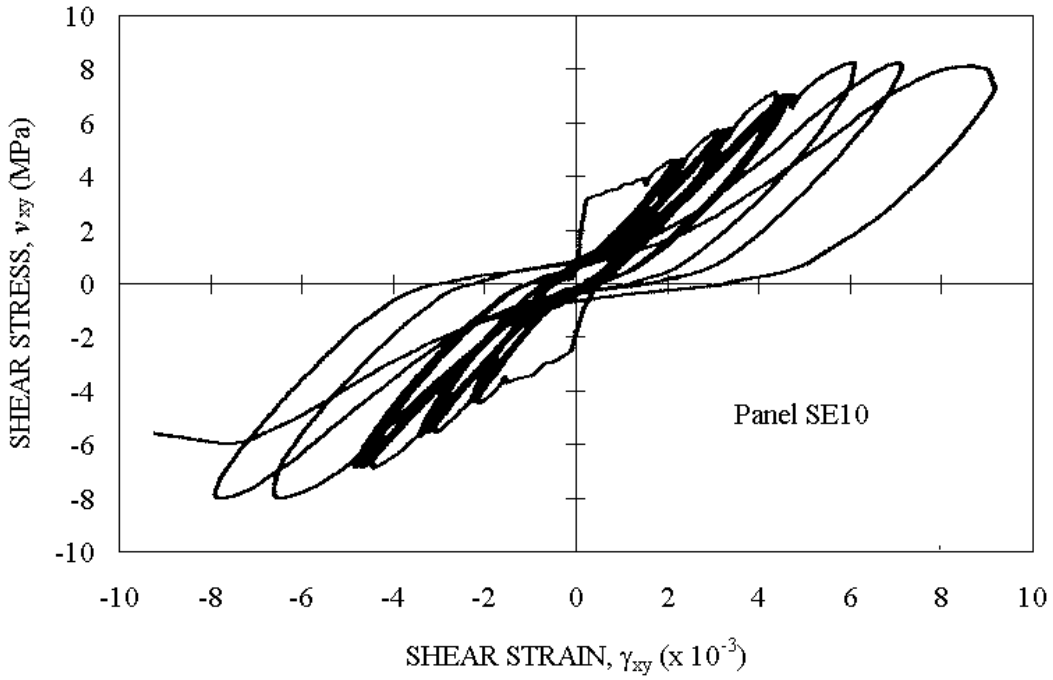

Figure 8.16 Shear Stress-Strain Response of SE10, taken from Stevens, Uzumeri, and Collins[26]

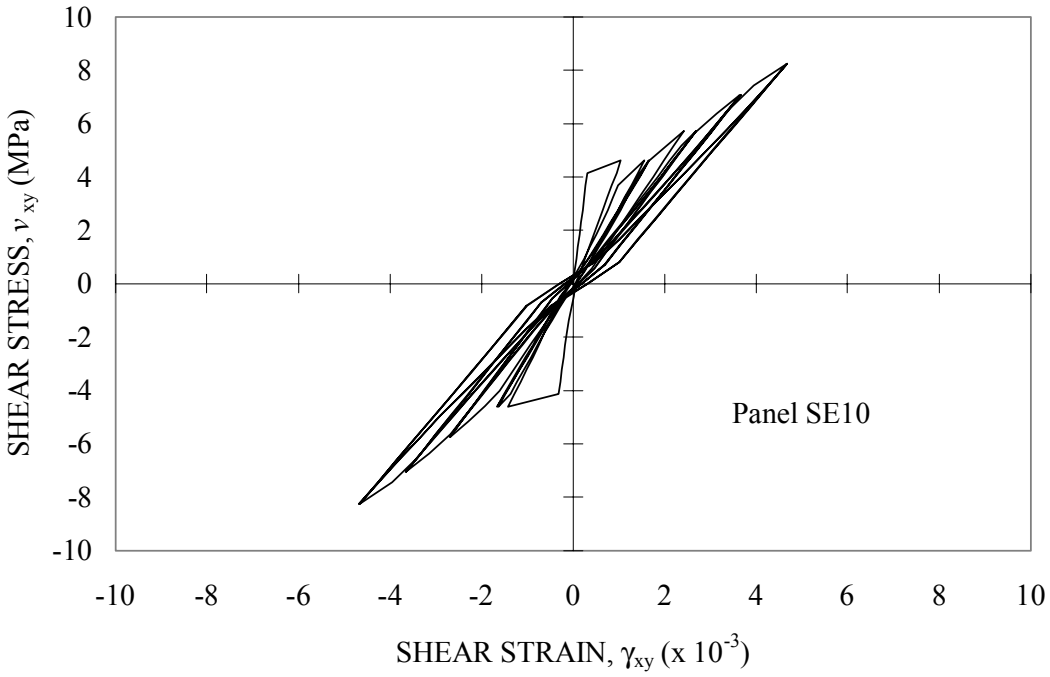

Figure 8.17 Calculated Response of SE10 Using Linear Cyclic Models

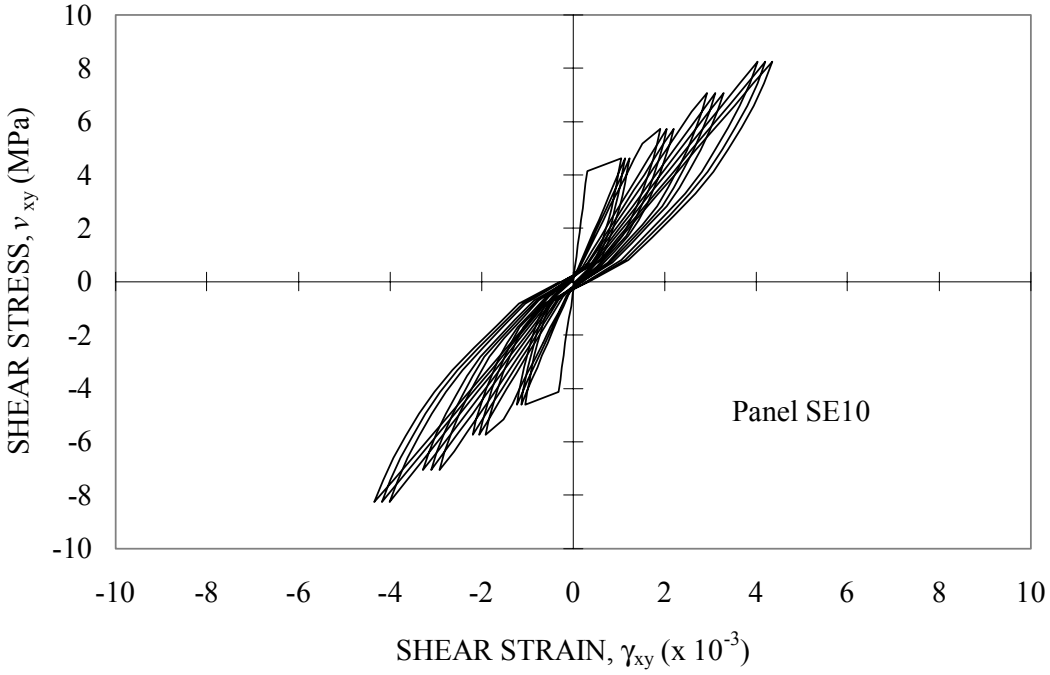

Figure 8.18 Calculated Response of SE10 Using Nonlinear Cyclic Models

The SE series of panels had failed due to concrete crushing, preceded by yielding of the reinforcement in the y-direction, which generally contained less reinforcement. During testing, the panels were cycled at intermediate loads prior to yielding of the reinforcement. The final load stage consisted of load cycling at a shear stress where yielding of the reinforcement in the y-direction was first observed. Cycling between peak shear stresses above yield caused large strain increments with each successive cycle, until the specimens failed by concrete crushing. The progressive expansion of the panel due to yielding increased the compressive softening effect. In the finite element results, yielding of the reinforcement was not calculated; however, local reinforcement strains were just below yielding. The stresses at crack locations were higher than currently calculated by the Modified Compression Field Theory. The analyses seemed to underestimate the strains in the transverse reinforcement due in part to neglecting the slip along crack surfaces. Also, the maximum allowable shear stress ($v_{ci\max}$) on a crack surface currently does not account for degradation under reversed cyclic loading conditions, and seems to be another contributing factor to underestimating the reinforcement strains.

For Panels SE8 and SE10, the analyses calculate reinforcement strains slightly less than yield, thus, failure could not be realized, and for Panel SE9, there appears to be experimental factors affecting the observed results. For the three panels, loading was incremented until first yielding and then cycled to failure. Thus, a more realistic analysis of the panels would be to provide loading to a specific displacement rather than stress level. Further, Stevens, Uzumeri, and Collins reported that biaxial straining causes an additional degradation to the compressive strength of the concrete. Panel SE10 was further analyzed using the nonlinear cyclic models. The panel was loaded to the point of

yielding of the y-direction reinforcement, and then the load was cycled until failure. Figure 8.19 depicts the results of SE10 cycled in the post-yield range.

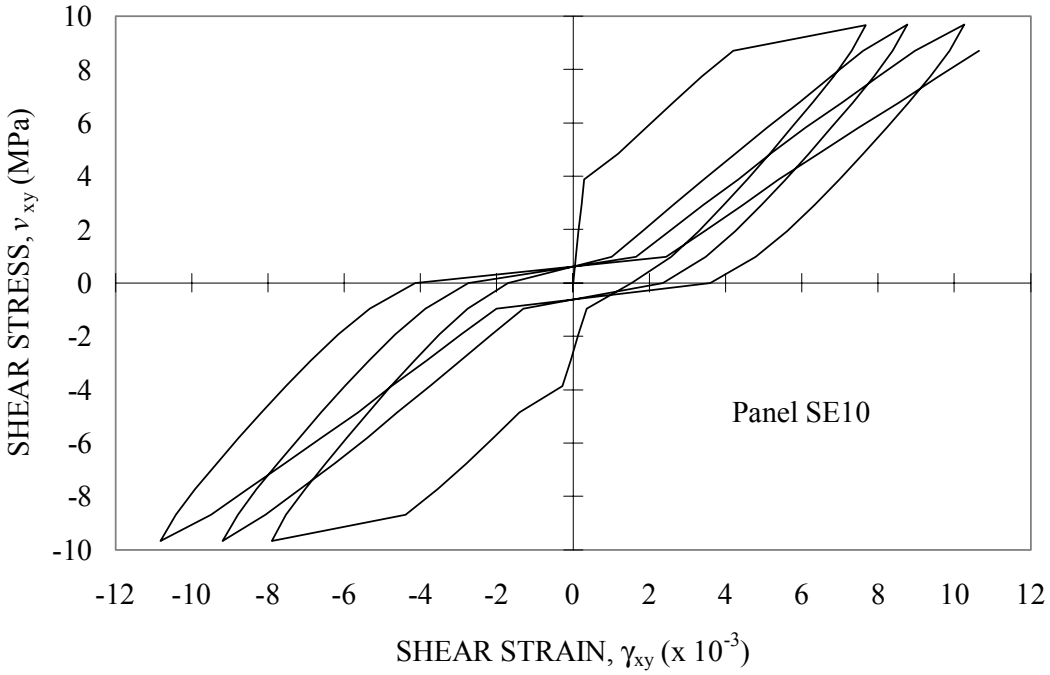

Figure 8.19 Calculated Post-Yield Response of SE10

Failure of SE10 was calculated to occur during loading to the forth cycle at a shear stress of 9.67 MPa, somewhat larger than the 8.25 MPa measured during testing. However, a shearing strain at first yield of 7.67 x10^{-3} was estimated by the analysis, which was comparable to the observed strain of 8.0 x 10^{-3}. The mode of failure in the analysis involved crushing of the concrete. Yielding of the reinforcement in the y-direction was calculated during the first cycle to 9.67 MPa. The reinforcement stresses in the x-direction were well below yield. The overall load-deformation response showed better correlation with the actual response and indicated that the nonlinear cyclic models

can accurately calculate the responses of panels provided that yielding of the reinforcement is captured.

The analyses of shear panels have indicated that while the response using the nonlinear cyclic models with stiffness degradation parameters provides a realistic representation of the reported results, there still exist deficiencies at the elemental level. This can be significant in correctly calculating localized damage, failure modes, and failure loads in shear or compression critical structures. Further study is required in modeling crack-closing, crack shear-slip, and the tensile and compressive softening parameters due to cyclic loading. This should provide better simulations of the PDV panel series, where the analyses were deficient in calculating damage to the concrete and the energy dissipation in the hysteresis loops. The analyses of the SE series of panels grossly underestimated the straining in the reinforcement. This deficiency seems to be linked to modeling of slip along crack surfaces. Proper modeling of the SE panels requires calculating the initiation of yielding in the transverse reinforcement.

8.5 APPLICATION TO SHEAR WALLS

8.5.1 PCA Shear Walls

The series of walls tested by the Portland Cement Association[30] (PCA) are widely regarded as benchmarks against which theoretical formulations are calibrated. The PCA reinforced concrete walls were a one-third-scale representation of a five-storey wall. The PCA specimens were barbell-shaped, measuring 1910 mm in total width and 4570 mm in height. The web walls were 102 mm thick, and the boundary elements were 305 mm square. The specimens were built integral with a heavy base slab and stiff top slab. The

specimens included in this investigation exhibited yielding of the flexural and vertical web reinforcement prior to failure. Figure 8.20 provides the dimension details of a typical test specimen, and Figure 8.21 shows the layout of the reinforcement.

Test specimen B1 contained 0.31 percent horizontal reinforcement and 0.29 percent vertical reinforcement in the web wall. The boundary elements were reinforced with 1.11 percent vertical reinforcement relative to the gross concrete area of the boundary elements and did not have any confining steel. Material properties of the specimen are given in Table 8.3. Loading consisted of imposing two cycles at predetermined displacement levels to the top slab, with the displacement incremented in steps of 25.4 mm (1 in.). No imposed axial load was present on B1. Failure of test specimen B1 included bar buckling of the flexural reinforcement in the boundary elements, initially occurring in the first excursion to 76.2 mm (3 in.) and continuing in subsequent cycles. The measured load-displacement response of B1 is shown in Figure 8.22. The response is typical of relatively high height-to-width wall ratios, where the response demonstrates significant energy dissipation and large residual strains. The behaviour of B1 was controlled by the response of the vertical reinforcement.

Finite element analyses were performed to calculate the behaviour of PCA wall B1, using the linear and nonlinear cyclic models previously discussed. The finite element mesh shown in Figure 8.23 consisted of 252 constant strain rectangular elements. The mesh was divided into a flange zone, a web zone, and a top slab zone collapsed to fit the width of the wall. The bottom slab was omitted from the analysis, and it was assumed that the wall section was fully fixed to the top of the base slab. Load increments of 20 percent of the peak displacement level were applied to the structure during the analyses

using displacement control. The analysis results are plotted in Figures 8.24 and 8.25, depicting the linear and nonlinear cyclic model responses, respectively.

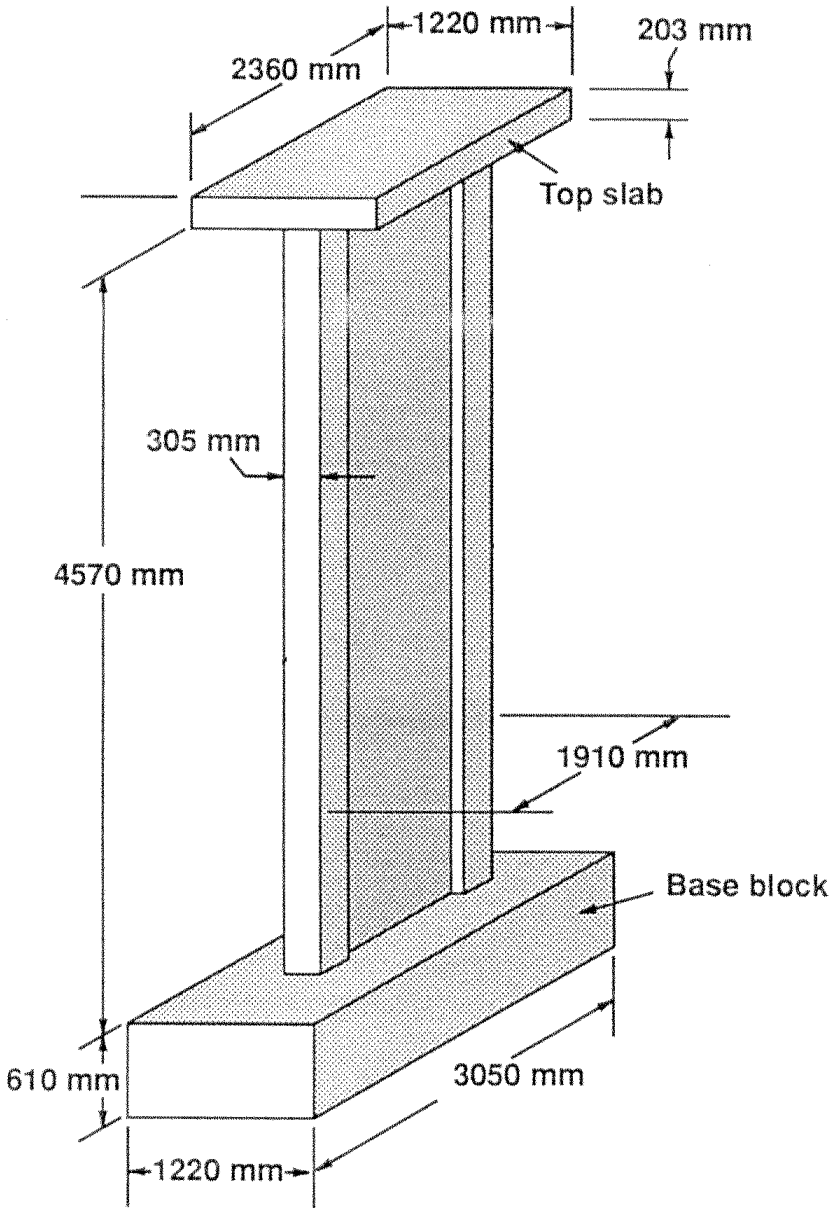

Figure 8.20 Details of PCA Walls, taken from Oesterle, Fiorato, Johal, Carptenter, Russell, and Corley[30]

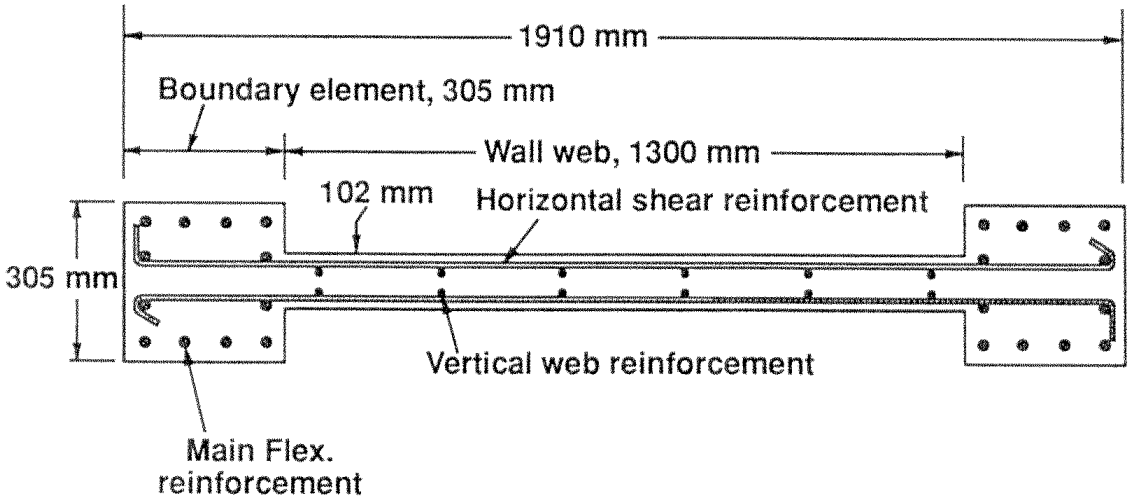

Figure 8.21 Typical Reinforcement Layout of PCA Walls, taken from Oesterle, Fiorato, Johal, Carptenter, Russell, and Corley[30]

Table 8.3 B1 Material Properties

Zone	Concrete		Horizontal Reinforcement		Vertical Reinforcement	
	f'_c (MPa)	E_c (MPa)	ρ (%)	f_y (MPa)	ρ (%)	f_y (MPa)
Web	53.0	32300	0.31	521	0.29	521
Flanges	53.0	32300	0.31	521	1.11	450

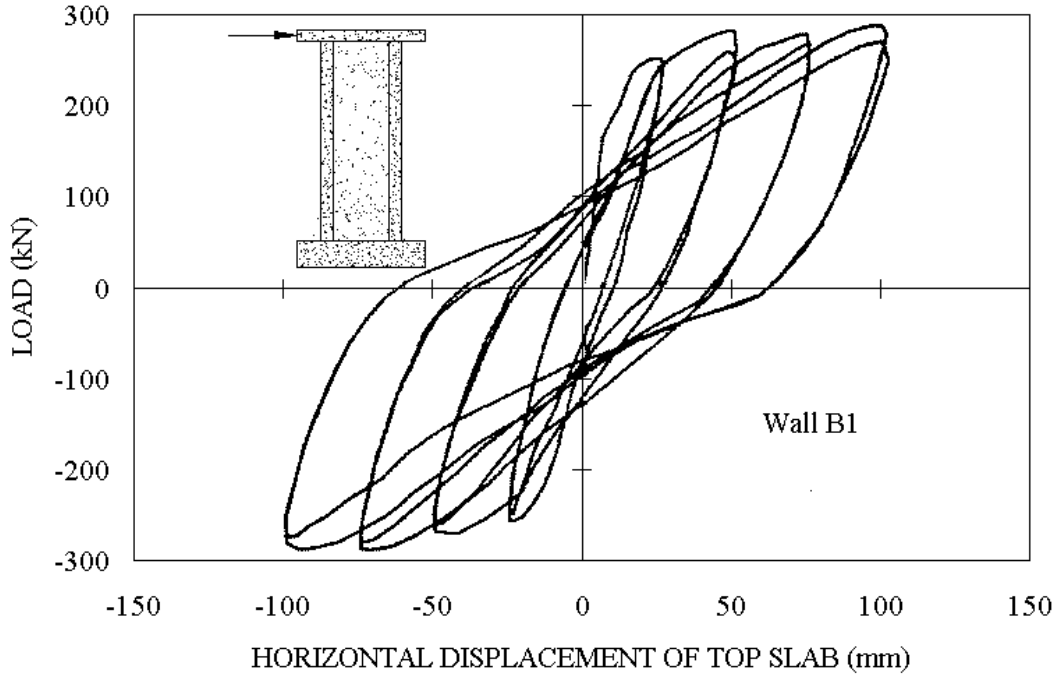

Figure 8.22 Load-Displacement Response of B1, taken from Oesterle, Fiorato, Johal, Carptenter, Russell, and Corley.[30]

The calculated load-displacement results from the linear and nonlinear cyclic models are similar. Yielding of the reinforcement controlled the responses, and the concrete's contribution was secondary to the overall behaviour. Relative to the experiment measured response, the analyses correlate well in terms of ultimate lateral resistance, residual displacements, energy dissipation, pre-cracking and post-cracking stiffness, degradation of the lateral stiffness, and overall hysteretic behaviour. The actual behaviour does, however, demonstrate more pinching of the hysteresis loops. The analyses seem to overestimate the tension stiffening, relieving the pinching effect. Related to this may be bond slip of the reinforcement, which tends to be an important phenomenon in reinforced concrete walls subjected to reversed cyclic loading and is

currently not considered in the FE analysis program. Also, slip along the crack surfaces is a further influencing factor, which is not considered by the Modified Compression Field Theory.

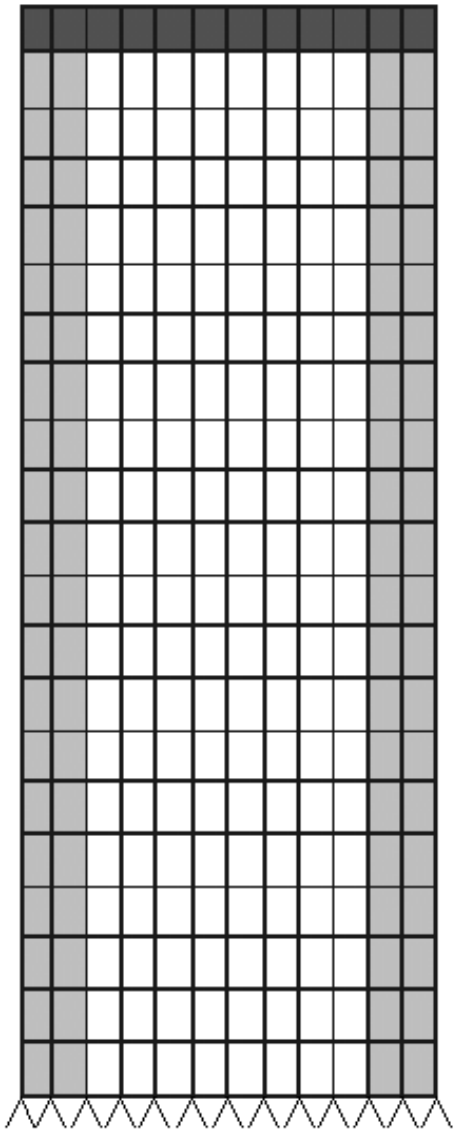

Figure 8.23 Finite Element Mesh for PCA Test Specimens

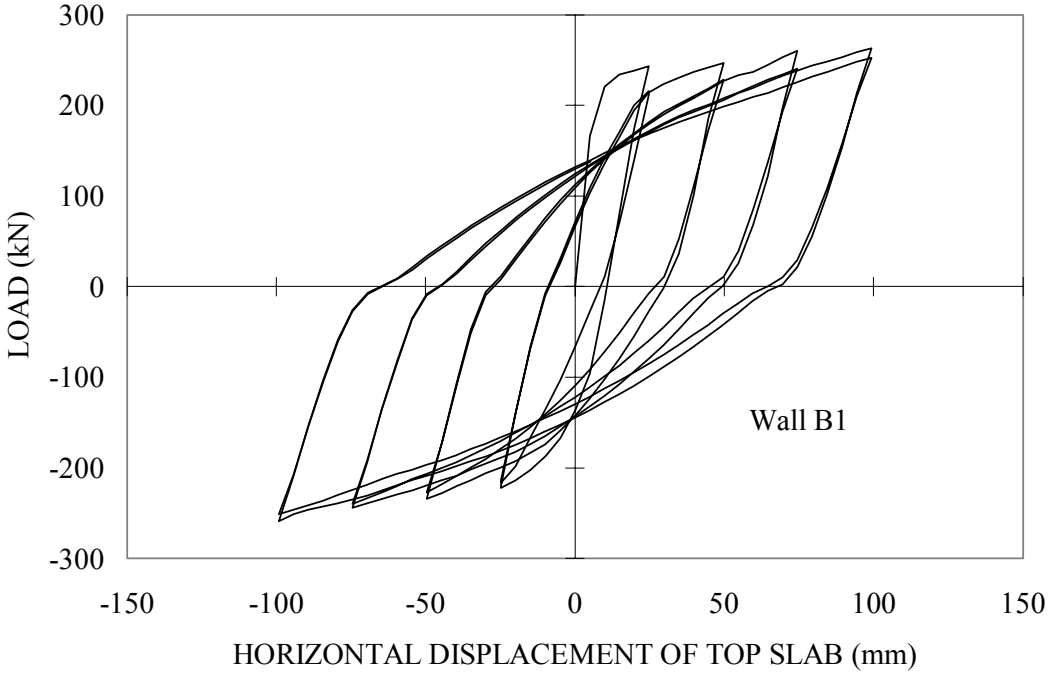

Figure 8.24 Calculated Response of B1 Using Linear Cyclic Models

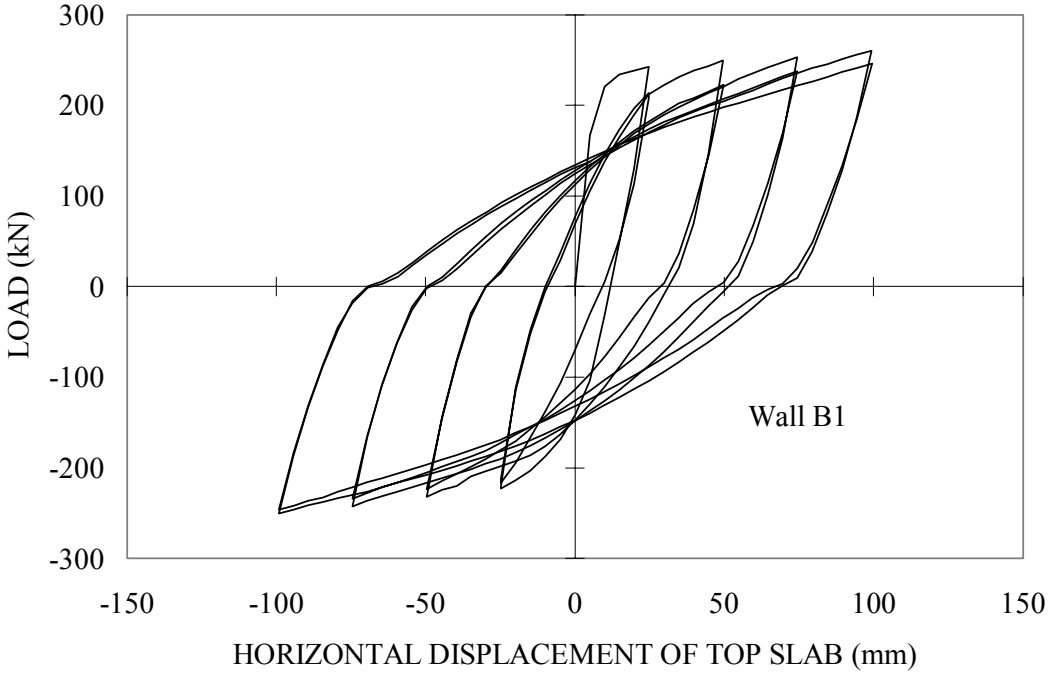

Figure 8.25 Calculated Response of B1 Using Nonlinear Cyclic Models

At 100 mm of displacement, loads of 263 kN and 260 kN were recorded for the linear and nonlinear cyclic models, compared to an approximate measured ultimate load of 280 kN. The resulting analytical-to-experimental lateral load resistance ratios were 0.94 and 0.92, respectively. Failure of B1 was reported as buckling of the flexural reinforcement, initially occurring in the first excursion to 75 mm and continuing throughout the test. The analysis program does not account for bar buckling and therefore, was not capable of capturing this effect. Significant indicators obtained from the analyses included local yielding of the horizontal and vertical reinforcement in the web wall on first cracking. At the peak load, the vertical reinforcement in the boundary elements near the base slab recorded strains 18-fold larger than the yield strain, and by the end of the analysis the bottom one-third rows of elements were showing yielding of the vertical reinforcement. Concrete crushing was also calculated to occur, but confined to the compressive toes in the web section, and was calculated to first occur at 100 mm of lateral displacement. The analysis using the linear cyclic models also experienced crushing of the concrete in the lower portion of the boundary elements. Crushing of the concrete dominated the calculated failure mechanisms.

Test specimen B2 was similar to B1, with the exception of larger quantities of flexural reinforcement in the boundary elements, and larger quantities of horizontal reinforcement throughout the wall. The web section of B2 contained 0.29 percent vertical reinforcement and 0.63 percent horizontal reinforcement. The boundary elements had 3.67 percent flexural reinforcement. The horizontal reinforcement in the web section extended into the boundary sections, otherwise, no other confining steel was provided. The material properties of specimen B2 are listed in Table 8.4.

Table 8.4 B2 Material Properties

Zone	Concrete		Horizontal Reinforcement		Vertical Reinforcement	
	f'_c (MPa)	E_c (MPa)	ρ (%)	f_y (MPa)	ρ (%)	f_y (MPa)
Web	53.6	32700	0.63	532	0.29	532
Flanges	53.6	32700	0.63	532	3.67	410

Loading consisted of imposing two excursions of displacement to the top slab of the structure beginning at 50.8 mm (2 in.). Each load stage was incremented by 25.4 mm (1 in.). No external axial load was applied. Failure was observed during the first excursion to -125 mm (5 in.), and ultimately involved web crushing of the concrete near the base slab. Buckling of the reinforcement was also recorded during the first excursion to 76.2 mm (3 in.). The observed load-displacement response of the top slab of B2 is shown in Figure 8.26. The response is similar to that of B1; however, the loads at each displacement level are higher, and more pinching is evident in the hysteresis response.

The modeling of B2, for the purposes of conducting finite element analyses, was similar to the modeling of B1. The results using the linear and nonlinear cyclic models are illustrated in Figures 8.27 and 8.28.

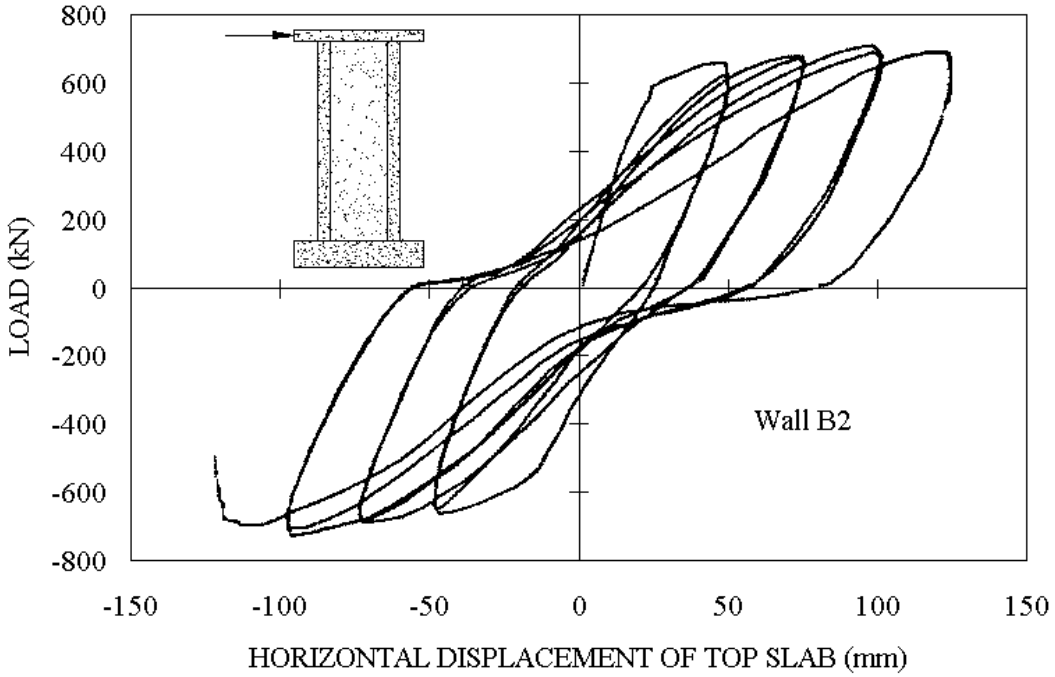

Figure 8.26 Load-Displacement Response of B2, taken from Oesterle, Fiorato, Johal, Carptenter, Russell, and Corley[30]

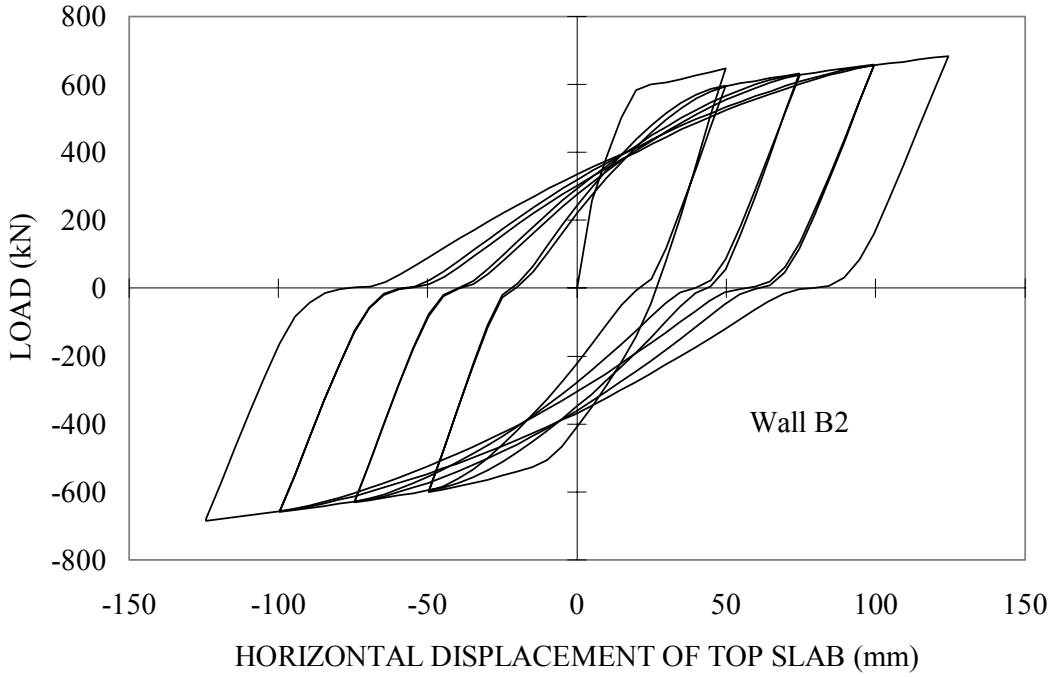

Figure 8.27 Calculated Response of B2 Using Linear Cyclic Models

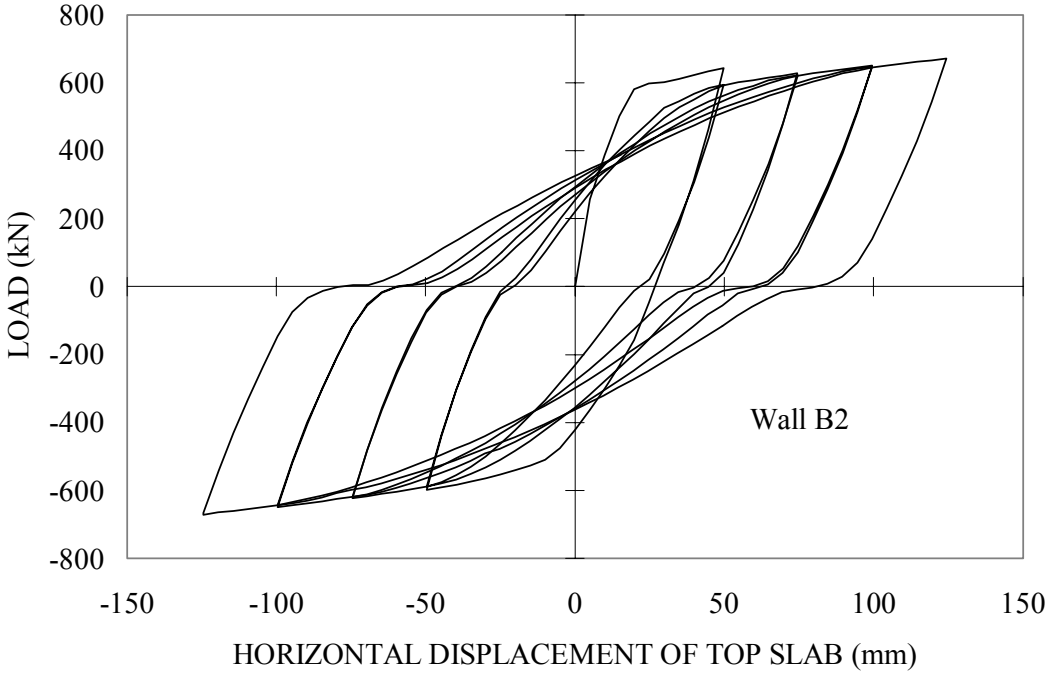

Figure 8.28 Calculated Response of B2 Using Nonlinear Cyclic Models

The analysis calculations using the linear and nonlinear cyclic models demonstrate similar behaviours. Yielding of the reinforcement, which is evident in the degree of energy dissipation through the hysteretic behaviour and in the near flat-top response, controls the response. Relative to the measured response, the analyses calculate the ultimate lateral resistance, residual displacements, pre-cracking and post-cracking stiffness, and energy dissipation reasonably well. The one notable discrepancy between the calculated and observed behaviours is the degree of pinching. Less noticeable is the slight underestimation of the degradation in the reloading stiffness of the second excursion of each displacement level.

The linear and nonlinear cyclic models, at 124.3 mm of lateral displacement, calculated loads of 683 kN and 671 kN, respectively. The measured maximum lateral

resistance was approximately 710 kN for B2 at 100 mm of displacement. The analytical-to-experimental lateral resistance ratios were 0.96 and 0.95, respectively. The analyses continued to record load with subsequent displacement, and no sudden failure was realized at 125 mm. The observed failure consisted of a sudden crushing of the concrete in the web, following buckling of the flexural reinforcement. At 125 mm of displacement, the analyses indicated that the web was experiencing extensive crushing over the bottom quarter rows of elements, that the vertical reinforcement was experiencing strains in excess of yield (20-fold larger) at the base over the bottom one-third rows of elements, and that the horizontal web reinforcement was yielding at one-third the height of the wall from the top of the base slab. Based on significant indicators from the analyses, the wall was failing due to concrete crushing in the web.

Test specimen B7 was similar to B2; however, it was tested under an applied axial stress of 3.77 MPa, and the boundary elements were reinforced with confining steel. The web wall was reinforced with 0.29 percent vertical reinforcement and 0.63 percent horizontal reinforcement. The boundary elements, at the sides of the web section, contained 3.67 percent flexural reinforcement and 1.35 percent confining steel. The material properties of specimen B7 are listed in Table 8.5.

B7 was subjected to horizontal cyclic displacements applied to the top slab. Loading consisted of two excursions to a pre-determined displacement level beginning at 12.7 mm (1/2 in.). The second load stage consisted of an imposed lateral displacement of 25.4 mm, after which displacements were incremented by 25.4 mm until failure. An imposed axial load of 3.77 MPa, applied to the top slab, was present throughout the course of testing. Failure was reported as web crushing occurring during + 150 mm (6

in.) displacement, following yielding of the flexural reinforcement. The load-displacement experimental response of B7 is shown in Figure 8.29.

Table 8.5 B7 Material Properties

Zone	Concrete		Horizontal Reinforcement		Vertical Reinforcement		Confining Reinforcement	
	f'_c (MPa)	E_c (MPa)	ρ (%)	f_y (MPa)	ρ (%)	f_y (MPa)	ρ (%)	f_y (MPa)
Web	49.3	30100	0.63	489	0.29	489	-	-
Flanges	49.3	30100	0.63	489	3.67	457	1.35	489

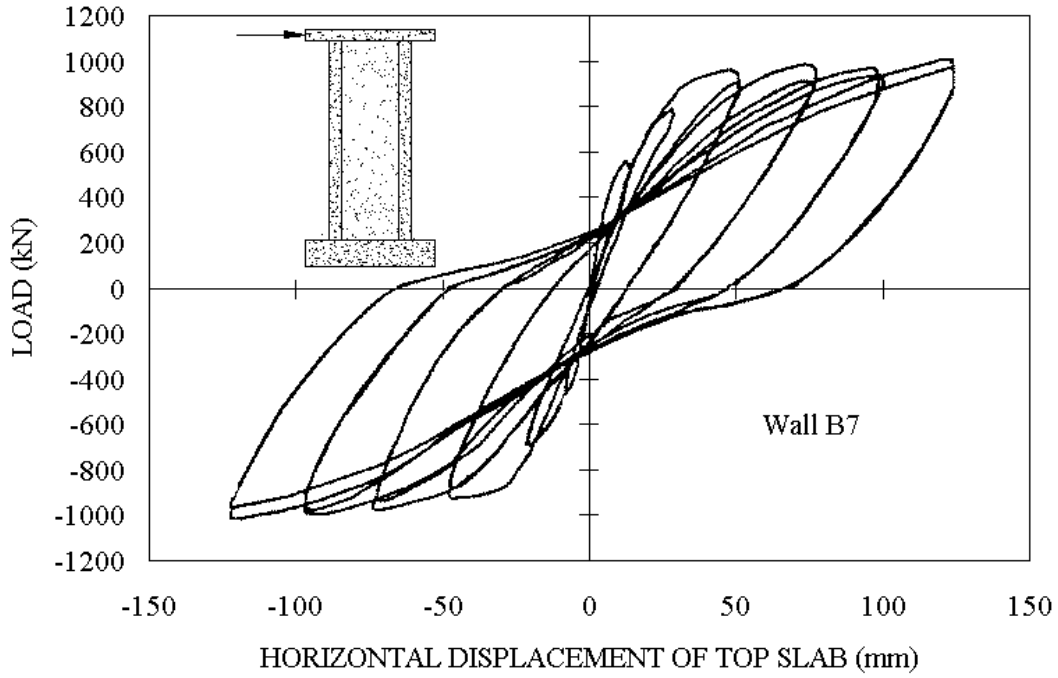

Figure 8.29 Load-Displacement Response of B7, taken from Oesterle, Fiorato, Johal, Carptenter, Russell, and Corley[30]

The inclusion of an applied axial load and confining steel in the boundary elements resulted in an increase of approximately 44 percent in terms of lateral load resistance in comparison to B2. Specimen B7 contained confining steel; otherwise it was reinforced identical to B2. The observed response demonstrates well-rounded hysteresis loops with significant residual deformations and energy dissipation, typical of flexure-dominant behaviour. The lateral load-displacement behaviour calculated by the linear and nonlinear cyclic models are shown in Figures 8.30 and 8.31, respectively. The applied axial was applied to the top slab using force control.

Similar to the previous calculations, the analytical behaviours of the linear and nonlinear cyclic models are nearly identical, and yielding of the reinforcement controls the responses. Apparently, altering the unloading/reloading models for concrete does not have a significant affect on the load-displacement response of slender walls dominated by flexural mechanisms. The calculated behaviours simulate reasonably well the ultimate lateral resistance, pre-cracking and post-cracking stiffness, and energy dissipation. Notable discrepancies between the calculated and observed behaviour include the degree of pinching at the end of unloading and the calculated residual deformations. However, in comparison to the analyses of B1 and B2, the pinching of B7 is better calculated. Also, there seems to be a slight underestimation of the degradation in the reloading stiffness of the second excursion of each displacement level.

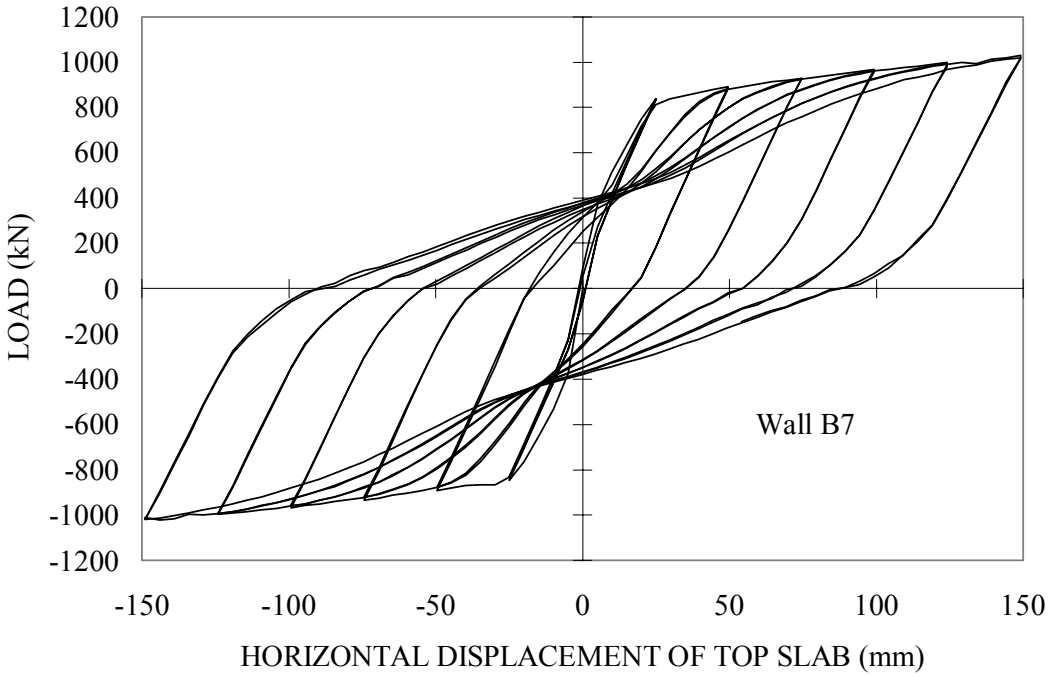

Figure 8.30 Calculated Response of B7 Using Linear Cyclic Models

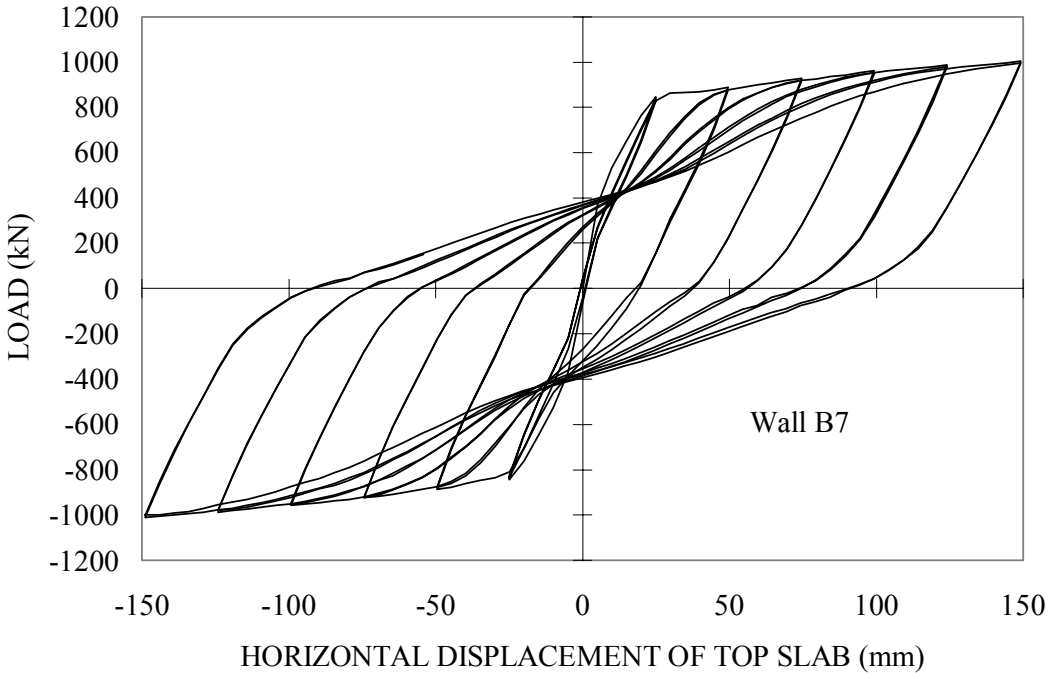

Figure 8.31 Calculated Response of B7 Using Nonlinear Cyclic Models

In terms of calculated lateral resistance, the linear and nonlinear cyclic model analysis recorded loads of 977 kN and 993 kN, in comparison to 1025 kN observed in the test. The resulting analytical-to-experimental resistance ratios were approximately 0.97 and 0.95 at 125 mm of displacement, respectively. The finite element analyses did not capture a sudden failure of the web during 150 mm of displacement as observed; however, the hysteresis loops did became unstable at this displacement level, and the indicators from the finite element model were pointing to significant damage throughout the structure. The bottom quarter of wall elements was indicating crushing of the concrete, and yielding of the vertical reinforcement was spread over the bottom one-third of the wall. Yielding of the horizontal reinforcement was also apparent throughout the web. Essentially, wall B7 failed due to crushing of the concrete in the web.

The final PCA wall structure investigated was B8, which was similar to B7 in terms of loading, but was reinforced with significantly more web horizontal reinforcement. The web wall contained 0.29 percent vertical reinforcement and 1.38 percent horizontal reinforcement. The boundary elements were reinforced with 3.67 percent flexural reinforcement and 1.35 percent confining steel. The material properties are listed in Table 8.6.

The loading regime was similar to that used for specimen B7. Failure for B8 was observed during 150 mm of lateral top slab displacement and was reported as web crushing. The experimental load-displacement behaviour is shown in Figure 8.32 and demonstrates a flexure-dominant response similar to the previous test specimens investigated. Figures 8.33 and 8.34 contain the analysis calculations using the linear and nonlinear cyclic models for concrete, respectively.

Table 8.6 B8 Material Properties

Zone	Concrete		Horizontal Reinforcement		Vertical Reinforcement		Confining Reinforcement	
	f'_c (MPa)	E_c (MPa)	ρ (%)	f_y (MPa)	ρ (%)	f_y (MPa)	ρ (%)	f_y (MPa)
Web	42.1	25600	1.38	489	0.29	455	-	-
Flanges	42.1	25600	1.38	489	3.67	448	1.35	455

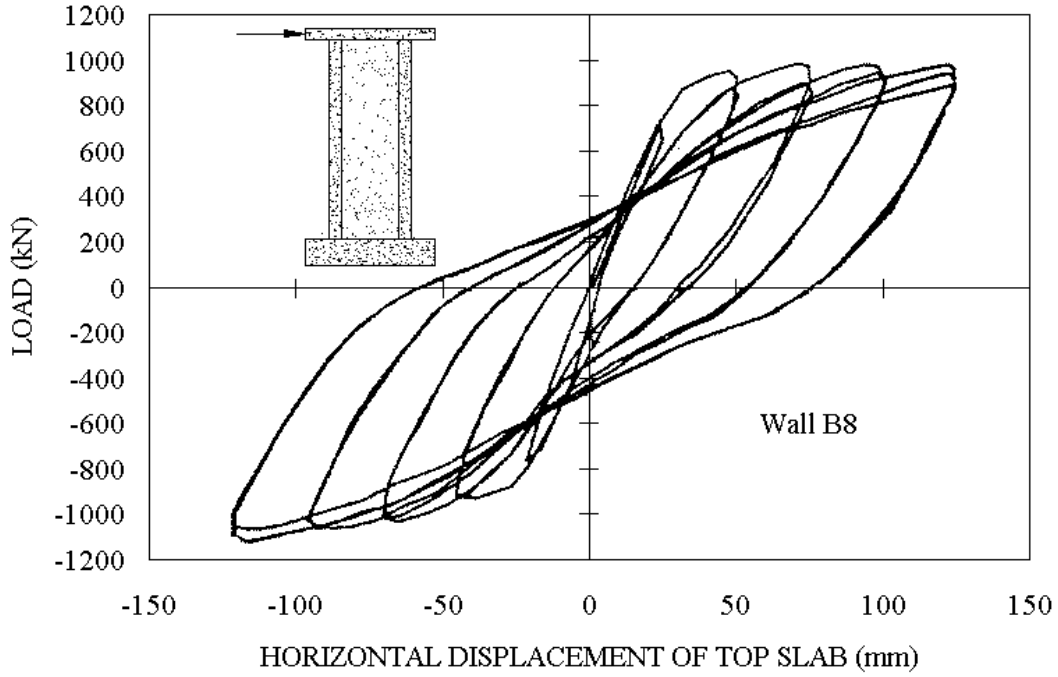

Figure 8.32 Load-Displacement Response of B8, taken from Oesterle, Fiorato, Johal, Carptenter, Russell, and Corley[30]

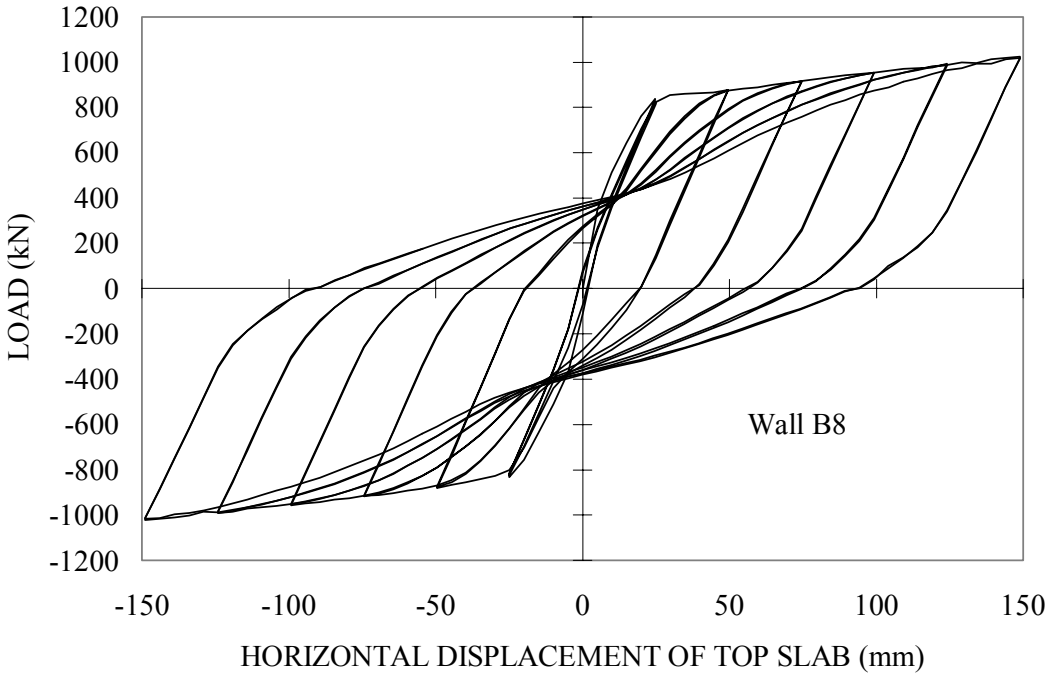

Figure 8.33 Calculated Response of B8 Using Linear Cyclic Models

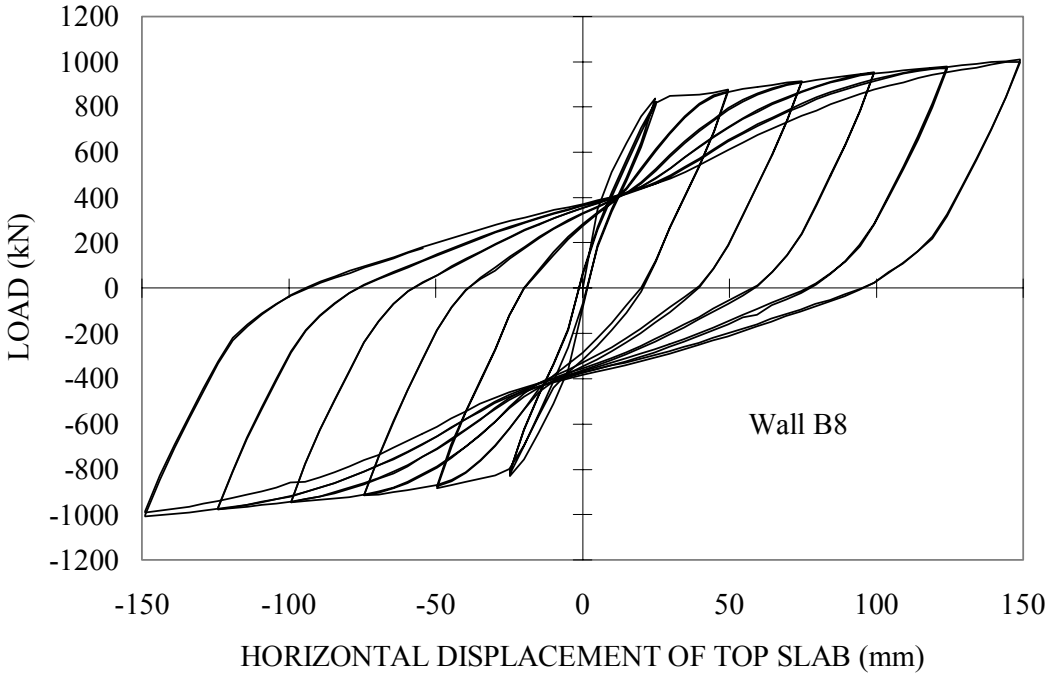

Figure 8.34 Calculated Response of B8 Using Nonlinear Cyclic Models

The finite element modeling of B8 using the linear and nonlinear cyclic models provides accurate results including: the ultimate resistance, pre-cracking and post-cracking stiffness, and the energy dissipation through hysteresis. However, some notable discrepancies do exist between the observed and calculated behaviours. These include the amount of pinching and the residual displacements. Less evident is the slight underestimation of the degradation in the reloading stiffness of the second excursion of each displacement level.

Lateral resistances of 993 kN and 980 kN were recorded by the finite element analyses for the linear and nonlinear cyclic models at 125 mm. The observed lateral resistance at +125 mm was 960 kN; the resulting analytical-to-experimental ratios were 1.03 and 1.02, respectively. Failure of wall B8, although not sudden in the analyses, seemed to occur during 150 mm as the hysteresis loops became unstable. At that point, the lower portion of the web wall and boundary elements had experienced crushing, and the bottom one-third of the wall was experiencing yielding of the vertical reinforcement. No strains in excess of yielding were calculated for the horizontal reinforcement. Essentially, wall B8 failed due to web crushing.

The analyses of the PCA series of structural walls have long been considered benchmarks against which theoretical calculations can be calibrated. However, this series of walls are dominated by flexural mechanisms, thus, the response is significantly controlled by yielding of the reinforcement. Therefore, the overall behaviour is marginally affected by the choice of a linear or nonlinear cyclic model for the concrete. The calculated responses for all cases were accurately simulated as expected. The model for the reinforcement is one that is commonly accepted amongst researchers and is well

understood. To better test the constitutive relations of the concrete, squat shear walls more heavily influenced by shear related mechanisms must be investigated. The response of squat shear walls are significantly influenced by the concrete, and these types of walls will be discussed in more detail in subsequent sections.

8.5.2 SW Shear Walls

Pilakoutas and Elnashai[31] conducted an extensive static cyclic experimental program on walls of 1:2.5 scale. The SW specimens were tested as isolated cantilever walls. The horizontal load was applied through a top beam, which was intended to spread the load onto the wall panel. The walls of test specimens SW4 through SW9 were rectangular, and were 1200 mm in height, 600 mm in length and 60 mm thick. Figure 8.35 shows the typical dimensional details of the test specimens. The walls also contained concealed columns at the ends of the wall, and Figure 8.36 illustrates a typical reinforcement pattern.

Loading of the walls was chosen to represent the extreme conditions experienced during a severe earthquake, where a large number of load reversals are expected at the lower displacement levels, increasing with increased displacements. An initial test by Elnashai, Pilakoutas, and Ambraseys[41], on a wall exposed to 10 cycles per displacement level, revealed that insignificant deterioration occurs after the second excursion up to yield. Owing to this, it was decided that a loading regime of two cycles at each displacement level be imposed to failure. The displacement level was incremented by 2 mm. Test specimens SW4-SW9 were tested under static conditions, and SW4-SW6 were chosen for this study.

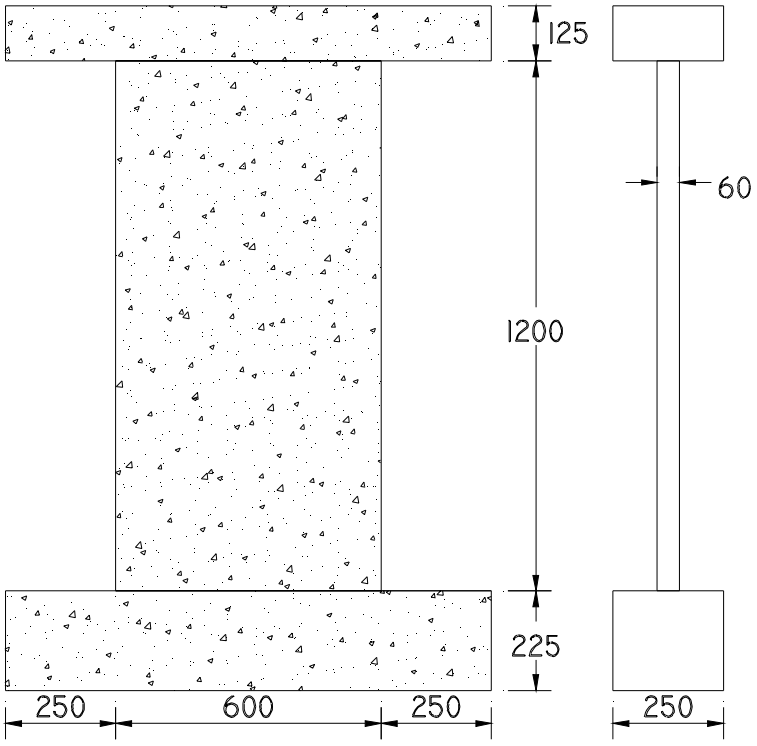

Figure 8.35 Details of SW Walls

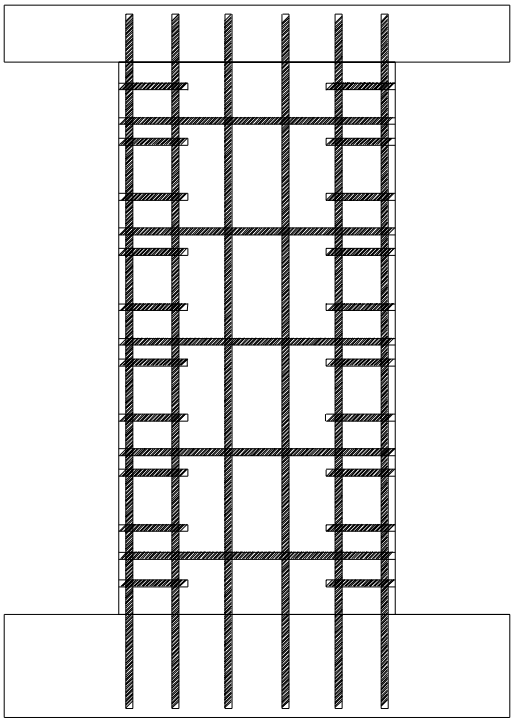

Figure 8.36 Typical Reinforcement Layout of SW Walls

Test specimen SW4 provides a test where significant yielding of the flexural reinforcement preceded failure by concrete crushing. SW4 contained 0.39 percent horizontal reinforcement and 0.50 percent vertical reinforcement. The latter was calculated over the web portion of the wall section, net of the 110 mm width boundary elements located at the ends of the wall. The boundary elements were reinforced with 6.86 percent flexural reinforcement, and 0.79 percent confining steel as a percentage of the vertical wall section. The material properties of SW4 are listed in Table 8.7.

Table 8.7 SW4 Material Properties

Zone	Concrete		Horizontal Reinforcement		Vertical Reinforcement		Confining Reinforcement	
	f'_c (MPa)	E_c (MPa)	ρ (%)	f_y (MPa)	ρ (%)	f_y (MPa)	ρ (%)	f_y (MPa)
Web	37.0	35240	0.39	545	0.50	545	-	-
Boundary	37.0	35240	0.79	545	6.86	470	0.43	545

The observed load-deformation response of SW4 is shown in Figure 8.37. The ultimate capacity of the wall was realized at 10 mm of displacement, and failure eventually occurred by concrete crushing at 24 mm of displacement, after significant out-of-plane displacement, but without much deterioration in strength. The flat-top response indicates that the post-peak response was dominated by yielding of the flexural reinforcement. Crushing of the concrete was generally confined to the lower portions of the boundary elements.

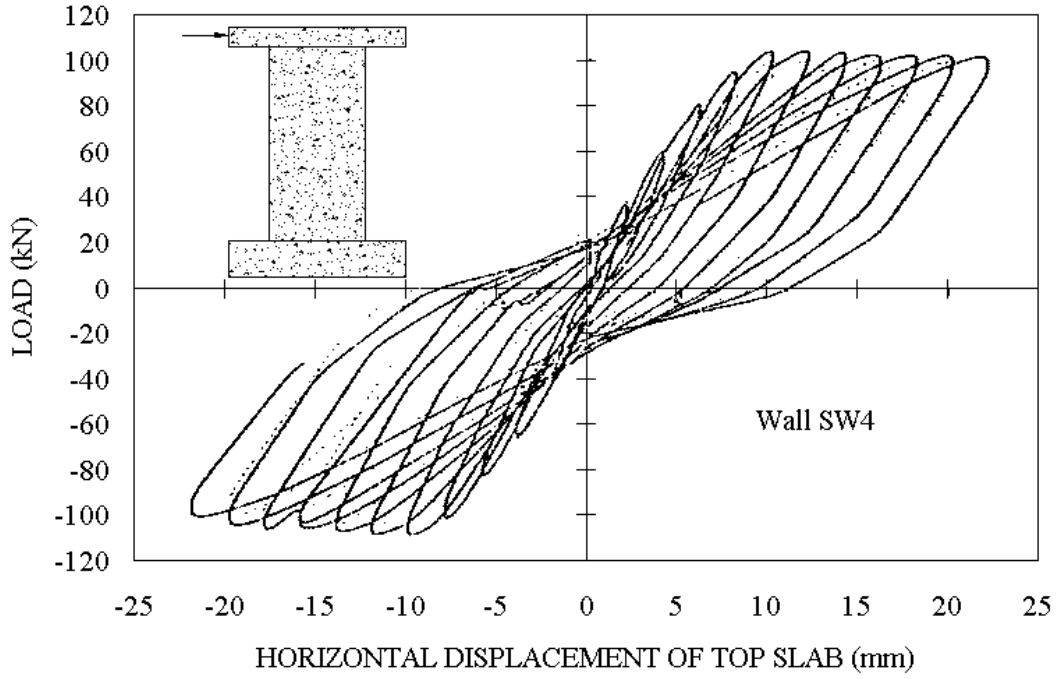

Figure 8.37 Load-Displacement Response of SW4, taken from Elnashai, Pilakoutas, and Ambraseys[41]

Finite element analyses were conducted on the SW series of walls using the linear and nonlinear cyclic models for concrete. The finite element mesh, shown in Figure 8.38, contained 117 constant strain rectangular elements. The mesh was divided into a web zone, a boundary element zone, and a top slab zone. The base slab was omitted, and the wall was assumed fully fixed at the base. Cyclic displacements were imposed at the top nodal joint of the slab section in increments of 2 mm, with two excursions per displacement level. Loading was incremented by 1.0 mm for displacement levels between 0 to 10 mm, and 2.0 mm thereafter. The analyses were performed using displacement control. The calculated load-displacement results using the linear and nonlinear cyclic models are shown in Figures 8.39 and 8.40.

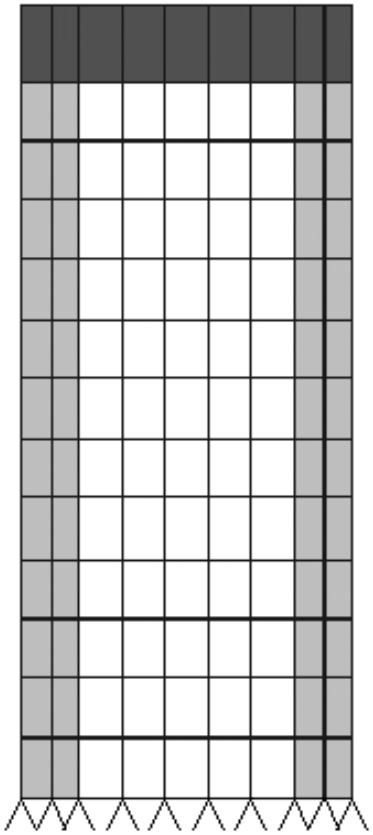

Figure 8.38 Finite Element Mesh for SW Series of Walls

In comparison to the observed behaviour, the analyses using the linear and nonlinear cyclic models provide reasonable simulations of the actual behaviour. The hysteresis loops, residual displacements, pinching, and flat-top response beyond 8 mm of displacement are all calculated well. The analyses are, however, deficient in accurately modeling the reloading stiffness; a stiffer response than that measured during testing was calculated. Peak loads of 101.4 kN for the linear cyclic model during loading to 16 mm, and 100 kN for the nonlinear cyclic model during loading to 10 mm were calculated. The observed ultimate resistance was 104.0 kN, corresponding to a displacement of 10 mm. The analytical-to-experimental ratios were 0.98 and 0.96, respectively.

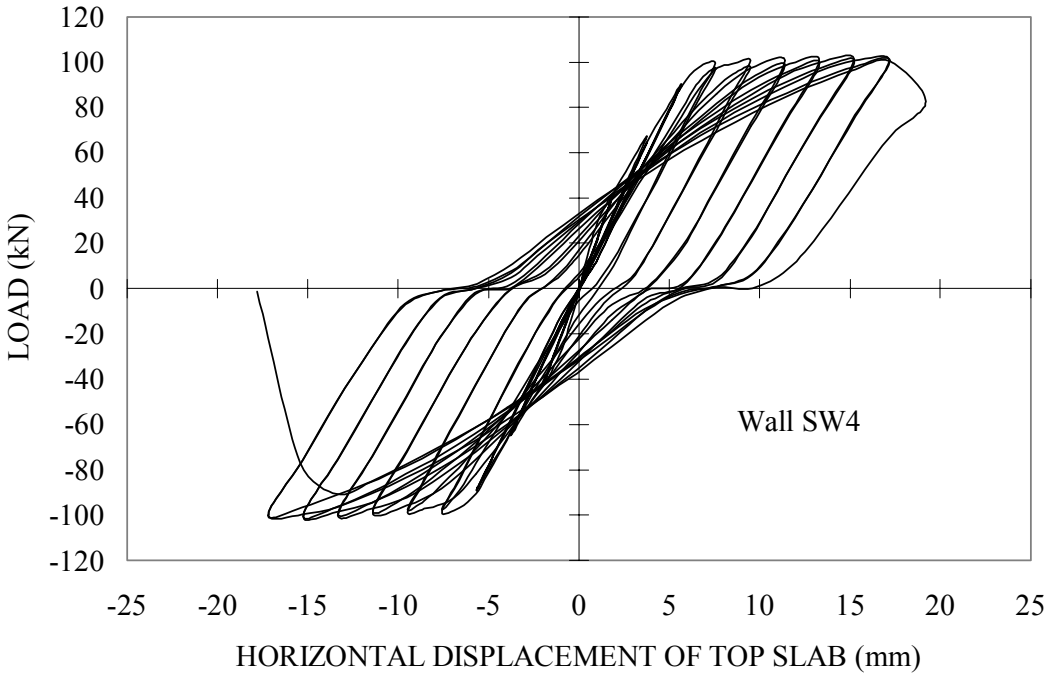

Figure 8.39 Calculated Response of SW4 Using Linear Cyclic Models

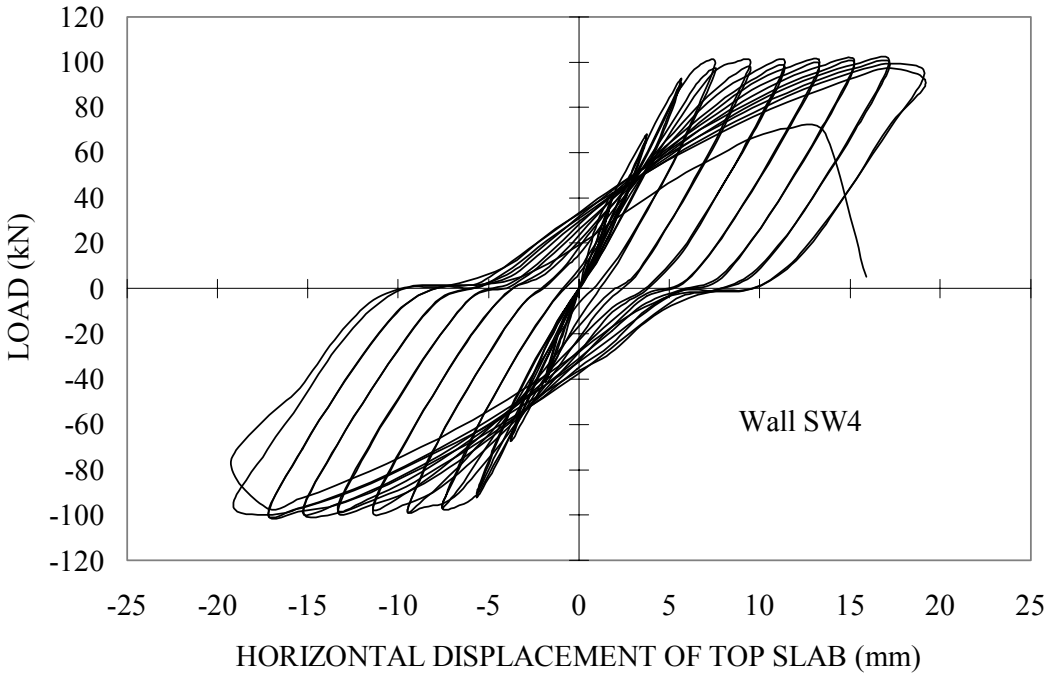

Figure 8.40 Calculated Response of SW4 Using Nonlinear Cyclic Models

The results using the nonlinear cyclic model calculated failure to occur during the first excursion to 22 mm of displacement by crushing of the concrete at the boundary elements, followed by the formation of a sliding shear plane near the base. A similar failure mechanism was obtained using the linear cyclic model; however, it was calculated to occur during the first excursion to –20 mm of displacement. In both cases, significant yielding of the flexural reinforcement preceded crushing of the concrete. The nonlinear cyclic model retained more lateral resistance near failure. Similar to the PCA series of walls, yielding of the reinforcement controlled the observed response, and failure was eventually governed by concrete crushing.

Specimen SW5 differed somewhat from SW4 in terms of reinforcement layout, and the boundary elements were reduced to 60 mm in width at each end of the wall. A large portion of the flexural reinforcement was concentrated at the extreme fibres, and only the bottom half of the boundary elements contained confining steel. Table 8.8 lists the material properties and reinforcement ratios.

The wall was subjected to two excursions per displacement level up to 8 mm. At 10 mm displacement, the wall experienced a significant loss of load carrying capacity, and it was decided to impose one excursion per displacement level beginning at 10 mm until the end of testing. Displacements were incremented by 2 mm up to 12 mm of displacements, after which displacements were increased by 2 mm in each direction of loading. Figure 8.41 shows the observed load-displacement response for SW5.

Table 8.8 SW5 Material Properties

Zone	Concrete		Horizontal Reinforcement		Vertical Reinforcement		Confining Reinforcement	
	f'_c (MPa)	E_c (MPa)	ρ (%)	f_y (MPa)	ρ (%)	f_y (MPa)	ρ (%)	f_y (MPa)
Web	31.8	27820	0.31	400	0.59	545	-	-
Boundary	31.8	27820	0.31/0.66*	400	12.5	535	0.0/0.35*	400

*** represents the reinforcement in the bottom half of the boundary elements**

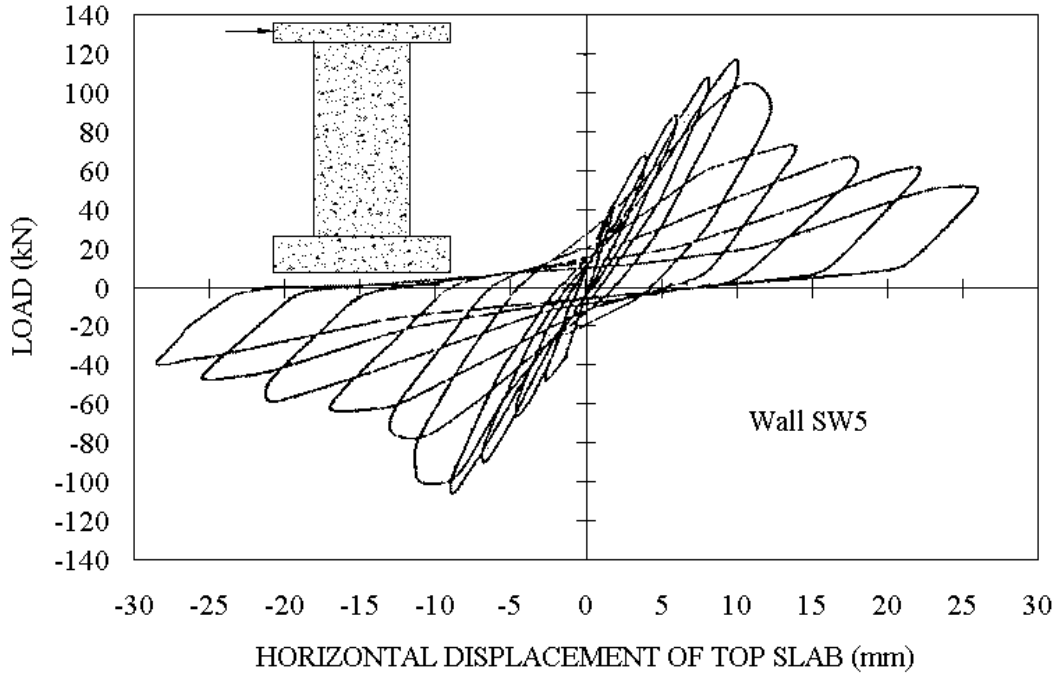

Figure 8.41 Load-Displacement Response of SW5, taken from Elnashai, Pilakoutas, and Ambraseys[41]

Failure was found to occur at the onset of opening of the main web cracks that extended into the compressive zone at 10 mm of displacement. Prior to failure, yielding

of the horizontal web reinforcement, followed by yielding of flexural reinforcement, was observed. Considerable horizontal expansion of the wall section was evident after 10 mm of displacement. The structure demonstrated a post-peak response, but the lateral resistance was significantly impaired beyond the peak load stage of 10 mm. Results of the finite element analyses are shown in Figures 8.42 and 8.43. Loading increments of 1.0 mm were imposed to the top slab up to 12 mm, after which the increments were increased to 2 mm. Calculating the expansion in the web wall of SW5, which significantly affected the actual behaviour, provides a challenge to the analysis.

The responses using the linear and nonlinear cyclic models calculated similar load-displacement behaviours. Maximum loads were attained during loading to 10 mm of displacements and were 122.5 kN and 123.6 kN for the linear and nonlinear cyclic models, respectively. The observed maximum lateral resistance was 117.3 kN, resulting in analytical-to-experimental strength ratios of 1.04 and 1.05, respectively, for responses of the linear and nonlinear cyclic models. The failure mechanisms were also similar to that observed. In the analyses, at failure the wall experienced significant horizontal expansion as a result of yielding of the horizontal web reinforcement, and crushing of the concrete was also evident near the compression toes. After extensive expansion, a sliding shear plane formed near the base of the wall. Yielding of the flexural reinforcement was also calculated, but only after the web horizontal reinforcement had yielded. The general behaviours simulated the experimental results reasonably well up to the peak load; however, the post-peak response was not well calculated. Failure in both analyses occurred suddenly during loading to 18 mm of displacement. The observed behaviour was able to sustain some lateral resistance up to 26 mm of displacement.

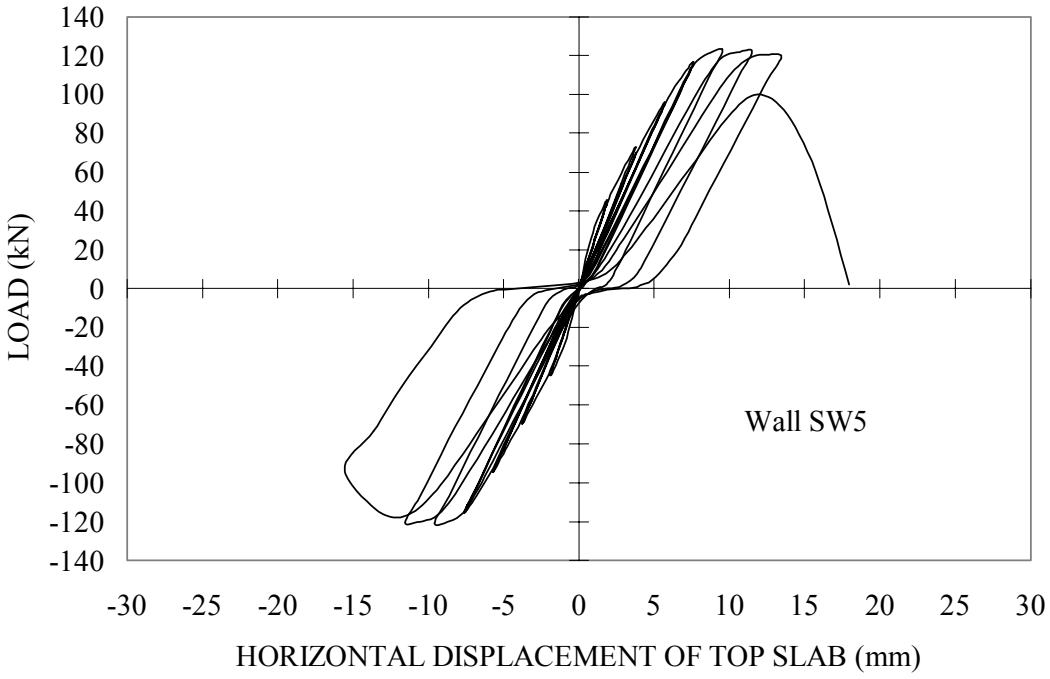

Figure 8.42 Calculated Response of SW5 Using Linear Cyclic Models

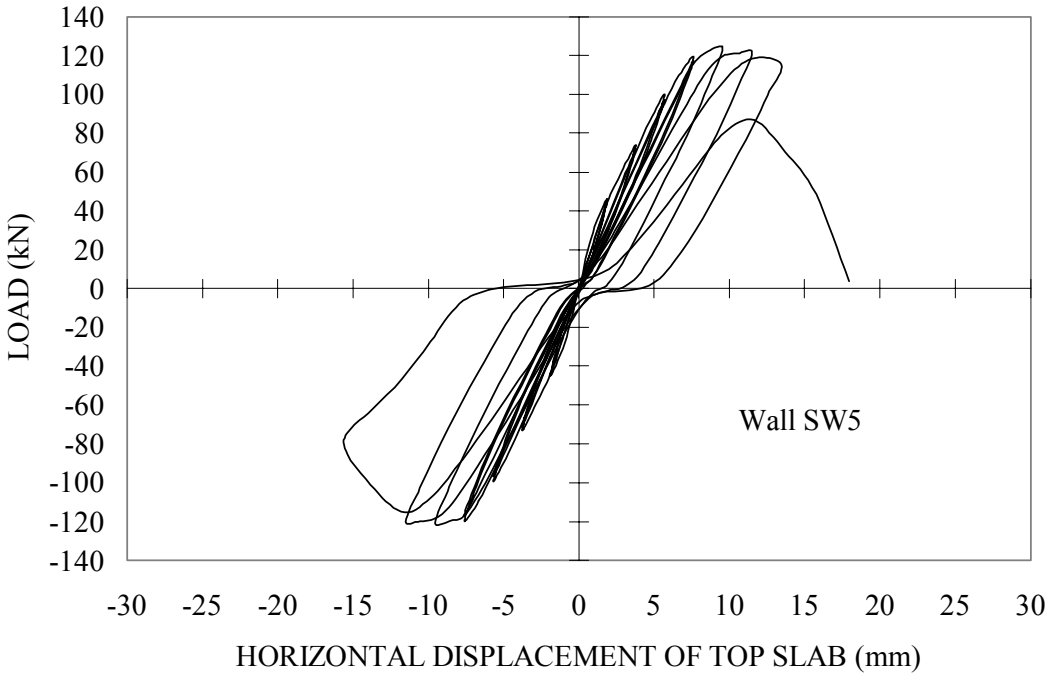

Figure 8.43 Calculated Response of SW5 Using Nonlinear Cyclic Models

Capturing a post-peak response, where a significant loss of capacity occurs, in a finite element analysis is a challenging task. As elements begin to experience crushing, adjacent elements are quick to degrade and failure follows soon after. Whereas in a laboratory setting, where the loading conditions can be controlled, a structure can be cycled well into the post-peak range even after significant damage has occurred. The plain reinforcement used as shear reinforcement is another possible cause of discrepancy between the analyses and the observed behaviour. The shear reinforcement experienced significant yielding, and contributed to the horizontal expansion of the wall. Properly accounting for the loss of bond, which is more severe in plain bars than deformed bars especially under repeated load, is crucial. The initial gradual loss of lateral resistance may be attributable to the loss of bond in the plain reinforcement. The analyses assumed all bars to be deformed and perfectly bonded to the concrete.

Test specimen SW6 was similar to SW4, except it contained less shear reinforcement, and confining reinforcement was concentrated in the bottom half of the boundary elements. Plain reinforcing bars were used in SW6 as shear reinforcement compared to deformed bars in SW4, which may partly account for the difference in behaviour. Material properties for SW6 are listed in Table 8.9 and the observed load-deformation response is given in Figure 8.44. The rounded response seems more influenced by the concrete and should provide a better test for the unloading/reloading models assumed for the concrete.

Table 8.9 SW6 Material Properties

Zone	Concrete		Horizontal Reinforcement		Vertical Reinforcement		Confining Reinforcement	
	f'_c (MPa)	E_c (MPa)	ρ (%)	f_y (MPa)	ρ (%)	f_y (MPa)	ρ (%)	f_y (MPa)
Web	38.6	36075	0.31	400	0.50	545	-	-
Boundary	38.6	36075	0.31/0.66*	400	6.86	470	0.0/0.19*	400

*** represents the reinforcement in the bottom half of the boundary elements**

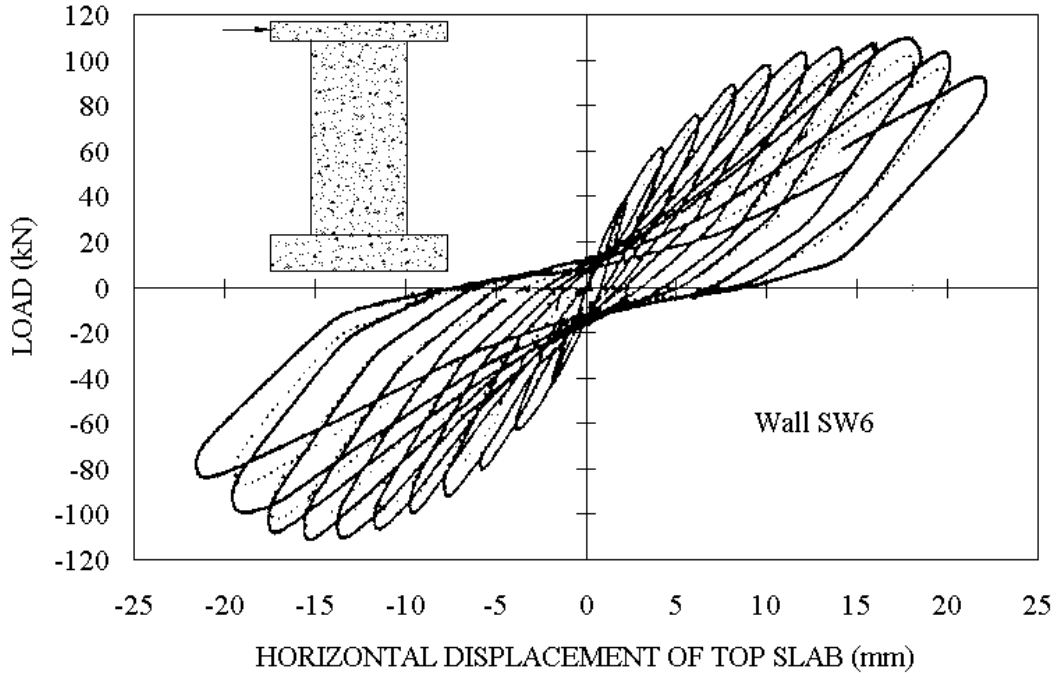

Figure 8.44 Load-Displacement Response of SW6, taken from Elnashai, Pilakoutas, and Ambraseys[41]

SW6 was exposed to two excursions per displacement level up to 22 mm of displacement. Failure was reported to have occurred during 22 mm of displacement by

opening of the diagonal cracks. Yielding of the flexural reinforcement and crushing of the concrete in the compressive zones were evident prior to failure. The ultimate lateral resistance was realized at 18 mm of top slab displacement.

The analysis predictions are shown in Figures 8.45 and 8.46 for the linear and nonlinear cyclic models, respectively. The analyses demonstrate only subtle differences in the load-displacement behaviours. They include slightly more pinching and more strength degradation in the post-peak range for the nonlinear cyclic model; otherwise, the overall responses are similar. Ultimate capacities of 102 kN and 101.8 kN were calculated using the linear and nonlinear cyclic models, respectively, compared to the observed resistance of 107.8 kN. This corresponded to analytical-to-experimental strength ratios of 0.95 and 0.94, respectively. The peak loads were calculated to occur during loading to 16 mm of displacement using the linear cyclic model and to 10 mm displacement using the nonlinear cyclic model. The actual displacement at peak resistance occurred during loading to 18 mm of displacement. This is not to suggest that the calculated displacements are grossly in error. The calculated behaviours both assumed a near flat-top response, and very little difference in loads was calculated for displacements in the 10 to 20 mm range.

A failure mechanism similar to that observed was calculated by the analyses and involved a sliding shear plane near the base slab. Prior to failure, crushing of the concrete was evident in the compressive toes of the walls, along with yielding of the flexural and web horizontal reinforcement. The wall had also experienced significant horizontal expansion just prior to failure.

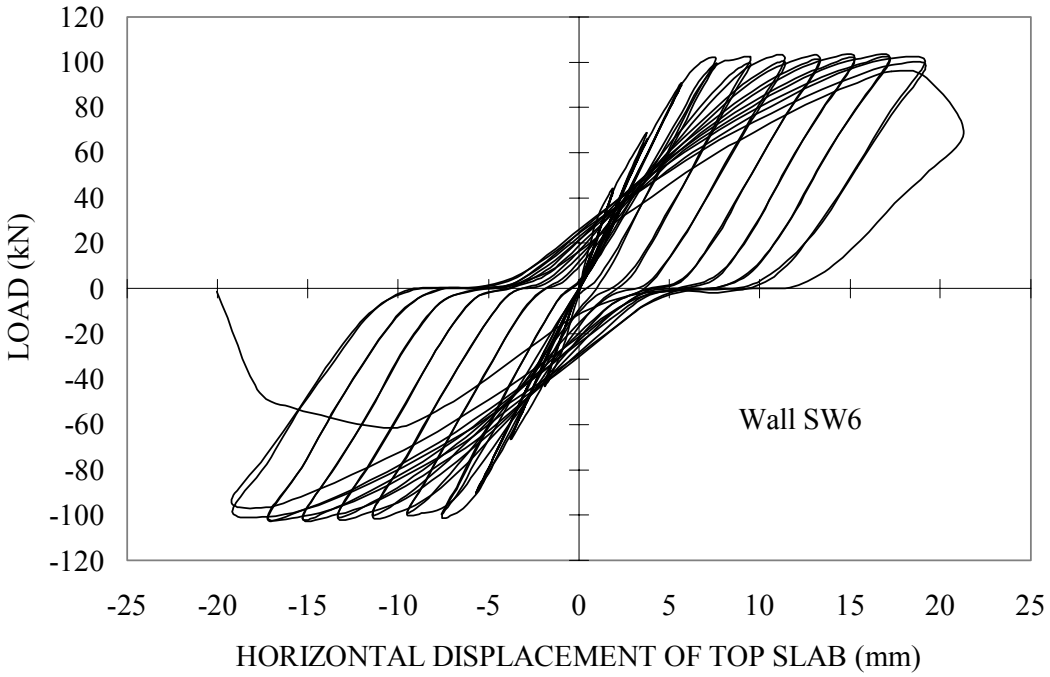

Figure 8.45 Calculated Response of SW6 Using Linear Cyclic Models

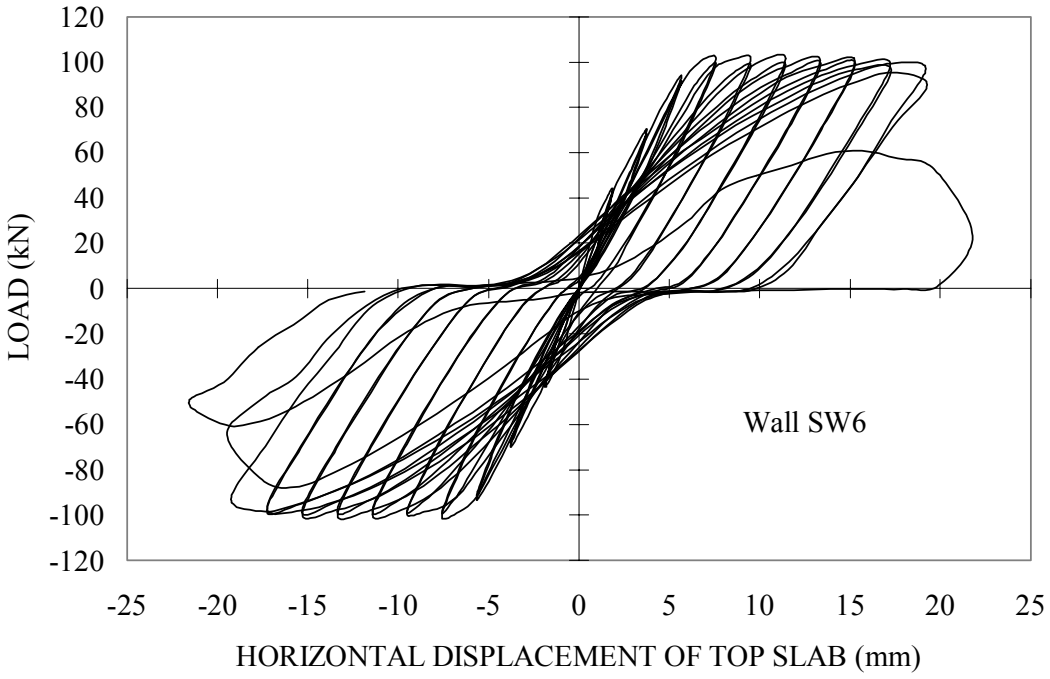

Figure 8.46 Calculated Response of SW6 Using Nonlinear Cyclic Models

The actual overall behaviour appears to have been significantly affected by the concrete response, as is evident by the rounded response. Although failure in the analyses involved crushing of the concrete, the overall behaviours were significantly affected by yielding of the reinforcement, as is evident by the near flat-top behaviour. The initial stiffer response of the analyses is a result of overestimating the strains in the longitudinal reinforcement. Accounting for crack shear-slip should address this problem. Slip along the cracks increases the strains in the transverse reinforcement, while reducing the strains in the longitudinal reinforcement. Added to this is the potential for bond slip of the plain bars for shear reinforcement at higher load stages, which is not accounted for in the analyses. The plain bars were susceptible to bond slip, as the strains experienced were well beyond yield. Slip of the reinforcement would also cause further expansion of the wall diagonal cracks, causing a larger horizontal expansion in the web wall, and in turn, increasing the compression softening effect of concrete.

As with the PCA series of walls, the choice of linear or nonlinear unloading/reloading rules for concrete did not seem to affect the overall wall behaviour when examining the SW series of walls. The analyses, to this point, have focused on structures where yielding of the reinforcement dominates the behaviour. Thus, the hysteresis response of the concrete, whether modeled as linear or nonlinear with decay, has no significant impact. To more clearly demonstrate the differences between the concrete models, analyses on the DP series of walls follows, where the observed responses were dominated by the extensive crushing of the concrete in the web wall.

8.5.3 DP Shear Walls

An objective of this research project was to complement current data readily available in the literature with data from squat shear walls more heavily influenced by shear related mechanisms. Such mechanisms place more demand on the concrete, and failure is quite often associated with shear crushing of the concrete. These types of walls are bested suited to corroborate constitutive models for concrete subjected to cyclic loading. Details of DP1 and DP2 are reviewed in Chapter 4. Tables 8.10 and 8.11 contain some of the material properties used in the finite element analyses for DP1 and DP2, respectively.

Table 8.10 DP1 Material Properties

Zone	Concrete		Horizontal Reinforcement		Vertical Reinforcement	
	f'_c (MPa)	E_c (MPa)	ρ (%)	f_y (MPa)	ρ (%)	f_y (MPa)
Web	21.7	25900	0.74	605	0.79	605
Flanges	21.7	25900	0.58	605	0.63/0.23*	605
Top Slab	43.9	43700	0.63	550	0.37	550
Bottom Slab	34.7	36900	0.65	550	0.37	550

*** 0.23 % represents reinforcement in the flange tips**

Table 8.11 DP2 Material Properties

Zone	Concrete		Horizontal Reinforcement		Vertical Reinforcement	
	f'_c (MPa)	E_c (MPa)	ρ (%)	f_y (MPa)	ρ (%)	f_y (MPa)
Web	18.8	18580	0.74	605	0.79	605
Flanges	18.8	18580	0.58	605	0.63/0.23*	605
Top Slab	38.0	37570	0.63	550	0.37	550
Bottom Slab	34.7	36900	0.65	550	0.37	550

The finite element mesh, shown in Figure 8.47, consisted of 540 constant strain rectangular elements. Given that the finite elements used were low-powered, one must consider whether the mesh used was sufficiently fine. The mesh selected for the finite element analyses provided a compromise between being able to capture important phenomenon and the insignificant return of further refinement. Vecchio[42] conducted a parametric study on mesh size using the NUPEC shear wall U-1, which investigated improvements in behaviour with mesh refinement.

The mesh in Figure 8.47 was divided into four zones: the web wall, flange walls, and top and bottom slabs. The base slab was assumed fully fixed to the laboratory strong floor. Horizontal displacements were imposed on the second nodal joint from the top of the top slab, and the axial load was spread along the joints of the last two rows of the top slab directly above the walls. The full width of the flanges, assumed to be fully effective in contributing to the lateral load resistance, was concentrated into a single element in the

2-D model. Issues relating to three-dimensional behaviour arise when the flange walls are assumed fully effective in a 2-D analysis, and will these be discussed in detail later.

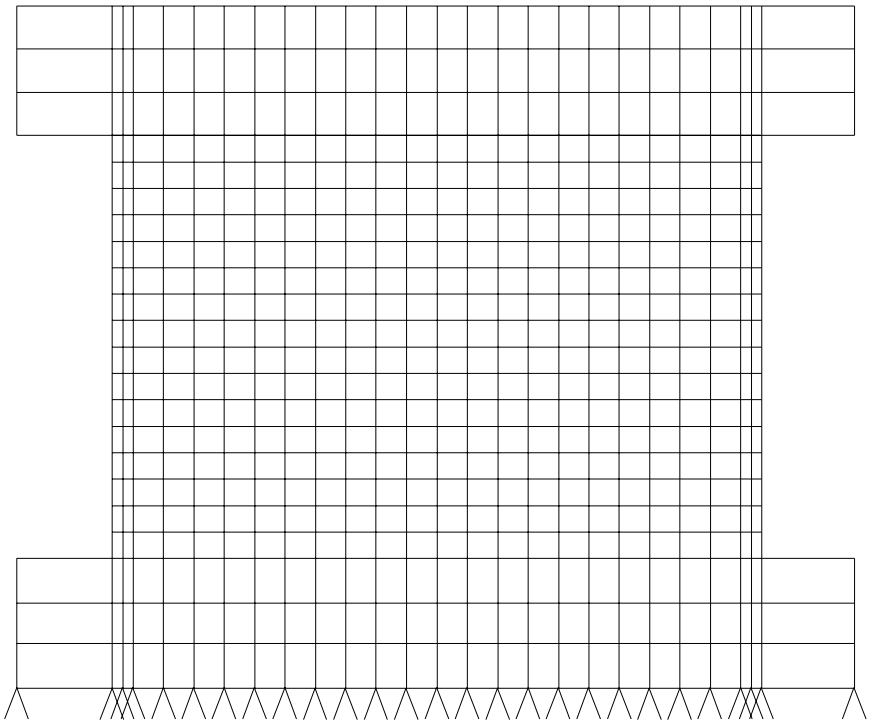

Figure 8.47 DP Finite Element Mesh

Displacements were incremented by 0.25 mm between 0 and 4 mm, by 0.50 mm between 5 and 7 mm, and by 1.0 mm from 8 mm to failure using displacement control. A shrinkage strain of -0.4×10^{-3} was applied first in the analysis to account for the delay in testing from the time of casting and was held constant throughout testing. [Shrinkage has the effect of causing tensile stresses in the concrete, which can lead to cracking, resulting in a reduction in the stiffness of the structure.] The axial load was applied to the structure during the second load stage using force control, followed by the cyclic displacements during the third load stage; the process being consistent with the actual loading sequence.

The experimental results of the lateral load versus the horizontal displacement of the top slab for DP1 are shown in Figure 8.48. The response, discussed in detail in

Chapters 5 and 6, is typical of shear-dominant behaviour. The hysteresis loops are highly pinched, and the energy dissipation is insignificant in comparison to that observed in walls with flexure-dominated responses. The latter is related to yielding of the reinforcement. Also evident in the behaviour is the degradation of the reloading stiffness during the second excursion for each displacement level, becoming more pronounced in the post-peak range.

The calculated responses for DP1 are shown in Figures 8.49 and 8.50 for the linear and nonlinear cyclic models, respectively.

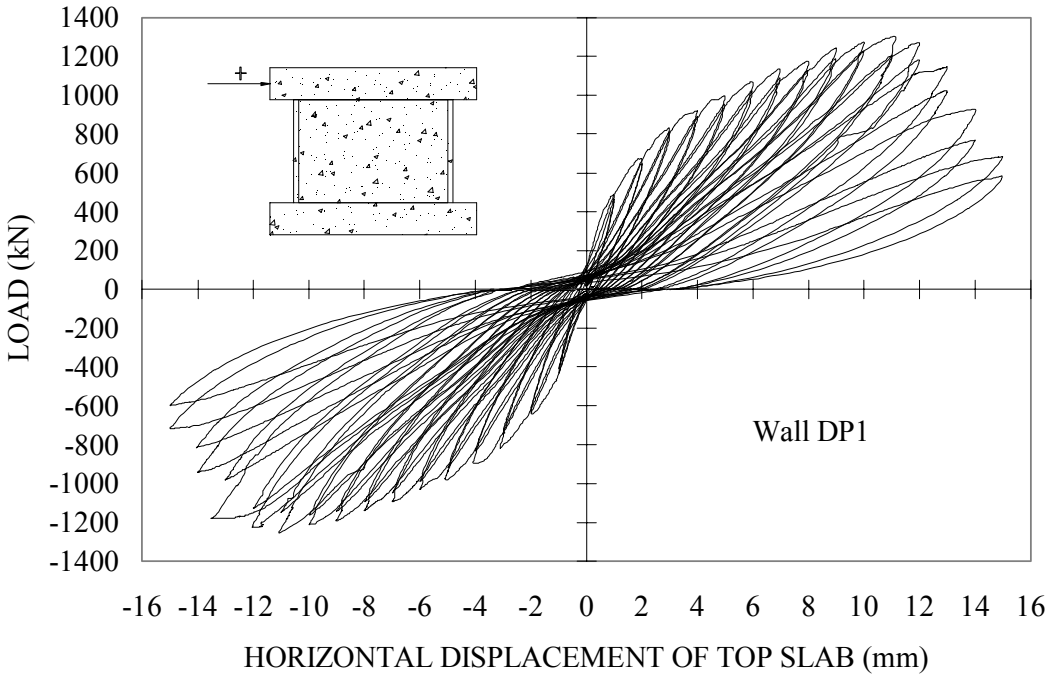

Figure 8.48 Experimental Load Displacement Response of DP1

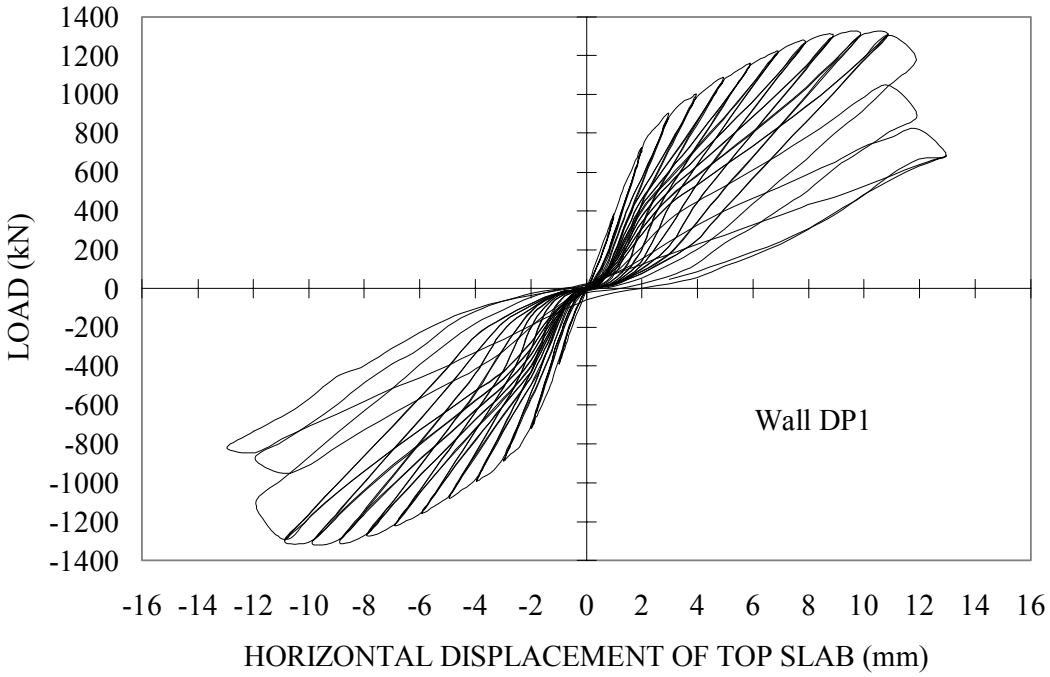

Figure 8.49 Calculated Response of DP1 Using Linear Cyclic Models

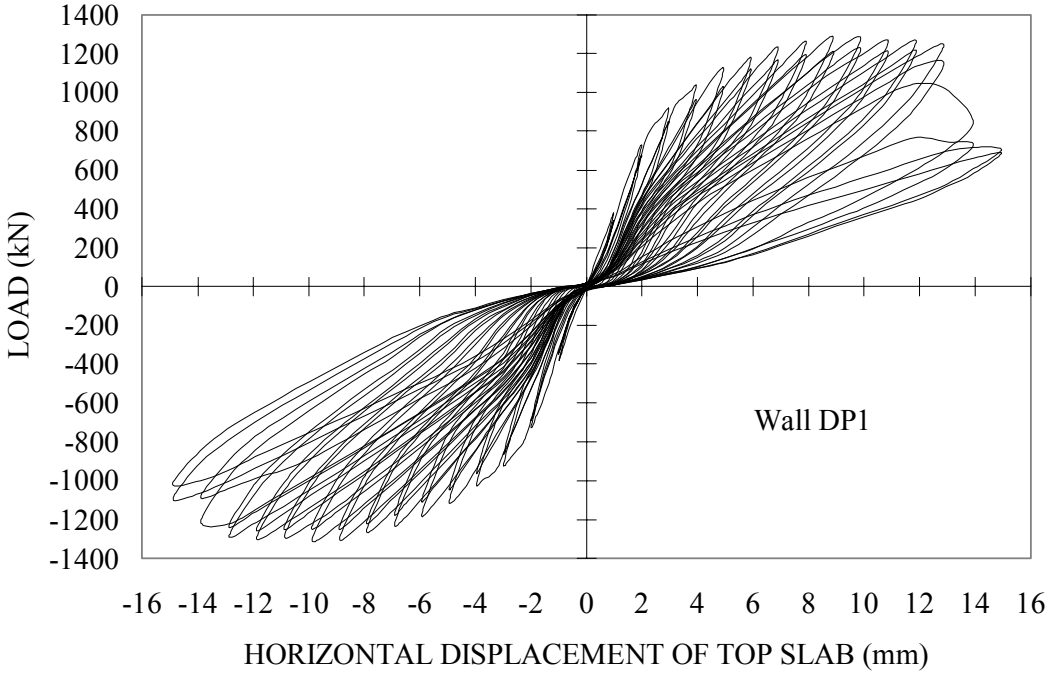

Figure 8.50 Calculated Response of DP1 Using Nonlinear Cyclic Models

The analyses using the linear and nonlinear cyclic models provide fairly accurate simulations of behaviour of specimen DP1. The ultimate lateral resistance, ductility, residual displacements, and energy dissipation through hysteresis are well calculated. The analysis using the nonlinear cyclic model does, however, demonstrate a better representation of the actual behaviour, including the post-peak response, the progressive degradation in the reloading stiffness, and the damage experienced during the second excursion of displacement. The second excursion to each displacement level produces a lateral resistance less than that resisted during the first excursion, which is consistent with the observed behaviour. The second excursion of reloading, for the linear cyclic model, calculates the same resistance as that experienced in the first excursion, thus neglecting the damage induced during reloading.

The calculated maximum loads and the corresponding displacements using the linear and nonlinear cyclic models, corresponding to the first excursion for the positive and negative directions of loading, are listed in Table 8.12.

Table 8.12 Analytical Results for DP1

Analysis	F_{exp}	F_{calc}	F_{calc}/F_{exp}	Δ_{exp}	Δ_{calc}	$\Delta_{calc}/\Delta_{exp}$
+ DP1-1	1298	1310	1.01	11.14	9.89	0.89
+ DP1-3	1298	1307	1.01	11.14	9.87	0.89
- DP1-1	-1255	1313	1.05	11.09	9.88	0.89
- DP1-3	-1255	1283	1.02	11.09	8.89	0.80

Note: 1 denotes linear model; 3 denotes nonlinear model
+ refers to positive direction; - refers to negative direction

The results indicate that the peak strength of the structure was calculated with more accuracy than the displacement at peak load. The overly stiff calculation of displacement at peak load is likely a consequence of modeling the full width of the flanges into the plane of the web.

Significant differences in the linear and nonlinear cyclic models are evident when comparing the failure mechanisms as shown in Figures 8.51 and 8.52, respectively, for the linear and nonlinear cyclic models. The failure mechanisms calculated by the linear cyclic model ultimately involved a sliding shear plane forming in the web wall near the base slab. Initially, crushing of the concrete was calculated in the web wall along the wall-flange intersection. The formation of the horizontal sliding plane first became evident at 12 mm displacement, which corresponded to a significant drop in lateral resistance of the wall. The initiation of sliding along the base caused yielding of the horizontal web reinforcement, followed by yielding of the flexural reinforcement in the flanges. No yielding of the vertical reinforcement in the web wall was calculated. However, as previously described, DP1 experienced six vertical slip planes spaced evenly along the web at the end of testing, and did not involve sliding shear along the base as calculated by the linear cyclic model. The nonlinear cyclic model, as shown in Figure 8.52 produced a failure mechanism consistent with the observed behaviour. The web wall experienced extensive crushing throughout, followed by the formation of five vertical slip planes at the end of the analysis. No yielding of the flange flexural or web horizontal reinforcement was found; however, there was some local yielding of the vertical web reinforcement. The vertical slip planes were first calculated at 10 mm of displacement and formed near the flange walls, which was similar to what was observed.

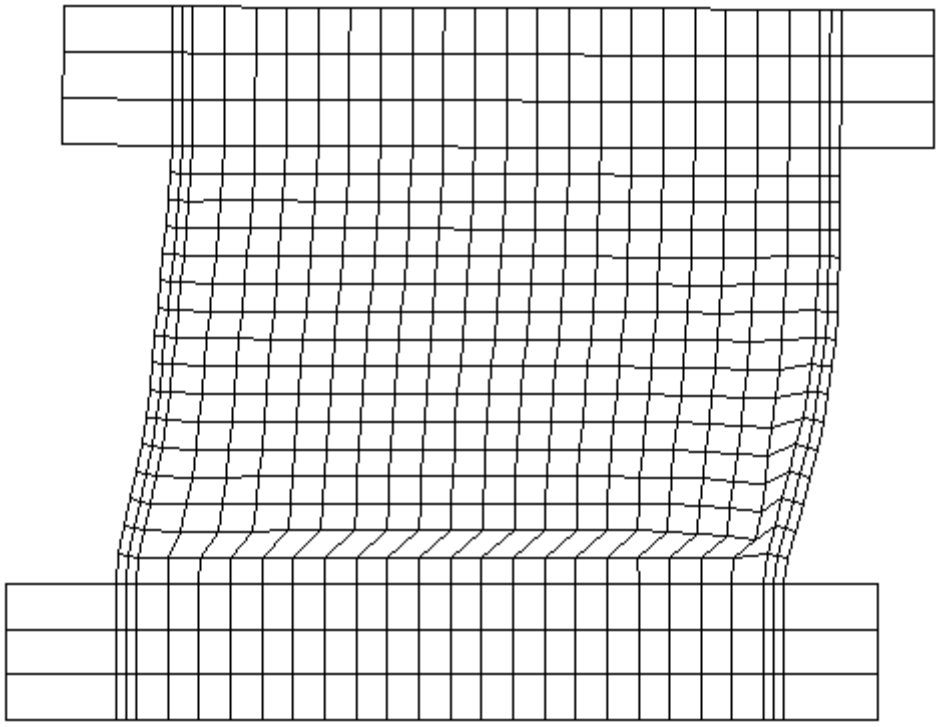

Figure 8.51 DP1 Failure - Linear Cyclic Model

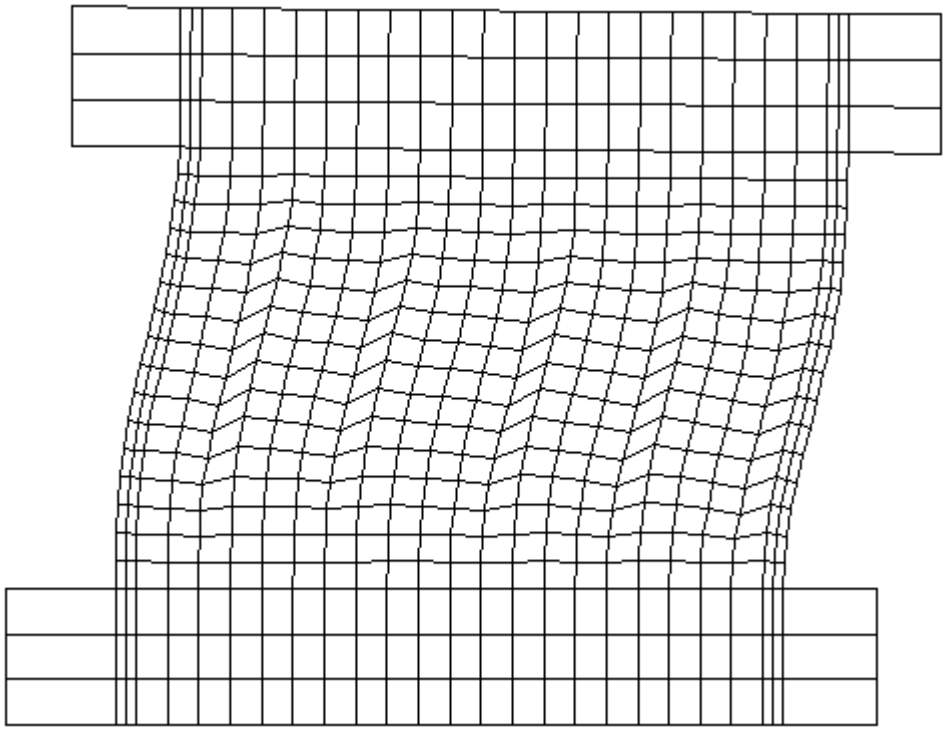

Figure 8.52 DP1 Failure - Nonlinear Cyclic Model

Figures 8.53 and 8.54 are plots of the envelope responses for the analytical and experimental load-displacement behaviours.

For the first excursion envelope results, the linear and nonlinear cyclic model calculations were similar up to the peak lateral resistance, after which the response using the linear cyclic models experienced a significant drop in load resistance, occurring at approximately ± 13 mm of displacement. The linear cyclic model slightly underestimated the post-peak capacity of DP1, and was the result of calculating a sliding shear failure. The nonlinear cyclic model better followed the gradual softening post-peak behaviour observed in the test; the result of calculating vertical slip planes.

The nonlinear cyclic model simulated more accurately the test results for the second excursion envelope, including the post-peak descending branch. This was partly due to the stiffness degradation parameters used for both the compression and tension regimes for the concrete, and partly the result of the calculated mode of failure.

To further demonstrate differences between the linear and nonlinear models, plots of the analytical and experimental results of the peak load stage (11 mm) for the first and second excursions are shown in Figures 8.55 and 8.56.

For both the first and second excursion, the nonlinear cyclic model better simulated the unloading portion of the response, due to the assumed nonlinear unloading model for concrete. In turn, the hysteresis loops of the nonlinear cyclic model captured more energy dissipation. It also seemed to calculate the peak strength, for each excursion, with slightly better accuracy. However, for the most part, both models slightly overestimated the reloading stiffness.

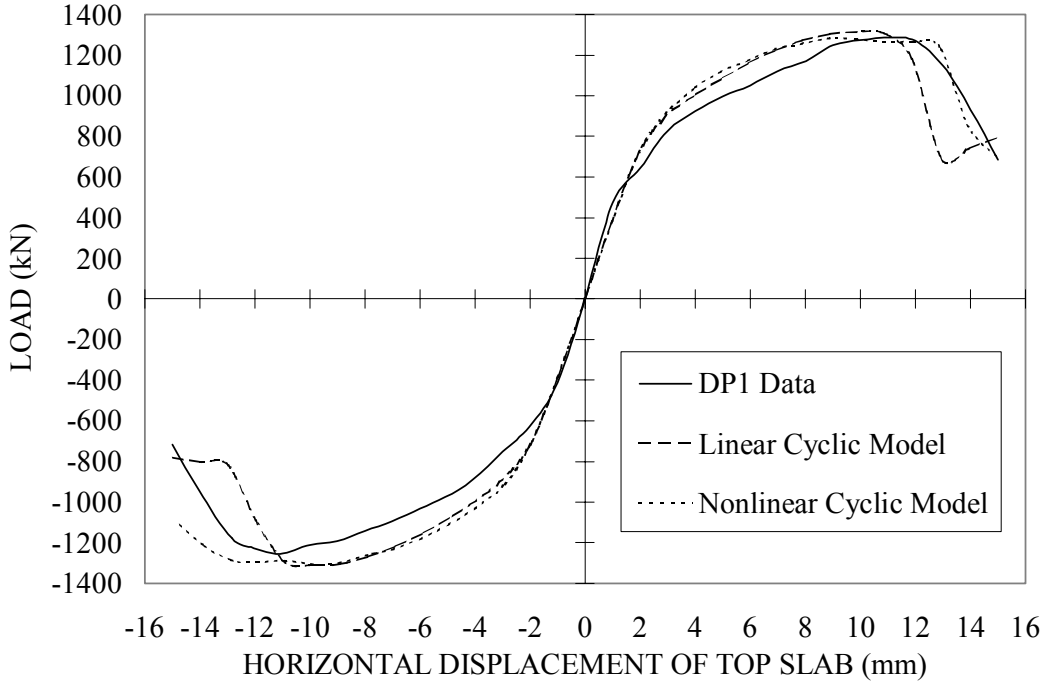

Figure 8.53 First Excursion Envelope Response of DP1

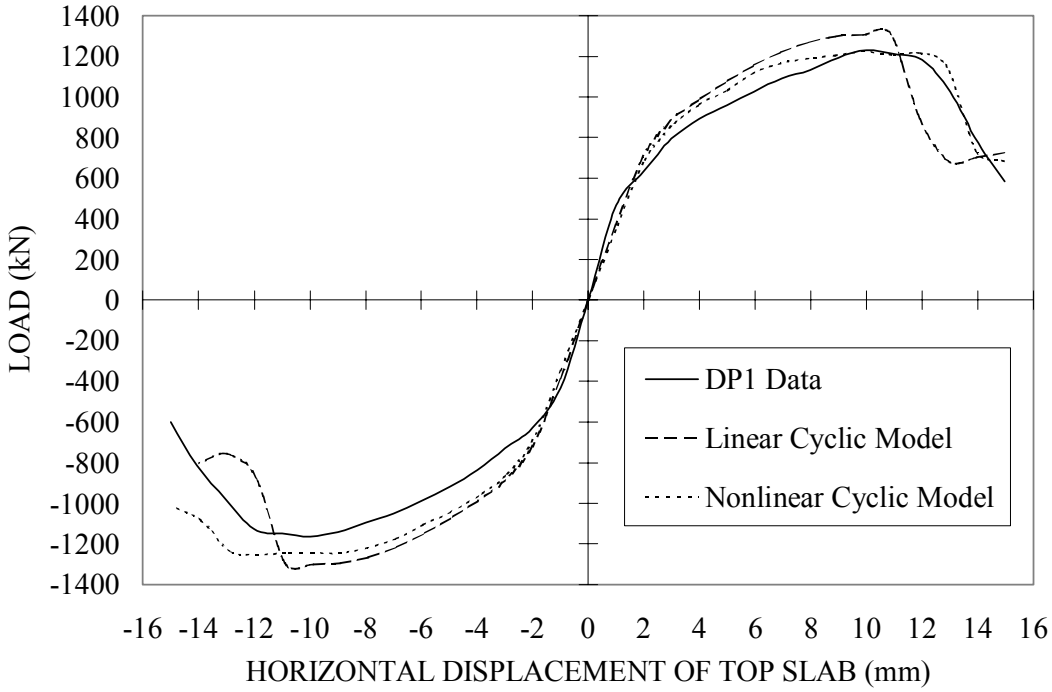

Figure 8.54 Second Excursion Envelope Response of DP1

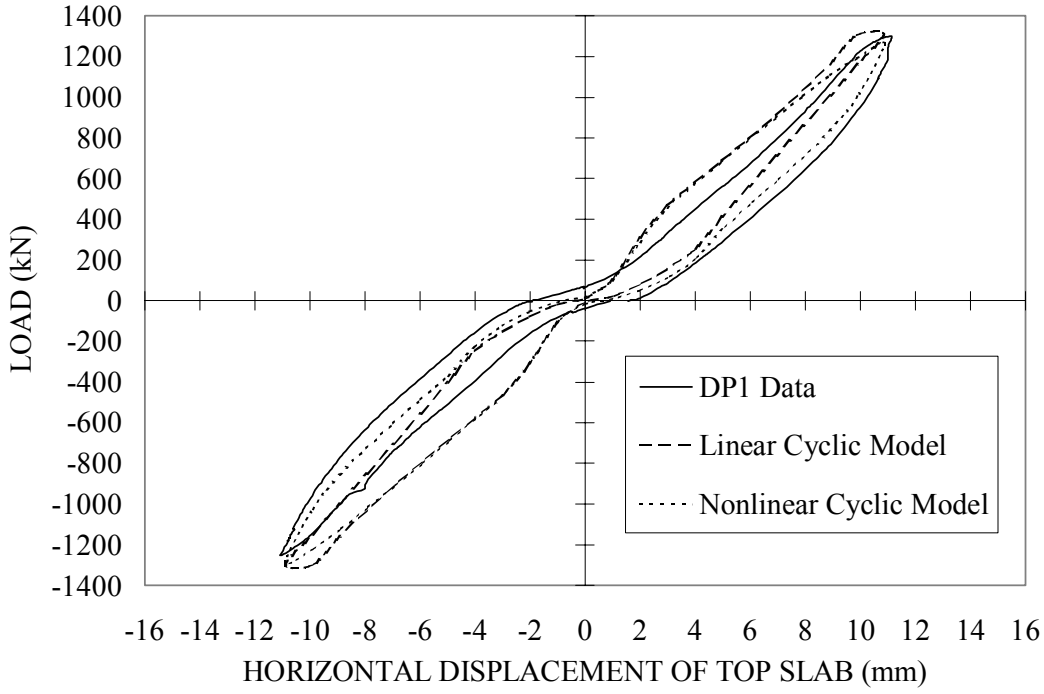

Figure 8.55 DP1 First Excursion At 11 mm

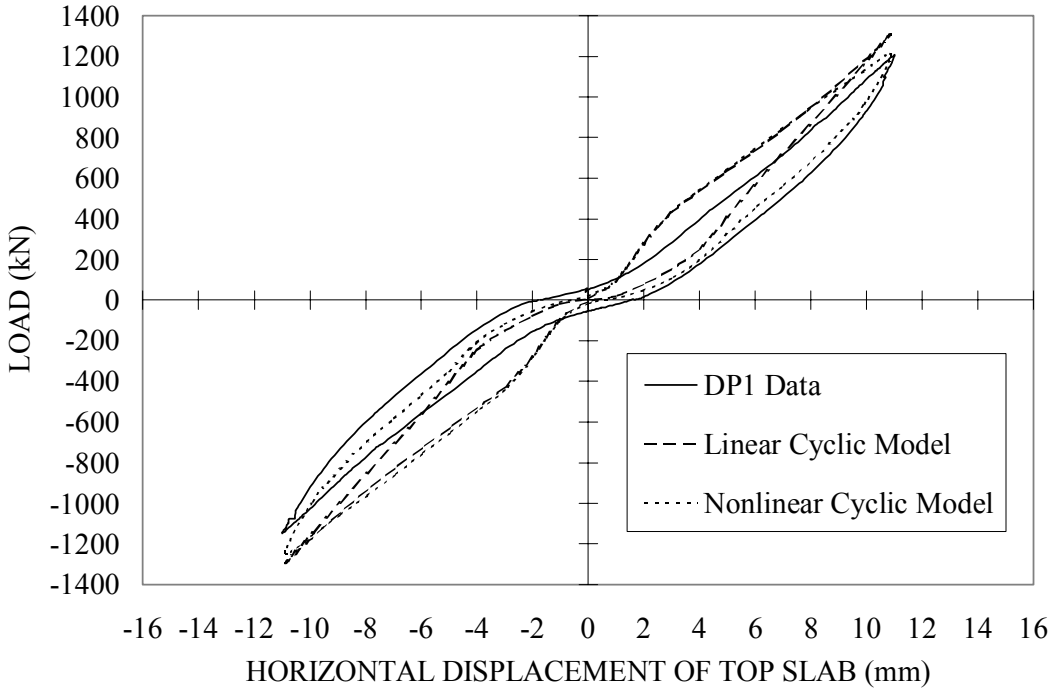

Figure 8.56 DP1 Second Excursion At 11 mm

A comparison between the observed and calculated horizontal expansion of the web wall further demonstrates the ability of the nonlinear cyclic model to simulate behaviour. The horizontal expansion, which is a second-order phenomenon, is a measure of the dilation of the web wall due to cracking and yielding of the web reinforcement and indicates the extent of compression softening of the concrete in the web wall. Figures 8.57 and 8.58 are the observed and calculated responses for DP1, respectively.

The calculated horizontal expansion of the web wall correlates reasonable well in the following aspects: the overall hysteretic behaviour, stiffness, and post-peak response. The only notable discrepancy is the degree of pinching estimated by the analysis. This deficiency is partly the result of not calculating yielding of the horizontal reinforcement near the mid-height of the web wall, and, more importantly, neglecting crack-closing in the analytical modeling. The analysis assumes the compressive stresses remain zero until the cracks completely close. [Note: the observed behaviour of Figure 8.57 is a plot of the wall expansion at maximum and zero loads for each displacement level.]

A maximum horizontal expansion of 6.10 mm was calculated by the analysis during 15 mm displacement for DP1, compared to the observed expansion of 6.52 mm, which occurred during loading to 13 mm displacement.

The vertical elongation of the flange wall is another interesting second-order mechanism. The elongation is a measure of the extent of flexural cracking and the ratcheting in the flange walls. [Ratcheting is a term used to describe the vertical stretching of the flange wall due to the irrecoverable strains that accumulate in the post-yield cycles.] Figures 8.59 and 8.60 are plots of the observed and calculated responses of the elongation of the flange wall nearest the laboratory strong wall.

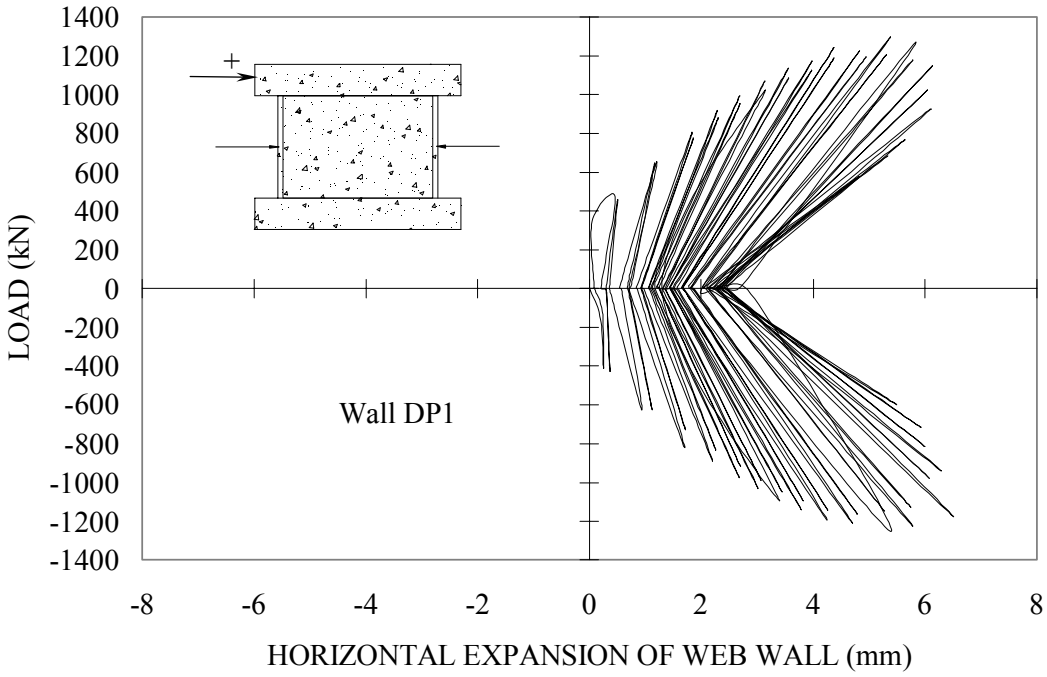

Figure 8.57 DP1 Observed Horizontal Expansion of Web Wall

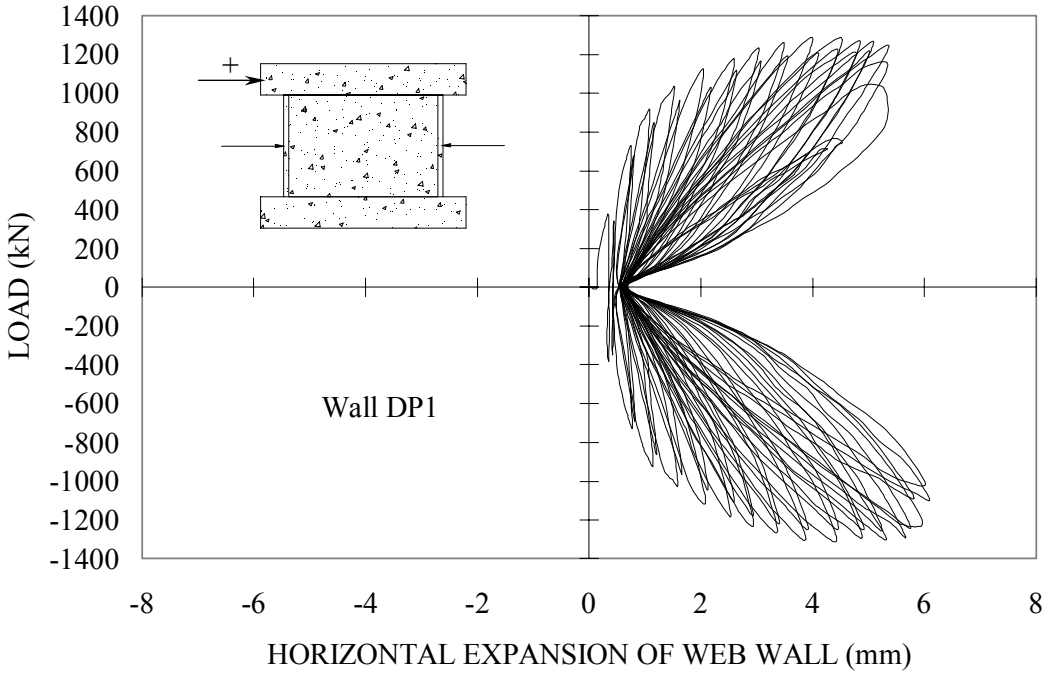

Figure 8.58 DP1 Calculated Horizontal Expansion of Web Wall

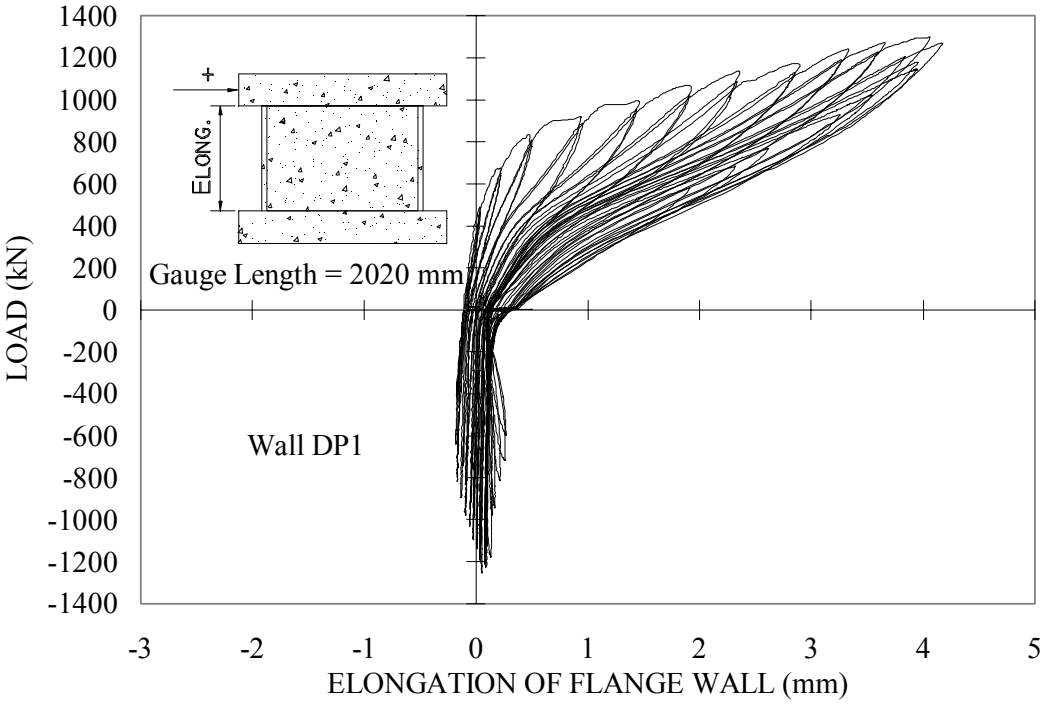

Figure 8.59 DP1 Observed Elongation of Flange Wall

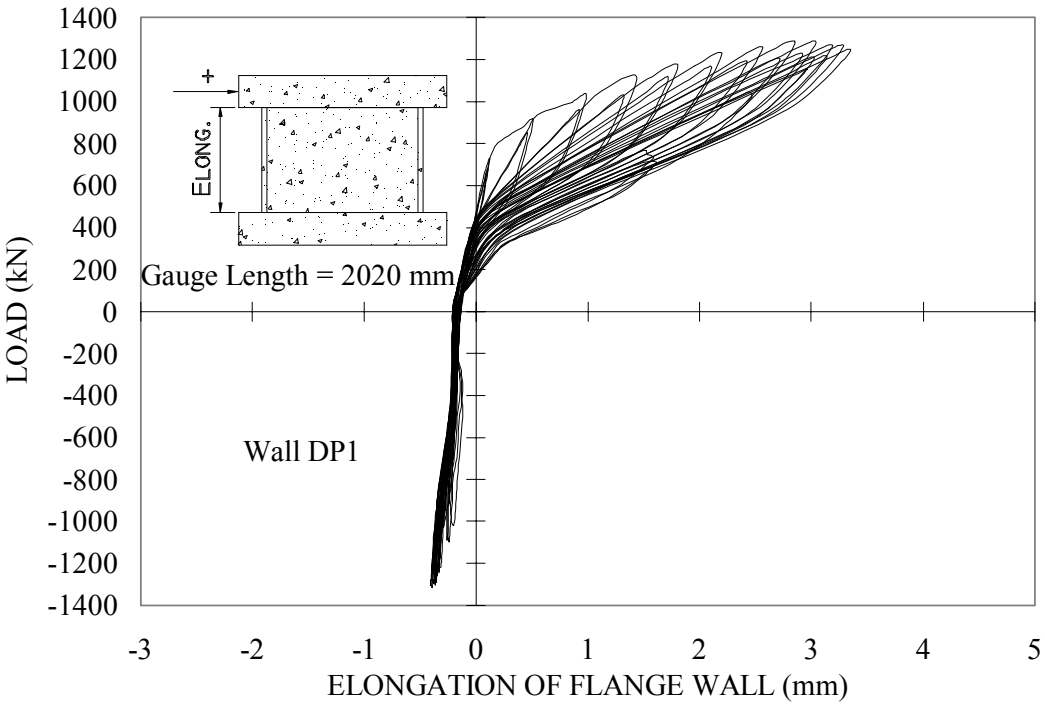

Figure 8.60 DP1 Calculated Elongation of Flange Wall

The calculated response using the nonlinear cyclic models for concrete demonstrates reasonable simulation of the flange wall elongation. This includes: the overall behaviour, stiffness, hysteresis curves, degradation of the reloading path during the second repetition of displacement, and the recovery of the vertical stretching in the post-peak region. The only notable difference is the estimated degree of pinching, which is a further result of neglecting the compressive stresses associated with crack-closing.

The nonlinear cyclic model calculated a maximum vertical elongation of 3.35 mm during loading to 13 mm displacement, compared to the observed elongation of 4.18 mm attained at 12 mm of lateral displacement. Bond slip at the base, neglected in the analyses, may potentially account for the discrepancy.

The web horizontal reinforcement is utilized to resist the shear stresses and control the horizontal expansion of the web wall. Therefore, calculating the horizontal expansion is significantly dependent on accurately modeling the behaviour of the horizontal reinforcement. Figure 8.61 is the observed response of strain gauge WH17, and Figure 8.62 is the calculated response of the horizontal reinforcement in the vicinity of WH17.

The analytical response calculated by the nonlinear cyclic model provides reasonable calculations of the reinforcement strains. In general, the overall behaviour, stiffness, hysteresis, and degradation occurring during the second repetition of displacement are well captured. The residual displacements are underestimated by the analysis, and, similar to the horizontal expansion of the web wall and elongation of the flange wall, this is a consequence of ignoring compressive stresses that arise when cracked surfaces come into contact in the tensile domain. Another discrepancy, to a

lesser extent, is the slightly smaller reinforcement strains calculated by the analysis at each displacement level.

Maximum strains of 3.05×10^{-3} and 3.55×10^{-3} were calculated by the analysis and observed during testing for DP1, respectively. The maximum reinforcement strains occurred during loading to 15 mm and 13 mm displacement, respectively, for the calculated and observed behaviours.

The larger strains measured in the web horizontal reinforcement during testing resulted in slighter more horizontal expansion of the web wall, as shown in Figure 8.57. Accounting for crack shear-slip in the analysis would result in better calculations of the straining in the transverse reinforcement. The Disturbed Stress Field Model, discussed in more detail in section 8.5.5, accounts for crack shear-slip.

The second wall in the DP series, DP2, was subjected to the same loading regime as DP1 with the exception of the externally applied axial load. The top slab, however, accounted for an axial load of 260 kN. The sequence of loading for the finite element analyses was identical to DP1, and included a shrinkage strain of -0.4×10^{-3} to account for the delay between casting of the concrete and the start of testing.

The observed load-displacement behaviour, previously discussed, is shown in Figure 8.63. Figures 8.64 and 8.65 are the calculated behaviours using the linear and nonlinear cyclic models for concrete, respectively. The highly pinched response of DP2 is also characteristic of a shear-dominated behaviour. The small amount of energy dissipation through the hysteresis loops and the small residual displacements are other shear-dominant qualities. The observed response did not realize a post-peak behaviour; a sudden loss of capacity followed the maximum lateral resistance.

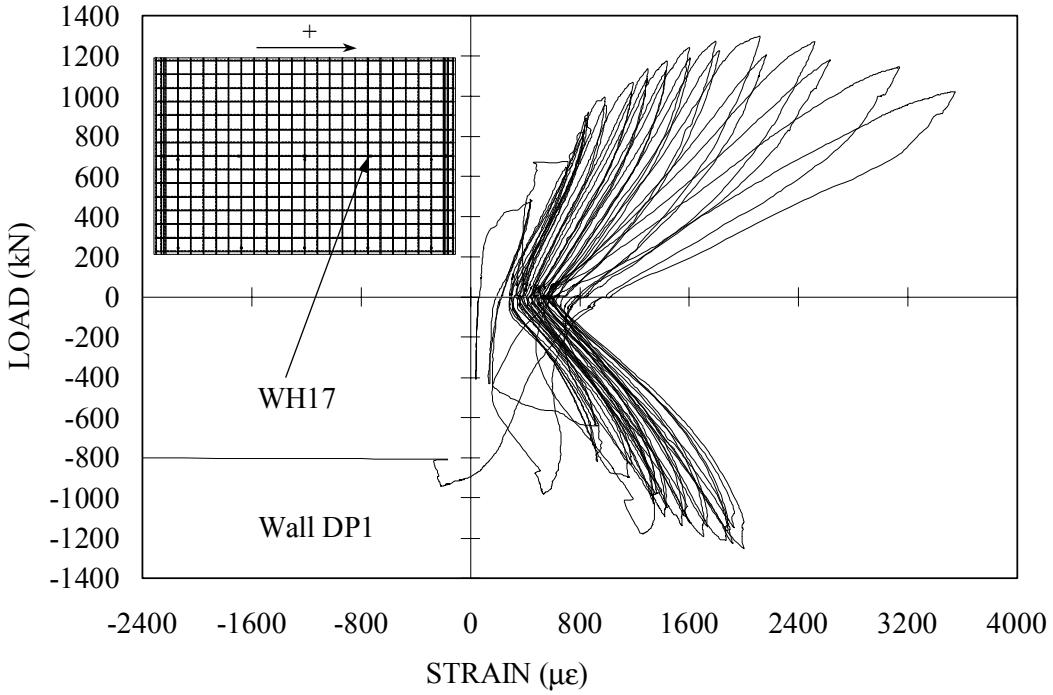

Figure 8.61 DP1 Observed Reinforcement Strains

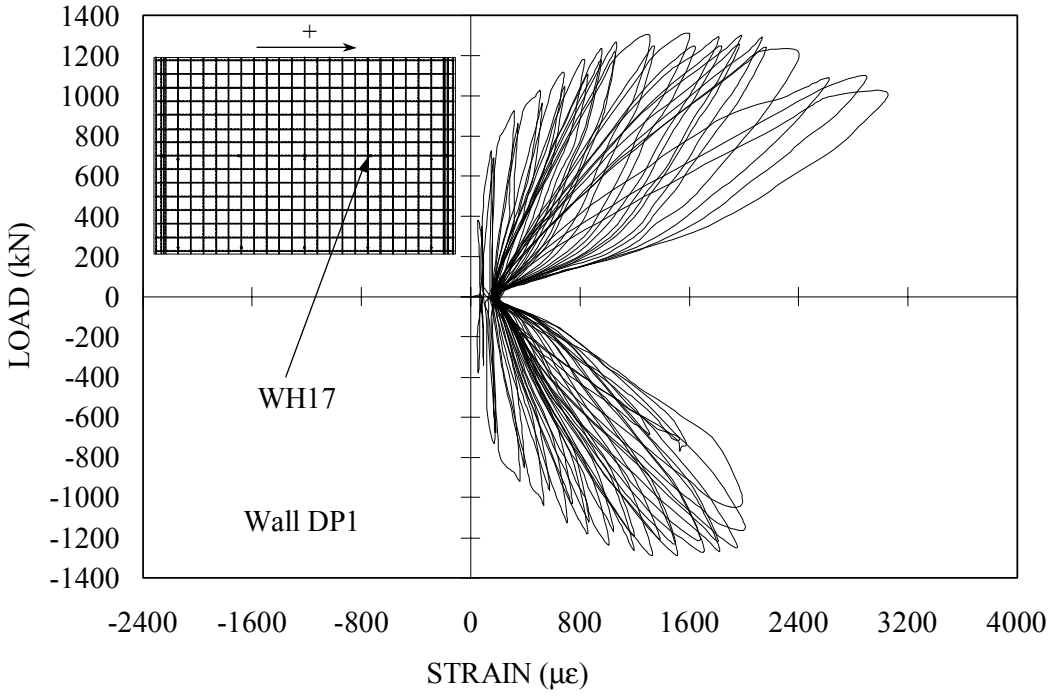

Figure 8.62 DP1 Calculated Reinforcement Strains

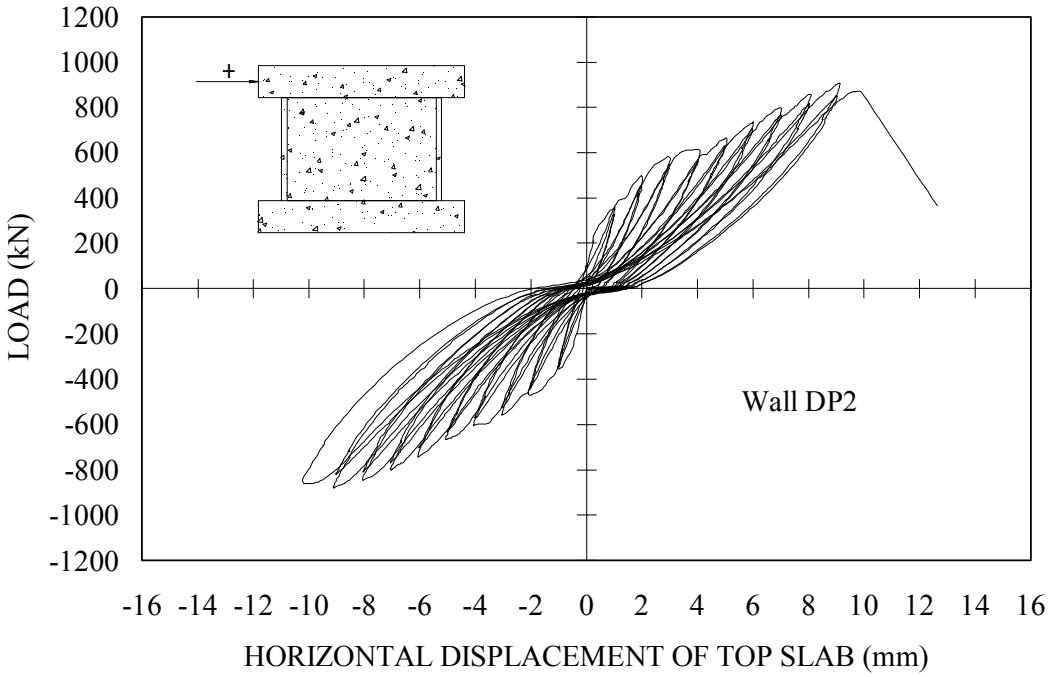

Figure 8.63 Experimental Load Displacement Response of DP2

Table 8.13 lists the maximum lateral resistances and the corresponding displacements.

Table 8.13 Analytical Results for DP2

Analysis	F_{exp}	F_{calc}	F_{calc}/F_{exp}	Δ_{exp}	Δ_{calc}	$\Delta_{calc}/\Delta_{exp}$
+ DP2-1	904	1059	1.17	9.15	12.82	1.40
+ DP2-3	904	1031	1.14	9.15	11.84	1.29
- DP2-1	-879	1060	1.21	9.08	12.82	1.41
- DP2-3	-879	1025	1.17	9.08	10.85	1.19

Note: 1 denotes linear model; 3 denotes nonlinear model
+ refers to positive direction; - refers to negative direction

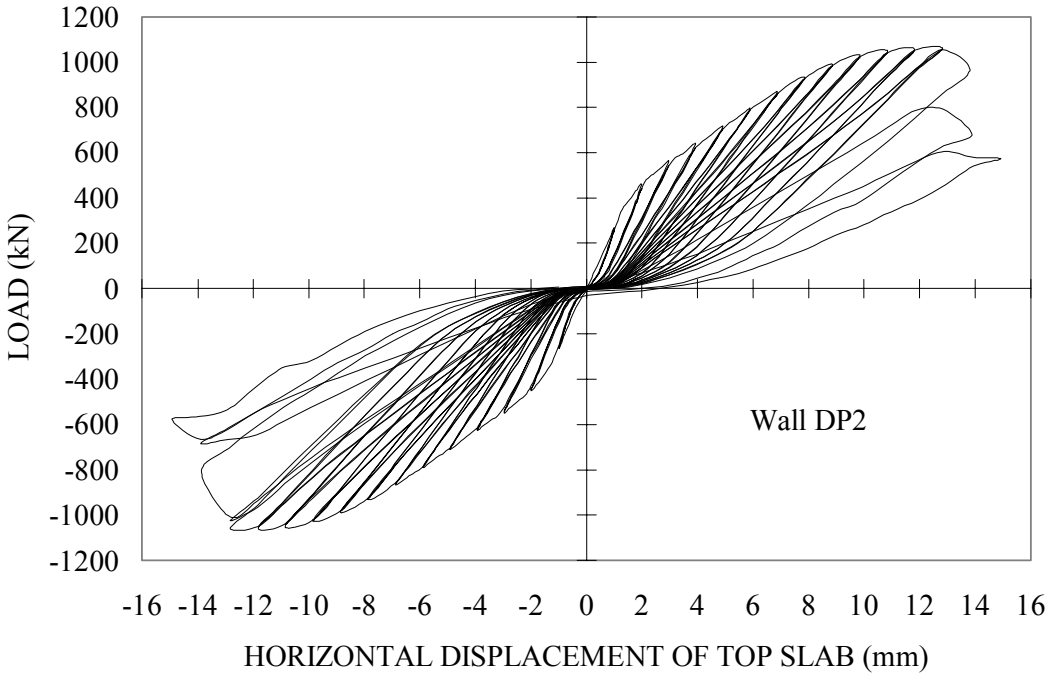

Figure 8.64 Calculated Response of DP2 Using Linear Cyclic Models

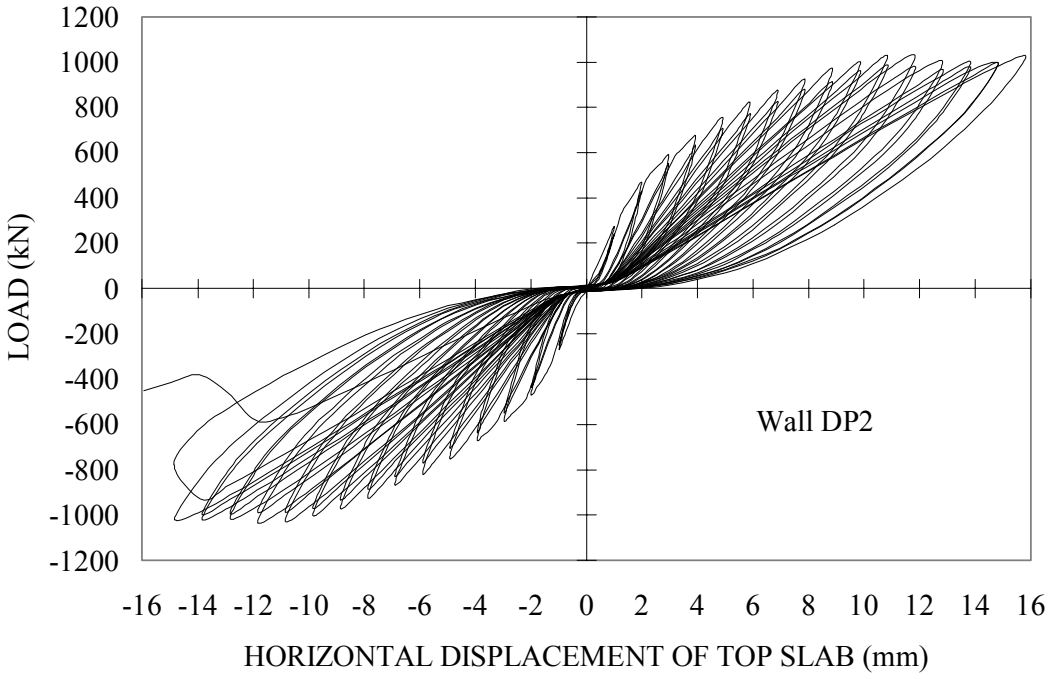

Figure 8.65 Calculated Response of DP2 Using Nonlinear Cyclic Models

The calculated responses captured the actual behaviour of DP2 reasonably well up to 9 mm of displacements, after which the wall failed suddenly. The nonlinear cyclic model more accurately simulated the hysteresis loops including nonlinear unloading and damage in concrete that was evident during the second excursion per displacement level.

The maximum loads were calculated with slightly more accuracy than the corresponding displacements, and the nonlinear cyclic model provided a better estimation of the observed strengths and displacements. A more appropriate comparison would be to determine the calculated lateral resistances at 9 mm of displacement (the last load stage before failure). The linear cyclic model recorded a load of 985 kN at 8.86 mm, and the nonlinear cyclic model calculated 969 kN at a corresponding displacement of 8.86 mm. The analytical-to-experimental strength ratios for the results at 9 mm of displacement were 1.09 and 1.07. Failure mechanisms as calculated by the finite element analyses are shown schematically in Figures 8.66 and 8.67, respectively, for the linear and nonlinear cyclic models.

The finite element analyses calculated sliding shear failures for both models, occurring at 14 mm for the linear cyclic model and –15 mm for the nonlinear cyclic model. Note that in Figures 8.66 and 8.67 the top slab demonstrated more rotation for both analyses, which wasn't evident for DP1. The release of the applied axial load resulted in more freedom for the top slab. The response using the linear cyclic model indicated the formation of a horizontal failure plane a distance of 125 mm from the base slab. A significant portion of the crushed concrete was confined to the compressive toes of the web wall, and some crushing was evident along the main compression strut. Yielding of the web horizontal reinforcement, and local yielding of the flexural

reinforcement in the flanges were calculated after the formation of the sliding shear plane. However, indicators of the finite element analysis at failure, using the nonlinear cyclic model, indicated subtle differences in terms of the calculated damage. The formation of a horizontal failure plane 375 mm from the base slab dominated the response in the negative direction; however, vertical crushing planes, similar to DP1, were evident in the positive cycles. Concrete crushing was more widespread than that assumed by the linear cyclic model. Preceding the sliding shear was yielding of the horizontal reinforcement in the web and local yielding of the flange flexural reinforcement. The nonlinear cyclic model for concrete more accurately captured the extensive damage experienced by the concrete throughout the web wall. This was due to the damage parameters formulated to calculate the degradation of the reloading stiffness due to cycling. To further demonstrate the differences between the linear and nonlinear cyclic models, envelope responses are shown in Figures 8.68 and 8.69 for the first and second excursions, respectively.

The envelope responses indicate that the linear and nonlinear cyclic models provided reasonable results up to 9 mm of displacements. For the first excursion envelope, there seems to be very little difference in the results, except that the linear cyclic model calculated a reduction in the lateral load carrying capacity before the nonlinear cyclic model. The second excursion results, however, demonstrates the influence of the reloading stiffness degradation parameters of the nonlinear cyclic model. With increasing lateral displacements, the nonlinear cyclic model calculated significantly less load carrying capacity in comparison to the linear cyclic model.

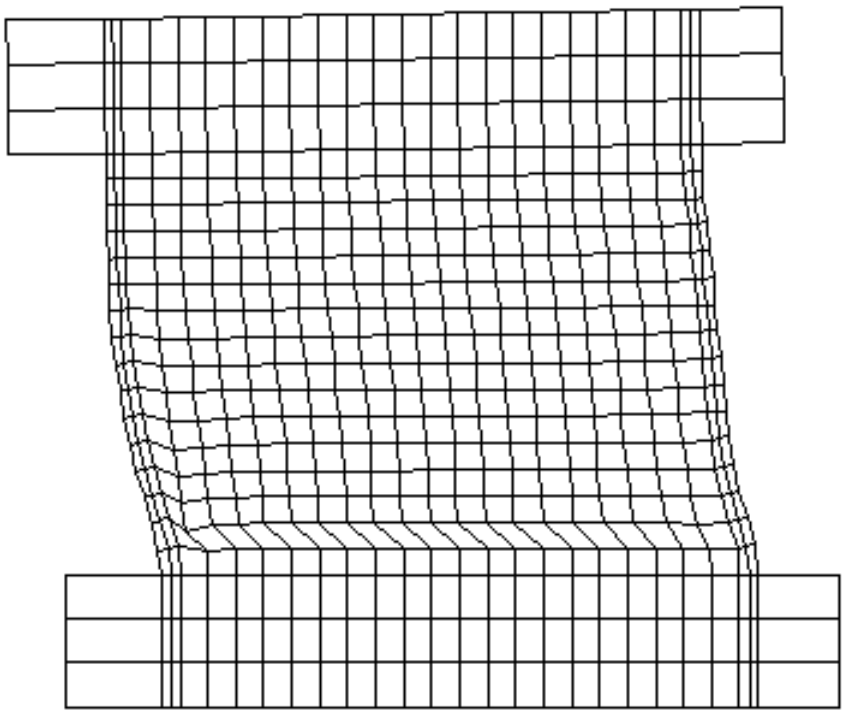

Figure 8.66 DP2 Failure – Linear Cyclic Model

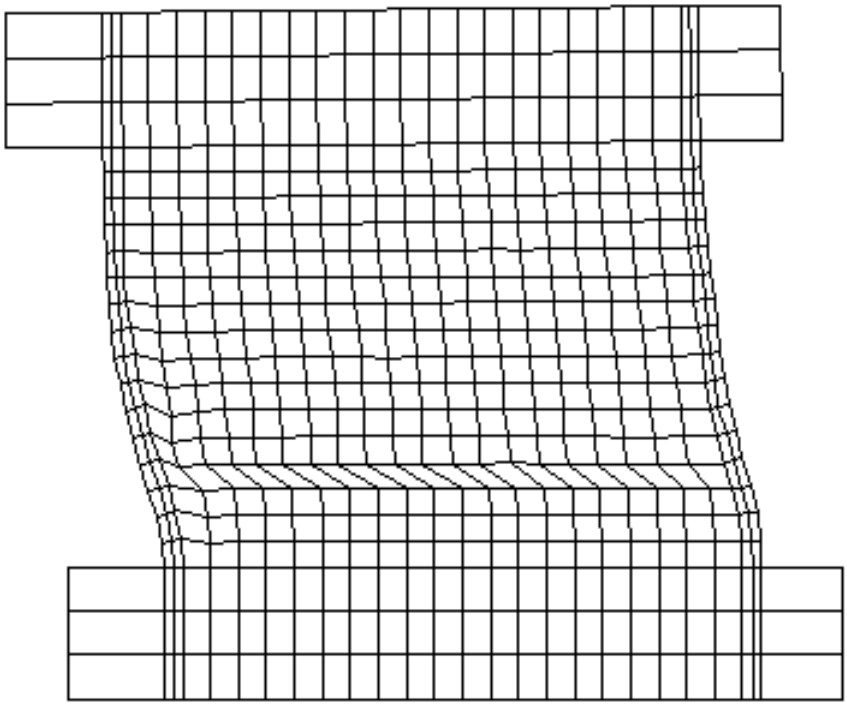

Figure 8.67 DP2 Failure – Nonlinear Cyclic Model

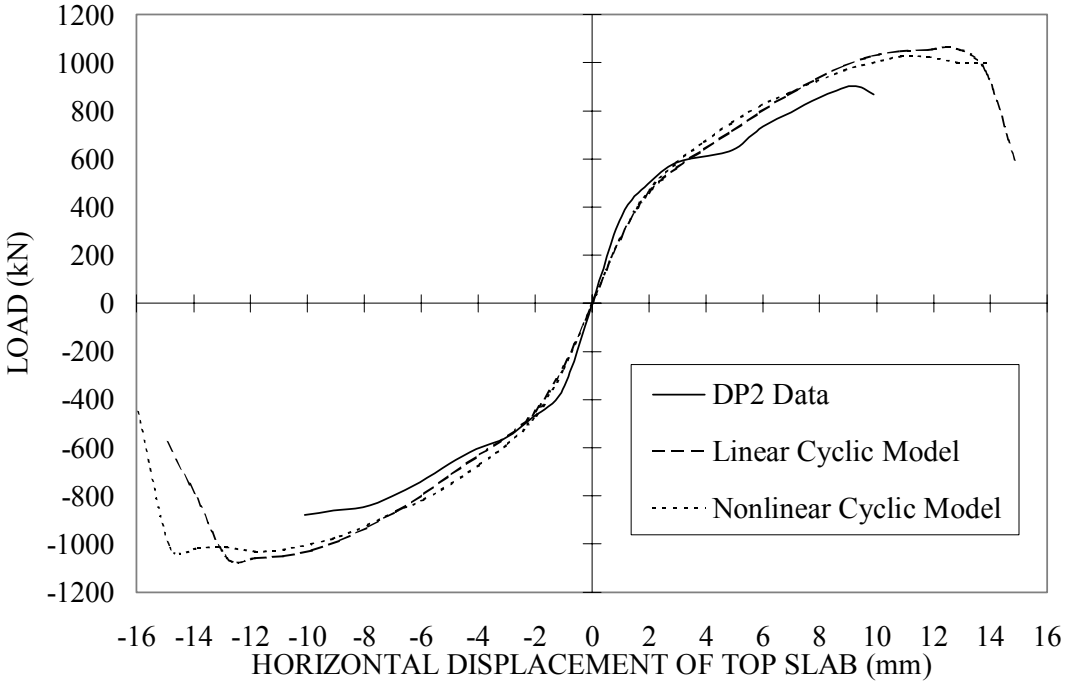

Figure 8.68 First Excursion Envelope Response of DP2

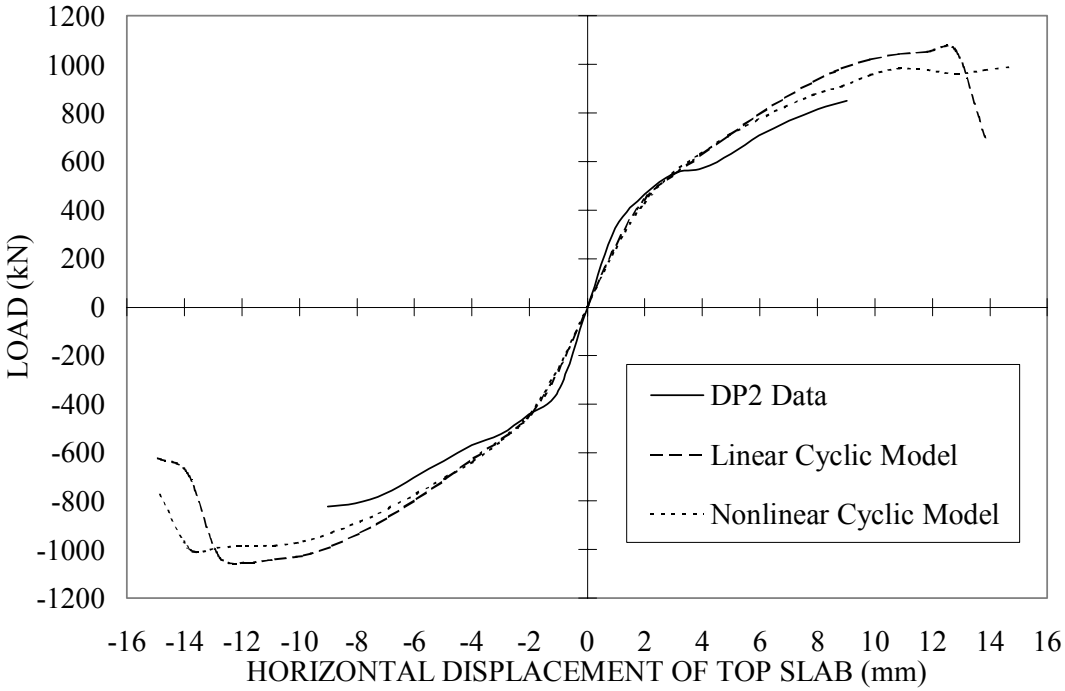

Figure 8.69 Second Excursion Envelope Response of DP2

Plots of the experimental peak load stage (9 mm) are shown in Figures 8.70 and 8.71 to further compare the analytical models with the experimental data.

The most significant difference, in the responses to 9 mm of displacement, is the unloading path. The nonlinear cyclic model accurately represented the actual unloading behaviour of DP2, whereas the initial unloading response for the second excursion of the linear cyclic model produced a pinched behaviour, which disagrees with the observed data. The experimental results also seemed to suggest that there was more damage during reloading than currently calculated by either model. A possible cause was the compression softening of the concrete due to history of cyclic loading in the transverse direction. Stevens, Uzumeri, and Collins[26] proposed an analytical model based on the test results of panel elements, however the model needs to be corroborated to structural members.

A further analysis was conducted on DP2, using the nonlinear cyclic model, to investigate the observed failure mechanism. It was previously suggested that weaker concrete in the wall section near the top slab was a possible cause of failure. In the analysis, the concrete in the top four rows of elements in the web and flange zones was reduced to 70 percent of cylinder strength, resulting in a compressive strength of approximately 13.2 MPa. The results of the analysis are shown in Figure 8.72.

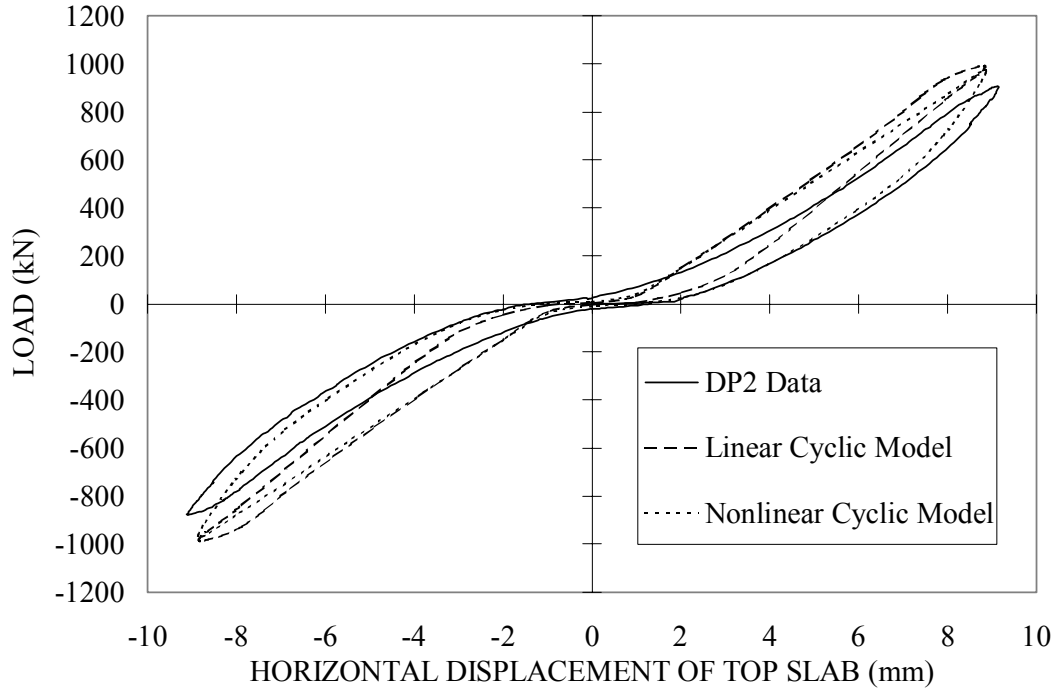

Figure 8.70 DP2 First Excursion At 9 mm

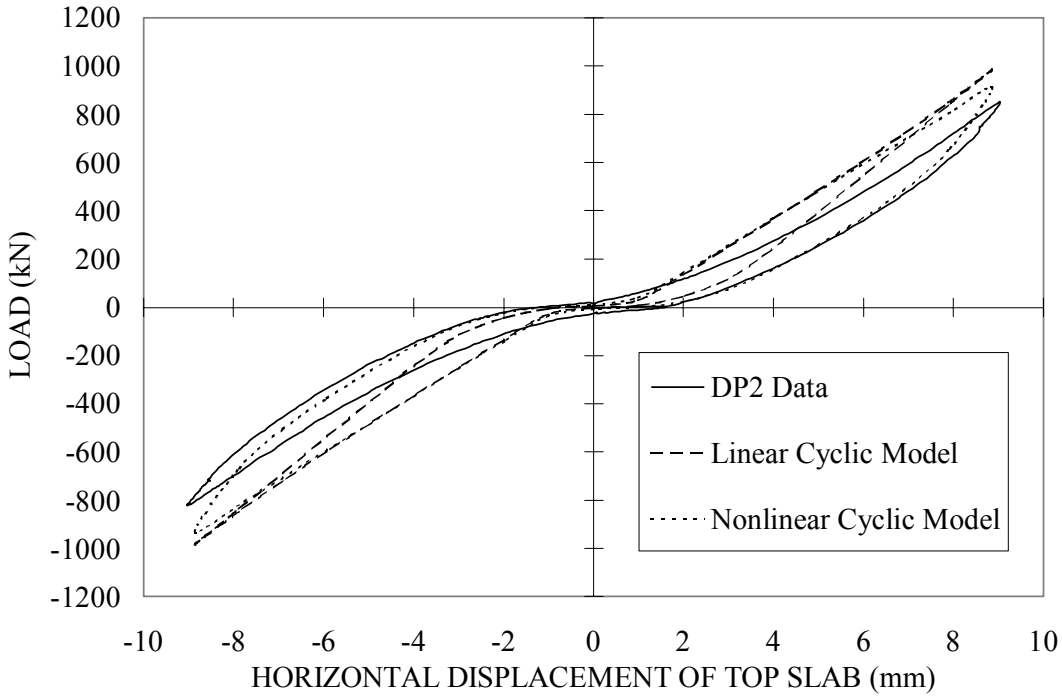

Figure 8.71 DP2 Second Excursion At 9 mm

The results indicate that the wall fails abruptly during loading to 12 mm of displacement, compared to the observed failure displacement of 10 mm. Peak loads of 975 kN and 983 kN for the positive and negative directions were recorded. The analytical-to-experimental lateral load resistances were 1.08 and 1.12, respectively. Failure was calculated as sliding shear approximately 375 mm from the top slab, which was similar to that observed in the test. Extensive crushing was calculated in the top corners of the wall prior to the formation of the sliding shear plane. No yielding of the reinforcement was calculated prior to failure. However, yielding of the horizontal web reinforcement was noted in the web wall following the sliding shear failure. Crushing of the concrete in the compression toes near the base slab was also calculated, and first crushing was calculated in the compression toes at 6 mm of lateral displacement. These damage indicators were consistent with what was observed during testing. A further reduction in the compressive strength of the concrete would initiate failure at smaller displacements in the web wall near the top slab. Therefore, it appears that weaker concrete in the upper part of the walls in DP2 was possibly responsible for the sudden sliding shear failure of the web wall near the top slab. Figure 8.73 illustrates the calculated failure mechanism of DP2 using 70 % of the concrete cylinder strength in the top region of the web wall.

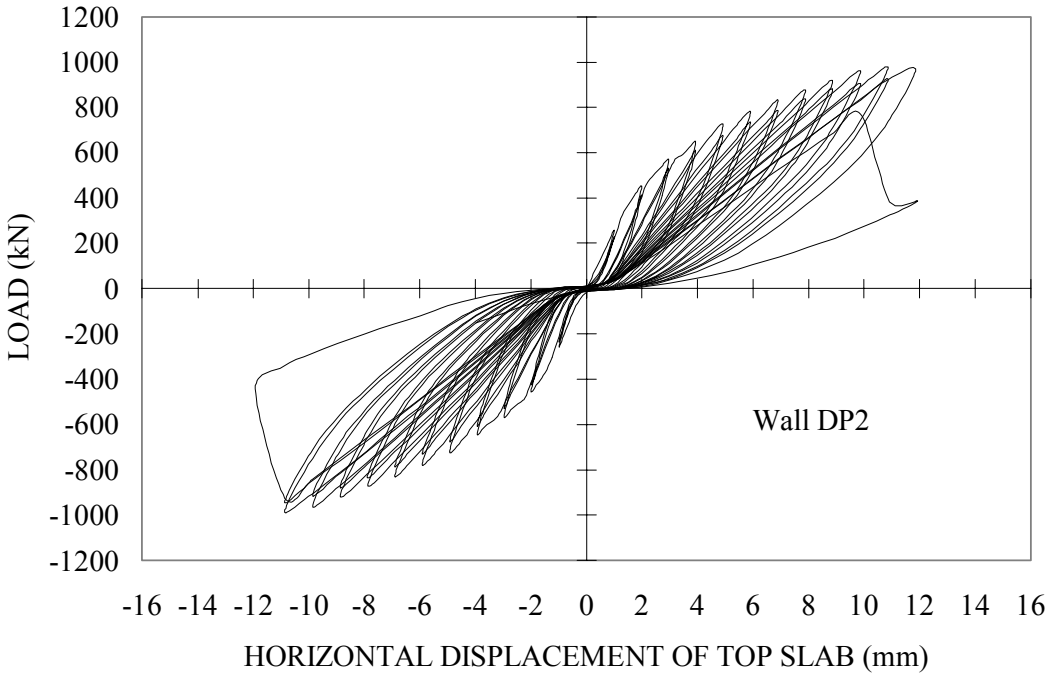

Figure 8.72 Load-Displacement Response of DP2 Modified

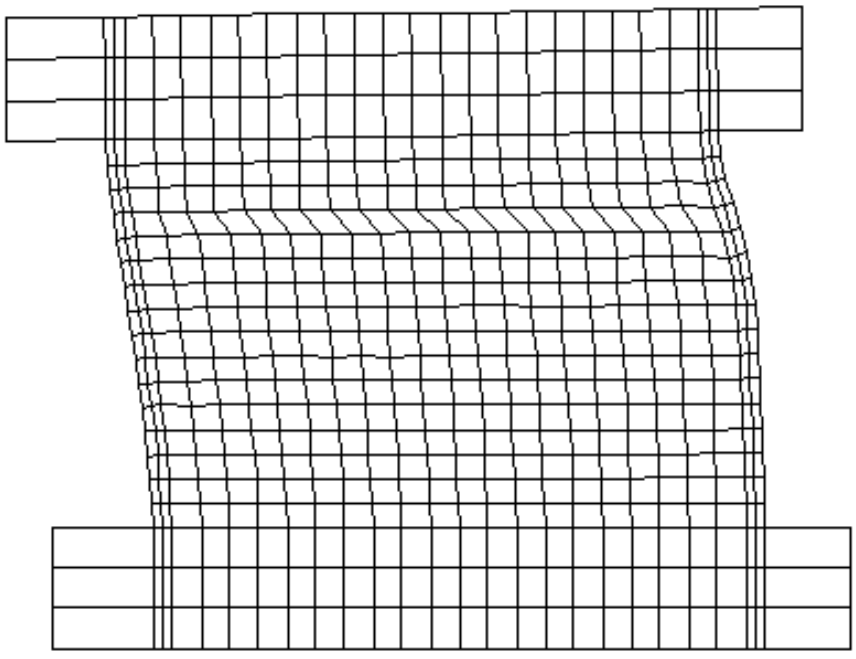

Figure 8.73 Predicted Failure Mode of DP2

Comparisons between the observed and calculated horizontal expansion of the web wall further demonstrate the effectiveness of the nonlinear cyclic models for concrete. Figures 8.74 and 8.75 are plots of the experimental and analytical responses, respectively. [Note that the analytical results were terminated at 10 mm displacement, at which point Specimen DP2 failed abruptly during testing.] The analysis provides, for the most part, accurate simulations of the horizontal expansion including: the overall response, stiffness, hysteresis, degree of expansion at each displacement level, and degradation experienced in the second repetition of displacement. The only notable difference is the degree of pinching, which is overestimated by the analysis, and can be attributed to the omission of a suitable crack-closing model. The tensile unloading regime assumes the re-contact strain of cracks is zero. Also, the analysis did not calculate yielding of the web horizontal reinforcement, which to a lesser extent contributed to the significantly pinched response.

A comparison at 10 mm displacement indicates that the analysis calculated a maximum web wall expansion of 3.95 mm, and the observed horizontal expansion was 4.62 mm.

The vertical elongation of the flange wall nearest the laboratory strong wall further illustrates the efficiency of the nonlinear cyclic model for concrete. The observed and the calculated response to the first excursion of 10 mm lateral displacement are shown in Figures 8.76 and 8.77, respectively.

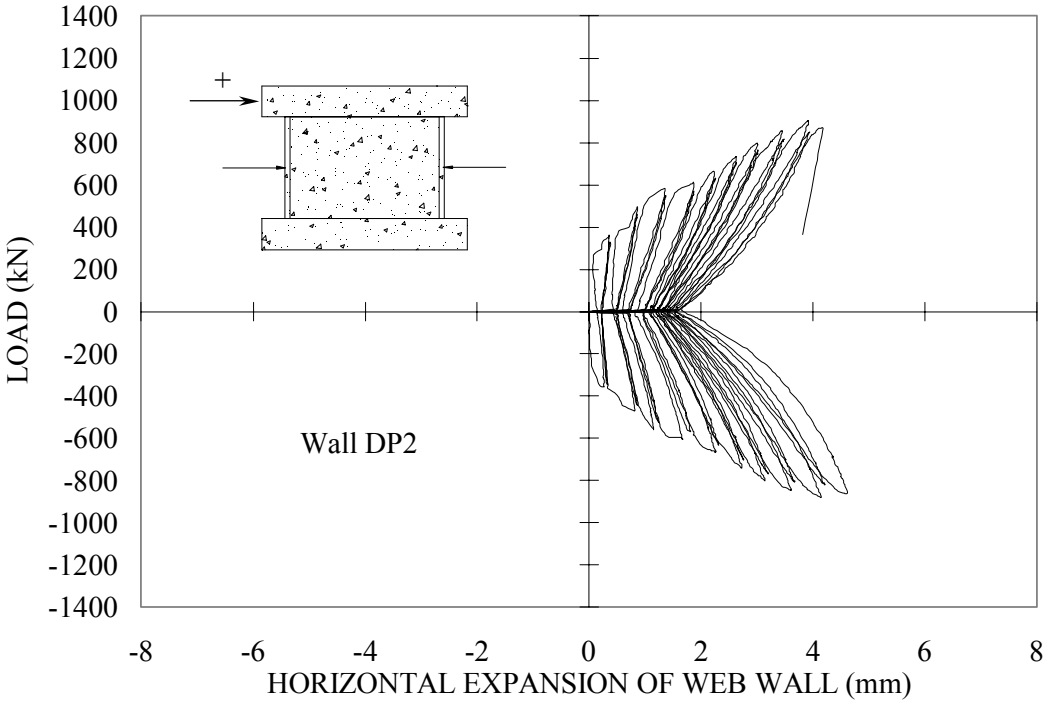

Figure 8.74 DP2 Observed Horizontal Expansion of Web Wall

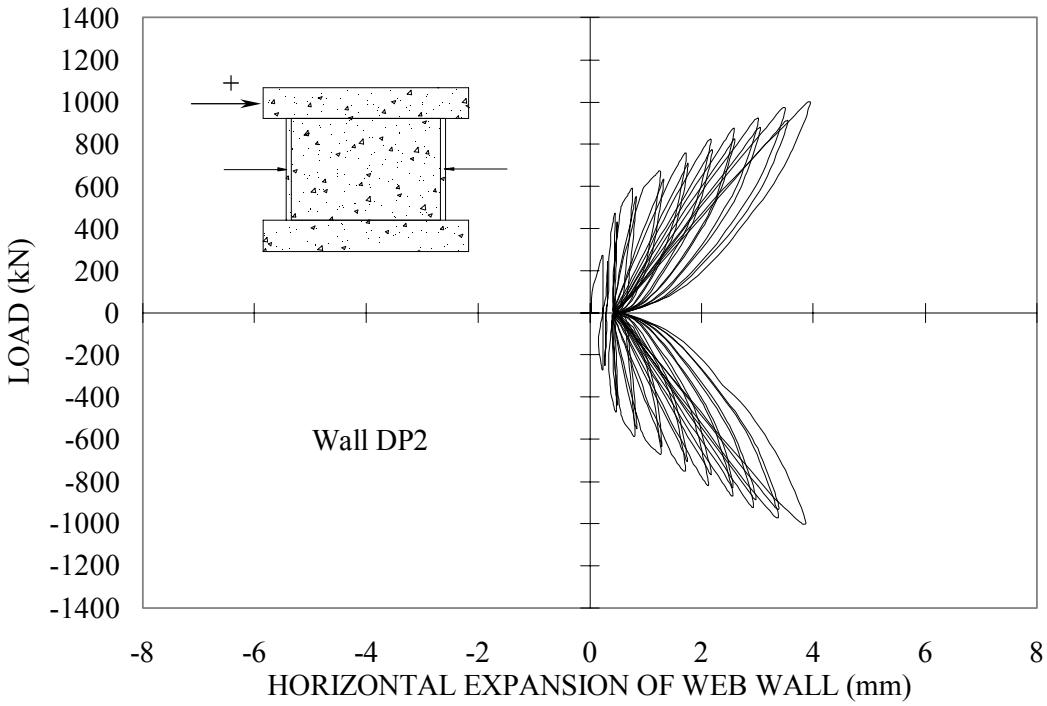

Figure 8.75 DP2 Calculated Horizontal Expansion of Web Wall

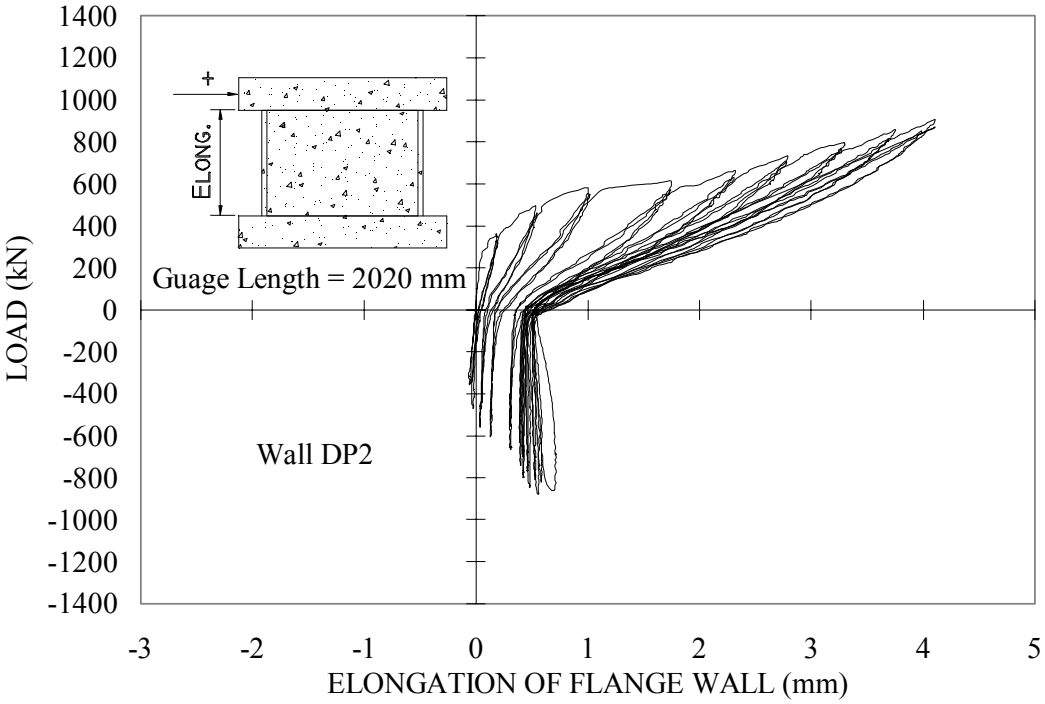

Figure 8.76 DP2 Observed Elongation of Flange Wall

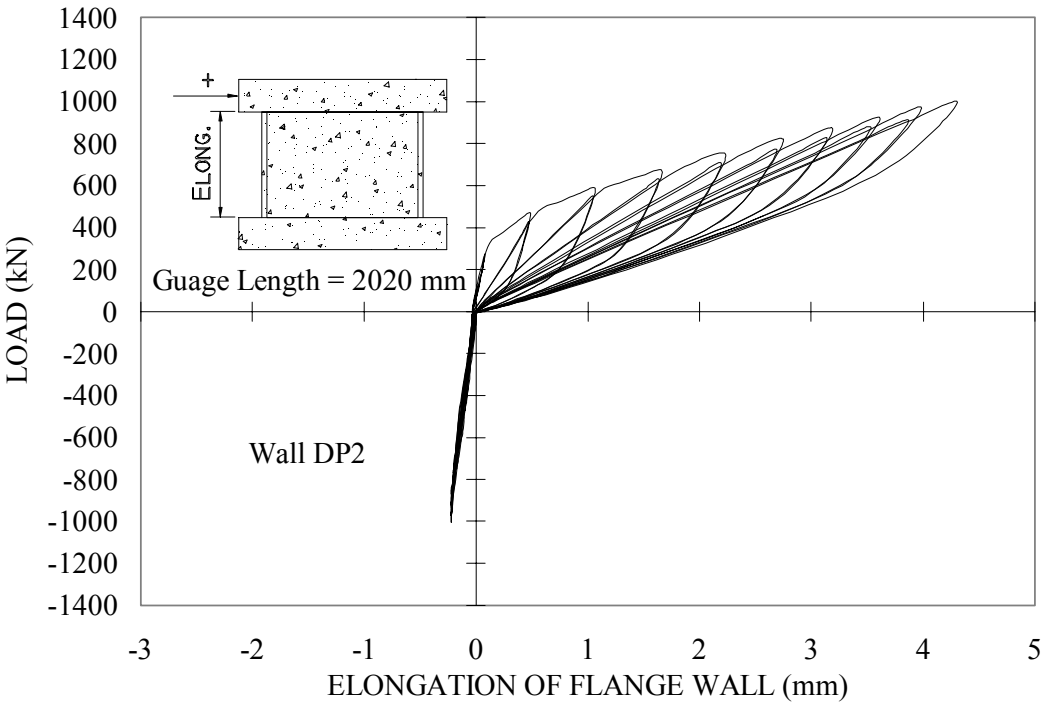

Figure 8.77 DP2 Calculated Elongation of Flange Wall

The overall behaviour, pre and post-cracking stiffness, hysteresis, degradation on loading to the second repetition, and degree of elongation at each displacement level are well simulated by the analysis. The significantly more pinched behaviour calculated by the analysis can be resolved by including a crack-closing formulation to account for the compressive stresses that arise before the cracks completely close. At 10 mm lateral displacement, the analysis calculated a maximum vertical elongation of 4.31 mm, and the observed elongation of the flange wall was 4.11 mm.

Related to the horizontal expansion of the web wall is the straining of the web horizontal reinforcement. Accurate calculation of the web expansion is significantly influenced by properly accounting for the strains in the transverse reinforcement. Figures 8.78 and 8.79 illustrate the observed and calculated response for a horizontal reinforcing bar located at the mid-height of the web wall.

More horizontal expansion of the web wall was observed than calculated as a result of larger strains measured during testing than calculated by the analysis using the nonlinear cyclic models for concrete. At 10 mm displacement, a maximum strain of 1.37×10^{-3} was calculated by the analysis, and the actual strain measured was 2.02×10^{-3}. The analysis also underestimates the residual displacements; otherwise, the overall response, hysteresis, stiffness, and reloading degradation are well simulated. The slighter more pinching calculated by the analysis is the result of ignoring the compressive stresses associated with crack-closing, and accounting for crack shear-slip would address the smaller strains calculated by the analysis. A further discrepancy is noted in the first few displacements of the observed behaviour, which illustrates significant strains as the result of cracking in the flanges and in the vicinity of the strain gauge.

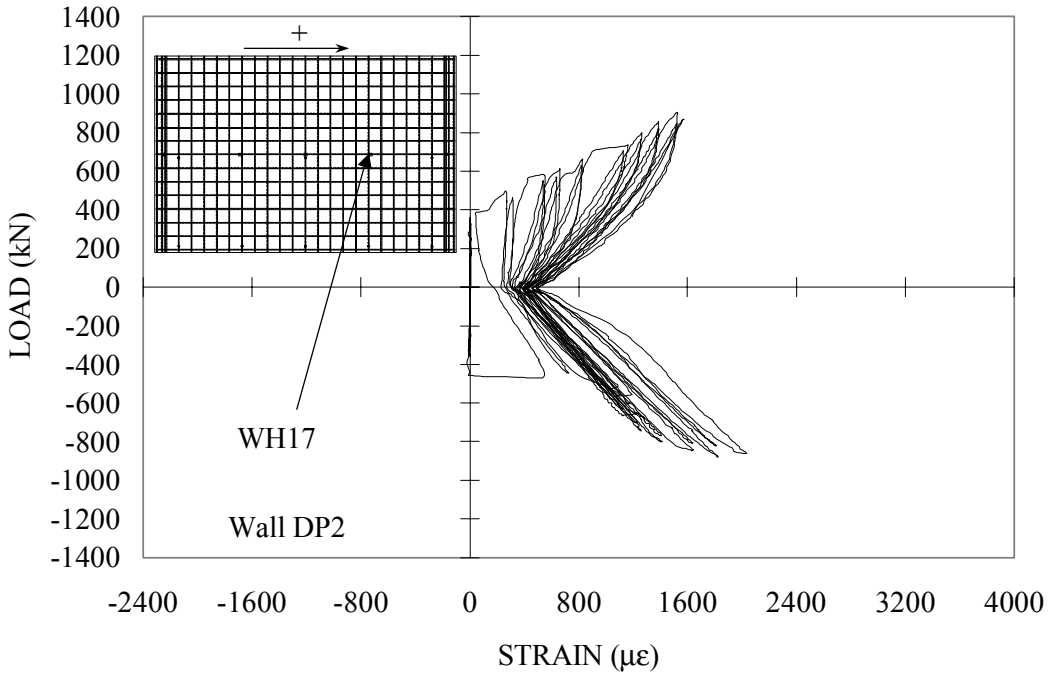

Figure 8.78 DP2 Observed Reinforcement Strains

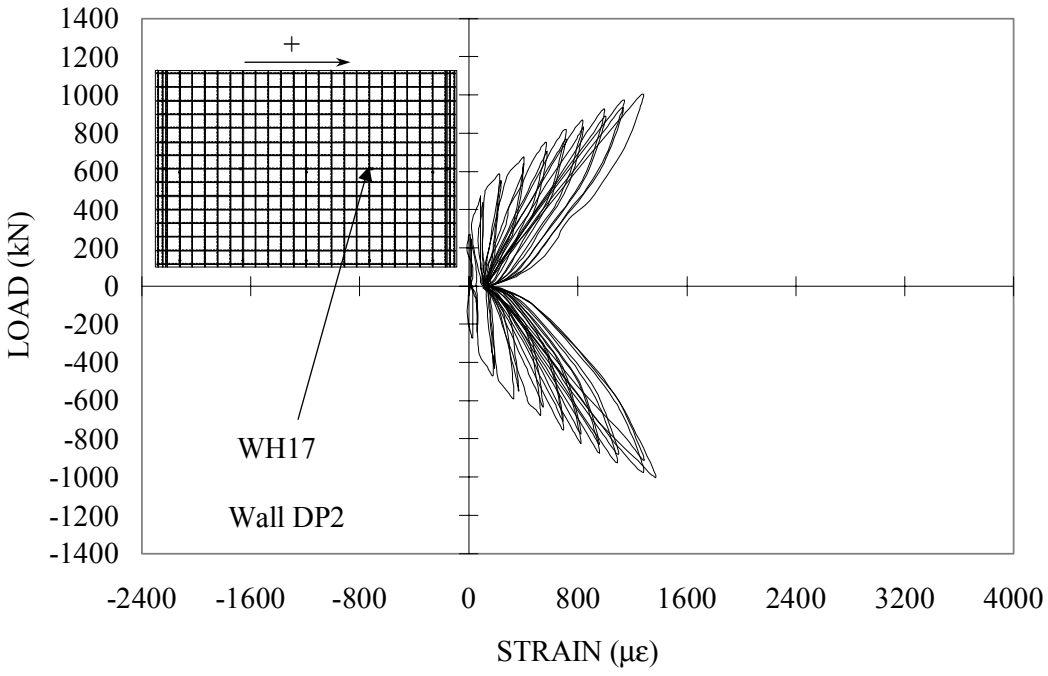

Figure 8.79 DP2 Calculated Reinforcement Strains

8.5.4 Three-Dimensional Analyses

Although DP1 and DP2 represent complex wall configurations, the 2-D analyses yielded reasonable results. Three-dimensional issues, however, must be addressed, and for DP1 and DP2 this includes the effectiveness of the flange width in contributing to the lateral load resistance of the wall. Concentrating the full width of the flanges into a single element in the 2-D model has several significant implications. The very stiff flange elements are assumed fully connected to the web elements. Thus, the degree of lateral and vertical confinement they provide to the web may be overestimated. Further, the shear lag effect that occurs in the out-of-place direction in the 3-D model, and in reality, is not considered. Finally, the ability of the flange elements to carry a lateral shear can be overstated when full fixity to the web is assumed. Relative to a 3-D analysis, these factors can contribute to overestimating the strength and stiffness of 3-D walls when conducting a 2-D analysis. Also, failure mechanisms such as flange punching, which are common in flanged shear walls, cannot be captured in a 2-D analysis. Vecchio[42] has identified these factors in the 3-D analysis of the NUPEC shear walls.

Pushover analyses of DP1 and DP2 were performed using VecTor2 and VecTor3 to identify differences between the 2-D and 3-D models. The 2-D finite element mesh shown in Figure 8.80 consisted of 325 constant strain rectangular elements. The mesh was divided into three zones: the web wall, the flange walls, and the top slab. The bottom slab was omitted, and the mesh was slightly coarser than that used in the cyclic analyses to be consistent with the 3-D model and to reduce computation time. The walls were assumed fully fixed along the base. The 3-D finite element mesh consisted of 1026

constant strain hexahedral elements. Similar to the 2-D model, the mesh was divided into the same three zones. To reduce computation time, only half of the actual structure was modeled. Figure 8.80 represents the web wall view of the 3-D model, and Figure 8.81 illustrates the top views of the finite element mesh of the walls and top slab, respectively. [Note: In the 3-D model, the discretization of the web wall was identical to that in the 2-D model.] For each pushover analysis, displacements, imposed at the top of the top slab, were incremented in steps of 0.25 mm until failure. All other loading conditions were similar to those used in the cyclic analyses, and included a constant shrinkage strain of -0.4×10^{-3} and an externally applied axial load of 940 kN for DP1. In addition, the top slab accounted for 260 kN of axial load.

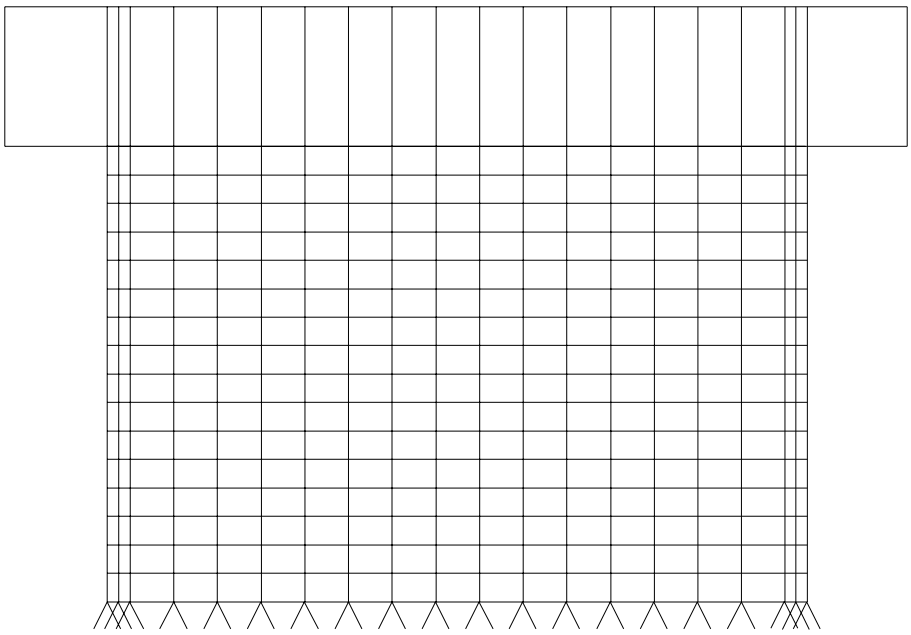

Figure 8.80 VecTor2 Finite Element Mesh for DP Wall Series

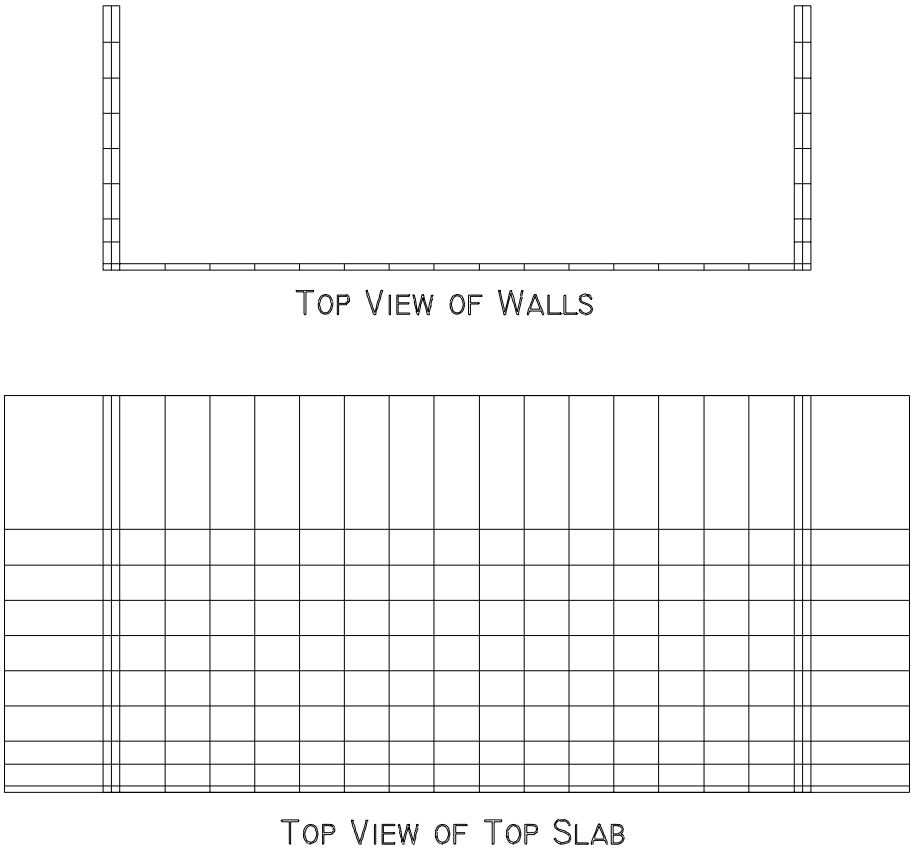

Figure 8.81 VecTor3 Finite Element Mesh Top View

Figure 8.82 shows the results of the pushover analyses along with the positive first excursion envelope for DP1. The 3-D analysis using VecTor3 calculated smaller lateral loads with increasing displacement in comparison to the 2-D analysis. From 2 mm to 10.75 mm of displacement, the 3-D results provided excellent agreement with the experimental data. Beyond 10.75 mm of displacement, VecTor3 calculated a progressive reduction in the lateral resistance. The post-peak response of the observed behaviour was realized at 12 mm of displacement, however, the softening response was more gradual than that calculated by either analysis. The 2-D analysis, although calculating slightly larger loads, seemed to better calculate the displacement at peak load. VecTor2 and

VecTor3 calculated maximum lateral loads of 1359 kN and 1265 kN, respectively. The corresponding displacements were 11.5 mm and 10.5 mm, respectively. The 2-D and 3-D analysis calculated similar shear failures in the form of diagonal compression. Extensive crushing in the compressive toe and along the main compressive strut was calculated at the peak loads, and a sliding shear plane eventually became evident near the base of the web walls. No yielding of the reinforcement was calculated. Crushing was initially calculated at 5 mm and 5.75 mm of lateral displacement for the 2-D and 3-D analysis, respectively.

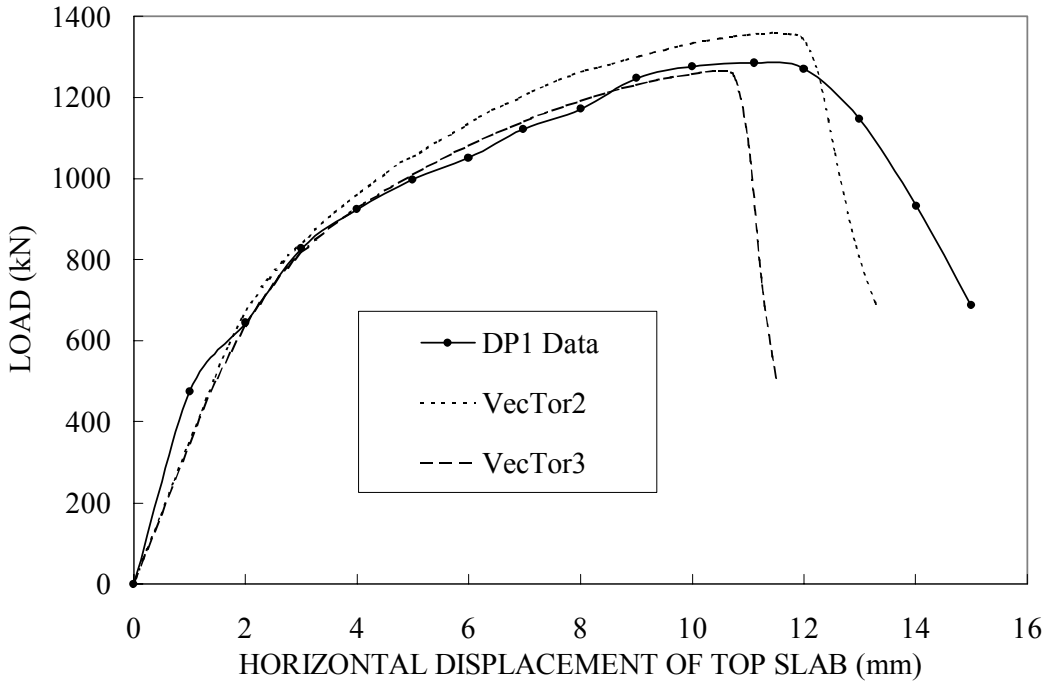

Figure 8.82 Pushover Analyses for DP1

Although the failure mechanisms were similar for the two analyses, VecTor3 calculated a significant decrease in lateral load beginning at 10.5 mm of displacement. High shear stresses were calculated on the flange elements near the base at the web-flange connection causing punching of the flange. From 6 mm of displacement on, shear

stresses of 6.3 MPa were calculated. Punching of the flange, in the 3-D analysis, seems to have contributed to failure of DP1. Punching of the flange is a 3-D phenomenon and thus, is not accounted for in the 2-D analysis.

Flanged shear walls, for the most part, seem to experience punching of the flanges, as was the case for the NUPEC test specimen U-1. A 3-D analysis is required to capture this phenomenon. A possible factor affecting the 3-D analysis results of DP1 was in modeling the flange elements with only two elements across the thickness of the flange. A finer mesh might better represent the shear stresses through the flanges and delay the onset of flange punching.

Figure 8.83 shows the results of the pushover analyses, with the first excursion envelope in the positive loading direction for DP2.

The analysis results of DP2 demonstrated similar trends as DP1. VecTor3 calculated smaller lateral loads than VecTor2, and failure was calculated at a lower displacement level. Maximum loads of 1094 kN and 1045 kN corresponding to displacements of 13.75 mm and 12.25 mm were calculated by the 2-D and 3-D analysis, respectively. From 4 mm to 9 mm lateral displacement, the 3-D analysis provided excellent agreement with the actual behaviour. The two analyses calculated similar modes of shear failure (diagonal compression). Extensive concrete crushing was calculated in the compression toe area and along the main compressive strut at peak loads, which eventually led to the formation of a sliding shear plane along the base of the web wall. Yielding of the flexural reinforcement in the tension flange wall near the base was calculated by the 2-D analysis beginning at 10.25 mm. No yielding of the reinforcement was calculated by the 3-D analysis. The 3-D analysis calculated the onset

of failure at a lower displacement level than the 2-D analysis, and like the analysis of DP1, was the result of high shear stresses on the flange elements near the base at the web-flange intersection causing punching of the flanges. Shear stresses in excess of 6 MPa were calculated from 9 mm of displacement on.

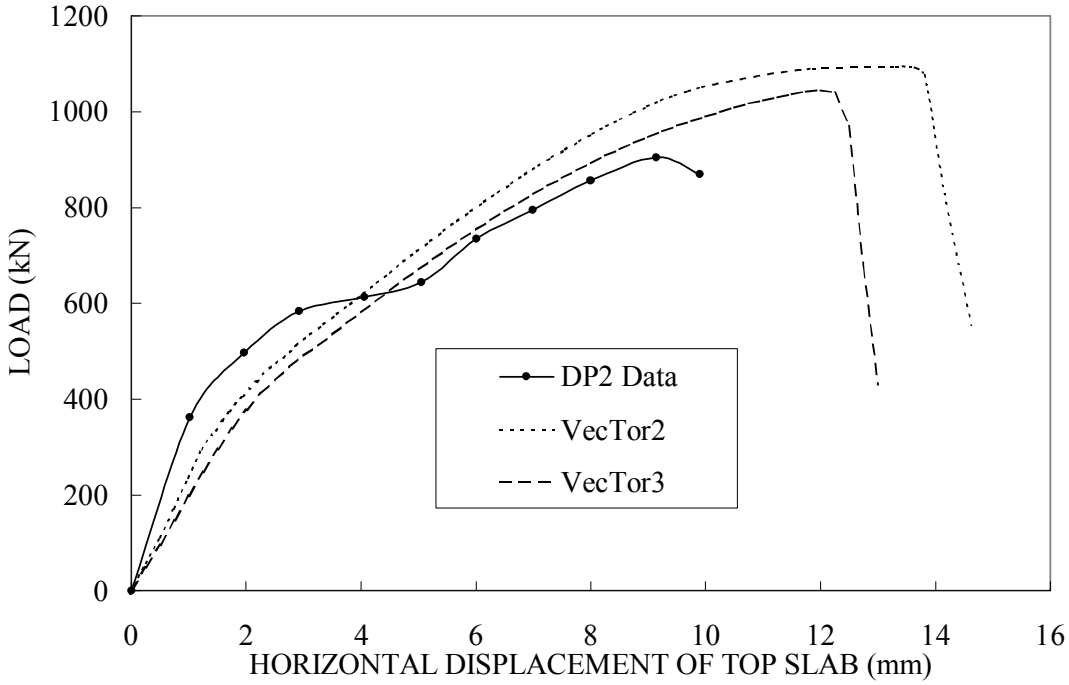

Figure 8.83 Pushover Analyses for DP2

Although the 3-D analysis seems to calculate the onset of failure reasonably well for DP2, it is important to note that the zones of damage leading to failure occurred in a significantly different area of the web wall. The failure mechanisms of the analyses were not consistent with the observed failure mode of DP2. The observed failure of DP2 did involve crushing of the concrete and the formation of a sliding shear plane leading to a punching of the flange wall; however, damage and failure of DP2 was observed near the top of the walls.

Three-dimensional analyses of the DP test specimens revealed some interesting points. Firstly, smaller lateral loads were calculated with increasing displacement in comparison to the 2-D analyses. Secondly, the assumption of fully effective flanges in contributing to the lateral resistance in the 2-D analysis seemed to provide acceptable results; however, damage in the flanges, such as punching, could not be calculated. Finally, it appeared that punching of the flanges seemed to initiate failure at smaller displacement levels. Also, neither the 2-D nor the 3-D pushover analyses calculated the observed failure mechanisms for these two cyclically loaded specimens.

The 2-D pushover analyses yielded reasonable results even though the strength, stiffness, and ductility were overestimated. Improvements to the 2-D model are achieved by conducting cyclic analyses. In this case, additional degradation in the strength, stiffness, and ductility arising from cyclic loading are accounted for.

8.5.5 Disturbed Stress Field Model

The accuracy and reliability of the Modified Compression Field Theory (MCFT) has been generally good in the analyses conducted on concrete structures. However, experience has revealed deficiencies in specific situations with respect to panel elements, as follows:

i) Predicted reductions in concrete strength are somewhat overstated for elements containing heavy amounts of reinforcement in both directions, in elements subjected to high biaxial compressions in addition to shear, or in elements where the reinforcement and loading conditions are such that there is no rotation of the principal stress or strain conditions.

ii) Shear strengths are generally overestimated for uniaxially reinforced elements, or for elements containing very light reinforcement in the transverse directions.

The Disturbed Stress Field Model (DSFM)[5] attempted to address these deficiencies, by removing the restriction that the concrete stress and strain fields be coincident, and by improving the treatment of shear stresses on cracks. Data from the initial panel tests, used to formulate the MCFT, showed that there was a tendency for the change in principal stress direction to lag behind the change in the principal strain direction. In terms of shear stresses on cracks, the MCFT initially made no allowance for discontinuous shear-slip along the crack.

In the formulation of the DSFM, compatibility assumes that the apparent strains, those that would be measured by extensometers during testing, are composed of strains induced by stress, shear-slip, and elastic and plastic offsets. The model explicitly allows for crack shear-slip in the element, and removes the crack shear stress check that was found to be troublesome and sometimes ignored by others in their implementation of the MCFT. In relating crack shear-slips to crack shear stresses, the DSFM incorporated formulations based on the works of Walraven[32], Okamura and Maekawa[24], and Vecchio and Lai[43]. While a number of models are available for representing crack shear mechanisms, those mentioned are the most suitable for implementation in the DSFM owing to their simplicity and adaptability to a secant stiffness formulation. Refer to Vecchio and Lai[43] for more details regarding the formulations.

A further analysis of DP1 was performed using the DSFM formulations with the linear cyclic models for concrete and the Walraven formulation for crack shear-slip

deformations. Figure 8.84 shows the load-top slab displacement results. The DSFM analysis using the linear cyclic models for concrete calculated maximum lateral resistances during the first excursion to 10 mm of displacement; 1431 kN and -1428 kN, respectively, for the positive and negative directions. The DSFM calculated loads slightly larger than the analysis using the MCFT (see Figure 8.49) for the most part. The observed lateral resistances for DP1 were 1298 kN and -1255 kN, resulting in analytical-to-experimental strength ratios of 1.10 and 1.14 for the DSFM results. Not accounting for degradation in the maximum allowable shear stress at cracks under cyclic loads contributed to overestimating the lateral loads. Under cyclic loading, the aggregate interlock between crack surfaces degrades causing slip along the cracks. Slip deformations increase the strains in the transverse reinforcement, while reducing the strains in the longitudinal reinforcement. The corresponding displacements at maximum loads were 9.85 mm for both directions of loading, and were similar to those calculated by the MCFT analysis.

The calculated failure involved a sliding shear plane forming approximately 125 mm from the base slab, with the concrete at the point of sliding extensively crushed throughout the web wall. Yielding of the web horizontal reinforcement was calculated after the formation of the sliding shear plane. Local yielding of the flexural flange reinforcement was also evident after failure. The failure mechanism was also similar to that obtained by the MCFT.

A difference with the DSFM calculations includes less energy dissipation in the hysteresis loops producing more pinching. Generally though, both the DSFM and MCFT seem to provide similar and fairly reasonable results of the DP1 test specimen. There

were no visual signs of cracks rotating during testing, and combined with nearly similar reinforcement in the longitudinal and transverse directions in the web walls seems to have resulted in minimal slip along the crack surfaces. Therefore, significant improvements by the DSFM in comparison to the MCFT were not expected.

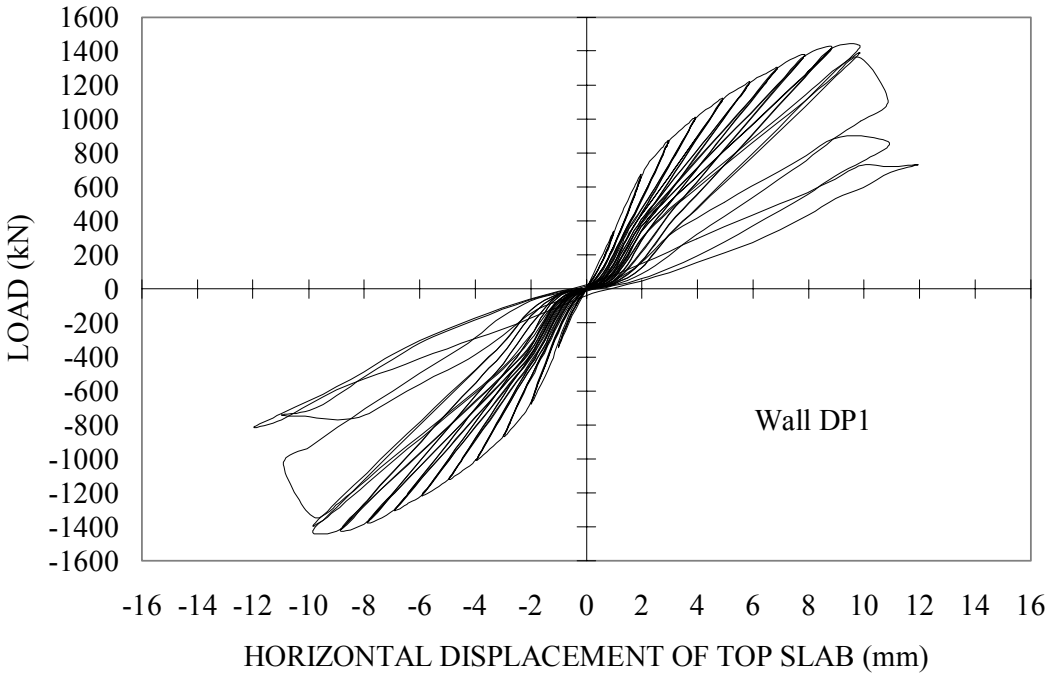

Figure 8.84 DSFM Results of DP1

In a study between the MCFT and DSFM by Lai[44], it was found that the DSFM was able to better calculate maximum displacements and pinching in the hysteresis curves for structures subjected to reversed cyclic loading. Generally, the DSFM calculates more straining of the transverse reinforcement as a result of accounting for slip along crack surfaces. In comparison to the MCFT, the DSFM would likely result in improved modeling of the Stevens panels, where yielding of the transverse reinforcement was not captured by the MCFT analyses.

8.6 REVIEW OF ANALYSES

The analyses conducted in this chapter revealed some interesting observations regarding modeling of concrete under cyclic loading. The overall load-displacement response appears to be unaffected by the choice of unloading/reloading rules for concrete, when the actual behaviour is flexure-dominant and yielding of the reinforcement precedes failure. This was evident in the analyses conducted on the PCA and SW series of walls. However, in situations where shear is the dominant mechanism, and the concrete experiences significant damage prior to yielding of the reinforcement, a nonlinear cyclic model with decay more accurately captures the overall behaviour and, more importantly, better calculates the failure mechanisms. Even though a nonlinear cyclic model with decay may not influence the macroscopic behaviour of flexural walls, it would be significant in correctly calculating localized damage, failure modes, and failure loads.

Given that it was demanding to reproduce every aspect of measured behaviour, the proposed analytical models were successful in reproducing those aspects that are crucial and include: load capacity, failure mode, deformation capacity, and energy dissipation. Further, the numerical models have demonstrated the ability to identify walls for which the cyclic response was controlled by the concrete.

Although the observed cracking patterns of walls DP1 and DP2 revealed that there were no visual signs of crack rotation, the numerical models were developed to be compatible with a rotating crack approach. Analytical calculations of these walls using the fixed crack philosophy would also provide reasonable simulations of behaviour. The main objective of this research project was to develop models compatible with the

rotating crack assumption of the Modified Compression Field Theory. By considering rotating cracks, the models could be used to reproduce behaviour of structural elements subjected to reversed cyclic loading where cracking has been observed to rotate. This includes situations where a structural element is lightly reinforced in the transverse direction and where yielding of the reinforcement initiates. Thus, the proposed models can be used in situations where cracks remain relatively fixed in direction, such as squat shear walls with similar web reinforcement in both directions; or for the more general case, where varying amounts of reinforcement causes cracks to rotate.

CHAPTER 9

Conclusions & Recommendations

9.1 SUMMARY

Results from two large-scale flanged structural walls, tested under cyclic displacements, were presented. The behaviour of the walls was dominated by shear-related mechanisms and, as a consequence, the web elements sustained heavy damage. The literature consists of walls mostly influenced by flexural mechanisms; thus, the current body of data will benefit from the experimental results of this research. As well, the DP series of wall tests involved complex wall configurations, in which three-dimensional effects may be influential; again, relevant literature in this regard is lacking.

The experimental results provide useful data to corroborate concrete models for cyclic loading, to investigate the effects of axial load and end flange walls, to investigate failure mechanisms associated with shear-dominant behaviours, and to determine the degree of damage incurred during excursions to a set displacement level. Other secondary wall behaviours exposed include the horizontal expansion of the web wall, which is a measure of the relative horizontal displacement in the plane of the web between the two flanges. It is an indication of the tensile straining, which leads to compression softening of the concrete, and an indication of the straining in the web horizontal reinforcement. These effects significantly contribute to the load capacity and failure mode. Another second-order mechanism is elongation of the flange wall, and

determines the extent of ratcheting due to yielding of the flexural reinforcement, which may be prevalent in walls subjected to reversed cyclic loading.

The comprehensive database acquired also contains information regarding reinforcement strains throughout the web and flange walls, and concrete surface strains.

A significant contribution of the analytical work was in modeling the reversed cyclic behaviour of reinforced concrete in the context of a rotating crack model based on a secant stiffness-based algorithm. The models are also easily adaptable in programs assuming either fixed cracks or fixed principal stress directions.

The concrete cyclic models consider both concrete in compression and concrete in tension. The unloading and reloading rules are linked to backbone curves, which are represented by the monotonic response curves. The backbone curves are adjusted for compressive softening and confinement in the compression regime, and for tension stiffening and tension softening in the tensile region.

Unloading is assumed nonlinear and is modeled using a Ramberg-Osgood formulation, which considers boundary conditions at the onset of unloading and at zero stress. The boundary conditions defined describe the stiffness of the unloading branch at the onset of unloading and at the end of unloading. Unloading, in the case of full unloading, is terminated at the plastic strain. Models for the compressive and tensile plastic strains have been formulated as a function of the unloading strain on the backbone curve.

Reloading is modeled as linear with a degrading reloading stiffness. Essentially, the reloading path does not return to the backbone curve at the previous unloading strain, and further straining is required to intersect the backbone curve. The degrading reloading

stiffness is a function of the strain recovery during unloading, and is bounded by the unloading strain on the backbone curve and the plastic strain. The reloading stiffness is also limited by a stability limit curve, under which no further damage is accumulated due to load cycling.

The models also consider the general case of partial unloading and partial reloading in the region below the previous maximum unloading strain.

A preliminary crack-closing model was presented. However, it was not implemented into the finite element program due to numerical stability problems.

The reinforcement model used in the analyses was adapted from Seckin[21]. The monotonic response is assumed to be tri-linear; unloading is modeled as linear, and reloading assumes a nonlinear behaviour using a Ramberg-Osgood formulation that accounts for the Bauschinger effect.

Corroboration of the concrete cyclic model included examination of shear panels, and shear walls dominated by flexural mechanisms and shear-related mechanisms. The proposed formulations were also compared against linear unloading/reloading rules for concrete initially presented by Vecchio[3].

Analyses of shear panels illustrated deficiencies in the models at the elemental level, and improvements can be significant in correctly calculating localized damage, failure loads, and failure modes. The analyses also demonstrated differences between the linear cyclic model and the proposed nonlinear cyclic model with decay.

Analyses were conducted on two sets of shear walls available in the literature and on those tested as part of this research. The analyses models provide reasonably accurate simulations of the overall load-displacement behaviours, ultimate lateral resistance,

ductility, residual displacements, and energy dissipation through the hysteresis loops. The analyses of the flexural-dominant walls, including the PCA and SW series, appeared to be unaffected by the choice of a linear or nonlinear concrete cyclic model. For these walls, yielding of the reinforcement controlled the behaviours, for the most part, and the concrete's contribution to the lateral resistance was relatively minor. However, for the DP series of walls, where shear-related mechanisms were dominant, the nonlinear cyclic model illustrated improvements in the behaviour including the damage experienced in the concrete in the second excursion per displacement level. More importantly, it was able to better simulate the failure mechanisms.

Further analyses included the investigation of three-dimensional effects. Generally, the 2-D analyses on the DP flanged shear walls provided reasonable simulations of the load-displacement results, even though fully effective flange walls were assumed in the 2-D model. The 3-D analyses provided excellent agreement in terms of load and displacement; however, failure was calculated at slightly lower displacements than with the 2-D analyses and was the result of predicting punching of the flanges.

9.2 CONCLUSIONS

Based on the experimental work presented in this report, the following conclusions are made:

1. Imposed axial loads, and wall configurations consisting of end flange walls, significantly influence the ultimate strength and failure modes of squat shear walls.

2. The stiffness of the flange walls restrained the opening of web shear cracks and caused the formation of vertical slip planes in DP1.
3. Weaker concrete in the upper part of the walls may have been responsible for premature failure of DP2. A sliding shear failure of the web wall formed near the top slab and caused a punching of the flanges near the top slab.
4. Squat shear walls produce highly pinched hysteresis curves with little energy dissipation in comparison to slender walls and are more influenced by shear-related mechanisms.
5. In the pre-peak cycles, cycling beyond the first unloading/reloading excursion to a specific displacement level produces negligible damage. However, in the post-peak region, the amount of damage in subsequent excursions is similar to that experienced by the first unloading/reloading excursion.
6. Static cyclic testing can potentially be a viable alternative to dynamic testing for the set of loading conditions to which test specimens DP1 and U-1 were exposed. Static testing can also provide a database useful in formulating constitutive models for reinforced concrete.
7. Second-order effects, namely the elongation of the flange walls and horizontal expansion of the web wall, are key indicators in determining the extent of damage and significantly affect the lateral resistance and failure mechanisms of squat shear walls.

Based on the analytical work, the following conclusions are derived:

1. A smeared rotating crack model for concrete based on a secant stiffness-based algorithm can be modified to provide accurate simulations of the behaviour of reinforced concrete under cycling loading.
2. Generally, the analytical procedure calculates well the macroscopic behaviour, energy dissipation through hysteresis, ultimate lateral resistance, residual displacements, and failure mechanisms for both squat and slender shear walls.
3. The analyses of shear panels illustrated some remaining deficiencies in the current modeling. Improvements at the elemental level can be significant in accurately calculating localized damage, failure modes, and failure loads.
4. The overall behaviour of flexure-dominant walls is unaffected by the choice of unloading/reloading rules for concrete.
5. A nonlinear cyclic model for concrete, incorporating nonlinear unloading rules and stiffness degradation in the reloading regime, more accurately simulates the load-displacement response, hysteresis response, energy dissipation, and failure mechanisms of squat walls, which are heavily influenced by shear related mechanisms.
6. Generally, the nonlinear cyclic model for concrete was able to better represent damage in the concrete, failure mode, strength, and energy dissipation.
7. Two-dimensional analyses assuming fully effective flange walls provide reasonable simulations of the DP wall series; however, 3-D issues must be addressed when modeling flanged shear walls.

8. The DSFM may lead to improved calculations, in being able to model shear-slip on cracks. However, the maximum allowable shear stress at cracks under cyclic loading needs to be addressed.

9.3 RECOMMENDATIONS

Further experimental testing should address the following research needs:

1. Experimental data is required to corroborate the proposed models for concrete subjected to cyclic tension. Data is also required to investigate the effects of compression softening due previous compressive loading in the transverse direction. Similarly, data is required to determine the effects on tension softening due to previous tensile loading in the transverse direction.
2. Experimental data is required to investigate the effects of strain recovery in the modeling of the degrading stiffness for both the compression and tension regimes. Currently, the strain recovery is limited to each domain and does not consider excursions into the tensile regime for the compression model, or excursions into the compressive region for the tension model.
3. Further data is required to formulate: crack-closing models, which will affect the elemental behaviour of reinforced concrete; and the bond slip of reinforcement, which may be prevalent in the case of reversed cyclic loading.
4. More reinforced concrete panel tests under reversed cyclic loading are required to refine the proposed cyclic models for concrete and provide data to investigate the degradation of the maximum allowable shear stress at cracks under cyclic loading conditions.

5. Additional analytical work is required to implement a tension offset and a compression crack-closing model. Also, a model for the degradation of the maximum allowable shear stress at cracks due to cyclic loading is required for the Disturbed Stress Field Model.

REFERENCES

1. Vecchio, F. J., "Nonlinear Finite Element Analysis of Reinforced Concrete Membranes," ACI Structural Journal, Vol. 86, No. 1, 1989, pp. 26-35.
2. Vecchio, F. J., and Selby, R. G., "Towards Compression Field Analysis of Reinforced Concrete Solids," ASCE, Journal of Structural Engineering, Vol. 117, No. 6, 1991, pp. 1740-1758.
3. Vecchio, F. J., "Towards Cyclic Load Modeling of Reinforced Concrete," ACI Structural Journal, Vol. 96, No. 2, 1999, pp. 132-202.
4. Vecchio, F. J., and Collins, M. P., "The Modified Compression-Field Theory for Reinforced Concrete Elements Subjected to Shear," ACI Journal, Vol. 83, No. 3, 1986, pp. 219-231.
5. Vecchio, F. J., "Disturbed Stress Field Model for Reinforced Concrete: Formulation," ACSE, Journal of Structural Engineering, Vol. 126, No. 9, 2000, pp. 1070-1077.
6. Vecchio, F. J., Polak, M. A., and Selby, R. G., "Nonlinear Analysis of Reinforced Concrete: The University of Toronto Experience," Proceedings of the Third Asian-Pacific Conference on Computational Mechanics, Seoul, Korea, 1996.
7. Nuclear Power Engineering Corporation of Japan (NUPEC), "Comparison Report, Seismic Shear Wall ISP, NUPEC's Seismic Ultimate Dynamic Response

Test," Report No. NU-SSWISP-D014, Organization for Economic Co-Operation and Development, Paris, 1996, 407 pp.

8. Palermo, D., "Testing of a 3-D Shear Wall Under Cyclic Loading," M.A.Sc. Thesis, University of Toronto, 1998, 240 pp.
9. Bucci, F., "Finite Element Analysis of Repaired Concrete Structures," M.A.Sc. Thesis, University of Toronto, 1998, 158 pp.
10. Haro de la Peña, O. A., "Modelling and Analysis of Retrofitted Concrete Structures," M.A.Sc. Thesis, University of Toronto, 2001, 242 pp.
11. Sinha, B. P., Gerstle, K. H., and Tulin, L. G., "Stress-Strain Relations for Concrete Under Cyclic Loading," Journal of the American Concrete Institute, Vol. 61, No. 2, 1964, pp. 195-211.
12. Karsan, I. K., and Jirsa, J. O., "Behaviour of Concrete Under Compressive Loadings," ASCE, Journal of the Structural Division, Vol. 95, No. 12, 1969, pp. 2543-2563.
13. Park, R., Kent, D. C., and Sampson, R. A., "Reinforced Concrete Members With Cyclic Loading," ASCE, Journal of the Structural Division, Vol. 98, No. ST7, 1972, pp. 1341-1358.
14. Darwin, D., and Pecknold, D. A., "Analysis of RC Shear Panels Under Cyclic Loading," ASCE, Journal of the Structural Division, Vol. 102, No. ST2, 1976, pp. 355-369.
15. Buyukozturk, O., and Tseng, T. M., "Concrete in Biaxial Cyclic Compression," ASCE, Journal of Structural Engineering, Vol. 110, No. 3, 1984, pp. 461-476.

16. Popovics, S., "A Numerical Approach to the Complete Stress-Strain Curve of Concrete," Cement and Concrete Research, Vol. 3, No. 5, 1973, pp. 583-599.

17. Yankelevsky, D. Z., and Reinhardt, H. W., "Model for Cyclic Compressive Behaviour of Concrete," ASCE, Journal of Structural Engineering, Vol. 113, No. 2, 1987, pp. 228-240.

18. Yankelevsky, D. Z., and Reinhardt, H. W., "Uniaxial Behaviour of Concrete in Cyclic Tension," ASCE, Journal of Structural Engineering, Vol. 115, No. 1, 1989, pp. 166-182.

19. Yankelevsky, D. Z., and Reinhardt, H. W., "Response of Plain Concrete to Cyclic Tension," ACI Materials Journal, Vol. 84, No. 5, 1987, pp. 365-373.

20. Bahn, B. Y., and Hsu, C. T., "Stress-Strain Behaviour of Concrete Under Cyclic Loading," ACI Materials Journal, Vol. 95, No. 2, 1998, pp. 178-193.

21. Seckin, M., "Hysteretic Behaviour of Cast-in-Place Exterior Beam-Column Sub-Assemblies," Ph. D. Thesis, University of Toronto, 1981, 266 pp.

22. Mander, J. B., Priestley, M. J. N., and Park, R., "Theoretical Stress-Strain Model for Confined Concrete," ASCE, Journal of Structural Engineering, Vol. 114, No. 8, 1988, pp. 1804-1826.

23. Sittipunt, W., and Wood, S. L., "Influence of Web Reinforcement on the Cyclic Response of Structural Walls," ACI Structural Journal, Vol. 92, No. 6, 1995, pp. 745-756.

24. Okamura, H., and Maekawa, K., "Nonlinear Analysis and Constitutive Models of Reinforced Concrete," Giho-do Press, University of Tokyo, 1991, 182 pp.

25. Teigen, G. T., "Nonlinear Analysis of Concrete Structures Based on a 3D Shear-Beam Element Formulation," Ph. D. Thesis, University of Oslo, 1994, 243 pp.
26. Stevens, N. J., Uzumeri, S. M., and Collins, M. P., "Analytical Modelling of Reinforced Concrete Subjected to Monotonic and Reversed Loadings," Publication No. 87-1, Department of Civil Engineering, University of Toronto, Toronto, 1987, 201 pp.
27. Fintel, M., "Shearwalls - An Answer for Seismic Resistance," ACI, Concrete International, Vol. 3, No. 7, 1991, pp. 48-53.
28. Paulay, T., "Earthquake-Resisting Shearwalls – New Zealand Design Trends," ACI Journal, Vol. 77, No. 3, 1981, pp. 144-152.
29. Paulay, T., Priestley, M. J. N., and Synge, A. J., "Ductility in Earthquake Resisting Squat Shearwalls," ACI Journal, Vol. 79, No. 4, 1982, pp. 257-269.
30. Oesterle, R. G., Fiorato, A. E., Johal, L. S., Carptenter, J. E., Russell, H. G., and Corley, W. G., "Earthquake-Resistant Structural Walls-Tests of Isolated Walls," Report to National Science Foundation, Construction Technology Laboratories, Portland Cement Association, Skokie, Ill, 1976, 315 pp.
31. Pilakoutas, K., and Elnashai, A., "Cyclic Behaviour of Reinforced Concrete Cantilever Walls, Part I: Experimental Results," ACI Structural Journal, Vol. 92, No. 3, 1995, pp. 271-281.
32. Walraven, J. C., "Fundamental Analysis of Aggregate Interlock," ASCE, Journal of Structural Engineering, Vol. 107, No. 11, 1981, pp. 2245-2270.

33. Hognestad, E., Hansen, N. W., and McHenry, D., "Concrete Stress Distribution in Ultimate Strength Design," ACI Journal Proceedings, Vol. 52, No. 4, 1955, pp. 455-480.

34. Lefas, I. D., Kotsovos, M. D., and Ambraseys, N. N., "Behaviour of Reinforced Concrete Structural Walls: Strength, Deformation Characteristics, and Failure Mechanism," ACI Structural Journal, Vol. 87, No. 1, 1990, pp. 23-31.

35. Smith, G. M., and Young, L. E., "Ultimate Theory in Flexure by Exponential Function," Journal of the American Concrete Institute, Vol. 52, No. 3, 1955, pp. 349-359.

36. Gopalaratnam, V. S., and Shah, S. P., "Softening Response of Plain Concrete in Direct Tension," ACI Journal, Vol. 82, No. 3, 1985, pp. 310-323.

37. Collins, M. P., and Mitchell, D. Prestressed Concrete Basics, Canadian Prestressed Concrete Institute, Ottawa, Canada, 1987, 614 pp.

38. Vecchio, F. J., and Bucci, F., "Analysis of Repaired Reinforced Concrete Structures," ASCE, Journal of Structural Engineering, Vol. 125. No. 6, 1999, pp. 644-652.

39. Vecchio, F. J., "Reinforced Concrete Membrane Element Formulations," ASCE, Journal of Structural Engineering, Vol. 116, No. 3, 1990, pp. 730-750.

40. Villani, D. R., "Reinforced Concrete Subjected to Cyclic Loads: A Pilot Study," B.A.Sc. Thesis, University of Toronto, 1995, 45 pp.

41. Elnashai, A., Pilakoutas, K., and Ambraseys, N. N., "Experimental Behaviour of Reinforced Concrete Walls Under Earthquake Loading," Earthquake Engineering and Structural Dynamics, Vol. 19, 1990, pp. 389-409.

42. Vecchio, F. J., "Lessons From The Analysis of a 3-D Concrete Shear Wall," Structural Engineering and Mechanics, Vol. 6, No. 4, 1998, pp. 439-455.

43. Vecchio, F. J., and Lai, D., "Crack Shear-Slip in Reinforced Concrete Elements," submitted to ASCE, Journal of Structural Engineering.

44. Lai, D., "Crack Shear-Slip in Reinforced Concrete Elements," M.A.Sc. Thesis, University of Toronto, 2001, 154 pp.

Available upon request.